

2017

Probabilistic Seismic Performance Assessment of Low-Ductility Concentrically Braced Frames in East Coast U.S.

Xin Chu
Lehigh University

Follow this and additional works at: <https://preserve.lehigh.edu/etd>



Part of the [Civil Engineering Commons](#)

Recommended Citation

Chu, Xin, "Probabilistic Seismic Performance Assessment of Low-Ductility Concentrically Braced Frames in East Coast U.S." (2017). *Theses and Dissertations*. 2940.
<https://preserve.lehigh.edu/etd/2940>

This Dissertation is brought to you for free and open access by Lehigh Preserve. It has been accepted for inclusion in Theses and Dissertations by an authorized administrator of Lehigh Preserve. For more information, please contact preserve@lehigh.edu.

**Probabilistic Seismic Performance Assessment of Low-Ductility
Concentrically Braced Frames in East Coast U.S.**

by

Xin Chu

Presented to the Graduate and Research Committee

of Lehigh University

in Candidacy for the Degree of

Doctor of Philosophy

in

Structural Engineering

Lehigh University

August 2017

© Copyright by Xin Chu 2017

All Rights Reserved

Approved and recommended for acceptance as a dissertation in partial fulfillment of the requirements for the degree of Doctor of Philosophy.

Date

Dr. Richard Sause
Dissertation Co-advisor

Dr. James M. Ricles
Dissertation Co-advisor

Dr. Shamim N. Pakzad
Dissertation Co-advisor

Approved Date

Committee Members

Dr. John L. Wilson
Committee Chairperson

Dr. Anne S. Meltzer
External member

Acknowledgements

The research presented in this dissertation was conducted at the Engineering Research Center for Advanced Technology for Large Structural System (ATLSS), Department of Civil and Environmental Engineering at Lehigh University, Bethlehem, Pennsylvania. The financial support from the Department of Civil and Environmental Engineering at Lehigh University is greatly appreciated. The National Science Foundation (NSF) is also acknowledged for providing the funding for the research presented in Chapter 3 through Award No. CMMI-1219447.

I would like to express my deepest gratitude to my research advisors Dr. Richard Sause, Dr. James M. Ricles, and Dr. Shamim N. Pakzad and for their excellent guidance, advice, and patience during my research and study. I would also like to thank Dr. John L. Wilson, the chairperson of my research committee, for his advice and constant support for me throughout my PhD study. The time, input, and contributions of the external committee member, Dr. Anne S. Meltzer, are also greatly appreciated.

I would like to thank my friends and colleagues at Lehigh University, especially my fellow graduate students and scholars at the ATLSS Engineering Research Center. There are so many people who helped me through this arduous journey that I cannot list all of their names here. The input and help from Chinmoy Kolay, Brent Chancellor, Tom Matarazzo, Leary Pakiding, Haiying Ma, Benjin Zhu, Ying-Cheng Lin and Siavash Dorvash is greatly appreciated. I also appreciate the support and assistance of ATLSS personnel, specifically Peter Bryan and Tommy Marullo. Last but not least, I am indebted to my family for their endless love.

Table of contents

List of tables.....	xii
List of figures.....	xviii
Abstract.....	1
Chapter 1 Introduction.....	4
1.1 Motivation.....	4
1.2 Research objectives.....	7
1.3 Research scope.....	8
1.4 Outline of the dissertation.....	11
Chapter 2 Background.....	13
2.1 Introduction.....	13
2.2 Origins and design feature of low-ductility CBF.....	13
2.3 Experimental investigation of low-ductility CBF.....	16
2.4 Analytical investigation of low-ductility CBFs.....	19
2.5 Summary.....	23
Chapter 3 Response simulation and performance assessment of an ECUS CBF during 2011 Virginia earthquake.....	44
3.1 Introduction.....	44
3.2 Virginia earthquake and building description.....	44

3.3 Damage reconnaissance	46
3.4 FEM simulation of seismic response during Virginia earthquake.....	48
3.4.1 Linear model	48
3.4.1.1 Finite element modeling and model validation.....	48
3.4.1.2 Seismic response simulation and investigation on the reason for damage	51
3.4.2 Nonlinear model.....	53
3.5 Fragility analysis and performance evaluation	54
3.5.1 Generation of hazard compatible ground motion	56
3.5.2 Limit State of Structural Damage, EDP and Intensity Measure	58
3.5.3 Development of fragility curve for structural damage.....	60
3.5.4 Fragility curve for nonstructural damage.....	62
3.5.5 Retrofit of the structure	66
3.5.6 Probability of exceeding various limit states	67
3.6 Summary and findings	68
Chapter 4 Development of prototype building design and collapse simulation model of low-ductility CBF	91
4.1 Introduction.....	91
4.2 Review of typical design variation in ECUS low-ductility CBF	91
4.3 Design of prototype building	96
4.3.1 Gravity load	96

4.3.2 Seismic load.....	96
4.3.3 Wind load.....	99
4.3.4 Other load.....	100
4.3.5 Load combinations.....	101
4.3.6 Design result	102
4.4 Modeling of low-ductility CBF system	104
4.4.1 Modeling of CBF	105
4.4.2 Modeling of gravity system	111
4.4.3 Modeling of damping with damping substructure	113
4.4.4 Validation of numerical model	115
4.4.5 Alternative modeling approach.....	116
Chapter 5 Development of an ECUS ground motion set.....	166
5.1 Introduction.....	166
5.2 Motivation.....	167
5.2.1 FEMA set.....	168
5.2.2 NGA-East GM database	171
5.3 Methodology for GM simulation	172
5.4 Development of Rock GM set	175
5.5 Development of Soil GM set	179
5.6 Comparison and discussion of various GM sets	183

Chapter 6 Uncertainty in collapse performance assessment of ECUS low-ductility CBF	215
6.1 Introduction	215
6.2 Background and critique of FEMA P695 collapse performance assessment methodology	216
6.3 Uncertainty considered in this study	221
6.3.1 Uncertainty in seismic demand	223
6.3.2 Variation in structural design	225
6.3.3 Uncertainty in model parameters	226
6.3.4 Uncertainty of the modeling approach	230
6.4 Comparison with uncertainty considered in the FEMA P695 methodology	232
6.4.1 Modeling Uncertainty	232
6.4.2 Test Data Uncertainty	234
6.4.3 Design Requirements Uncertainty	235
Chapter 7 Assessment of collapse performance of ECUS low-ductility CBFs	253
7.1 Introduction	253
7.2 Collapse performance evaluation using FEMA P695 methodology	254
7.2.1 Insight into pushover response of ECUS low-ductility CBFs with design variation	257

7.2.2 Critique of FEMA P695 methodology to determine median collapse capacity	261
7.2.3 Effect of design variation on collapse performance	263
7.2.3.1 Effect of weld design strength	264
7.2.3.2 Effect of beam design strength	266
7.2.3.3 Effect of brace configuration	268
7.3 Collapse performance evaluation using ECUS GM set	269
7.3.1 Spectral shape effect	270
7.3.2 RTR variability	273
7.4 Effect of modeling approach uncertainty on collapse performance	274
7.4.1 Effect of modeling brace re-engagement	274
7.4.2 Effect of modeling beam strength deterioration	276
7.4.3 Effect of modeling gravity load system	277
7.5 Effect of model parameter uncertainty on collapse performance	278
7.5.1 Sensitivity study	278
7.5.1.1 Effect of weld strength R_c	280
7.5.1.2 Effect of brace LCF strength ϵ_0	281
7.5.1.3 Effect of brace re-engagement strength F_{re}	282
7.5.1.4 Effect of brace initial imperfection e/L	283
7.5.1.5 Effect of brace yield strength $F_{y_{br}}$	284

7.5.1.6 Summary of sensitivity study	285
7.5.2 Monte Carlo Simulation.....	286
7.5.2.1 Median collapse capacity.....	287
7.5.2.2 Dispersion of collapse capacity	291
7.6 Discussion and summary of effect of various sources of uncertainty	293
7.7 Collapse performance evaluation using modified FEMA P695 methodology	294
Chapter 8 Summary and conclusions.....	395
8.1 Summary.....	395
8.1.1 Motivation.....	395
8.1.2 Research objective	396
8.1.3 Research scope.....	397
8.2 Research findings.....	400
8.2.1 Findings in Chapter 3.....	400
8.2.2 Findings in Chapter 4.....	401
8.2.3 Findings in Chapter 5.....	401
8.2.4 Findings in Chapters 6 and 7	402
8.3 Conclusions.....	405
8.4 Original contributions	406
8.5 Limitation and recommended future research	407
References.....	409

Vita..... 425

List of tables

Table 2.1 Design requirement for different CBF systems	26
Table 3.1 Eccentricity between CR and CM for each case in parametric study (unit: ft) 71	
Table 3.2 Comparison of measured and SAP model period for different modes (unit: s) 71	
Table 3.3 Comparison of measured and OpenSees model period for different modes (unit: s).....	71
Table 3.4 Coefficient for PSDM (in the form of Eq. (3.2)) for different cases	72
Table 3.5 Coefficients for fragility function shown in Figure 3.19	72
Table 3.6 Dimension and friction property of the different types of cabinets	72
Table 3.7 Parameters for different PSDM for floor acceleration (in the form of $a_{max} = a_{Sab}$)	73
Table 3.8 Probability of exceeding various limit states at different hazard level.....	73
Table 4.1 Building designs reviewed.....	120
Table 4.2 Information on beam design from existing buildings and evaluation of beam strength under unbalanced brace force	120
Table 4.3 Connection design in Hines et al. (2009).....	121
Table 4.4 Example of different level of weld overstrength as a result of different design convention.....	122
Table 4.5 Weld size design guideline from Marstellar et al. (2002).....	122
Table 4.6 Design dead load.....	123
Table 4.7 Design live load	123
Table 4.8 T_1 (s) obtained from SAP model for each design variant	123
Table 4.9 Summary of seismic design information	124

Table 4.10 Equivalent lateral force at each floor level per frame due to seismic load...	125
Table 4.11 Summary of wind design information	125
Table 4.12 Calculation of design wind pressure.....	126
Table 4.13 Summary of CBF design variants for prototype building.....	126
Table 4.14 Member sections for chevron CBF.....	127
Table 4.15 Member sections for split-X CBF.....	127
Table 4.16 Member sections for gravity system.....	127
Table 4.17 Information on weak weld (Design 1) for chevron CBF	128
Table 4.18 Information on strong weld (Design 2) for chevron CBF	129
Table 4.19 Information on weak weld (Design 1) for split-X CBF.....	130
Table 4.20 Information on strong weld (Design 2) for split-X CBF	131
Table 5.1 Summary of FEMA GM set (adapted from FEMA P695 (FEMA 2009)).....	187
Table 5.2 Six seismological models used in the NGA-East project	189
Table 5.3 Seismic hazard deaggregation for MR bins with more than 1.5% contribution	189
Table 5.4 Number of ground motions to be selected for each MR bin and ϵ interval....	190
Table 5.5 Four ground motions selected for R=393.4 km, M=7.39 bin using A04 model	190
Table 5.6 Summary of M, R, ϵ information for all 44 ground motions selected by using A04 model.....	191
Table 5.7 Comparison of $S_a(1s)$ values from median spectrum of ground motion sets generated using 6 seismological models and MCE hazard level	192
Table 5.8 Characteristic period for each soil profile.....	193

Table 5.9 Number of ground motions sampled for each soil profile and their corresponding bedrock motion index	194
Table 5.10 Comparison of $Sa1s$ for Rock GM and Soil GM and $Sa1s$ of MCE hazard level from various sources	196
Table 6.1 Example of archetype buildings and performance groups (FEMA 2009).....	238
Table 6.2 Example of performance evaluation for archetype buildings and performance groups (FEMA 2009).....	239
Table 6.3 Partial list of variation in structural design of low-ductility CBF	240
Table 6.4 Archetype designs and performance groups in this study	240
Table 6.5 Partial list of model parameters with uncertainty	241
Table 6.6 Summary of statistical distribution of uncertain model parameters considered in this study.....	242
Table 6.7 Summary of types of uncertainty considered in FEMA P695 and current study	242
Table 7.1 Pushover analysis results and calculation of SSF for each archetype model .	301
Table 7.2 Median collapse capacity and CMR for each archetype model.....	301
Table 7.3 Period-based ductility and RTR variability for each archetype model.....	301
Table 7.4 β values for various sources of uncertainty for different ratings and corresponding total uncertainty and acceptable CMR (selected rating is shown in italic)	302
Table 7.5 Comparison of adjusted CMR and acceptable CMR for each archetype model and performance group	302

Table 7.6 Comparison of median collapse capacity from FEMA P695 methodology and actual collapse S_{ac}, m	303
Table 7.7 Comparison of collapse response under GM25 for chevron CBF models with strong beam design and different weld design strength.....	304
Table 7.8 Comparison of collapse response under GM14 for chevron CBF models with weak beam design and different weld design strength	305
Table 7.9 Comparison of collapse response under GM39 for split-X CBF models with different weld design strength.....	306
Table 7.10 Comparison of collapse response under GM21 for chevron CBF models with weak weld design and different beam design strength	307
Table 7.11 Comparison of collapse response under GM18 for chevron CBF models with strong weld design and different beam design strength.....	308
Table 7.12 Comparison of collapse response under GM16 for split-X CBF models with different beam design strength.....	309
Table 7.13 Comparison of collapse behavior under GM19 for models with weak weld design and different brace configuration	310
Table 7.14 Comparison of collapse behavior under GM23 for models with strong weld design and different brace configuration	311
Table 7.15 Comparison of collapse capacity from IDA using ECUS GM set and FEMA GM set and from FEMA P695 methodology.....	312
Table 7.16 Comparison of $\sigma_{\ln}(S_{ac})$ from IDA result for ECUS GM set and FEMA GM set and β_{RTR} from FEMA P695 methodology	312
Table 7.17 Effect of brace re-engagement.....	313

Table 7.18 Effect of beam strength deterioration	313
Table 7.19 Effect of gravity system modeling.....	313
Table 7.20 Variation of uncertain model parameters for sensitivity study.....	314
Table 7.21 Median collapse capacity of model C1 using different modeling approaches	314
Table 7.22 Summary of FEMA P695 methodology with variations	315
Table 7.23 Median collapse capacity and ACMR for each archetype model using Mod1 variation of FEMA P695 methodology.....	316
Table 7.24 Performance evaluation for each archetype model using Mod1 variation of FEMA P695 methodology	316
Table 7.25 Summary of IDA result for each archetype model using Mod2 variation of FEMA P695 methodology	317
Table 7.26 Performance evaluation for each archetype model using Mod2 variation of FEMA P695 methodology	317
Table 7.27 Summary of IDA result for archetype model C1 and C2 using Mod3 variation of FEMA P695 methodology.....	318
Table 7.28 Performance evaluation for archetype model C1 and C2 using Mod3 variation of FEMA P695 methodology.....	318
Table 7.29 Summary of IDA result for archetype model C1 using Mod4 variation of FEMA P695 methodology	319
Table 7.30 Performance evaluation for each archetype model C1 using Mod4 variation of FEMA P695 methodology	319

Table 7.31 Summary of IDA result for each archetype model using Mod5 variation of FEMA P695 methodology	320
Table 7.32 Performance evaluation for each archetype model using Mod5 variation of FEMA P695 methodology	320
Table 7.33 Summary of performance evaluation result using different variations of FEMA P695 methodology	321

List of figures

Figure 2.1 Potential limit states unique to R=3 CBF	27
Figure 2.2 Test specimen and setup (Sizemore et al. 2015)	28
Figure 2.3 (a) brace local buckling; (b) brace low cycle fatigue; (c) global hysteresis (Sizemore et al. 2015).....	29
Figure 2.4 (a) brace-gusset weld fracture; (b) brace re-engagement (Sizemore et al. 2015)	30
Figure 2.5 Base shear vs Story 1 Drift (Sizemore et al. 2015)	30
Figure 2.6 Test specimen and setup (Bradley et al. 2015).....	31
Figure 2.7 Test hysteretic behavior (Bradley et al. 2015).....	31
Figure 2.8 Weld fracture during the test: (a)&(b) fracture of story 1 upper mid span brace gusset connection; fracture of story 1 bottom mid span beam gusset connection (Bradley et al. 2015)	32
Figure 2.9 (a) Typical CBF connection studied (b) Test setup (Davaran et al. 2014).....	32
Figure 2.10 Hysteresis behavior of brace re-engagement (Davaran et al. 2014).....	33
Figure 2.11 Connection details: (a) CN1; (b) CN2; (c) CN3; (d) CN4; (e) CN5; (f) CN6; (g) CN7; (h) CN8 (Stoakes and Fahnestock 2011).....	33
Figure 2.12 Normalized moment versus story drift: (a) CN1; (b) CN2; (c) CN3; (d) CN4; (e) CN5; (f) CN6; (g) CN7; (h) CN8 (Stoakes and Fahnestock 2011)	34
Figure 2.13 Specimen elevation, typical sections and geometry: (a) Specimen 1; (b) Specimen 2; (c) Specimen 3; (d) Specimen 4 (Sen et al. 2016a).....	35

Figure 2.14 Base shear versus drift hysteresis: (a) Specimen 1; (b) Specimen 2; (c) Specimen 3; (d) Specimen 4 (Sen et al. 2016a)	35
Figure 2.15 Specimen 1 test: (a) a south first-story brace local buckling; (b) a south first-story brace fracture; (c) north first-story brace-to-gusset plate connection fracture (Sen et al. 2016a).....	36
Figure 2.16 Test specimen and setup (Simpson et al. 2013)	36
Figure 2.17 Shear vs drift ratio (Simpson et al. 2013).....	37
Figure 2.18 Test setup (Sen et al. 2016b)	37
Figure 2.19 Connection detail of test specimens: (a) Specimen 1; (b) Specimen 2 and 3; (c) Specimen 4; (d) Specimen 5 and 6; (e) Specimen 7; (f) Specimen 8 (Sen et al. 2016b)..	38
Figure 2.20 Hysteresis behavior: (a) Specimen 1; (b) Specimen 2; (c) Specimen 3; (d) Specimen 4; (e) Specimen 5; (f) Specimen 6; (g) Specimen 7; (h) Specimen 8 (Sen et al. 2016b)	39
Figure 2.21 Brace connection hysteresis model used in (Gryniuk 2008)	40
Figure 2.22 Brace hysteresis response in one analysis in (Hines et al. 2009)	40
Figure 2.23 Some IDA analysis that show convergence problems in (Hines et al. 2009)	41
Figure 2.24 Force-deformation relation of SDOF system in (Li and Fahnstock 2013)..	41
Figure 2.25 IDA of prototype CBF in (Sizemore et al. 2004): (a) baseline; (b) brace re-engagement; (c) enhanced B-C connection; (d) fixed bases in braced frame; (e) all column bases fixed; (f) combined (b) + (c) +(e) (Sizemore et al. 2014)	42
Figure 2.26 Abaqus model in (Sen 2014)	43
Figure 2.27 Comparison of test result with FEM simulation: (a) Specimen 1; (b) Specimen 2; (c) Specimen 3; (d) Specimen 4 (Sen 2014).....	43

Figure 3.1 (a) Aerial view of MSC (http://www.bing.com/map); (b) Floor plan of MSC74	
Figure 3.2 (a) Typical elevation of Pod, Office and mezzanine; (b) Steel mezzanine inside Pod; (c) Typical braced bay	75
Figure 3.3 (a) RC beam-column joint failure; (b) crack in masonry wall; (c) sliding of T beams	76
Figure 3.4 Type and distribution of damage in the first story of the steel mezzanine in Pod 1.....	77
Figure 3.5 Nonstructural damage: (a) toppling of a storage cabinet; (b)&(c) sliding of cabinet; (d) cabinet dislodged; (e) storage content damage.....	78
Figure 3.6 Isometric view of SAP2000 FEA model of steel mezzanine	78
Figure 3.7 Illustration of cabinet content weight distribution and resultant total floor weight over floor plan: (a) Case I; (b) Case II; (c) Case III; (d) Case IV; (e) Case V; (f) Case VI; (g) Case VII.....	79
Figure 3.8 Location of the CM within the floor plan of the mezzanine for each cabinet content weight case.....	79
Figure 3.9 Response spectrum of ground motion of Virginia earthquake at bedrock and ground surface level (a) component in the long direction (b) component in the short direction	80
Figure 3.10 Peak axial stress response in 1st story braces in SAP model for Case I	81
Figure 3.11 Time history for translation of joints at the top of columns in east and west perimeters: (a) response to ground motion in NS direction; (b) response to ground motion in EW direction; (c) response to bi-directional ground motion	81

Figure 3.12 Response spectra of two components of ground motion and structural periods	82
Figure 3.13 Mode shape of SAP2000 model in Case I.....	83
Figure 3.14 (a) Imposed brace displacement history of displacement-control cyclic load; (b) Hysteretic force-displacement response of one diagonal brace (tension force is positive)	84
Figure 3.15 Peak axial stress in braces of 1 st story in OpenSees model in response to Virginia earthquake.....	84
Figure 3.16 Shear wave velocity profile of soil strata used in site response analysis for records used in fragility analysis.....	85
Figure 3.17 Individual and median value of ensemble of bedrock motion, ground surface motion and target spectrum for (a) DBE hazard level and (b) MCE hazard level.....	86
Figure 3.18 PSDM generated using different ground motions sets for braces in (a) long direction; (b) short direction and (c) combined directions of structure	87
Figure 3.19 Fragility curve for different parts of the structure for onset of damage	87
Figure 3.20 (a) Criteria for different types of motion in parameter space; (b) definition of various parameters	88
Figure 3.21 Fragility curve for different parts of the structure for onset of damage	88
Figure 3.22 Fragility curves for initiation of motion for different types of cabinets.....	89
Figure 3.23 PSDM for floor acceleration for structures using braces of different yield strength.....	89

Figure 3.24 Cabinet fragility curves for structures using braces of different yield strength: (a) Type 348 rocking; (b) Type 348 sliding; (c) Type 220 rocking; (d) Type 220 sliding; (e) Type 395 rocking; (f) Type 395 sliding;	90
Figure 4.1 Variation of brace configuration from existing CBF design (from Building 1): (a) single diagonal, multi-story X; (b) inverted chevron; (c) split X; (d) chevron	132
Figure 4.2 Brace and beam section for Building 2	133
Figure 4.3 Brace and beam section for Building 3	134
Figure 4.4 Different types of brace-gusset plate connections: (a) welded connection for slotted HSS brace; (b) bolted connection for single angle brace; (c) bolted connection for double angle brace; (d) bolted connection for wide flange brace; (e) hybrid connection for HSS brace at beam column joint; (f) hybrid connection for HSS brace at brace beam joint	135
Figure 4.5 Brace connection design in Building 2.....	135
Figure 4.6 Connection design parameter for Building 2 (second story has been highlighted)	136
Figure 4.7 Connection detail in Marstellar et al. (2002).....	137
Figure 4.8 Floor plan of prototype building.....	138
Figure 4.9 Elevation of prototype building: (a) chevron brace configuration variant; (b) split-X brace configuration variant	139
Figure 4.10 Distribution of design wind pressure.....	140
Figure 4.11 Member sections: (a) beams at typical floors; (b) beams at roof; (c) columns	142

Figure 4.12 Weld connection detail (Design 1) for second story at beam-column joint in chevron CBF: (a) location; (b) EW bay; (c) NS bay	144
Figure 4.13 Weld connection detail (Design 1) for second story at chevron point in chevron CBF: (a) location; (b) EW bay; (c) NS bay	146
Figure 4.14 Weld connection detail (Design 1) for second story at BC joint in split-X CBF: (a) location; (b) EW bay; (c) NS bay	148
Figure 4.15 Weld connection detail (Design 1) for second story at brace beam joint in split-X CBF: (a) location; (b) EW bay; (c) NS bay	150
Figure 4.16 Schematic of CBF model in OpenSees	151
Figure 4.17 Modeling detail at (a) beam column joint and (b) chevron point.....	152
Figure 4.18 Illustration of brace and connection model	153
Figure 4.19 Illustration of brace gusset weld connection model (a) weld fracture component; (b) brace re-engagement component; (c) numerical stability component...	153
Figure 4.20 Increase of contact surface during brace re-engagement (Sizemore et al. 2015)	154
Figure 4.21 Behavior of brace re-engagement model (a) Imposed displacemnt history; (b) hysteretic behavior	154
Figure 4.22 Schematic of beam model using CPH approach	155
Figure 4.23 Hysteretic response and definition of input parameters for IMK material (Lignos et al. 2011) to model strength deterioration in beam plastic hinge	155
Figure 4.24 Local buckling in beam plastic hinge observed in Bradley et al. (2015)	155
Figure 4.25 (a) Backbone curve and definition of material parameters; (b) Moment-rotation hysteresis of rotational spring to model BC connection with gusset plate	156

Figure 4.26 Different modeling approaches for gravity system: (a) LOC-pin; (b) LOC-continuous; (c) LOC-continuous-fiber; (d) EGF	157
Figure 4.27 (a) Backbone curve and definition of input parameters; (b) Moment-rotation hysteresis of rotational spring to model BC connection in gravity system.....	158
Figure 4.28 Illustration of damping substructure model.....	159
Figure 4.29 Assembly of CBF, gravity system and damping substructure (gravity system shown in EGF approach)	159
Figure 4.30 Drift history during the second phase of Sizemore et al. (2015).....	160
Figure 4.31 Comparison of analytical model response and test result in Sizemore et al. (2015).....	160
Figure 4.32 Plastic hinge developed in chevron point during “long link EBF” response in Sizemore (2015).....	161
Figure 4.33 Moment rotation response of beam plastic hinge at chevron point in the analytical model	162
Figure 4.34 Comparison of analytical model response and test result in Bradley et al. (2015)	162
Figure 4.35 Alternative model for beam using forceBeamColumn element with fiber section	163
Figure 4.36 Proposed brace model to include local buckling.....	163
Figure 4.37 Comparison of analytical and experimental response for west brace of 2 nd story in Simpson et al. (2013) when proposed brace model is used	164
Figure 4.38 Moment rotational response of the rotational spring at the middle of the brace	164

Figure 4.39 Comparison of analytical and experimental response for roof drift vs base shear in Simpson et al. (2013) when proposed brace model is used	165
Figure 4.40 Comparison of analytical and experimental response for west brace of 2 nd story in Simpson et al. (2013) when conventional brace model is used	165
Figure 5.1 Response spectra for uncaled FEMA GM set and its median spectrum	197
Figure 5.2 Comparison of the felt area of ECUS earthquake with WUS earthquake of similar magnitude (Horton and Williams 2012)	198
Figure 5.3 Median ε of FEMA GM set.....	198
Figure 5.4 Comparison of magnitude and distance of ground motion records in NGA-East and NGA-West2 database (Boore 2013)	199
Figure 5.5 Response spectra of example records from NGA-East database: (a) 2002 Charleston ground motion (unscaled); (b) 2011 Mineral ground motion (unscaled); (c) comparison; (d) comparison up to 1g	200
Figure 5.6 Procedure of ground motion simulation in SMSIM (Boore 2003).....	201
Figure 5.7 Seismic hazard deaggregation result for MCE hazard level at $T = 1s$ for Philadelphia.....	202
Figure 5.8 (a) Spectra for the 800 generated ground motions, median spectrum, median plus one standard deviation and median plus two standard deviations spectrum; (b) log standard deviation for 800 generated ground motions for $M=7.39$, $R=393.4$ using A04 model.....	203
Figure 5.9 Response spectrum for an example ground motion with $\varepsilon = 1.35$, selected for $R=393.4$ km, $M=7.39$ bin using A04 model	204

Figure 5.10 Response spectra for ground motions selected for R=393.4 km, M=7.39 bin using A04 model	205
Figure 5.11 44 ground motions selected using A04 model	206
Figure 5.12 Comparison of median spectra of ground motion sets from 6 seismological models and $Sa(T = 1s)$ for MCE hazard level.....	207
Figure 5.13 Shear wave velocity profile at a site at Drexel University, Philadelphia	207
Figure 5.14 Original and uniform layer profile of shear wave velocity for DXL site	208
Figure 5.15 Response spectra for surface ground motions from site response analyses using Rock GM set as bedrock motion input for: (a) uniform layer profile; (b) original profile	209
Figure 5.16 Comparison of median spectra of ground motion sets obtained from site response analyses using different soil profiles: (a) profiles with $v_s = 180m/s$; (b) profiles with $v_s = 465m/s$;	210
Figure 5.17 Response spectra for Soil GM set and its median spectrum	211
Figure 5.18 Comparison of median spectra of Rock GM set and Soil GM set	212
Figure 5.19 Comparison of the median response spectra for Soil GM set and FEMA GM set when scaled to the same $Sa(T=1s)$	213
Figure 5.20 Comparison of Rock GM set median spectrum, Rock GM set median spectrum, ASCE7 MCE (rock, Site Class A and soil, Site Class D) spectra and USGS UHS	214
Figure 6.1 Illustration of Incremental Dynamic Analyses (IDA)	243
Figure 6.2 Fragility curve generated according to FEMA P695 methodology and fitted lognormal CDF to collapse data points directly obtained from IDA.....	244
Figure 6.3 Summary of categories of uncertainty considered in this study	244

Figure 6.4 Different scaling methods for IDA shown with FEMA GM set: (a) and (b) “Sa component scaling method” scaled to 0.1g and 0.2g for $Sa(1s)$; (c) and (d) PGV scaling method scaled to 0.1g and 0.2g for $Sa(1s)$	245
Figure 6.5 Illustration of relative strength between brace and connection with uncertainty	246
Figure 6.6 Brace-to-gusset plate fillet weld specimens from tests by Sizemore et al. (2015): (a) with equal gap; (b) with unequal gap	247
Figure 6.7 Monte Carlo Simulation procedure to study model parameter uncertainty ..	247
Figure 6.8 Schematic showing uncertainty (except for RTR variability) considered in FEMA P695 and current study	248
Figure 6.9 Schematic illustration of modeling uncertainty: (a) model not capturing important limit states leading to larger modeling uncertainty; (b) model capturing important limit states leading to smaller modeling uncertainty	248
Figure 6.10 Schamatic illustration of modeling uncertainty from design variation: (a) using one IAM to cover entire design space, leading to a larger modeling uncertainty; (b) using multiple IAMs to cover the entire design space, leading to a smaller modeling uncertainty	249
Figure 6.11 Schamatic illustration of relation of test data uncertainty to model parameter uncertainty: (a) larger uncertainty for model parameters without test data; (b) smaller uncertainty for input model parameters with calibration with good quality test data	250
Figure 6.12 Schamatic illustration of design requirement uncertainty for brace and connection design: (a) low-ductility CBF with poor design requirements, leading to uncertain limit state sequence and unintended behavior from higher design requirement	

uncertainty; (b) SCBF with good design requirements, leading to controlled limit states and lower design requirement uncertainty.....	251
Figure 6.13 Schematic illustration of the relation of design variation (DV) to MDL uncertainty and DR uncertainty	252
Figure 7.1 Idealized pushover curve and definition of δu according to 80% base shear reduction rule (FEMA 2009)	322
Figure 7.2 IDA results using PGV scaling method for archetype models: (a) C1; (b) C2; (c) C3; (d) C4; (e) X1; (f) X2; (g) X3; (h) X4	323
Figure 7.3 Pushover analysis results for: (a) archetype models with chevron bracing and (b) archetype models with split-X bracing.....	324
Figure 7.4 Notation for brace members and welds: (a) Chevron CBF; (b) Split-X CBF	325
Figure 7.5 Pushover response for model C1	326
Figure 7.6 Stages of pushover response for model C1	326
Figure 7.7 Pushover response for model C3.....	327
Figure 7.8 Stages of pushover response for model C3	327
Figure 7.9 Pushover response for model C2.....	328
Figure 7.10 Stages of pushover response for model C2	328
Figure 7.11 Pushover response for model X3.....	329
Figure 7.12 Stages of pushover response for model X3	329
Figure 7.13 Pushover response for model X4.....	330
Figure 7.14 Stages of pushover response for model X4	330
Figure 7.15 IDA result of C3 model ($SCT = 0.6g$ according to FEMA P695 methodology)	331

Figure 7.16 Median spectral acceleration for ground motion set <i>STCuTa</i> vs. <i>Sa(CuTa)</i> using IDA result for model C3 under GM1	331
Figure 7.17 Comparison of <i>Sa(CuTa)</i> causing collapse for each ground motion with <i>Sa(CuTa)</i> for each ground motion used to calculate <i>SCT</i> using IDA results for model C3	332
Figure 7.18 Response of archetype model C1 for GM25 at <i>STCuTa</i> = 0.8 <i>g</i> : (a) brace hysteresis; (b) first story hysteresis; (c) drift history	333
Figure 7.19 Response of archetype model C2 for GM25 at <i>STCuTa</i> = 0.8 <i>g</i> : (a) brace hysteresis; (b) first story hysteresis; (c) drift history	334
Figure 7.20 Response of archetype model C2 for GM25 at <i>STCuTa</i> = 1.1 <i>g</i> : (a) brace hysteresis; (b) first story hysteresis; (c) drift history	335
Figure 7.21 Response of archetype model C3 for GM14 at <i>STCuTa</i> = 0.9 <i>g</i> : (a) brace hysteresis; (b) first story hysteresis; (c) drift history	336
Figure 7.22 Response of archetype model C3 for GM14 at <i>STCuTa</i> = 1.2 <i>g</i> : (a) brace hysteresis; (b) first story hysteresis; (c) drift history	337
Figure 7.23 Response of archetype model C4 for GM14 at <i>STCuTa</i> = 0.9 <i>g</i> : (a) brace hysteresis; (b) first story hysteresis; (c) drift history	338
Figure 7.24 Response of archetype model X1 for GM39 at <i>STCuTa</i> = 0.5 <i>g</i> : (a) brace hysteresis; (b) second story hysteresis; (c) drift history.....	339
Figure 7.25 Response of archetype model X1 for GM39 at <i>STCuTa</i> = 0.6 <i>g</i> : (a) brace hysteresis; (b) second story hysteresis; (c) drift history.....	340
Figure 7.26 Response of archetype model X2 for GM39 at <i>STCuTa</i> = 0.5 <i>g</i> : (a) brace hysteresis; (b) first story hysteresis; (c) drift history	341

Figure 7.27 Response of archetype model C1 for GM21 at $STCuTa = 0.5g$: (a) brace hysteresis; (b) first story hysteresis; (c) drift history	342
Figure 7.28 Response of archetype model C3 for GM21 at $STCuTa = 0.5g$: (a) brace hysteresis; (b) first story hysteresis; (c) drift history	343
Figure 7.29 Response of archetype model C3 for GM21 at $STCuTa = 0.7g$: (a) brace hysteresis; (b) first story hysteresis; (c) drift history	344
Figure 7.30 Response of archetype model C2 for GM18 at $STCuTa = 0.9g$: (a) brace hysteresis; (b) first story hysteresis; (c) drift history	345
Figure 7.31 Response of archetype model C2 for GM18 at $STCuTa = 1.1g$: (a) brace hysteresis; (b) first story hysteresis; (c) drift history	346
Figure 7.32 Response of archetype model C4 for GM18 at $STCuTa = 0.9g$: (a) brace hysteresis; (b) first story hysteresis; (c) drift history	347
Figure 7.33 Response of archetype model X2 for GM16 at $STCuTa = 0.4g$: (a) brace hysteresis; (b) first story hysteresis; (c) drift history	348
Figure 7.34 Response of archetype model X4 for GM16 at $STCuTa = 0.4g$: (a) brace hysteresis; (b) first story hysteresis; (c) drift history	349
Figure 7.35 Response of archetype model C1 for GM19 at $STCuTa = 0.7g$: (a) brace hysteresis; (b) first story hysteresis; (c) drift history	350
Figure 7.36 Response of archetype model X1 for GM19 at $STCuTa = 0.7g$: (a) brace hysteresis; (b) first story hysteresis; (c) drift history	351
Figure 7.37 Response of archetype model C2 for GM23 at $STCuTa = 0.5g$: (a) brace hysteresis; (b) first story hysteresis; (c) drift history	352

Figure 7.38 Response of archetype model C2 for GM23 at $STCuTa = 0.7g$: (a) brace hysteresis; (b) first story hysteresis; (c) drift history	353
Figure 7.39 Response of archetype model X2 for GM23 at $STCuTa = 0.5g$: (a) brace hysteresis; (b) first story hysteresis; (c) drift history	354
Figure 7.40 IDA results using ECUS GM set for model: (a) C1; (b) C2; (c) C3; (d) C4; (e) X1; (f) X2; (g) X3; (h) X4	355
Figure 7.41 Response of the pushover analysis and tangent first mode period at each load step during the pushover analysis for model C3	356
Figure 7.42 First story hysteresis response of model C3 under GM10 at $Sa(1s) = 1.0g$	357
Figure 7.43 Tangent first mode period at each time step during the response of model C3 under GM10 at $Sa(1s) = 1.0g$ in IDA	357
Figure 7.44 Response spectrum of (a) FEMA set; (b) ECUS GM set when all ground motions are scaled to $Sa(1s)=0.1g$	358
Figure 7.45 Comparison of standard deviation of $\ln(Sa)$ at each period between FEMA and ECUS GM set at $Sa(1s)=0.1g$ using “Sa component scaling method”	359
Figure 7.46 Illustration on brace re-engagement effect: free body diagram on chevron point	359
Figure 7.47 IDA results for model C1 under GM16 with and without modeling brace re-engagment	360
Figure 7.48 First story hysteresis of model C1 under GM16 at $Sa(1s)=0.3g$ with and without modeling brace re-engagment	360

Figure 7.49 Comparison of IDA results for model C1 under GM25 with and without including brace re-engagment.....	361
Figure 7.50 Comparison first story hysteresis of model C1 under GM25 at $S_a(1s)=0.5g$ with and without including brace re-engagment.....	361
Figure 7.51 IDA results for model C2 under GM2 when CPH approach or fiber approach is used for beam modeling	362
Figure 7.52 First story drift history of model C2 under GM2 at $S_a(1s)=0.6g$ when CPH approach or fiber approach is used for beam modeling.....	362
Figure 7.53 Beam moment response at chevron point of model C2 under GM2 at $S_a(1s)=0.6g$ when CPH approach or fiber approach is used for beam modeling	363
Figure 7.54 Pushover analysis results for C1 model with different gravity load system modeling approaches	363
Figure 7.55 Variation of median collapse capacity as individual model parameters are varied to lower and upper values: (a) model C1; (b) model C2.....	364
Figure 7.56 Effect of weld strength on the collapse capacity for model C1 for 5 ground motions.....	365
Figure 7.57 IDA for GM12 for model C1 with variation on weld strength.....	365
Figure 7.58 Response for GM12 at $S_a(1s)=0.1g$ for model C1 with median and lower value of weld strength.....	366
Figure 7.59 Response for GM12 at $S_a(1s)=0.2g$ for model C1 with median and upper value of weld strength.....	367
Figure 7.60 Brace 1-2 buckling strength with different Weld 1-2 strength in sensitivity analysis for (a) model C1; (b) model C2	368

Figure 7.61 IDA result for GM44 for model C1 with different LCF strength.....	369
Figure 7.62 Brace 3-2 hysteresis with different brace LCF strength: (a) upper value; (b) lower value.....	369
Figure 7.63 Timeline of important limit states for GM44 at Sa=0.8g for model C1 with different LCF strength.....	370
Figure 7.64 First story drift history for GM44 at Sa=0.8g for model C1 with different LCF strength (BF: brace fracture).....	370
Figure 7.65 IDA result for GM12 for model C2 with different brace LCF strength.....	371
Figure 7.66 Brace 1-2 and first story hysteresis response for GM12 at Sa=0.3g for model C2 with different LCF strength.....	371
Figure 7.67 IDA result for GM5 for model C1 with different brace re-engagement strength.....	372
Figure 7.68 Force history of Brace 1-1 and Brace 1-2 for GM5 at Sa=0.6g for model C1 with different brace re-engagement strength	373
Figure 7.69 First story drift history for GM5 at Sa=0.6g for model C1 with different brace re-engagement strength.....	373
Figure 7.70 IDA result for GM2 for model C1 with different brace re-engagement strength.....	374
Figure 7.71 Comparison of (a) First story and (b) Brace 1-2 hysteresis response for GM2 at Sa=0.5g for model C1 with different brace re-engagement strength.....	374
Figure 7.72 Buckling strength of Brace 1-2 with different e/L value and Weld 1-2 strength in mode C1 and model C2	375

Figure 7.73 Brace 3-1 hysteresis response for GM5 at $S_a=0.4g$ for model C1 with different brace initial out of straightness (e/L)	375
Figure 7.74 Timeline of limit states for GM5 at $S_a=0.4g$ for model C1 with different brace initial out of straightness (e/L)	376
Figure 7.75 First story drift history for GM5 at $S_a=0.4g$ for C1 model with different brace initial out of straightness (e/L)	376
Figure 7.76 Buckling strength of Brace 1-2 with different yield strength and weld 1-2 strength in model C1 and model C2	377
Figure 7.77 IDA result for GM19 for model C1 with different brace yield strength	377
Figure 7.78 Brace 1-1, Brace 1-2, and first story hysteresis response for GM19 at $S_a=0.5g$ for model C1 with different brace yield strength	378
Figure 7.79 Correlation between random variables in MCS	379
Figure 7.80 IDA results for 20 sample models for model C1 (continued)	381
Figure 7.81 IDA results for 20 sample models for model C2 (continued)	383
Figure 7.82 Median collapse capacity with different number of sample models included (a) C1 model; (b) C2 model	384
Figure 7.83 Median collapse capacity for each sample model, median collapse capacity considering all 20 sample models, and median collapse capacity of median model for: (a) model C1 and (b) model C2	385
Figure 7.84 First story weld strength and corresponding $S_{ac,m}(1s)$ for each of the 20 sample models and for the median model for model C1	386
Figure 7.85 IDA results for sample model 3 and median model of model C1	386

Figure 7.86 IDA result for of GM5 for sample model 3 and median model of model C1	387
Figure 7.87 Comparison of first story brace response and first story hysteresis between sample model 3 and median model for model C1 for GM5 at $Sa(1s)=0.5g$	387
Figure 7.88 Notation for some collapse modes observed in IDA.....	388
Figure 7.89 Percentage of collapse modes exhibited in (a) IDA of median model (model C1) under 44 GMs; (b) IDA of 20 sample models (model C1) in MCS under GM1	389
Figure 7.90 Log standard deviation of collapse capacity for each sample model $\sigma_{ln}(Sac)$, for median model $\sigma_{ln}(Sac)$, and log standard deviation considering all sample models $\sigma_{ln}(Sac)$, <i>MCS</i>	390
Figure 7.91 IDA results for: (a) sample model 1 under 44 GMs; (b) 20 sample models under GM1	391
Figure 7.92 Log standard deviation of collapse capacity from different sample models under each GM: (a) model C1; (b) model C2.....	392
Figure 7.93 Comparison of RTR variability β_{RTR_Sa} and model parameter uncertainty β_{MP}	393
Figure 7.94 Median collapse capacity for each sample model of archetype model C1 and median collapse capacity for the median model of each archetype model	393
Figure 7.95 Median collapse capacity for each sample model of the baseline model (MA1) for archetype model C1 and for the median model with different modeling approaches for archetype model C1	394

Abstract

The overall objective of this dissertation is to advance knowledge on the seismic behavior and performance of low-ductility concentrically braced frames (CBF) in the mid-Atlantic east coast region of the United States (ECUS). Low-ductility CBFs in the ECUS are usually designed with a Response Modification Factor R equal to 3 and without seismic detailing to promote ductile behavior. While low-ductility CBFs constitute a large portion of the building inventory in low to moderate seismic zones of the United States such as the ECUS, there is a lack of understanding of their seismic response, and more importantly, whether they provide satisfactory performance in the context of ECUS seismic hazard environment. This research emphasizes the collapse performance of low-ductility CBFs and how it is influenced by various sources of uncertainty. The scope of the research includes: (1) seismic response simulation and performance evaluation of an ECUS CBF during the 2011 Virginia earthquake; (2) developing of a prototype building design and numerical models for collapse simulation of low-ductility CBFs; (3) developing of an ECUS ground motion set for collapse performance assessment; (4) identifying and categorizing different sources of uncertainty associated with seismic performance assessment; (5) evaluating the seismic performance of low-ductility CBFs under various sources of uncertainty; and (6) examining the application of the FEMA P695 methodology for collapse performance assessment to low-ductility CBFs and propose modifications to the methodology.

Damage reconnaissance, response simulation and fragility analysis were conducted on an existing ECUS CBF which was considerably damaged during the 2011 Virginia earthquake. The focus of fragility analysis was non-collapse performance, i.e., limit states

at onset of structural damage and non-structural damage. It was found that the probability of non-structural damage is significant even under the Design Basis Earthquake (DBE) level. In addition, the site soil amplification effect on the ground motion was found to have played an important role in the seismic performance of this building.

To evaluate collapse performance of the general building stock of low-ductility CBFs in the ECUS, a set of 8 archetype buildings representing design variations were created. Key design variables and their corresponding variation were identified by reviewing existing designs and literature. Numerical models that capture the unique behavior of low-ductility CBFs, such as weld fracture and brace re-engagement were developed. Experimental data was used to validate and calibrate the numerical models.

A set of synthetic ground motions representing the ECUS seismic hazard was developed. Synthetic ground motions at the bedrock level were generated from current seismological models. The bedrock ground motions consider the variation in earthquake sources and the effect of spectral shape. Site response analyses were performed using a set of potential Site Class D soil profiles to account for variation in the site soil amplification effect. It was found that the median spectrum of the soil ground motion set is smaller than the current Maximum Considered Earthquake (MCE) spectrum for Site Class D.

Various sources of uncertainty affecting the seismic performance of low-ductility CBFs were identified and categorized, including uncertainty in seismic demand, design variation, modeling approach uncertainty, and model parameter uncertainty. The relation between these categories and the uncertainty categories considered in the FEMA P695 methodology

was explored. Strategies to investigate different categories of uncertainty were proposed. Probability distribution for model parameter uncertainties were established.

Incremental Dynamic Analysis (IDA) was performed on different archetype models to investigate the effect of design variation of collapse capacity. The IDA results from a FEMA P695 ground motion set and the ECUS ground motion set were compared. It was found that the empirical formulas from the FEMA P695 methodology for the spectral shape effect and record-to-record variability do not apply to ECUS low-ductility CBFs. The effect of modeling approach uncertainty was studied. It was found that including the lateral resistance of the gravity load system has a significant impact on the collapse capacity. The effect of model parameter uncertainty on the collapse capacity was explicitly quantified using Monte Carlo Simulation. It was found that the dispersion in collapse capacity due to model parameter uncertainty is relatively smaller compared to other documented dispersion in collapse capacity. It was also discovered that IDA results for the median model do not provide the median collapse capacity. In parallel, deficiencies from directly applying the FEMA P695 methodology to low-ductility CBFs were found and modifications were proposed. The collapse performance of low-ductility CBFs was evaluated using the original FEMA P695 procedure as well as the modified versions. It was found that using the original FEMA P695 methodology, low-ductility CBFs do not have adequate collapse capacity. However, they may have satisfactory collapse performance using the modified versions of the FEMA P695 methodology.

Chapter 1

Introduction

1.1 Motivation

Earthquakes are a major natural hazard that causes economic losses, human casualties, and indirect social impacts. Driven by the potential for heavy losses, there is a growing interest in the earthquake engineering community in evaluating the seismic performance of the built environment for future seismic events. For the past two decades, the development of Performance-based Earthquake Engineering (PBEE) methods has enabled seismic performance assessment in a more rigorous way by integrating seismic hazard, structural response, damage, and various loss estimates to provide a quantitative and probabilistic description of the seismic risk. The end-product of this seismic performance provides a wealth of information that enables comparison of different design methodologies for new structures and identification of existing structures that are vulnerable and pose a threat to their occupants.

Steel concentrically braced frames (CBFs) are a very popular type of lateral force resisting system (LFRS) which provides large elastic stiffness while being economical. Past and current building codes permit CBFs in vast areas of the United States (US), which are in low to moderate seismic zones, such as the mid-Atlantic east coast region of the United States (ECUS), to be designed with a Response Modification Factor R equal to 3 and without seismic detailing to promote ductility. While the design and construction of low-

ductility CBFs are pervasive in the US, there is very little understanding of their inelastic behavior and seismic performance. Therefore, the seismic performance of this class of CBFs is of concern. On the other hand, the seismic hazard in the ECUS is also not well characterized, compared to the western United States (WUS, west of the Rocky Mountains). The 2011 Mineral, Virginia earthquake increased public awareness of potential seismic hazard in low to moderate seismic zones and motivated researchers to investigate the seismic performance of low-ductility CBFs in the ECUS seismic hazard environment. Due to the infrequent nature of seismic events in the ECUS, the performance objectives for low-ductility CBFs is focused on preventing life-threatening collapses (Nelson 2007; Nordenson and Bell 2000). In some cases, however, the non-collapse performance can be of concern for stakeholders for special reasons.

Variability in the collapse capacity of the building inventory, which comes from various sources of uncertainty, is a critical component in a probabilistic seismic performance evaluation. This variability is of special importance to low-ductility CBF systems because the variation in their collapse capacity may be larger than that of special concentrically braced frame (SCBF) which are detailed to have higher ductility. Current design code provisions do not preclude undesirable brittle failure mode (e.g. brace connection fracture) in low-ductility CBFs. Therefore, low-ductility CBFs may have various limit states occurring in various sequences and do not follow a clear hierarchy of limit states like SCBFs, which respond with selected limit states occurring (brace yielding and buckling). The inherent uncertainty of the structural properties, for example, material properties and design variations, may trigger a variation of the governing limit states and create different paths to failure. Furthermore, low-ductility CBFs are reported to have the so called “reserve

capacity” (Li and Fahnstock 2013) that are not considered in design but may contribute to collapse prevention after the primary LFRS becomes severely damaged. The uncertain nature of the reserve capacity contributes to the total uncertainty in the collapse capacity. Therefore, it is important to evaluate all significant sources of uncertainty in the collapse response and to comprehensively assess the seismic performance of a general inventory of low-ductility CBFs.

FEMA P695 (FEMA 2009) provides a methodology to evaluate the collapse performance of a structural system type considering the effects of uncertainties. This methodology was developed based on ductile reinforced concrete (RC) moment resisting frames (MRFs) in WUS. It is not known whether this methodology applies to evaluating ECUS structures for several reasons. For example, the FEMA ground motion set that is used to capture the uncertainty in seismic demand consists of recorded ground motions mainly from WUS. The spectral shape factor (SSF) to address the spectral shape effect is based on ductile structures. The β factors that account for various sources of uncertainty in the collapse capacity are also developed for ductile structures. Therefore, it is necessary to examine the application of FEMA P695 methodology to the evaluation of the collapse capacity of ECUS structures.

Recent large scale tests on low-ductility CBFs (Bradley et al. 2015; Sen 2014; and Sizemore et al. 2015) provide insight and valuable data on the seismic behavior of low-ductility CBF at a fundamental level. However, these tests were limited to certain structural parameters, configurations and designs, and do not address the effect of uncertainty. In addition, the test results (mostly from static cyclic loading) do not provide direct

information on the collapse capacity. Numerical studies that explore the behavior of low-ductility CBF in broader parametric space and evaluate the collapse performance are necessary.

Motivated by the above factors, this research seeks to develop accurate numerical models facilitated by recent test data and to evaluate the seismic performance of low-ductility CBF in the context of the ECUS seismic hazard environment. Special attention is given to the collapse performance and how it is affected by various sources of uncertainty. The FEMA P695 methodology (FEMA 2009) was used as a baseline reference to evaluate the collapse performance. The application of the FEMA P695 methodology for collapse performance assessment of low-ductility CBFs in the ECUS is examined and modifications in the methodology are proposed.

1.2 Research objectives

The overall objective of this research is to advance knowledge on the seismic response and performance of low-ductility CBFs in the ECUS. The specific objectives are as follows:

1. Investigate the non-collapse performance of low-ductility CBFs through a case study of an ECUS CBF that was significantly damaged during the 2011 Virginia earthquake.
2. Develop numerical models for low-ductility CBFs for collapse response analysis. The numerical models need to capture the unique limit states of low-ductility CBFs that are important to collapse response (e.g. weld fracture and brace re-engagement).

3. Investigate the effect and sensitivity of various sources of uncertainty (e.g., design approach, modeling parameters, modeling approach, and ground motions) on the collapse capacity of low-ductility CBFs.
4. Examine the application of the FEMA P695 methodology to assess the collapse capacity of ECUS low-ductility CBF in the presence of various sources of uncertainty and propose modifications that could improve applicability to ECUS low-ductility CBFs.
5. Evaluate the collapse performance of low-ductility CBFs under the ECUS seismic hazard environment.

1.3 Research scope

The following tasks were accomplished to achieve the objectives of this research:

- 1) Response simulation of an existing ECUS CBF in the MSC building during the 2011 Virginia earthquake and performance evaluation.

Damage reconnaissance was conducted on an ECUS CBF which was considerably damaged during the 2011 Virginia earthquake. A numerical model of the building was developed in OpenSees and validated using dynamic properties from field vibration testing. The seismic response of the building during the 2011 Virginia earthquake was simulated and the results were consistent with the observed damage. A set of ground motions that incorporates the soil amplification effect was developed for seismic fragility analysis. The focus of the fragility analysis was on non-collapse performance. Fragility curves for the limit states of onset of structural damage and non-structural damage were developed. The

performance of the structure was evaluated at several hazard levels and the implications are presented.

- 2) Development of the prototype building design and numerical model for collapse simulation of low-ductility CBFs

This research seeks to evaluate the seismic performance of an inventory of structures as opposed to an individual building. Therefore, design variation was considered. The key design variables were identified by reviewing existing designs and literature. A three-story R=3 prototype CBF with 8 design variants were created. The design variation covers the variation in brace connections, beam design strength and brace configuration. The site of the prototype building is Philadelphia, a low seismic zone in the ECUS.

Nonlinear numerical models that capture the unique behavior of low-ductility CBFs, such as weld fracture and brace re-engagement were developed in OpenSees for the purpose of collapse simulation. Experimental data was used to validate and calibrate the numerical models. Alternative modeling approaches are conducted.

- 3) Development of an ECUS ground motion set for seismic collapse performance assessment;

A set of synthetic ground motions representing the ECUS seismic hazard characteristic was developed for collapse performance assessment of ECUS low-ductility CBFs. The synthetic ground motion set for sites in Philadelphia at the bedrock level was generated from current seismological models from the NGA East project (Goulet et al. 2011). The bedrock ground motions consider the variation in earthquake sources and consider the

effect of spectral shape. Site response analysis were performed using a set of potential Site Class D soil profiles to account variation in the soil amplification effect. The response spectra for the ECUS ground motion set were compared with the FEMA Far Field set, Uniform Hazard Spectrum (UHS) from USGS (Petersen et al. 2008), and the Maximum Considered Earthquake (MCE) spectrum in ASCE7-10 (ASCE 2010).

4) Identify and categorize different sources of uncertainty in seismic collapse performance assessment

The various sources of uncertainty affecting the seismic collapse performance of ECUS low-ductility CBFs were identified and categorized, including are uncertainty in seismic demand, design variation, modeling approach uncertainty, and model parameter uncertainty. The relation between these categories and the uncertainty categories considered in the FEMA P695 methodology (FEMA 2009) was explored. Probability distributions for the model parameter uncertainties were developed. Strategies to investigate the different sources of uncertainty were proposed.

5) Investigate the effects of various sources of uncertainty on the seismic collapse performance of ECUS low-ductility CBFs

Incremental Dynamic Analyses (IDA) were performed to determine the collapse capacity of low-ductility CBFs and subsequently to evaluate the effects of various sources of uncertainty. The dynamic responses of the CBFs were analyzed in detail to obtain insight on the effect of various sources of uncertainty on the collapse response. The IDA results from two sets of ground motions (the FEMA set and the ECUS set) were compared.

Collapse responses of structures with different designs were compared. The IDA results based on different modeling approaches were compared. The effect of model parameter uncertainty was studied by sensitivity analysis. In addition, Monte Carlo Simulation (MCS) was used to create sample models to understand and quantify the effect of model parameter uncertainty on the collapse capacity.

- 6) Examine the application of the FEMA P695 methodology to ECUS low-ductility CBFs and propose modifications.

The seismic collapse performance of low-ductility CBFs was evaluated using the original FEMA P695 methodology. Several modifications to the FEMA P695 methodology were proposed, including for example, using the ECUS ground motion set, and including the lateral resistance of the gravity load system. The collapse performance was evaluated using modified versions of the FEMA P695 methodology.

1.4 Outline of the dissertation

Chapter 1 presents the motivation of this research, the research objectives, and the scope.

Chapter 2 reviews the relevant previous research on low-ductility CBFs.

Chapter 3 presents a study of the seismic response and fragility analysis of an ECUS low-ductility CBF during the 2011 Virginia earthquake. The focus is on non-collapse performance assessment.

Chapter 4 presents the development of the prototype building with design variants. It also presents the development and validation of the nonlinear numerical model.

Chapter 5 presents the development of an ECUS ground motion set for seismic collapse performance.

Chapter 6 discusses the identification and categorization of various sources of uncertainty that affect the collapse performance of low-ductility CBFs

Chapter 7 presents the evaluation of the collapse performance of ECUS low-ductility CBFs under various sources of uncertainty. It also examines the application of the FEMA P695 methodology to ECUS low-ductility CBFs and proposed modifications.

Chapter 8 summarizes the findings of this research, draws conclusions, and suggests future research.

Chapter 2

Background

2.1 Introduction

This chapter presents the background information about low-ductility CBFs. It first introduces the history of low-ductility CBFs and its design features. Next, results from recent experimental study are presented. Then previous numerical investigations on the low-ductility CBFs are reviewed. In the end, important findings from the experimental study and the weakness of previous numerical study are summarized.

2.2 Origins and design feature of low-ductility CBF

From the 1970s to 1990s, the seismic design provision that originated from California had been expanding towards the east coast, through the development of Tentative Provisions for the Development of Seismic Regulations for Buildings (Applied Technology Council 1978) and National Earthquake Hazard Reduction Program (NEHRP). This nationwide expansion of seismic design reached a climax when the 3 regional building codes: Building Officials and Code Administrators (BOCA) in the northeast, Standard Building Code (SBC) in the southeast and Uniform Building Code (UBC) in the west were unified into the first draft of nationwide building code International Building Code (IBC) in 1997 (International Code Council 1997) which requires mandatory seismic design at a national scope. Nevertheless, during the introduction of the seismic design provision to the east coast, a lot of resistance was met from local structural engineers who argue that the new

design requirements are overconservative and lead to significant increase in construction cost, particularly due to seismic detailing requirement (Gryniuk and Hines 2004). Therefore, the designers from the east coast try to avoid the new seismic design requirement by taking advantages of loop holes in the design code. A very common strategy is to use a high R factor that reduce the seismic design base shear to be smaller than wind load and argue that seismic design can be ignored and therefore there is no need for seismic detailing either (Carter 2009). This is clearly against the intent of the design provision that the use of high ductile system (with a high R factor) must guarantee its inelastic deformation capability.

As a solution to fix this loop hole and aid the acceptance of the new seismic design provision in the east coast, Henry Martin from the American Iron and Steel Institute (AISI) came up with the idea of R=3 steel structure (Carter 2009) which first appeared in the 1997 AISC Seismic Provision (AISC 1997). The 1997 AISC Seismic Provision indicated that “systems designed and detailed to meet the requirements in the LRFD Specification but not the requirements of Part I (seismic provisions for structural steel buildings)” should be designed with R=3. The rationale behind the R=3 structures is that R=3 can “represent the normal ductility, reserve strength, and redundancies present in the steel framing systems used in traditionally non-seismic regions” (Carter 2009). Since the introduction in the 1997 AISC Seismic Provision, R=3 steel buildings have gained enormous popularity in low to moderate seismic region due to its exemption of the costly seismic detailing.

Table 2.1 shows the difference in the design requirement between R=3 braced frames (low-ductility CBF), ordinary concentrically braced frames (OCBF) and special concentrically

braced frames (SCBF) according to 2010 AISC Seismic Provision (AISC 2010a). As we can see, one important distinction of the design of R=3 CBFs from the more ductile CBFs is that the structural elements and connections adjacent to braces are not capacity-designed to have enough strength and deformation capacity to accommodate brace yielding and buckling. For example, the brace-gusset plate weld is designed by the required strength P_u , which is also used to size the braces. As the brace capacity is usually governed by compressive buckling strength, the tensile yield strength may be much larger than the design strength of the connection. Therefore, the connection is likely to fracture before the brace can yield. The beam is also not design to sustain the unbalanced brace force in the post-buckling stage. Therefore, the beam may develop plastic hinge at brace-beam intersection point. Besides, R=3 CBF does not restrict the use of non-compact brace section which may be susceptible to local buckling and rapid fracture due to low cycle fatigue. In comparison, SCBF requires to use compact sections to achieve a more stable post-buckling brace hysteric behavior and longer low cycle fatigue life. Overall, the SCBF is trying to achieve a stable energy dissipation mechanism of brace yielding in tension and buckling in compression by seismic detailing. Without the benefit of ductile detailing, R=3 CBF lacks a controlled yielding sequence and have more possible limit states (Figure 2.1). R=3 CBF offers significant flexibility in design since there is few, if any, prescriptive requirement that the designer need to follow. Therefore, considerable design variation exists among the inventory of R=3 CBF.

2.3 Experimental investigation of low-ductility CBF

There is almost no experimental investigation on the seismic behavior of low-ductility CBF until very recently. These recent tests are not limited to $R=3$ CBF in the ECUS. They also include OCBF with modest ductility and low-ductility (pre-1988) CBF in western United States (WUS). Due to the overall scarcity of the test data, experiments on OCBF and WUS low-ductility CBF are also reviewed as they may also provide insight in the low-ductility structural behavior similar to $R=3$ CBFs.

Sizemore et al. (2015) conducted cyclic static testing on a full-scale one-bay two-story chevron CBF designed with $R=3$ and without any seismic detailing (Figure 2.2). The test showed that $R=3$ CBFs may experience brittle failure mechanism that leads to significant reduction in lateral resistance from braces. For example, local buckling occurred in the non-compact braces in the second story (Figure 2.3 (a)), which leads to a significant degradation in the brace force and rapid fracture due to low cycle fatigue (Figure 2.3 (b)). However, it also demonstrated that the so-called “reserve capacity”, lateral force resisting mechanisms outside of the primary load path (from braces) can still provide considerable strength and ductility after brittle failure happens in the primary load path. For instance, after the brace-gusset connection fracture (Figure 2.4 (a)), the brace is still able to maintain its resistance in compression by re-engaging the gusset plate with the edge of the brace slot (Figure 2.4 (b)). The system with only one intact brace can also develop a “long link EBF system” and maintain ductile and stable lateral force response up till 6% of drift (Figure 2.5). It is worth noticing that, the brace-gusset plate weld connection, which was expected to fracture naturally during the loading due to lack of capacity design, did not fracture under

original loading protocol (likely due to material overstrength or actual construction condition) and had to be manually weakened in order to fracture. This manifests the uncertainty associated with the failure mechanism and response of low-ductility CBFs: brittle failure (e.g. weld fracture) is not bound to occur even though seismic detailing is lacking.

Bradley et al. (2015) conducted cyclic testing on a full scale one-bay two-story split-X OCBF (Figure 2.6). This OCBF has modest seismic detailing compared to the R=3 CBF that has no seismic detailing at all. The frame exhibited ductile behavior up to 1.5% of drift by brace yielding and buckling. During this stage, the braces did not suffer from local buckling and had stable post-buckling hysteresis (Figure 2.7). This can be attributed to the compact section of the braces. The frame then experienced brittle fracture in one of the brace-gusset plate connection weld (Figure 2.8). Ironically, this weld fractured even though it had been capacity designed while the weld in R=3 CBF tested by Sizemore et al. (2015) could not fail naturally even with no seismic detailing at all. This in another perspective reflects the uncertainty associated with the damage mechanism and seismic response of low-ductility CBFs. Brace re-engagement was also observed upon loading in the opposite direction which gave the frame almost the same strength in the previous cycles. Gusset plate-beam connection weld fracture happened a few cycles later and the frame's capacity was substantially reduced.

Experimental investigations of low-ductility CBF also exist at component level focusing on exploring the sources that provide reserve capacity. Davaran et al. (2014) tested 6 typical brace gusset connection specimens to investigate the effect of brace-reengagement (Figure

2.9). It was found that the typical slotted-tube gusset plate fillet weld connection can develop brace re-engagement in compression after connection damage or fracture. The compressive strength of brace re-engagement depends on the failure mode of the connection. It ranges between $0.38P_y$ and $0.16P_y$ where P_y is the nominal yield strength of the brace section (Figure 2.10).

Stoakes and Fahnestock (2011) investigated the cyclic flexural response of beam-column connections with gusset plate in CBFs (Figure 2.11). It is found that these connections possess considerable strength and ductility that is ignored in the design stage (Figure 2.12). The significant flexural strength and deformation capacity provide a source of reserve lateral force resistant capacity in low-ductility CBF as they can increase the frame action after brace fractures.

Sen et al. (2016a) examined the cyclic response of 4 two-story one-bay chevron CBF specimens representing a typical low-ductility CBF design in west coast along with 3 rehabilitation schemes (Figure 2.13). The low-ductility CBF is designed with a weak beam that may yield under the unbalanced brace force in the post-buckling stage. However, the weak beam design is found able to provide comparable lateral strength and deformation capacity with the strong beam design, provided that other ductile detailing is applied (Figure 2.14). The test also shared some similar findings with Sizemore et al. (2015) such as that non-compact brace section will suffer from severe local buckling and will fracture at very small drift level. Contrary to the second story of the specimen in Sizemore et al. (2015) in which both brace buckled, the first story of specimen 1 in (Sen et al. 2016a) only have one brace buckled (Figure 2.15 (a)). The other brace suffered from connection fracture

in later cycles (Figure 2.15 (c)). Both 2 specimens have the same brace configuration and are designed without seismic dealings. Their different failure hierarchies corroborate the uncertainty associated with the response of low-ductility CBFs.

Simpson et al. (2013) conducted cyclic testing on a two-story one-bay chevron NCBF (Figure 2.16). The braces in the second story buckled at around 0.4% of roof drift. Local buckling occurred and the brace force significantly deteriorates. The brace fractured rapidly in subsequently cycles at 0.9% of roof drift (Figure 2.17). The test further demonstrated the detrimental effect of local buckling in non-compact brace sections.

Sen et al. (2016b) conducted cyclic testing on 8 one-bay one-story low-ductility CBF specimens with a single diagonal brace (Figure 2.18). The impact of different brace and connection deficiency was examined in the study (Figure 2.19, Figure 2.20). The non-compact braces and inadequate brace-gusset plate weld was found to be the most detrimental design deficiency to the drift capacity of the structure. The weld joining gusset plate to the frame was found susceptible to fracture even if they have sufficient strength according to brace yielding capacity (but not the gusset plate yielding capacity). More rotational clearance in the gusset plate is found to be correlated with increased drift capacity. Shear plate bolt fracture has limited influence on the structures' performance and is deemed a low priority in retrofit.

2.4 Analytical investigation of low-ductility CBFs

Analytical investigations on the seismic performance on low-ductility CBFs precede recent experimental investigation. Therefore, numerical models employed in those studies were

not validated by the recent test data and failed to capture many critical behaviors. Besides, numerical analysis technique back then was not as robust as today, which causes lots of numerical convergence problems in the dynamic analysis. In addition, there was no standardized methodology in performance evaluation such as FEMA P695.

The first analytical study on low-ductility CBF is from Gryniuk (2008) who investigated the collapse performance of multiple benchmark R=3 Chevron CBFs in Boston, Ma using the software package Ruaumoko (Carr 2004). A set of 28 GMs at MCE level is applied to the 5 models with different height for nonlinear time history analysis. He concluded that structures with inadequate connection strength are more likely to collapse than those with enough connection strength. However, critical issues exist in terms of the validity of the analytical model. For example, the brace connection is modeled as a strength degradation hysteresis model that cannot fracture immediately after capacity is reached (Figure 2.21). The brace model is admitted by the author himself to be not reliable as it does not consider limit state such as brace fracture. Furthermore, the collapse criterion is defined as the point when the analytical model fails to converge. This is inappropriate because nonlinear analysis code of poor quality may cause the analysis to terminate prematurely due to convergence problem without reaching actual collapse.

Hines et al. (2009) studied the seismic collapse capacity on 11 low-ductility CBFs with four different heights and three different R factors designed for seismic load of Boston. In addition, the performance of a braced frame designed for wind load only coupled with a light moment frame reserve system, called “wind plus reserve system” is also examined. Gravity load systems were explicitly modeled to account for their lateral force resistance

as “reserve capacity”. The authors found that R=3 CBF has an approximately 30% probability of collapse under MCE hazard level. The paper concludes that reserve capacity from the gravity load system is more effective in collapse prevention than strength of the primary system. However, the authors reported significant numerical convergence difficulties when trying to model damage to the structure such as brace buckling and fracture. As a result, some simple hysteresis models are used which compromises the accuracy of the model (Figure 2.22). In addition, the author assumes in the numerical model that the brace weld connection will fracture at nominal strength while the brace buckling strength employs the expected buckling strength. Since it is well established that the weld material is significantly over-strengthened, this unfairly assumes that all weld will fracture in R=3 CBF. It can also be clearly seen from the IDA curves that many analyses failed to converge at early stage (Figure 2.23). Many non-converged results are even defined as the collapse point, which makes the obtained collapse capacity questionable. Furthermore, the effect of brace re-engagement that is revealed by later testing (Sizemore et al. 2015) is not modeled.

Hines et al. (2011) pointed out the challenge of numerical modeling of low-ductility systems due to discontinuity in strength and stiffness. Numerical convergence in the nonlinear collapse analysis is more difficult to achieve than the ductile systems. In the absence of test data, they cross validated the analysis result from a simplified model in OpenSees and Ruaumoko in order to strengthen confidence in the collapse modeling. The authors admitted that solving convergence problems is still a mystery to them. The authors also pointed out the need for large scale test data to improve modeling accuracy.

Li and Fahnstock (2013) studied the seismic response of single-degree-of-freedom (SDOF) systems representing low-ductility CBF with reserve capacity (Figure 2.24). Consistent with Hines et al. (2009), they also found that increasing the primary LFRS strength only provides a small performance enhancement and more uniform performance enhancement is obtained by increasing the reserve capacity. But the strength of the reserve capacity has to be more than 60% of the primary LFRS in order to reliably achieve collapse prevention in moderate seismic zone. Therefore, they indicate that typical CBFs may not have adequate inherent reserve capacity for collapse prevention. However, the authors also pointed out that the simplified nature the SDOF model may render the result conservative and more complex model that accurately capture the evolution of damage is needed to study the behavior of low-ductility CBF.

Sizemore et al. (2014) studied the effect of various types of reserve capacity, including enhanced beam column connection with seat angle, brace re-engagement in compression and column base fixity, on collapse capacity on R=3 CBF. It is found that column base fixity, especially those in the gravity load system, can dramatically increase the collapse capacity (Figure 2.25). The prototype structure is modeled using OpenSees with substantial increase in model sophistication compared to earlier numerical studies. However, the model still made several unjustified assumptions. For example, it is presumed that the weld will always fracture before brace buckles. In addition, it is assumed that after the failure of the first brace connection weld, the weld connection in the remaining brace will fracture at 1% of story drift regardless. These assumptions are later invalidated by their own experiment (Sizemore et al. 2015). While the modeling approach is adequate in determining the relative importance of different sources of reserve capacity in collapse

prevention, it is not suitable for investigating the absolute collapse performance on R=3 CBFs.

Sen (2014) developed high resolution finite element models in Abaqus to reproduce the response of four low-ductility CBF test specimens (Figure 2.26). The models agree well with the experiment result (Figure 2.27). However, the model is not able to simulate weld fracture without a priori knowledge of the test result. The weld elements in the model are manually deleted at the instance of actual fracture in the test. Furthermore, the computational cost of this model is expected to be very high and may not be suitable for IDA in collapse analysis.

Shen et al. (2015) studied the near-collapse behavior of low-ductility CBF with focus on the influence of gravity load system. Three different ways of modeling the lateral forces resistance of the gravity load system is investigated. It was found that the inclusion of lateral resistance from gravity load system significantly increases the collapse capacity of low-ductility CBF. For example, the collapse capacity increases by a factor of 3 for the three-story building and the ground motion used in this study. However, the brace connection is not modeled in a realistic way which assumes a fracture capacity equal to the brace buckling capacity. In addition, the study only involves with one ground motion and cannot speak for the general situations.

2.5 Summary

It can be seen that the seismic behavior and performance of low-ductility CBFs has received more and more attention from the engineering community. Significant progress

has been made recently in the experimental research in low-ductility CBF which increases our understanding on their seismic behavior and features. They are summarized as follows:

- Low-ductility CBFs can develop brittle damage mechanism such as weld connection fracture, brace local buckling, etc. These damage states are rarely seen in SCBFs.
- Low-ductility CBFs can develop significant reserve capacity after brittle damage happen to the braces.
- The response of low-ductility CBF is subjected to uncertainty. Some brittle limit states may not happen even if they are not designed with seismic detailing. Alternative failure hierarchies may develop into different response path to ultimate failure.

These test results also serve as an opportunity to facilitate more accurate numerical modeling of low-ductility CBFs. However, most analytical studies on the seismic performance of low-ductility CBFs were conducted before recent tests. The numerical models used in those studies have not benefitted from the recent test data which can help improve accuracy. They also have significant drawbacks which are summarized below:

- Due to limitation of modeling technique at the time of the research, many models lack simulation accuracy. They also do not incorporate important behavior that is revealed by later experiment, e.g. brace re-engagement;
- Many numerical analyses suffer from numerical convergence problems due to limitation on robust of numerical solution technique at the time of the research;

- Many numerical models neglect the uncertainty associated with the property and response of low-ductility CBF and make unfair or oversimplified assumption;
- The collapse analysis is not conducted under systematic collapse assessment methodology such as FEMA P695

While these numerical analyses provide some preliminary observations on the seismic behavior and performance of low ductility CBF, they are far from adequate and comprehensive. More research is needed to evaluate the performance of low-ductility using more accurate numerical models that are validated by recent test data and consider the effect of various sources of uncertainty.

Table 2.1 Design requirement for different CBF systems

Item	R=3 CBF	OCBF	SCBF
R	3	3.25	6
Required tensile strength for brace connection	P_u	$\Omega_0 P_u$ capped by $R_y F_y A_g$	$R_y F_y A_g$
Required compressive strength for brace connection	P_u	$\Omega_0 P_u$ capped by $\min(R_y F_y A_g, 1.14 F_{cre} A_g)$	$1.1 \min(R_y F_y A_g, 1.14 F_{cre} A_g)$
Brace expected buckling strength	-	$\min(R_y F_y A_g, 1.14 F_{cre} A_g)$	$\min(R_y F_y A_g, 1.14 F_{cre} A_g)$
Lateral bracing of beam	-	At least one set of lateral bracing required at the braces intersection point	At least one set of lateral bracing required at the braces intersection point
Strength of beam under unbalanced load	-	Tension brace: $\min(R_y F_y A_g, \Omega_0 P_u, P_{max})$ Compression brace: $0.3 P_n$	Tension brace: $R_y F_y A_g$ Compression brace: $0.3 \min(R_y F_y A_g, 1.14 F_{cre} A_g)$
Net section reinforcement	-	-	Required
Gusset plate rotation capacity	-	-	$2t$ clearance
Brace b/t	-	Compactness limit (b/t) for moderately ductile member	Compactness limit for highly ductile member
Brace KL/r	-	$KL/r \leq 4\sqrt{E/F_y}$	$KL/r \leq 200$
<p>Note:</p> <p>P_u: required strength (factored load)</p> <p>Ω_0: overstrength factor</p> <p>R_y: expected to nominal yield strength ratio</p> <p>F_y: nominal yield strength</p> <p>F_{cre}: brace buckling strength using expected material yield strength</p> <p>P_{max}: the maximum force that can be developed by the system</p> <p>P_n: nominal buckling strength</p> <p>A_g: gross section area</p> <p>t: thickness of gusset plate</p> <p>K: effective length factor</p> <p>L: lateral unbraced length of the member (brace)</p> <p>r: radius of gyration</p> <p>E: elastic modulus of steel</p>			

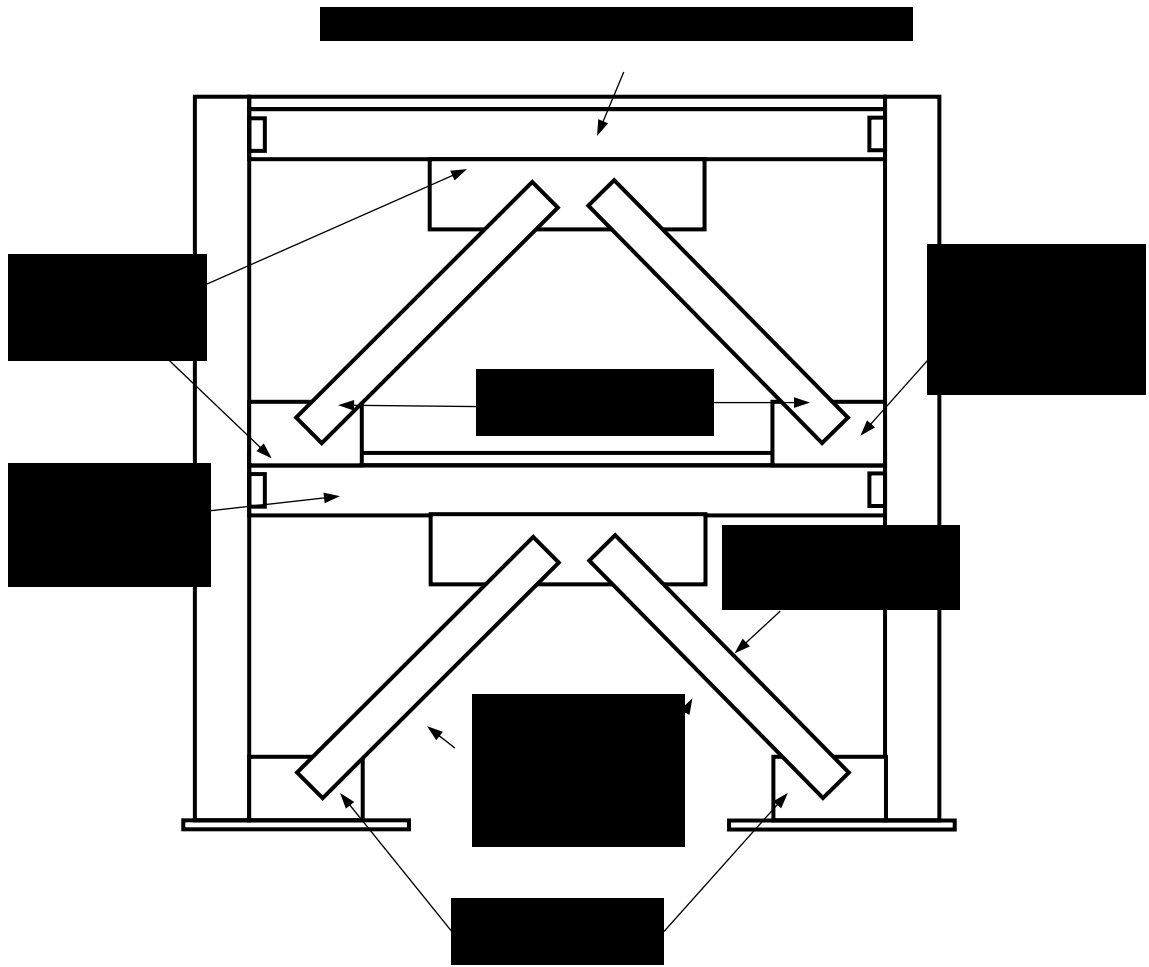
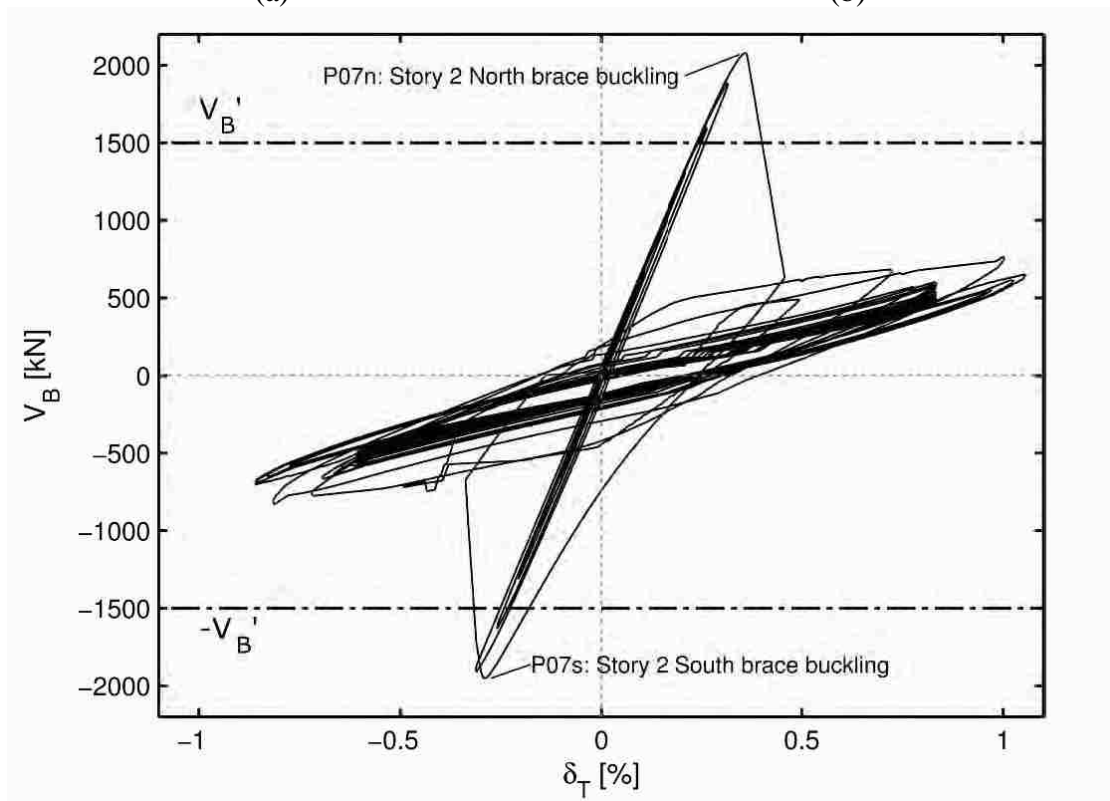


Figure 2.1 Potential limit states unique to R=3 CBF



(a)

(b)



(c)

Figure 2.3 (a) brace local buckling; (b) brace low cycle fatigue; (c) global hysteresis (Sizemore et al. 2015)



Figure 2.4 (a) brace-gusset weld fracture; (b) brace re-engagement (Sizemore et al. 2015)

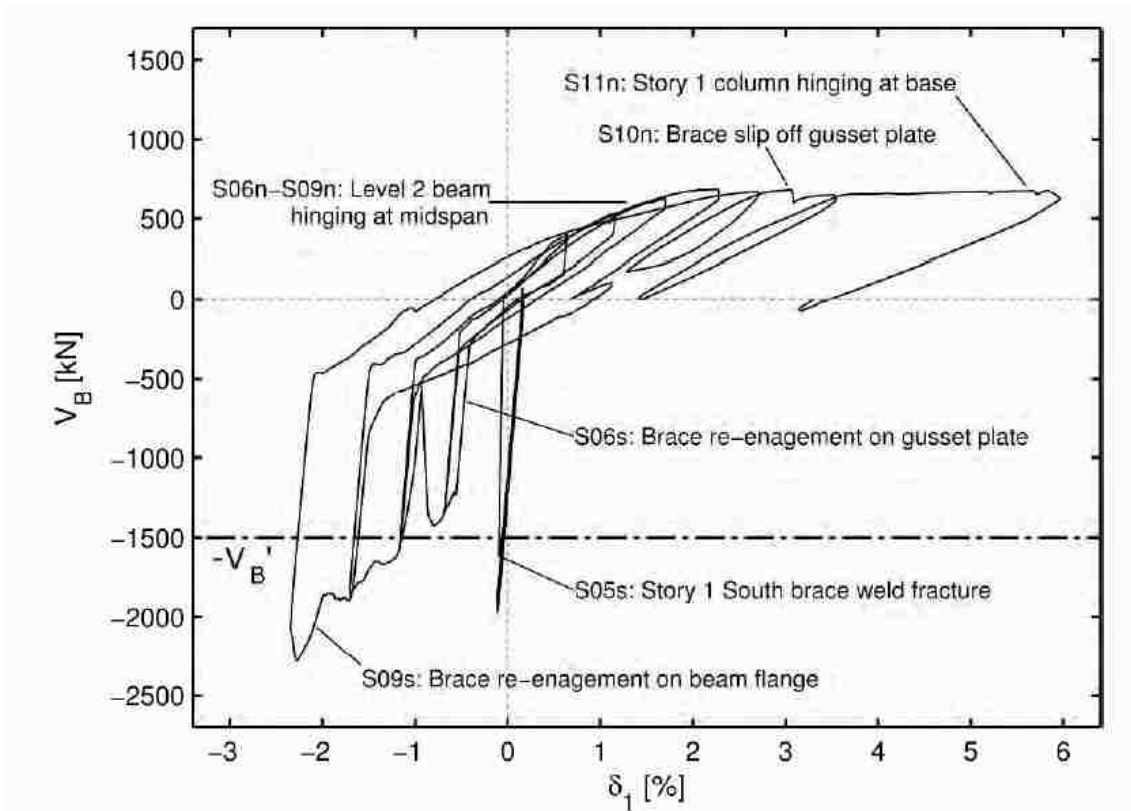


Figure 2.5 Base shear vs Story 1 Drift (Sizemore et al. 2015)

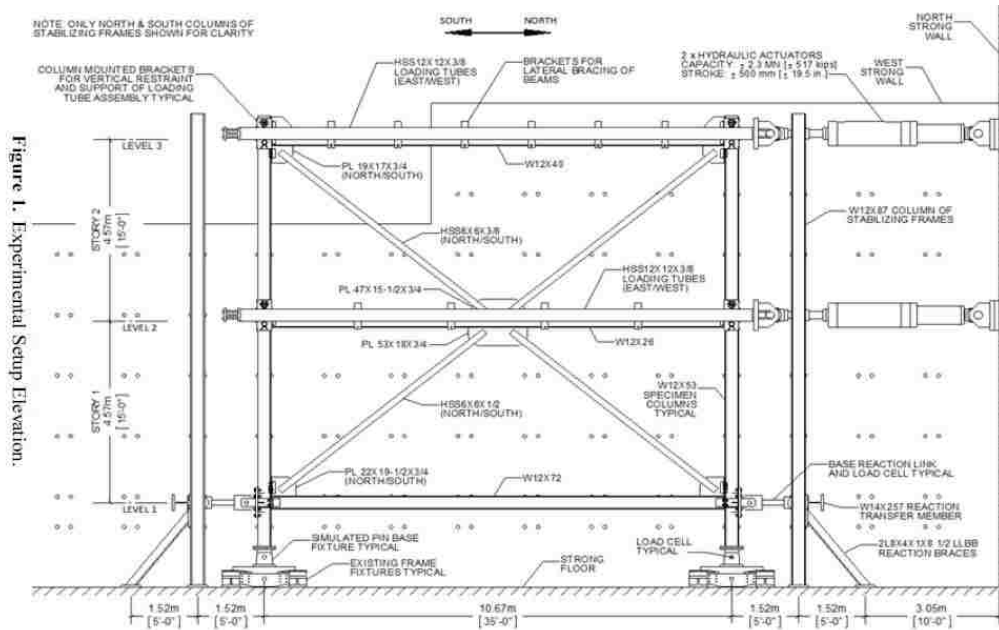


Figure 1. Experimental Setup Elevation.

Figure 2.6 Test specimen and setup (Bradley et al. 2015)

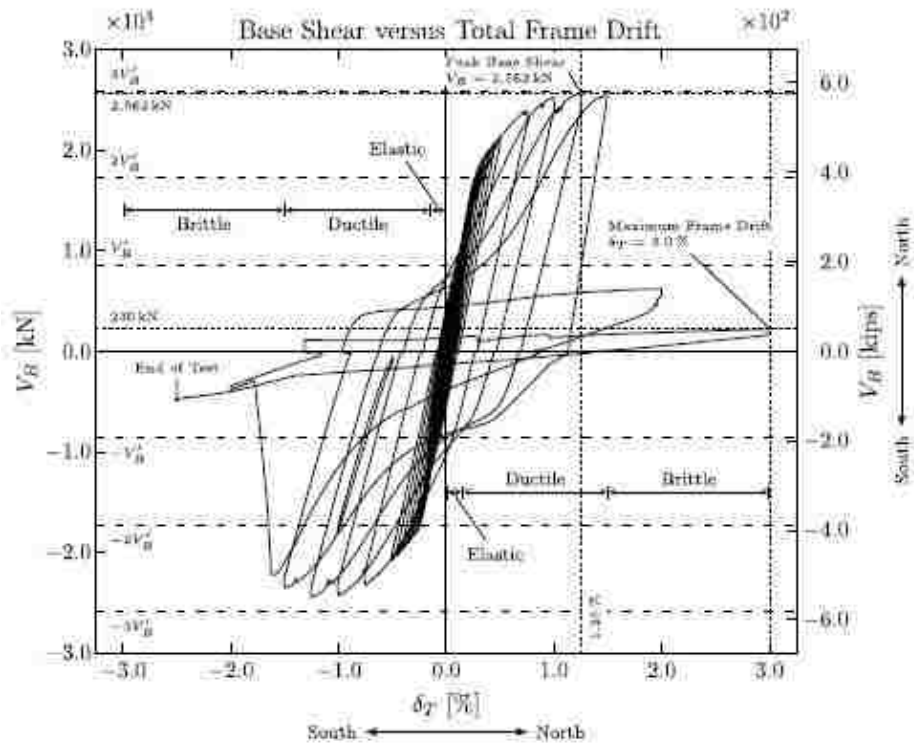


Figure 2.7 Test hysteretic behavior (Bradley et al. 2015)

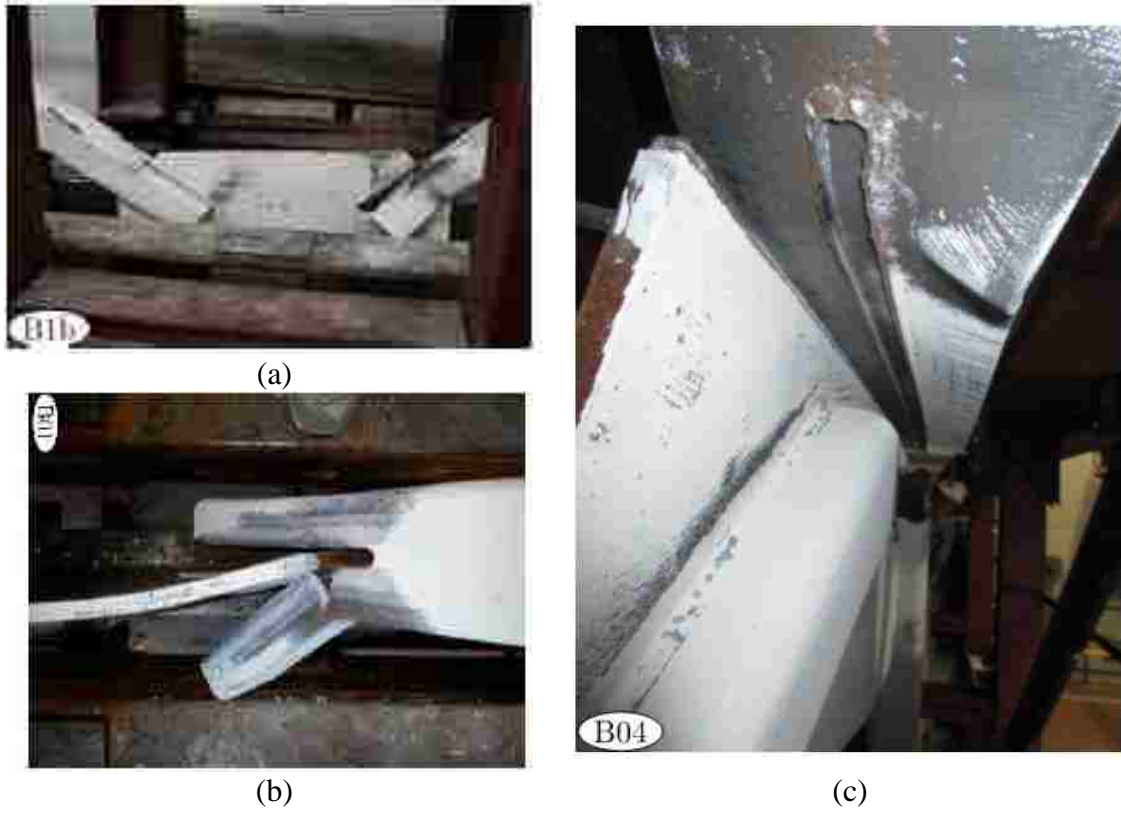


Figure 2.8 Weld fracture during the test: (a)&(b) fracture of story 1 upper mid span brace gusset connection; fracture of story 1 bottom mid span beam gusset connection (Bradley et al. 2015)

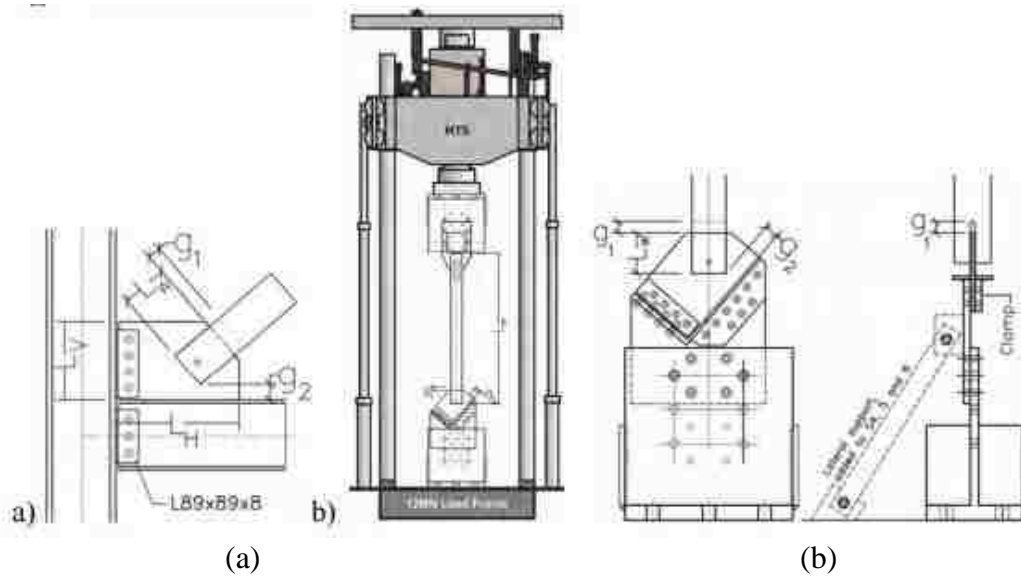


Figure 2.9 (a) Typical CBF connection studied (b) Test setup (Davaran et al. 2014)

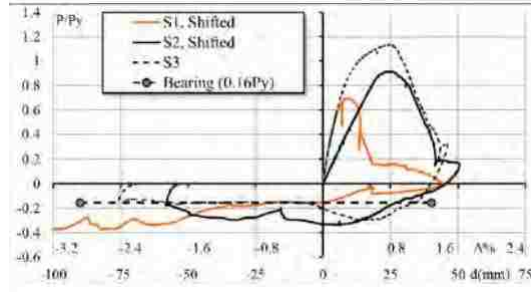


Figure 2.10 Hysteresis behavior of brace re-engagement (Davaran et al. 2014)

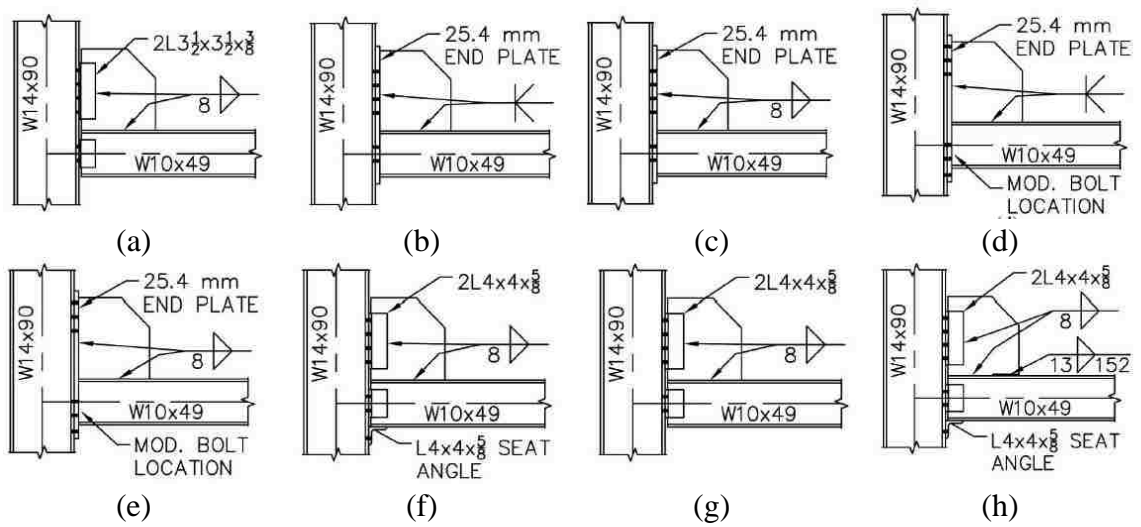


Figure 2.11 Connection details: (a) CN1; (b) CN2; (c) CN3; (d) CN4; (e) CN5; (f) CN6; (g) CN7; (h) CN8 (Stoakes and Fahnestock 2011)

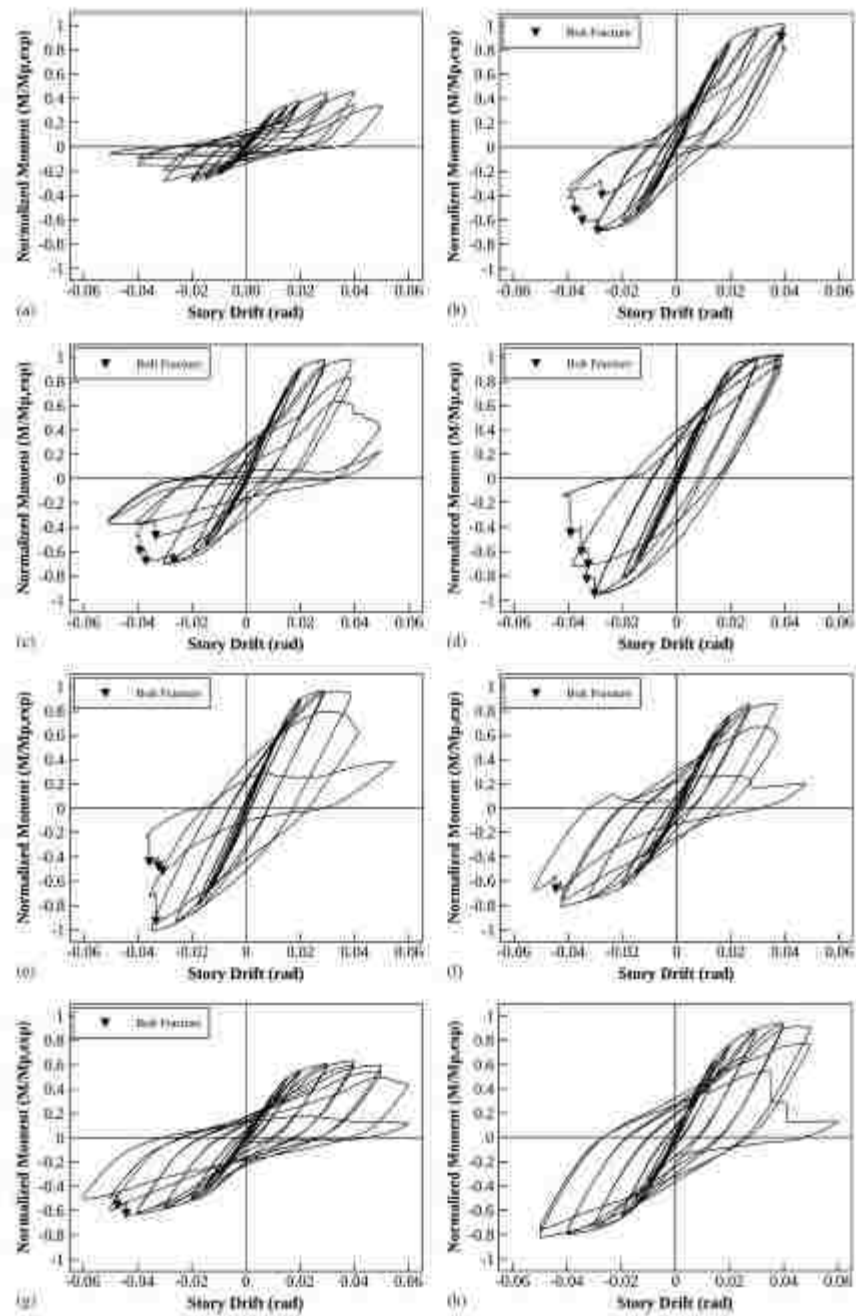


Fig. 7. Normalized moment) versus story drift: (a) CN1; (b) CN2; (c) CN3; (d) CN4; (e) CN5; (f) CN6; (g) CN7; (h) CN8

Figure 2.12 Normalized moment versus story drift: (a) CN1; (b) CN2; (c) CN3; (d) CN4; (e) CN5; (f) CN6; (g) CN7; (h) CN8 (Stoakes and Fahnestock 2011)

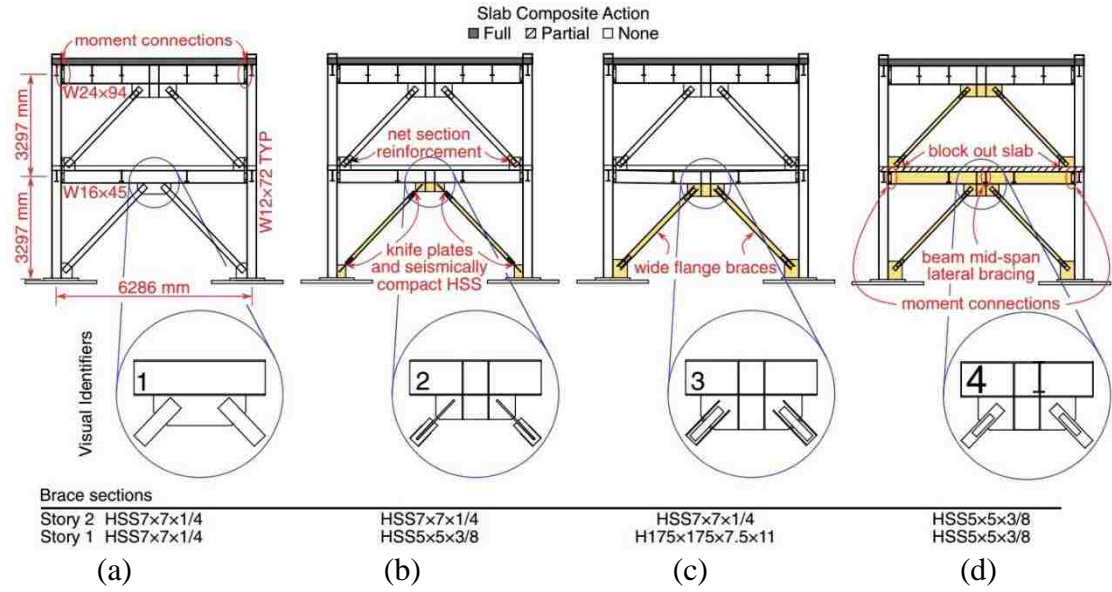


Figure 2.13 Specimen elevation, typical sections and geometry: (a) Specimen 1; (b) Specimen 2; (c) Specimen 3; (d) Specimen 4 (Sen et al. 2016a)

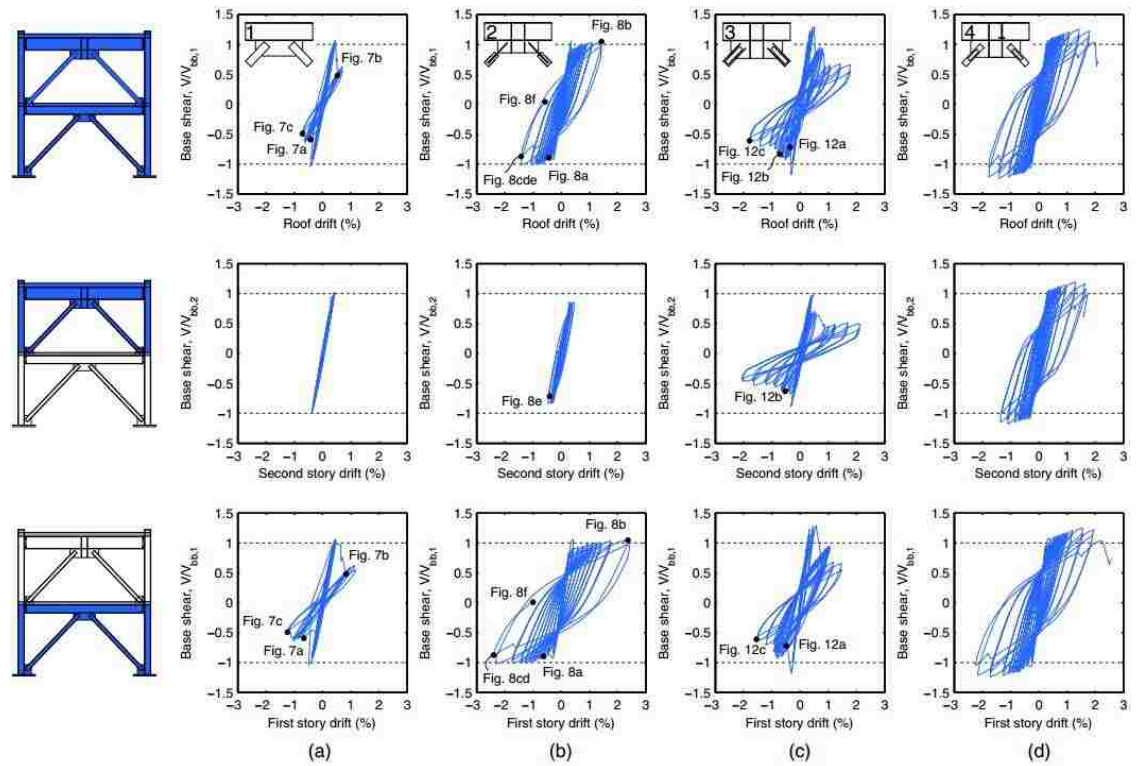


Figure 2.14 Base shear versus drift hysteresis: (a) Specimen 1; (b) Specimen 2; (c) Specimen 3; (d) Specimen 4 (Sen et al. 2016a)

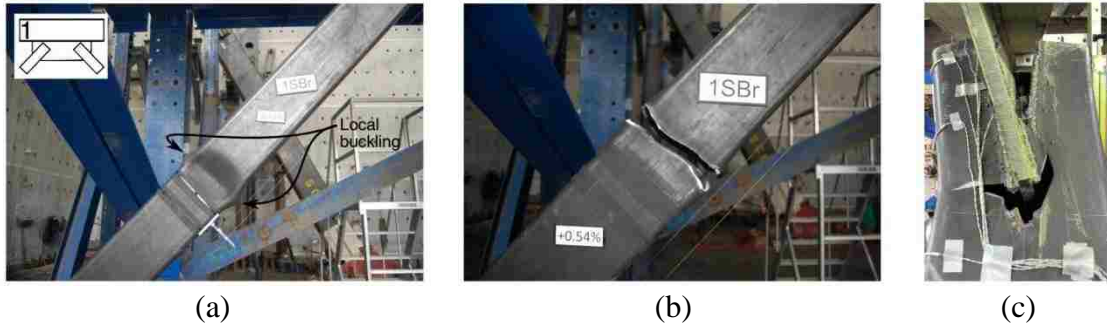


Figure 2.15 Specimen 1 test: (a) a south first-story brace local buckling; (b) a south first-story brace fracture; (c) north first-story brace-to-gusset plate connection fracture (Sen et al. 2016a)

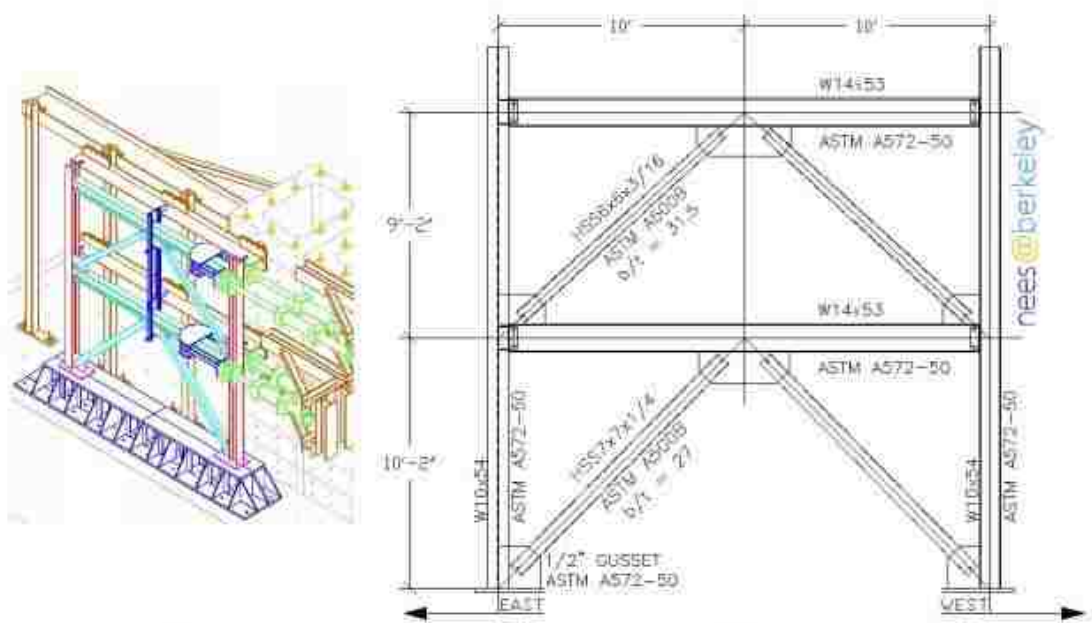


Figure 2.16 Test specimen and setup (Simpson et al. 2013)

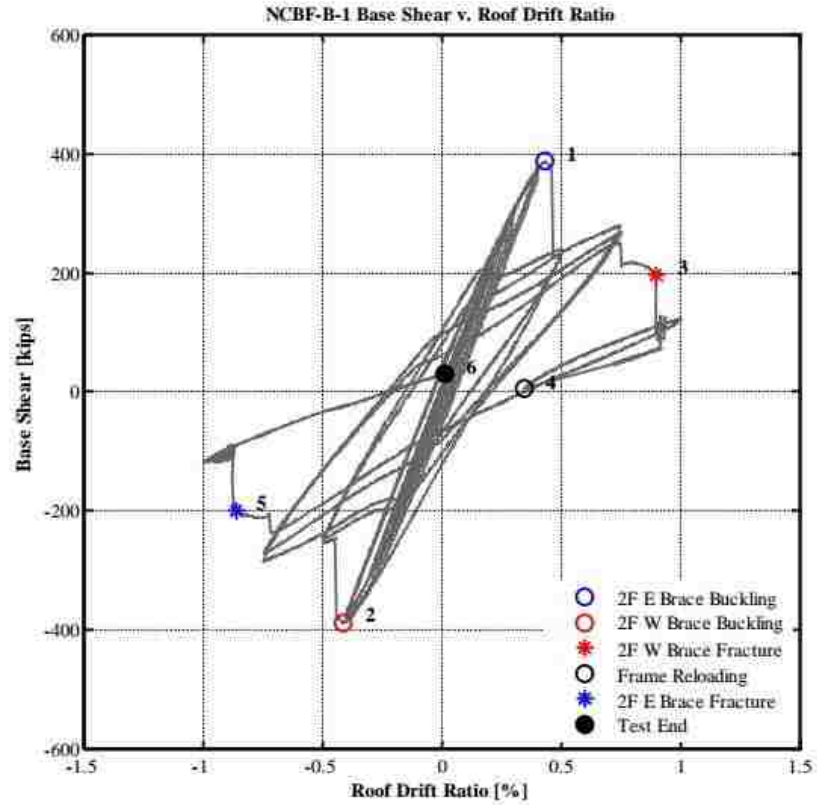


Figure 2.17 Shear vs drift ratio (Simpson et al. 2013)

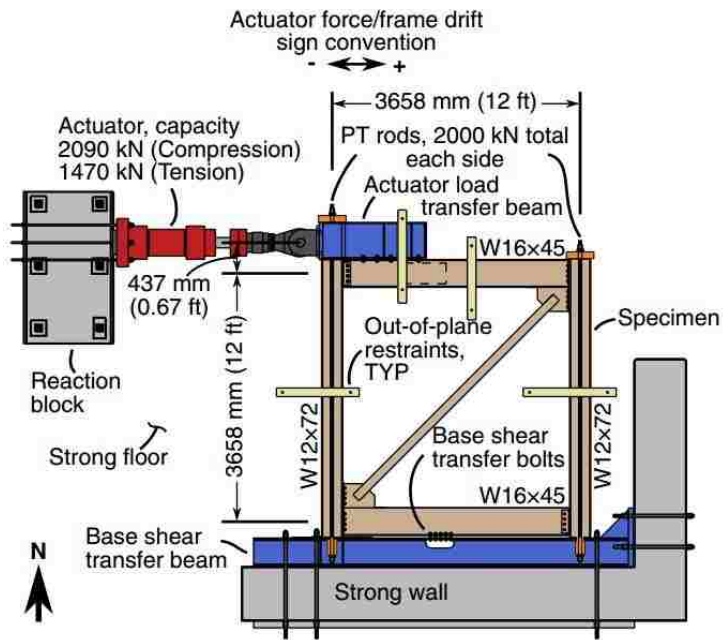


Figure 2.18 Test setup (Sen et al. 2016b)

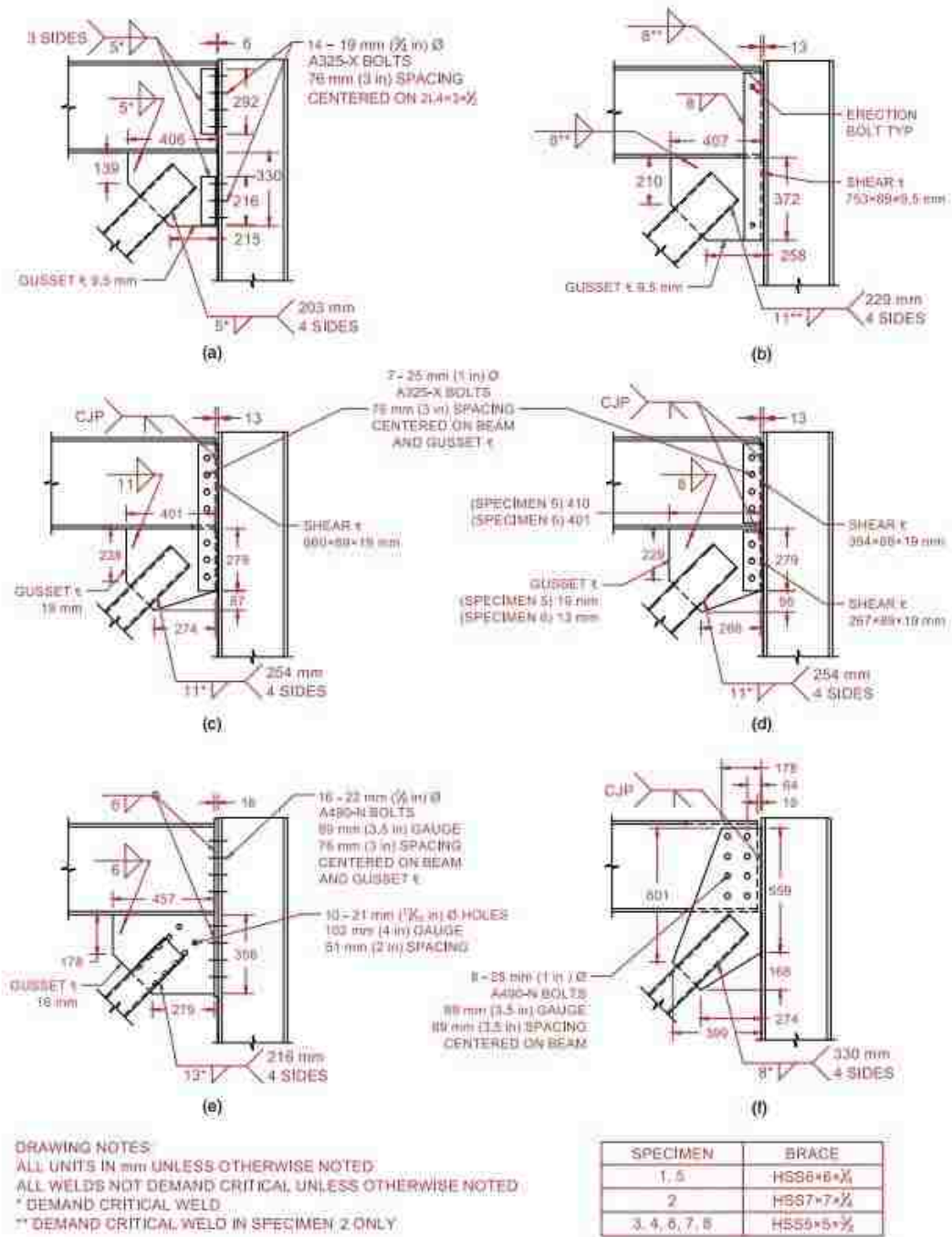


Figure 2.19 Connection detail of test specimens: (a) Specimen 1; (b) Specimen 2 and 3; (c) Specimen 4; (d) Specimen 5 and 6; (e) Specimen 7; (f) Specimen 8 (Sen et al. 2016b)

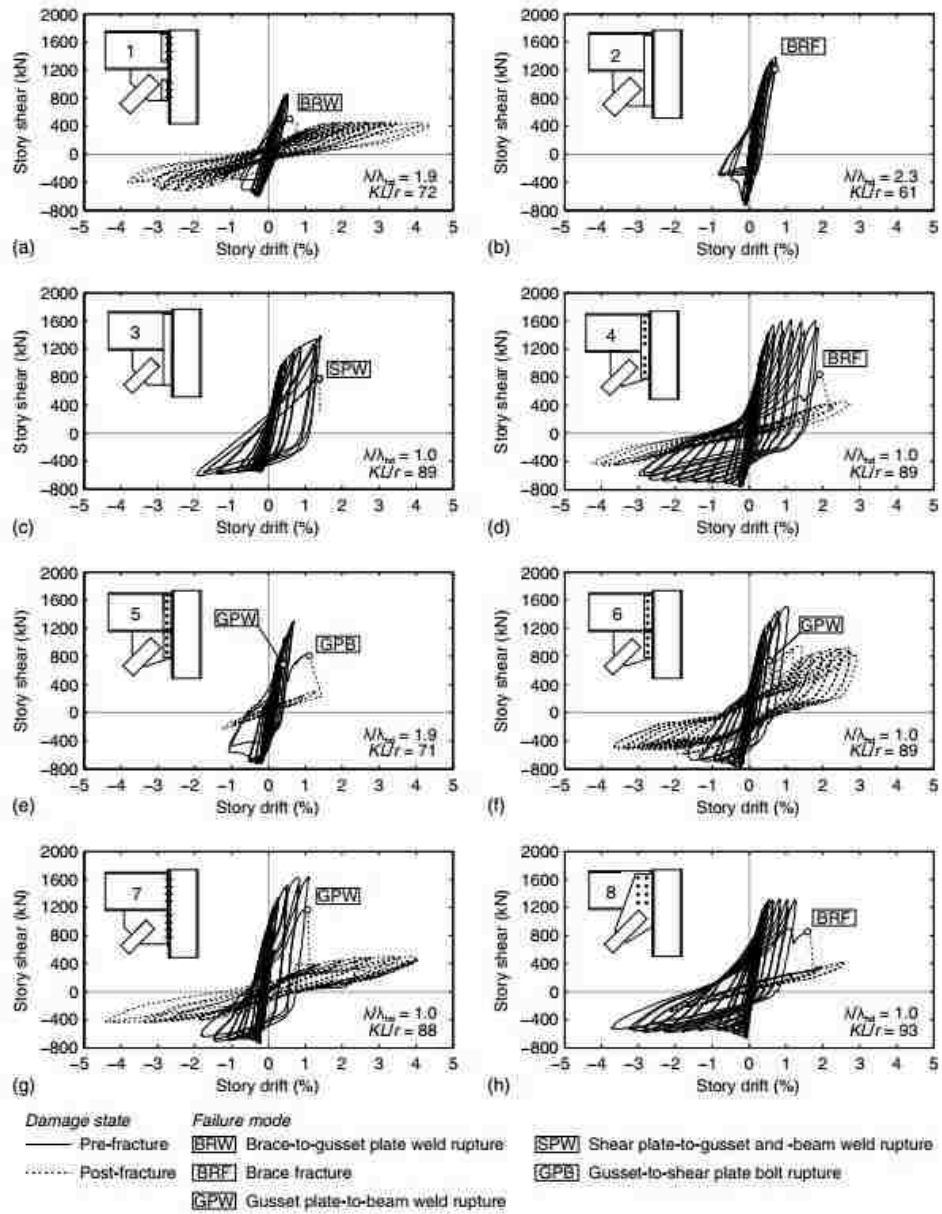


Figure 2.20 Hysteresis behavior: (a) Specimen 1; (b) Specimen 2; (c) Specimen 3; (d) Specimen 4; (e) Specimen 5; (f) Specimen 6; (g) Specimen 7; (h) Specimen 8 (Sen et al. 2016b)

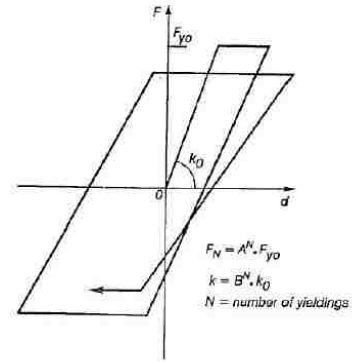


Figure 2.21 Brace connection hysteresis model used in (Gryniuk 2008)

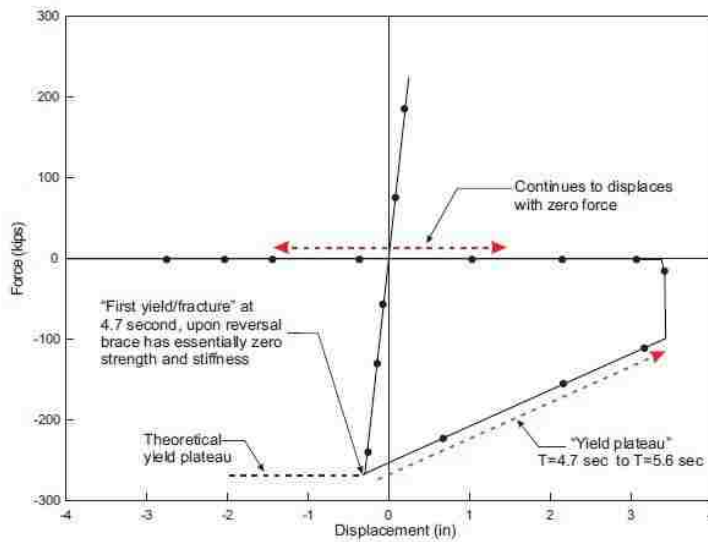


Fig. A-2. A 6-story/R3/GM3 first-story brace hysteresis loop.

Figure 2.22 Brace hysteresis response in one analysis in (Hines et al. 2009)

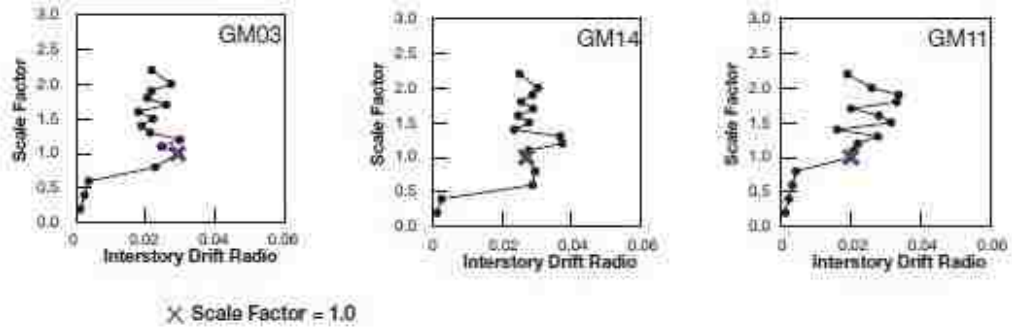


Figure 2.23 Some IDA analysis that show convergence problems in (Hines et al. 2009)

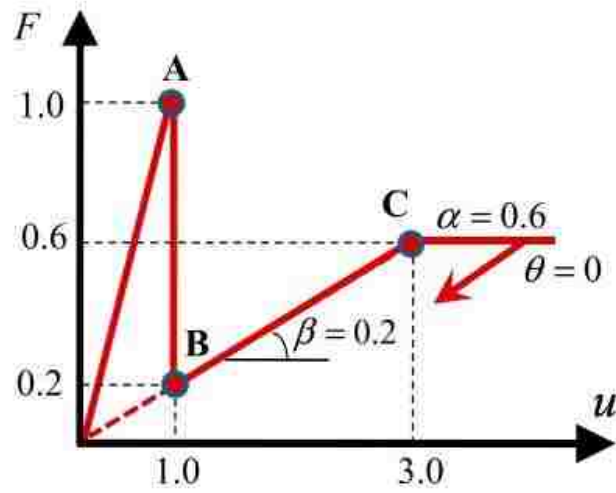


Figure 2.24 Force-deformation relation of SDOF system in (Li and Fahnestock 2013)

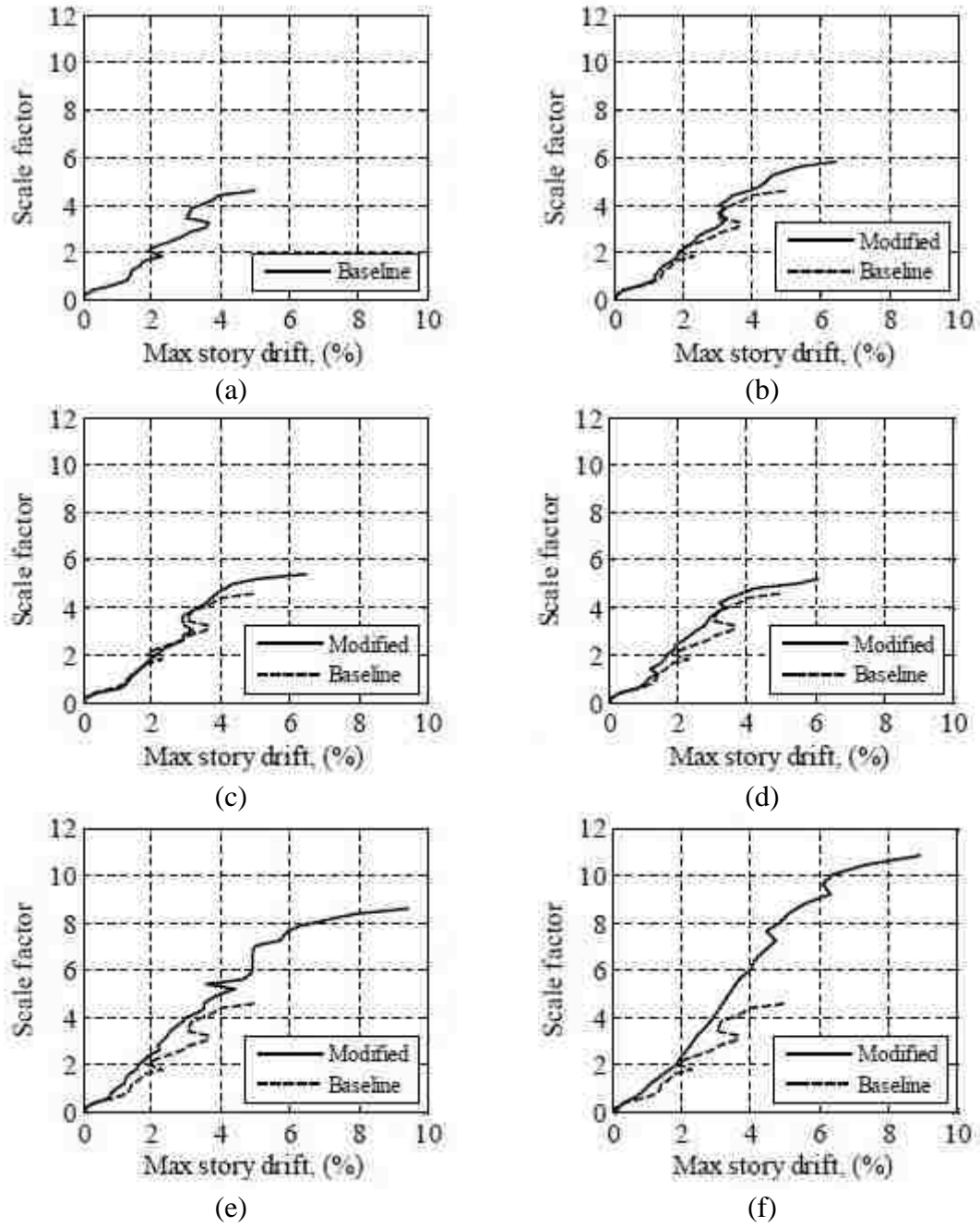


Figure 2.25 IDA of prototype CBF in (Sizemore et al. 2004): (a) baseline; (b) brace re-engagement; (c) enhanced B-C connection; (d) fixed bases in braced frame; (e) all column bases fixed; (f) combined (b) + (c) +(e) (Sizemore et al. 2014)

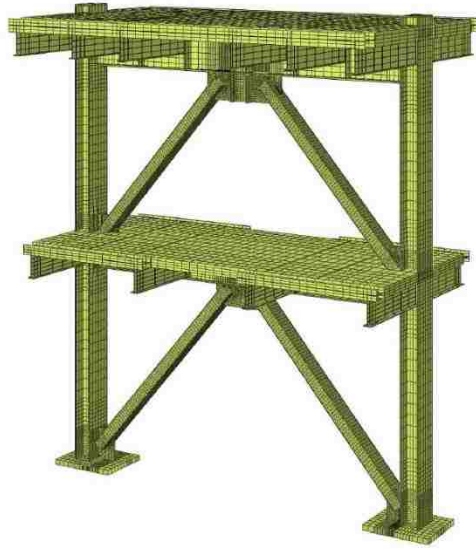


Figure 2.26 Abaqus model in (Sen 2014)

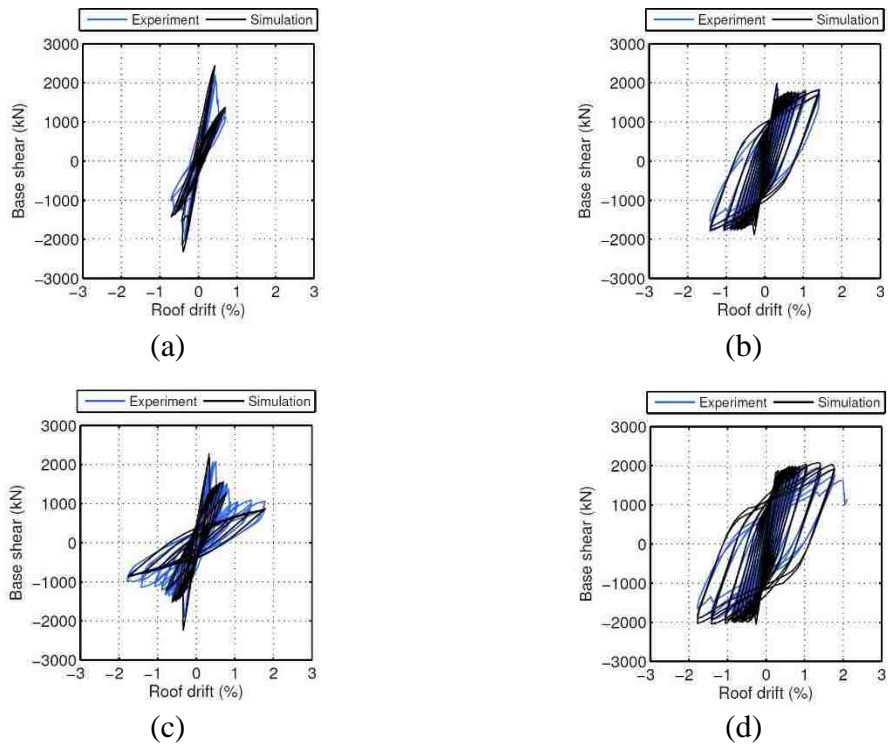


Figure 2.27 Comparison of test result with FEM simulation: (a) Specimen 1; (b) Specimen 2; (c) Specimen 3; (d) Specimen 4 (Sen 2014)

Chapter 3

Response simulation and performance assessment of an ECUS CBF during 2011 Virginia earthquake

3.1 Introduction

This chapter presents the simulated response and performance assessment of the Smithsonian Institute Museum Support Center (MSC), an existing ECUS CBF, during the 2011 Virginia earthquake. The Virginia earthquake and the engineering background of the building is first introduced. Next, the result of post-earthquake damage reconnaissance is presented. Finite element models (FEM) of the building were created to simulate the response of the structure during the earthquake and to investigate what caused the damage. Fragility analysis is conducted to develop fragility curves for structural as well as nonstructural damage. The non-collapse performance of the structure is evaluated by calculating the probability of exceeding various limit states under multiple hazard levels. The work in this chapter is based on the 2 papers (Chu et al. 2014, 2017) published by the author.

3.2 Virginia earthquake and building description

On 1:51 PM August 23, 2011, a magnitude 5.8 earthquake occurred in Mineral, Virginia. The 2011 Virginia earthquake, with a maximum perceived intensity of VII (very strong) on the Mercalli intensity scale, is the largest earthquake to strike the Central and Eastern United States (CEUS) in 70 years (Hough 2012). Research shows that the earthquake occurred as a shallow reverse rupture comprising of three sub-events (Chapman 2013). The

earthquake, although centered in central Virginia, was felt as far north as Canada and caused substantial damage to structures in the Washington D.C. Metro area that is about 90 miles away from the epicenter. Among those structures, the MSC experienced significant structural as well as non-structural damage.

The MSC (Figure 3.1(a)) is a museum warehouse complex for the conservation, study and storage of the off-display artifacts, which is located in Suitland, MD, approximately 6 miles southeast of Washington D.C. The 700,000 square feet zigzag-shaped complex is divided into three parts: the five “Pods”; five Offices; and an interconnecting corridor called the “Street” (Figure 3.1(b)). The Pods are one-story high bay concrete frames with in-filled masonry walls while the Offices are 2-story in-filled masonry precast concrete frames designed between 1979 and 1980. More information about the concrete structure can be found in Chu et al. (2014).

Inside each of Pods 1 and 2 is a 2-story steel mezzanine that was designed in 1988 and later added to the existing concrete structure. The mezzanine is anchored to the ground floor of the existing concrete structure by expansion bolts. With a two-inch gap between the perimeter edge of the floor slabs and the outer masonry walls of the Pod (Figure 3.2(a)), the mezzanines are designed and constructed to be structurally independent from the existing concrete frame, except for sharing the same foundation with the concrete structure. The mezzanines are steel concentrically braced frames with diagonal cross bracing in two orthogonal directions of the structure (Figure 3.2(b)). As each of the mezzanines has a longer dimension in the N-S direction than the E-W direction (Figure 3.2(b)), the N-S direction is referred to as long direction of the building while the E-W direction is defined

as short direction. A typical configuration of the braced bays is shown in Figure 3.2(c). The diagonal bracing comprises of A36 steel rectangular bars of 2”×0.25” size. The columns are A500 (Grade B) steel HSS sections including HSS3×3×5/16, HSS3×3×1/4, HSS4×2×1/4 and HSS6×2×1/4, while the beams are A36 W shapes including W6×9, W6×12, W6×15, W6×20 and W8×31. The floor system employs a composite slab with 6” thick concrete cast on top of metal decking supported by steel beams. The UBC 1985 was employed in the seismic design of the mezzanines. As capacity design is not introduced in UBC until 1988, this structure was designed without seismic detailing and belongs to low-ductility CBFs.

3.3 Damage reconnaissance

Following the earthquake, damage reconnaissance of the structure was conducted by an EERI reconnaissance team (Beavers et al. 2012; EERI 2011) as well as the author in subsequent reconnaissance. The 2011 Virginia earthquake resulted in wide-ranging damage to both the concrete and steel structures of the MSC. Typical damage observed in the concrete frames includes concrete spalling, T-beam sliding at the roof and cracking in the in-filled wall (Figure 3.3). Failure of a RC beam-column joint was found (Figure 3.3(a)) near the roof level at a corner of Office 1. This specific failure consists of concrete spalling at the ends of the beam and columns adjacent to the joint, buckling of the rebar and falling of the tile façade at the upper half of the corner. Figure 3.3(b) shows a crack of about ½” width in a masonry wall of Office 2 which extended throughout the entire height of the second floor. Other observed damage included at least five T beams in different locations having slid from their bearing. For example, Figure 3.3(c) shows sliding of a precast roof

T-beam in Pod 2 that had slid from its support bearing for about 2-inches. Cracks in the masonry wall were also observed in a number of places.

Damage was also observed in both steel mezzanines in Pods 1 and 2. However, the mezzanine in Pod 1 suffered more extensive damage than that in Pod 2. The type of damage included brace buckling and yielding at both stories, in addition to brace fracture and anchor bolt failure at the ground level. The second story sustained less damage than the first story, with only some minor yielding and buckling. Figure 3.4 shows the location and condition of damage of the steel mezzanine in the first story of Pod 1. The braces in the N-S direction of the structure and anchor bolts in some of the braced bays suffered significant damage. In contrast, there were no signs of structural damage in any of the beams or columns and the diagonal braces in the E-W direction of the structure. Among the damaged braces in the N-S direction, those in the east perimeter suffered more significant damage in the form of yielding and buckling than their counterparts along the west perimeter of the structure. In addition, in a braced bay near the south-east corner of the floor plan both diagonal braces had fractured.

The nonstructural (storage content) damage is observed to be mainly associated with the motion of cabinets induced by floor accelerations. The damage can be categorized into rocking (toppling) and sliding. Figure 3.5(a) shows the toppling of a cabinet as a consequence of excessive rocking. Figure 3.5(b) and Figure 3.5(c) show that numerous cabinets stacked on top of other cabinets have slid. Figure 3.5(d) shows the dislodging of some cabinets which may be caused by either rocking or sliding. Figure 3.5(e) shows a damaged artifact stored in a cabinet as a result of cabinet motion.

3.4 FEM simulation of seismic response during Virginia earthquake

The focus of this study is on the steel mezzanine in Pod 1 which suffered the most severe damage among all parts of the structure. Finite element models of the mezzanine were created to simulate the response during Virginia earthquake. A linear model in SAP2000 (Figure 3.6) is first created in order to identify the floor mass parameter through parametric study. The response of the linear model is used to explain what caused the damage and why the damage presents the unique pattern observed from damage reconnaissance. Using the mass parameter identified from the linear SAP2000 model, a nonlinear model is developed in OpenSees for fragility analysis. The OpenSees model is also validated by the modal testing result as well as the observed damage.

3.4.1 Linear model

3.4.1.1 Finite element modeling and model validation

The information obtained from structural drawings was utilized to construct the model. The columns are modeled according to the structural drawings using beam-column elements. Due to the composite action of the floor slab and the relatively small stiffness of the columns compared to the beams, the beams are considered axially and flexurally rigid. Therefore, the structure is modeled as a shear building with each floor modeled using a rigid diaphragm constraint. The methodology of Metelli (2013) is used to evaluate the effective slenderness ratio of the diagonal braces which are welded together at the mid-point. The lower limit for the effective slenderness ratio of braces with out-of-plane buckling is calculated assuming that a brace buckled in the second mode and the out-of-plane motion at mid-point is zero. Due to the variation of the geometry of each bay, the

effective slenderness ratio of the diagonal braces is between 385 and 530, corresponding to a compressive buckling stress of 1.02 to 1.94 ksi (i.e., a buckling load of 0.51 to 0.97 kips). As a result, the straps provide negligible compressive resistance during the earthquake and can be considered to be tension-only members. Therefore, to simulate the tension-only behavior of the braces during seismic response, only one of the crossing bracing members within each braced bay is modeled in the elastic SAP2000 model. The mass of the structure is considered lumped at the center of mass (CM) at each floor level.

However, the effective seismic mass of the structure is unknown. From design information and material property, the self-weight of the structure, including the floor slab and framing system, can be determined as 1770.8 kips per floor. As the steel mezzanine is used to store the off-site artifacts of the museum, the storage cabinets constitute a significant portion of the total weight of the mezzanine. Nevertheless, the exact weight of the cabinet is unknown. From a survey performed by the staff of the MSC the content weight inside the cabinets is estimated to range from 483.7 kips to 1802.1 kips for each floor while the self-weight of all the cabinets amounts to 632.3 kips per floor. A parametric study on the possible content weight distribution and a field vibration test were performed in order to identify the actual mass of the floor.

As there are more than 1000 cabinets on each floor, it will be prohibitively difficult to vary the weight of every single cabinet to obtain all the possible value on the amount and location of floor mass. So instead, seven extreme representative cases of mass distribution are considered, and are shown in the floor plan provided in Figure 3.7. In Cases I, II and VII, all the cabinets have minimum, maximum and average content weight distributed

uniformly over the floor plan of both floors, respectively. In Cases III and IV, the floor plan is trisected along its short direction (EW direction), with all the cabinets within each subarea having the same mass distribution. For example, in Case III, all the cabinets in the 2/3rds of the floor plan towards the east direction have the minimum mass while those in the lower 1/3 of the floor plan in the west direction have maximum mass. In Case V and VI, the floor plan is trisected along its long direction (NS direction), as shown in Figure 3.7(e) and (f).

The location of the center of mass (CM) for each case of content weight distribution and the center of rigidity (CR) are shown in Figure 3.8. A summary of the eccentricity between the CR and CM for each case is given in Table 3.1. The total floor weight and location of CM show a large variance due to a wide range of possible content weight.

A field vibration test was conducted on the mezzanine to capture the modal property of the structure and find the analytical model (among all 7 mass scenarios) that has consistent modal property. Both wired and wireless accelerometers were deployed around the second and third floor to measure the ambient vibrations. System identification algorithm in Chang and Pakzad (2014) is employed on measured acceleration time series to extract the modal property of the structure. Three vibration modes are identified. The modal property of each analytical model in the parametric study of floor mass is compared with the measured modal property. It is found that the model of Case I has a better match with the measured modal property than other cases. Table 3.2 presents the identified periods compared with analytical periods of model of Case I. The measured results have a better agreement with the as-built model when the compression is also modeled. The reason is that the behavior

of the braces is amplitude dependent. At ambient vibration level, the amplitude of the vibration is low, thus the compressive braces will not buckle and can still provide stiffness. However, under earthquake excitation, the vibration amplitude is very large and the braces will buckle at very early stage and are not effective in providing compression resistance. So, during earthquake excitation, it is reasonable to model the braces as tension-only while in ambient vibration tests the compression braces should also be considered. Therefore, the distribution of the content weight is identified as the distribution in Case I and the effective seismic weight of each floor is calculated accordingly.

3.4.1.2 Seismic response simulation and investigation on the reason for damage

Unfortunately, there is no recorded free-field ground motion in the DC region during Virginia earthquake. Therefore, the ground motions at the MSC are generated from ground motions that were recorded in Reston, VA. This process consists of conducting a deconvolution of the Reston surface ground motion into bed rock and then convoluting these motions up to ground surface of at the MSC utilizing measured soil profiles of the region. The detailed description of this method can be found in Shahidi et al. (2015).

The response spectrum of the ground motion at the bed rock and the ground surface level at MSC (rotated to the orthogonal directions of the mezzanine) are shown in Figure 3.9. It can be observed that the spectral response of 0.1s to 1s is significantly amplified by the local soil condition. It appears that soil amplification is one of the reasons that caused structural damage to the MSC, as the natural periods of the MSC fall in this range.

The tension-only model with the floor mass identified as Case I is subjected to the bidirectional ground motion at the ground surface level (Figure 3.9). Figure 3.10 shows the

peak axial tensile stress in the diagonal braces. The peak response is in the braces along the east perimeter, where the stress is as high as 40.4 ksi, exceeding the nominal yield stress of the 36 ksi (A36 steel). In comparison, the response of the diagonal braces along the west perimeter is smaller than their counterparts in the east perimeter. This is consistent with the observed damage pattern (Figure 3.4) in which the east perimeter of the structure suffered more damage than the west side.

By close examination, this unique damage pattern can be attributed to significant coupling between the translational and torsional displacement of the floor diaphragm induced by bi-directional ground motion excitation. The effect of bi-directional excitation is clearly demonstrated by comparing the response of the structure under uni-directional and bi-directional ground motion. Figure 3.11 presents the time-history of lateral displacement in the NS direction for two braced bays located respectively at the east and west perimeter (identified within the red circles in Figure 3.10) under uni-directional ground motion in the NS, EW and bi-directional ground motion, respectively. When the ground motion strikes in the EW direction (i.e., short direction of the building; Figure 3.11 (b)), the displacement demand in the NS (i.e., long direction of the building) direction is comparable to the case when the building is subjected to ground motion in the NS direction (Figure 3.11(a)). In addition, the non-uniform response in braces in the long direction of the building is also caused by ground motion in the short direction of the building. The reason is, in this case, the CR of the first floor deviates from the CM by 13.9' to the south and 1.2' to the east (Table 3.1). Larger eccentricity in the long direction creates a significant component of torsion in the second and third modes (Figure 3.13). In addition, the earthquake in the short direction has much larger magnitude than its perpendicular component, especially at the

second and third modes due to the effect of site soil amplification (Figure 3.12). Consequently, the torsional component from the second and third modes in response to the ground motion in the short direction will impose extra and non-uniform demand on the displacement response in the long direction.

Therefore, the potential causes of structural damage of steel mezzanine in Pod1 of MSC are

- Site soil amplification effect
- Combined effect of torsion and translation response
- Bi-directional earthquake demand

3.4.2 Nonlinear model

In order to perform the fragility analysis, it is important to model the nonlinear behavior of the structure, which is bound to occur as structural damage limit states are reached. Thus, a nonlinear model is created in OpenSees (McKenna et al. 2000).

To include nonlinearity, the columns are modeled according to the structural drawings using nonlinear force-based beam-column elements with fiber sections. A combination of a gap element, elastic-no-compression element and nonlinear force-based beam-column element is used in series to model the tension-only behavior of the strap braces (Figure 3.14). In the same way as the SAP2000 model, the structure is modeled as a shear building with each floor modeled using a rigid diaphragm constraint. The floor mass uses the same value as the SAP2000 model (Case I).

The model is validated using results from vibration tests and the observed damage pattern. The modal periods of the OpenSees model is compared with the results from the vibration tests in Table 3.3. OpenSees is able to calculate the modal periods based on the structural stiffness before and after brace buckling by performing an eigenvalue analysis before and after lateral load is applied to the model. The modal periods of the model with no brace buckling (i.e., pre-buckling) shows better agreement with the test result because the behavior of the braces is amplitude dependent. For the vibration test, the amplitude of the vibration is low and the braces do not buckle and can provide compressive stiffness. However, during seismic excitation the amplitude of vibration is large and the braces buckle (post buckling), and therefore are not able to provide stiffness.

The model is also subjected to ground motions from the 2011 Virginia earthquake. Figure 3.15 shows the peak axial stress response in the braces in the first story. It presents a pattern consistent with the observation (Figure 3.4) in which the axial stress in the braces along the east perimeter is larger than that along the west perimeter. The braces in the east perimeter have yielded (exceeding the nominal yield strength 36 ksi). The model appears to match well with the dynamic properties under low level of vibrations and the observed damage under higher levels of vibration, and is therefore deemed suitable for use in the fragility analysis.

3.5 Fragility analysis and performance evaluation

One of the key ingredients to systematically evaluate the seismic performance of a structure is to obtain its fragility curve for various limit states. The fragility curves for this study are analytically generated by performing nonlinear response time history analysis using the

OpenSees model described in the previous sections and a procedure that is commonly used (Choi et al. 2004; Ellingwood et al. 2007; Pan et al. 2010).

A fragility curve presents the probability that a structure exceeds a certain limit state at a given ground shaking intensity. A fragility function (Eq. (3.1)) typically takes the form of a lognormal cumulative distribution function (CDF) and is characterized by two parameters IM_C and β_C , which represent the median structural capacity and lognormal standard deviation that accounts for the uncertainty, respectively:

$$P_f = \Phi \left(\frac{\ln(IM/IM_C)}{\beta_C} \right) \quad (3.1)$$

In Eq. (3.1), IM is the ground shaking Intensity Measure (e.g., spectral acceleration S_a) and Φ is the standard normal CDF.

To obtain the value of IM_C and β_C , the Probabilistic Seismic Demand Model (PSDM) which describes the relationship between the ground shaking intensity and the Engineering Demand Parameter (EDP) should be established. The PSDM is generated by performing a regression analysis on the structural responses from nonlinear response time history analyses involving a set of ground motions. The PSDM in this study follows the form of a power relationship, which is shown to be valid for steel frame structures (Kinali and Ellingwood 2007):

$$\theta_d = aS_a^b \quad (3.2)$$

in which θ_d is seismic demand expressed in terms of EDP; S_a is the spectral acceleration; a and b are coefficients found from a regression analysis.

IM_C is then obtained by back calculating the IM corresponding to the EDP threshold of a limit state using the PSDM. β_C , which describes the uncertainty, should include both aleatoric and epistemic uncertainty, i.e., uncertainty in seismic demand σ_d , structural capacity σ_c , and structural modeling σ_m , where:

$$\beta_C = \sqrt{\sigma_d^2 + \sigma_c^2 + \sigma_m^2} \quad (3.3)$$

3.5.1 Generation of hazard compatible ground motion

A major contributor to the uncertainty in the structural response is the uncertainty in seismic demand caused by the inherent randomness of the ground motion characteristics. To characterize the uncertainty in seismic demand, a set of ground motions needs to be generated that represent the hazard level, the tectonic environment, and geological features at the site of the structure.

To account for the unique tectonic condition in the East Coast of the United States, the ground motion database developed by McGuire et al. (2001) is utilized. While most of the records in this database come from the west coast of the United States or a similar tectonically active region, the ground motions have been scaled by applying a transfer function to make them suitable for use in a tectonically inactive environment.

The database contains 151 sets of tri-directional ground motions at the bedrock level. To make those ground motions compatible with the hazard level at the site of the MSC, a scale factor f is found which minimizes the sum of square of the error (SSE) between the target spectrum S_a^{target} and the geometric mean spectrum for the two horizontal components of each ground motion set S_a^{record} over the period range between 0.0 to 2.0 second.

$$SSE = \sum_{i=1}^n [\ln(S_a^{target}(T_i)) - \ln(f * S_a^{record}(T_i))]^2 \quad (3.4)$$

in which,

$$S_a^{record}(T_i) = \sqrt{S_{ax}(T_i) \cdot S_{ay}(T_i)} \quad (3.5)$$

In Eq. (3.4), T_i is the period value between 0.0 to 2.0s at an interval of 0.01s, S_{ax} and S_{ay} are the spectral acceleration for the two horizontal components of a record set, f is the scale factor, and n is the total number of discretized periods.

The scale factor is applied to both horizontal components for each ground motion set. In the end, a set of 22 bidirectional ground motions with the smallest SSE among all the 151 sets are selected as the spectrum compatible bedrock motion for each hazard level. As a result, there is one set of ground motions for the Design Basis Earthquake (DBE) hazard level and another for the Maximum Considered Earthquake (MCE) hazard level. 22 pairs of ground motions are selected for a set in order to be consistent with the methodology in FEMA P-695 (FEMA 2009).

The USGS Uniform Hazard Response Spectra (UHRS) (Petersen et al. 2008) for the DBE and MCE hazard levels, which correspond to a return period of 475 years and 2475 years, respectively, at the site of the MSC are employed as the target spectra in selecting the bedrock motions. The site condition for the target spectrum is NEHRP Site Class A (BSSC 2009). As the USGS UHRS provides spectral acceleration values at several discrete points between 0.0 and 2.0s, this period range is selected for spectrum matching.

Since it has been determined that soil amplification effect played an important role in causing damage to the MSC during the Virginia earthquake (Tilshalski et al. 2015), it is essential to incorporate the effect of the underlying soil in developing the ground motions. To obtain the ground surface motions, a site response analysis is performed on each set of the selected bedrock ground motions using the open source software Deepsoil (Hashash et al. 2014). The soil profile (Figure 3.16) is the same as the one used in Chu et al. (2014) that results in a simulated response consistent with the observed damage. The measured shear wave velocity is limited to a soil depth of 82m, beyond which it is assumed that the shear wave velocity transitions to the bed rock velocity over a soil depth of 165m. The result of the selected bedrock motion sets and the developed ground surface motion sets for DBE and MCE hazard levels is shown in Figure 3.17.

The set of ground surface motions for DBE and MCE hazard levels are used in the nonlinear response time history analyses to generate the fragility curves. To account for the uncertainty in the direction of the earthquake, the two orthogonal components of the ground motion are interchanged with respect to the long and short direction of the building (Peruš and Fajfar 2005). As a result, there are 44 nonlinear response time history analysis for each hazard level.

3.5.2 Limit State of Structural Damage, EDP and Intensity Measure

This study is mainly focused on non-collapse performance and particularly the limit state “onset of damage”. This is because damage to the building is of major concern to the stakeholders.

According to the assessment of the finite element analysis results and observations from the damage reconnaissance, the initial damage in the steel mezzanine is most likely to take place in the diagonal braces. Therefore, the ductility demand on the diagonal braces (Eq. (3.6)) is chosen to be the engineering demand parameter (EDP) to characterize the seismic demand on the structure, where the brace ductility demand is defined as:

$$\mu = \frac{\Delta_{max}}{\Delta_{yield}} \quad (3.6)$$

in which

Δ_{max} is the maximum lateral displacement of the bay with diagonal bracing

Δ_{yield} is the lateral displacement of the bay to cause yielding of the brace.

It should be noted that all bays do not share the same ductility demand because of the torsional response of the building and different configuration of each individual bay. Hence, to account for the performance of the entire structure, the limit state of initiation of damage is considered to be achieved when the maximum ductility demand among all braced bays in the structure reaches the value of 1, i.e.:

$$\max(\mu_i) = 1 \quad (3.7)$$

in which μ_i is the ductility demand of each individual bay.

Alternatively, the fragility of a selected part of the structure can also be investigated by tracking the maximum ductility demand only in that specific region. In the absence of the material property testing, the yield displacement of each bay is calculated from kinematic

relationship using the nominal yield strength of 36 ksi for A36 steel. To account for ground shaking intensity of bidirectional ground motions, a nominal spectral acceleration $S_{a,nom}$ is proposed as follows:

$$S_{a,nom} = \sqrt{S_{a1}(T_1) * S_{a2}(T_2)} \quad (3.8)$$

in which $S_{a1}(T_1)$ is the spectral acceleration of the ground motion in the long direction of the building at the first mode; $S_{a2}(T_2)$ is the spectral acceleration of the ground motion in the short direction of the building at the second mode.

The basis for Eq. (3.8) is that the first mode of the structure is almost purely translational in the long direction while the second mode is torsional coupled with translation in the short direction (Chu, et al. 2014).

3.5.3 Development of fragility curve for structural damage

The PSDM is generated by performing a linear regression analysis on the natural log of the bracing maximum ductility demand from the nonlinear response time history analysis and the corresponding nominal spectral acceleration (from Eq. (3.8)) to obtain the coefficients a and b appearing in Eq. (3.2). In order to examine the relative vulnerability for different parts of the structure, PSDMs are developed for braces in the long direction of the building, short direction of the building, and the entire building (combined directions) by using the structural responses in the corresponding directions. To investigate the effect of the ground motion set on PSDM, for each part of the structure three PSDMs are determined by using structural response to DBE set only, MCE set only and a combination of these two sets,

respectively, resulting in the generation of nine PSDMs as presented in Figure 3.18 and Table 3.4.

The maximum ductility demand for braces in the short direction is smaller than those in the long direction. As a result, the PSDM for the combined directions is almost the same with that for the long direction. The minor difference is caused by a few cases in which the maximum ductility demand occurs in the short direction of the building as opposed to the long direction.

Another observation from Figure 3.18 is that the PSDM generated using response from different sets of ground motions is noticeably different. The PSDM generated using the combined set of DBE and MCE is more similar to those generated using only the DBE set when the ground shaking intensity is low, while they are more similar to those generated from MCE set when the ground shaking intensity is high.

Fragility curves are generated based on the PSDM obtained above using the combined sets for the DBE and MCE ground motions. Due to lack of material testing, the variability for material strength cannot be established. In addition, Celik and Ellingwood (2010) suggested the uncertainty in material strength makes limited difference in fragility analysis for limit states other than collapse. Therefore, the material strength in this study is treated as deterministic and the term to describe the uncertainty of structural capacity σ_c in Eq. (3.3) is set equal to zero. The uncertainty in finite element modeling σ_m in this same equation is set equal to 0.2, as suggested by Kinali and Ellingwood (2007).

Figure 3.19 shows the fragility curves for the onset of damage for the long direction, short direction and combined directions of the structure. Table 3.5 shows the coefficients for the fragility function in Eq. (3.1). The long direction of the structure is more fragile than the short direction. At the ground shaking intensity of the Virginia earthquake whose nominal spectral acceleration Sa_{nom} based on Eq. (3.8) is 0.09g, the long direction of the structure has a probability of 0.660 of sustaining damage while the short direction has a probability of only 0.054 of being damaged. The ground shaking level corresponding to a 50% probability of damage in the combined directions of the structure is small (0.079g). The probability of damage occurring in the combined directions of the structure is close to that for the long direction, corroborating with the previous conclusion that damage is much more likely to take place in the long direction of the structure.

3.5.4 Fragility curve for nonstructural damage

Since the purpose of the MSC is to provide storage to preserve artifacts, it is therefore important to investigate how safe the artifacts are during a future earthquake. The methodology to assess the safety of the artifacts during an earthquake is to develop fragility curves associated with the initiation of cabinet motion. Motion of the cabinet can lead to its contents being damaged from impact with other artifacts within the cabinet, or impact with the cabinet.

Cabinet motions are induced by floor acceleration. Based on physical principles, Shenton III (1996) developed criteria to initiate different kinds of motion for a rigid body resting on the ground subjected to ground acceleration. Depending on the floor acceleration intensity (a_{max}), coefficient of friction (μ_s) between the cabinet and the surface it rests on, the

location of center of gravity (β) and the aspect ratio (width-to-height, B/H), the cabinet may remain at rest, rock, or slide. Figure 3.20(a) shows the criteria in parameter space for a cabinet with its center of gravity located at βH from its bottom and an aspect ratio of 3. The definition of various parameters is illustrated in Figure 3.20(b). The Slide&Rock region identified in Figure 3.20(a) is a motion in which rocking occurs initially that is proceeded by sliding as the friction force diminishes. The other regions in Figure 3.20(a) indicate the respective condition of the cabinet for a given set of parameters.

According to these criteria, the fragility function for the rocking and sliding of a cabinet can be defined as follows:

$$F_{rocking}(S_a) = P[(a_{max} > \frac{B}{2\beta H}g) \cap (\mu_s > \frac{B}{2\beta H})|S_a] \quad (3.9)$$

$$F_{sliding}(S_a) = P\{[(a_{max} > \mu_s g) \cap (\mu_s < \frac{B}{2\beta H})] \cup [(a_{max} > A_g^*) \cap (\mu_s > \frac{B}{2\beta H})]|S_a\} \quad (3.10)$$

in which, S_a is the spectral acceleration associated with the ground shaking intensity; a_{max} is the maximum floor acceleration; g is the gravity acceleration, and A_g^* is defined as:

$$A_g^* = \frac{(1 + 4\gamma^2)\mu_s - 3\gamma}{4 + \gamma^2 - 3\gamma\mu_s} \quad (3.11)$$

$$\gamma = \frac{B}{2\beta H} \quad (3.12)$$

It should be noted that a_{max} is chosen to be the maximum floor acceleration in the N-S direction of the building in order to be compatible with the 1-D nature of the criteria developed in Shenton III (1996). The reason to choose the N-S direction as opposed to the E-W direction is because a cabinet is more likely to rock in the N-S direction due to the short direction of the cabinets being orientation in that direction (Figure 3.5(a)).

Similar to the approach to establish the PSDM for structural damage, a regression analysis is performed to develop the PSDM for maximum floor acceleration. The regressed relation for the absolute acceleration of the second floor in the long direction is shown in Figure 3.21 and expressed by Eq. (3.13) which gives the median value of maximum floor acceleration conditioned on the spectral acceleration. The absolute accelerations of the second floor were obtained from the nonlinear response time history analysis. The dispersion from the regression analysis is found to be 0.192 which is the lognormal standard deviation of the floor acceleration demand.

$$a_{max} = 0.95S a_{nom}^{0.65} \quad (3.13)$$

One of the important aspects in studying the fragility of these cabinets is the uncertainty on the capacity of the cabinets against motion, which is a result of the uncertainty in the coefficient of friction and the location of center of gravity. It is assumed that the coefficient of friction μ_s and the normalized height of the center of gravity β follow a normal distribution.

There are three types of cabinets in Pod 1: Type 348 (Figure 3.5(a) and (d)), Type 220 (Figure 3.5(b) and (c)) and Type 395 (bottom middle photograph in Figure 3.4). Table 3.6

lists their dimensions and friction properties. Dimensions of the cabinets were provided by MSC staff (Dietrich 2012). The mean value and standard deviation for the coefficient of friction are based on previous studies by Rabbat and Russell (1985) and Dooley (1957). It should be noted that the Type 220 cabinets are stacked on top of each other. The cabinets in the upper stack are selected for the study because the reduced coefficient of friction that exists between the steel-to-steel contact surface renders them more vulnerable to sliding.

Due to complex criteria involved in defining the initiation of cabinet motion, an analytical expression for the fragility function (Eq. (3.9) and (3.10)) is difficult to obtain. As a result, a Monte Carlo simulation approach is employed to calculate the fragility function. For a given ground shaking intensity S_a , one million samples of floor acceleration demand a_{max} are generated using the developed PSDM (Eq. (3.13)) along with the coefficient of friction (μ) and normalized height of center of gravity (β) using the normal distribution with the parameters specified in Table 3.6. The probability that motion is initiated can be calculated by dividing the number of samples that satisfy the corresponding criteria by the total number of samples. By repeating this process for a range of ground shaking intensity, the entire fragility curve can be developed numerically.

Figure 3.22 shows the probability of initiation of rocking and sliding for the three different types of cabinets that were obtained from the Monte Carlo simulations. It can be seen that Type 348 cabinet (Figure 3.5(a)) has the highest probability to rock. This is attributed to the large aspect ratio of this type of cabinet. On the contrary, Type 220 (Figure 3.5(b) and (c)) has a low probability to rock due to its small aspect ratio. However, the probability of sliding is the highest among the three types of cabinets. This is due to the smaller

coefficient of friction of the painted steel-to-steel contact surface of Type 220 cabinets. Type 395 has a smaller aspect ratio than Type 348 and a contact surface of steel and concrete, making its probability of both sliding and rocking moderate. It should be noted that the fragility curve does not resemble a conventional fragility curve that takes the form of a lognormal CDF. The reason is that, as explained above, the coefficient of friction, cabinet aspect ratio and center of gravity, and level of floor acceleration have an effect on the type of motion that a cabinet develops. For example, if the ground acceleration is large the probability that a Type 348 cabinet will rock cannot be one hundred percent if the coefficient of friction is small, as the cabinet will have the tendency to slide and not rock (Figure 3.20(a)). The uncertainty in the coefficient of friction keeps the probability of rocking from reaching one. In addition, the various uncertain parameters that determine the capacity of the cabinets against motion also do not follow a lognormal distribution.

3.5.5 Retrofit of the structure

The Smithsonian Institute is considering to seismically retrofit the mezzanine by replacing the diagonal strap braces with high strength steel cables with sufficient pretension to make them taut. The objective is to make the structure stronger and have less structural damage under a similar future earthquake. Past experience however shows that if a structure remains linear during an earthquake that the floor acceleration demand will increase. For the MSC, this will increase the probability for the storage contents in the cabinets to be damaged. Thus, the FEM is modified with increased brace yield strength to investigate its effect on the floor acceleration. Two cases are studied: one with brace yield stress of 72 ksi; the other with 150 ksi.

It was found from the subsequent nonlinear response time history analysis that were performed that for the case of 72 ksi yield strength that there are only a few ground motions that cause the braces to yield. However, in the latter case (150 ksi yield strength), no brace yields under any of the considered earthquakes. The results of the floor acceleration PSDM along with the original case ($F_y = 36 \text{ ksi}$) are shown in Figure 3.23 and Table 3.7. Figure 3.23 shows that by increasing the yield stress of the bracing, the floor acceleration demand has increased significantly, especially at a higher level of ground shaking intensity. Using the results for the PSDM for floor acceleration, the fragility of the cabinets for these different cases can be compared. Figure 3.24 shows the fragility curve for cabinet sliding and rocking limit states for different types of cabinet.

Increasing the brace yield strength causes the fragility of the cabinet to significantly increase. Considering that the braces are designed to yield and dissipate energy, the damage of bracing is acceptable. The purpose of the MSC is to preserve storage content. Thus, it is more important to keep the floor acceleration demand low by using a low yield strength to allow the braces to yield. Therefore, it is not recommended to retrofit the structure with high strength braces. Studies have shown that passive dampers are cost effective in reducing both story drift level and floor acceleration demand (Dong et al. 2016) and could be considered as possible alternative retrofit strategy. It is beyond the scope of this study however to study this type of retrofit.

3.5.6 Probability of exceeding various limit states

To put the fragility curves in Figure 3.19 and Figure 3.22 into perspective, the nominal spectral accelerations are calculated from the USGS UHRS (Petersen et al. 2008) for the

DBE and MCE level using Eq. (3.8). Using an actual ground motion, the nominal spectral acceleration of the Virginia earthquake is determined as well. Hence the probability of exceeding various limit states under various hazard levels can be assessed. The USGS spectrum originally provides spectral acceleration for Site Class B. To account for the soil amplification effect, the spectral acceleration is multiplied by the soil amplification factor $F_a=1.6$ from ASCE7-10 (ASCE 2010). The Virginia earthquake is believed to have a return period of 752 years (Chapman 2015). Plugging in the ground shaking intensity to the fragility curves developed in the previous sections, the probability of exceeding various limit states under different hazard levels are obtained and summarized in Table 3.8.

At the DBE level, the probability for the building to have structural damage is small (0.068). However, the probability to cause Type 220 cabinets to slide is considerable (0.431). At the MCE level, the structure is almost certain to have structural damage and sliding for Type 220 cabinets to occur. The probability for cabinet 348 to rock is also high under the MCE. At the ground shaking intensity of the Virginia earthquake, there is a relatively high probability for structural damage (0.677) and sliding of Type 220 cabinets (0.802) to occur. In addition, there is a considerable probability (0.103) for Type 348 cabinets to undergo rocking. At all hazard levels, the probability for motion to occur in Type 395 cabinets is small.

3.6 Summary and findings

This study performs a comprehensive investigation on the response and performance of the MSC located in Suitland, Maryland. The damage reconnaissance following the 2011 Mineral, Virginia earthquake is conducted. Through FEM simulation of the structure's

response during the Virginia earthquake, it is found that the seismic damage is attributed to: 1. soil amplification; 2. combined effect of torsion and translation response and 3. bi-directional earthquake demand. A nonlinear FEM was developed for the purpose of performing the fragility analysis. The model was validated using the results from a field vibration test as well as the observed damage pattern from the earthquake. To perform the fragility analysis, two sets of hazard compatible ground motions were selected from a CEUS ground motion database. The effect of soil amplification is accounted for by a site response analysis. The sets of ground motion are applied to the FEM for conducting the nonlinear response time history analysis, whose results are used to generate fragility curves. Fragility curves are developed for initiation of structural damage and acceleration-induced motion (rocking and sliding) for different types of storage cabinets in the MSC. The structural damage fragility for different parts of the structure is also studied. The effect of employing braces with different strength in possible seismic retrofit is investigated. The probability of exceeding various limit states at different hazard levels is determined to evaluate seismic risk.

It is found that the structure is more fragile in the N-S direction than the E-W direction. It is also discovered that increasing the yield strength of the braces will significantly increase the floor acceleration demand and thus increase the fragility of the contents in the cabinets.

It is discovered that the ground motion to cause structural damage in the mezzanine is not high. However, due to the low seismic hazard level at the site of MSC, the probability of structural damage to occur during the DBE is small. Considering the fact that both current and traditional seismic design practice in the U.S. employ a reduced seismic design force

to exploit the ductility of the structure, damage is expected to occur at the DBE hazard level. The acceptable amount for the probability of structural damage to occur should be determined by the owner of the building, as the repair process following structural damage may affect access to the stored artifacts.

There is a considerable probability that Type 220 cabinet will slide under the DBE earthquake. In addition, at ground shaking intensity of the 2011 Virginia earthquake, Type 348 cabinets also have an appreciable probability of rocking, which is detrimental to the storage contents. Considering that the purpose of the MSC is to preserve the invaluable museum collections, this might pose significant risk in terms of the normal functioning of this storage warehouse. This also reveals the threat faced by a large number of warehouses located in the East Coast U.S that do not possess measures to secure motions of storage contents, like connecting straps or restraining nets to avoid their motions. As there is no clear specification in building codes on the expected performance of the storage content in museum warehouses, this study simply provides the probability of possible content damage at different hazard level. It is up to the stakeholder whether such risk is acceptable and if any measures should be taken.

Table 3.1 Eccentricity between CR and CM for each case in parametric study (unit: ft)

	I	II	III	IV	V	VI	VII
NS	-13.9	1.4	-7.8	-4.1	-17.8	-15.5	-4.8
EW	1.2	1.8	7.9	7.6	2.2	2.1	1.6

Table 3.2 Comparison of measured and SAP model period for different modes (unit: s)

	Brace condition	Mode					
		1	2	3	4	5	6
Vibration Test Data	--	0.30	--	0.21	--	0.11	--
SAP2000 Model	Tension only	0.42	0.33	0.28	0.16	0.13	0.11
	As-built	0.32	0.25	0.21	0.12	0.10	0.08

Table 3.3 Comparison of measured and OpenSees model period for different modes (unit: s)

	Brace condition	Mode					
		1	2	3	4	5	6
Vibration Test Data	--	0.30	--	0.21	--	0.11	--
OpenSees Model	Post-buckling	0.43	0.33	0.28	0.17	0.13	0.11
	Pre-buckling	0.32	0.25	0.21	0.13	0.10	0.08

Table 3.4 Coefficient for PSDM (in the form of Eq. (3.2)) for different cases

Coefficient	Direction	DBE Set	MCE Set	Combined Sets
a	Long	8.469	8.221	11.358
	Short	2.144	5.73	7.903
	Combined	10.08	9.039	11.796
b	Long	0.854	0.772	0.961
	Short	0.616	0.907	1.100
	Combined	0.916	0.818	0.973

Table 3.5 Coefficients for fragility function shown in Figure 3.19

	IM_c	β_c
Long	0.0798	0.2907
Short	0.1527	0.329
Combined Directions	0.0791	0.281

Table 3.6 Dimension and friction property of the different types of cabinets

Type	B (in)	H (in)	B/H	Friction			Height of center of gravity	
				Contact Surface Material	μ_s		β	
					Mean	Standard Deviation	Mean	Standard Deviation
348	22.6	81.5	0.277	steel-concrete	0.6	0.15	0.5	0.1
220	38.6	40.75	0.947	steel-steel	0.15	0.05	0.5	0.1
395	50	81.5	0.613	steel-concrete	0.6	0.15	0.5	0.1

Table 3.7 Parameters for different PSDM for floor acceleration (in the form of $a_{max} = aS_a^b$)

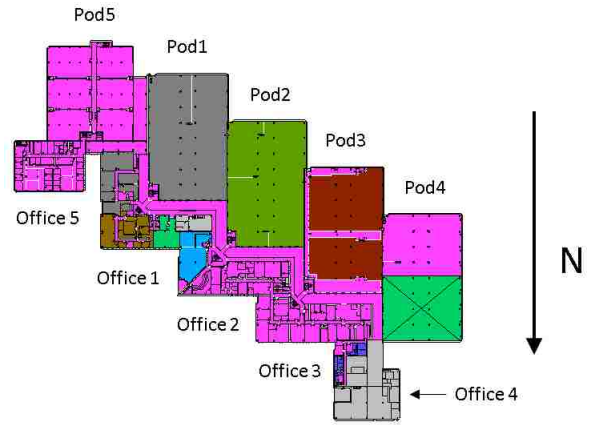
Brace yield stress (ksi)	a	b
36	0.9454	0.6469
72	2.221	0.9503
150	3.001	1.065

Table 3.8 Probability of exceeding various limit states at different hazard level

Hazard Level (Return Period)	Sa_{nom}, g	Probability of Structural Damage	Probability of Nonstructural Damage					
			Rocking			Sliding		
			Type 220	Type 348	Type 395	Type 220	Type 348	Type 395
DBE (475 years)	0.052	0.068	0	0.004	0	0.431	0.001	0
MCE (2475 years)	0.139	0.978	0	0.420	0	0.960	0.013	0.019
Virginia 2011 (752 years)	0.09	0.677	0	0.103	0	0.802	0.005	0.005



(a)



(b)

Figure 3.1 (a) Aerial view of MSC (<http://www.bing.com/map>); (b) Floor plan of MSC

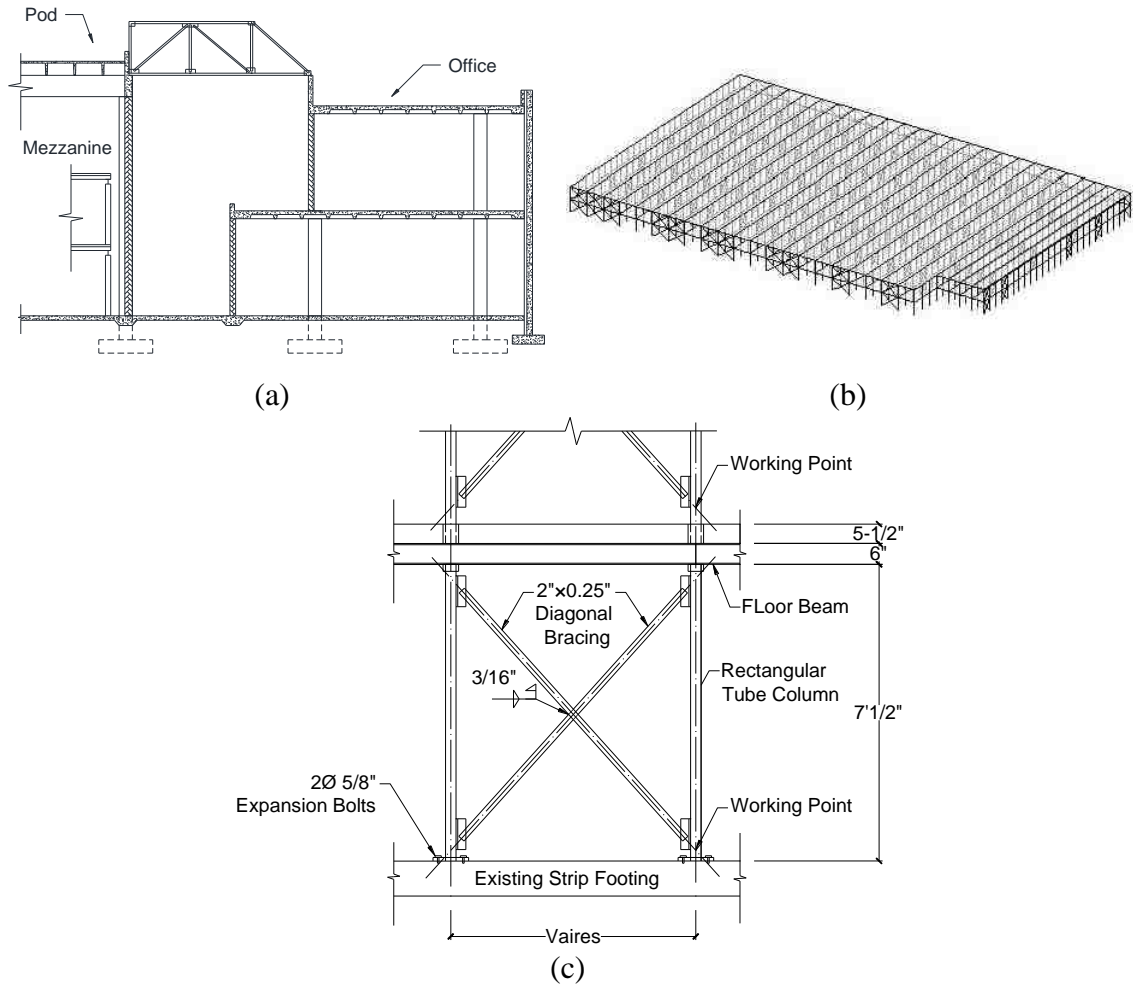


Figure 3.2 (a) Typical elevation of Pod, Office and mezzanine; (b) Steel mezzanine inside Pod; (c) Typical braced bay

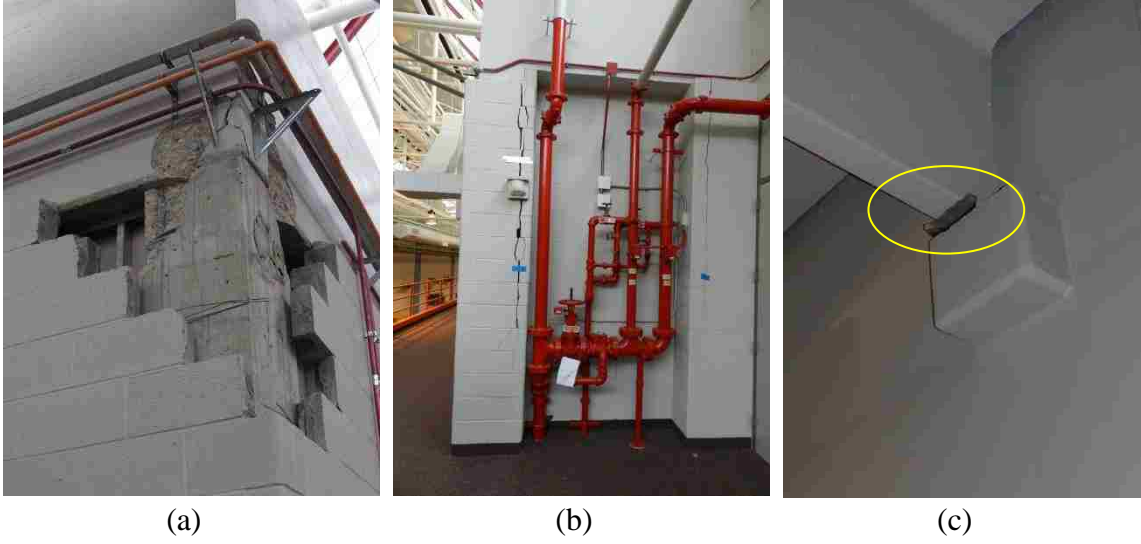


Figure 3.3 (a) RC beam-column joint failure; (b) crack in masonry wall; (c) sliding of T beams

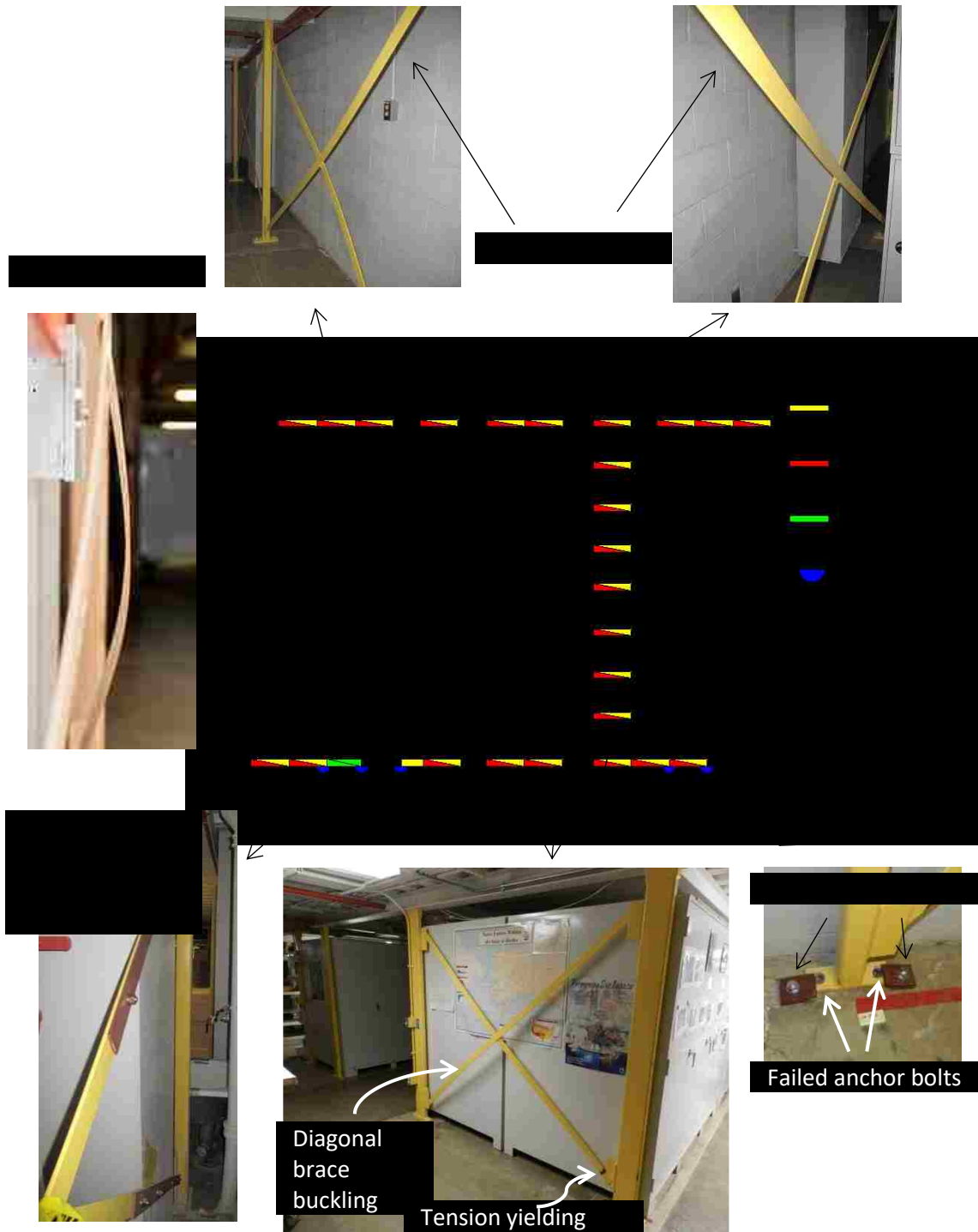


Figure 3.4 Type and distribution of damage in the first story of the steel mezzanine in Pod 1

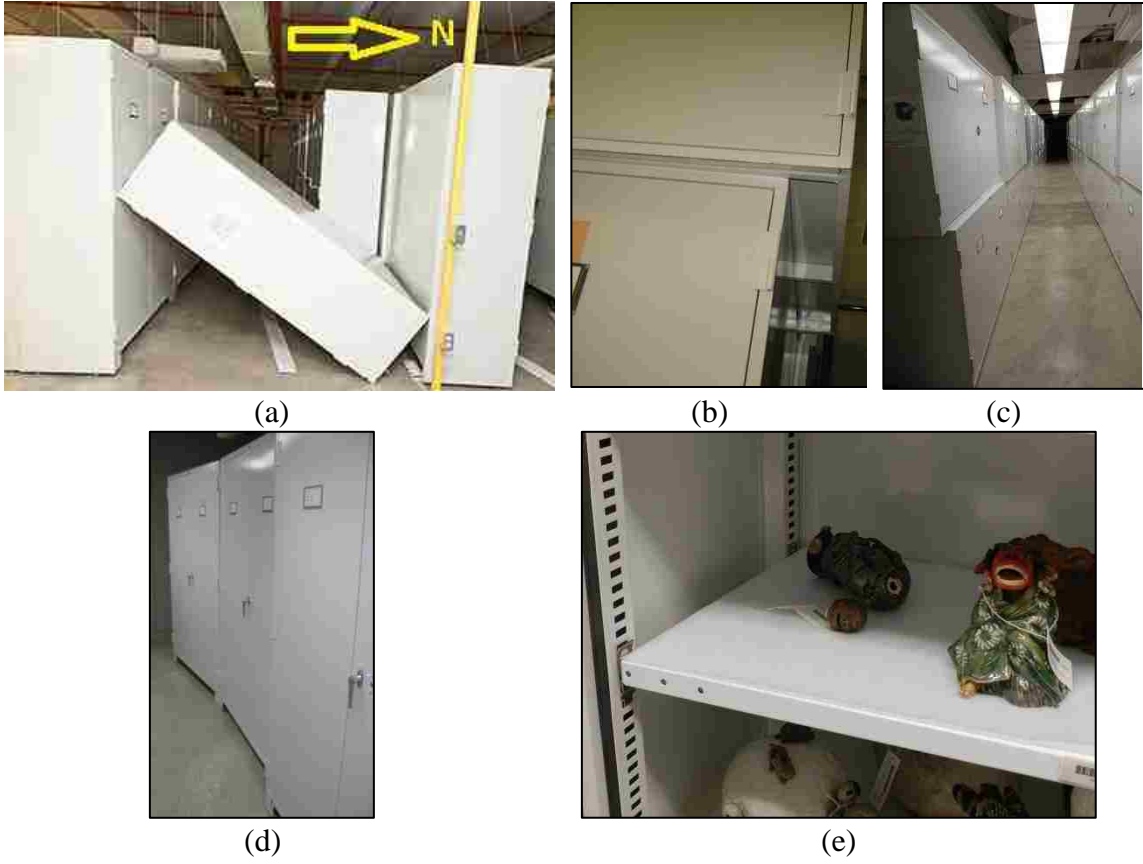


Figure 3.5 Nonstructural damage: (a) toppling of a storage cabinet; (b)&(c) sliding of cabinet; (d) cabinet dislodged; (e) storage content damage

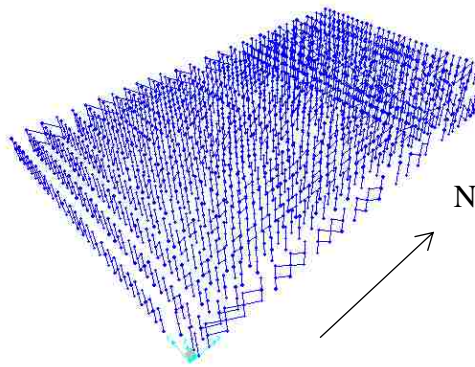


Figure 3.6 Isometric view of SAP2000 FEA model of steel mezzanine

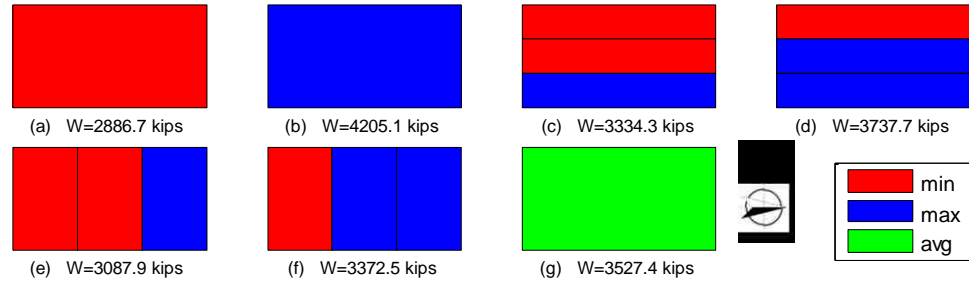


Figure 3.7 Illustration of cabinet content weight distribution and resultant total floor weight over floor plan: (a) Case I; (b) Case II; (c) Case III; (d) Case IV; (e) Case V; (f) Case VI; (g) Case VII

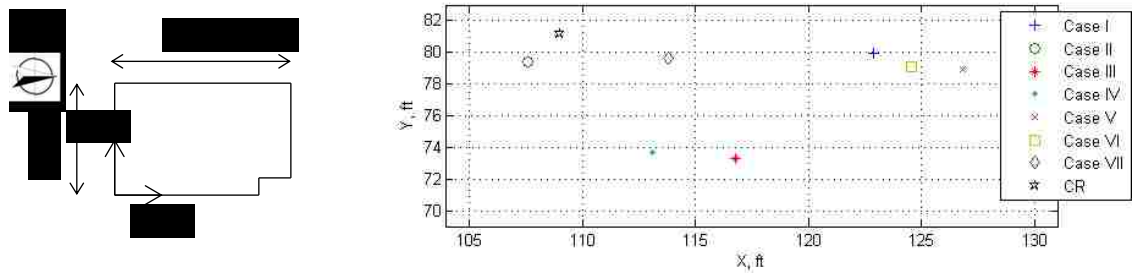


Figure 3.8 Location of the CM within the floor plan of the mezzanine for each cabinet content weight case

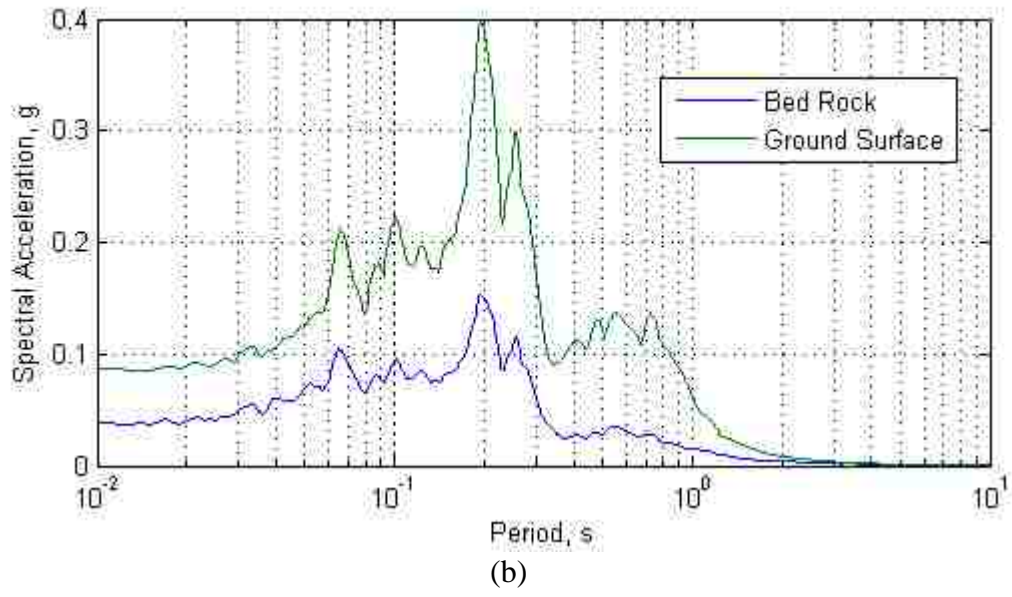
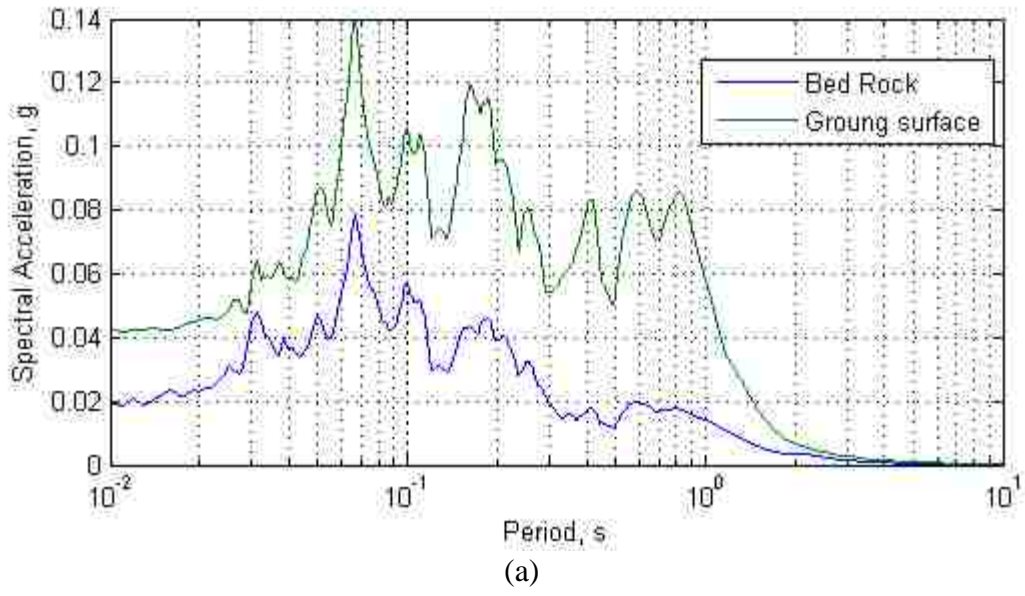


Figure 3.9 Response spectrum of ground motion of Virginia earthquake at bedrock and ground surface level (a) component in the long direction (b) component in the short direction

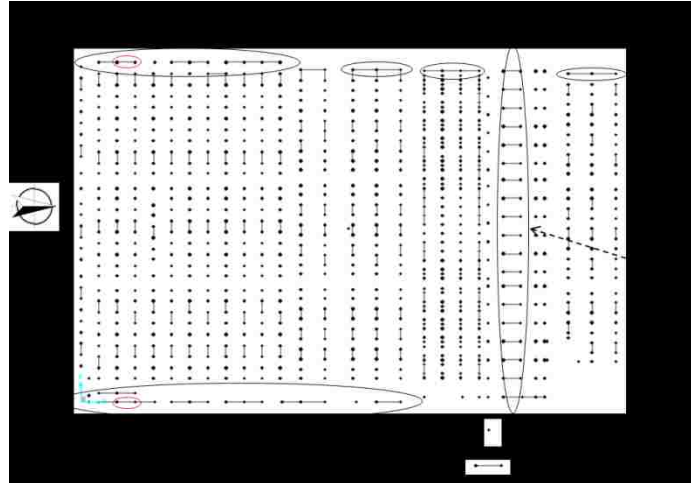
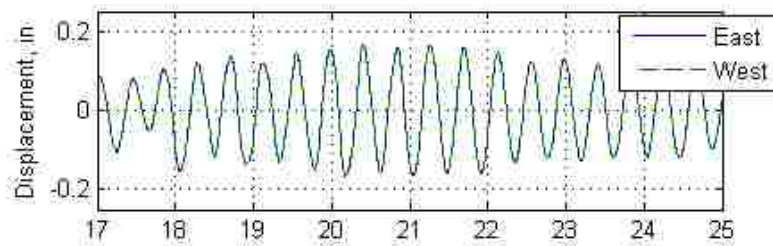
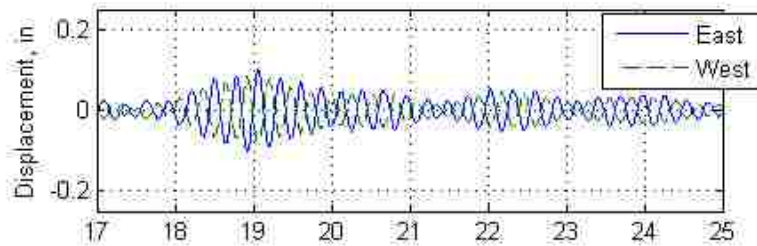


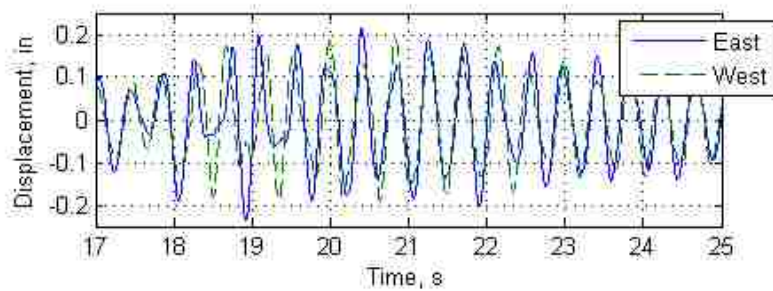
Figure 3.10 Peak axial stress response in 1st story braces in SAP model for Case I



(a)



(b)



(c)

Figure 3.11 Time history for translation of joints at the top of columns in east and west perimeters: (a) response to ground motion in NS direction; (b) response to ground motion in EW direction; (c) response to bi-directional ground motion

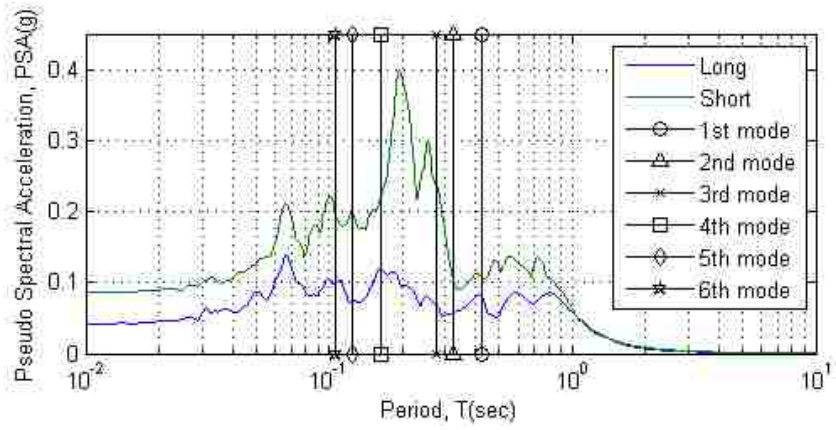


Figure 3.12 Response spectra of two components of ground motion and structural periods

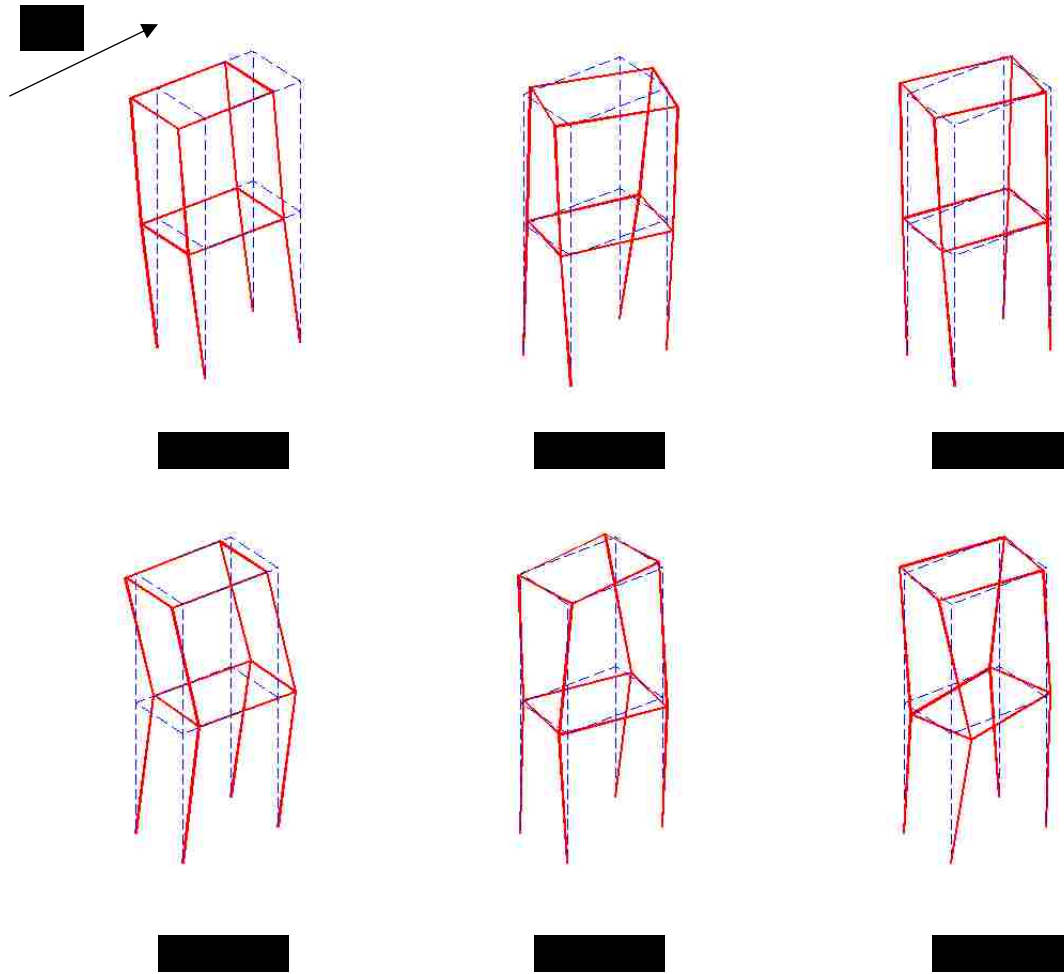


Figure 3.13 Mode shape of SAP2000 model in Case I

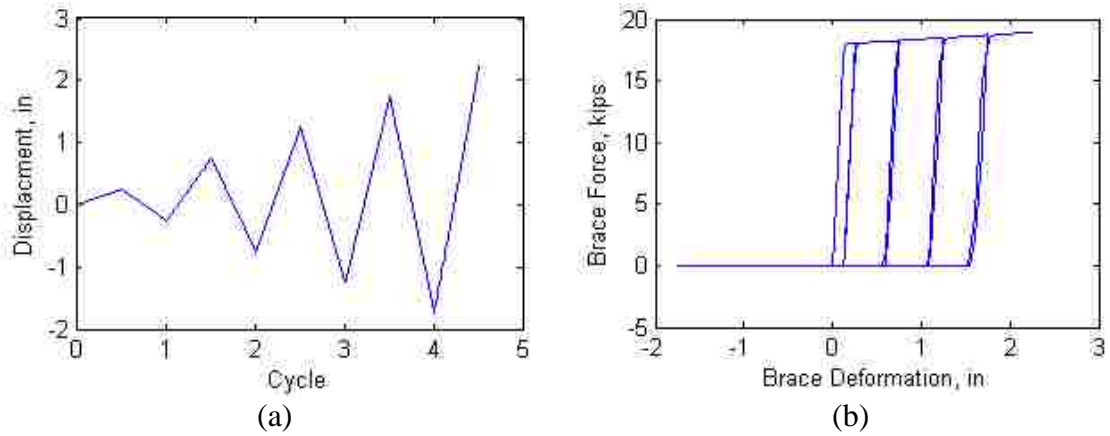


Figure 3.14 (a) Imposed brace displacement history of displacement-control cyclic load; (b) Hysteretic force-displacement response of one diagonal brace (tension force is positive)

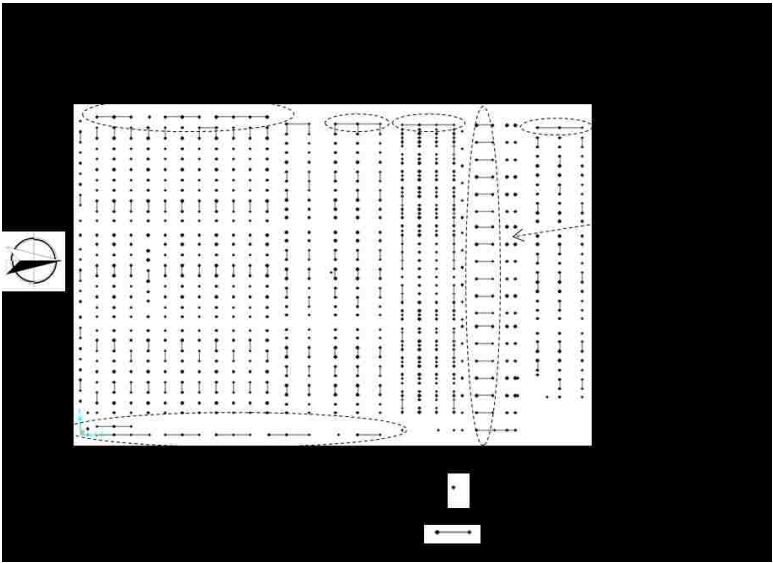


Figure 3.15 Peak axial stress in braces of 1st story in OpenSees model in response to Virginia earthquake

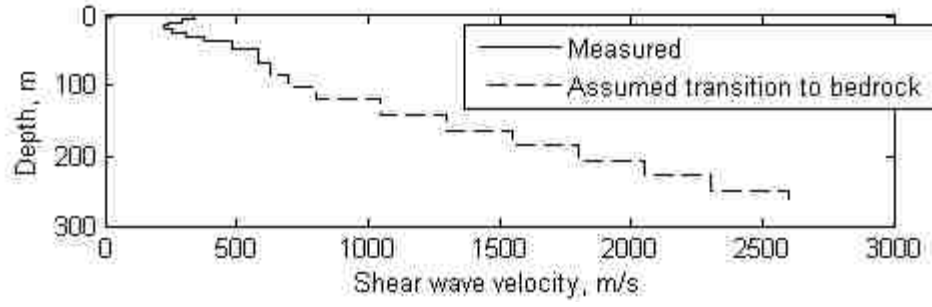
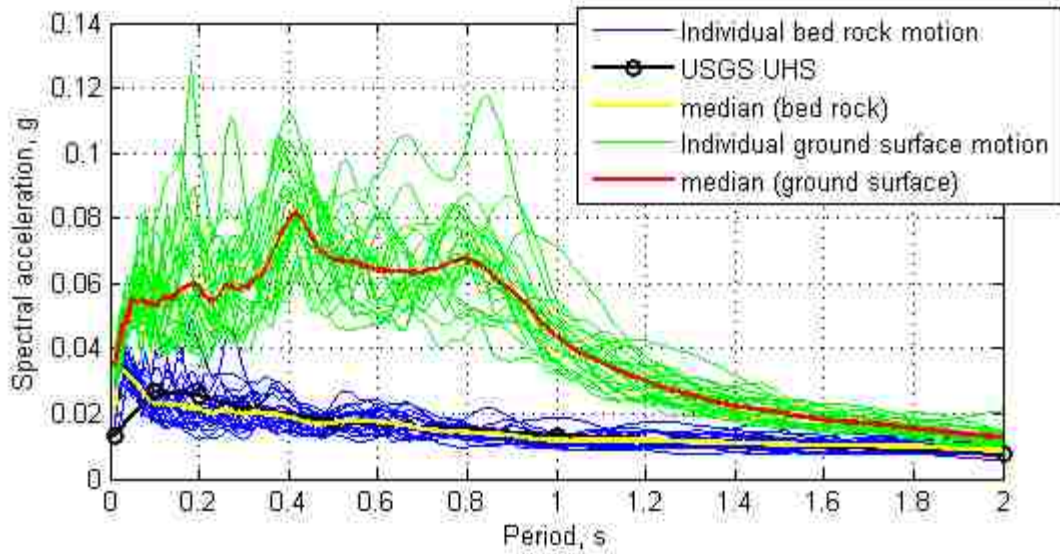
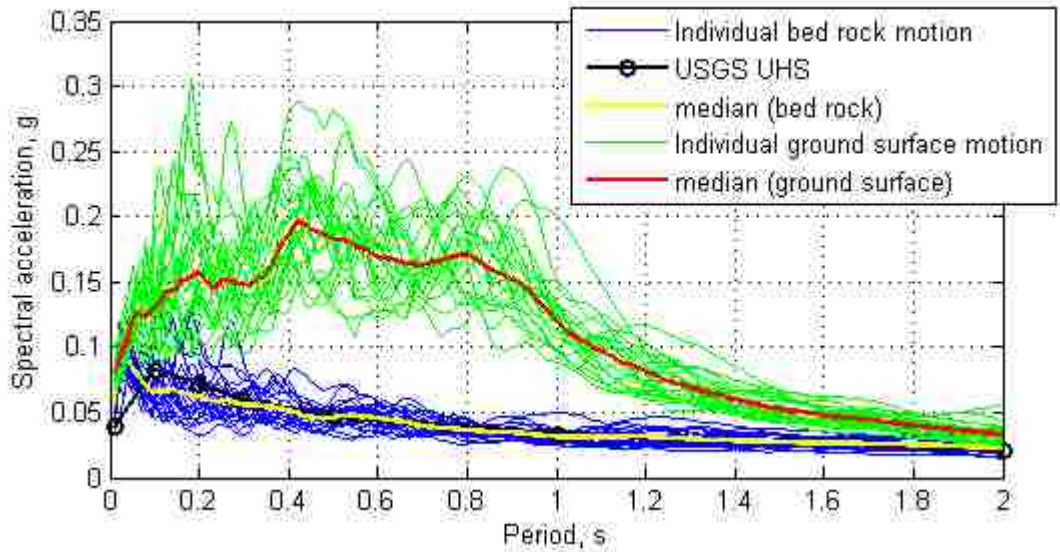


Figure 3.16 Shear wave velocity profile of soil strata used in site response analysis for records used in fragility analysis



(a)



(b)

Figure 3.17 Individual and median value of ensemble of bedrock motion, ground surface motion and target spectrum for (a) DBE hazard level and (b) MCE hazard level

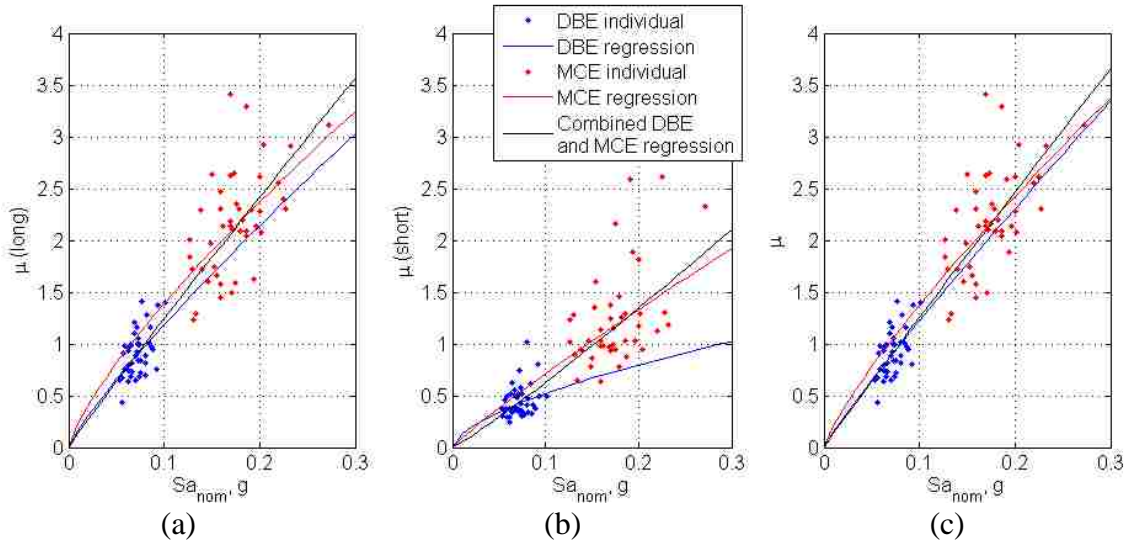


Figure 3.18 PSDM generated using different ground motions sets for braces in (a) long direction; (b) short direction and (c) combined directions of structure

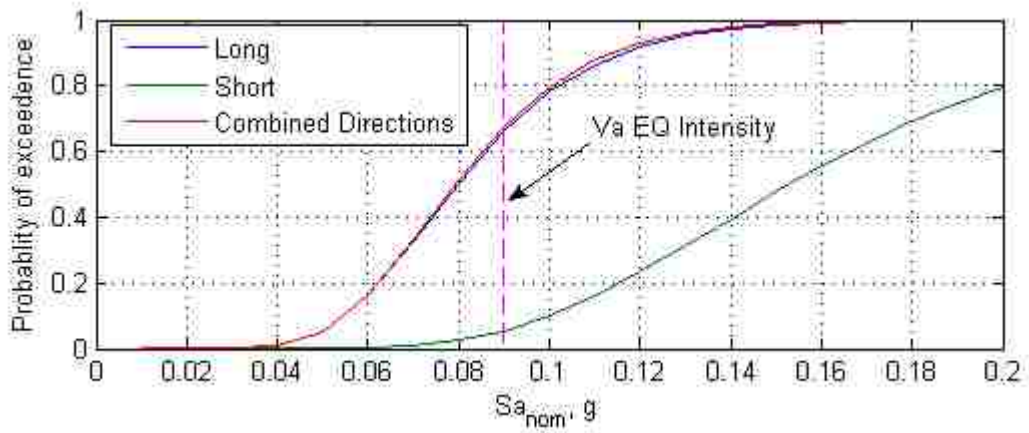


Figure 3.19 Fragility curve for different parts of the structure for onset of damage

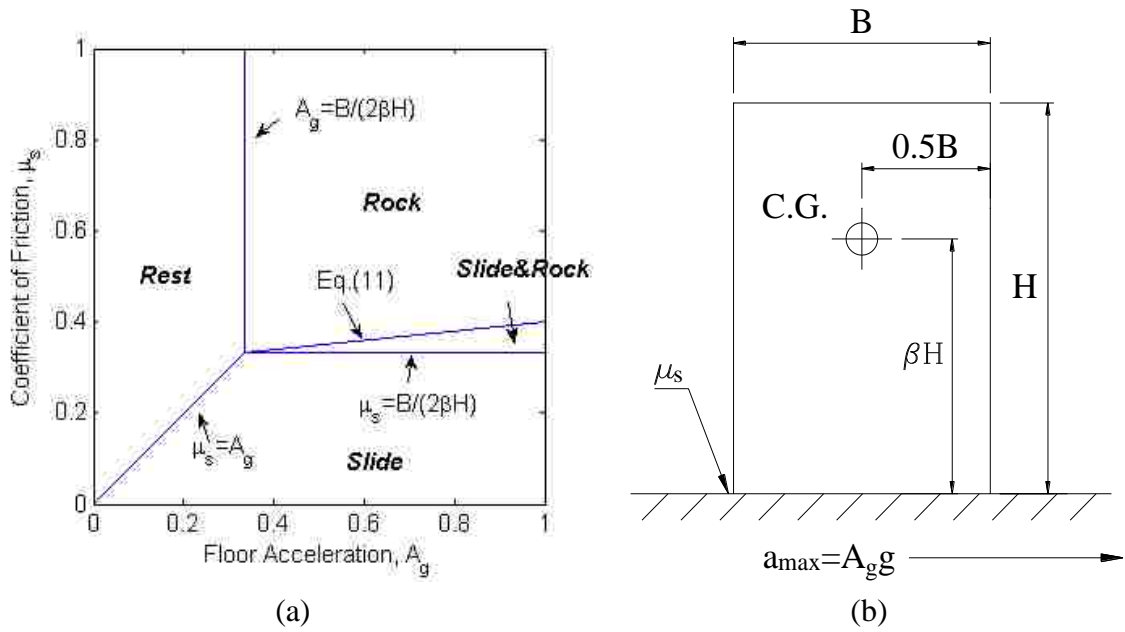


Figure 3.20 (a) Criteria for different types of motion in parameter space; (b) definition of various parameters

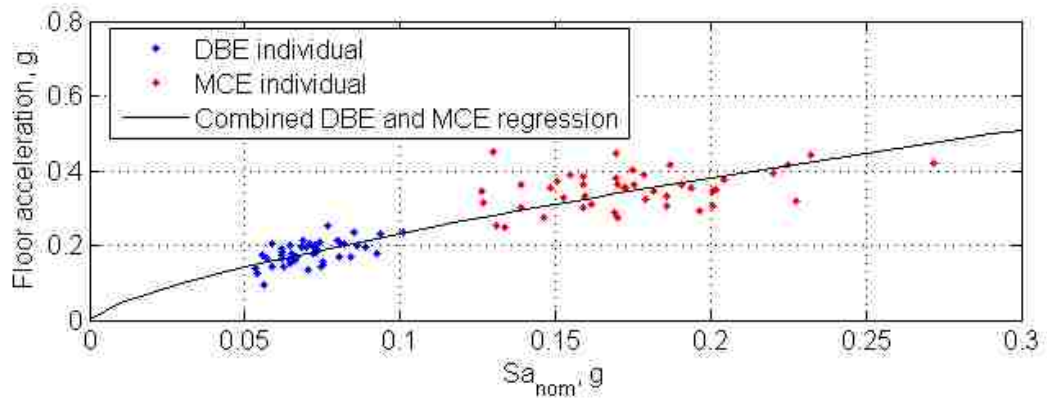


Figure 3.21 Fragility curve for different parts of the structure for onset of damage

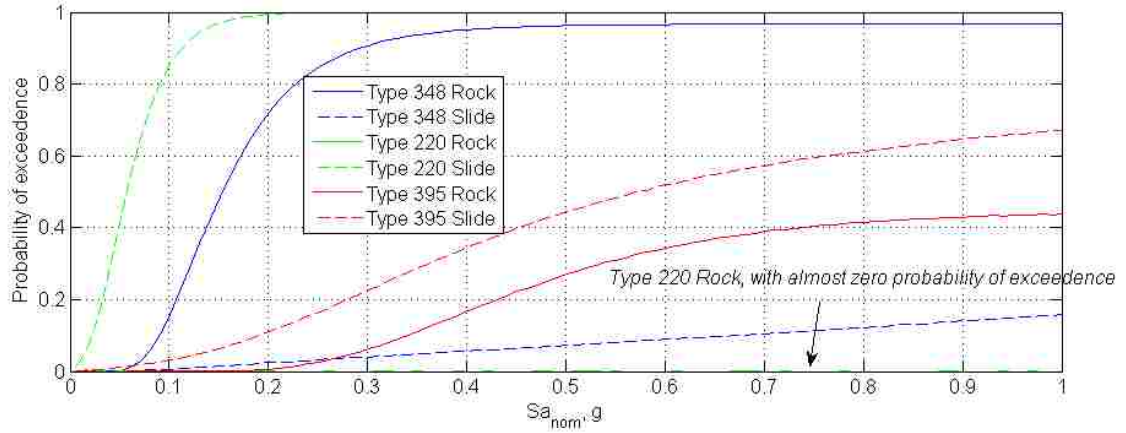


Figure 3.22 Fragility curves for initiation of motion for different types of cabinets

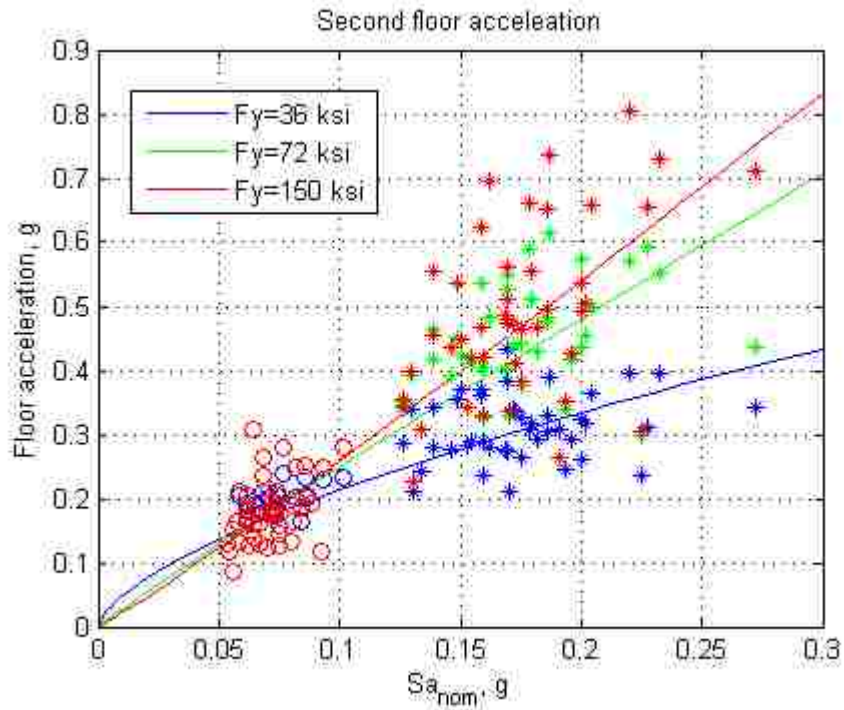


Figure 3.23 PSDM for floor acceleration for structures using braces of different yield strength

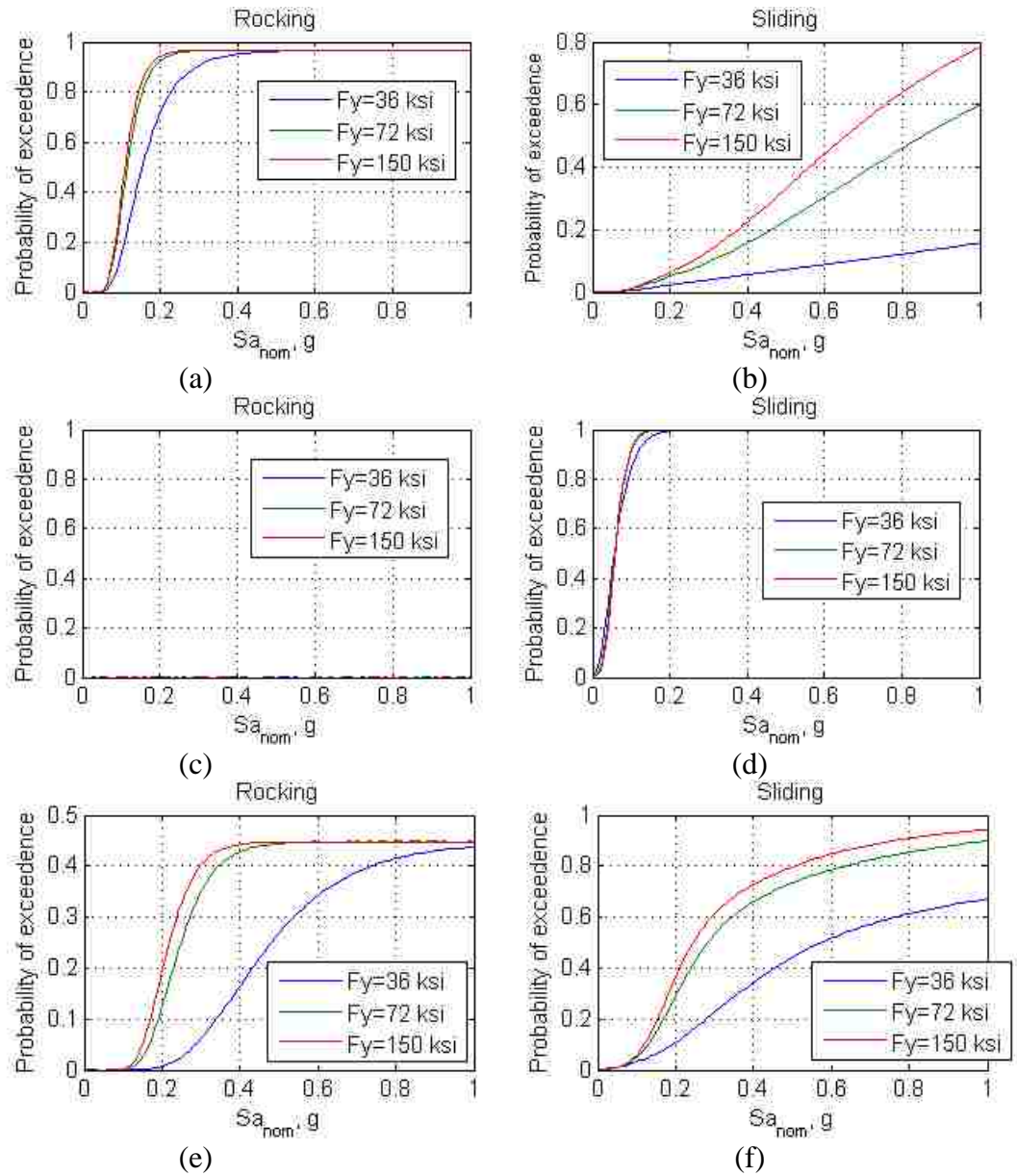


Figure 3.24 Cabinet fragility curves for structures using braces of different yield strength: (a) Type 348 rocking; (b) Type 348 sliding; (c) Type 220 rocking; (d) Type 220 sliding; (e) Type 395 rocking; (f) Type 395 sliding;

Chapter 4

Development of prototype building design and collapse simulation model of low-ductility CBF

4.1 Introduction

This chapter presents the development of prototype building designs representing low-ductility CBFs in the mid-Atlantic east coast region of the US (ECUS) and the numerical model for collapse simulation. It is important to incorporate the variation of design properties in the building inventory to evaluate the overall collapse performance of low-ductility CBFs especially considering the significant variation permitted by the relevant design code provisions. Several existing CBF building designs were reviewed and their design variations are summarized. Three key design variables were identified and selected for this study. A total of eight design variants of the prototype building were created with different values for the key design variables. In order to evaluate collapse performance, numerical models that are able to capture nonlinear behavior that could lead to collapse were developed for the prototype building. The numerical models are validated using experiment data from recent work by Bradley et al. (2015), Simpson et al. (2013), Sizemore et al. (2015) etc.. Some alternative numerical modeling approaches are also discussed.

4.2 Review of typical design variation in ECUS low-ductility CBF

Drawings for three existing CBF buildings and one connection design assembly that includes different types of connection details were reviewed. The buildings were designed

by three different design firms and the connection design assembly was from the company that designed one of the three buildings. These buildings and the design firms are from major metropolitan areas in ECUS and represent the regional design practice. The buildings are all designed with $R=3$ and without ductile detailing. The companies that designed the buildings will remain anonymous throughout the dissertation and are given aliases. The designs of these buildings are summarized in Table 4.1. In addition, some CBF designs from the literature are also reviewed. Three key design variables are extracted from the review. They are the brace configuration, beam design strength and brace-gusset plate weld connection design strength.

The drawing for Building 1 shows the variation in brace configuration in the design of low-ductility CBFs. Building 1 contains multiple CBFs. The CBFs employ different configurations for bracing, including X bracing in multiple bays and stories with single diagonal bracing (Figure 4.1(a)), split-X bracing (Figure 4.1(c)), chevron bracing (Figure 4.1(d)) and inverted chevron bracing (Figure 4.1(b)). The bracing configuration can have a significant influence on the inelastic behavior of the CBF especially in the brace post buckling range of behavior. In a chevron configuration, the vertical unbalance force from the braces (after one brace buckles) is resisted by the beam only and thus may cause beam yielding. In an X bracing configuration the unbalanced brace forces are carried by the braces in the upper levels or adjacent columns. The chevron and split-X bracing configuration are chosen for study in this dissertation.

The beam size also affects the inelastic behavior of a CBF, especially in a chevron bracing configuration. If the beam is not strong enough, it will develop flexural yielding under the

unbalanced brace force after one brace buckles. As the beam yields and deflects downward, the force in the tension brace will be limited, preventing the brace from reaching its yield force in tension. Therefore, in an SCBF, the beams are designed to withstand the the unbalanced brace forces demand. However, this consideration is not required for an R=3 CBF design. Therefore, for R=3 CBFs, engineers with different typical design practice may select beams of different strength relative to the unbalanced brace force demand. The AISC Seismic Provisions (AISC 2010a) was used to evaluate the strength of the beams relative to the unbalanced brace force demand (Eq. (4.1), (4.2) and (4.3)). The induced bending moment is compared with the unfactored bending moment capacity of the beam by calculating a Demand-Capacity Ratio (DCR). A DCR larger than 1 indicates that the beam is weak with respect to the unbalanced brace force demand. Figure 4.2 and Figure 4.3 show the beam and brace sections used in certain stories in Building 2 and Building 3.

$$T = R_y F_y A_g \quad (4.1)$$

$$C = 0.3 * \min(R_y F_y A_g, F_{cre} A_g) \quad (4.2)$$

$$V_{unbal} = (T - C) \sin \gamma \quad (4.3)$$

Table 4.2 shows the DCR of beams under unbalanced brace forces for Building 2 and Building 3. It can be seen that the beams in both buildings do not have adequate capacity to resist the unbalanced brace force. However, the extent that the demand exceeds the capacity varies significantly. In Building 2, the DCR is 2.9 while in Building 3 the DCR is 9.1. Therefore, the beam strength relative to the unbalanced brace force is considered to be

a key design variable. Its effect on the collapse performance of low-ductility CBF will be investigated in this dissertation.

The brace gusset plate connection design in a low-ductility CBF also has significant variation depending on the type of braces being joined. This connection mainly falls into 3 categories: welded connections (Figure 4.4 (a)), bolted connections (Figure 4.4 (b), (c) and (d)) and hybrid connections (Figure 4.4 (e) and (f)). Hybrid connections are usually used for unslotted tubular braces which are connected to the gusset plate by an angle that is bolted to the gusset plate and welded to the braces. During the review, it was found that the slotted tube-gusset plate fillet weld connection (Figure 4.4 (a)) is one of the most popular type of connection in the design of low-ductility CBFs. In addition, recent experimental studies (Bradley 2016; Davaran et al. 2014; Sizemore et al. 2015) on this type of connection provides invaluable data to facilitate numerical modeling. Therefore, this type of connection was selected for this dissertation.

In slotted tube-gusset plate fillet weld connections, the brace-to-gusset weld design strength was found to vary, depending on the design practice. Different engineers will apply different level of conservatism in designing the weld, which produces weld with different strengths. For $R=3$ CBFs, capacity design on the connecting fillet weld is not required. The weld needs to be designed for the factored load P_u , not the expected load from the brace. As a consequence, welds designed with different strengths will have different probabilities of fracture under the force that develop during seismic response. Therefore, the weld design strength plays an important role in the seismic behavior of low-ductility CBFs.

Figure 4.5 shows the brace gusset plate connection detail used in Building 2. It can be seen that this type of connection uses a 5/16” fillet weld universally. Figure 4.6 shows the factored load on the weld and the dimensions of the weld designed in an example story. From calculations, it can be seen that the weld length is always one inch longer than the minimum required length (the nearest integer rounded up). In comparison, the R=3 CBF design in Hines et al. (2009) uses multiple weld sizes and lengths; and the weld dimensions were selected without extra length to be conservative. Table 4.3 shows that the size and length of the welds are selected so that the capacity is larger than the design force demand. Therefore, the design approach produces a different level of weld overstrength. The DCR is calculated as the ratio between design force demand and weld capacity for the weld designs in these 2 buildings. The weld capacity is obtained using Eq. (4.4) from the AISC Specification (AISC 2010b), where l is the weld length, d is the weld size and F_{EXX} is the electrode strength, which equals to 70 ksi for E70. As is shown in Table 4.4, the DCRs of welds vary from 0.87 in Building 2 to 0.98 in Hines et al. (2009).

$$\phi R_n = 0.75 \cdot 0.6 F_{EXX} \cdot l \frac{d}{\sqrt{2}} \quad (4.4)$$

Design guidelines from Marstellar et al. (2002) (Table 4.5) suggest using multiple weld sizes depending on the brace section and design force demand. In summary, different design practice for welds will result in different levels of weld overstrength which will in turn affect the behavior of the low-ductility CBF.

4.3 Design of prototype building

To provide a realistic context to study the seismic performance of low-ductility CBFs in the ECUS, the prototype building is assumed to be located in Philadelphia, Pa. The building has a regular floor plan which consists of 5 bays of 30' wide in each orthogonal direction (Figure 4.8). The braced frame is located in the middle bay on the perimeter of the plan. The building has 3 stories with a first story height of 15 ft and the remaining story heights at 13 ft. The building is assumed to be an office building. The soil condition at the building site is assumed to be Site Class D according to ASCE7-10 (ASCE 2010). The building is designed using ASCE7-10 (ASCE 2010) and AISC Specification (AISC 2010b). Eight CBF design variants were developed for the prototype building to address the variations in the 3 key design variables identified in the previous section. Figure 4.9 shows building frame elevations for the 2 design variants with different brace configurations.

4.3.1 Gravity load

The design dead and live load for the building are shown in Table 4.6 and Table 4.7 respectively. The effective seismic weight of the structure and the seismic mass to be assigned to each floor level in the numerical model are calculated including the dead load and the partition load from the live load. The effective seismic weight of the entire building is determined as 5625 kips.

4.3.2 Seismic load

The equivalent lateral load procedure from ASCE7-10 (ASCE 2010) is used to for seismic design. The mapped MCE_R ("Risk Targeted" Maximum Considered Earthquake) spectral accelerations S_5 and S_1 is obtained from the USGS online seismic design tool

(<https://earthquake.usgs.gov/designmaps/us/application.php>) as 0.201g and 0.060g, respectively. The building belongs to Risk Category II and the importance factor $I_e = 1$. To consider the site soil conditions, soil amplification factors F_a and F_v were applied to S_S and S_1 to obtain the adjusted MCE_R spectral accelerations S_{MS} and S_{M1} as 0.322g and 0.145g. The DBE (Design Basis Earthquake) spectral accelerations S_{DS} and S_{D1} are 2/3 of the MCE_R spectral accelerations, and equal 0.215g and 0.096g. According to Table 11.16-1 and 11.6-2 in ASCE7-10 (ASCE 2010), the structure belongs to Seismic Design Category (SDC) B, representing a common scenario in teh ECUS. Consequently, the lateral system is designed with the Response Modification Factor $R = 3$, and without considering seismic detailing.

The seismic design base shear V is calculated using Eq. (4.5), where W is the effective seismic weight of the structure and C_s is the seismic response coefficient.

$$V = C_s W \quad (4.5)$$

C_s is calculated using Eq. (4.6) and is limited by the upper bounds of Eq. (4.7) and (4.8) and a lower bound of Eq. (4.9). The long-period transition period T_L for Philadelphia is 6s according to Figure 22-12 in ASCE7-10 (ASCE 2010). The fundamental period of the structure T is determined as the first mode period T_1 from eigenvalue analysis on the structural model of the prototype building and is capped by the upper limit from Eq. (4.10). Structural models of the design variants of the prototype building were developed in later sections to perform design calculation. It can be shown that T_1 for all models are larger than the period upper limit $C_u C_t h_n^x = 0.55s$ (Table 4.8). Therefore, the fundamental

period $T = 0.551s$ for all design variants. The information on the seismic design load is summarized in Table 4.9.

$$C_s = \frac{S_{DS}}{\left(\frac{R}{T_e}\right)} \quad (4.6)$$

$$C_s = \frac{S_{D1}}{T\left(\frac{R}{T_e}\right)} \text{ for } T \leq T_L \quad (4.7)$$

$$C_s = \frac{S_{D1}T_L}{T^2\left(\frac{R}{T_e}\right)} \text{ for } T > T_L \quad (4.8)$$

$$C_s = 0.044S_{DS}I_e \geq 0.01 \quad (4.9)$$

$$C_u T_a = C_u C_t h_n^x \quad (4.10)$$

The obtained base shear is distributed to each floor level using Eq. (4.11) and Eq. (4.12), where w_x and w_i is the effective seismic weight of the structure located at level x or i ; h_x and h_i is the height from the base to level x or i ; k is determined from Eq. (4.13). As the building has a symmetric floor plan, the obtained equivalent lateral force F_x is divided into half for each frame (

Table 4.10).

$$F_x = C_{vx}V \quad (4.11)$$

$$C_{vx} = \frac{w_x h_x^k}{\sum_{i=1}^n w_i h_i^k} \quad (4.12)$$

$$k = \begin{cases} 1 & \text{for } T \leq 0.5 \\ 0.5T + 0.75 & \text{for } 0.5 < T < 2.5 \\ 2 & \text{for } T \geq 2.5 \end{cases} \quad (4.13)$$

4.3.3 Wind load

In the ECUS, wind load can be significant compared to seismic load and is therefore considered in the design. Wind load on the Main Wind-Force Resisting System (MWFRS) of the building is determined using the directional procedure. The building is assumed to be located in Exposure B as it is situated in urban but not downtown Philadelphia area. The basic wind speed is determined from Figure 26.5-1A in ASCE7-10 to be 115 miles per hour (mph). The information for the wind load is summarized in Table 4.11. The design wind pressure p over the height of the structure is determined from Eq. (4.14) where $q = q_z$ for windward walls evaluated at height z above ground; $q = q_h$ for leeward walls evaluated at height h ; $q_i = q_h$ for internal pressure as a conservative measure; G is the gust-effect factor; C_p is the external pressure coefficient; GC_{pi} is the internal pressure coefficient. The velocity pressure q_z is obtained from Eq. (4.15), where K_z is the velocity pressure coefficient; K_{zt} is the velocity pressure coefficient; K_d is the wind directionality factor; V is the basic wind speed. The calculated wind pressure is displayed in Table 4.12 and Figure 4.10. Multiple load distribution scenarios exist because the internal pressure can take either positive or negative direction, and that C_p can take 2 values for the roof pressure. It is found that the base shear due to wind load for the entire building is 132.8 kips, smaller than that due to seismic load, which is 326.7 kips.

$$p = qGC_p - q_i(GC_{pi}) \quad (4.14)$$

$$q_z = 0.00256K_zK_{zt}K_dV^2 \quad (4.15)$$

However, it is found that for taller buildings the wind load will start to be the governing lateral load as the wind pressure increases with height while the seismic response coefficient C_s decreases with increasing design period. For example, for a 9-story building in the same location, the design base shear for wind is 524.6 kips while the seismic design base shear is 517.3 kips. It is for this reason that this dissertation focused on the 3-story prototype building which is dominated by seismic load, even though taller buildings constitute a significant portion of possible design variation of the low-ductility CBF inventory in the ECUS.

4.3.4 Other load

Snow load is calculated using Eq. (4.16) from ASCE7-10. The exposure factor $C_e = 0.9$ for Exposure B and fully exposed roof. The thermal factor $C_t = 1$. The importance factor $I_s = 1$ for Risk Category II. The ground snow load p_g is 25 psf in Philadelphia. The design snow load $p_f = 15.75 \text{ psf}$.

$$p_f = 0.7C_eC_tI_s p_g \quad (4.16)$$

Rain load is calculated from Eq. (4.17). d_s is the depth of water on the undeflected roof up to the inlet of the secondary drainage system when the primary drainage system is blocked. d_s is the additional depth of water on the undeflected roof above the inlet of the secondary drainage system at its design flow (ASCE 2010). The design rain load $R = 10.4 \text{ psf}$ with $d_s = 1.5''$ and $d_h = 5''$. As can be seen, both the snow load and the rain load are smaller than the roof live load (40 psf).

$$R = 5.2(d_s + d_h) \quad (4.17)$$

4.3.5 Load combinations

The following 7 load combinations from ASCE7-10 are used to design the building. The load factor on L is 0.5 in Eq. (4.20), (4.21) and (4.22) because the live load is less than 100 psf.

$$1.4D \quad (4.18)$$

$$1.2D + 1.6L + 0.5(L_r \text{ or } S \text{ or } R) \quad (4.19)$$

$$1.2D + 1.6(L_r \text{ or } S \text{ or } R) + (0.5L \text{ or } 0.5W) \quad (4.20)$$

$$1.2D + 1.0W + 0.5L + 0.5(L_r \text{ or } S \text{ or } R) \quad (4.21)$$

$$1.2D + 1.0E + 0.5L + 0.2S \quad (4.22)$$

$$0.9D + 1.0W \quad (4.23)$$

$$0.9D + 1.0E \quad (4.24)$$

The earthquake load effect E includes both horizontal force E_h and vertical force E_v . In load combination Eq. (4.22), the vertical earthquake force is applied downward to consider the worst-case scenario for column compression (Eq. (4.25)). For load combination in Eq. (4.24), the vertical earthquake force is applied upward to consider the worst-case scenario for column uplifting (Eq. (4.26)). $E_h = \rho Q_E$, where Q_E is the design seismic force determined from equivalent lateral procedure and the redundancy factor ρ is 1 for SDC B. E_v is determined from Eq. (4.27).

$$E = E_h + E_v \quad (4.25)$$

$$E = E_h - E_v \quad (4.26)$$

$$E_v = 0.2S_{DS}D \quad (4.27)$$

4.3.6 Design result

To carry out the design and analysis, a 2D model was created in SAP2000 (Computer and Structures 2010) for the perimeter frame in each orthogonal direction of the building and for each of the brace configuration variant. 2D analysis is used because ASCE7-10 allows the seismic design force to be applied in each of the orthogonal direction independently and ignore the orthogonal interaction effect for SDC B. The interior frames are designed by hand calculation as they are mainly controlled by gravity load. To address the variation of the 3 key design variables identified in Section 4.2, a total of 8 CBF design variants were developed (Table 4.13). They are represented by 4 SAP models as connection design is not included in those global models. To consider the variation in bracing configuration, the first 4 design variants use chevron bracing configuration (Figure 4.9 (a)) and the last 4 use split-X configuration (Figure 4.9 (b)).

As can be seen in the floor plan (Figure 4.8), the floor beams are oriented in the North-South (NS) direction, so the gravity load tributary to the NS girder in the perimeter frame is smaller than those in the East-West (EW) direction. Due to the smaller demand in gravity load, the girder of the frame in the NS direction is designed with smaller sections than those in the EW direction. Calculations show that the DCR of the unbalanced brace forces on the beam is 3.7 and 7.2 for NS and EW frame respectively in the current design. They

approximate the upper and lower bound (9.1 and 2.9 respectively) of the DCR of the unbalanced brace forces on the beam from survey of existing design in Section 4.2. Taking advantage of this, the CBFs in the EW and NS direction are considered to be 2 design variants to study the effect of different beam design strength on the collapse performance of low-ductility CBF.

The member section for the CBF in both 2 orthogonal directions for the Chevron and Split-X design variants of the building are shown in Table 4.14 and Table 4.15, respectively. The members for the interior gravity system are the same for all design variants (Table 4.16). The beams and columns use wide flange section with A992 steel. The braces use HSS square sections with A500 Gr. B steel.

The brace gusset plate connection follows a typical design found in existing buildings (Figure 4.4 (a)). The tubular brace is slotted and fillet welded to the gusset plate using E70 electro. The gusset plate is welded to the beam top flange. An angle welded to each side of the gusset plate is bolted to the column. The beam and column are connected by an angle on each of the 2 sides of the beam web. The angle is welded to the beam and bolted to the column. For connection where the brace joins the middle of the beam (e.g. chevron point), the gusset plate is welded to the flange of the beam.

Two different designs for the brace-to-gusset fillet weld are created to address the variation of weld design overstrength due to different design practice. The weak weld design, denoted as Design 1, follows the design practice from Hines et al. (2009) and Marsteller et al. (2002). It seeks to select fillet weld length and size to achieve minimum overstrength in terms of required strength. The only constraint on the weld length is that minimum length

is equal to the width of the tubular section. This is according to the AISC Specification (AISC 2010b) so that the shear lag factor can be calculated. As can be seen in Table 4.17, the available weld strength barely exceeds the required strength. The strong weld design, denoted as Design 2, follows the design practice found in Building 2. It employs 5/16" weld size universally and is also constrained by the minimal weld length which equals to the width of the tubular section. Because of this, there is significant overstrength of available weld strength compared to the required strength (Table 4.18).

Other elements of the brace-gusset plate connection such as the gusset plate and connecting angles are also designed as they are needed to calculate input parameters for numerical modeling. They are designed using Uniform Force Method from the AISC Steel Construction Manual which assumes no bending moment in beam-gusset interface, column-gusset interface and beam-column interface. Therefore, these connections only need to be designed for combined shear force and normal force. The connection design details are shown in Figure 4.12 to Figure 4.15. Only the drawings for Design 1 are shown here for brevity as Design 2 is only different with Design 1 in brace-to-gusset fillet weld dimension which is presented in Table 4.17 to Table 4.20.

4.4 Modeling of low-ductility CBF system

Numerical models for collapse simulation of low-ductility CBF system are developed in OpenSees computational framework (McKenna et al. 2000). Numerical model of the entire low-ductility CBF system includes the CBF which is the primary lateral force resisting system, the gravity load resisting system and the damping substructure. The contribution to resist lateral force from gravity system is usually ignored in the design phase. But in

reality, the gravity system is able to provide some degree of lateral force resistance and can be an important source of “reserve capacity” and significantly enhance the collapse performance (Elkady and Lignos 2015). Therefore, different numerical models considering different levels of contribution of lateral force resistance from the gravity system are created. The inherent elastic damping (Jehel et al. 2014) of the structure is modeled as damping substructure, a technique that avoids large artificial damping force when elements are severely damaged (Roke 2010). The numerical models are validated from recent test data. In the end, some alternative modeling approaches are also discussed.

4.4.1 Modeling of CBF

Low-ductility CBFs can develop unique limit states such as weld fracture, brace re-engagement and beam yielding etc., which are precluded in SCBF due to capacity design. These limit states are shown to have a great influence on the collapse behavior from experimental studies (Bradley et al. 2015; Davaran et al. 2014; Sizemore et al. 2015). Therefore, numerical models need to be able to capture these important limit states in order to have accurate collapse simulations. Due to symmetry of the building, a two-dimension (2D) finite element model was created and only one bay of the CBF is modeled. The schematic of the numerical model is shown in Figure 4.16.

In order to capture brace buckling, the braces are modeled using the approach proposed by Uriz and Mahin (2008). The brace is divided into 10 segments each of which is modeled using forceBeamColumn element. The brace takes a shape of a half sine with an initial imperfection e of $L/1500$ assigned to the middle node of the brace (Figure 4.18). Corotational geometric transformation is assigned to the brace elements to enable

simulation of large deformation and brace buckling. In reality, brace buckling for this type of connection and brace section happens out of plane. But due to the 2D simplification of the model, the brace is modeled to buckle in plane. As the building uses square HSS section, there is no need to change the orientation of the brace to facilitate in-plane buckling. The forceBeamColumn element is assigned with fiber section with Giuffre-Menegotto-Pinto (Steel02) material in OpenSees. Due to the 2D nature of the model, the sections are subdivided into multiple layers only in the direction perpendicular to the bending axis. The HSS brace section is divided into 10 fibers across the width and only one fiber is assigned across the thickness as the tube wall is very thin. The low cycle fatigue fracture of the braces is modeled by adding Fatigue material in OpenSees to the brace section material. This material uses a modified Rainflow cycle counting algorithm (Uriz 2005) to track the strain amplitude at each fiber and relate to damage according to Coffin-Manson relationship (Manson 1965) as shown in Eq (4.28). The damage is accumulated using Miner's rule (Miner 1945). Fracture is initiated once the accumulated damage of the fiber reaches 1.0 and the fiber is removed from the section. The 2 input parameters for the Fatigue material are ε_0 which is the strain amplitude that will cause fracture in one complete cycle, and m which controls the sensitivity between the strain amplitude of an individual cycle ε_i and N_f the number of cycle it takes to cause fracture at this strain amplitude. These two parameters have been empirically calibrated from a larger database of brace component tests and predictive formulas have been proposed for typical steel brace sections (Karamanci and Lignos 2014). Eq. (4.29) is the predictive formula for HSS brace section.

$$\varepsilon_i = \varepsilon_0(N_f)^m \quad (4.28)$$

$$\varepsilon_0 = 0.291 \cdot \left(\frac{kL}{r}\right)^{-0.484} \cdot \left(\frac{w}{t}\right)^{-0.613} \cdot \left(\frac{E}{F_y}\right)^{0.303} \quad (4.29)$$

To capture the limit state of brace-gusset connection weld fracture and brace re-engagement, a model for the brace end segment is developed to act as an axial spring (Figure 4.18). The brace end segment that is fillet welded to the gusset plate is modeled by a dispBeamColumn element assigned with a parallel of 3 materials (Figure 4.19) to simulate the effect of weld fracture and brace re-engagement. The first material (Figure 4.19 (a)) is a linear elastic material wrapped with Minmax material that simulates fracture in OpenSees. The linear elastic material is to account for the stiffness of the fillet weld. The stiffness of the fillet weld is determined according to Lesik and Kennedy (1990). The fracture strength of the Minmax material R_c is set as the expected strength of the weld which is determined from Fisher et al. (1978). It should be noted that the ductility of the weld is not considered as the dimension on the weld is so small compared to the entire brace therefore the ductile deformation of the weld is negligible. After fracture, the stiffness and stress of the first material is essentially reduced to zero. The second material (Figure 4.19(b)) is a compression-only gap material which is to simulate the effect of brace re-engagement by bearing onto the edge of the gusset plate. This material has zero stiffness and strength until the gap is reached in compression. After that the material act as a bilinear elastic plastic material of which the stiffness K_{re} and yield strength F_{re} is determined by calibration from test data shown in the following sections. The material has a strain hardening branch because it was observed in Sizemore et al. (2015) that as the gusset plate beared further onto the slot edge, the contact surface grew due to the flattening of the

deformed steel (Figure 4.20). The value of the gap dimension is set as the actual gap between the slot edge and the gusset plate edge which is 2 inches. The material has no stiffness or strength in the tension range simulating the fact that the connection is not effective in tension after weld fracture. It should be noted that another Minmax material should be wrapped with this gap material. The fracture deformation of this Minmax material in the tension range should be set as the length of the weld (a very large value is assigned to compression threshold). If the fracture threshold is reached in tension, the gap material will no longer be effective even if the deformation returns to the re-engagement range in compression. This is to simulate the phenomenon that if the tension deformation is too large after the brace connection fractures, the brace slot will be pulled out of the gusset plate and the brace will no longer be able to re-engage with the gusset plate. This phenomenon has been observed in Sizemore et al. (2015). The third material is simply a very flexible elastic material to provide numerical stability (Figure 4.19 (c)). The behavior of this model under cyclic load is demonstrated in Figure 4.21. At the beginning, when the force is smaller than the weld strength, the connection acts linear elastically. In the subsequent half cycle in compression, the weld fractures after the force exceeds the weld strength and the connection becomes ineffective until the gap is closed between the brace slot and the edge of the gusset plate. With the brace re-engaging with the gusset plate, the connection is effective in compression. In the later tension cycle, the connection is not able to transfer forces and the slot is pulled out of the gusset plate when the tensile deformation exceeds the length of the weld. Subsequently, brace is no longer able to re-engage with the gusset plate and provide compression even if the compressive deformation exceeds the gap

distance. It is assumed in the model that weld fracture and brace re-engagement only happens in the brace end at beam column connection.

The gusset plate rotational flexibility is modeled by a rotational spring (red circle in Figure 4.17) following the method in Hsiao et al. (2012). Steel02 material is used for this nonlinear spring. The rotational stiffness and yielding moment for this material is based on the geometry of the connection detail design (Figure 4.12) and determined using the empirical formula from Hsiao et al. (2012).

The beams are modeled using concentrated plastic hinge (CPH) approach in which a zero-length rotational spring is attached to each of the 2 ends of an elasticBeamColumn element (Figure 4.22). The rotational spring is assigned with Ibarra-Medina-Krawinkler (IMK) hysteretic material (Ibarra et al. 2005) that is able to capture both the in-cycle and between-cycle stiffness and strength deterioration (Figure 4.23) due to local buckling. The IMK material is calibrated by a large test database of steel beam-to-column subassemblies. The input parameters for the material (M_y , M_c , θ_p , θ_{pc} , Λ) are provided by the empirical formulas developed by Lignos and Krawinkler (2011). The advantage of using CPH model is that it can capture the strength deterioration in beam plastic hinge due to local buckling. This limit state often happens at the beam-brace joint when the structure becomes a “long link EBF” which is an important collapse mechanism of the low-ductility CBF (Figure 4.24).

Recent testing shows that beam-column (BC) connection with gusset plate can develop considerable flexural stiffness and strength (Stoakes and Fahnestock 2011) and can improve collapse performance by increasing the frame action. Therefore, they are also

included in the model. The beam-column connection with only one gusset plate on top of the beam in chevron braced frame (Figure 4.12 (b) and (c)) is modeled with a rotational spring located at the beam column interface (green circle in Figure 4.16 and Figure 4.17(a)) and assigned with Pinching4 material in OpenSees following the suggestion of Karamanci and Lignos (2014). This material is able to capture the asymmetric hysteresis behavior due to gusset plate and pinching phenomenon due to bolt slip and angle bearing (Figure 4.25 (b)). The material is defined by a backbone curve along with some other parameters that controls the pinching and deterioration property (Figure 4.25 (a)). The initial stiffness and ultimate moment capacity M_c of the connection is determined based on the size and location of the bolt and angle using the predictive formula proposed in Stoakes and Fahnestock (2012). The yielding moment M_y and residual moment M_r is assumed to be $M_c/1.1$ and $0.1M_c$, respectively. The deformation capacity and hysteresis parameters use the recommended value from calibration result from Karamanci and Lignos (2014). The beam-column connection with gusset plate on both top and bottom of the beam in split-X braced frame (Figure 4.14 (b) and (c)) is modeled as a rigid connection, as 2 gusset plates resulted in very large moment arm and thereby significantly increase the rotational stiffness and strength. The beam-column connection without a gusset plate (the one on roof of chevron braced frame and the one on the first story of split-X braced frame) is modeled as pin connection since the beam is only connected to the column by a shear tab.

As the IMK material is developed for beam section without axial load, it's not considered to be appropriate to be used in column section in which considerable axial load exists. For this reason, columns are modeled with forceBeamColumn element with fiber sections that is able to capture Axial-Moment Interaction. 12 fibers are used along the depth of the web

and 4 fibers are used across the thickness of the flange. Steel02 material is assigned to the fibers.

The rigid offset at the connection of elements are modeled with very stiff elasticBeamColumn elements (shown in black thick line in Figure 4.16 and Figure 4.17). The rigid zone at the end of the brace extends from the working point of beam-column connection to the end of the actual brace. The rigid offset in the beam stems from the column centerline to the outer edge of gusset plate while the rigid zone in the column ranges from the beam bottom surface up to the top edge of the gusset plate (Figure 4.17).

4.4.2 Modeling of gravity system

In order to assess the effect of gravity system on the collapse performance of low-ductility CBF, four different approaches are used to model the gravity system accounting for the different levels of contribution of lateral resistance (Figure 4.26):

- (i) The gravity system is modeled as a lean-on-column (LOC) with elastic elements that are pin connected between each story and at the base. The area and moment of inertia of the LOC is based on the summation of the area and moment of inertia of all gravity columns in the tributary area (half of the total floor area). All gravity load tributary to the gravity system is applied to the LOC. P-Delta transformation is applied to the LOC to account for the destabilizing effect of gravity. It can be noted that this modeling approach completely ignores any lateral resistance contributed by the gravity system and purely considers P- Δ effect. This modeling approach is denoted as LOC-pin.

- (ii) The gravity system is modeled as a LOC with elastic elements that are continuous between each story and pin connected at the base. All other aspects remain the same as the LOC-pin model. This modeling approach considers some degree of lateral resistance in preventing soft story mechanism and drift concentration due to continuous stiffness of the gravity columns. This modeling approach is denoted as LOC-continuous.
- (iii) The gravity system is modeled as a LOC with forceBeamColumn elements with fiber sections. The Steel02 material is assigned to the fiber sections. All other aspects remain the same as the LOC-continuous model. This model considers the effect of yielding in columns. This modeling approach is denoted as LOC-continuous-fiber.
- (iv) The gravity system is modeled as a one-bay frame called “equivalent gravity frame” (EGF) proposed by Elkady and Lignos (2015). In addition to the lateral force resistance contribution from the continuity of gravity columns, this modeling approach also considers the flexural strength and stiffness from beam-column connections in the gravity system. The beam-column connection with single angle shear tab and composite slab that is typical in gravity system design is found able to develop considerable flexural strength due to composite action (Liu and Astanteh-Asl 2000). The equivalent gravity frame consists of forceBeamColumn elements with fiber sections to model the columns and elasticBeamColumn elements with rotational springs attached at two ends to model the beam-column connection. As the shear tab composite slab connection is usually characterized by a pinched moment-rotation hysteresis

with strength and stiffness degradation, the rotational spring is assigned with Pinching4 material. The material parameters (Figure 4.27 (a)) follow the guideline from Elkady and Lignos (2015). An example of the hysteresis behavior of the beam-column connection model is shown in Figure 4.27 (b). The connection can resist significant moment before the concrete floor slab failed and the strength and stiffness of the connection is deteriorated. Each column is assigned with the flexural stiffness and strength property that equal to half of the sum of those columns in the tributary area. Each beam and its hinge is assigned with the flexural stiffness and strength property that equals the sum of those beams in the tributary area. This modeling approach is denoted as EGF.

4.4.3 Modeling of damping with damping substructure

OpenSees allows Rayleigh damping (Eq. (4.30)) to be assigned to the entire structure or certain region of the structure (by nodes or element). a_0 and a_1 can be calculated according to Eq. (4.31) to anchor the damping ratio of mode i and j , with natural frequency ω_i and ω_j , at ζ . Charney (2008) showed that if stiffness proportional damping based on initial stiffness matrix is assigned to elements where severe damage happens, large artificial damping forces may be generated in nonlinear analysis. One solution is to use tangent stiffness based proportional damping to the region where nonlinearity may happen. However, this solution often brings challenge in numerical convergence as tangent stiffness may become negative at some time step (e.g. due to geometric stiffness after brace buckling) and thereby cause damping matrix to become negative too. Another solution is to exclude stiffness proportional damping from elements where significant damage is

expected to take place, e.g. brace elements in CBFs. Nevertheless, this approach may grossly underestimate the inherent elastic damping of the structure because the braces are major contributors to the lateral stiffness and therefore provide significant elastic damping for CBF.

$$\mathbf{c} = a_0 \mathbf{m} + a_1 \mathbf{k} \quad (4.30)$$

$$a_0 = \zeta \frac{2\omega_i \omega_j}{\omega_i + \omega_j} \quad a_1 = \zeta \frac{2}{\omega_i + \omega_j} \quad (4.31)$$

Therefore, the inherent elastic damping of the structure is modeled by damping substructure which avoids the drawback of the 2 approaches above. In the damping substructure approach, the inelastic CBF is not assigned with any stiffness proportional damping. In compensation, the damping substructure, a duplicate CBF modeled with elastic elements, is created and attached with the inelastic CBF. The elements in damping substructure are all assigned with a reduced elastic modulus $E_{DS} = E/10000$, where E is the young's modulus of steel, thereby reducing the lateral stiffness of the damping substructure by 10000 times and minimize its influence on the lateral resistance of the entire system. The stiffness proportional damping is assigned to all elements in damping substructure base on initial stiffness matrix (since tangent stiffness remains the same as initial stiffness for elastic elements). The stiffness proportionate coefficient a_1 in front of the stiffness matrix is amplified 10000 times to restore the right amount of damping since the stiffness of the damping substructure is reduced 10000 times from the original elastic stiffness. The process is illustrated by Figure 4.28 where \mathbf{k}_{DS} denotes stiffness matrix of damping substructure. As the damping substructure remains elastic, no artificial damping

forces will be produced due to member yielding. In this way, the inherent elastic damping from all elements of the CBF is preserved in the damping substructure at the right amount. Tangent stiffness based proportional damping is assigned to the gravity system using the original stiffness proportionate coefficient a_1 . The mass proportional damping remains the same for the entire structural system. $\zeta = 2\%$ of damping is assigned to the first and second mode of the structure. The natural frequency of the structure is obtained by performing eigenvalue analysis after gravity load is applied and thereby includes the second order effect. Both the damping substructure and the gravity system is attached to the inelastic CBF by rigid link (Figure 4.29).

4.4.4 Validation of numerical model

To verify that the modeling approach is able to capture the unique limit states of brace connection fracture, brace re-engagement and beam hinging at chevron point developed during “long link EBF” response, the test data on the first story response from the second test phase of Sizemore et al. (2015) is utilized as these 3 limit states were exhibited by the test unit. In addition, the brace re-engagement response during the test is used to calibrate the input parameters for brace re-engagement model. During the second test phase, load was only applied to the first story of the test unit which remained undamaged during the first test phase. The test specimen is modeled using the above modeling approach and applied the displacement history during the test (Figure 4.30). A trial and error process is used to calibrate the parameters of the gap material to model brace re-engagement. The elastic stiffness and yield strength of the gap material is normalized by the brace axial stiffness and brace yield force in order to provide general modeling guideline. Through calibration, it is found that the analytical response match well with the test result for brace

re-engagement response when the elastic stiffness K_{re} , yield strength F_{re} and strain hardening ratio is $9 \frac{EA_{br}}{L_{br}}$, $0.2F_y A_{br}$ and 0.001, respectively (E is the elastic modulus of steel; A_{br} is the area of the brace section; L_{br} is the actual brace length; F_y is the nominal yield strength of brace material). The comparison of analytical model response and test result is presented in Figure 4.31. It can be seen that the limit states of weld fracture and “long link EBF” response (positive drift range) are also captured very well by the analytical model. During the “long link EBF” response (Figure 4.32), local buckling developed in beam plastic hinge at the chevron point which caused strength deterioration. This is captured by the analytical model which uses the IMK material to model plastic hinge (Figure 4.33). Therefore, it is validated that the model can capture the unique limit states of low-ductility CBF.

To verify that the model is able to capture brace global buckling, the test result of the OCBF from Bradley et al. (2015) is used. The test specimen uses compact sections for brace and local buckling did not occur during global buckling of the brace. The test unit is modeled using the above approach and applied with the displacement history during the test. The comparison of the model response and experiment result is shown in Figure 4.34. It can be seen that the global buckling of the brace is well captured by the model.

4.4.5 Alternative modeling approach

Apart from the modeling approach discussed above, two alternative modeling approaches are also studied as they have both advantage and disadvantage. They are:

- Using forceBeamColumn element with fiber section to model beams

- Modeling local buckling in braces

The IMK material can model flexural strength deterioration in beam plastic hinge. However, it cannot capture the axial-moment interaction in the beam. To avoid this problem, the beam between the rigid offset can be directly modeled as a forceBeamColumn element assigned with fiber sections and Steel02 material (Figure 4.35). Five integration points are used for the elements. However, the fiber-based element is not able to capture the strength deterioration in the beam due to local buckling. These 2 different approaches in modeling beam is compared in Chapter 7 to investigate whether it is more important to capture strength deterioration effect or moment-axial interaction for the collapse response of low-ductility CBF.

While it is verified that the conventional brace modeling approach in Section 4.4.1 is able to model brace global buckling, it cannot capture the rapid strength deterioration in the post buckling range due to local buckling of non-compact section. The reason is that at the location of local buckling, the section is distorted and the plane section no longer remains plane. The effective strength and stiffness of the section has deteriorated. However, in the current modeling approach, plane section is still assumed to remain plane and the strength and stiffness of the section does not have deterioration. Therefore, it can only model the global buckling effect not local buckling. To solve this problem, a new method to model the brace is proposed as shown in Figure 4.36. A rotational spring is inserted at the midpoint of the brace to attach left and right half of the brace. The rotational spring is assigned with Steel02 material to represent the lumped behavior of the local buckled region. The R0 parameter of the material is set as a low value (5~7) to artificially amplify the Baushinger

effect which can be utilized to model the rapid strength and stiffness deterioration of sections in the local buckled region as shown in Figure 4.38. The initial stiffness of the hinge material is set between $5EI/L$ to $10EI/L$, where E is the Young's modulus of steel, I is the moment of inertia of the brace, L is the brace length. The yield moment of hinge is set around the nominal bending moment capacity of HSS section M_n determined using Eq. (F7-2) from AISC Specification (AISC 2010b). All other aspects of the model including element type and material for the brace etc. remain the same as the conventional modeling approach described in section 4.4.1. The test data in (Simpson et al. 2013) is used to validate the modeling approach. The test result of the 2 story frame in Figure 2.16 which utilized non-compact braces and experienced local buckling (Simpson et al. 2013) is used to validate the new modeling approach. As can be seen in Figure 4.37, the rapid strength deterioration of local buckled brace is captured by the proposed method. Figure 4.38 shows the hysteresis behavior of the hinge which simulates the deterioration of the effective stiffness and strength of the local buckled section. The global behavior of the frame is also captured as shown in Figure 4.39. In comparison, if the original method is used to model the brace, the post buckling strength in later cycles remains high and the local buckling effect is not captured (Figure 4.40). It should be noted that, however, when the local buckling hinge is introduced to model braces, the uniaxial strain of the fibers in the brace sections will be different from the case where the brace is modeled in the conventional way without the hinge. As the empirical formula to predict brace fatigue life (Eq. (4.29)) is based on calibration using conventional brace model, it does not apply to the proposed model. A new calibration process using the proposed brace model is needed to develop a new formula that predicts the input parameter for the fatigue material. This is beyond the

scope of this dissertation and is considered as future work. Therefore, in order to utilize the established result to model brace fatigue fracture, the brace is still modeled in the conventional way described in section 4.4.1 for the rest of the analysis in this dissertation.

It should be noted that, among the different modeling approaches previously discussed, the base line model uses CPH approach to model beams; the gravity load system is modeled using the LOC-pin approach, denoted as approach (i) in section 4.4.2. Brace re-engagement is also included in the baseline model. The baseline model was used in the subsequent analyses unless otherwise stated.

Table 4.1 Building designs reviewed

Drawing	Content	Design Firm Alias
1	Building 1	DF1
2	Building 2	DF2
3	Building 3	DF3
4	Connection assembly	DF2

Table 4.2 Information on beam design from existing buildings and evaluation of beam strength under unbalanced brace force

		Building 2	Building 3
Beam	Section	W18×119	W18×40
	M_p (kips·ft)	1092.2	326.7
Brace	Section	HSS 8×8×5/8	HSS 6×6×1/2
	Expected tension (kips) Eq. (4.1)	1056.2	627.3
	Expected post-buckling strength (kips) Eq. (4.2)	244.2	92.8
	Resultant vertical force (kips) Eq. (4.3)	643.6	357.5
	Induced bending moment	3217.8	2681.4
	Demand Capacity Ratio (DCR)	2.9	9.1

Table 4.3 Connection design in Hines et al. (2009)

Table 3. R3 Design Brace Sizes and Connection Forces						
Story	Design Load	Brace	Expected Strength	Weld (x4)	Weld Capacity	
(1)	(2)	(3)	(4)	(5)	(6)	
3 Story	3	81 k	6x6x¼	201 k	¾"x6"	134 k
	2	121 k	7x7x¼	268 k	¼"x7"	208 k
	1	158 k	8x8x¼	302 k	¼"x8"	238 k
6 Story	6	63 k	6x6x¼	201 k	¾"x6"	134 k
	5	99 k	6x6x¼	201 k	¾"x6"	134 k
	4	125 k	7x7x¼	268 k	¼"x7"	208 k
	3	153 k	8x8x¼	332 k	¼"x8"	238 k
	2	167 k	8x8x¼	332 k	¼"x8"	238 k
	1	197 k	8x8x ⁵ / ₁₆	371 k	¼"x9"	267 k
9 Story	9	62 k	6x6x¼	201 k	¾"x6"	134 k
	8	95 k	6x6x¼	201 k	¾"x6"	134 k
	7	119 k	7x7x¼	268 k	¼"x7"	208 k
	6	140 k	7x7x¼	268 k	¼"x7"	208 k
	5	158 k	8x8x¼	332 k	¼"x8"	238 k
	4	172 k	8x8x¼	332 k	¼"x8"	238 k
	3	182 k	8x8x¼	332 k	¼"x9"	267 k
	2	189 k	8x8x¼	332 k	¼"x9"	267 k
	1	218 k	9x9x ⁵ / ₁₆	453 k	¼"x10"	297 k
12 Story	12	57 k	5x5x¼	134 k	¾"x5"	111 k
	11	87 k	6x6x¼	201 k	¾"x6"	134 k
	10	110 k	7x7x¼	268 k	¾"x7"	156 k
	9	130 k	7x7x¼	268 k	¼"x7"	208 k
	8	148 k	7x7x¼	268 k	¼"x7"	208 k
	7	163 k	8x8x¼	332 k	¼"x8"	238 k
	6	176 k	8x8x¼	332 k	¼"x8"	238 k
	5	186 k	8x8x¼	332 k	¼"x9"	267 k
	4	194 k	8x8x¼	332 k	¼"x9"	267 k
	3	200 k	8x8x ⁵ / ₁₆	409 k	¼"x9"	267 k
	2	204 k	8x8x ⁵ / ₁₆	409 k	5/16"x8"	297 k
	1	233 k	9x9x ⁵ / ₁₆	453 k	5/16"x9"	334 k

Table 4.4 Example of different level of weld overstrength as a result of different design convention

Design	Location	Weld size (inch)	Weld length (inch)	Weld capacity (kips)	Design force demand (kips)	DCR
Building 2	second story	5/16	14	389.8	338.0	0.87
6 story building Hines et al. (2009)	first story	1/4	9	200.5	197.0	0.98
9 story building Hines et al. (2009)	first story	1/4	10	222.7	218.0	0.98

Table 4.5 Weld size design guideline from Marstellar et al. (2002)

Chevron Bracing in Low-Rise Buildings							
Unfactored Loads (Kips)		30	50	75	100	150	200
HSS	Round HSS ASTM A500, Gr. B	HSS 5.000x0.375 (18.5 lb/ft)	HSS 6.000x0.312 (19.0 lb/ft)	HSS 6.000x0.500 (29.4 lb/ft)	HSS 6.875x0.500 (34.1 lb/ft)	HSS 8.625x0.500 (43.4 lb/ft)	HSS 9.625x0.500 (48.8 lb/ft)
	Square HSS ASTM A500, Gr. B	HSS5x5x1/4 (16 lb/ft)	HSS6x6x1/4 (19 lb/ft)	HSS6x6x1/4 (19 lb/ft)	HSS7x7x1/4 (22 lb/ft)	HSS8x8x5/16 (32 lb/ft)	HSS8x8x3/8 (38 lb/ft)
	Weld	"a" (in) [See Details]	3/16	3/16	1/4	1/4	5/16
	"b" (in) ** [See Details]	7	8	8	9 (Round) 10 (Square)	12 (Round) 11 (Square)	13 (Round) 11 (Square)

Table 4.6 Design dead load

Item	Description	Equivalent uniform load (psf)	
		Typical floors	Roof
Slab	3 ½ inch on 2 inch, lightweight concrete	44	-
Metal deck	18 gage metal deck	3	3
Ceiling		5	5
Finish	Carpet	2	-
Mechanical/electrical		10	20
Fireproofing		2	2
Curtain wall	25 psf on vertical projection	9	-
Steel structure	Beams, girders, columns, etc.	10	10
Total		85	40

Table 4.7 Design live load

Item	Equivalent uniform load (psf)	
	Typical floors	Roof
Office	50	40
Partition	20	-
Total	70	40

Table 4.8 T_1 (s) obtained from SAP model for each design variant

Chevron		Split X	
EW	NS	EW	NS
0.76s	0.82s	0.78s	0.79s

Table 4.9 Summary of seismic design information

Location	Philadelphia, Pa
Occupation	Office building
Soil condition	Site D
S_S	0.201g
S_1	0.060g
Importance factor I_e	1.0
F_a	1.6
F_v	2.4
S_{MS}	0.322g
S_{M1}	0.145g
S_{DS}	0.215g
S_{D1}	0.096g
Seismic Design Category (SDC)	B
Design period T	0.551s
Response modification factor R	3
Seismic response coefficient C_s	0.058
Effective seismic weight	5625 kips
Design base shear	326.7 kips

Table 4.10 Equivalent lateral force at each floor level per frame due to seismic load

Floor level	$\frac{F_x}{2}$ (kips)
1	42.2
2	78.9
3	43.6

Table 4.11 Summary of wind design information

Dimension (ft)	Topography	Exposure	Building Risk Category	Basic Wind Speed V (mph)
150×150×41	Urban	B	II	115 mph

Table 4.12 Calculation of design wind pressure

Surface		z (ft)	q (psf)	Cp	External pressure (psf)	Internal pressure (psf)		Total pressure (psf)	
Windward wall		0 to 15	16.4	0.8	10.7	12.4	-12.4	23.2	-1.7
		20	17.8	0.8	11.7	12.4	-12.4	24.1	-0.7
		25	19.0	0.8	12.4	12.4	-12.4	24.9	0.0
		30	20.1	0.8	13.2	12.4	-12.4	25.6	0.8
		40	21.9	0.8	14.3	12.4	-12.4	26.8	1.9
		45	22.6	0.8	14.8	12.4	-12.4	27.2	2.4
Leeward wall		All	22.6	-0.5	-9.3	12.4	-12.4	3.2	-21.7
Side walls		All	22.6	-0.7	-13.0	12.4	-12.4	-0.5	-25.4
Roof	1 st Cp value	0 to 22.5	22.6	-0.9	-16.7	12.4	-12.4	-4.2	-29.1
		22.5 to 45	22.6	-0.9	-16.7	12.4	-12.4	-4.2	-29.1
		45 to 90	22.6	-0.5	-9.3	12.4	-12.4	3.2	-21.7
		90 to 150	22.6	-0.3	-5.6	12.4	-12.4	6.9	-18.0
	2 nd Cp value	0 to 22.5	22.6	-0.18	-3.3	12.4	-12.4	9.1	-15.8
		22.5 to 45	22.6	-0.18	-3.3	12.4	-12.4	9.1	-15.8
		45 to 90	22.6	-0.18	-3.3	12.4	-12.4	9.1	-15.8
		90 to 150	22.6	-0.18	-3.3	12.4	-12.4	9.1	-15.8

Table 4.13 Summary of CBF design variants for prototype building

Bracing configuration	Bay direction	Beam relative strength	Weld design	Weld relative strength
Chevron	EW	Strong	Design 1	Weak
			Design 2	Strong
	NS	Weak	Design 1	Weak
			Design 2	Strong
Split-X	EW	Strong	Design 1	Weak
			Design 2	Strong
	NS	Weak	Design 1	Weak
			Design 2	Strong

Table 4.14 Member sections for chevron CBF

Story	Bay direction					
	EW			NS		
	Beam	Column	Brace	Beam	Column	Brace
1	W24×62	W12×40	HSS7×7×5/16	W16×36	W12×40	HSS7×7×1/4
2	W24×62	W12×40	HSS6×6×5/16	W16×36	W12×40	HSS6×6×5/16
3	W21×44	W12×40	HSS5×5×3/16	W14×26	W12×40	HSS5×5×3/16

Table 4.15 Member sections for split-X CBF

Story	Bay direction					
	EW			NS		
	Beam	Column	Brace	Beam	Column	Brace
1	W24×62	W12×40	HSS7×7×5/16	W16×36	W12×40	HSS7×7×5/16
2	W24×62	W12×40	HSS6×6×5/16	W16×36	W12×40	HSS6×6×5/16
3	W21×44	W12×40	HSS5×5×3/16	W14×26	W12×40	HSS5×5×3/16

Table 4.16 Member sections for gravity system

Story	Bay direction						Column
	EW			NS			
	Interior girder	Exterior girder	Floor Beam	Interior girder	Exterior girder	Exterior and corner	Interior
1	W24×62	W24×62	W16×36	W16×36	W16×36	W12×40	W14×53
2	W24×62	W24×62	W16×36	W16×36	W16×36	W12×40	W14×53
3	W21×44	W21×44	W14×26	W14×26	W14×26	W12×40	W14×53

Table 4.17 Information on weak weld (Design 1) for chevron CBF

Location		Brace Section	Required strength P_u (kips)	Weld size d (1/16 inch)	Weld length l (inch)	Available strength $4 * \phi R_n$ (kips)
NS	1st floor	HSS 7×7×1/4	130.5	3	8	133.6
	2nd floor	HSS 6×6×5/16	97.1	3	6	100.2
	3rd floor	HSS 5×5×3/16	33.7	3	5	83.5
EW	1st floor	HSS 7×7×5/16	150.8	4	7	155.9
	2nd floor	HSS 6×6×5/16	112.2	3	7	116.9
	3rd floor	HSS 5×5×3/16	39.7	3	5	83.5

Table 4.18 Information on strong weld (Design 2) for chevron CBF

Location		Brace Section	Required strength P_u (kips)	Weld size d (1/16 inch)	Weld length l (inch)	Available strength $4 * \phi R_n$ (kips)
NS	1st floor	HSS 7×7×1/4	130.5	5	7	194.9
	2nd floor	HSS 6×6×5/16	97.1	5	7	194.9
	3rd floor	HSS 5×5×3/16	33.7	5	5	139.2
EW	1st floor	HSS 7×7×5/16	150.8	5	7	194.9
	2nd floor	HSS 6×6×5/16	112.2	5	7	194.9
	3rd floor	HSS 5×5×3/16	39.7	5	5	139.2

Table 4.19 Information on weak weld (Design 1) for split-X CBF

Location		Brace Section	Required strength P_u (kips)	Weld size d (1/16 inch)	Weld length l (inch)	Available strength $4 * \phi R_n$ (kips)
NS	1st floor	HSS 7×7×5/16	140.7	4	7	155.9
	2nd floor	HSS 6×6×5/16	92.8	3	6	100.2
	3rd floor	HSS 5×5×3/16	33.4	3	5	83.5
EW	1st floor	HSS 7×7×5/16	154.0	4	7	155.9
	2nd floor	HSS 6×6×5/16	95.3	3	6	100.2
	3rd floor	HSS 5×5×3/16	39.0	3	5	83.5

Table 4.20 Information on strong weld (Design 2) for split-X CBF

Location		Brace Section	Required strength P_u (kips)	Weld size d (1/16 inch)	Weld length l (inch)	Available strength $4 * \phi R_n$ (kips)
NS	1st floor	HSS 7×7×5/16	140.7	5	7	194.9
	2nd floor	HSS 6×6×5/16	92.8	5	7	194.9
	3rd floor	HSS 5×5×3/16	33.4	5	5	139.2
EW	1st floor	HSS 7×7×5/16	154.0	5	7	194.9
	2nd floor	HSS 6×6×5/16	95.3	5	7	194.9
	3rd floor	HSS 5×5×3/16	39.0	5	5	139.2

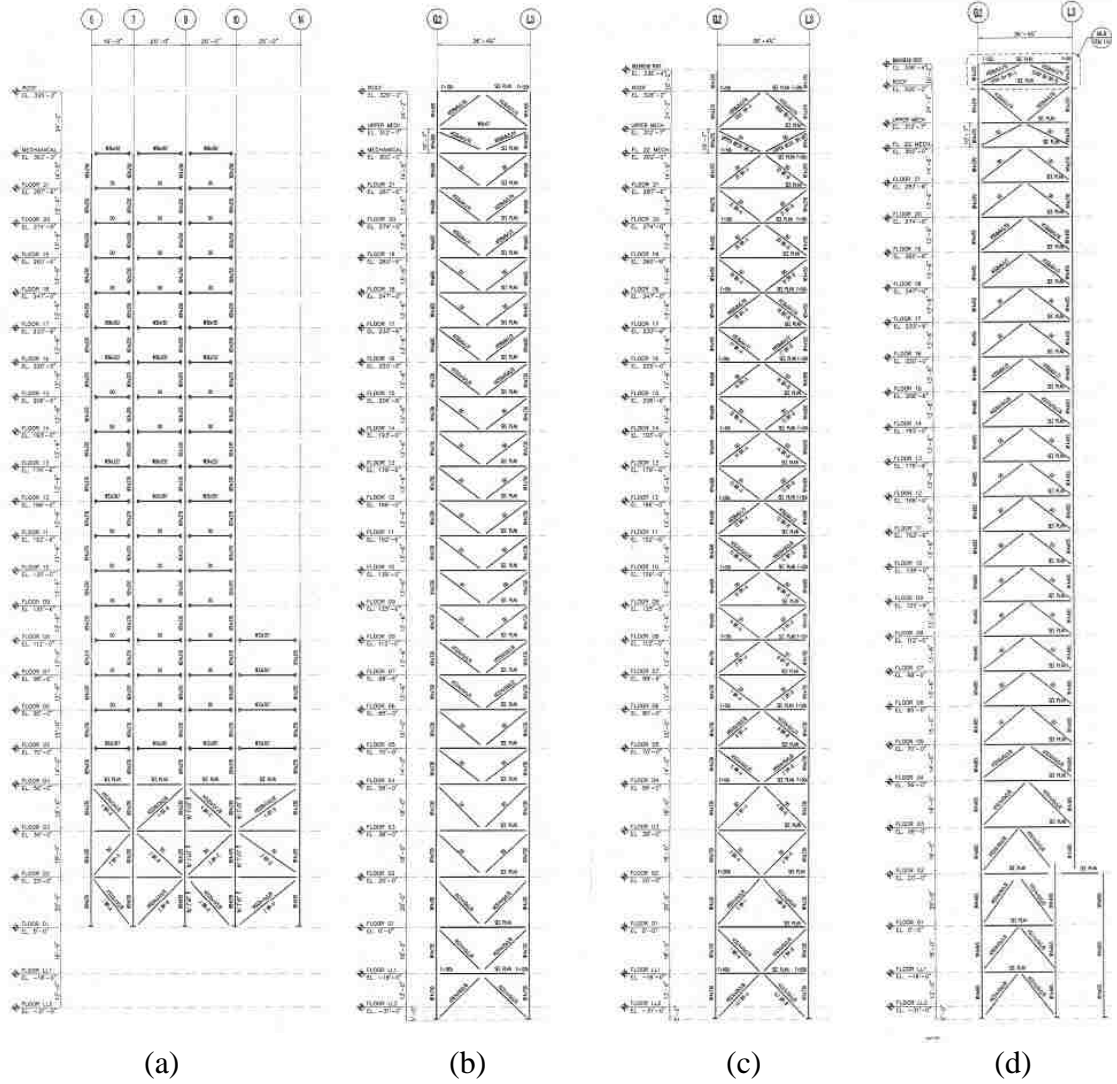


Figure 4.1 Variation of brace configuration from existing CBF design (from Building 1): (a) single diagonal, multi-story X; (b) inverted chevron; (c) split X; (d) chevron

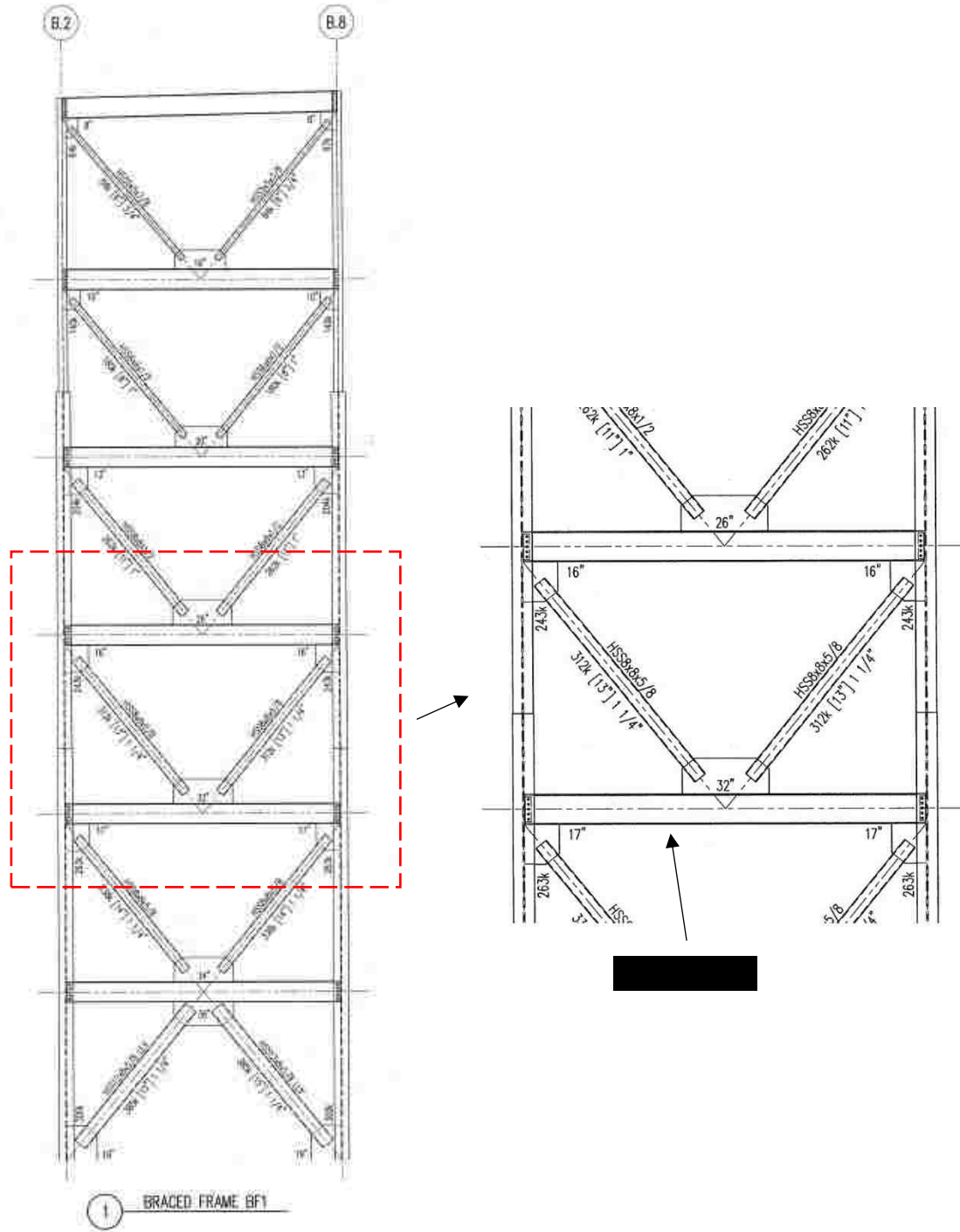


Figure 4.2 Brace and beam section for Building 2

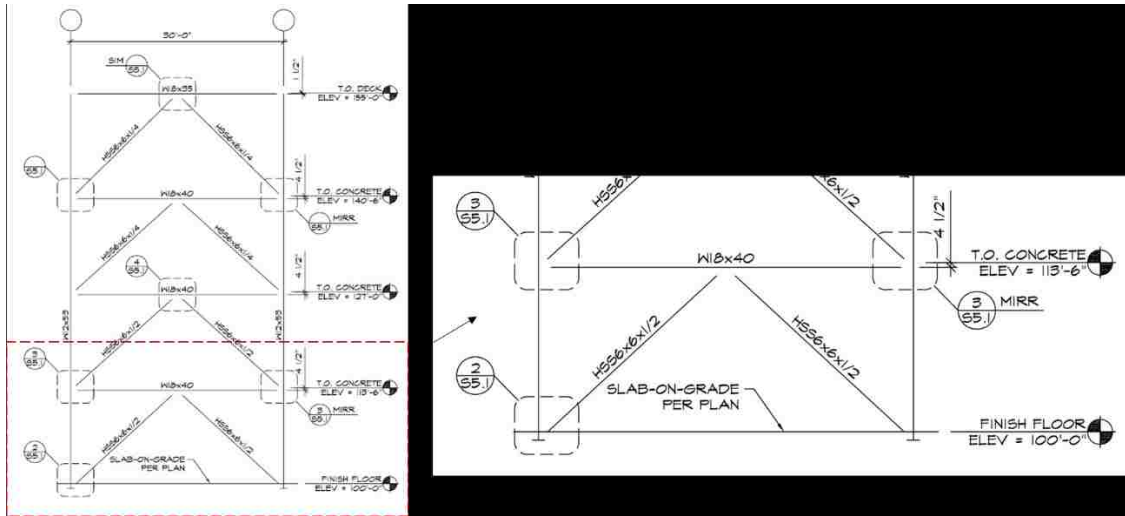
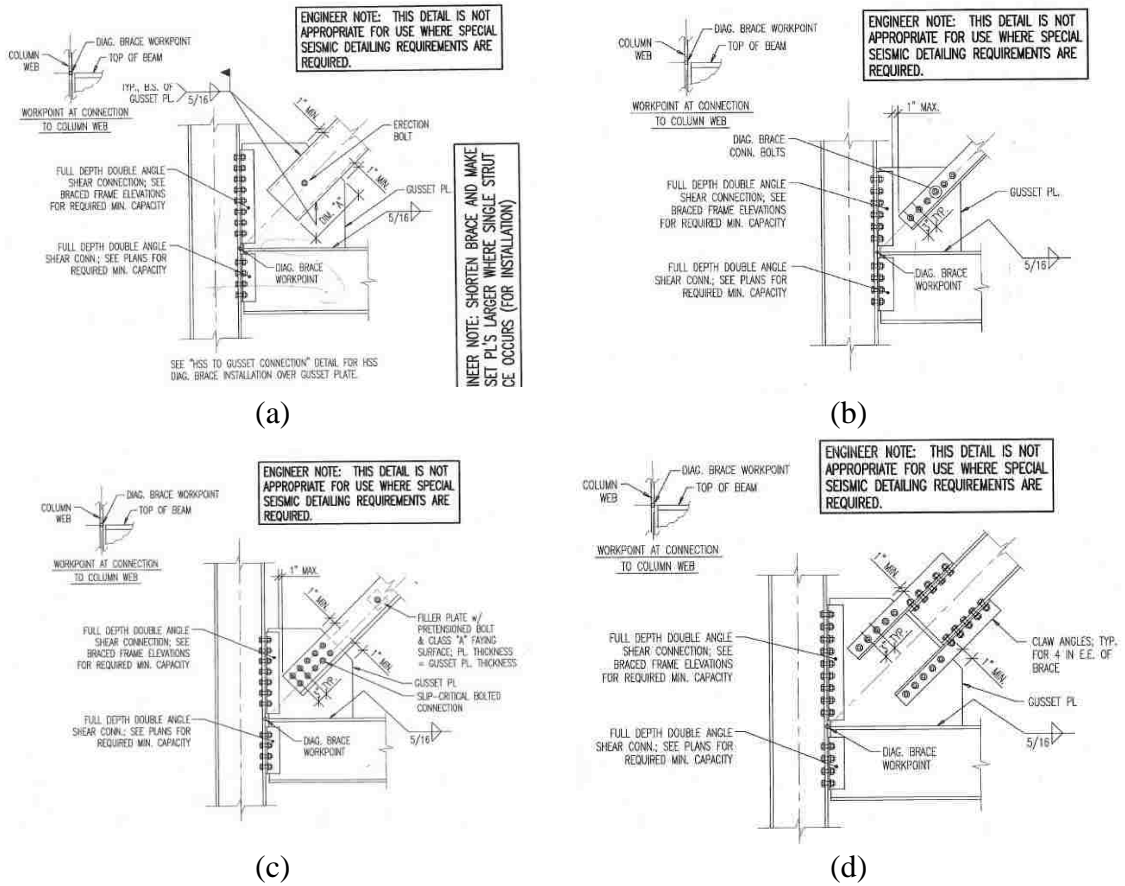


Figure 4.3 Brace and beam section for Building 3



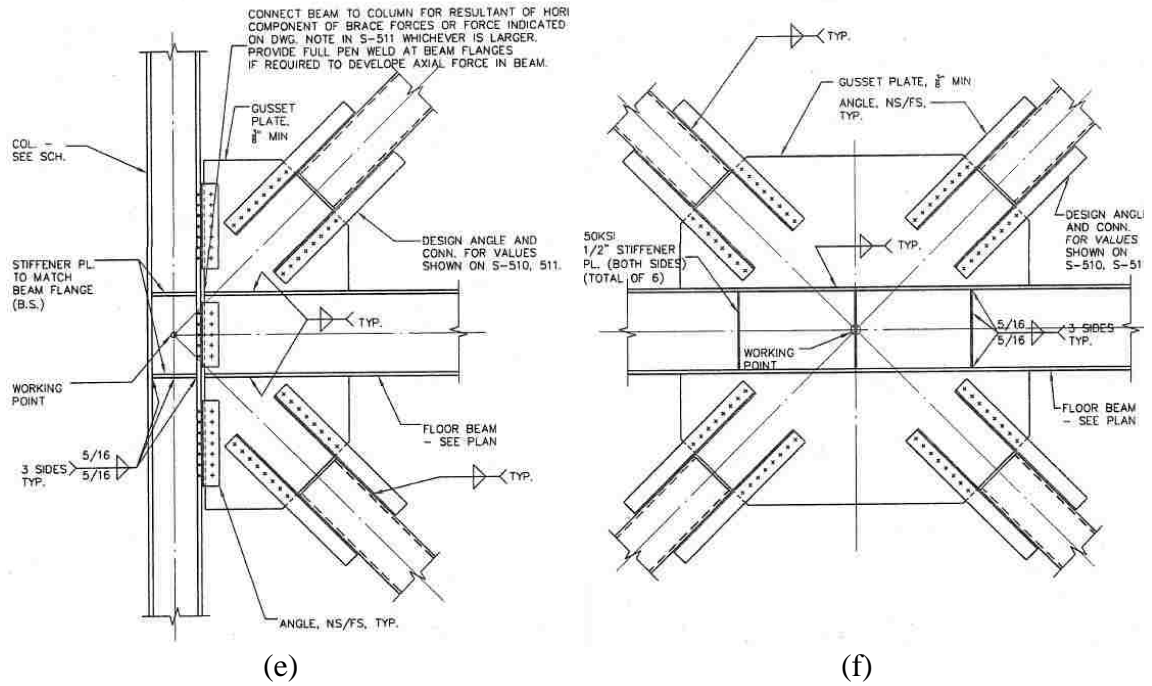


Figure 4.4 Different types of brace-gusset plate connections: (a) welded connection for slotted HSS brace; (b) bolted connection for single angle brace; (c) bolted connection for double angle brace; (d) bolted connection for wide flange brace; (e) hybrid connection for HSS brace at beam column joint; (f) hybrid connection for HSS brace at brace beam joint

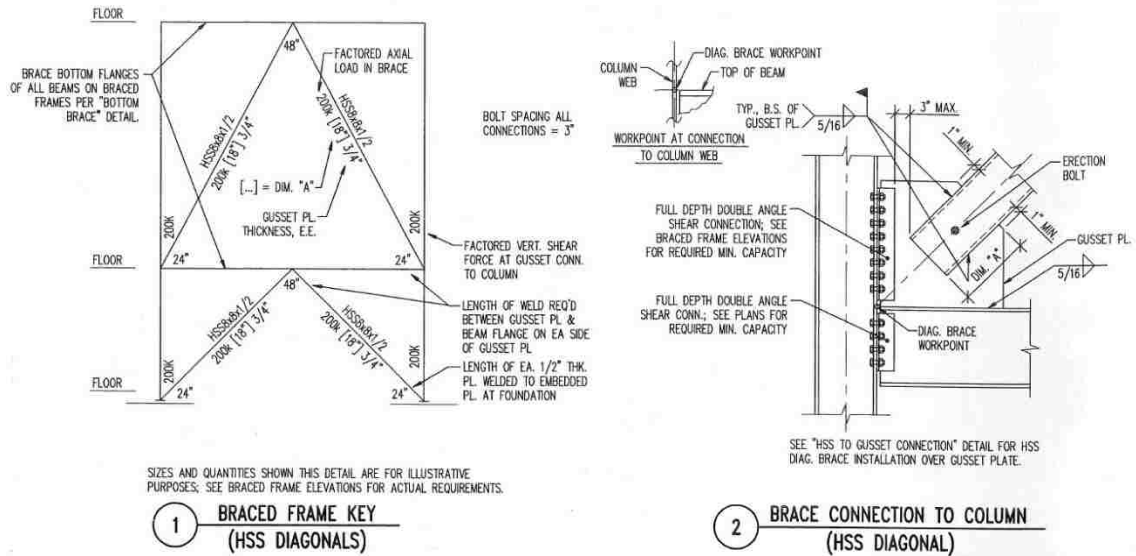


Figure 4.5 Brace connection design in Building 2

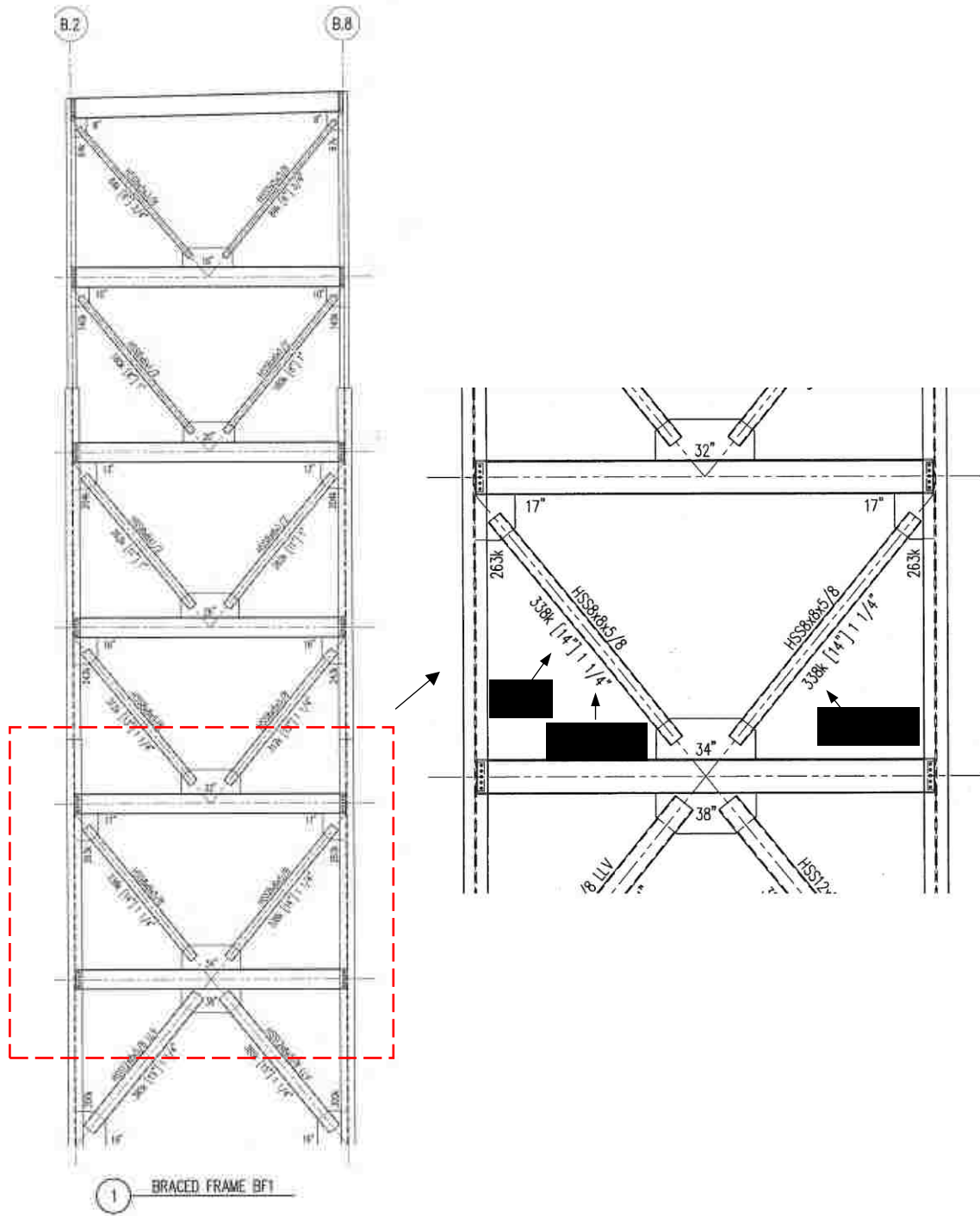


Figure 4.6 Connection design parameter for Building 2 (second story has been highlighted)

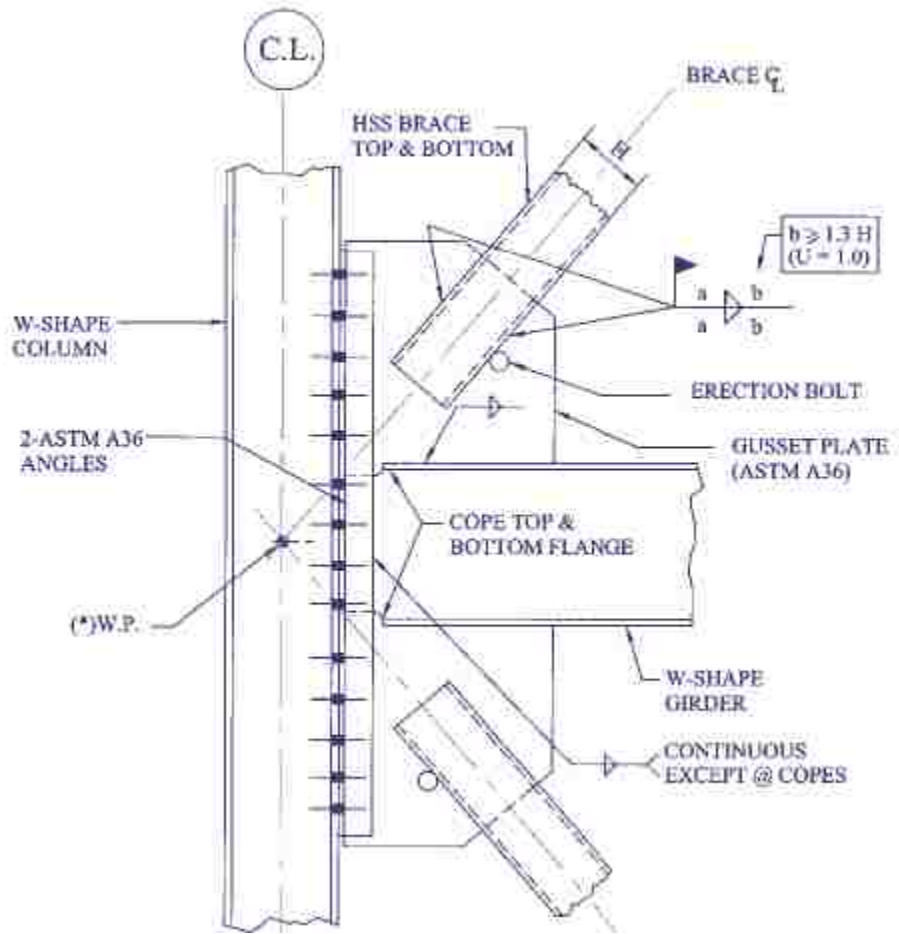


Figure 4.7 Connection detail in Marstellar et al. (2002)

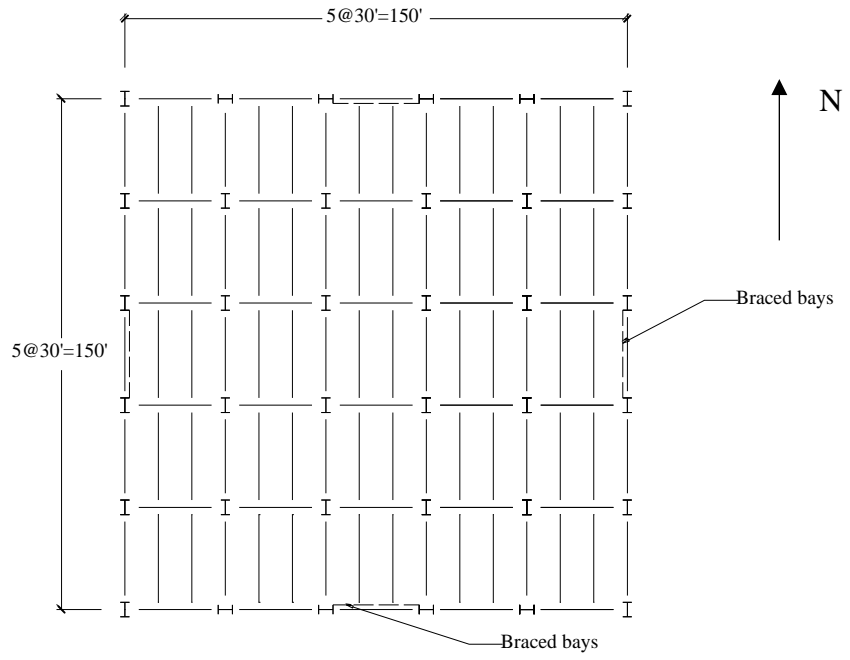
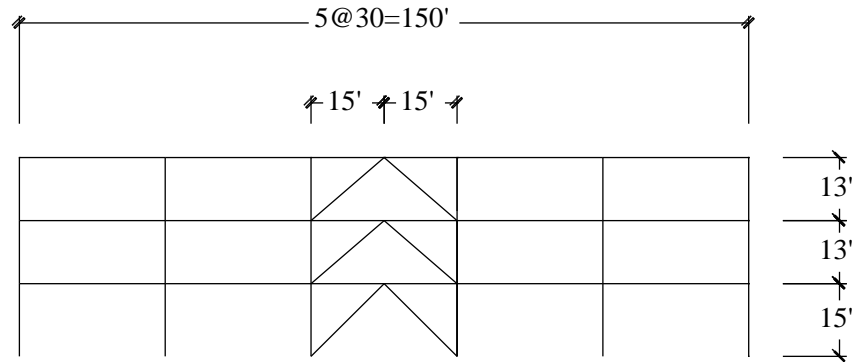
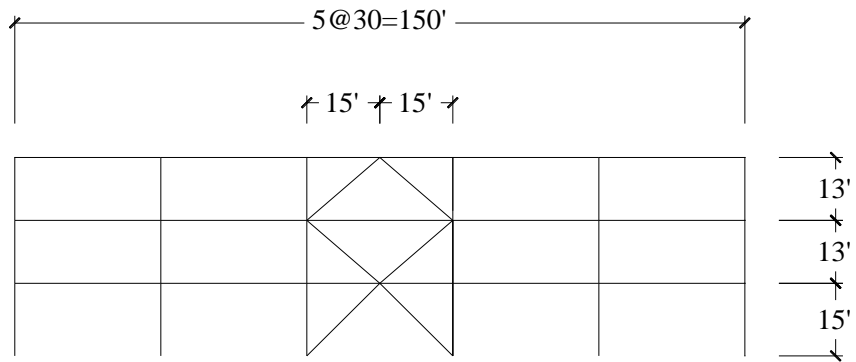


Figure 4.8 Floor plan of prototype building



(a)



(b)

Figure 4.9 Elevation of prototype building: (a) chevron brace configuration variant; (b) split-X brace configuration variant

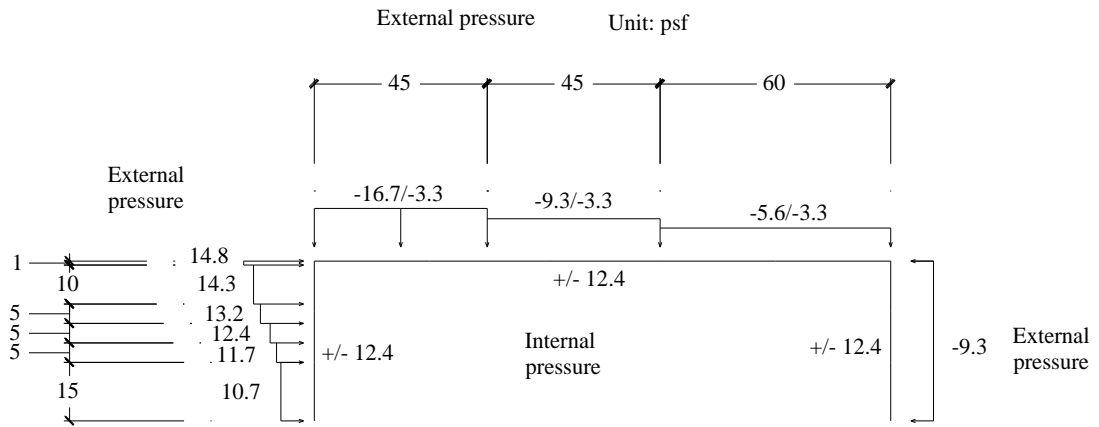
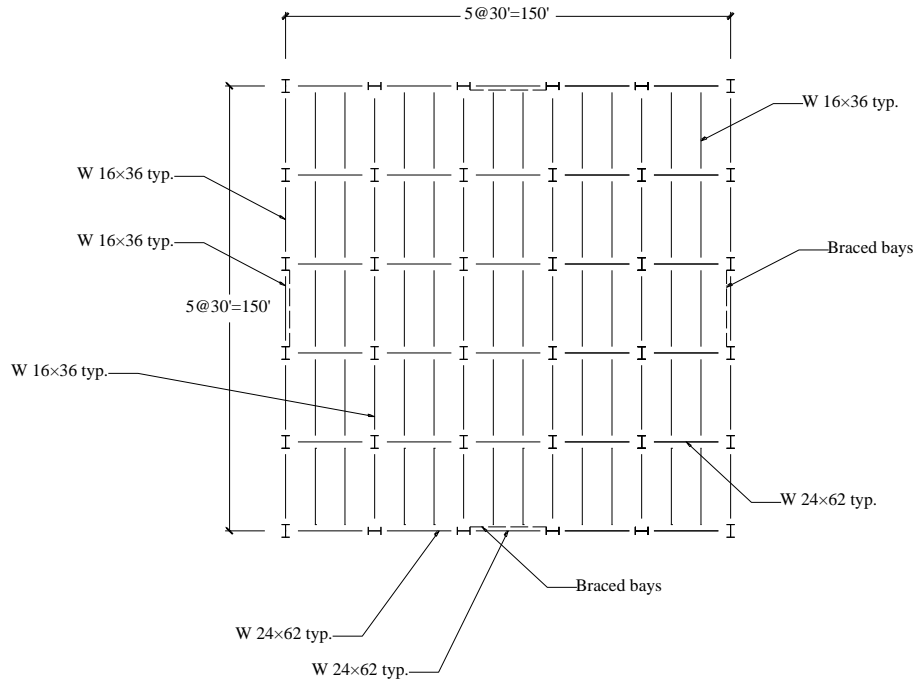


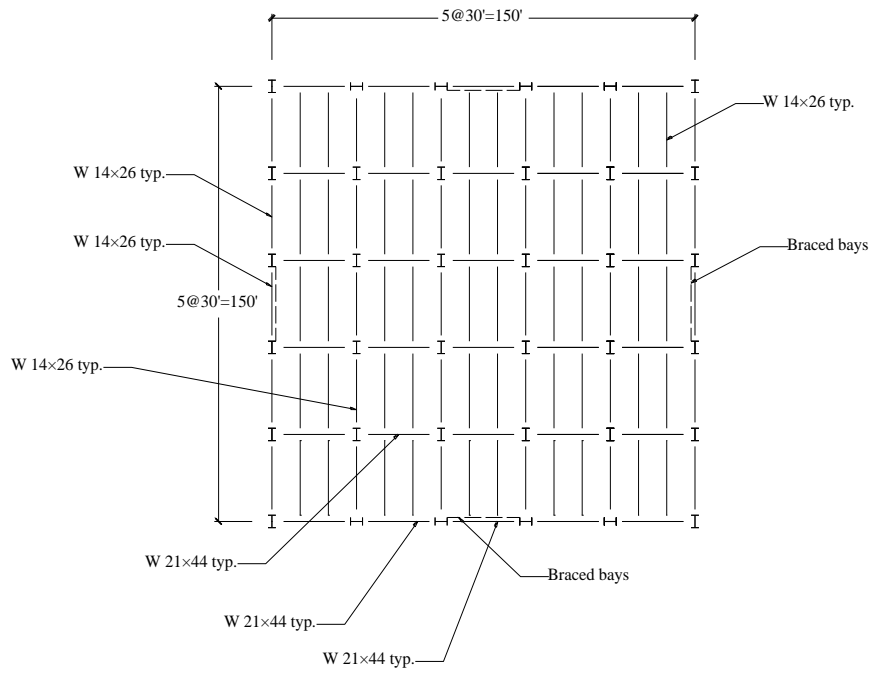
Figure 4.10 Distribution of design wind pressure

Normal floor beam section selection



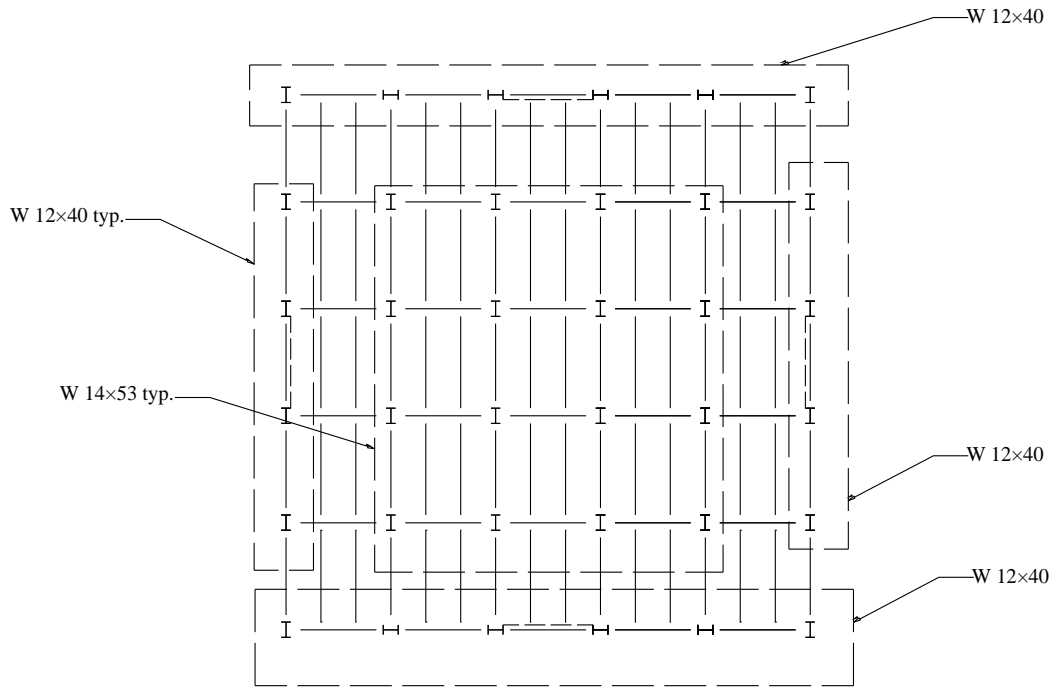
(a)

Roof floor beam section selection



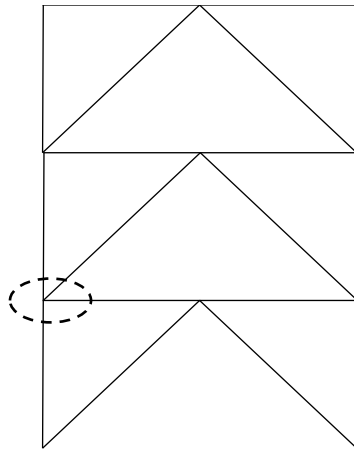
(b)

Column section selection

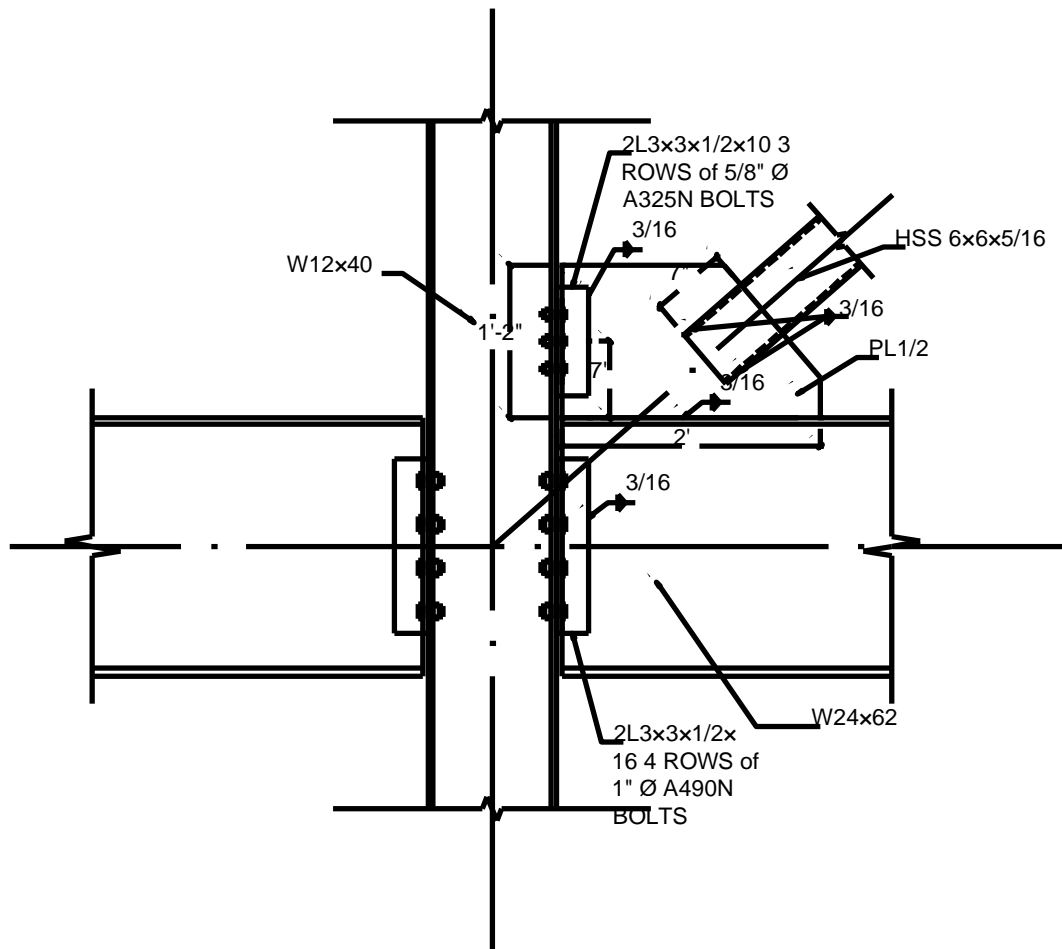


(c)

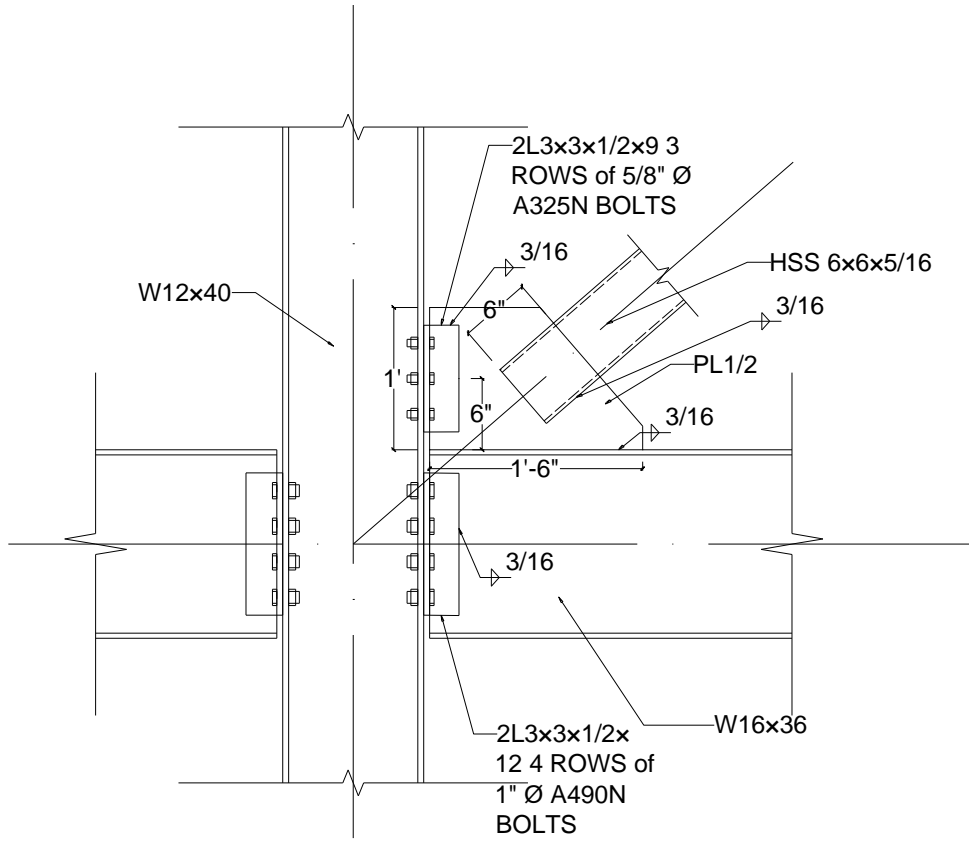
Figure 4.11 Member sections: (a) beams at typical floors; (b) beams at roof; (c) columns



(a)

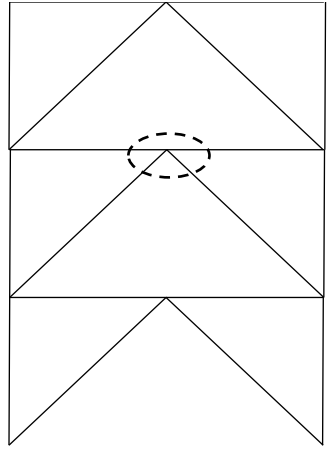


(b)

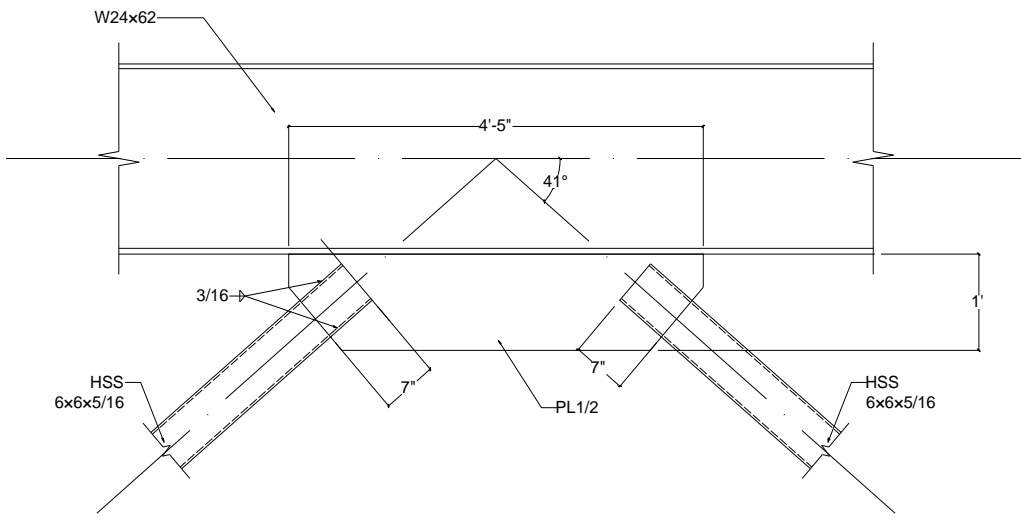


(c)

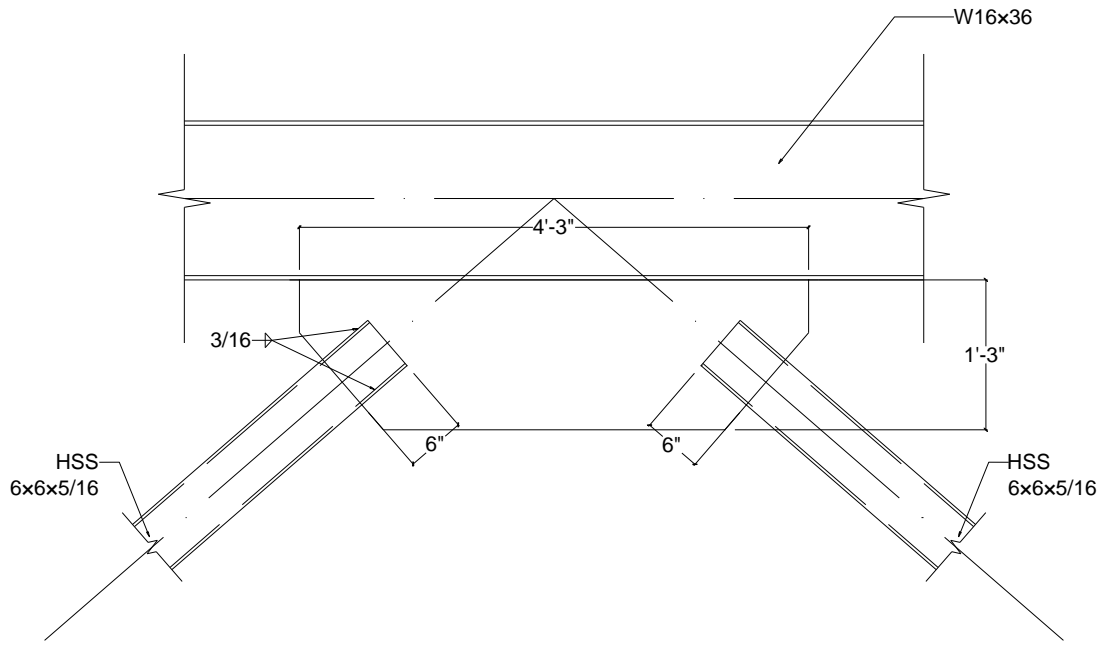
Figure 4.12 Weld connection detail (Design 1) for second story at beam-column joint in chevron CBF: (a) location; (b) EW bay; (c) NS bay



(a)

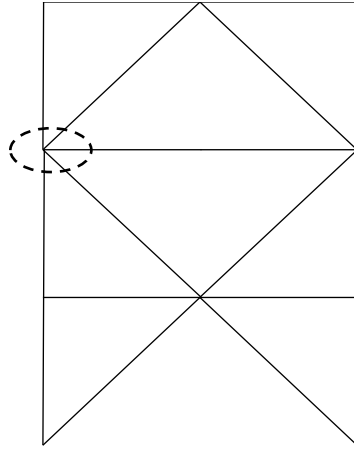


(b)

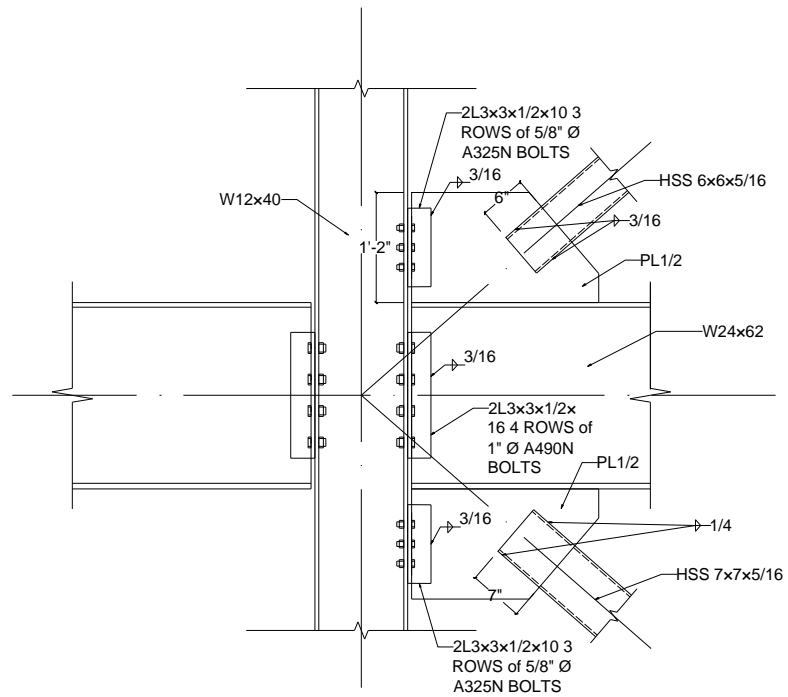


(c)

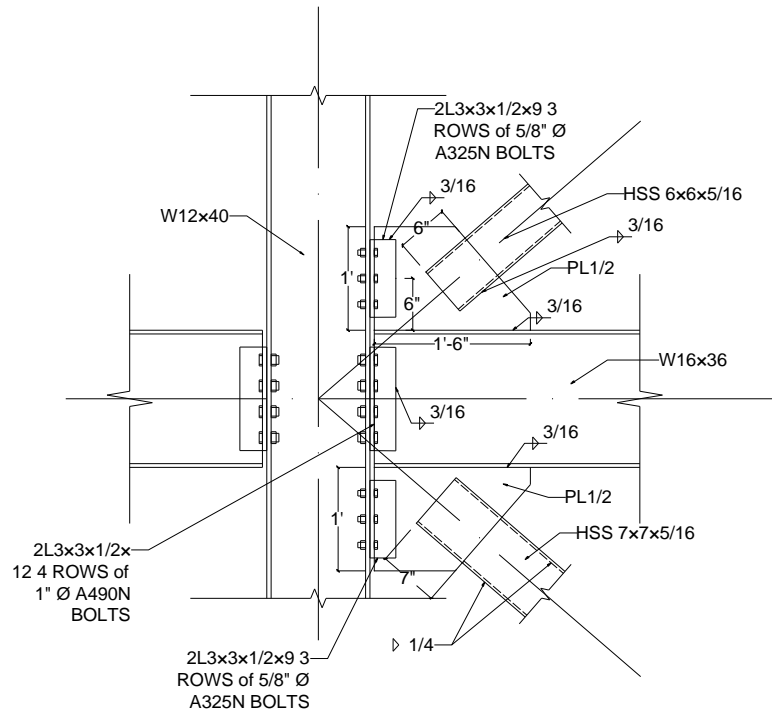
Figure 4.13 Weld connection detail (Design 1) for second story at chevron point in chevron CBF: (a) location; (b) EW bay; (c) NS bay



(a)

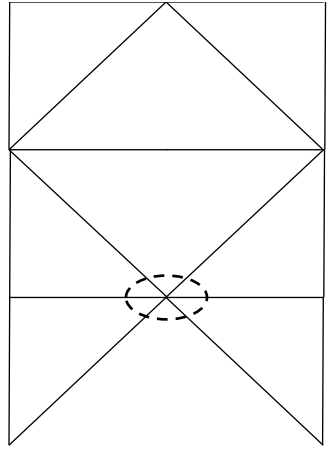


(b)

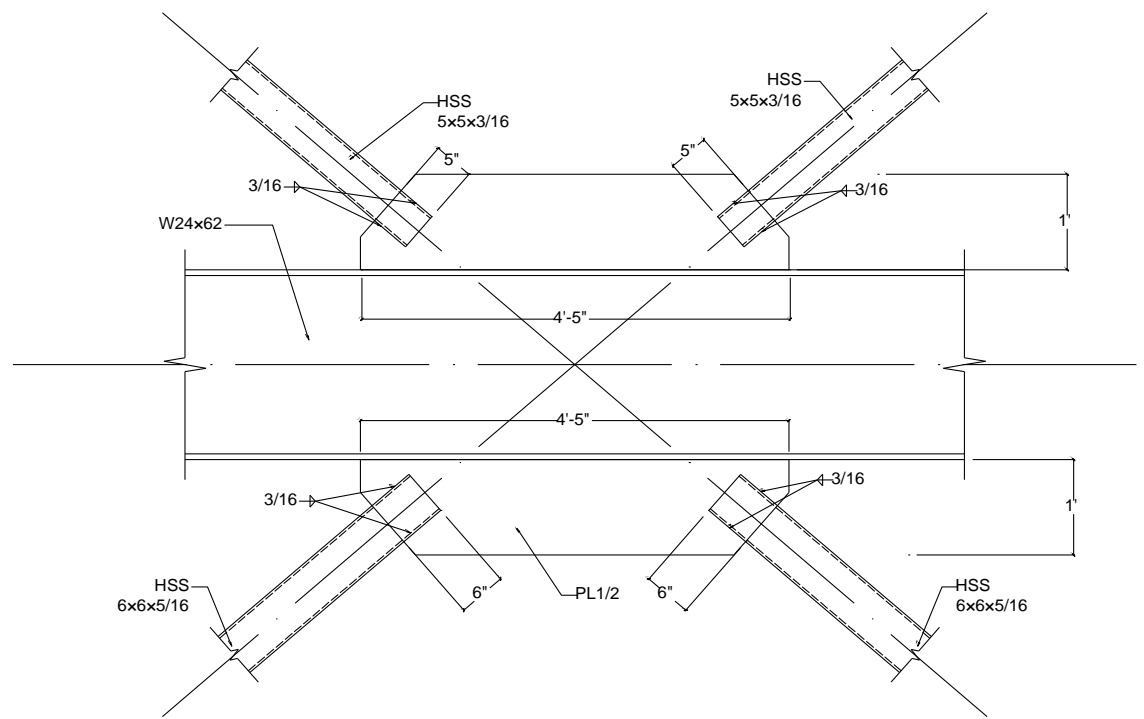


(c)

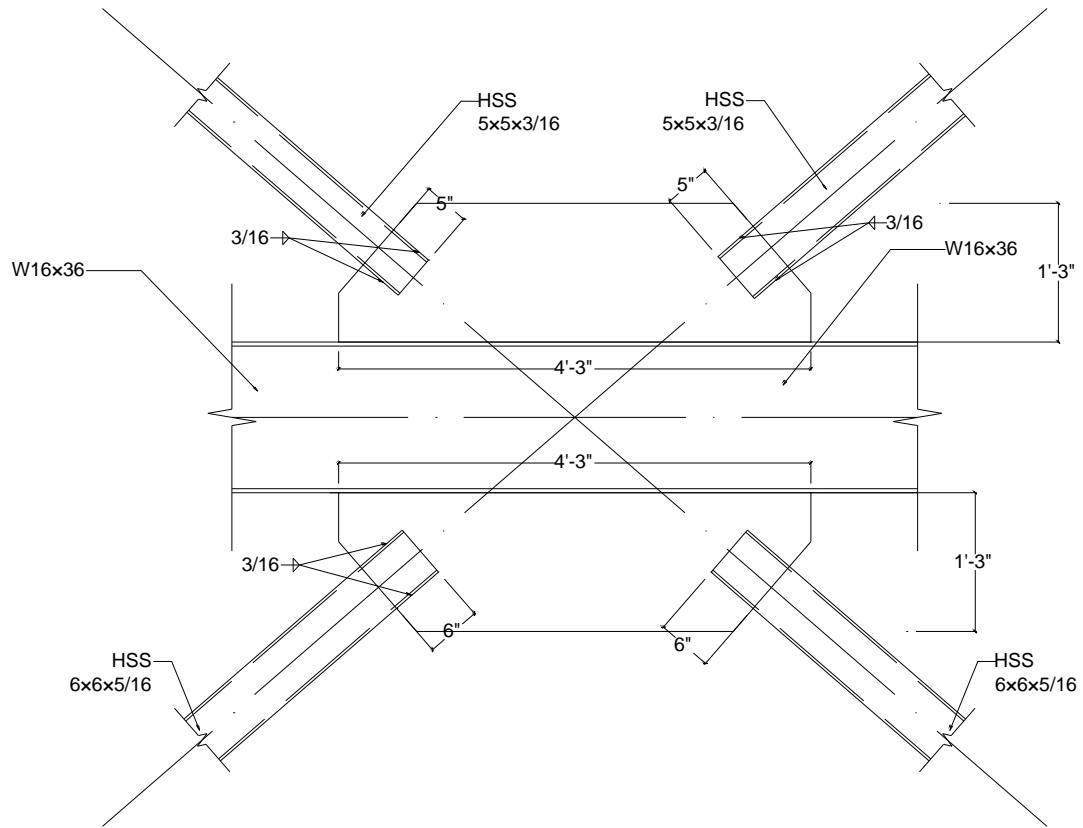
Figure 4.14 Weld connection detail (Design 1) for second story at BC joint in split-X CBF: (a) location; (b) EW bay; (c) NS bay



(a)



(b)



(c)

Figure 4.15 Weld connection detail (Design 1) for second story at brace beam joint in split-X CBF: (a) location; (b) EW bay; (c) NS bay

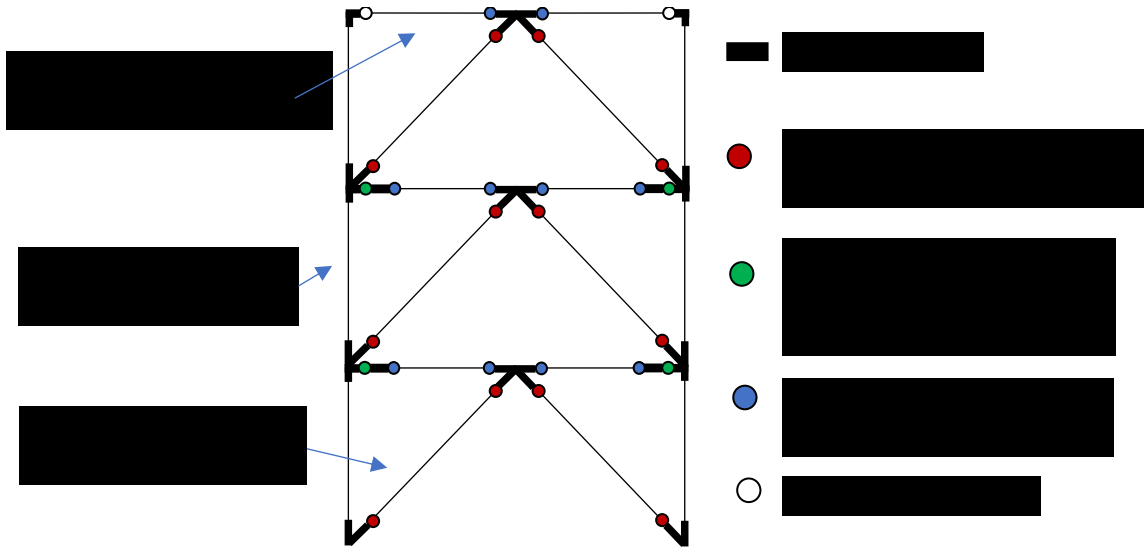


Figure 4.16 Schematic of CBF model in OpenSees

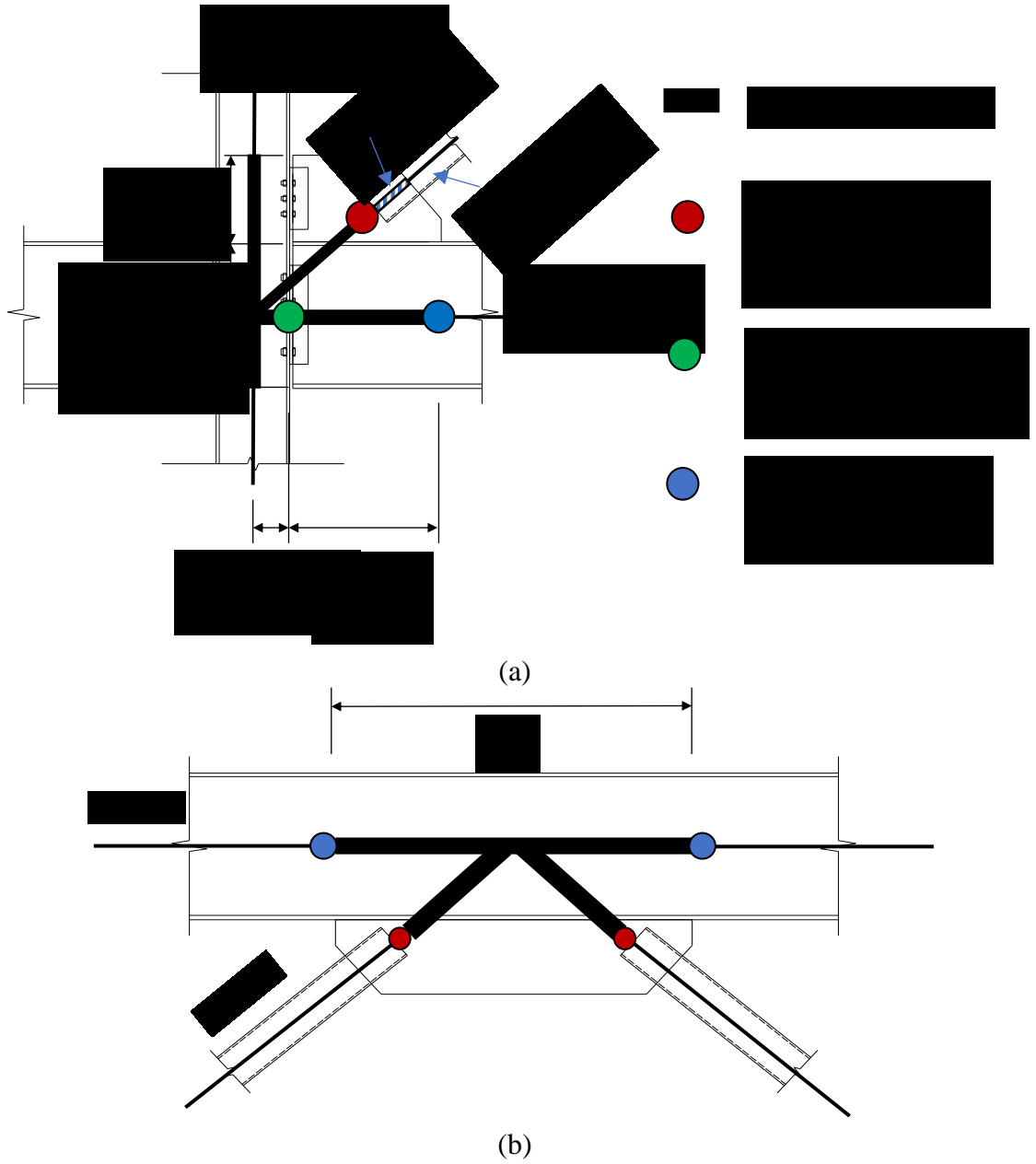


Figure 4.17 Modeling detail at (a) beam column joint and (b) chevron point

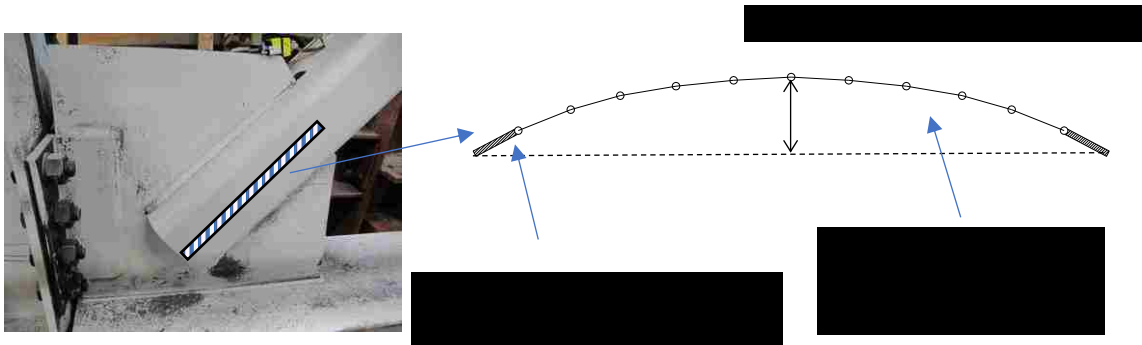


Figure 4.18 Illustration of brace and connection model

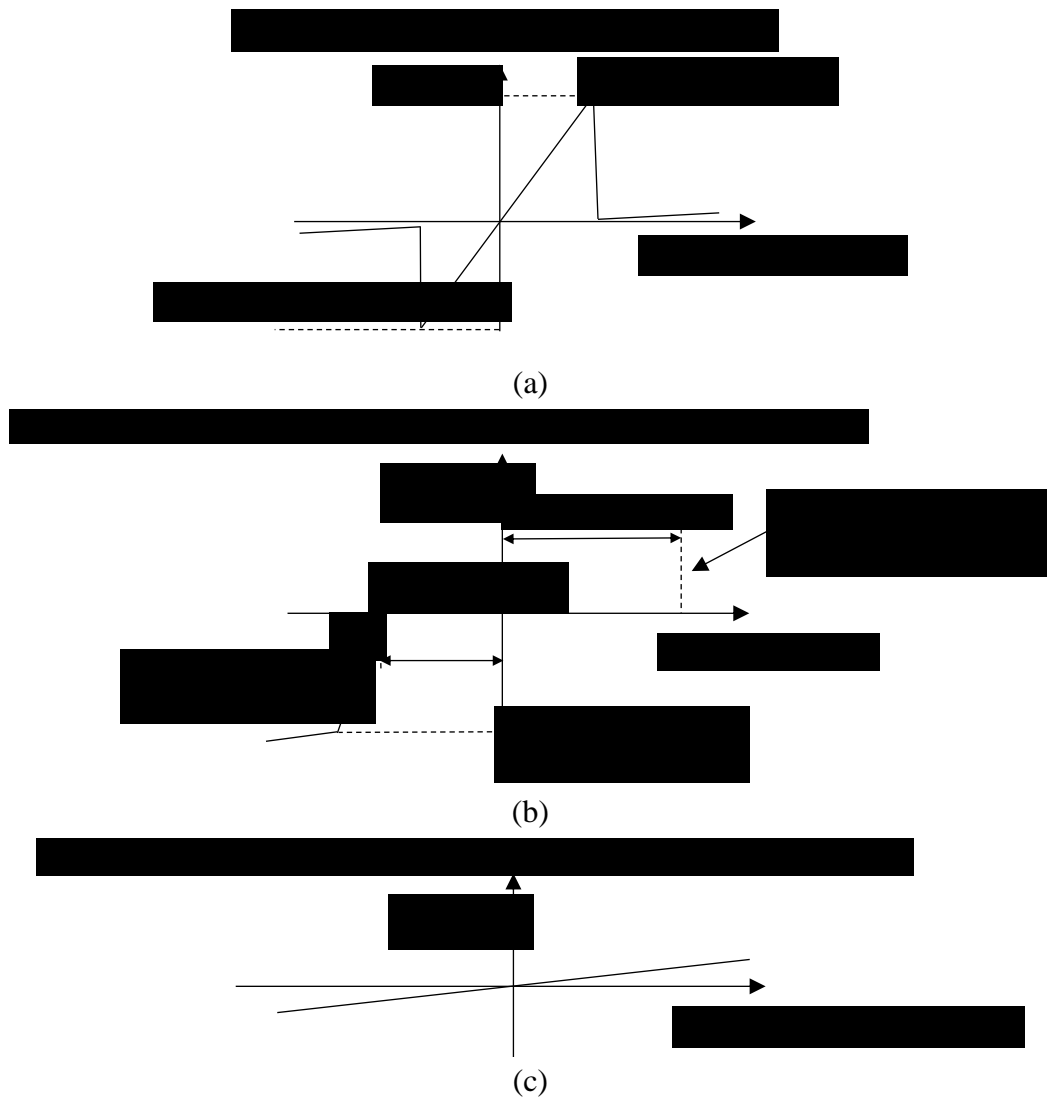
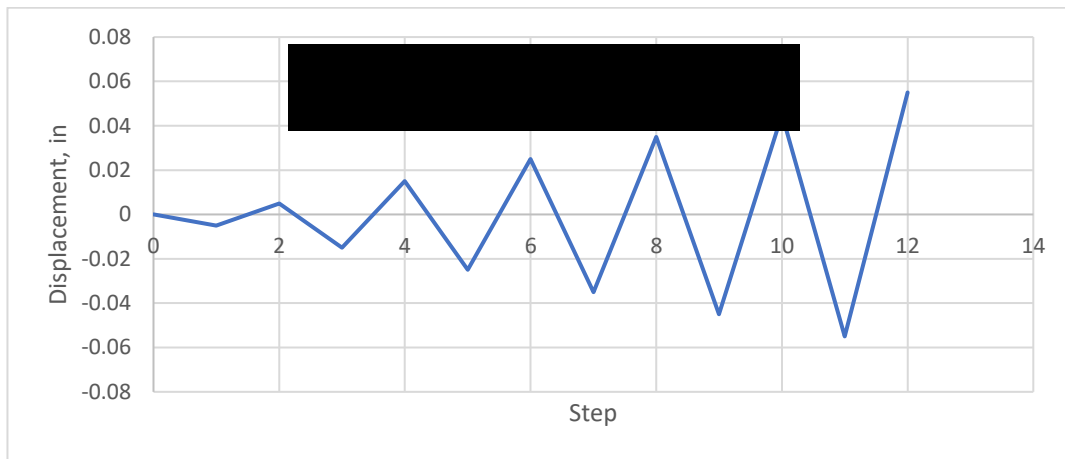


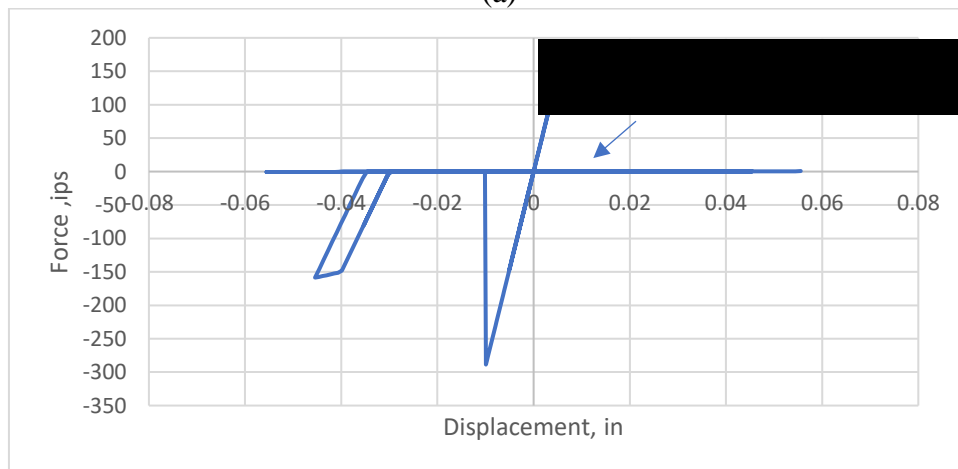
Figure 4.19 Illustration of brace gusset weld connection model (a) weld fracture component; (b) brace re-engagement component; (c) numerical stability component



Figure 4.20 Increase of contact surface during brace re-engagement (Sizemore et al. 2015)



(a)



(b)

Figure 4.21 Behavior of brace re-engagement model (a) Imposed displacement history; (b) hysteretic behavior

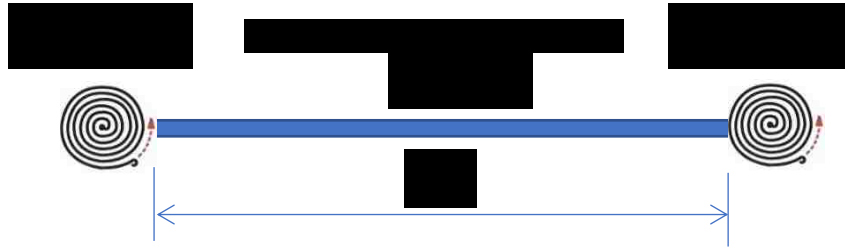


Figure 4.22 Schematic of beam model using CPH approach

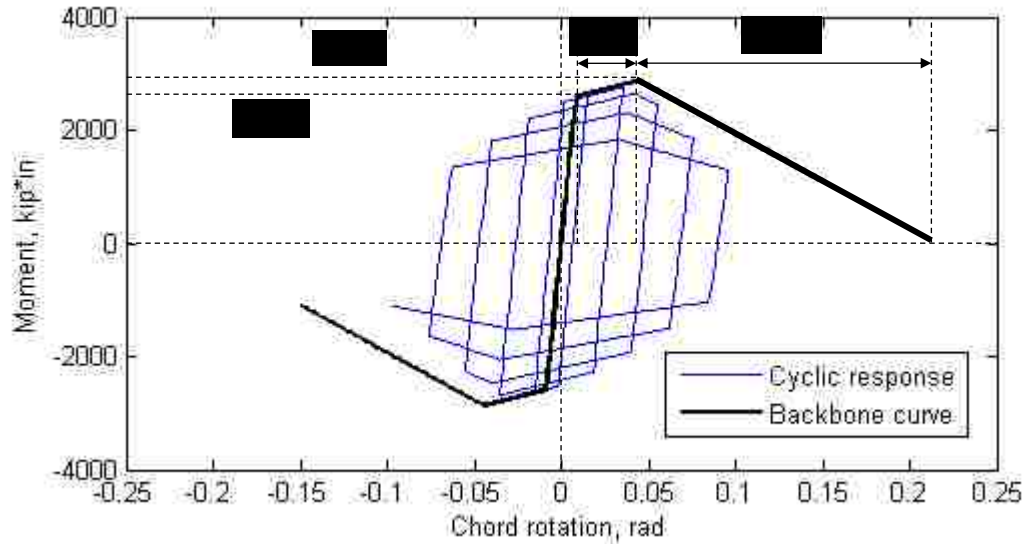
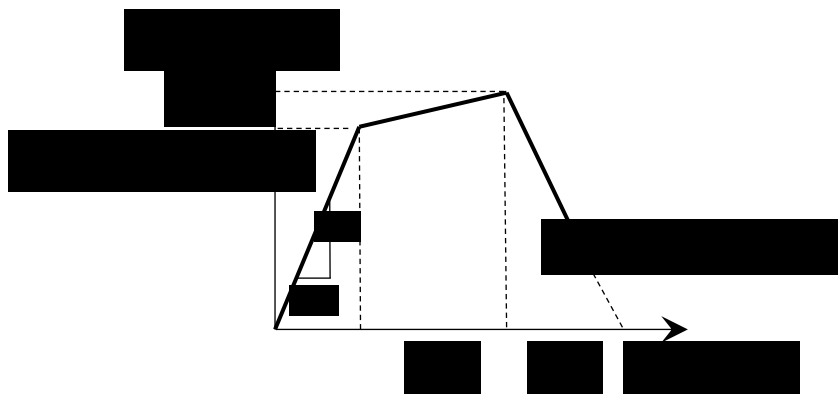


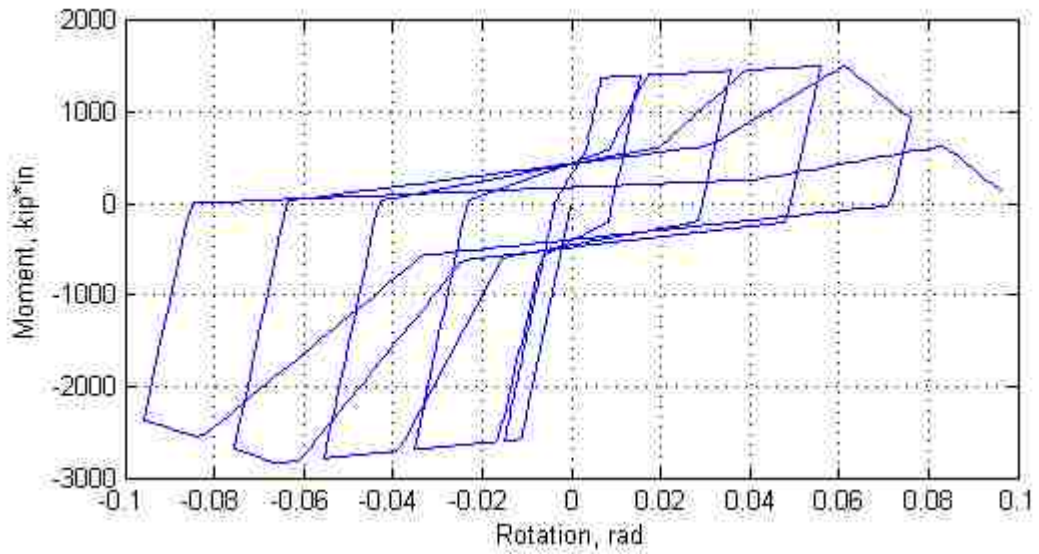
Figure 4.23 Hysteretic response and definition of input parameters for IMK material (Lignos et al. 2011) to model strength deterioration in beam plastic hinge



Figure 4.24 Local buckling in beam plastic hinge observed in Bradley et al. (2015)



(a)



(b)

Figure 4.25 (a) Backbone curve and definition of material parameters; (b) Moment-rotation hysteresis of rotational spring to model BC connection with gusset plate

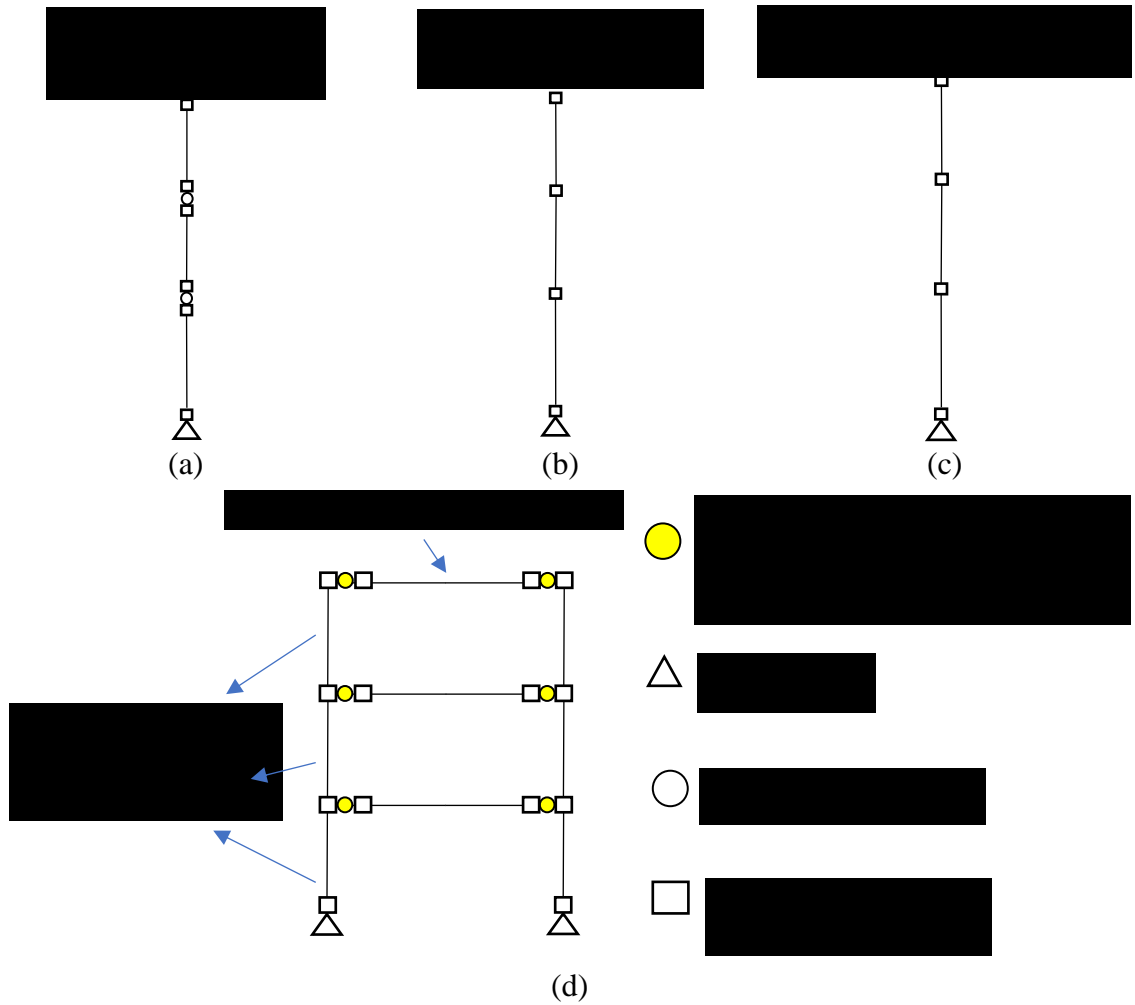
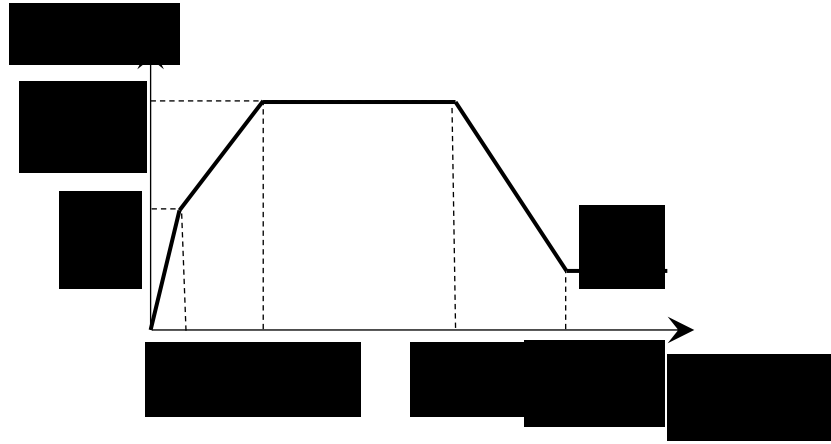
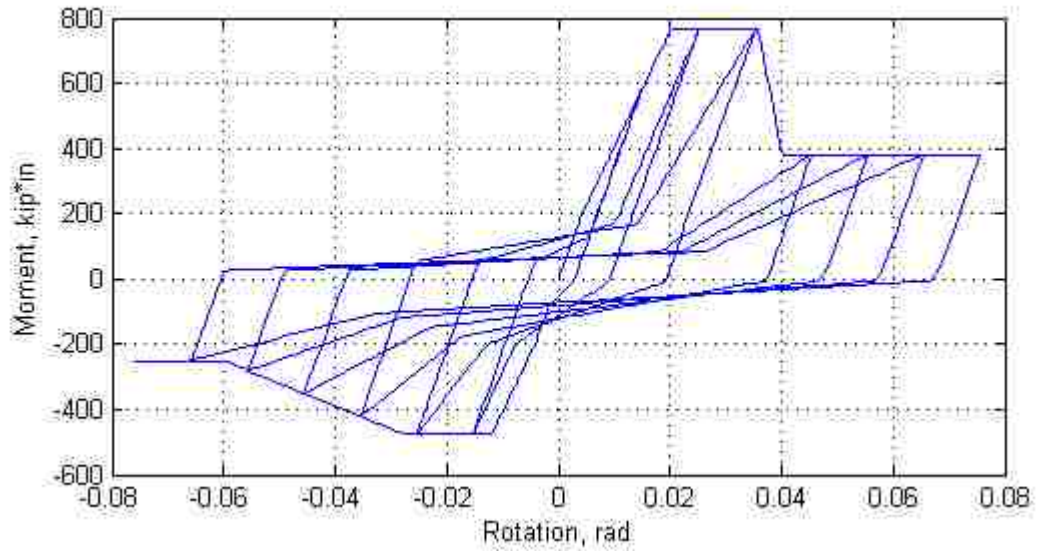


Figure 4.26 Different modeling approaches for gravity system: (a) LOC-pin; (b) LOC-continuous; (c) LOC-continuous-fiber; (d) EGF



(a)



(b)

Figure 4.27 (a) Backbone curve and definition of input parameters; (b) Moment-rotation hysteresis of rotational spring to model BC connection in gravity system

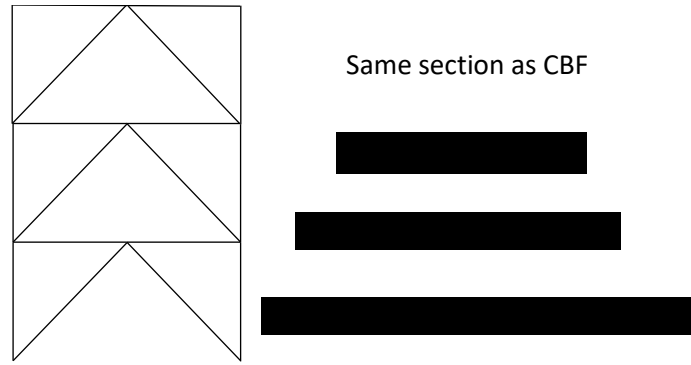


Figure 4.28 Illustration of damping substructure model

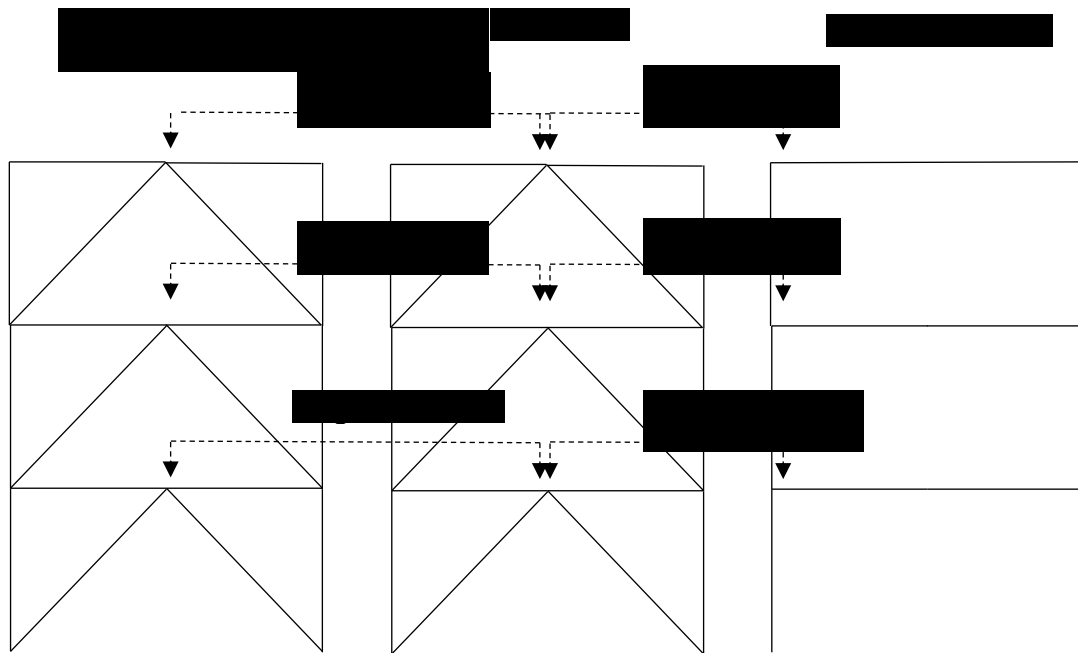


Figure 4.29 Assembly of CBF, gravity system and damping substructure (gravity system shown in EGF approach)

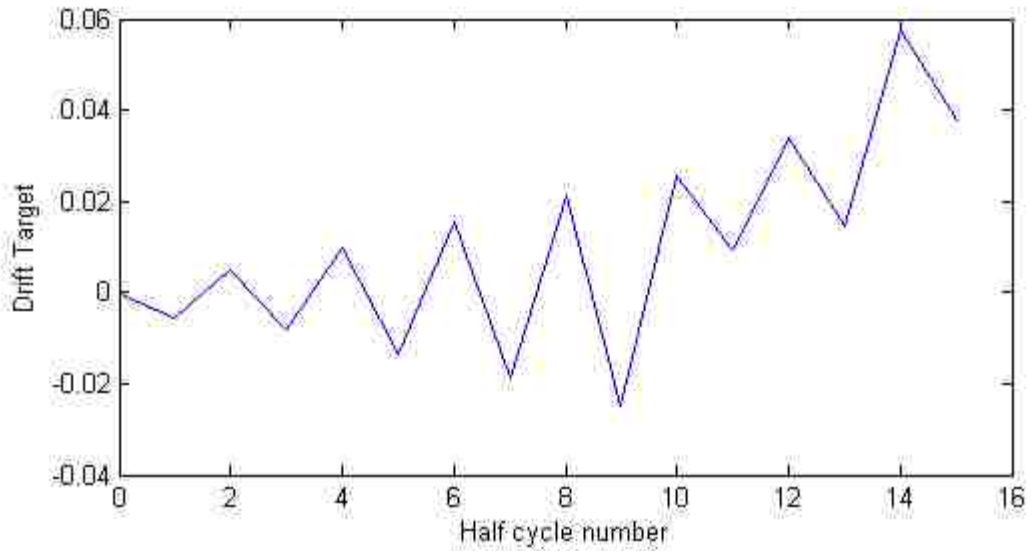


Figure 4.30 Drift history during the second phase of Sizemore et al. (2015)

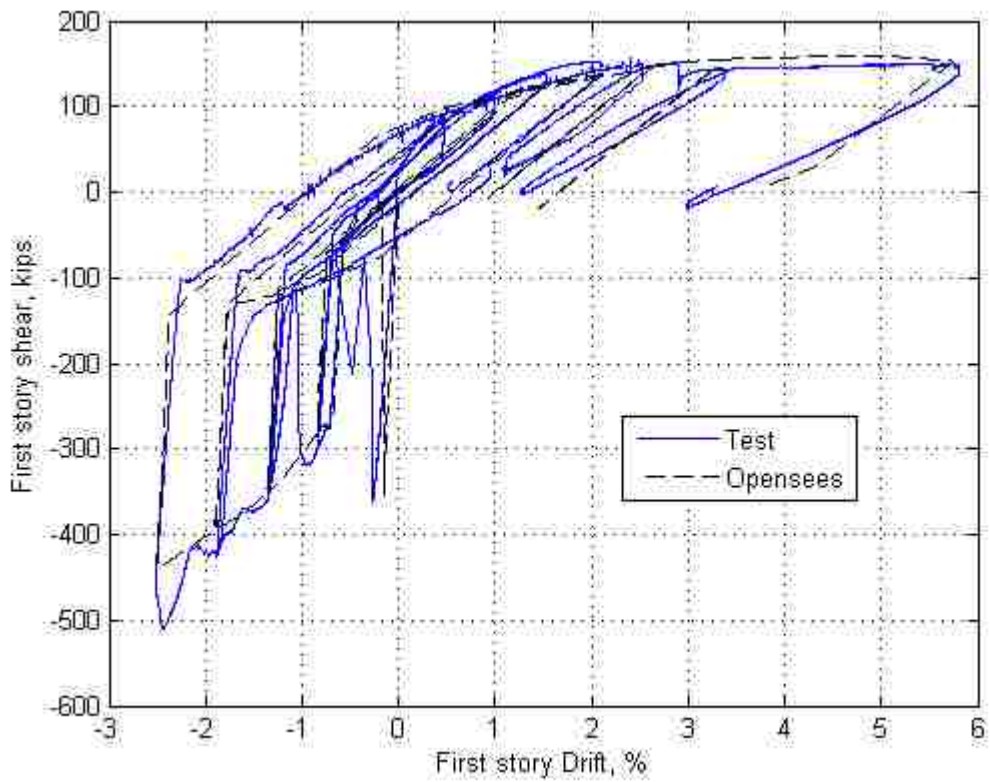


Figure 4.31 Comparison of analytical model response and test result in Sizemore et al. (2015)

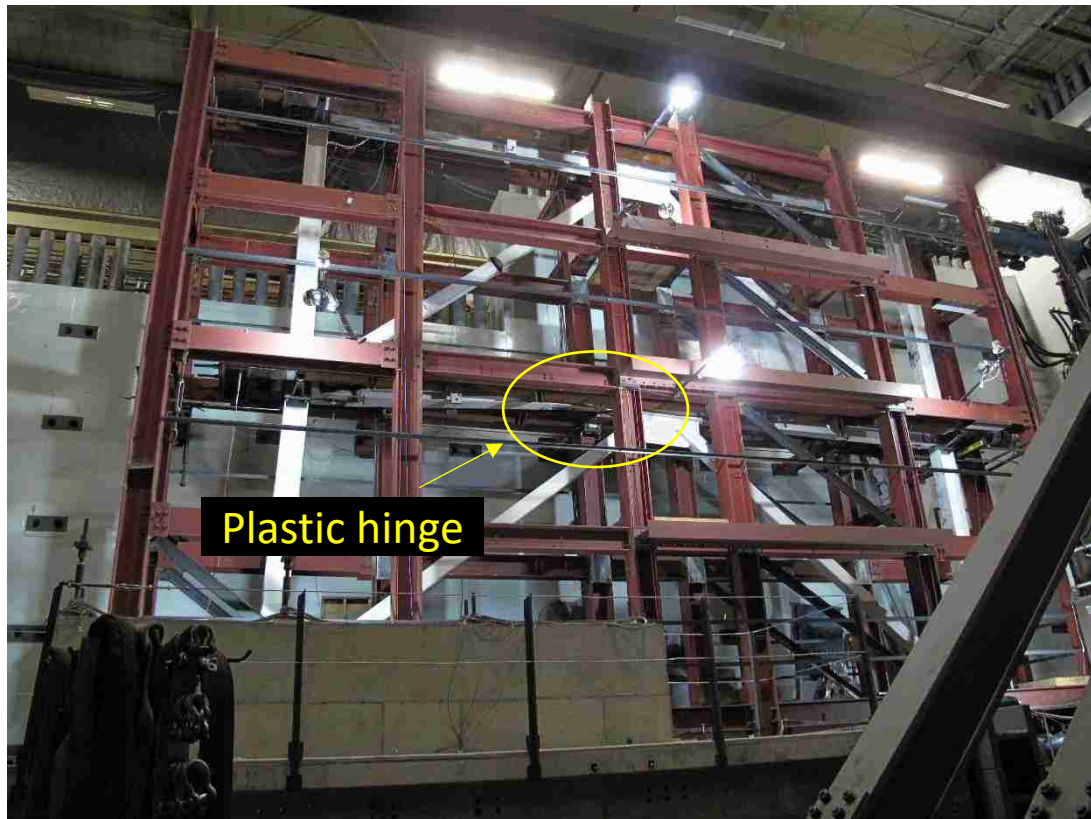


Figure 4.32 Plastic hinge developed in chevron point during “long link EBF” response in Sizemore (2015)

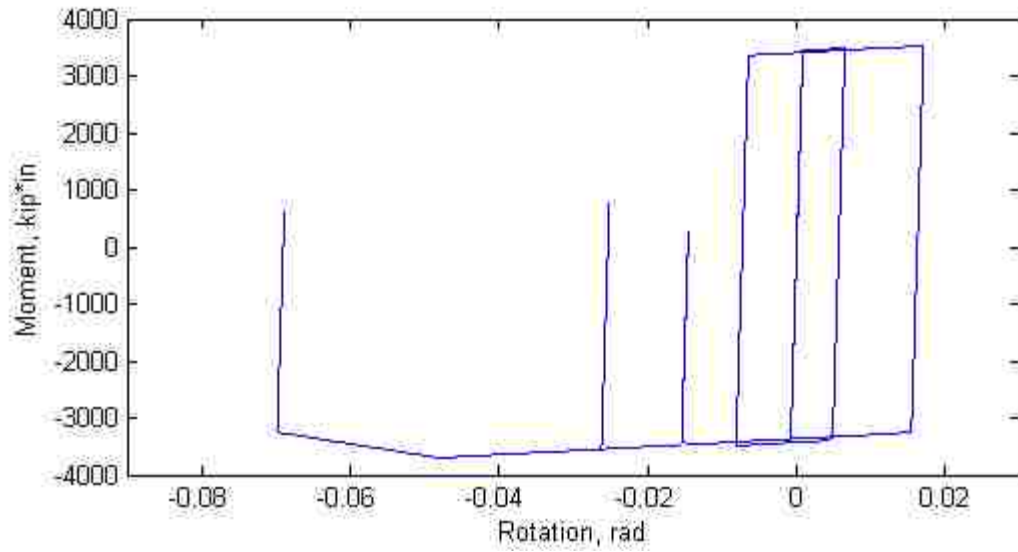


Figure 4.33 Moment rotation response of beam plastic hinge at chevron point in the analytical model

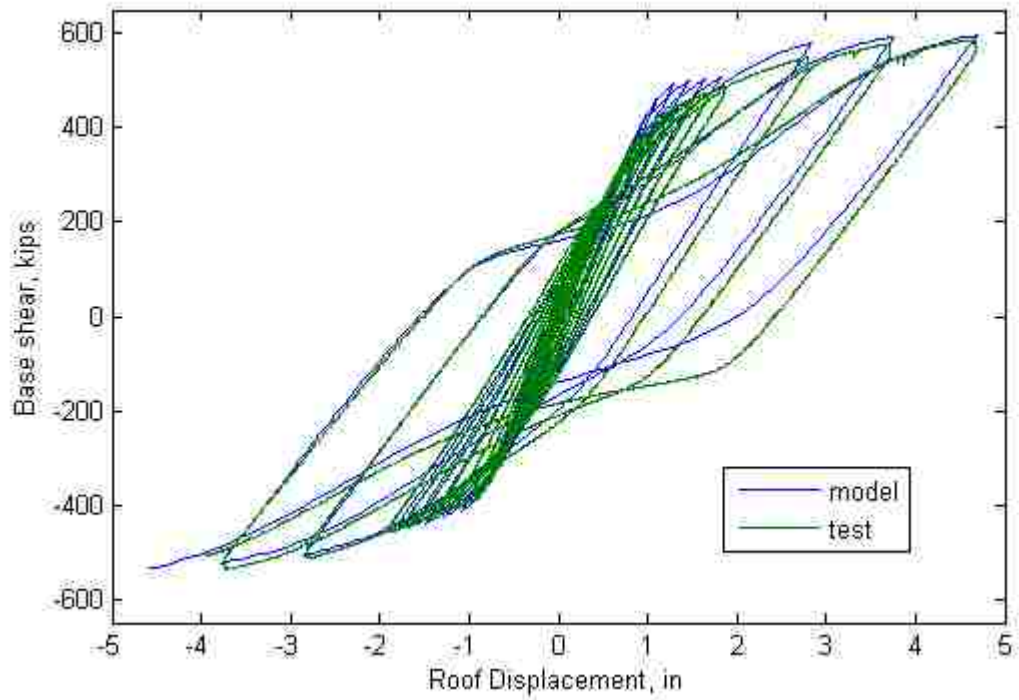


Figure 4.34 Comparison of analytical model response and test result in Bradley et al. (2015)

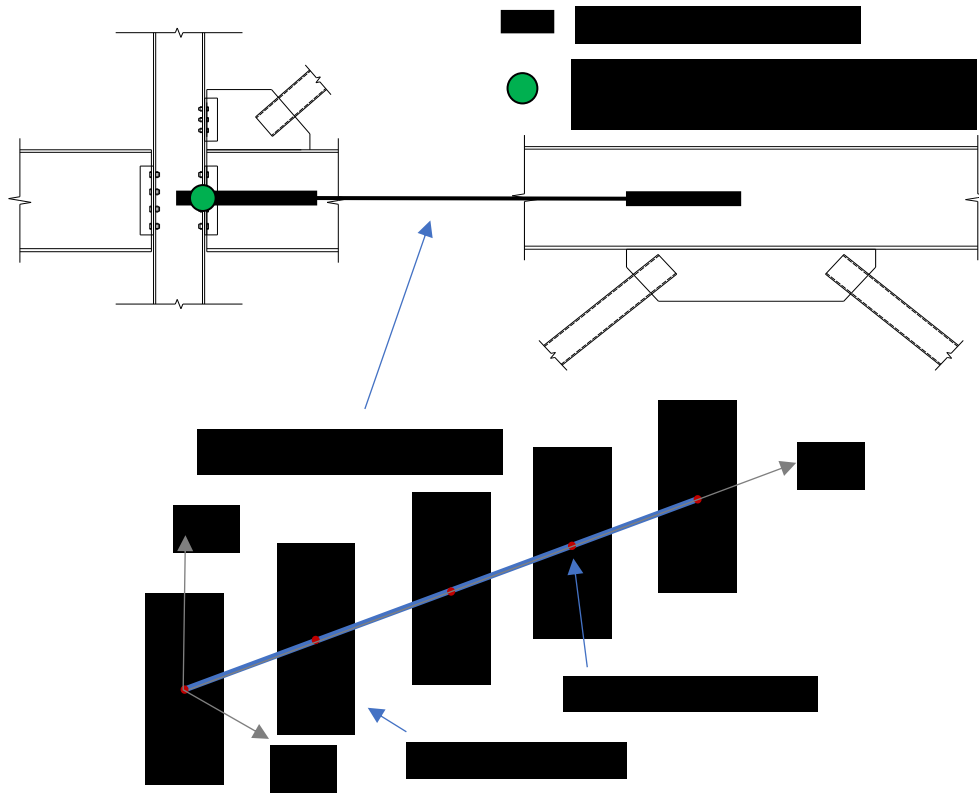


Figure 4.35 Alternative model for beam using forceBeamColumn element with fiber section

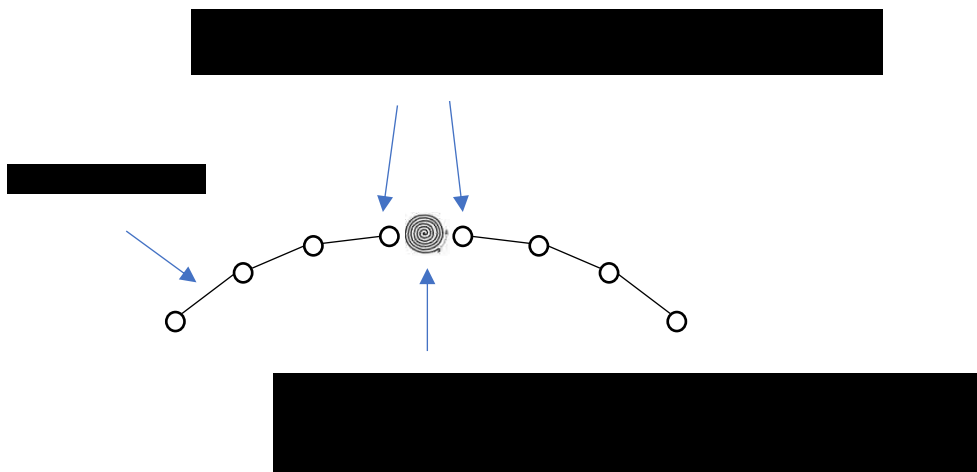


Figure 4.36 Proposed brace model to include local buckling

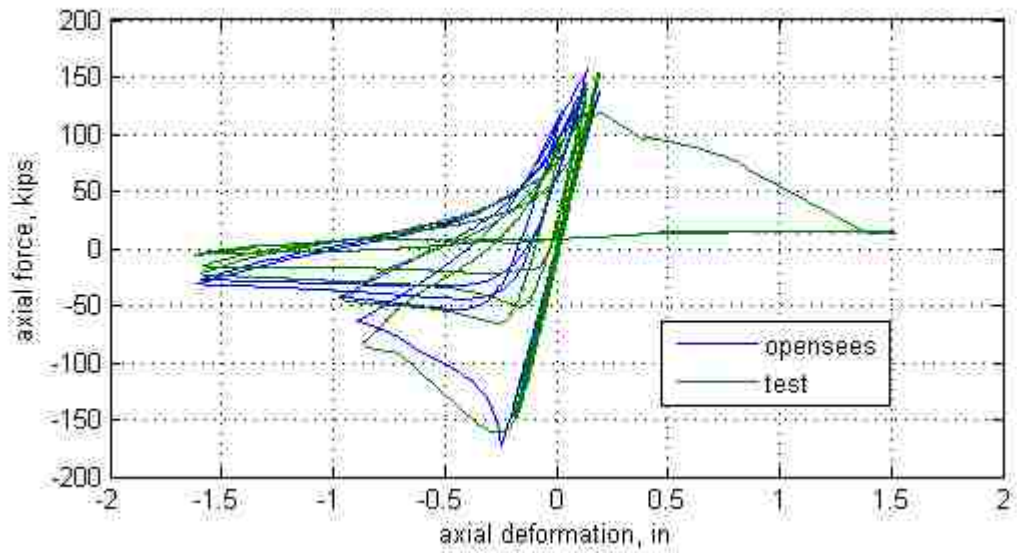


Figure 4.37 Comparison of analytical and experimental response for west brace of 2nd story in Simpson et al. (2013) when proposed brace model is used

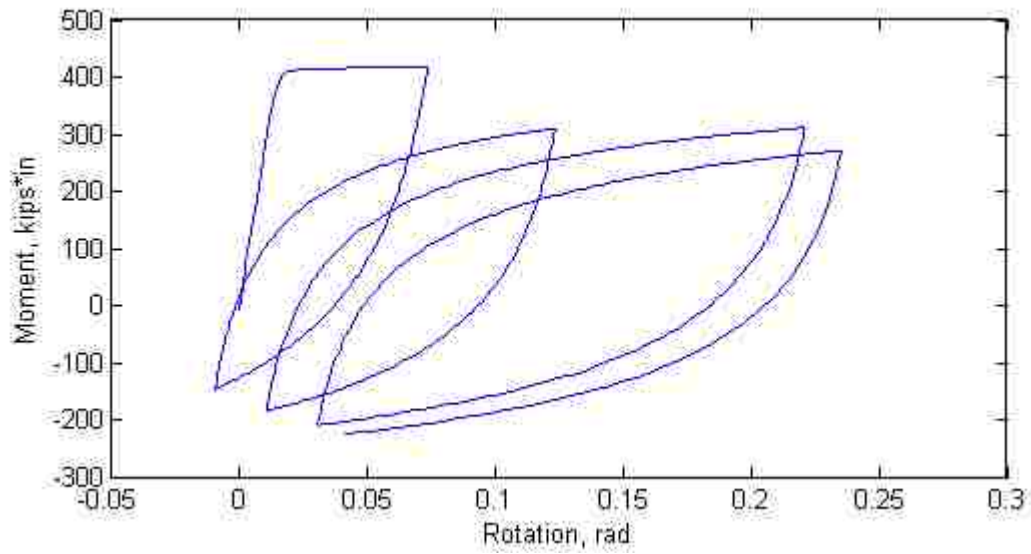


Figure 4.38 Moment rotational response of the rotational spring at the middle of the brace

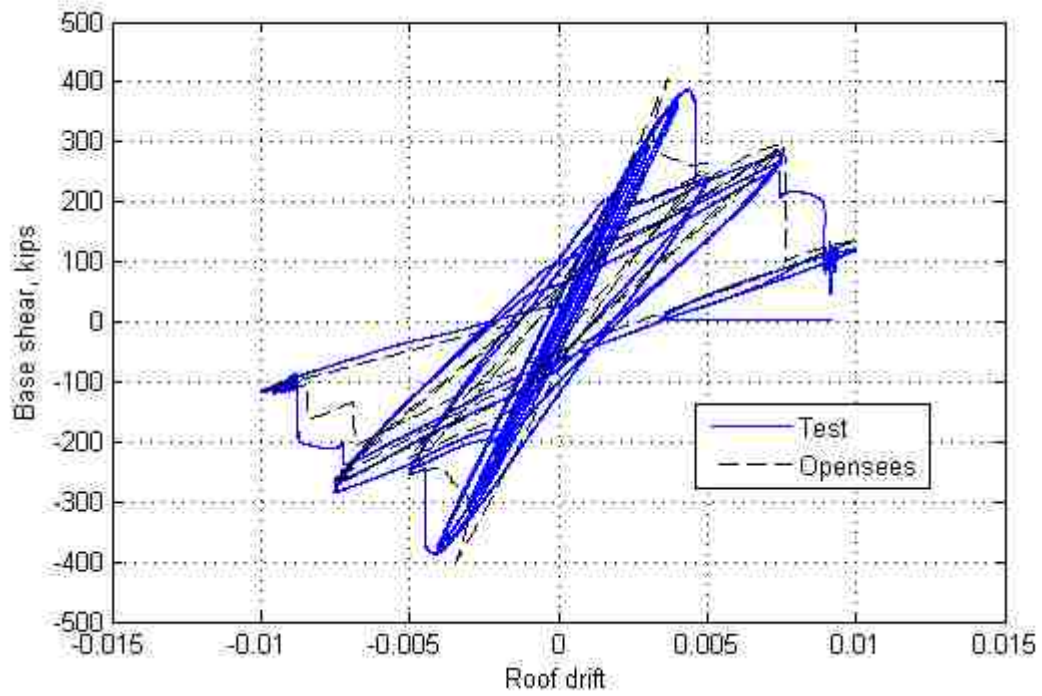


Figure 4.39 Comparison of analytical and experimental response for roof drift vs base shear in Simpson et al. (2013) when proposed brace model is used

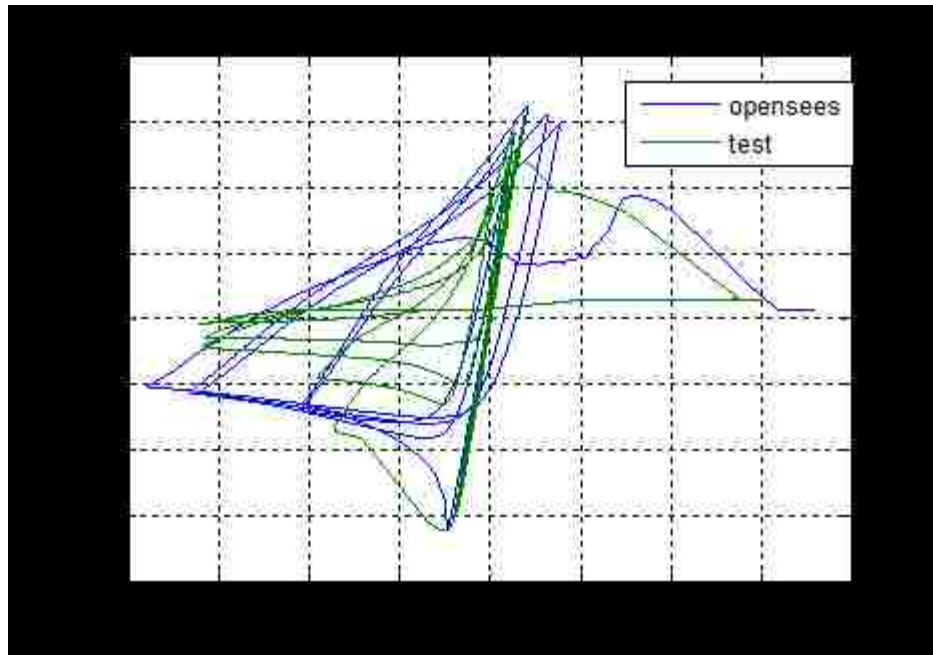


Figure 4.40 Comparison of analytical and experimental response for west brace of 2nd story in Simpson et al. (2013) when conventional brace model is used

Chapter 5

Development of an ECUS ground motion set

5.1 Introduction

This chapter presents the development of an ECUS ground motion (GM) set for assessing the collapse performance of ECUS low-ductility CBFs. The ECUS GM set consists of 44 synthetic surface ground motions that consider current seismological models, uncertainty in the seismic hazard sources, the spectral shape effect, and site soil amplification. The motivation is first introduced, which includes the reasons for not using one of the existing FEMA ground motion sets (FEMA 2009) and not using natural ground motions from the newly-developed NGA-East ground motion database (Goulet et al. 2014).

The ground motions at the bedrock level are generated using the program SMSIM (Boore 2003) which implements a stochastic ground motion generation method and the 6 seismological models used in the NGA-East Project (Goulet et al. 2011). The hazard deaggregation results for the prototype building site for Magnitude (M), Distance (R) and ϵ are used as the input for generating synthetic ground motions and subsequently selecting a set of these ground motions (called the Rock GM set hereafter). This ground motion set includes the uncertainty in seismic sources and the spectral shape effect. To include the site soil amplification effect, 1-D equivalent-linear site response analyses are performed using the Rock GM set ground motions as input. To represent the variation in the possible site soil conditions in Philadelphia, a set of 8 soil profiles with different soil profile heights and shear wave velocities is used. The properties of the soil profiles are randomly sampled and the resulting surface ground motions are aggregated into a single set of ground motion at

the ground surface level (named Soil GM set hereafter). The Soil GM set, which is the ECUS ground motion set to be used in the subsequent collapse analysis, is then compared with the FEMA Far-Field GM set (FEMA 2009). The intensities of both the Rock GM and Soil GM sets are also compared with the MCE hazard level intensity based on of ASCE (ASCE 2010) and USGS (Petersen et al. 2008). It is shown that the developed GM set can directly address the effect of spectral shape. It is also discovered that the Soil GM set suggests lower level of ground shaking intensity at the MCE level than the ASCE MCE (ASCE 2010) spectrum for Site Class D.

5.2 Motivation

An important component of seismic performance evaluation is establishing the seismic hazard at the site of the structure. The hazard is often quantified by a Probabilistic Seismic Hazard Analysis (PSHA), which determines the ground motion intensity corresponding to a certain hazard level. Then, a set of ground motions is created to represent the seismic hazard along with the potential record-to-record (RTR) variability for use in the subsequent nonlinear time history analyses needed to estimate the seismic performance of the structure. The ground motions need to be consistent with the expected ground shaking characteristics at the site of the structures including the peak intensity, time-varying amplitude, strong-motion duration, and frequency content (spectral shape), etc. Among them, spectral shape is of particular importance to the collapse performance.

The Far-Field ground motion set developed and presented in FEMA P695 (FEMA 2009) has been commonly used for collapse performance evaluations. In addition, the new NGA-East ground motion database includes a large number of natural ground motions from east

coast seismic events, which may have the potential to be used into a GM set for seismic performance evaluation. However, due to drawbacks discussed in the following sections, it is doubtful that these ground motion sets are appropriate for the seismic collapse evaluations for the ECUS low-ductility CBF buildings presented in this dissertation. Therefore, a set of synthetic ground motion was developed as part of this dissertation reserved to use in the seismic collapse performance evaluation of the prototype low-ductility CBF located in Philadelphia.

5.2.1 FEMA set

The FEMA Far-Field ground motion set (FEMA set hereafter) consists of 22 pairs of orthogonal horizontal ground acceleration records (44 individual components) selected from the PEER NGA (currently called NGA-West2) Database (PEER 2006). These ground motions are from 14 earthquake events that occurred between 1971 and 1999 from active tectonic regions (ATRs) such as western United States (WUS). The FEMA set is intended to be “site general” and was selected based on the broad criteria shown below:

- Magnitude > 6.5
- Distance > 10km
- Site Class C or D
- Source type: strike-slip or reverse fault, typical of shallow crustal earthquake in West Coast
- PGA > 0.2g; PGV > 15cm/s
- No more than 2 pairs of records from one earthquake event

The ground motions in the FEMA set are summarized in Table 5.1. Figure 5.1 shows the unscaled spectrum of FEMA GM set along with its median spectrum. Two major drawbacks exist for the FEMA set which cast doubt on its usefulness for evaluating the seismic collapse performance of ECUS low-ductility CBFs.

First, the ground motions in the FEMA set are all from inter-plate earthquakes, representative of the ATR of the WUS, which is located at a tectonic plate boundary. In comparison, the ECUS is situated in a Stable Continental Region (SCR) where intra-plate earthquakes occur. These two types of earthquake differ significantly in two key factors: seismic source and propagating path. In terms of seismic source characteristics, inter-plate earthquakes can be explained by plate relative motions and the causative faults are well-understood (Atkinson 2007). In comparison, it is generally not well-understood why intraplate earthquakes happen (Talwani 1999) and their sources are usually based on postulated faults. Regarding the propagating path, intraplate earthquake energy in the ECUS region travels more efficiently (with less loss per unit distance) than the inter-plate earthquakes in the WUS. This efficient propagation can be attributed to the harder and less fractured bedrock in the ECUS (Nikolaou et al. 2012). Consequently, an earthquake in the ECUS is usually felt over a larger area than an earthquake in the WUS of similar magnitude (Figure 5.2). Considering the differences in these two key factors, it is reasonable to believe that ground motions from these two types of earthquake have different characteristics and that the FEMA set may not be representative of ground motion characteristics in the ECUS.

Second, the FEMA set, owing to its broad selection criteria, does not directly include the spectral shape effect. Baker and Cornell (2006) found that the shape of the pseudo-

acceleration spectrum ($Sa(T)$) has a significant impact in evaluating the structural collapse capacity. The ε factor, defined in Eq. (5.1) as the number of lognormal standard deviations between the unscaled ground motion intensity (measured as the natural log of the spectral acceleration at a certain period) and the median intensity from a Ground Motion Prediction Equation (GMPE), is a good indicator of spectral shape. The expected shape of ground motion for a specific site may have a positive ε value at the period of interest. However, the FEMA set is an “ ε -neutral” set. Figure 5.3 shows that the median ε value for the FEMA ground motion set is close to 0 for most of the period range. Therefore, the FEMA P695 approach for seismic collapse evaluation uses a spectra shape factor (SSF) for adjustment. The SSF in FEMA P695 (FEMA 2009) follows several empirical formulas developed based on the nonlinear analysis results for special reinforced concrete moment resisting frames (RC MRF) (Haselton 2007). The nonlinear behavior of low-ductility CBFs is very different from that of special RC MRFs. Low-ductility CBFs often experience abrupt changes in force versus deformation behavior due to connection fracture or brace buckling while special RC MRFs have relative smooth transition in force versus deformation behavior as they experience material yielding. Hence, it is doubtful whether the empirical formulas from FEMA P695 (FEMA 2009) apply to low-ductility CBFs and consequently whether the “ ε -neutral” FEMA set can be used to correctly evaluate the collapse capacity of low-ductility CBFs.

$$\varepsilon(T) = \frac{\ln Sa(M, R) - \mu_{\ln Sa}(M, R, T)}{\sigma_{\ln Sa}(T)} \quad (5.1)$$

5.2.2 NGA-East GM database

The recently developed NGA-East database (Goulet et al. 2014) was also evaluated for its potential to provide ground motions to assess the collapse performance of ECUS low-ductility CBFs. The NGA-East database contains over 29000 records from 81 earthquake events and 1379 recording stations in the Central and Eastern North America (CENA) since 1988 (Goulet et al. 2014). While the ground motions in the NGA-East database may have ground shaking characteristics of SCR such as the ECUS, critical issues exist that prevent them from being used directly in nonlinear time history analyses to evaluate collapse capacity.

Most recorded ground motions in the NGA-East database are earthquakes of small magnitude ($M < 5$) recorded at large distance ($R > 100$ km) as shown in Figure 5.4. As a result, most records in the NGA-East database have a small amplitude of shaking, and would require a large scale factor to induce appreciable motion in the structure which may lead to collapse. For example, one of the record for the 2002 Charleston earthquake ($M=4.03$) has a spectral acceleration at the period of 1s ($Sa(T = 1s)$) of $4.67 \times 10^{-5}g$. A scaled factor of 2140 is needed to bring $Sa(T = 1s)$ up to 0.1g in order to cause significant motion in a structure. A large scale factor lacks technical legitimacy, as it will introduce bias (Luco and Bazzurro 2007). Apart from that, these records, particularly those with small amplitude, also suffer from problems caused by high frequency noise. Due to the low amplitude of the actual ground acceleration signals, a low signal-to-noise acceptance threshold was used in processing those records (Goulet et al. 2014). Therefore, the short period content of the records is often contaminated by significant high frequency noise. Taking the example of the Charleston record again, the record has very large $Sa(T)$ in the

short period range compared to its long period range (Figure 5.5(a)). When the record is scaled to have the same $Sa(T = 1s)$ as the 2011 Mineral, Virginia record, it can be clearly seen that the low period content is contaminated by noise as it reaches as high as 15g (Figure 5.5(c)). Even though the long period content seems reasonable (Figure 5.5(d)), this record is not suitable for nonlinear time history analysis. It should be mentioned that the Mineral, Virginia (M5.8) record has a moderate amplitude ($Sa(T = 1s) = 0.11g$) (Figure 5.5 (b)). However, such unscaled records with adequate amplitude are rare in the NGA-East database. Most records are similar to the Charleston record, and are contaminated by short period noise and require a large scale factor. Therefore, the records from the NGA-East database were not used to develop a ground motion set to evaluate the collapse capacity of ECUS low-ductility CBF.

5.3 Methodology for GM simulation

A set of synthetic ground motions was developed that is consistent with the ECUS ground motion characteristics, has expected large amplitude, and directly includes the effect of spectral shape. Two major types of ground motion simulation are hybrid broadband (HBB) simulation and stochastic simulation (Atkinson et al. 2011). Stochastic simulation can be further divided into finite fault simulation and point-source simulation, depending on how the earthquake source is modeled (Atkinson et al. 2011).

HBB simulation uses a stochastic method to simulate high frequency (short period) motion and uses deterministic kinematic models to simulate low frequency (long period) motion (Shahjouei and Pezeshk 2015). The low frequency content is then spliced together with the high frequency content. HBB can simulate ground motion time histories across a broad

range of frequency and produces a realistic treatment of the low frequency (long period) content of ground motions (Burks et al. 2015). Nevertheless, it requires additional information and input parameters such as fault geometry, timing and distribution of slip and stress drop during the rupture process, etc., which is not available for the ECUS where the faults are poorly characterized. Hence, the additional complexity of HBB simulation may not lead to improved accuracy (Atkinson et al. 2011).

In comparison, stochastic simulation treats the ground motion as a random process across the entire frequency range. While it does not aim to provide a realistic treatment of the low frequency content of ground motions, it has been useful for simulating ground motions in the frequency range ($f > 0.1\text{Hz}$, $T < 10\text{s}$) of most interest to structural engineers (Boore 2003). Stochastic simulation with a finite fault model (Motazedian and Atkinson 2005) is usually used for simulating near-fault ground motions which are not considered in this dissertation. In addition, it requires parameters for the fault geometry. Therefore, the finite fault model is not used in this study.

This study employs the program SMSIM (Stochastic-Method SIMulation) which implements a point-source model to generate synthetic ground motions (Boore 2003). The essence of stochastic method is to use a target Fourier Amplitude Spectrum (FAS) defined by a parametrized seismological model and a random phase spectrum to generate ground motion time-histories.

The procedure for generating ground motion time histories using SMSIM is described in Figure 5.6. First, a white noise signal with a random phase spectrum, and of appropriate duration is generated in the time domain. Next, a window is applied to the white noise in

the time domain to simulate the increase and decrease in ground acceleration over time. Then a Fourier Transform is applied to the windowed white noise to transform the signal into the frequency domain. The FAS of the windowed white noise signal is then normalized by its root mean square (RMS) so that the average squared amplitude is unity. Then this normalized FAS of the windowed white noise signal is multiplied by the target FAS, at each frequency in the spectrum. In the end, the resulting FAS along with the phase spectrum of the windowed white noise signal is transformed back into the time domain. The generated ground acceleration includes the frequency characteristics defined by the target FAS, the effect of random phase, and the specified time window and duration.

Seismological models define the functional form and parameters of the target FAS of a ground motion Y which include 3 key factors, the source (E), path (P) and site (G) as shown in Eq.(5.2), where M_0 is the seismic moment, R is the source to site distance, f is the frequency. The seismic moment M_0 is related to the moment magnitude M by Eq. (5.3) from Hanks and Kanamori (1979). Past research have developed seismological models that account for the underlying physics of earthquake process and wave propagation in a SCR like CENA. Among them, 6 models are chosen in the recent NGA-East Project to generate synthetic ground motions that are in turn utilized to develop updated Ground Motion Prediction Equation (GMPE) for the CENA region (PEER 2015). Hence, these 6 models are also used to generate synthetic ground motions and develop a set of ECUS ground motions in the next section. Information of these 6 models are listed in Table 5.2. The major differences between these 6 models are the distance-dependent geometric spreading function $Z(R)$ and frequency-dependent attenuation $Q(f)$ which compose the term for the path effect $P(R, f)$ in Eq. (5.4), where C_Q is the seismic wave velocity. The stress drop

value in the source term $E(M_0, f)$, which also depends on $P(R, f)$ has been calibrated with ground motion data from the NGA-East database for each seismological model (PEER 2015). In order to be compatible with the hazard deaggregation described in the following section, the site term $G(f)$ uses the frequency-amplification pair for a hard rock site with $v_{s30} = 2000 \text{ m/s}$. More details about the 6 models can be found in PEER (2015).

$$Y(M_0, R, f) = E(M_0, f)P(R, f)G(f) \quad (5.2)$$

$$M = \frac{2}{3} \log(M_0) - 10.7 \quad (5.3)$$

$$P(R, f) = Z(R) \exp(-\pi f R / (Q(f) C_Q)) \quad (5.4)$$

5.4 Development of Rock GM set

A set of 44 ground motions was developed to include the spectral shape effect and record-to-record variability. Synthetic ground motions were generated and selected according to seismic hazard deaggregation results for the site, which provides information on the magnitude, distance and ε value of the earthquakes that contribute to the total seismic hazard at the site. Unfortunately, hazard deaggregation using the USGS online tool (<https://geohazards.usgs.gov/deaggint/2008/>) for sites in the ECUS is only available for rock sites. Consequently, a set of ground motions at the bedrock level was generated first and then propagated through the soil profile to account for the soil amplification effect. The procedure to develop the ground motion set for the bedrock level is described as follows:

Step 1. Seismic hazard deaggregation

Seismic hazard deaggregation was performed for a site in Philadelphia (latitude/longitude = 39.953/-75.165) for $Sa(1s)$ at MCE hazard level (2% of exceedance in 50 years). The site soil condition was assumed to be hard rock, with v_{s30} (average shear wave velocity of upper 30m of soil) of 2000m/s (Site Class A). The USGS online tool for seismic hazard deaggregation was used (<https://geohazards.usgs.gov/deaggint/2008/>). The hazard is deaggregated at $T = 1s$ because the tool permits deaggregation at only discrete periods such as 0.5s and 1s and, the fundamental periods of the SAP models in the previous chapter (Table 4.8) are around 0.8s. ECUS low-ductility CBFs sustain significant damage before they collapse, so period elongation is expected. Therefore, $Sa(1s)$ is assumed to be a good intensity measure for the seismic collapse evaluation of the prototype building and the hazard is deaggregated at the period of 1s. The MCE level is selected because the seismic collapse evaluation is based on the MCE hazard level (FEMA 2009). v_{s30} is assumed to be 2000 m/s to be consistent with the typical rock site condition in the ECUS. The result for the hazard deaggregation is shown in Figure 5.7, where $Sa(1s) = 0.039g$ for MCE hazard level.

Step 2. Determine the number of ground motions for each magnitude (M), distance (R) bin from the hazard deaggregation result.

As can be seen in Figure 5.7, the seismic hazard in Philadelphia is from earthquake events of various magnitudes and distances. The deaggregation results indicate that the hazard is from a total of 121 contributions of Magnitude (M) and distance (R), which are termed MR bins. A set of 44 ground motions cannot consider the contributions from all the bins. Therefore, only bins with more than a 1.5% contribution to the total hazard were

considered, which reduces the number of MR bins to 16. Table 5.3 shows the MR bins that were considered. It can be seen that the contribution from a single MR bin is further divided into contribution from different ε intervals. The number of ground motions from each ε interval within a MR bin was determined roughly by its contribution relative to the total contribution of the 16 bins multiplied by 44 (size of the ground motion set). For example, the bin M=6.22, R=35.2 has a contribution of 1.379% within the interval of $0 < \varepsilon < 1$. The number of ground motions used to represent this contribution is $\frac{1.379\%}{31.771\%} \times 44 \approx 2$ where 31.771% is the total contribution from the 16 bins. The number of ground motions needed for each MR bin and ε interval is shown in Table 5.4.

Step 3. Generate candidate ground motion set and determine median spectrum and standard deviation for each M, R bin

In order to select ground motions according to ε , the median spectrum of the ground motions generated for a particular M and R, as well as the associated standard deviation, need to be obtained. For the WUS, the median spectrum and standard deviation can be obtained from analysis of spectra of many natural ground motion records. However, for the ECUS, the median spectra and standard deviation must be determined from statistical analysis of the simulated ground motions.

Therefore, 800 ground motions were generated using SMSIM and a certain seismological model (Table 5.2) for each MR bin, and the response spectra for the simulated ground motions were calculated. It was assumed that the spectral acceleration response for ground motions for a given M and R follows a lognormal distribution, and the median spectrum for the 800 generated ground motions and the standard deviation was obtained. The

obtained median spectrum and standard deviation are considered to represent the predicted median spectrum and associated standard deviation for the given M and R. For example, Figure 5.8(a) shows the response spectra for the 800 generated ground motions using A04 seismological model for the bin with M=7.39, R=393.4km along with the median spectrum, and the median plus one and median plus two standard deviation spectra. Figure 5.8(b) shows the standard deviation of natural log of Sa at each period obtained from the 800 ground motions. The set of 800 ground motions for each MR bin also offers candidate ground motions to be considered, for the final ground motion set.

Step 4. Select required number of ground motions for each MR bin and ε interval

With the median spectrum and standard deviation obtained from Step 3, the ε value for each ground motion can be calculated according to Eq. (5.1). For each MR bin, the ground motions with ε values in the target interval are randomly selected from the 800 generated ground motion set. Figure 5.9 shows one of the ground motions selected for the bin M = 7.39, R = 393.4km and $1 < \varepsilon < 2$. This particular ground motion has $\varepsilon(1s) = 1.35$. The spectral shape effect can be clearly seen in this figure. While the spectral acceleration around $T = 1s$ is more than one standard above the median spectrum, the Sa values in part of the period range away from 1s exceed the median spectrum by a smaller extent. Some Sa values are even below the median. According to Table 5.4, 4 ground motions are needed for the bin with M=7.39, R=393.4km, and 3 ground motions should have $1 < \varepsilon < 2$, one ground motion should have $0 < \varepsilon < 1$. Figure 5.10 shows the response spectra for the 4 ground motions selected for this bin. Table 5.5 shows the ε values for all the 4 ground motions for this bin.

This process was repeated for each MR bin and a set of 44 ground motions was selected. For example, Figure 5.11 shows the response spectra for the 44 selected ground motions along with its median spectrum generated from A04 seismological model. The information on M, R and ϵ of these 44 ground motions is presented in Table 5.6.

Step 5. Repeat Step 3 and Step 4 for each seismological model and determine one final set

Steps 3 and 4 were repeated for each seismological model and one set of ground motion was developed for each model. The median spectrum of the ground motion set for each of the 6 models are displayed in Figure 5.12. It can be seen that these 6 spectra have similar shape, but have different amplitude. The ground motion set developed from seismological model A04 is seen to have a median $Sa(1s)$ closest to the target hazard $Sa(1s)$ value (Table 5.7). Therefore, the ground motion set from the A04 model was selected as the Rock GM set.

5.5 Development of Soil GM set

The results presented in Chapter 3 indicate site soil amplification of seismic input may have a significant impact on the ground motion and the associated seismic response of a structure on the site, especially for ECUS sites. Therefore, site response analyses were conducted using the Rock GM set as input to develop a set of ground motions which include the site soil amplification effect. To evaluate the collapse capacity of ECUS low-ductility CBFs in Philadelphia, the soil GM set used in the collapse evaluation should reflect site soil conditions in the Philadelphia area. Therefore, the variation of soil profiles in Philadelphia was considered. Unfortunately, only one soil profile from the Philadelphia

area is publicly available, which is a set of shear wave velocity measurements at Drexel University by Kayen et al. (2015). The shear wave velocity data is shown in Figure 5.13. The average shear wave velocity for the upper 30m of this soil profile v_{s30} is 353.4m/s, making it a Class D site according to ASCE7-10 (ASCE 2010). Due to a lack of soil profile datasets, the variation of the shear wave velocity over the depth of the soil profile cannot be established, and similarly, the variation of the depth of soil to bedrock across the perpendicular area cannot be established. As a result, this study uses a uniform layer approximation to perform the site response analyses to study the effect of variation of soil profile. In this method, the soil profile is assumed to be a single uniform layer with depth H and shear wave velocity v_s on top of the bedrock. The shear wave velocity of the uniform layer is calculated according to Eq. (5.5) as the average shear wave velocity \bar{v}_s from each layer of the actual soil profile $v_{s,i}$ weighted by the layer thickness d_i .

$$\bar{v}_s = \frac{\sum d_i v_{s,i}}{\sum d_i} \quad (5.5)$$

The uniform layer approximation approach was validated using site response analyses for a site with the Drexel (DXL) profile. The average shear wave velocity for the uniform layer approximation is $\bar{v}_s = 465m/s$ as shown in Figure 5.14 along with the original shear wave velocity (v_s) profile for DXL site. Site response analyses were performed using the entire rock GM set as input for both the uniform layer profile and the original profile. Response spectra for the resulting ground surface motions are shown in Figure 5.15. It can be seen using these 2 profiles yield ground motions with similar response spectra. Therefore, the uniform layer approximation is validated and used in the subsequent analyses.

According to the theory of site response analysis (Kramer 1996), for a single uniform soil column on rigid bedrock, the soil amplification effect is controlled by shear wave velocity v_s and soil column height H . The characteristic period of the soil column, which the period with the largest site amplification effect, can be calculated according to Eq. (5.6).

$$T_s = \frac{4H}{v_s} \quad (5.6)$$

To consider the variation of the site soil amplification effect, 8 different soil profiles with different H and v_s values are considered. The 8 soil profiles encompass a possible range of v_s and H of soil profiles in the Philadelphia area. As the prototype building is assumed to be located on Site Class D, the lower bound for v_s of the uniform soil layer is set to 180m/s which is the lower bound for v_{s30} for Site Class D. The upper bound for v_s is set to 465m/s instead of 360 m/s which is the upper bound for v_{s30} for Site Class D. The reason 465m/s was used is because v_{s30} is the average shear wave velocity considers for the upper 30m of the soil profile, and the shear wave velocity for soil more than 30m from the surface is usually larger, causing the average shear wave velocity for a soil profile greater than 30m deep to be greater than v_{s30} . For example, for the DXL profile, the $v_{s30} = 353.4m/s$ close to the upper bound for v_{s30} of Site Class D. But the average shear wave velocity of the entire soil profile is 465m/s. Therefore, 465m/s is selected to be a representative upper bound for the average shear wave velocity for the Philadelphia area for the uniform layer approximation. Bausher and Pazzaglia (2015) studied the possible bedrock depth in Philadelphia from well logs and boring data from the Pennsylvania Groundwater Information System (PaGWIS). They found that the bedrock depth in Philadelphia ranges from 4m to 120m. 4 possible bedrock depths were selected from this range: 30m, 50m,

80m and 110m. 30m was selected as the lower bound because when the bedrock depth is less than 30m, the site is not likely to be Site Class D. Bausher and Pazzaglia (2015) also shows that the bedrock depth does not vary significantly within proximity, further justifying the use of uniform layer approximation. The characteristic periods of the 8 soil profiles are shown in Table 5.8.

The open source software DEEPSOIL (Hashash et al. 2014) that was described in Chapter 3 was used for the site response analyses described in this chapter. Equivalent linear behavior is used as an approximation for the nonlinear behavior of the soil. The detailed description of the theory behind the response analysis method is presented in Kramer (1996). Site response analyses were performed using the entire Rock GM set as input bedrock motion for each of the 8 soil profiles. The median spectrum for the surface ground motions with the Rock GM set as bedrock motion input for each of the 8 soil profiles are shown in Figure 5.17. It can be seen that the 8 different soil profiles have different site soil amplification effects. The period with peak site soil amplification varies, but is consistent with the characteristic period in Table 5.8. Therefore, different soil profiles result in different spectral shapes for the surface ground motions. To consider the site soil amplification effect from the range of possible soil profiles, the resulting surface ground motions from the 8 soil profiles were randomly sampled to create a set of 44 ground motions, denoted the Soil GM set. Each of the 8 soil profiles is treated as equal likely, so ground motions resulting from each soil profile are equally represented in the Soil GM set. To maintain randomness, the ground motion from the Rock GM set used to represent the bedrock motion in the site response analysis for the selected surface ground motion for each soil profile is not repeated. The corresponding relation between the input bedrock

motion from the Rock GM set and soil profile is shown in Table 5.9. The final Soil GM set and its median spectrum are shown in Figure 5.17. It can be seen that the peak in the spectral shape at $T = 1s$ is preserved.

5.6 Comparison and discussion of various GM sets

Figure 5.18 shows the comparison of the median spectrum of the Rock GM set and the Soil GM set. It can be seen that the Soil GM set has been amplified from the Rock GM set but the shapes of the median spectrum of these 2 ground motion sets are similar. Even though it is shown by Figure 5.16 that the soil amplification from an individual soil profile significantly alter the spectrum shape of the resulted motion at the ground surface level, the fact that we are sampling ground motions resulted from 8 soil profiles makes the change in spectral shape insignificant. The local peak of Sa around $T = 1s$ still remains in the median spectrum of the Soil GM set.

The spectral shape of the Soil GM set is also compared with that of the FEMA GM set. Figure 5.19 shows the median spectrum of these 2 sets of ground motions when they are scaled to have the same $Sa(1s)$. It can be seen the intended spectral shape effect is achieved in the Soil GM set. The median spectrum has a peaked shape at $T=1s$. At periods away from $T = 1s$, the Sa values decrease rapidly from FEMA set.

The ground motion intensity of both the Rock GM set and Soil GM set is compared with the MCE hazard level intensity indicated by various reference sources from ASCE and USGS. As the Rock GM set is developed based on the hazard deaggregation result of the MCE hazard level for $Sa(1s)$, it should reflect the ground motion intensity for the MCE

hazard level in Philadelphia for rock site (Site Class A). Consequently, the Soil GM set is supposed to reflect the MCE hazard level for Site D in Philadelphia. Table 5.10 lists the $S_a(1s)$ value of the median spectrum of the Rock and Soil GM sets, $S_a(1s)$ value obtained from USGS seismic hazard deaggregation, USGS Uniform Hazard Spectrum (UHS), both at MCE hazard level for Site Class A, and ASCE MCE spectrum for different site conditions. Several observations can be made:

- I. The MCE intensity from USGS seismic hazard deaggregation is consistent with that of the UHS (0.039g). But both of them are considerably smaller than the value indicated by the ASCE MCE spectrum for Site Class A (0.048g). This is because the USGS UHS is purely based on the 2008 version of United States National Seismic Hazard Maps (Petersen et al. 2008) which corresponds to a 2% probability of exceedance in 50 years. However, the ASCE MCE spectrum applies some modifications over the 2008 National Hazard Map: 1. The S_a is modified to give a 1% probability of collapse in 50 years based on generic structural fragility curves; 2. A factor of 1.1 is applied to adjust from a geometric mean to the maximum response regardless of direction (ASCE 2010).
- II. The $S_a(1s)$ value of the Rock GM set (0.036g) is smaller than the USGS UHS (0.039g). This can be attributed to several reasons. First, the Rock GM set is developed by using current seismological models (PEER 2015) while the UHS is based on 2008 seismic hazard map which uses older GMPEs (Petersen et al. 2008). In fact, the more updated 2014 National Hazard Map (Petersen et al. 2014) indicates a smaller MCE ground motion intensity for the Philadelphia

location, a trend consistent with findings in this study (Petersen et al. 2015). Second, the method to develop the Rock GM set does not account for all the seismic sources (MR bins) contributing to the total hazard due to limit size of the GM.

- III. The more significant difference is between the $Sa(1s)$ value of the Soil Set (0.065g) and that indicated by the ASCE MCE Spectrum for Site D (0.144g). The primary reason is because of the different soil profiles used in the site response analysis to obtain the Soil GM set. It can be seen from Figure 5.16 that not all the soil profiles have peak amplification effect at the same period. For example, for the soil column with $V_s=465\text{m/s}$ and $H=120\text{m}$, it has peak amplification period around 1s. The amplification ratio is $0.1042\text{g}/0.0358\text{g}=2.91$, close to the amplification ratio of $2.4/0.8=3$ from Site A to Site D according to the F_v factor from ASCE 7-10. But for the soil profile with $V_s=465\text{m/s}$ and $H=30\text{m}$, the peak amplification is around 0.25s. Its amplification for $Sa(1s)$ is very limited. Since the Soil Set is sampled from site response analysis result from the 8 soil profiles on roughly an equal likely basis, the average amplification effect (at $T = 1s$) of the entire ground motion set cannot be as high as the case when all peak amplification happen at 1s. In the design stage, it is not known what specific soil profile the structure may encounter. To be conservative, the spectral accelerations in a range of period are all amplified using the worst-case scenario where peak amplification happens. But in our application where we want to evaluate the expected performance of the structure on a generic Site Class D site in Philadelphia, it

may not be appropriate to use a conservative estimation on the seismic hazard. It is more appropriate to estimate the expected ground motion intensity according to the expected geological condition for Site Class D sites in Philadelphia. Besides a smaller soil amplification effect, the difference between the Soil GM set and ASCE MCE Spectrum (Site D) at $Sa(1s)$ is also contributed by the $Sa(1s)$ value of median spectrum of the Rock Set which is smaller than the UHS and further smaller than the ASCE MCE at rock site.

Figure 5.20 compares the entire median spectrum for the Rock and Soil Set, ASCE MCE Spectrum for Site A and D and USGS UHS for Site A. Because of the reason stated in the third observation above, the $Sa(1s)$ value of the Rock and Soil set is smaller than that of the ASCE MCE Spectrum of the corresponding site condition. Because of the spectral shape effect, the Sa at other periods are even smaller than the ASCE MCE spectrum. It should be noted that FEMA P695 methodology requires MCE ground motion intensity be determined according to the ASCE MCE spectrum which is much larger than the MCE ground motion intensity indicated by the ground motion set developed in this chapter.

Table 5.1 Summary of FEMA GM set (adapted from FEMA P695 (FEMA 2009))

ID No.	Earthquake			Recording Station Name	Site Data		Source (Fault Type)	Site-Source Distance ¹ (km) Campbell
	M	Year	Name		Site Class	V_{s30} (m/s)		
1	6.7	1994	Northridge	Beverly Hills - Mulhol	D	356	Thrust	17.2
2	6.7	1994	Northridge	Canyon Country-WLC	D	309	Thrust	12.4
3	7.1	1999	Duzce, Turkey	Bolu	D	326	Strike-slip	12.4
4	7.1	1999	Hector Mine	Hector	C	685	Strike-slip	12
5	6.5	1979	Imperial Valley	Delta	D	275	Strike-slip	22.5
6	6.5	1979	Imperial Valley	El Centro Array #11	D	196	Strike-slip	13.5
7	6.9	1995	Kobe, Japan	Nishi-Akashi	C	609	Strike-slip	25.2
8	6.9	1995	Kobe, Japan	Shin-Osaka	D	256	Strike-slip	28.5
9	7.5	1999	Kocaeli, Turkey	Duzce	D	276	Strike-slip	15.4
10	7.5	1999	Kocaeli, Turkey	Arcelik	C	523	Strike-slip	13.5
11	7.3	1992	Landers	Yermo Fire Station	D	354	Strike-slip	23.8
12	7.3	1992	Landers	Coolwater	D	271	Strike-slip	20

¹ Campbell distance (Campbell and Bozorgnia 2003) is used.

Table 5.1 (continued) Summary of FEMA GM set (adapted from FEMA P695 (FEMA 2009))

ID No.	Earthquake			Recording Station Name	Site Data		Source (Fault Type)	Site-Source Distance (km) Campbell ²
	M	Year	Name		Site Class	V_{s30} (m/s)		
13	6.9	1989	Loma Prieta	Capitola	D	289	Strike-slip	35.5
14	6.9	1989	Loma Prieta	Gilroy Array #3	D	350	Strike-slip	12.8
15	7.4	1990	Manjil, Iran	Abbar	C	724	Strike-slip	13
16	6.5	1987	Superstition Hills	El Centro Imp. Co.	D	192	Strike-slip	18.5
17	6.5	1987	Superstition Hills	Poe Road (temp)	D	208	Strike-slip	11.7
18	7	1992	Cape Mendocino	Rio Dell Overpass	D	312	Thrust	14.3
19	7.6	1999	Chi-Chi, Taiwan	CHY101	D	259	Thrust	15.5
20	7.6	1999	Chi-Chi, Taiwan	TCU045	C	705	Thrust	26.8
21	6.6	1971	San Fernando	LA - Hollywood Stor	D	316	Thrust	25.9
22	6.5	1976	Friuli, Italy	Tolmezzo	C	425	Thrust	15.8

² Campbell distance (Campbell and Bozorgnia 2003) is used.

Table 5.2 Six seismological models used in the NGA-East project

Model abbreviation	Reference
AB95	Atkinson and Boore (1995)
SGD02	Silva et al. (2002)
A04	Atkinson (2004)
BCA10d	Boore et al. (2010)
BS11	Boatwright and Seekins (2011)
AB14	Atkinson and Boore (2014)

Table 5.3 Seismic hazard deaggregation for MR bins with more than 1.5% contribution

Distance R (km)	Magnitude M (Mw)	Contribution to hazard (%)						
		All ϵ	$\epsilon > 2$	$1 < \epsilon < 2$	$0 < \epsilon < 1$	$-1 < \epsilon < 0$	$-2 < \epsilon < -1$	$\epsilon < -2$
393.4	7.39	2.591	0.345	1.748	0.499	0	0	0
35.2	6.22	2.404	0.108	0.643	1.379	0.274	0	0
390.6	7.01	2.347	0.719	1.61	0.018	0	0	0
123.9	6.79	2.286	0.141	0.84	1.305	0	0	0
33.8	5.81	2.108	0.188	1.071	0.848	0.001	0	0
34.9	6.01	2.073	0.12	0.717	1.16	0.076	0	0
35.2	6.42	1.984	0.069	0.413	1.034	0.465	0.003	0
390	6.79	1.952	1.153	0.799	0	0	0	0
123.7	7	1.945	0.087	0.517	1.248	0.094	0	0
122.9	6.42	1.801	0.208	1.228	0.364	0	0	0
391.8	7.19	1.786	0.361	1.316	0.109	0	0	0
637	7.4	1.776	0.983	0.793	0	0	0	0
85.2	6.79	1.747	0.087	0.518	1.123	0.019	0	0
32.3	5.4	1.68	0.459	1.13	0.091	0	0	0
33.3	5.62	1.671	0.218	1.042	0.411	0	0	0
122.5	6.22	1.62	0.35	1.269	0.002	0	0	0

Table 5.4 Number of ground motions to be selected for each MR bin and ϵ interval

Distance R (km)	Magnitude M (Mw)	Number of ground motion to select						
		All ϵ	$\epsilon > 2$	$1 < \epsilon < 2$	$0 < \epsilon < 1$	$-1 < \epsilon < 0$	$-2 < \epsilon < -1$	$\epsilon < -2$
393.4	7.39	4	0	3	1	0	0	0
35.2	6.22	3	0	1	2	0	0	0
390.6	7.01	3	1	2	0	0	0	0
123.9	6.79	3	0	1	2	0	0	0
33.8	5.81	3	0	2	1	0	0	0
34.9	6.01	3	0	1	2	0	0	0
35.2	6.42	3	0	1	1	1	0	0
390	6.79	3	2	1	0	0	0	0
123.7	7	3	0	1	2	0	0	0
122.9	6.42	3	0	2	1	0	0	0
391.8	7.19	3	1	2	0	0	0	0
637	7.4	2	1	1	0	0	0	0
85.2	6.79	2	0	1	1	0	0	0
32.3	5.4	2	1	1	0	0	0	0
33.3	5.62	2	0	1	1	0	0	0
122.5	6.22	2	0	2	0	0	0	0

Table 5.5 Four ground motions selected for R=393.4 km, M=7.39 bin using A04 model

GM Index	Distance R (km)	Magnitude M (Mw)	ϵ	ϵ range
1	393.4	7.39	1.35	$1 < \epsilon < 2$
2	393.4	7.39	1.18	
3	393.4	7.39	1.05	
4	393.4	7.39	0.66	$0 < \epsilon < 1$

Table 5.6 Summary of M, R, ε information for all 44 ground motions selected by using A04 model

GM Index	R	M	ε
1	393.4	7.39	1.35
2	393.4	7.39	1.18
3	393.4	7.39	1.05
4	393.4	7.39	0.66
5	35.2	6.22	1.91
6	35.2	6.22	0.53
7	35.2	6.22	0.77
8	390.6	7.01	2.69
9	390.6	7.01	1.25
10	390.6	7.01	1.24
11	123.9	6.79	1.71
12	123.9	6.79	0.69
13	123.9	6.79	0.03
14	33.8	5.81	1.34
15	33.8	5.81	1.42
16	33.8	5.81	0.98
17	34.9	6.01	1.54
18	34.9	6.01	0.38
19	34.9	6.01	0.29
20	35.2	6.42	1.48
21	35.2	6.42	0.76
22	35.2	6.42	-0.15
23	390	6.79	2.01
24	390	6.79	2.30
25	390	6.79	1.54
26	123.7	7	1.46
27	123.7	7	0.56
28	123.7	7	0.81
29	122.9	6.42	1.15
30	122.9	6.42	1.53
31	122.9	6.42	0.56
32	391.8	7.19	3.36
33	391.8	7.19	1.23
34	391.8	7.19	1.59
35	637	7.4	2.48
36	637	7.4	1.14
37	85.2	6.79	1.70
38	85.2	6.79	0.68

Table 5.6 (continued) Summary of M, R, ε information for all 44 ground motions selected by using A04 model

GM Index	R	M	ε
39	32.3	5.4	2.38
40	32.3	5.4	1.82
41	33.3	5.62	1.19
42	33.3	5.62	0.73
43	122.5	6.22	1.49
44	122.5	6.22	1.04

Table 5.7 Comparison of $Sa(1s)$ values from median spectrum of ground motion sets generated using 6 seismological models and MCE hazard level

Model	$Sa(1s)$ for median spectrum (g)
A04	0.036
AB14	0.033
AB95	0.033
BCA10D	0.025
BS11	0.032
SGD02	0.023
MCE Hazard Level	0.039

Table 5.8 Characteristic period for each soil profile

v_s (m/s)	H (m)	T_s (s)
180	30	0.667
	50	1.111
	80	1.778
	120	2.667
465	30	0.258
	50	0.430
	80	0.688
	120	1.032

Table 5.9 Number of ground motions sampled for each soil profile and their corresponding bedrock motion index

v_s (m/s)	H (m/s)	Number of ground motions	Rock GM set index for bedrock motion
180	30	5	24
			41
			21
			8
			16
	50	5	4
			15
			34
			29
			9
	80	6	12
			22
			17
			1
			18
			39
	120	6	38
			10
			19
			3
7			
30			

Table 5.9 (continued) Number of ground motions sampled for each soil profile and their corresponding bedrock motion index

v_s (m/s)	H (m/s)	Number of ground motions	Rock GM set index for bedrock motion
465	30	6	27
			35
			20
			33
			32
			28
	50	6	11
			13
			36
			37
			14
			26
	80	5	44
			23
			42
			5
			43
	120	5	2
			25
			31
6			
40			

Table 5.10 Comparison of $Sa(1s)$ for Rock GM and Soil GM and $Sa(1s)$ of MCE hazard level from various sources

Source	$Sa(1s)$ (g)	Site Class	Note
USGS UHS	0.039	A	Obtained from https://geohazards.usgs.gov/hazardtool/application.php
USGS deaggregation	0.039	A	Obtained from https://geohazards.usgs.gov/deaggint/2008/
ASCE7-10 design map	0.060	B	Referring to seismic design web tool https://earthquake.usgs.gov/designmaps/us
ASCE7-10 design map	0.048	A	Multiple by $F_v = 0.8$
ASCE7-10 design map	0.144	D	Multiple by $F_v = 2.4$
Rock GM set	0.036	A	Developed using USGS seismic hazard deaggregation
Soil GM set	0.065	D	Developed using site response analysis from 8 soil profiles

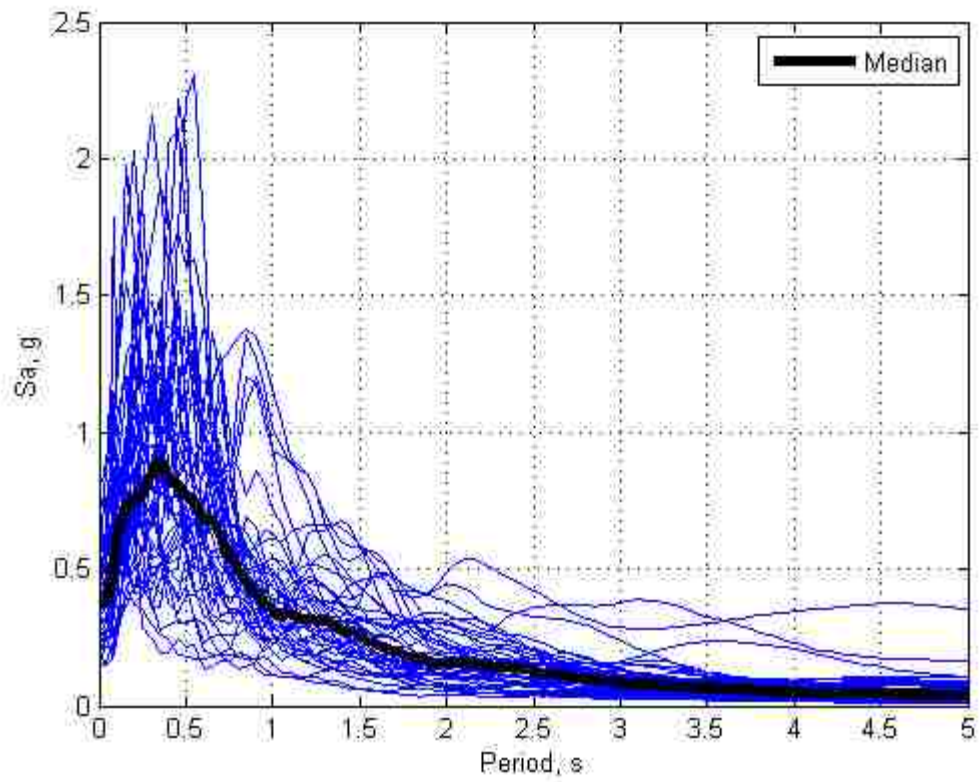


Figure 5.1 Response spectra for uncalibrated FEMA GM set and its median spectrum

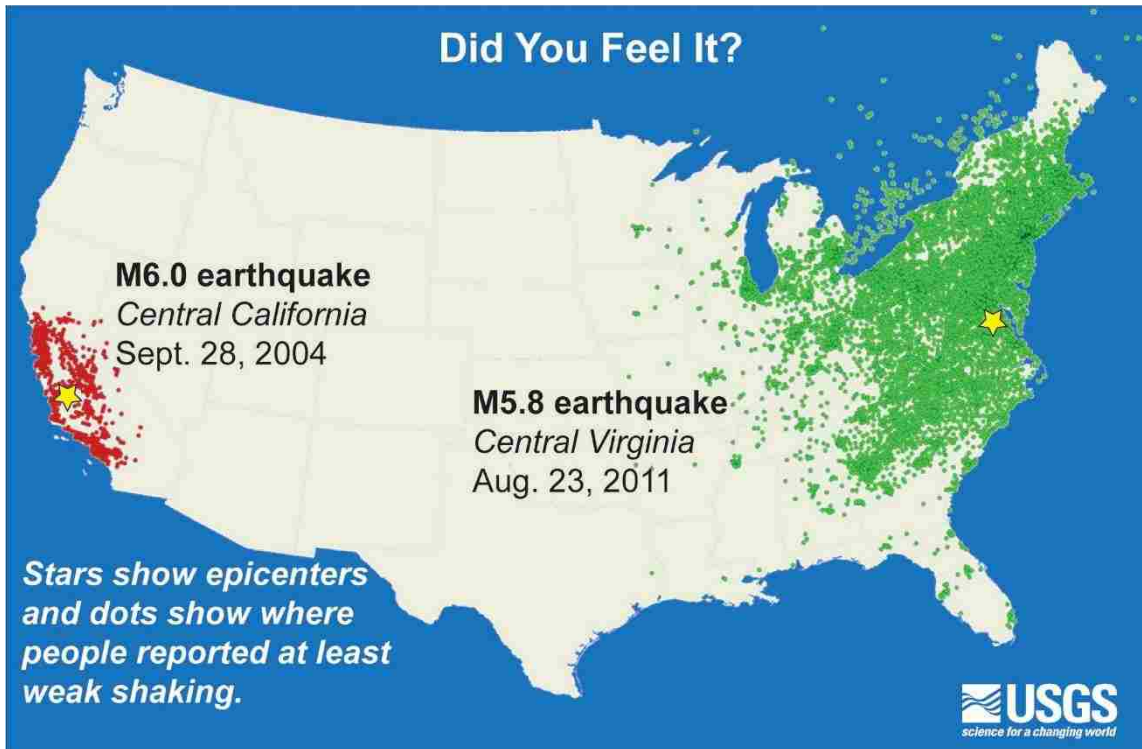


Figure 5.2 Comparison of the felt area of ECUS earthquake with WUS earthquake of similar magnitude (Horton and Williams 2012)

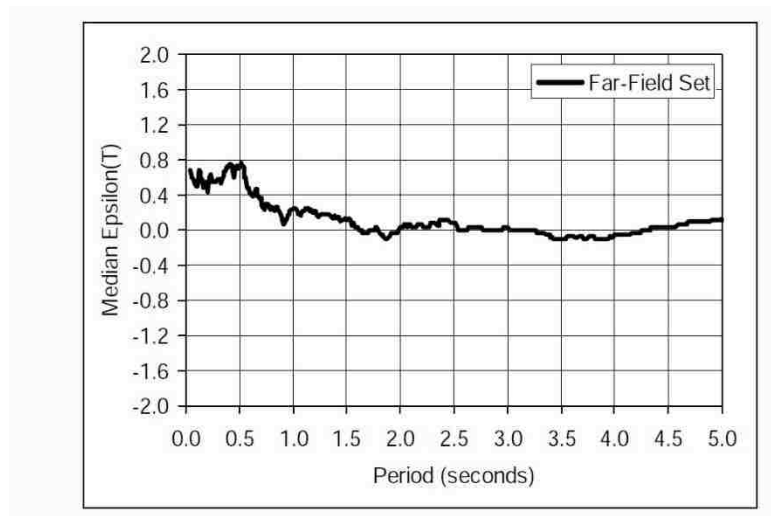


Figure 5.3 Median ϵ of FEMA GM set

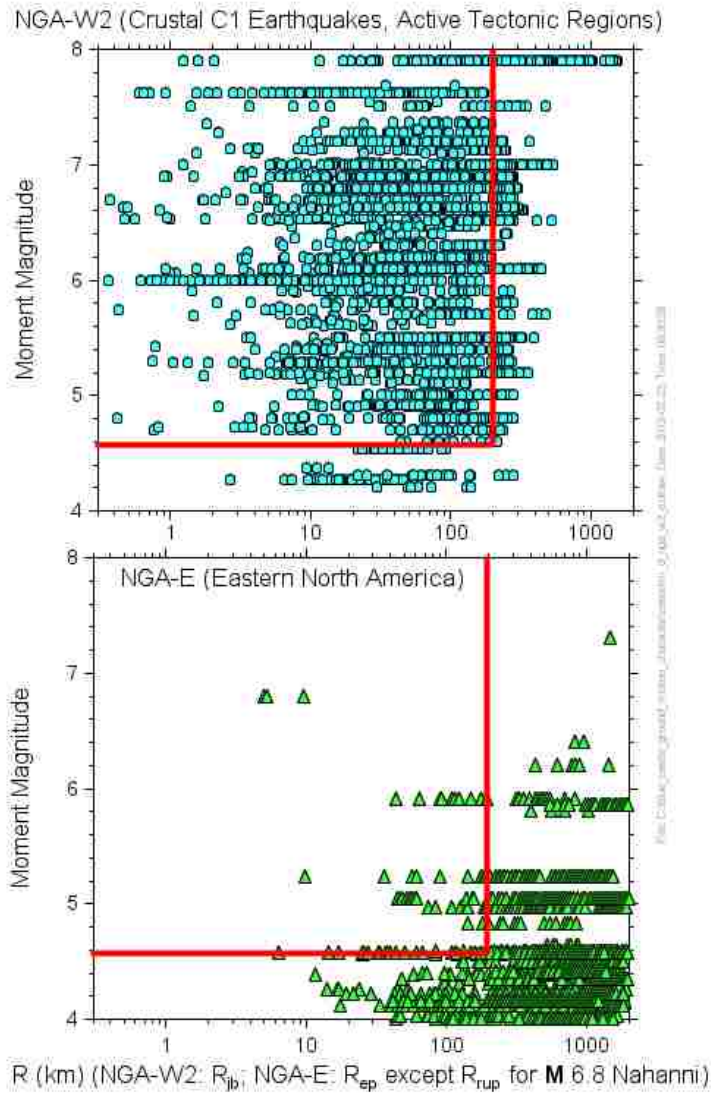
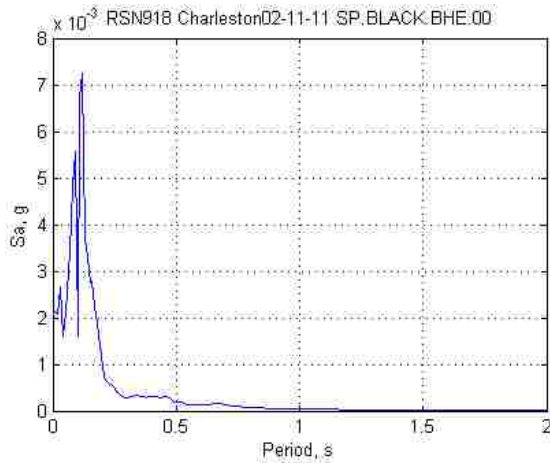
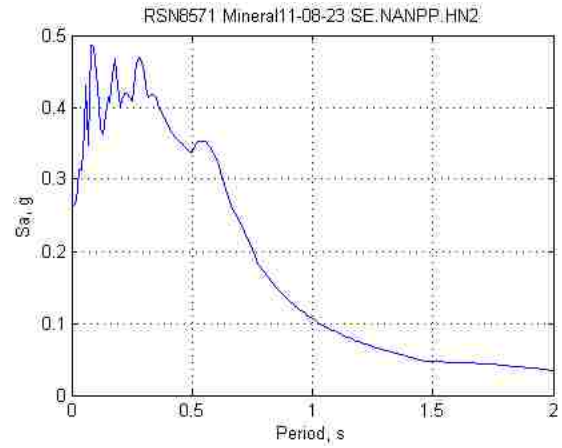


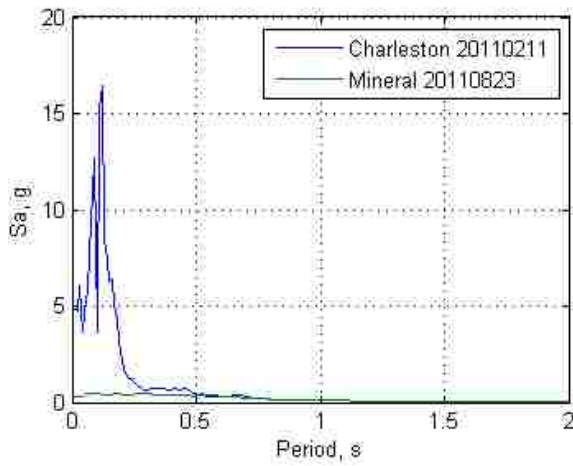
Figure 5.4 Comparison of magnitude and distance of ground motion records in NGA-East and NGA-West2 database (Boore 2013)



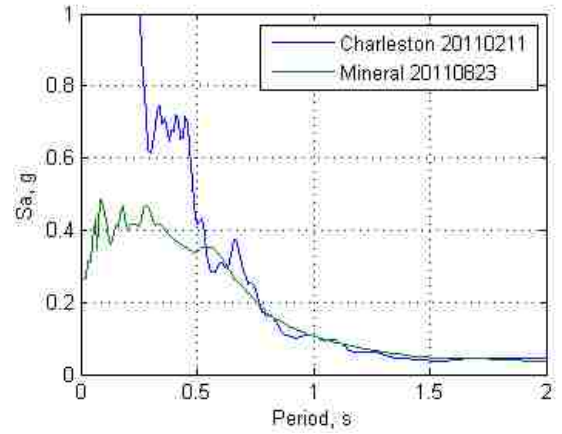
(a)



(b)



(c)



(d)

Figure 5.5 Response spectra of example records from NGA-East database: (a) 2002 Charleston ground motion (unscaled); (b) 2011 Mineral ground motion (unscaled); (c) comparison; (d) comparison up to 1g

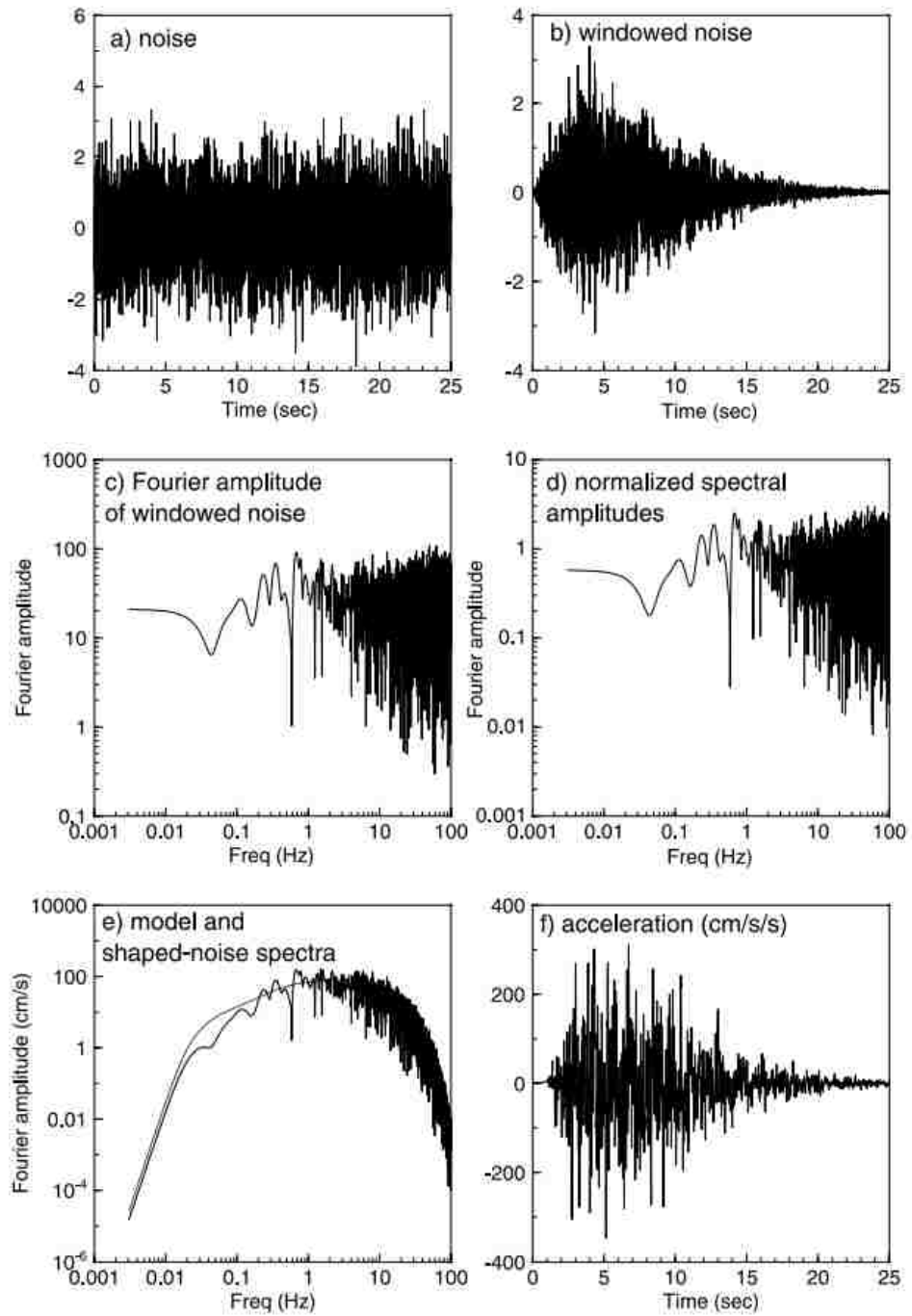
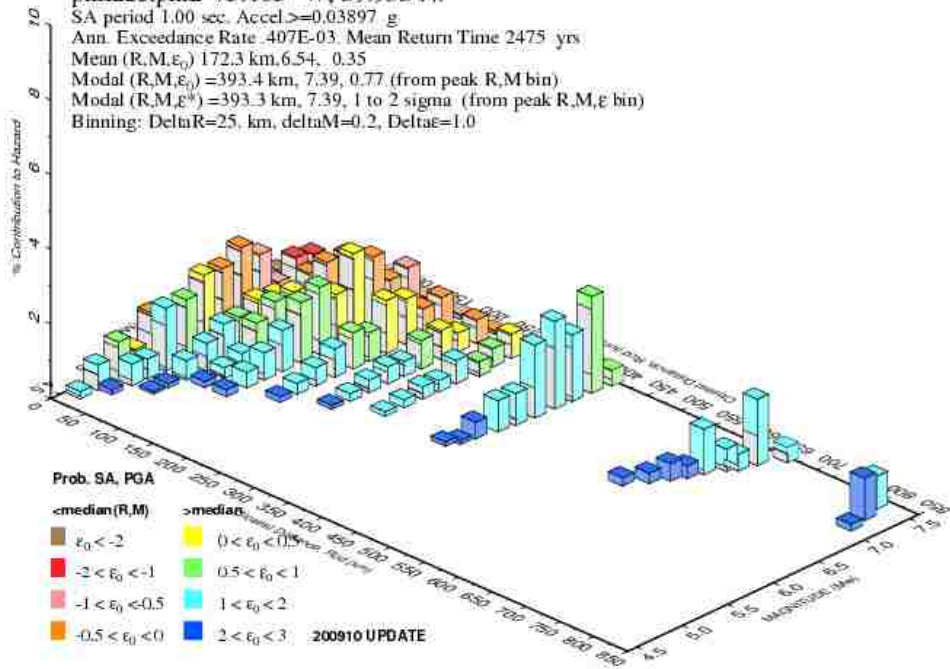


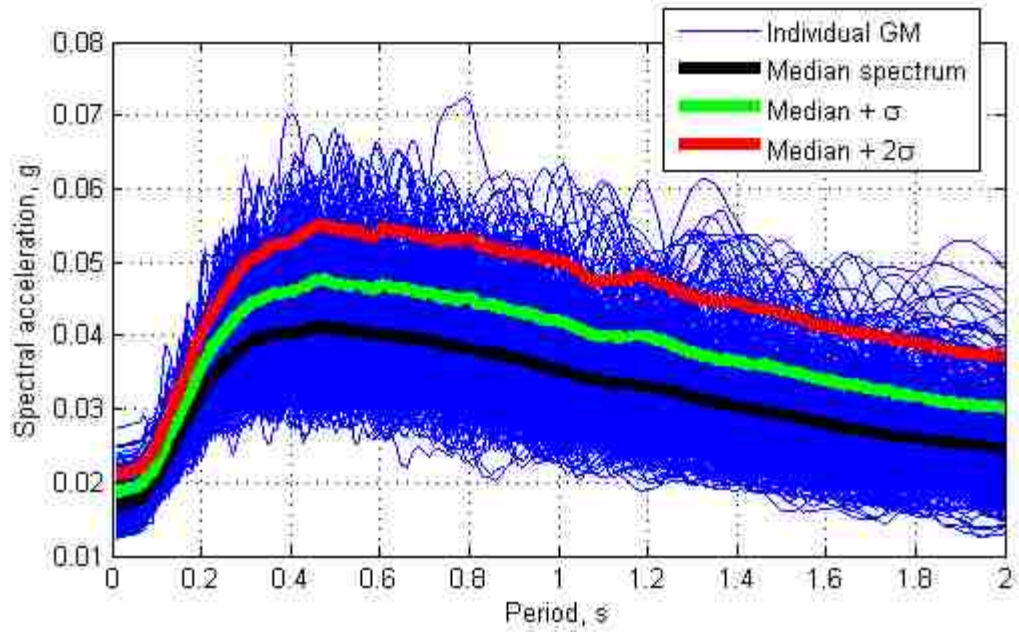
Figure 5.6 Procedure of ground motion simulation in SMSIM (Boore 2003)

PSH Deaggregation on NEHRP A rock
 Philadelphia 75.165° W, 39.953 N.
 SA period 1.00 sec, Accel. ≥ 0.03897 g
 Ann. Exceedance Rate 407E-03, Mean Return Time 2475 yrs
 Mean (R,M, ϵ_0) 172.3 km, 6.54, 0.35
 Modal (R,M, ϵ_0) = 393.4 km, 7.39, 0.77 (from peak R,M bin)
 Modal (R,M, ϵ_0^*) = 393.3 km, 7.39, 1 to 2 sigma (from peak R,M, ϵ bin)
 Binning: DeltaR=25, km, deltaM=0.2, Delta ϵ =1.0

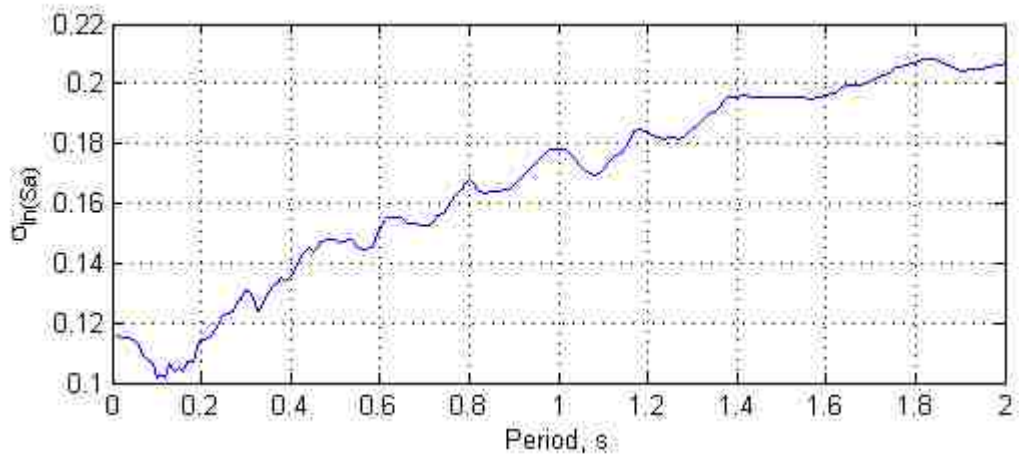


GMT 2015 Dec 10 00:21:05 Distance (R), magnitude (M), epsilon (E) deaggregation for a site on rock with average vs=2000, rns top 30m, USGS CG-IT PSHA2008 UP DATE Bins with 110.00% contrib. omitted

Figure 5.7 Seismic hazard deaggregation result for MCE hazard level at $T = 1$ s for Philadelphia



(a)



(b)

Figure 5.8 (a) Spectra for the 800 generated ground motions, median spectrum, median plus one standard deviation and median plus two standard deviations spectrum; (b) log standard deviation for 800 generated ground motions for $M=7.39$, $R=393.4$ using A04 model.

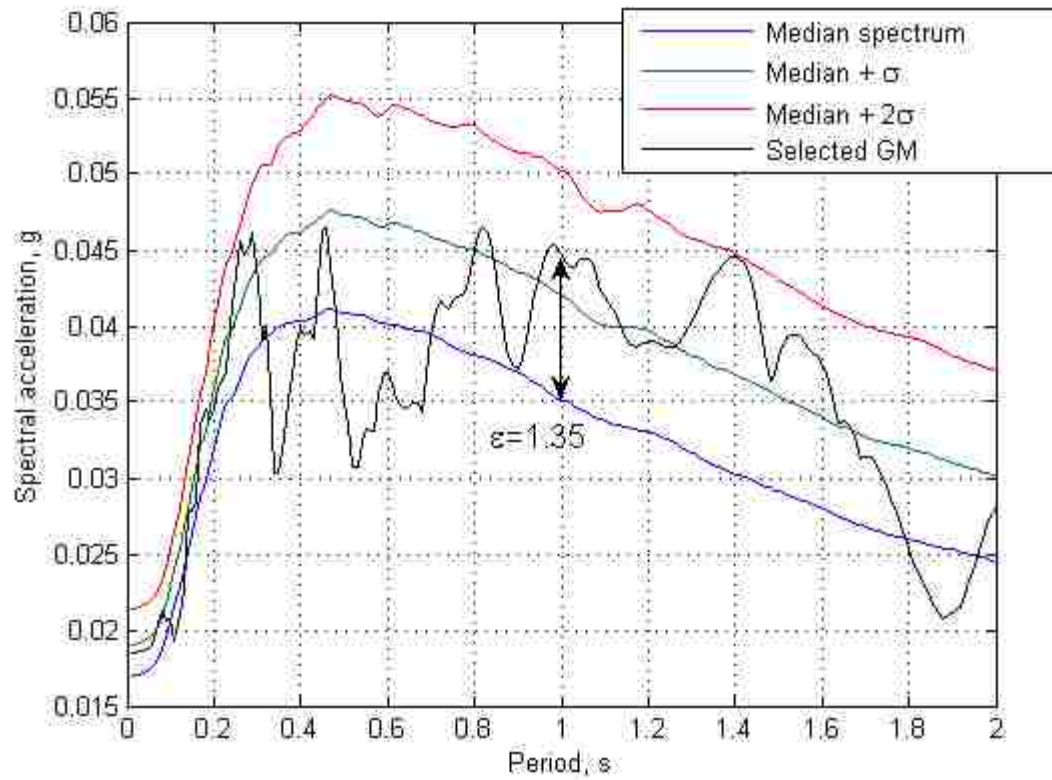


Figure 5.9 Response spectrum for an example ground motion with $\epsilon = 1.35$, selected for $R=393.4$ km, $M=7.39$ bin using A04 model

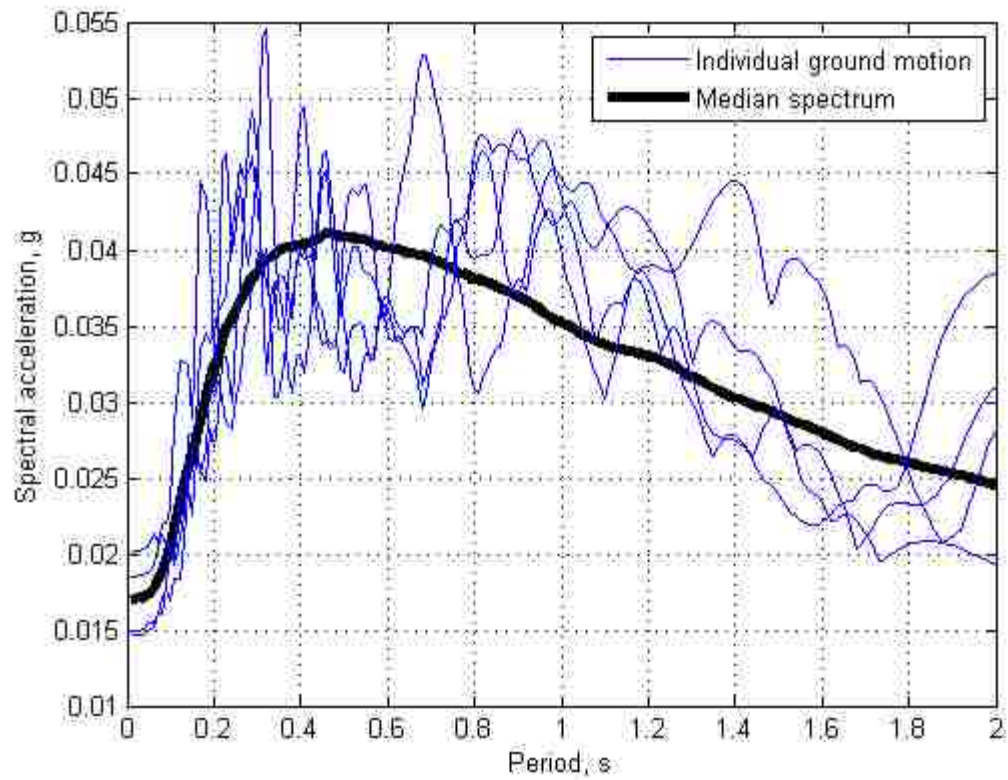


Figure 5.10 Response spectra for ground motions selected for $R=393.4$ km, $M=7.39$ bin using A04 model

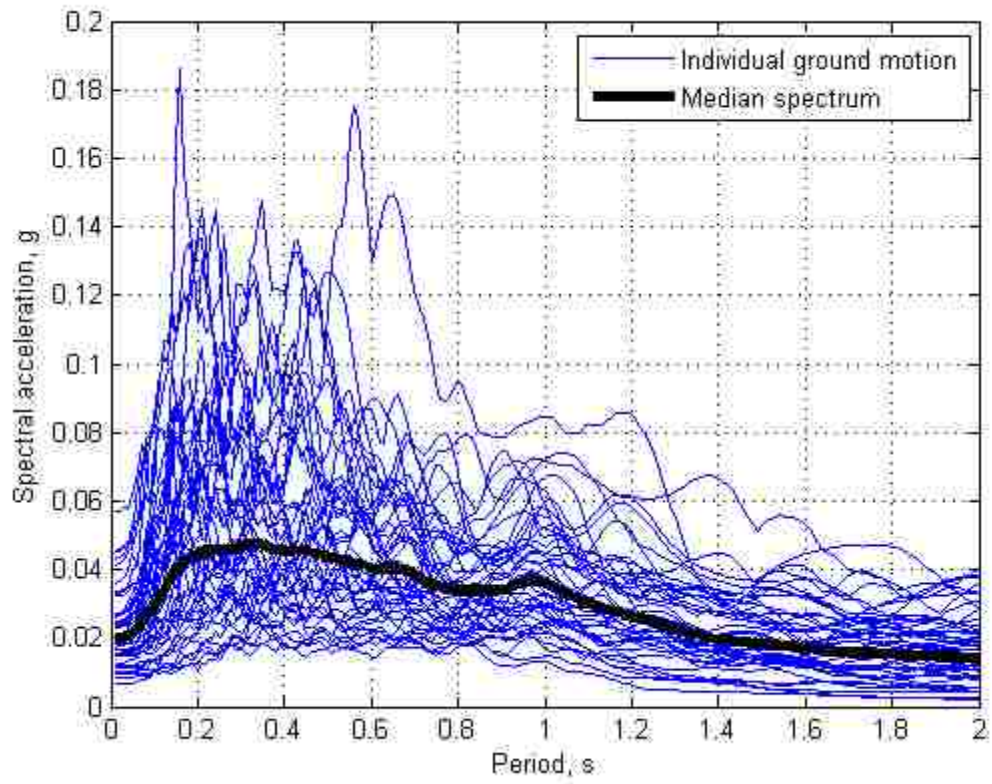


Figure 5.11 44 ground motions selected using A04 model

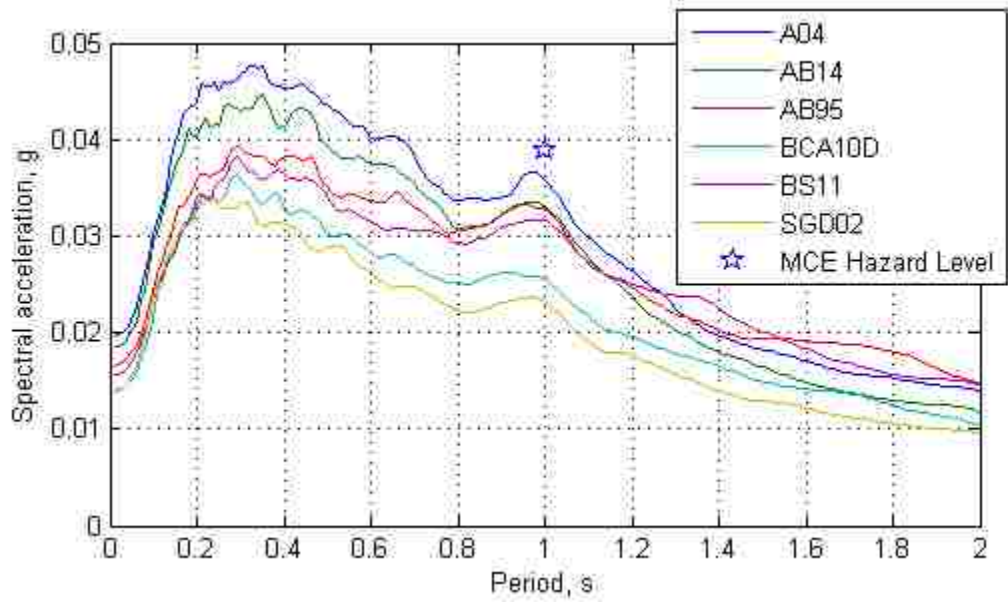


Figure 5.12 Comparison of median spectra of ground motion sets from 6 seismological models and $Sa(T = 1s)$ for MCE hazard level

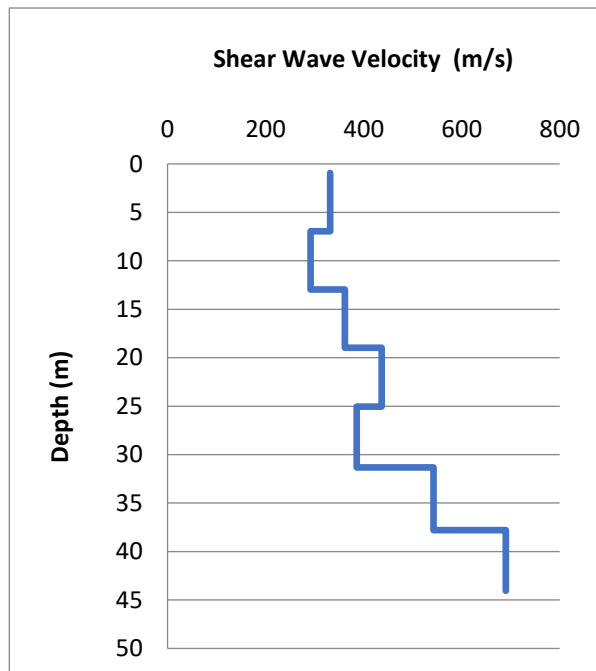


Figure 5.13 Shear wave velocity profile at a site at Drexel University, Philadelphia

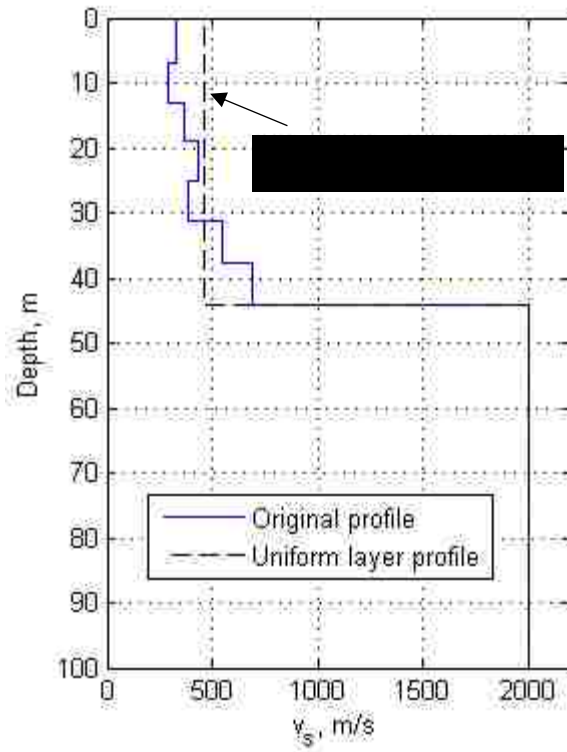
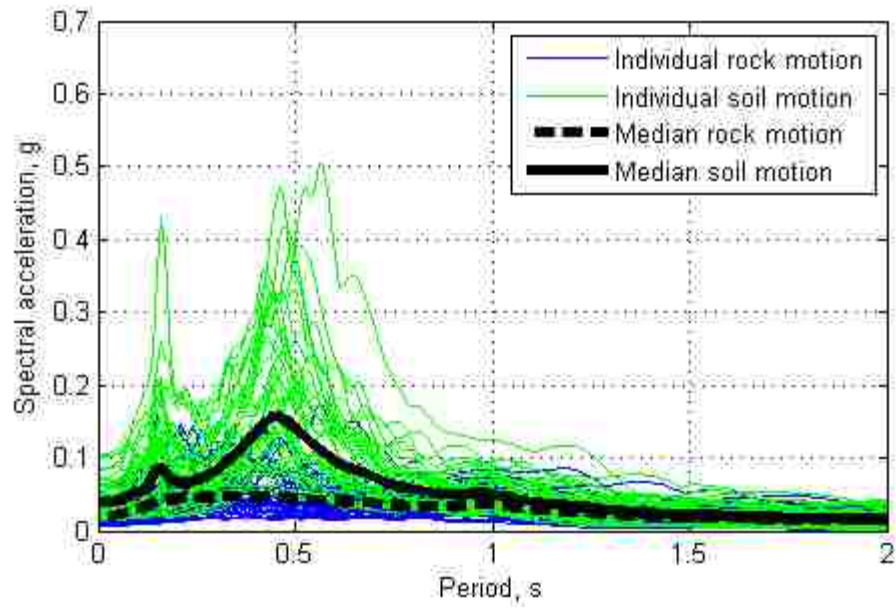
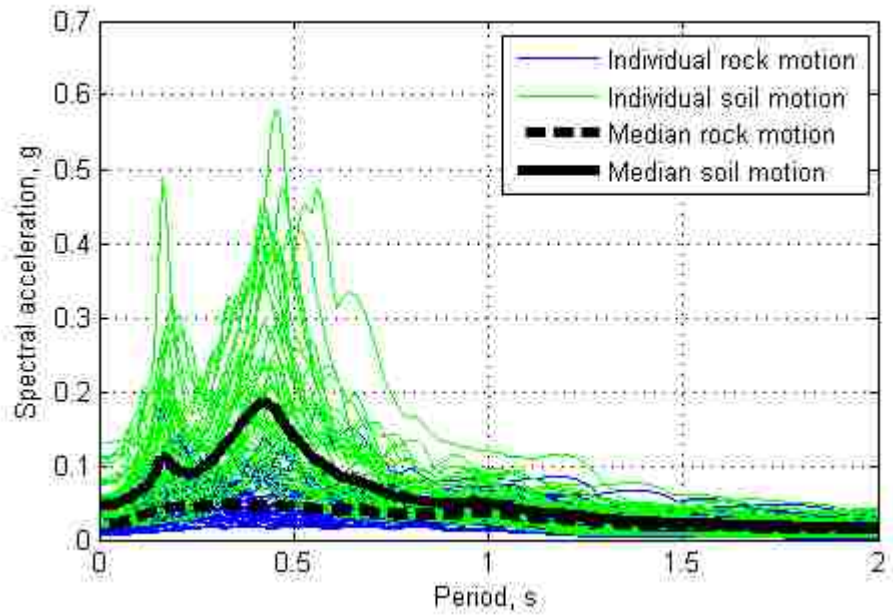


Figure 5.14 Original and uniform layer profile of shear wave velocity for DXL site

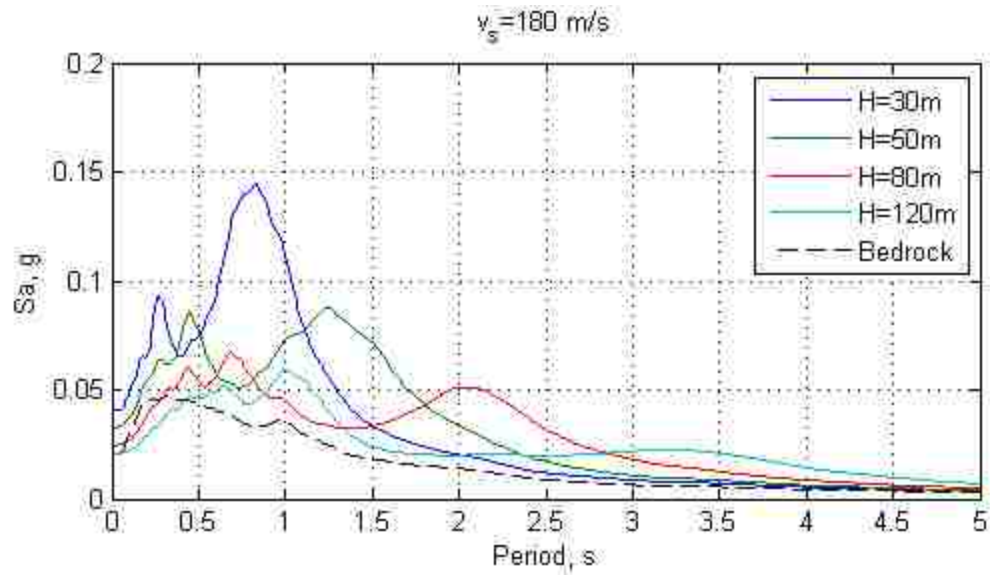


(a)

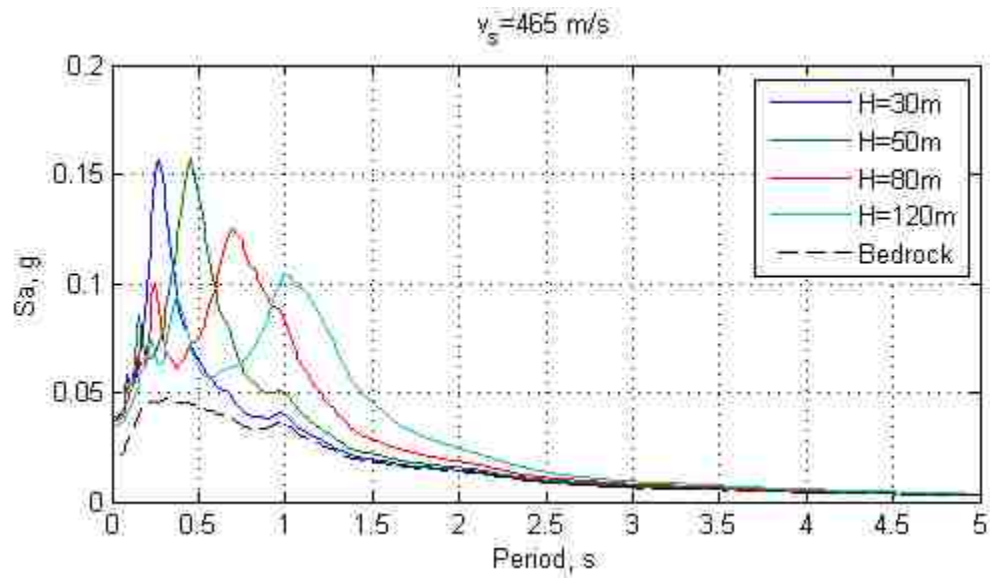


(b)

Figure 5.15 Response spectra for surface ground motions from site response analyses using Rock GM set as bedrock motion input for: (a) uniform layer profile; (b) original profile



(a)



(b)

Figure 5.16 Comparison of median spectra of ground motion sets obtained from site response analyses using different soil profiles: (a) profiles with $v_s = 180 \text{ m/s}$; (b) profiles with $v_s = 465 \text{ m/s}$;

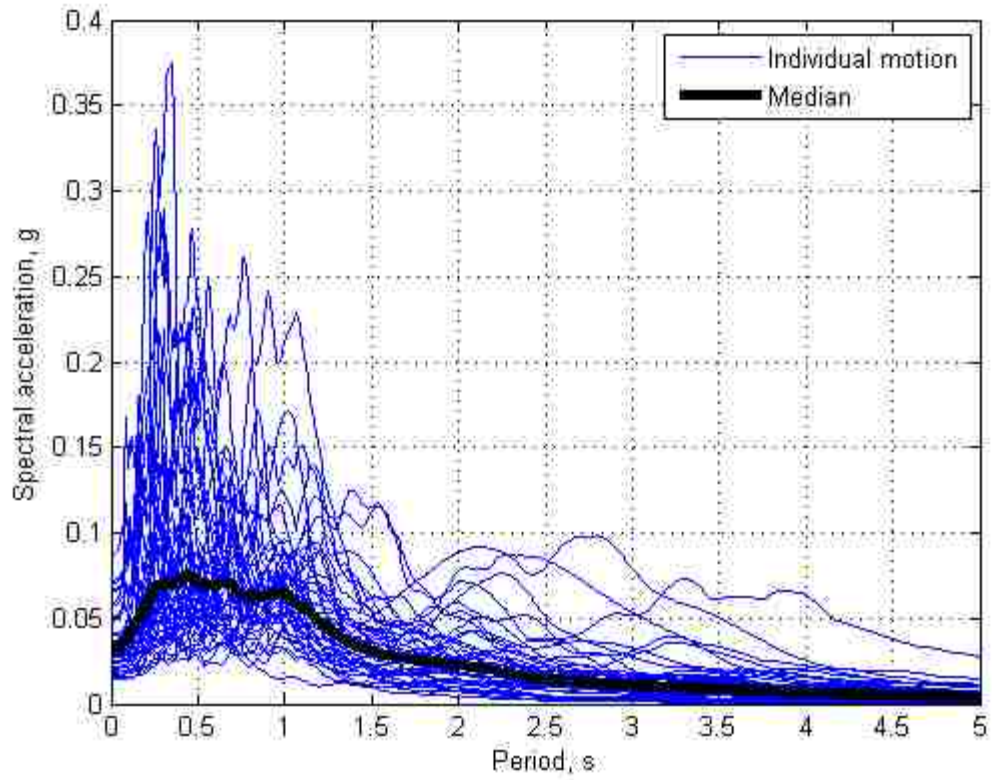


Figure 5.17 Response spectra for Soil GM set and its median spectrum

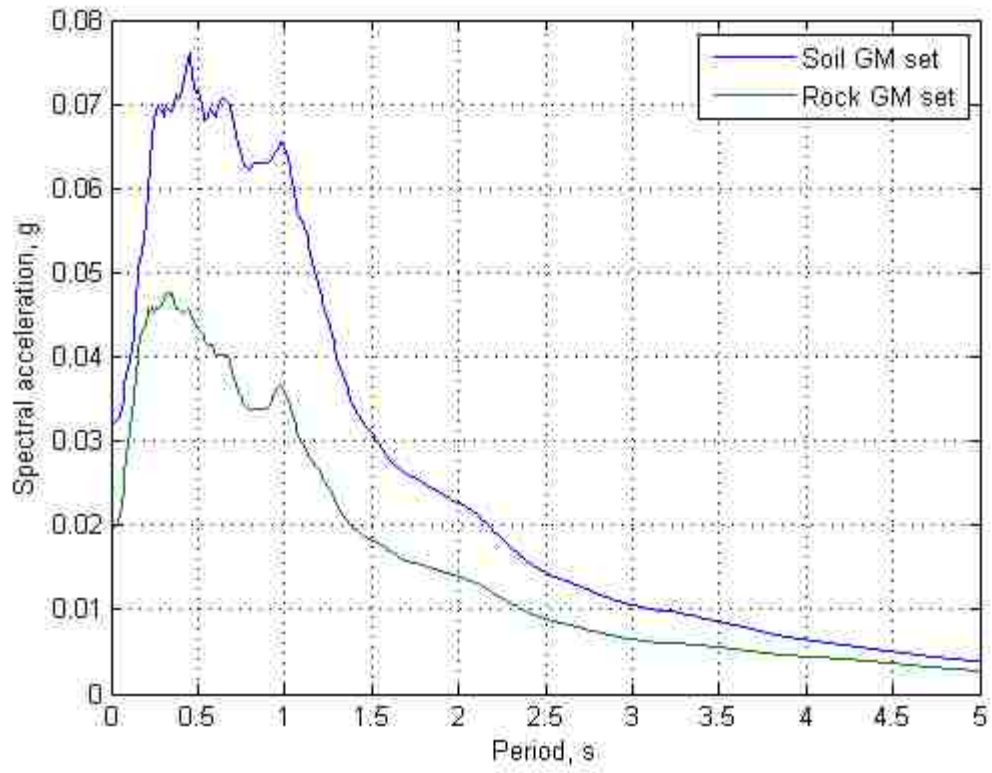


Figure 5.18 Comparison of median spectra of Rock GM set and Soil GM set

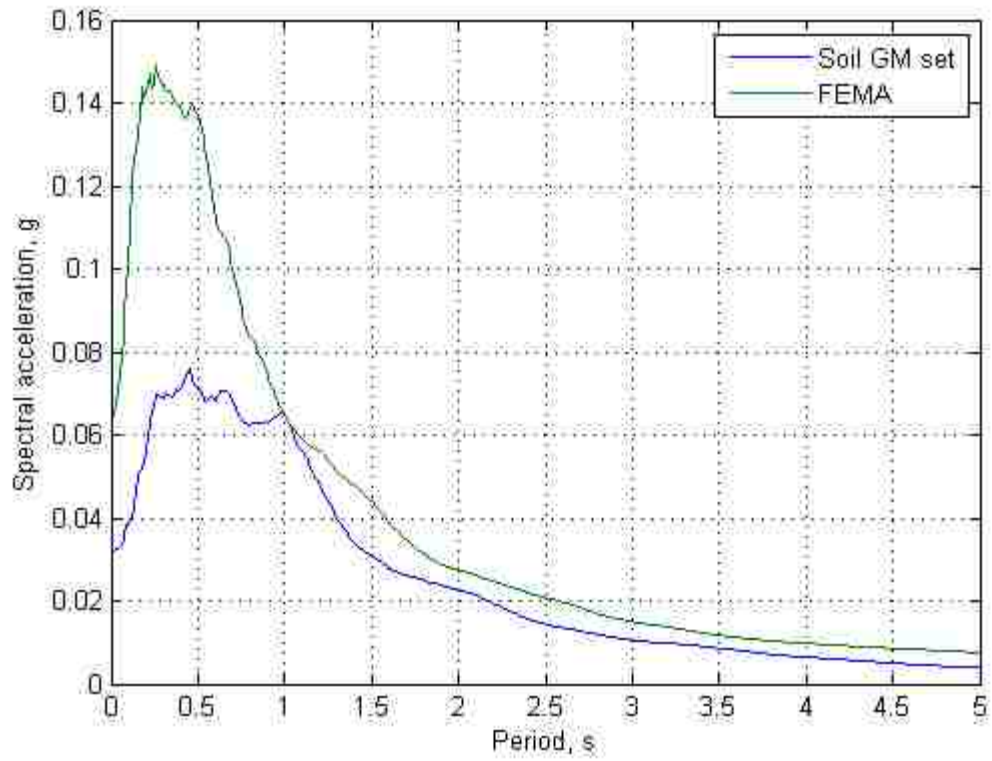


Figure 5.19 Comparison of the median response spectra for Soil GM set and FEMA GM set when scaled to the same $S_a(T=1s)$

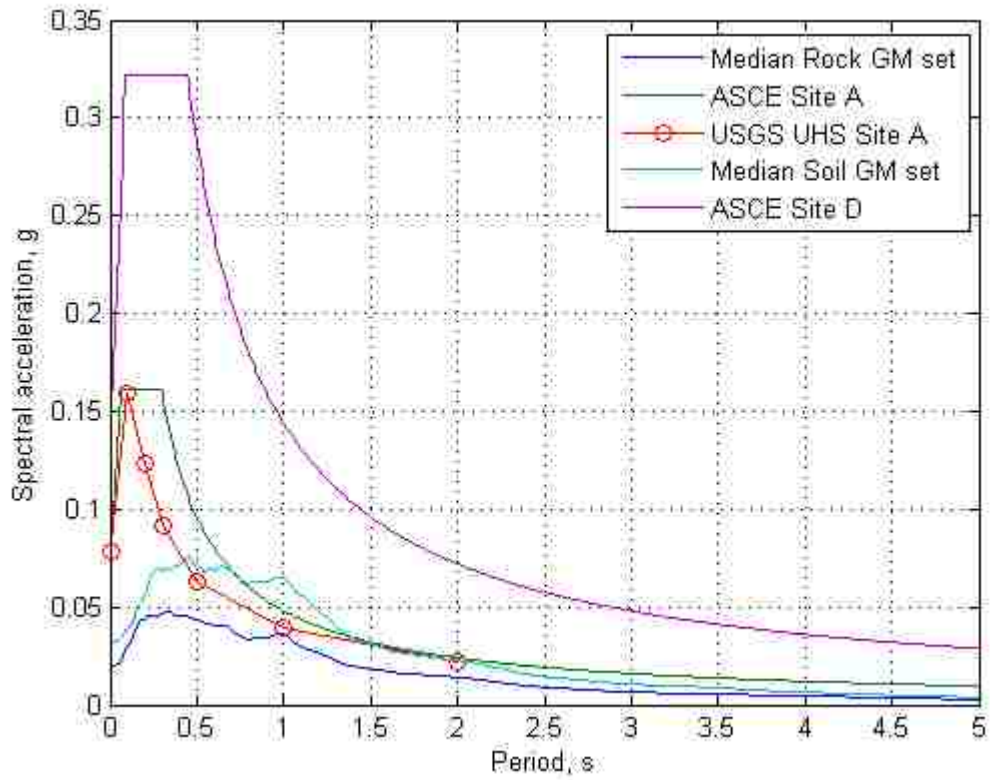


Figure 5.20 Comparison of Rock GM set median spectrum, Rock GM set median spectrum, ASCE7 MCE (rock, Site Class A and soil, Site Class D) spectra and USGS UHS

Chapter 6

Uncertainty in collapse performance assessment of ECUS low-ductility

CBF

6.1 Introduction

This chapter introduces the various sources of uncertainty associated with the collapse performance assessment of ECUS low-ductility CBFs. First, it introduces the background information on the FEMA P695 methodology for evaluating collapse performance. Next, concerns are raised about how the uncertainties are addressed in the FEMA P695 methodology, which assigns predefined dispersion values to develop a fragility function without explicitly quantifying uncertainties in the collapse assessment. In order to examine the validity of this approach for collapse performance assessment of ECUS low-ductility CBFs as well as to conduct performance evaluation in a more complete probabilistic manner, the various sources of uncertainty affecting collapse of ECUS low ductility CBF were categorized and identified. Different strategies were proposed to assess the impact of different categories of uncertainty. The categories of uncertainty considered in this study are compared with those in FEMA P695 and their corresponding relationship is explored to facilitate examination of the validity of the FEMA P695 approach in addressing the uncertainty associated with the collapse performance assessment of ECUS low-ductility CBFs.

6.2 Background and critique of FEMA P695 collapse performance assessment methodology

With a methodology to address various sources of uncertainties, FEMA P695 provides a standard procedure to quantify the collapse potential of a structural system type instead of an individual structure. While FEMA P695 claims to be intended to apply broadly to all buildings, it also realizes that this objective may not be fully achieved for certain seismic environments and building configurations (FEMA 2009). Therefore, it can serve as a valuable reference, but not necessarily with exact compliance, to assess the collapse performance of the ECUS low-ductility CBF.

The first step of FEMA methodology is to design a set of archetype buildings that are representative of the design variation expected from the building code design provision for the structural system type. The archetype buildings should cover a range of structural features and design parameters such as building height, structural configuration, level of gravity load, design ground motion intensity, etc. Then, those archetype buildings are assembled into different “performance groups” depending on the change of major structural features. An example of performance group and archetype buildings are shown in Table 6.1.

The second step is to develop a numerical model for subsequent nonlinear time history analysis. The numerical model needs to include the nonlinear behavior of the archetype buildings under seismic loading, particularly the various mechanism for strength and stiffness deterioration, which are important contributors to structural collapse. Test data is

needed to calibrate the numerical model so that the model can predict the nonlinear structural response with accuracy.

The third step is to evaluate the collapse capacity of each building structure using Incremental Dynamic Analysis (IDA) developed by Vamvatsikos and Cornell (2002). An individual IDA involves performing nonlinear time history analysis at the structure for a ground motion that is scaled to increasing intensity levels until the structure reaches incipient collapse. For an individual IDA, a curve of a structural response quantity, termed an “engineering demand parameter” (EDP, e.g. max story drift) versus ground motion intensity (e.g. $Sa(T_1)$), denoted as an IDA curve. The incipient collapse may be determined as the point where the slope of an IDA curve reduces to less than 20% of the initial slope or the point where the max story drift exceeds 10% (Vamvatsikos and Cornell 2004).

The collapse capacity of a structure is usually quantified by the $Sa(T_1)$ of the ground motion that causes the incipient collapse. As ground motions are inherently random, as shown in Chapter 5, each ground motion with the same $Sa(T_1)$ does not cause the same seismic response for a nonlinear multi-degree-of-freedom (MDOF) structure. In other words, the $Sa(T_1)$ value for each ground motion to cause incipient of collapse of a nonlinear structure may vary, which is called record-to-record (RTR) variability. Therefore, a set of IDA using a set of ground motions is necessary to address the RTR variability in the collapse capacity. In FEMA P695 methodology, the set of 44 ground motions described in Section 5.2.1 is used for a set of IDA to account for RTR variability. Figure 6.1 presents an example of IDA using the FEMA ground motion set where the criterion for incipient collapse is story drift exceeding 10%.

The last step is to generate a collapse fragility curve and quantify the collapse performance by calculating the Collapse Margin Ratio (CMR). The collapse fragility curve describes the probability of collapse at a given ground motion intensity (e.g. $Sa(T_1)$). The fragility function underlying the fragility curve provides the probability of the ground motion intensity Sa exceeding the collapse capacity S_{CT} (Eq. (6.1)). The actual collapse capacity is uncertain and is assumed to follow a lognormal distribution. Therefore, the fragility function is usually expressed as a lognormal cumulative distribution function (CDF) defined by 2 parameters: the median collapse capacity \hat{S}_{CT} and the total dispersion β_{TOT} (Eq. (6.2)). In the FEMA P695 methodology, the median collapse capacity is obtained from the IDA using the set of 44 ground motions. The dispersion value β_{TOT} , however, is not obtained from the IDA but is obtained by aggregating 4 predefined β value. Each β value represents the uncertainty from a specific source, as shown in Eq.(6.3).

$$P_{collapse} = P(Sa > S_{CT}) \quad (6.1)$$

$$P(Sa > S_{CT}) = \Phi\left(\frac{\ln(Sa/\hat{S}_{CT})}{\beta_{TOT}}\right) \quad (6.2)$$

$$\beta_{TOT} = \sqrt{\beta_{RTR}^2 + \beta_{DR}^2 + \beta_{TD}^2 + \beta_{MDL}^2} \quad (6.3)$$

β_{RTR} : record to record variability

β_{MDL} : modeling uncertainty

β_{DR} : design requirement uncertainty

β_{TD} : test data uncertainty

As shown by Eq. (6.3), the 4 categories of uncertainty considered are: RTR variability, modeling uncertainty, design requirement uncertainty, and test data uncertainty. The RTR variability is determined by Eq. (6.4) with an upper bound of 0.4, where μ_T is related to the inelastic deformation capacity of the structure. β for the other 3 sources of uncertainty are determined from a subjective quality rating scheme as follows: (A) Superior, $\beta = 0.1$; (B) Good, $\beta = 0.2$; (C) Fair, $\beta = 0.35$; and (D) Poor, $\beta = 0.5$. The judgment criteria for the quality rating scheme are in FEMA P695 (FEMA 2009). Therefore, the collapse fragility curve generated according to the FEMA P695 methodology is not the same as would be obtained as fitting the lognormal CDF to the collapse data from the IDA (Figure 6.2).

$$\beta_{RTR} = 0.1 + 0.1\mu_T \leq 0.4 \quad (6.4)$$

With the fragility curves developed, the probability of collapse of an archetype building under any ground motion intensity level can be calculated. The FEMA P695 methodology defines a satisfactory collapse performance as less than 20% of collapse probability for an individual archetype building and 10% for a set of archetype buildings (performance group) under the MCE ground motion intensity S_{MT} . To conveniently assess the collapse performance, the collapse margin ratio (CMR), defined as the ratio of median collapse capacity \hat{S}_{CT} and the MCE ground motion intensity S_{MT} (Eq.(6.5)), is calculated. To consider the spectral shape effect, a spectral shape factor (SSF) is applied to the CMR to obtain the adjusted collapse margin ratio (ACMR) (Eq.(6.6)).

$$CMR = \hat{S}_{CT}/S_{MT} \quad (6.5)$$

$$ACMR = SSF \times CMR \quad (6.6)$$

Acceptable collapse margin ratios corresponding to a 10% (ACMR10) and a 20% (ACMR20) probability of collapse under various values of dispersion value are tabulated in FEMA P695 (FEMA 2009). The ACMR for the individual archetype building and the mean ACMR for a performance group is compared with the ACMR20 value and ACMR10 value respectively. Satisfactory collapse performance for the structural system type is obtained if ACMR for all individual archetypes is greater than ACMR20 and the mean ACMR is greater than ACMR10. An example performance evaluation is given in Table 6.2.

As can be seen from the FEMA P695 methodology discussed above, while the median collapse capacity is determined from the IDA, the characterization of various sources of uncertainty is not an explicit consideration in the IDA. Rather, uncertainty is treated by assigning default β values in the fragility function. The following concerns about the application of FEMA P695 methodology to the collapse performance assessment of ECUS low-ductility CBF have been identified:

1. β_{RTR} is based on Eq. (6.4) instead of using the variability of the collapse capacities obtained from the IDA using the 44 ground motions (the computed β_{RTR}). Eq. (6.4) is an empirical formula developed from the computed β_{RTR} from IDA of a number of WUS RC MRFs using the FEMA GM set. However, in evaluating the collapse performance of ECUS low-ductility CBFs, the GM set developed for the ECUS in Chapter 5 is utilized. The east coast GM set has different characteristics than the FEMA GM set. In addition, ECUS low-ductility CBFs have different seismic

behavior than WUS RC MRF. Therefore, it is questionable whether Eq. (6.4) gives appropriate characterization of the RTR variability of low-ductility CBF using the ECUS GM set.

2. The uncertainty related to the numerical model used in the IDA is not addressed in a comprehensive probabilistic manner. Instead, three β values (β_{MDL} , β_{DR} and β_{TD}) address this uncertainty in the fragility function. These β values are determined using a subjective rating scheme and are not quantitatively verified in the FEMA P695 document (FEMA 2009) or other supporting documents. For example, there is uncertainty related to the input parameters of the numerical models. However, this uncertainty is not explicitly considered and propagated through the IDA. A numerical model with median values for the input model parameters is used in the IDA, assuming it produces median response. The dispersion of the response is addressed by the selected β values. Since ECUS low-ductility CBFs do not have a clear failure hierarchy, their failure modes may be more sensitive to the value of the input model parameters. Using the median model and selected β values may not accurately represent the variability of the collapse capacity.

Therefore, the impact of various sources of uncertainty on the collapse performance of ECUS low-ductility CBFs was studied and the accuracy of using the FEMA P695 methodology to address these uncertainties was examined.

6.3 Uncertainty considered in this study

Figure 6.3 describes the types of uncertainty considered in this study. The uncertainties are broken into different types based on their nature and how their impact can be explicitly

evaluated. This classification of uncertainty is different from the categories in FEMA P695 (FEMA 2009). The reason, as will be mentioned in the next section, is because each category of uncertainty in FEMA P695 combines 2 different types of uncertainty (from Figure 6.8) that will be evaluated by different methods in this study.

Collapse assessment is a comparison of seismic demand and structural capacity. The uncertainty in seismic demand includes RTR variability due to different seismic sources, propagating paths and local site effects etc. for the ground motions that the structure is likely to experience. The uncertainty in the structural capacity of the structural system type comes from 2 sources. First, there is variation in how a given structure is designed among all the possibilities within a given structural system type. Structures with different design features and characteristics will have different structural capacity. Second, even if the design of a given structure is fully known, there is uncertainty in the seismic response (and thereby the collapse capacity) of the given structure as its response is simulated by a numerical model. This uncertainty is called structural response modeling uncertainty or simply structural response uncertainty. The cause of this uncertainty is two-folded. On one hand, the value of the input parameters to the numerical model are uncertain, which reflects variability in the physical properties and behavior of a structure. On the other hand, every modeling approach is based on assumptions and has limitations in capturing the actual structural response. Therefore, the modeling uncertainty can be further differentiated into uncertainty in model parameters and uncertainty of the modeling approach.

6.3.1 Uncertainty in seismic demand

Seismic demand of a ground motion is the response of the structure (usually quantified by an EDP) to that ground motion at a given (hazard) intensity measure (e.g. $Sa(T_1)$). For a nonlinear MDOF structure, the $Sa(T_1)$ alone does not determine the structural response. For example, spectral contents at periods other than T_1 also affects the structural response due to the elongation of effective period when nonlinearity happens as well as higher mode response. Therefore, ground motions with the same intensity measure but different other characteristics may cause different structural response. Uncertainty in seismic demand reflects the variability on the various characteristics of ground motions that the structure is likely to experience in the future seismic events. As a result of the uncertainty in seismic demand, the collapse capacities for the same structure under different earthquakes are different, leading to RTR variability (Figure 6.1).

In this study, uncertainty in seismic demand is addressed by subjecting the structure to the ECUS GM set developed in Chapter 5 for IDA and calculating RTR variability. The ECUS GM set considers the underlying reason for variability of ground motion characteristics which is the uncertainty on seismic sources, propagating path, local soil effect etc. (Boore 2003). The RTR variability is computed as the log standard deviation of the collapse capacity Sa_c for all the ground motions of the set using Eq. (6.7) and (6.8), where $N = 44$ is the total number of ground motions and i is the index for each ground motion. The collapse capacity is quantified as the $Sa(1s)$ value of the ground motion to cause collapse. The reason to choose $Sa(1s)$ as the intensity measure because the ECUS GM set is developed according to the seismic hazard deaggregation at $T = 1s$. Therefore, the spectral

shape effect is addressed at $T = 1s$. The hazard intensity is also defined at $T = 1s$ for future evaluation purpose.

$$\mu_{\ln Sa} = \frac{1}{N} \sum_{i=1}^N \ln Sa_c^{(i)} \quad (6.7)$$

$$\sigma_{\ln(Sa_c)} = \sqrt{\sum_{i=1}^N \frac{(\ln Sa_c^{(i)} - \mu_{\ln Sa})^2}{N - 1}} \quad (6.8)$$

It should be noted that in the IDA of this study, the ground motions are scaled using the “Sa component scaling method” mentioned in Appendix A of FEMA P695 (FEMA 2009). In the component scaling method, the ground motions are scaled individually so that each ground motion has precisely the target intensity measure when applied in each analysis of the IDA (Figure 6.4 (a)&(b)). In this way, the ground motion intensity of each collapse data point in the IDA can be directly used to calculate β_{RTR} . It should also be noticed that the empirical formula FEMA uses to determine the β_{RTR} (Eq. (6.4)) is also based on IDA results using the “Sa component scaling method” (FEMA 2009).

The “Sa component scaling method” is in contrast with the PGV scaling method used by FEMA P695 to determine the median collapse capacity. In the PGV scaling method, all the ground motions are first normalized to have the same PGV (Peak Ground Velocity) and then scaled up collectively using a common scale factor in IDA (Figure 6.4 (c)&(d)). The median spectrum of the ground motion set is used as the intensity measure for each individual ground motion in plotting the IDA curves. The median collapse capacity is considered as the median spectrum intensity of the GM set at which half of the ground

motions in the set cause collapse. However, the result from IDA using this scaling method cannot be used directly to determine the RTR variability since the intensity of the collapse point in each IDA curve is not the intensity of each ground motion. Besides, there is inconsistency within the way FEMA P695 calculates the median collapse capacity using the IDA results from PGV scaling method. This is discussed in detail in Chapter 7. Hence, this study chooses “Sa component scaling method” in IDA to investigate RTR.

6.3.2 Variation in structural design

Variation in structural design is due to the different practices of engineers when applying the building code to design buildings, as well as the different architectural requirement constraints within the building stock. An example of design variation due to engineering practice is the additional strength an engineer may provide in the brace-to-gusset connection compared to the code-required strength. An example of design variation due to different architecture requirements is using the chevron or X bracing configuration. ECUS low-ductility CBFs have larger design variation than WUS SCBFs because the exemption of seismic detailing permits more variation.

Table 6.3 provides a partial list of possible design for ECUS low-ductility CBFs. This study focuses on the first 3 items of Table 6.3, as they are identified as key design variables from reviewing existing CBF designs as summarized in Chapter 4. The design variation is studied by creating archetype buildings with different values for the key design variables and investigating the collapse performance of each building. Each key design variable takes 2 possible values representing the variation identified in Chapter 4. The brace configuration varies between chevron and split-X. The beam strength can be either strong or weak

relative to the unbalanced brace force demand from the braces. The brace-to-gusset weld connection can be either strong or weak depending on the additional strength, relative to the required strength, provided by the engineer. Therefore, the 8 design variants of the prototype building described in Chapter 4 (Table 4.13) are utilized as the archetype buildings. In reference to the FEMA methodology, the 8 archetype buildings are divided into 2 performance groups (Table 6.4) depending on the bracing configuration.

6.3.3 Uncertainty in model parameters

Uncertainty in input model parameters of a numerical model reflects both (1) the variability of the properties of a structure characterized by model parameters and (2) the uncertainty in the structural behavior characterized by phenomenological parameters. An example of the variability of a structural property is the material yield strength of the steel column in a ECUS low-ductility CBF. If the column is made from A992 material with a nominal yield strength $F_y = 50ksi$, the actual yield strength of the material is uncertain, which can be reflected by uncertainty in the material yield strength model parameter in the numerical model. An example of the uncertainty in the structural behavior is the initiation of low cycle fatigue (LCF) fracture of the braces in a low-ductility CBF. LCF of a brace is modeled using a phenomenological model in OpenSees, as described Section 4.4.1. and the uncertainty of the brace LCF life can be reflected by the uncertainty of the controlling model parameter ϵ_0 .

Table 6.5 provides a partial list of model parameters with uncertainty which are categorized by the structural components of the CBF system. The uncertainty for these parameters encompass both aleatory and epistemic uncertainty. For example, the brace yield strength

$F_{y_{br}}$ exhibits aleatory uncertainty due to the random nature of steel material properties. The parameters for the hysteretic behavior for Beam-to-Column (BC) connection, based on empirical formulas, exhibit epistemic uncertainty due to lack of knowledge. It can be seen that there are numerous model parameters with uncertainty. It is impractical to consider all the uncertain model parameters, even from a research perspective. Since the braces are the main source of lateral force resistance in the CBF system, this study focuses on the uncertainty of the parameters related to the braces and brace connections in this study. Specifically, the 5 uncertain parameters for the braces and brace connections listed in Table 6.5 are considered in this study. As the brace and its connection weld to the gusset plate is in series, whether or not the weld will fracture is influenced by the relative and actual strength of the brace and the connection (Figure 6.5). In addition to the brace weld connection strength R_c itself, the initial imperfection e/L and yield strength $F_{y_{br}}$ of the brace will also affect the probability of the fracture of the brace connection. This is because a smaller initial imperfection of the brace than the code specified value or by a larger yield strength $F_{y_{br}}$ than the nominal yield strength will result in overstrength of the brace capacity and allow larger force to be developed in the brace during the seismic response. Brace connection fracture is a failure mode unique to low-ductility CBFs. Previous experiments reviewed in Chapter 2 show it has a significant influence on the failure hierarchy (sequence and types of yielding and failure modes) of the structure. For example, the second story in the test specimen of Sizemore et al. (2015) did not have weld fracture and subsequently developed brace LCF (Figure 2.3(c)) while the first story had weld fracture and subsequently developed brace re-engagement and “long link EBF” (Figure 2.5). The ε_0 value determines when the brace will fracture due to LCF. Fracture of the

brace will result in a significant loss of lateral force resistance of the structure and could lead to collapse. Brace reengagement may provide a secondary source of lateral force resistance after the brace connection fracture. The strength of brace re-engagement F_{re} (Figure 4.19(b)) will influence how much this secondary force transfer mechanism contributes to collapse prevention.

The probability distributions of the above 5 uncertain model parameters are listed in Table 6.6. Fisher et al. (1978) found fillet strength of the weld material follows a lognormal distribution with a median value of 1.45 times the nominal strength and a coefficient of variation (c.o.v.) of 0.11. However, the actual strength of a fillet weld connection depends on the weld quality and quality of fit between parts, even if the actual material strength is known. The evidence for the effect of weld and fit quality is provided by Figure 6.6 which shows the profiles of 2 brace-to-gusset plate fillet connections specimens from the tests of Sizemore et al. (2015). The weld in Figure 6.6(b) has an uneven gap at each side of the gusset plate due to weld and fit quality. The strength of this weld will be significantly different from the one in Figure 6.6(a) which has a fairly even gap. Therefore, the weld connection strength R_c is assumed to follow a lognormal distribution with a median value of $1.45R_n$, where R_n is the nominal strength of the weld given by the AISC design formula (Eq. 4.4). To consider the larger dispersion of the actual weld strength due to weld and fit quality, the c.o.v. of R_c is increased to 0.3.

The ε_0 parameter that controls the fatigue strength of the brace material is assumed to follow a lognormal distribution. The median value is determined by Eq. (4.9), an empirical formula developed from calibration against test results (Karamanci and Lignos 2014). The

log standard deviation of ε_0 is 0.249 which is the prediction uncertainty obtained from the regression analysis. The re-engagement strength of the brace connection F_{re} is assumed to follow a uniform distribution between $0.16P_y$ and $0.38P_y$ which are the lower and upper bounds of the brace re-engagement strength found in the tests by Davaran et al. (2014). The initial out of straightness of the braces e/L is assumed to be lognormally distributed. The literature indicates variation of the magnitude of the initial out-of-straightness of an HSS member. Bjorhovde and Birkemoe (1979) found that the average out-of-straightness of HSS section to be in the order of 1/6000. However, Goggins and Salawdeh (2013) found the out-of-straightness to be around 1/500 for the HSS braces in a full-scale single-story CBF specimen. Therefore, it is decided to use 1/1500, which has been used in developing the AISC column compressive strength formula (Bjorhovde 1988), as the median value of e/L . The c.o.v. of the e/L is assumed to be 0.3. The actual yield strength of the HSS brace material (A500 Gr. B) $F_{y_{br}}$ is assumed to follow a normal distribution with a mean of $1.3F_y$ and a C.O.V. of 0.08 (Liu et al. 2007).

The model parameter uncertainty was studied by sensitivity analysis and by Monte Carlo Simulation (MCS). The sensitivity study was conducted by systematically perturbing each of the 5 model parameters individually in the numerical model to study the effect of the perturbation on the collapse performance. The sensitivity study shows the influence of an individual parameter on the collapse capacity of the ECUS low-ductility CBF and establishes the relative importance of the parameters. However, the sensitivity study does not show the interaction between multiple uncertain parameters. Nor does it show the overall impact of model parameter uncertainty on the collapse performance. Therefore,

MCS is used to generate sample models where the 5 uncertain model parameters are random variables following the distributions described above. IDA are performed on each sample model propagate the uncertainty and show its effect. The results from IDA on all sample models are combined and analyzed to quantify the effect of model parameter uncertainty. Figure 6.7 illustrate the MCS procedure, which is discussed further in Chapter 7.

6.3.4 Uncertainty of the modeling approach

Uncertainty of the modeling approach reflects uncertainty about the capability of the numerical model to predict the seismic response and collapse capacity, due to assumption and limitation of the model. The numerical model response is an uncertain representation of the actual seismic response of the structure. An example is the uncertain effect of using a 2-D model to study the seismic response of a building. The true seismic response of the building, even under unidirectional earthquake, will differ from the 2-D model result because of omission of the possible accidental torsional response. Bradley (2013) states that, ideally, this type of uncertainty should be quantified by systematic validation of a numerical seismic response model against observational data from sub-system or system-level tests. However, the scarcity of test data at the system level makes it challenging to quantify this uncertainty. Another way to address modeling approach uncertainty is to use multiple modeling approaches, similar to the logic tree approach (Kulkarni et al. 1984) commonly employed in the probabilistic seismic hazard analysis (PSHA). In PSHA, multiple ground motion prediction models are used, since each model has certain limitation and it is uncertain which model (if any) accurately represents the true hazard. Different weights are assigned to different models reflecting confidence in the model. Similar to

sampling uncertain parameters, here we are sampling uncertain modeling approaches. However, there is controversy on how to combine the results from different models with weights (Marzocchi et al. 2015). Therefore, this study uses a logic tree approach in a qualitative way, to compare the collapse capacity of the same structure using different modeling approaches and study differences in the seismic response. Instead of quantifying the dispersion of the collapse capacity due to the modeling approach, this study focuses on aspects of the modeling approach that influence the collapse of the structure.

The following 3 aspects of modeling approach uncertainty are investigated:

- Using fiber section or Concentrated Plastic Hinge (CPH) approach to model beam nonlinearity
- Including or not including brace re-engagement model
- Different models for the gravity load system

As mentioned in Chapter 4, two alternative way to model for the beam are: (1) using a fiber section in the beam, which includes M-P interaction but does not capture strength deterioration; and (2) CPH method which captures strength deterioration but not M-P interaction. The effect of choosing one of these 2 modeling approaches on collapse capacity of the structure was studied. The brace re-engagement model was developed from the tests result by Sizemore et al. (2015) and Davaran et al. (2014). Whether this model represents the typical low-ductility CBF response is uncertain. It is also uncertain whether brace re-engagement always happen. Therefore, the seismic response and collapse capacity of the model with and without modeling brace re-engagement effect was studied. The gravity load system is usually considered to have no lateral resistance in the design stage and in

many seismic analysis applications. In reality, the gravity load system provides lateral resistance to some extent (Elkady and Lignos 2015). The 4 different ways of modeling the gravity load system mentioned in section 4.4.2 are investigated to study the effect of modeling gravity system on the collapse capacity of low-ductility CBF systems.

6.4 Comparison with uncertainty considered in the FEMA P695 methodology

The FEMA P695 methodology addresses uncertainty is by selecting β values from tabulated predefined values based on quality ratings. Hence, the possibility of explicitly considering the uncertainty identified in section 6.3 is studied, first by understanding the uncertainty represented by each β in the FEMA P695 methodology and how it relates to the uncertainties described in section 6.3. The categories of uncertainties considered in the FEMA P695 methodology and the current study (section 6.3) are listed in Table 6.7. It is found that only the RTR variability in the FEMA P695 methodology and the current study share the same meaning. The other 3 types of uncertainties in the FEMA P695 methodology and the current study are related but do not correspond to each other. Their relationship is demonstrated in Figure 6.1. As can be seen, each of the other 3 types of uncertainty considered in this study has overlap with 2 types of uncertainty considered in the FEMA P695 methodology. In the following sections, each of the other 3 types of uncertainty in the FEMA P695 methodology is in relation to the uncertainty considered in this study.

6.4.1 Modeling Uncertainty

The uncertainty to be included in the collapse fragility function is the uncertainty of the collapse capacity Sa of a structure of the target structural system type based on the collapse

analysis of one or more numerical models. The various β factors mentioned earlier (Eq. (6.3)) represent the dispersion of the collapse capacity Sa . It is important to understand that the FEMA P695 methodology (FEMA 2009) is a method that uses numerical analysis on a finite number of numerical models of the archetype buildings, called index archetype model (IAM), to evaluate the collapse performance of all buildings with the type of structural system being studied. Therefore, the modeling (MDL) uncertainty represented by β_{MDL} , according to the definition in FEMA P695 document (FEMA 2009), contains the following 2 aspects

- How well the IAMs represent the collapse response or the accuracy of model prediction.
- How well the IAMs cover the full range of the expected design space.

The first aspect can be illustrated as shown by Figure 6.9. In this illustration (and the following illustrations), the collapse capacity Sa is shown as a probability density function based on the predicted collapse capacity Sa (i.e., predicted from IAMs). IAMs that capture important failure modes will predict actual collapse capacity Sa with less uncertainty. Therefore, the distribution of the collapse capacity Sa will have a smaller variation with respect to the predicted collapse capacity Sa , and is indicated by a smaller β_{MDL} (Figure 6.9 (b)). On the contrary, IAMs that fail to capture the important failure modes predict the collapse capacity with greater uncertainty (Figure 6.9 (b)). Therefore, a larger β_{MDL} is assigned. This aspect of MDL uncertainty is related to the modeling approach (MA) uncertainty considered in this study which accounts for the accuracy of the modeling approach.

The second aspect of MDL uncertainty is illustrated by Figure 6.10. Since the FEMA P695 methodology is trying to cover the entire design space for a structural system, it needs to address the variation of potential designs not represented by the limited number of IAMs that are analyzed. Using an extreme example, if only one IAM is used to represent the entire design space, the collapse capacity Sa for any building in the design space will have a large variation with respect to the predicted collapse capacity Sa for the IAM (Figure 6.10 (a)), leading to and is indicated by a larger β_{MDL} . If more IAMs, each intended to represent a part of the design space, are used to represent the entire design space, then the predicted collapse capacity Sa from each IAM, which represents possible designs only in only part of the design space will have a smaller variation (Figure 6.10 (b)).

6.4.2 Test Data Uncertainty

According to the FEMA P695 document, test data is needed to establish material properties, calibrate and validate component models, and confirm behavior so that the numerical model can predict the seismic response of structures with accuracy (FEMA 2009). Test data (TD) uncertainty in the collapse performance assessment is related to the quality and completeness of the test data. Test data uncertainty is related to model parameter uncertainty (MP) and modeling approach uncertainty (MA) in the following ways: 1. Good quality test data, usually at the component level (Bradley 2013), can produce accurate estimates of the value of the input model parameters, which will lead to less uncertainty in the collapse capacity (Figure 6.11 (a)); a smaller value of β_{TD} can be used. If good quality test data is not used to determine model parameters, the uncertainty in these parameters is larger and the uncertainty in the collapse capacity is larger (Figure 6.11 (b)); a larger value of β_{TD} should be used. This aspect of test data uncertainty is related to the epistemic

uncertainty in the model parameters (MP) considered in the current study (i.e., due to lack of knowledge). 2. Good quality test data, usually at the system level (Bradley 2013), will lead to a more accurate modeling approaches that are able to predict the collapse capacity S_a with less uncertainty. This aspect of TD uncertainty is related to the modeling approach (MA) uncertainty in a similar way as MDL uncertainty.

6.4.3 Design Requirements Uncertainty

Design requirements (DR) uncertainty is uncertainty whether the sequence of limit states of the structure under severe seismic loading, and the resulting strength, ductility, and energy dissipation will be as intended to provide safety to the structure and its occupants. Poor design requirements less reliability against unintended or undesirable limit states and do not ensure that yielding or other ductile limit states will occur, so that non-ductile failure modes may occur (FEMA 2009). A structure designed with poor design requirements will exhibit unanticipated limit states and failure modes that may not be included in the numerical model. Therefore, a larger β_{DR} should be assigned to the collapse capacity S_a predicted from numerical analysis.

The difference between the intended limit states (those that produce acceptable strength, ductility, and energy dissipation) and the actual limit states and failure modes are due to variations of the design properties (section sizes, connection strength, etc.) and variation in material properties, workmanship, etc., that are permitted by design requirements and specifications, but can lead to undesirable limit states. These variations are related to design variation (DV) and uncertainty in model parameters (MP) considered in this study, respectively. For example, in a CBF design, the braces are intended to carry to the lateral

forces. But fracture of a brace connection before brace buckling or yielding will result in the structure response different from the intended behavior. The fracture of a brace connection is controlled by the actual connection strength versus the actual brace compressive/tensile strength, both of which follow a probability distribution around their median strength due to the uncertainty of various structural property and material properties. In addition, the median strength of the braces and connections are determined from the design process, which also affects the probability of connection fracture. In designing an R=3 CBF, the brace connection is not required to be made stronger than the associated brace by “capacity design”. The as-designed strength of the connection may be close to the as-designed compression strength of the brace. Therefore, there is considerable probability that the brace connection will fracture which is not the intended limit state and leads to unanticipated behavior (Figure 6.12 (a)); a large β_{DR} should be used. In comparison, in designing SCBF, the connection is required to be designed for the expected strength of the brace (i.e., by “capacity design”). The as-designed strength of the connection is, therefore, much higher than the as-designed brace strength, and the probability of brace connection fracture is very small. The structure will be more likely to have the intended behavior (Figure 6.12 (b)); small β_{DR} should be used.

It should be noted that both DR uncertainty and MDL uncertainty are related to uncertainty due to design variation (DV). But they use 2 different metrics to describe the amount of design variation represented by one design, as illustrated by Figure 6.13. For a smaller DR uncertainty, the design variation (represented by one IAM) is reduced by more prescriptive design requirements and thereby shrinking the entire design space. For a smaller MDL

uncertainty, the design variation is reduced by dividing the design space into smaller design subspaces and using more IAMs to represent each design subspace.

Table 6.1 Example of archetype buildings and performance groups (FEMA 2009)

Archetype ID	No. of Stories	Key Archetype Design Parameters						$S_{SR}(T)$ [g]
		Framing (Gravity Loads)	Seismic Design Criteria					
			SDC	R	T [sec]	T_1 [sec]	V/W [g]	
Performance Group No. PG-5 (Short Period, 20' Bay Width Configuration)								
2069	1	P	D_{max}	8	0.26	0.71	0.125	1.50
2064	2	P	D_{max}	8	0.45	0.66	0.125	1.50
--	3	P	D_{max}	8	0.63	--	0.119	1.43
Performance Group No. PG-6 (Long Period, 20' Bay Width Configuration)								
1003	4	P	D_{max}	8	0.81	1.12	0.092	1.11
1011	8	P	D_{max}	8	1.49	1.71	0.050	0.60
5013	12	P	D_{max}	8	2.13	2.01	0.035	0.42
5020	20	P	D_{max}	8	3.36	2.63	0.022	0.27
Performance Group No. PG-1 (Short Period, 20' Bay Width Configuration)								
2061	1	S	D_{max}	8	0.26	0.42	0.125	1.50
1001	2	S	D_{max}	8	0.45	0.63	0.125	1.50
--	3	S	D_{max}	8	0.63	--	0.119	1.43
Performance Group No. PG-3 (Long Period, 20' Bay Width Configuration)								
1008	4	S	D_{max}	8	0.81	0.94	0.092	1.11
1012	8	S	D_{max}	8	1.49	1.80	0.050	0.60
5014	12	S	D_{max}	8	2.13	2.14	0.035	0.42
5021	20	S	D_{max}	8	3.36	2.36	0.022	0.27
Selected Archetypes - Performance Group Nos. PG-4 and PG-8 (20' Bay Width)								
6011	8	P	D_{min}	8	1.60	3.00	0.013	0.15
6013	12	P	D_{min}	8	2.28	3.35	0.010	0.10
6020	20	P	D_{min}	8	3.60	4.08	0.010	0.065
6021	20	S	D_{min}	8	3.60	4.03	0.010	0.065
Selected Archetypes - Performance Group Nos. PG-10 and PG-14 (30' Bay Width)								
1009	4	P-30	D_{max}	8	1.03	1.16	0.092	1.03
1010	4	S-30	D_{max}	8	1.03	0.86	0.092	1.03

Table 6.2 Example of performance evaluation for archetype buildings and performance groups (FEMA 2009)

Arch. ID	Design Configuration			Computed Overstrength and Collapse Margin Parameters					Acceptance Check	
	No. of Stories	Framing (Gravity Loads)	SDC	Static Ω	CMR	μ_T	SSF	ACMR	Accept ACMR	Pass/Fail
Performance Group No. PG-5 (Short Period, 20' Bay Width Configuration)										
2069	1	P	D_{max}	1.6	1.18	14.0	1.33	1.57	1.52	Pass
2064	2	P	D_{max}	1.8	1.50	19.6	1.33	2.00	1.52	Pass
--	3	P	D_{max}	1.7*	--	--	--	2.13*	--	--
Mean of Performance Group:				1.7*	1.34	16.8	1.33	1.90*	1.90	Pass
Performance Group No. PG-6 (Long Period, 20' Bay Width Configuration)										
1003	4	P	D_{max}	1.6	1.61	10.9	1.41	2.27	1.52	Pass
1011	8	P	D_{max}	1.6	1.25	9.8	1.61	2.01	1.52	Pass
5013	12	P	D_{max}	1.7	1.22	7.4	1.58	1.93	1.52	Pass
5020	20	P	D_{max}	2.6	0.82	4.1	1.40	1.15	1.52	Fail
Mean of Performance Group:				1.9	1.23	8.1	1.50	1.84	1.90	Fail
Performance Group No. PG-1 (Short Period, 20' Bay Width Configuration)										
2061	1	S	D_{max}	4.0	1.96	16.1	1.33	2.61	1.52	Pass
1001	2	S	D_{max}	3.5	2.06	14.0	1.33	2.74	1.52	Pass
--	3	S	D_{max}	3.1 ¹	--	--	--	2.63*	--	--
Mean of Performance Group:				3.5 ¹	2.01	15.0	1.33	2.66*	1.90	Pass
Performance Group No. PG-3 (Long Period, 20' Bay Width Configuration)										
1008	4	S	D_{max}	2.7	1.78	11.3	1.41	2.51	1.52	Pass
1012	8	S	D_{max}	2.3	1.63	7.5	1.58	2.58	1.52	Pass
5014	12	S	D_{max}	2.8	1.59	8.6	1.61	2.56	1.52	Pass
5021	20	S	D_{max}	3.5	1.25	4.4	1.42	1.78	1.52	Pass
Mean of Performance Group:				2.8	1.56	8.0	1.51	2.36	1.90	Pass
Selected Archetypes - Performance Group Nos. PG-4 and PG-8 (20' Bay Width)										
6011	8	P	D_{min}	1.8	2.12	3.0	1.21	2.56	1.52	Pass
6013	12	P	D_{min}	1.8	2.00	3.7	1.24	2.47	1.52	Pass
6020	20	P	D_{min}	1.8	1.73	2.8	1.20	2.08	1.52	Pass
6021	20	S	D_{min}	3.4	3.70	3.3	1.22	4.51	1.52	Pass
Selected Archetypes - Performance Group Nos. PG-10 and PG-14 (30' Bay Width)										
1009	4	P-30	D_{max}	1.6	1.98	13.4	1.41	2.79	1.52	Pass
1010	4	S-30	D_{max}	3.3	2.50	13.2	1.41	3.53	1.52	Pass

Table 6.3 Partial list of variation in structural design of low-ductility CBF

1	<i>Brace configuration</i>
2	<i>Beam design strength</i>
3	<i>Brace connection weld design strength</i>
4	Type of brace connection
5	Type of brace section
6	Beam in gravity system: composite or non-composite
7	Column splice location
8	Building fundamental period in seismic design: T_a or $C_u T_a$
9	Number of stories (building height)

Table 6.4 Archetype designs and performance groups in this study

Archetype ID	Bracing configuration	Beam relative strength	Weld relative strength
Performance Group No. PG-1 (chevron braced frame)			
C1	Chevron	Strong	Weak
C2	Chevron	Strong	Strong
C3	Chevron	Weak	Weak
C4	Chevron	Weak	Strong
Performance Group No. PG-2 (split-X braced frame)			
X1	Split-X	Strong	Weak
X2	Split-X	Strong	Strong
X3	Split-X	Weak	Weak
X4	Split-X	Weak	Strong

Table 6.5 Partial list of model parameters with uncertainty

Parameter	Physical meaning or structural behavior represented	Illustration
<u>Brace and brace connection:</u>		
R_c	Brace weld connection strength	Figure 4.19(a)
ε_0	Brace Low Cycle Fatigue (LCF) life	Eq. (4.28)
F_{re}	Brace re-engagement strength	Figure 4.19(b)
e/L	Brace (relative) initial imperfection	Figure 4.18
$F_{y_{br}}$	Brace yield strength	
<u>Beam, column and BC connection in the lateral system:</u>		
$F_{y_{col}}$	Column yield strength	
$M_y, M_c, \theta_p, \theta_{pc}, \Lambda^1$	Flexural hysteretic behavior for plastic hinge	Figure 4.23 & Lignos and Krawinkler (2011)
$k, M_y, M_c, \theta_p, \theta_{pc}, M_r$	Flexural hysteretic behavior for BC connection with gusset plate	Figure 4.25(a)
<u>Column and BC connection in the gravity system:</u>		
$F_{y_{col}}$	Column yield strength	
$M_s, M_{max}, M_r, \theta_s, \theta_{m1}, \theta_{m2}, \theta_{drop}$	Flexural hysteretic behavior for BC connection with composite slab	Figure 4.27(a)
<u>System level property:</u>		
D, L	Gravity (dead and live load)	
W	Mass (seismic weight)	
ζ	Damping ratio	
Note: 1. Λ is a parameter controlling the rate for between-cycle strength and stiffness deterioration. See Lignos and Krawinkler (2011).		

Table 6.6 Summary of statistical distribution of uncertain model parameters considered in this study

Uncertain model parameter	Physical meaning	Probability distribution	Defining parameters	Reference
R_c	Brace weld connection strength	Lognormal	Median: $1.45R_n$ c.o.v.: 0.3	Fisher et al. (1978)
ε_0	Brace Low Cycle Fatigue (LCF) Strength	Lognormal	Median: Eq. (4.28) c.o.v.: 0.249	Karamanci and Lignos (2014)
F_{re}	Brace re-engagement strength	Uniform	Upper bound: $0.38P_y$ Lower bound: $0.16P_y$	Davaran et al. (2014)
e/L	Brace initial imperfection	Lognormal	Median: 1/1500 c.o.v.: 0.3	Bjorhovde and Birkemoe (1979) Goggins and Salawdeh (2013)
$F_{y_{br}}$	Brace yield strength	Normal	Mean: $1.3F_y$ c.o.v.: 0.08	Liu et al. (2007)
<p>Notes;</p> <ol style="list-style-type: none"> 1. R_n is the nominal strength of fillet weld connection calculated by Eq. (4.4); 2. P_y is the nominal yield strength of brace section; 3. F_y is the nominal yield strength of brace material. 				

Table 6.7 Summary of types of uncertainty considered in FEMA P695 and current study

FEMA P695	Current Study
Record to Record (RTR) Variability	Record to Record (RTR) Variability
Uncertainty in Test Data (TD)	Uncertainty in Model Parameters (MP)
Uncertainty in Modeling (MDL)	Uncertainty due to Modeling Approach (MA)
Uncertainty in Design Requirements (DR)	Design Variation (DV)

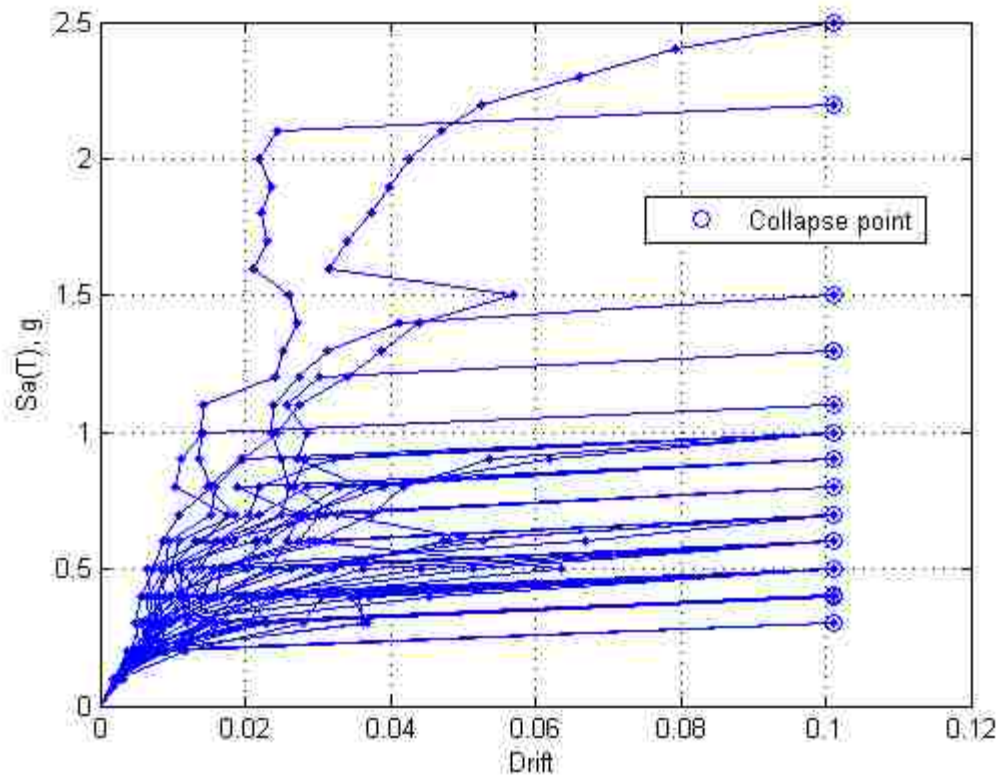


Figure 6.1 Illustration of Incremental Dynamic Analyses (IDA)

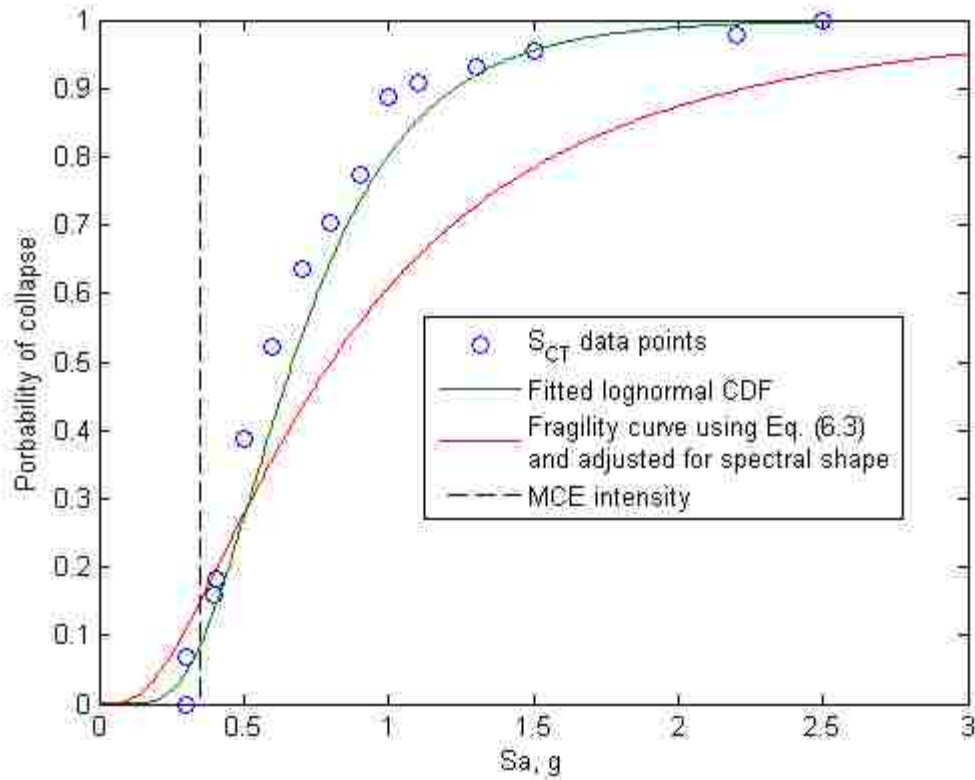


Figure 6.2 Fragility curve generated according to FEMA P695 methodology and fitted lognormal CDF to collapse data points directly obtained from IDA

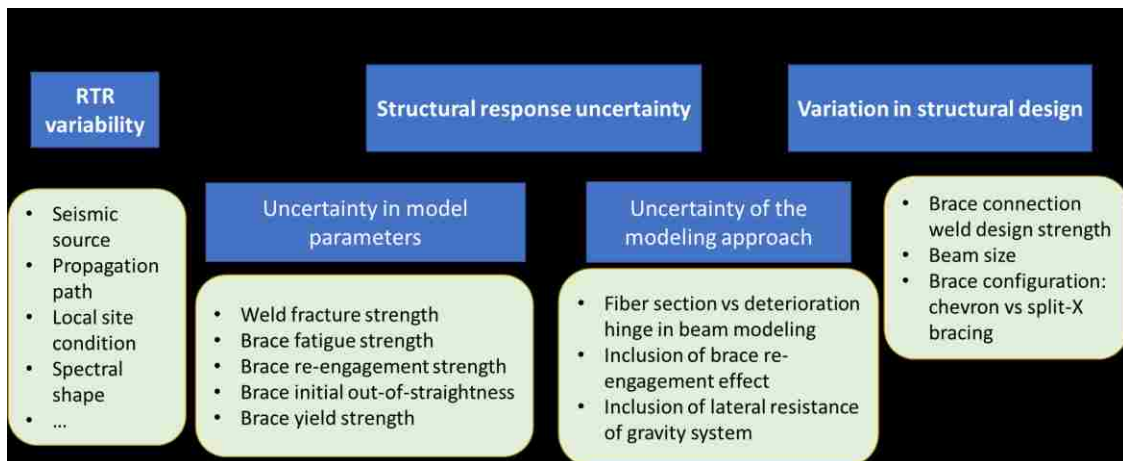


Figure 6.3 Summary of categories of uncertainty considered in this study

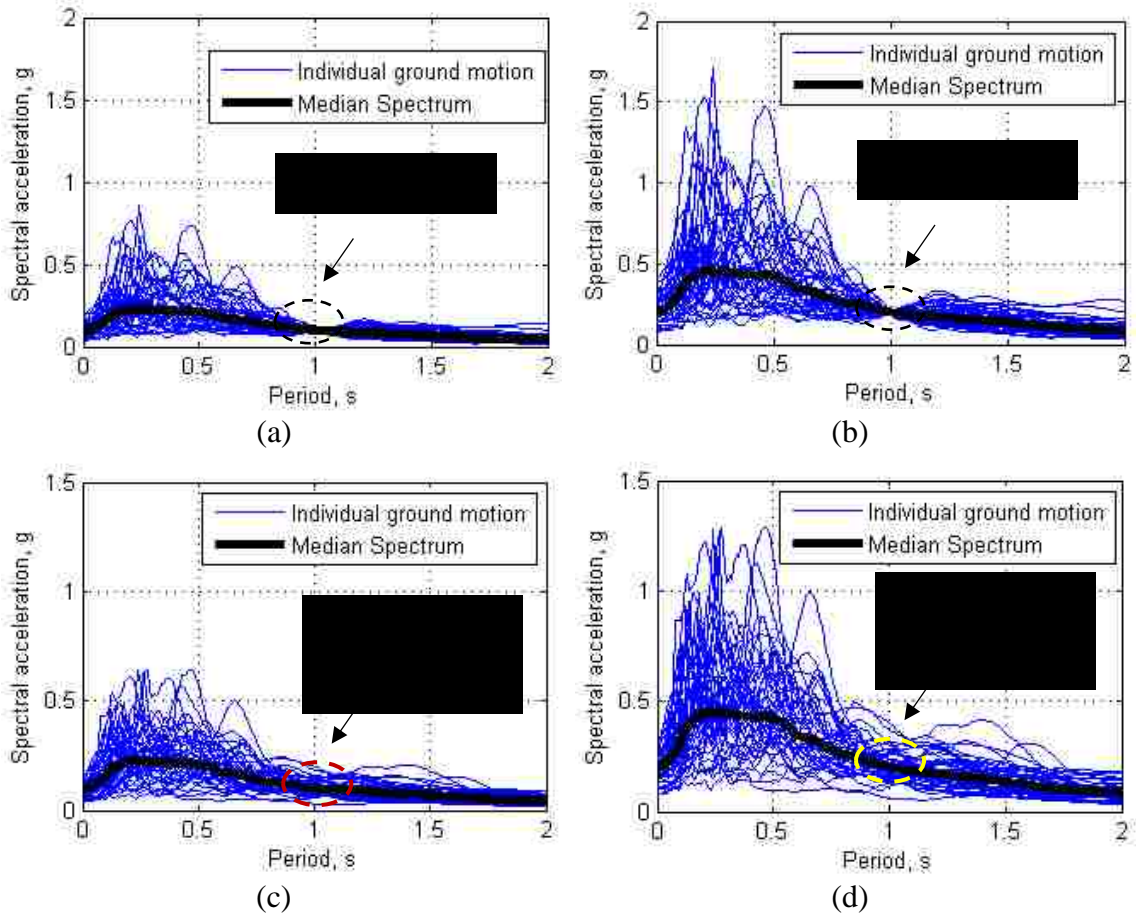


Figure 6.4 Different scaling methods for IDA shown with FEMA GM set: (a) and (b) “Sa component scaling method” scaled to 0.1g and 0.2g for $Sa(1s)$; (c) and (d) PGV scaling method scaled to 0.1g and 0.2g for $Sa(1s)$

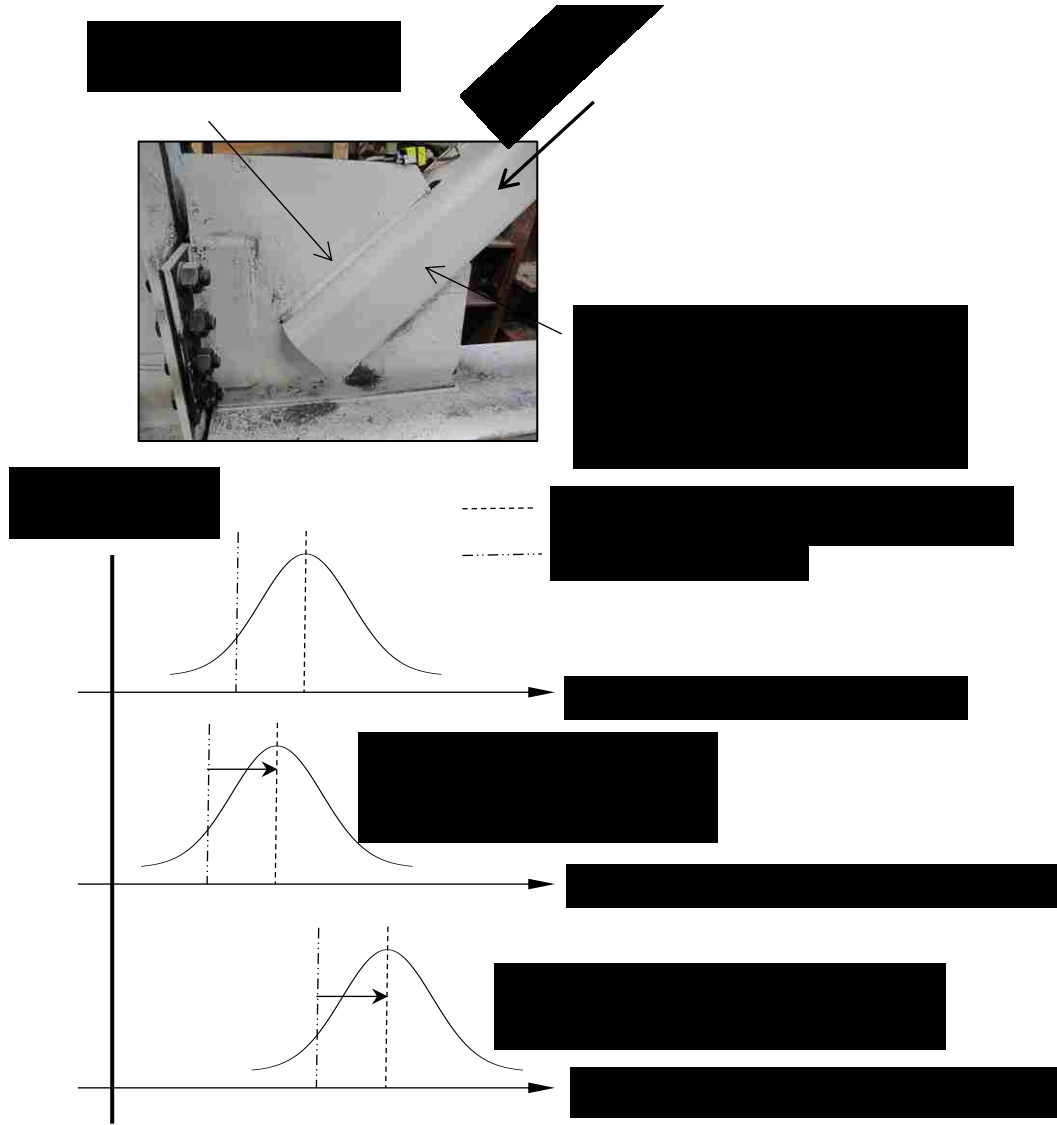


Figure 6.5 Illustration of relative strength between brace and connection with uncertainty

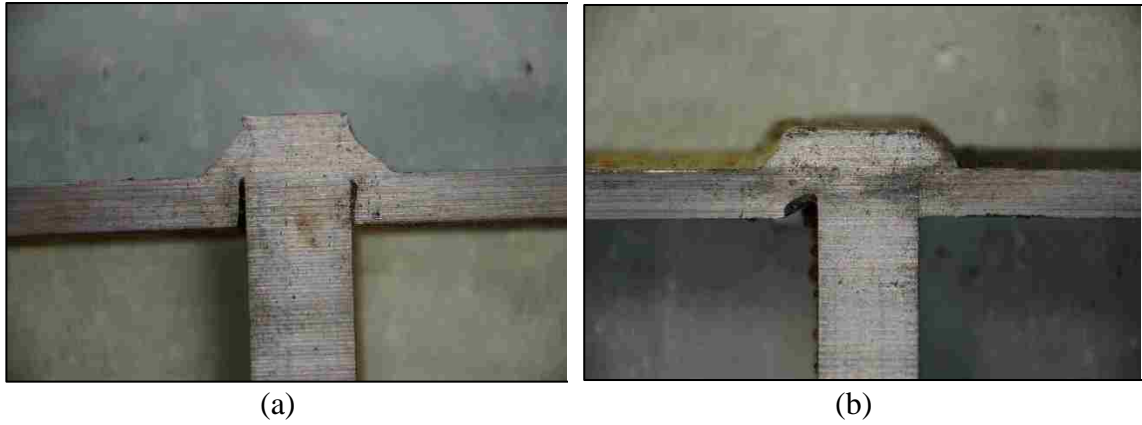


Figure 6.6 Brace-to-gusset plate fillet weld specimens from tests by Sizemore et al. (2015): (a) with equal gap; (b) with unequal gap

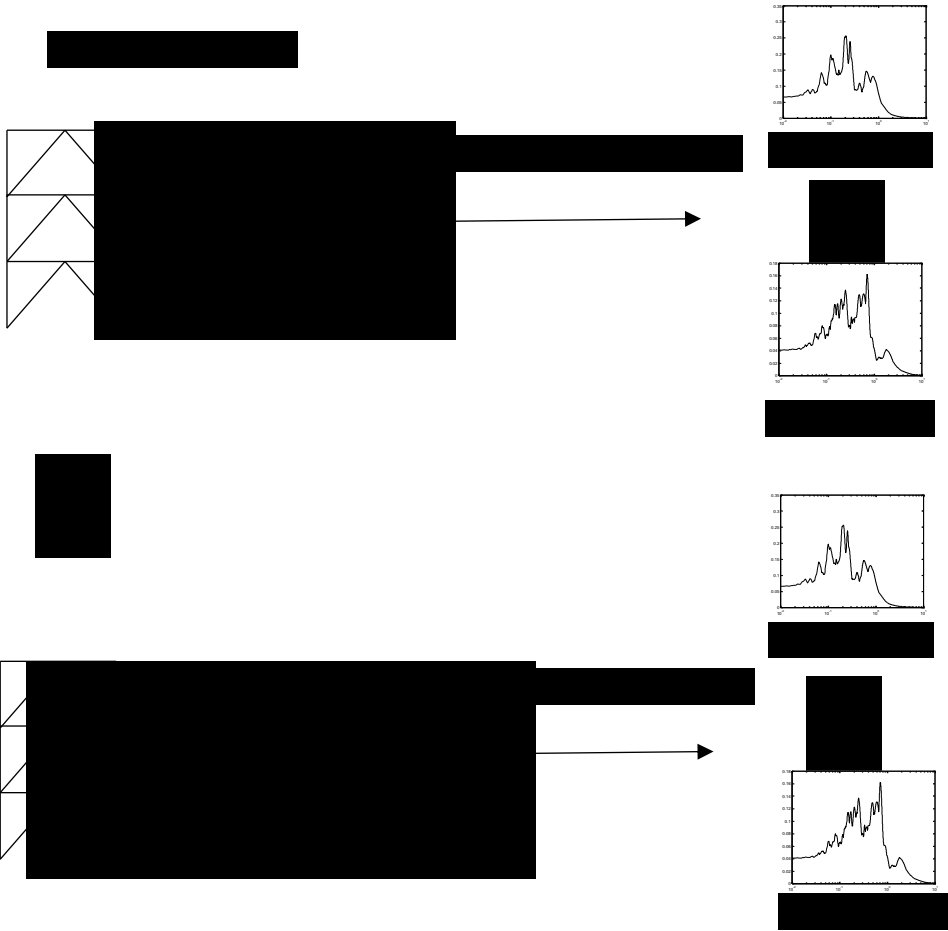


Figure 6.7 Monte Carlo Simulation procedure to study model parameter uncertainty

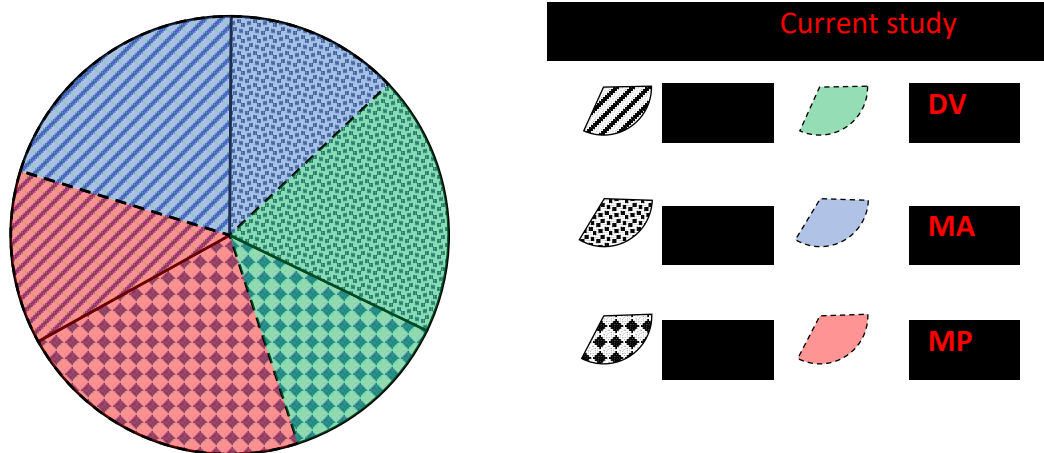


Figure 6.8 Schematic showing uncertainty (except for RTR variability) considered in FEMA P695 and current study

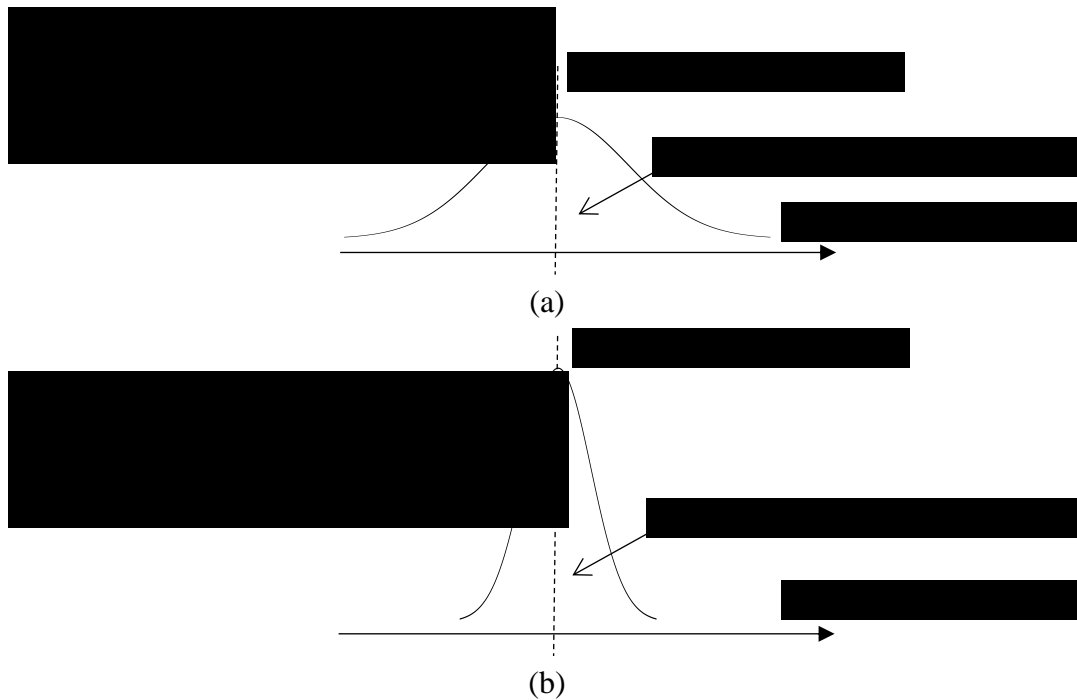


Figure 6.9 Schematic illustration of modeling uncertainty: (a) model not capturing important limit states leading to larger modeling uncertainty; (b) model capturing important limit states leading to smaller modeling uncertainty

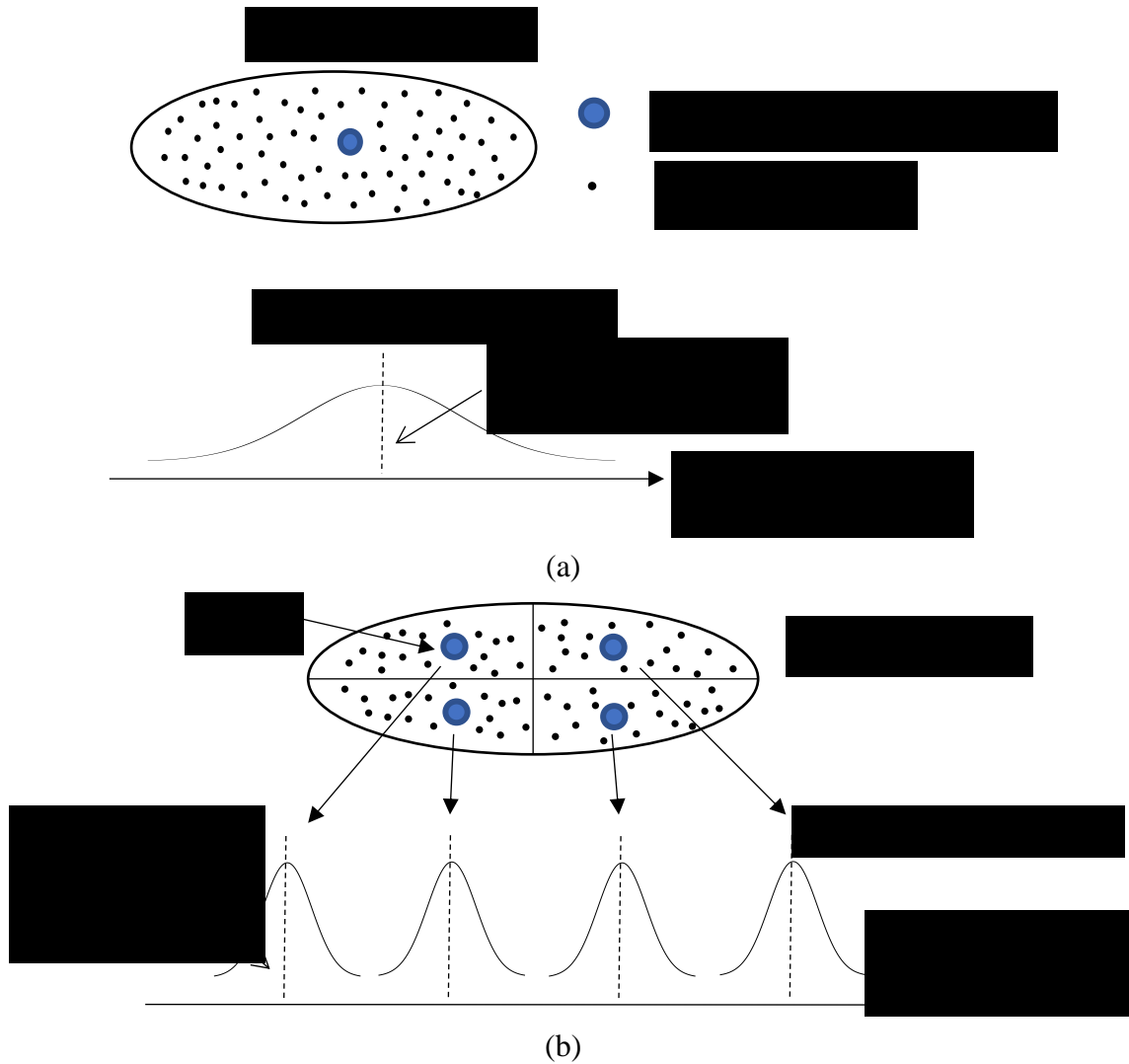


Figure 6.10 Schematic illustration of modeling uncertainty from design variation: (a) using one IAM to cover entire design space, leading to a larger modeling uncertainty; (b) using multiple IAMs to cover the entire design space, leading to a smaller modeling uncertainty

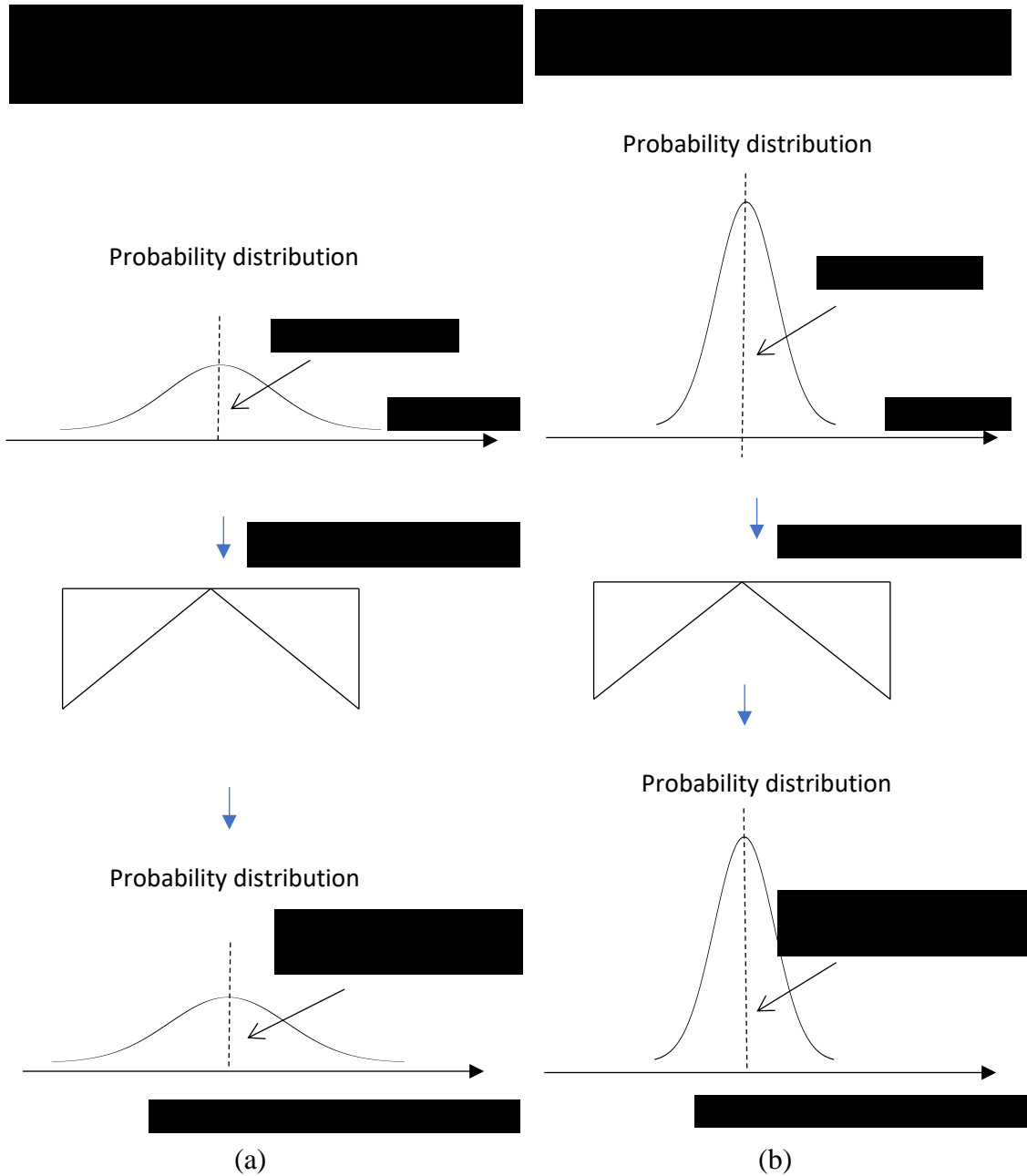


Figure 6.11 Schematic illustration of relation of test data uncertainty to model parameter uncertainty: (a) larger uncertainty for model parameters without test data; (b) smaller uncertainty for input model parameters with calibration with good quality test data

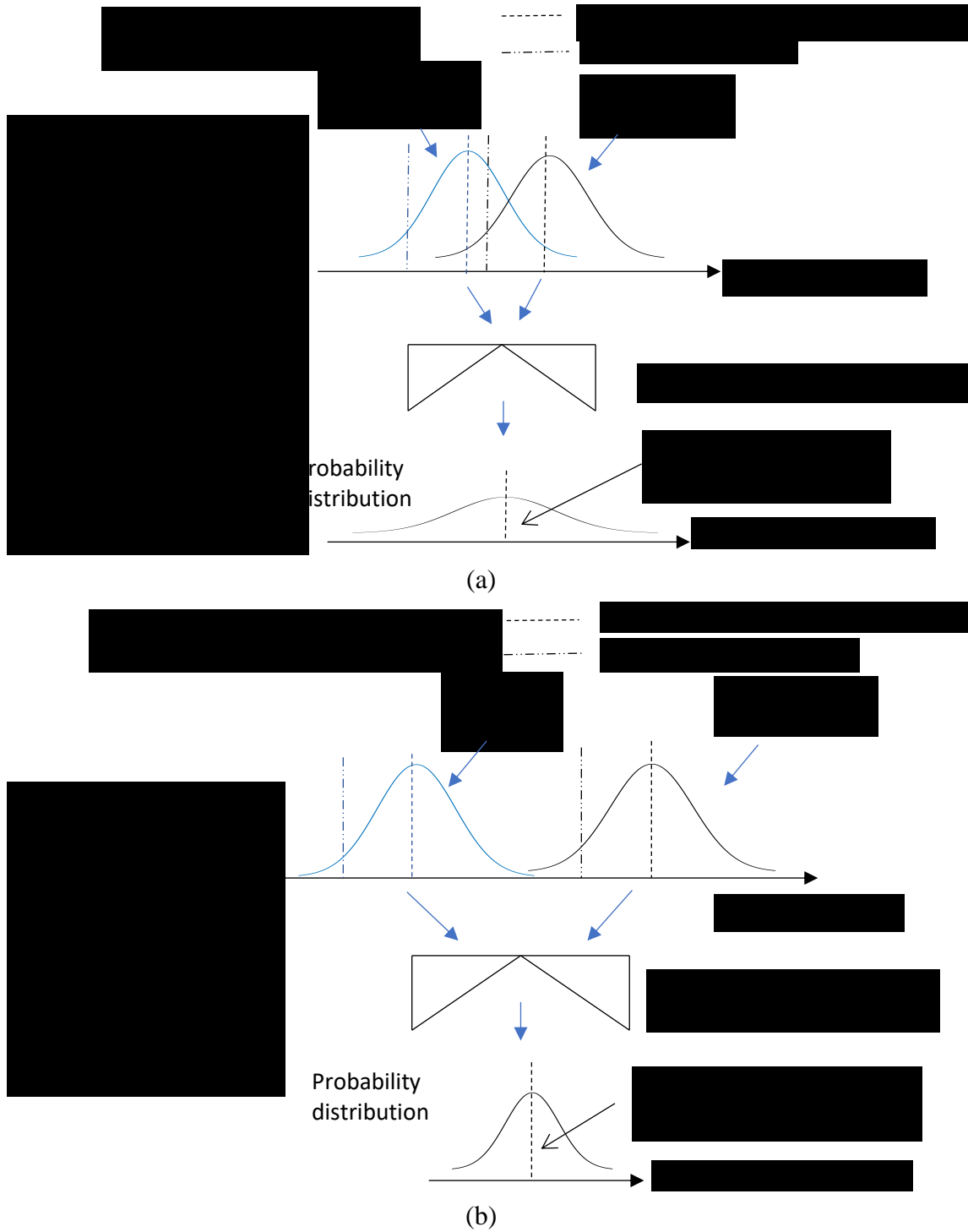


Figure 6.12 Schematic illustration of design requirement uncertainty for brace and connection design: (a) low-ductility CBF with poor design requirements, leading to uncertain limit state sequence and unintended behavior from higher design requirement uncertainty; (b) SCBF with good design requirements, leading to controlled limit states and lower design requirement uncertainty.

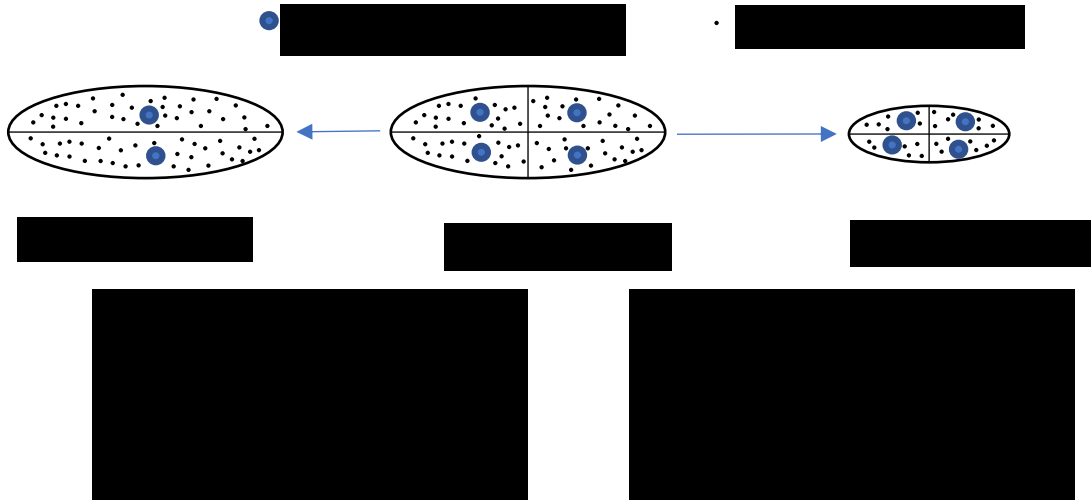


Figure 6.13 Schematic illustration of the relation of design variation (DV) to MDL uncertainty and DR uncertainty

Chapter 7

Assessment of collapse performance of ECUS low-ductility CBFs

7.1 Introduction

This chapter presents an assessment of the collapse performance of ECUS low-ductility CBFs and investigates how the collapse performance is influenced by various sources of uncertainty identified in Chapter 6. In parallel, the application of FEMA P695 methodology (FEMA 2009) for evaluating the collapse performance of low-ductility CBFs is examined and necessary modifications are proposed. First, a collapse performance evaluation which follows the FEMA P695 methodology is presented. The effect of design variation is explored. Some on the behavior of low-ductility CBFs from pushover analysis is presented. In addition, a critique of the method used in the FEMA P695 methodology to determine the median collapse capacity is made. Next, an evaluation of the collapse performance using the ECUS GM set developed in Chapter 5 is given, which addresses the effect of uncertainty in seismic demand. The formula from the FEMA P695 methodology to calculate the SSF and RTR variability are examined regarding the applicability to ECUS low-ductility CBF. Then the modeling approach uncertainty is studied before the effect of model parameter uncertainty is explored by sensitivity analysis and Monte Carlo Simulation. The effects of various sources of uncertainty are summarized and compared. Finally, the collapse performance of the structure is evaluated using the FEMA P695 methodology with modifications.

7.2 Collapse performance evaluation using FEMA P695 methodology

IDA are performed on the 8 archetype models which are listed in Table 6.4 and represent design variation of the prototype building in Philadelphia. According to the FEMA P695 methodology (FEMA 2009), the ground motions in an IDA are scaled up by the “PGV scaling method” which scales up the ground motion set collectively after normalizing all the ground motions to the same PGV. The median spectrum of the ground motion set at $C_u T_a$, the approximate design period of the structure, $S_T(C_u T_a)$ is defined as the intensity measure for the IDA results. The median collapse capacity \hat{S}_{CT} is defined as the $S_T(C_u T_a)$ at which 22 of the 44 ground motions produce collapse. The results of the IDA are shown in Figure 7.2 from which the median collapse capacity \hat{S}_{CT} is determined. It should be noted that the robustness of the numerical models and nonlinear analyses is achieved by carefully conducting the analyses and eliminating the numerical convergence problems as they are encountered. According to the FEMA P695 methodology, the MCE intensity is obtained from the ASCE MCE spectrum as shown by Eq. (7.1). The CMR for each archetype model is calculated using Eq. (6.5) and is presented in Table 7.2.

$$S_{MT} = \frac{S_{M1}}{T} = \frac{S_{M1}}{C_u T_a} = 0.26g \quad (7.1)$$

To consider the spectral shape effect, the SSF is calculated according to the procedure in Appendix B in FEMA P695 and using empirical formulas (FEMA 2009) which relate the period elongation effect to the inelastic deformation capacity of the structure. The inelastic deformation capacity of the structure is characterized by the period-based ductility μ_T

determined from Eq. (7.2) and (7.3) and the results of the pushover analysis of each archetype model.

$$\delta_{y,eff} = C_0 \frac{V_{max}}{W} \left[\frac{g}{4\pi^2} \right] (\max(T, T_1))^2 \quad (7.2)$$

$$\mu_T = \delta_u / \delta_{y,eff} \quad (7.3)$$

In Eq. (7.2) and (7.3), C_0 is a coefficient relating the SDOF displacement to the roof displacement, computed according to ASCE/SEI 41-06 Section 3.3.3.3 (ASCE 2007); V_{max} is the maximum base shear determined from pushover analysis; W is the effective seismic weight of the structure; T is the approximate fundamental period from design which equals to $C_u T_a$; T_1 is the first mode period from eigenvalue analysis; $\delta_{y,eff}$ is the effective yield displacement; δ_u is defined as the roof displacement where the base shear is reduced to the 80% of V_{max} (Figure 7.1).

The results of pushover analysis of each archetype model are shown in Figure 7.3. It can be observed that the base shear decreases drastically after weld fracture or brace buckling. Even though there is some recovery in base shear due to, for example brace re-engagement, the base shear in most cases never reaches 80% of V_{max} again. In this situation, according to the 80% base shear reduction rule, δ_u is determined as the displacement where V_{max} is reached, since the base shear drops to less than 80% and does not recover to above 80% of V_{max} again. As a result, δ_u is only slightly larger than $\delta_{y,eff}$. This leads to a small μ_T and, in turn, a very small SSF of only 1.03 or 1.04 (Table 7.1). As the ECUS low-ductility CBF behaves in a very different way than the idealized pushover curve assumed by FEMA (Figure 7.1), section 7.3.1 presents a study of whether the SSF procedure in the FEMA

P695 methodology is applicable to ECUS low-ductility CBFs. The SSF is multiplied with the CMR to obtain the adjusted CMR (ACMR) for each archetype model. The results are shown in Table 7.2.

According to the FEMA P695 methodology (FEMA 2009), the RTR variability β_{RTR} is determined from an empirical formula (Eq. (6.6)). The result is shown in inTable 7.3.

The β value for other sources of uncertainty are determined according to quality rating scheme in the FEMA P695 document (FEMA 2009). Using this scheme, the design requirements are rated as poor ($\beta_{DR} = 0.5$), because the low-ductility CBF design does not provide adequate safeguard against undesirable failure modes nor does it ensure an appropriate sequence of limit states. The test data quality ($\beta_{TD} = 0.5$) is also rated as poor, since there is very limited experimental data for low-ductility CBF at either the component level or the system level. The modeling quality is rated as fair ($\beta_{MDL} = 0.35$). Although significant progress has been made in modeling the limit states of low-ductility CBFs (e.g. weld fracture, brace re-engagement, beam local buckling), there are complicated types of behaviors for low-ductility CBFs that may be important contributors to collapse but are not modeled. For example, strength deterioration and low cycle fatigue of the fillet weld of the brace connection has been observed during the experiment by Sizemore et al. (2015)m but this behavior is not included in the current model. Therefore, the model may underestimate the probability of weld fracture and affect the evaluation of collapse performance. The above rating result and assignment of β value is considered to be the reasonable, and was selected for the collapse assessment. However, the rating process is inevitably subjective. Other possible quality ratings and β values are also listed in Table 7.4. The total collapse

capacity uncertainty is obtained by the SRSS rule using Eq. (6.3). The corresponding ACMR10 and ACMR20 are given in Table 7.4.

To evaluate the collapse performance for ECUS low-ductility CBFs using the FEMA P695 methodology, the ACMR for each archetype model and the average ACMR for the performance group are compared with ACMR10 and ACMR20 in Table 7.5. It can be observed that for each archetype model, the ACMR is larger than ACMR20 but smaller than ACMR10. The average ACMR of each of the two performance groups is also smaller than ACMR10. Therefore, the probability of collapse under the MCE intensity for each archetype model is between 10% and 20%. According to the acceptance criteria in the FEMA P695 methodology (FEMA 2009), each individual archetype needs to have ACMR larger than ACMR20 meaning less than 20% probability of collapse under the MCE, and the average ACMR of a performance group need to be larger than ACMR10, indicating less than 10% probability of collapse under the MCE. Therefore, the ECUS low-ductility CBF system does not provide acceptable collapse performance according to the FEMA P695 methodology.

7.2.1 Insight into pushover response of ECUS low-ductility CBFs with design variation

The results of the pushover analyses are examined to provide some insight about the response of low-ductility CBFs and how the response is affected by design variation. This study provides some understanding of the seismic response. To help explain the limit states during the pushover responses, the braces and the associated welds are given a notation according to their location (Figure 7.4). This notation is used throughout the rest of the

dissertation. As mentioned earlier, weld fracture is modeled at only one end of the brace, as shown by the notation in Figure 7.4.

Figure 7.5 shows the base shear vs. roof drift for model C1 (weak weld and strong beam) from pushover analysis. The response is divided into different stages which are separated by important limit states. The sequence of stages up to collapse and the corresponding limit states are illustrated in Figure 7.6. The structure behaves elastically until Weld 1-2 of the compression brace fractures (stage I). Despite having the same strength, the compressive brace weld fractures first because the gravity load creates compression in both braces. After Weld 1-2 fractured, the lateral resistance of the structure drops significantly and recovers slowly as the gap between the brace edge and the gusset plate is closing (stage II). After the gap is closed, brace 1-2 becomes effective again to resist compressive force through re-engagement and after re-engagement (stage III), the base shear recovers rapidly. After the brace re-engagement produces local yielding at the re-engagement location of the connection, the recovery of base shear becomes slower with respect to the roof drift. With increasing drift, the force in the tension brace and weld increases and Weld 1-1 fractures. After Weld 1-1 fractures, a significant decrease in base shear occurs and the remaining lateral resistance becomes very small as there is no effective brace in this story (stage IV). Brace 1-2 will re-engage with the gusset plate again with increasing drift and lead to some recovery in the base shear (stage V). At this drift level, the P-delta effect from the gravity load becomes dominant and overcomes the lateral resistance from the CBF after brace re-engagement yielding. The base shear decreases with increasing drift leading to collapse.

Figure 7.7 and Figure 7.8 illustrate the pushover response of model C3 (weak weld and weak beam). The limit states are similar to those of model C1, including weld fracture in the compression brace and subsequent brace re-engagement. The differences arise from the difference in strength and stiffness of the beams. During stage II and III, the first floor beam is not strong enough to sustain the unbalanced force in the vertical direction from Brace 1-1 and 1-2. Therefore, the beam in model C3 undergoes larger downward deflection than the beam of model C1 and model C3 develops a plastic hinge in the beam at the chevron point. At the same drift level, the downward deflection of the beam relieves the force/deformation demand on the tension brace and weld. Therefore, the structure can sustain a larger lateral drift before Weld 1-1 fractures.

Figure 7.9 and Figure 7.10 illustrate the pushover response of model C2 (strong weld and strong beam). Compared with model C1 and model C3, Brace 1-2 is able to buckle because of stronger weld. After buckling, the system resists lateral force by post-buckling response of Brace 1-2 and tension force in Brace 1-1, leading to a recovery of the base shear (stage II). As the lateral drift increases, the tension force in Brace 1-1 increases while the post-buckling force in Brace 1-2 decreases, resulting in increasing unbalanced force in the vertical direction on the beam. The beam eventually yields and develops a plastic hinge. After yielding, the beam will deflect downward and relieves the deformation demand on Brace 1-1, reducing the tension force in Brace 1-1. The lateral resistance of the CBF is overcome by the P-delta effect from gravity load (stage III), and the base shear decreases with increasing drift. The slope of this decrease becomes steeper after the beam hinge suffers local buckling and strength deterioration.

Figure 7.11 and Figure 7.12 illustrate the pushover response of model X3, representing the behavior of a split-X CBF with a weak weld design. The difference between chevron CBF with weak welds and the split-X CBF with weak welds is that the tension brace weld will fracture immediately after the compression brace weld fractures in a split-X CBF, because the deformation of the beam is restrained by the braces in the adjacent story. After the compression brace weld (Weld 2-1) fractures, the beam is not able to deform freely and relieve the force demand on the tension brace and weld (Weld 2-2). Therefore, the tension brace weld (Weld 2-2) fractures immediately after the compression brace weld (Weld 2-1) fractures. In the chevron CBF, the beam has enough flexibility to relieve the demand on the tension brace and weld, preventing immediate fracture. As the split-X CBF (model X3) deforms laterally, the compression brace will re-engage. The slope of the base shear vs. roof drift becomes negative immediately after the brace re-engagement location yields locally, since there is no effective tension brace. This response is different than the response of the chevron CBF (Figure 7.7), where there is a considerable plateau of base shear during the compression brace re-engagement response due to the effective tension brace.

Figure 7.13 and Figure 7.14 illustrate the pushover response of model X4, representing the behavior of a split-X CBF with a strong weld design. This response is similar to the response of a chevron CBF upon the buckling of the first compression brace (Brace 1-2). The differences arise in the post-buckling stage. The braces in the second story sustain the vertical unbalanced force from the braces in the first story. Unlike chevron CBF (Figure 7.9), the beam does not yield and develop a plastic hinge or a large downward deflection. The force in Weld 1-1 increases and the weld eventually fractures. After Weld 1-1

fractures, the story has only a buckled brace to resist the lateral force. The resistance of the CBF is overcome by the P-delta effect from gravity, leading to collapse.

While the pushover analysis provides significant insight about the response of low-ductility CBFs with different designs, it does not fully represent their seismic response. It should be noted that in a pushover analysis, the lateral loading has a constant pattern. The important limit state of low cycle fatigue of the braces, which happens under dynamic response, is not exposed under static loading. Also, the constant lateral load pattern is not representative of the dynamic load pattern under seismic response. The dynamic response of low-ductility CBFs is examined in section 7.2.3 to explore the influence of design variation on collapse capacity.

7.2.2 Critique of FEMA P695 methodology to determine median collapse capacity

The FEMA P695 (FEMA 2009) normalizes the ground motions to have the same PGV and then scale all the ground motions by a common scale factor. The median spectral acceleration of the ground motion set $S_T(C_u T_a)$ is defined as the ground motion intensity and used in the IDA. The median collapse capacity \hat{S}_{CT} is defined as the $S_T(C_u T_a)$ at which 22 of the 44 ground motions have caused collapse. This method to calculate median collapse capacity is examined. Some drawback and inconsistency within the method itself is found.

First, the spectral acceleration $Sa(C_u T_a)$ for each individual ground motion when the GM set is scaled to $S_T(C_u T_a) = \hat{S}_{CT}$ is not the $Sa(C_u T_a)$ causing collapse for each ground motion. Taking the IDA results for model C3 for example (Figure 7.15), when the ground motion set is scaled to $S_T(C_u T_a) = 0.6g$, 22 of the 44 GMs have caused collapse.

According to the FEMA P695 methodology, the median collapse capacity $\hat{S}_{CT} = 0.6g$. Figure 7.16 shows the IDA result of model C3 under GM1 plotted using the median spectral acceleration of the ground motion set $S_T(C_uT_a)$ (blue curve using left y axis) and the spectral acceleration of the GM1 $Sa(C_uT_a)$ (red curve using right y axis). It can be seen that $Sa(C_uT_a)$ of GM1 when $S_T(C_uT_a) = 0.6g$ is 0.88g, which is less than the $Sa(C_uT_a)$ when GM1 produces collapse (1.17g).

Using results similar to those in Figure 7.16, the $Sa(C_uT_a)$ which determines the value of \hat{S}_{CT} in the FEMA P695 methodology is compared with the $Sa(C_uT_a)$ which results in collapse for each ground motion using the IDA results for model C3. The results are shown in Figure 7.17. It can be observed that for many ground motions, $Sa(C_uT_a)$ which determines \hat{S}_{CT} is significantly less than value of $Sa(C_uT_a)$ when the ground motion produces collapse, defined as $Sa_c(C_uT_a)$.

Hence, a definition of the median collapse capacity, based on $Sa_c(C_uT_a)$ from each ground motion is introduced. Considering $Sa_c(C_uT_a)$ as a random variable, the median collapse capacity is calculated as the geometric mean of $Sa_c(C_uT_a)$ for all the ground motions using Eq. (7.4), where $Sa_c(C_uT_a)^{(i)}$ is $Sa_c(C_uT_a)$ for ground motion i ; $N = 44$ is the total number of ground motions. $Sa_{c,m}(C_uT_a)$ is compared with \hat{S}_{CT} in Table 7.6. It can be seen that \hat{S}_{CT} from the FEMA P695 methodology is systematically smaller than $Sa_{c,m}(C_uT_a)$. For the rest of the dissertation, the median collapse capacity is $Sa_{c,m}$. It should be clarified that $Sa_{c,m}$ represents the generic concept median collapse capacity, which is not necessarily constrained to be calculated at a certain period such as C_uT_a as shown in Eq. (7.4).

$$Sa_{c,m}(C_u T_a) = \exp\left[\frac{1}{N} \sum_{i=1}^N \ln Sa_c(C_u T_a)^{(i)}\right] \quad (7.4)$$

Second, the RTR variability β_{RTR} in the fragility function in the FEMA P695 (FEMA 2009) methodology is computed as the dispersion of $Sa_c(C_u T_a)$ (for each individual ground motion) obtained using the “Sa component scaling method”. Thus, the FEMA P695 definition of the median collapse capacity is inconsistent with the definition of β_{RTR} . In the later sections of the dissertation, the RTR variability is calculated as $\sigma_{\ln(Sa_c)}$ using Eq. (6.7) and (6.8).

7.2.3 Effect of design variation on collapse performance

$Sa_{c,m}(C_u T_a)$ for the 8 archetype models in Table 7.6 are compared to see the effect of design variation on the collapse capacity of ECUS low-ductility CBFs. Specifically, the response of the structure during the IDAs is closely examined to understand how the collapse capacity is influenced by weld design strength, beam design strength and brace configuration. Overall, it is observed that the influence of these design variables on collapse capacity is interdependent. For chevron CBFs, when the beam strength increases as the brace connection weld strength creases, or when the beam strength decreases as the brace connection weld strength decreases, a larger collapse capacity can be achieved. It should be noted that the $S_T(C_u T_a)$ corresponding to the collapse of the structure under a particular ground motion is used in explaining the effect of design variation. This is because the effect of design variation on the collapse response can be demonstrated as long as the intensity measure can reflect the relative intensities at which structures with different design collapse under a particular earthquake. Another reason is to facilitate cross referencing the raw data

of the IDA in this section, which was performed using $S_T(C_u T_a)$ as the intensity measure according to FEMA P695 methodology.

7.2.3.1 Effect of weld design strength

The following comparisons are made to study the effect of weld design strength: C1 vs. C2, C3 vs. C4, X1 vs. X2 and X3 vs. X4. It is found that the influence of weld strength is not independent from the other design variables, i.e. the beam strength and brace configuration. For chevron CBF with a strong beam (C1 vs. C2), a stronger weld design leads to a larger collapse capacity. For chevron CBF with weak beam (C3 vs. C4), weaker weld design leads to a larger collapse capacity. For a Split-X CBF (X1 vs. X2 and X3 vs. X4), a weaker weld design leads to a larger collapse capacity regardless of the beam strength.

The responses of model C1 and model C2 to GM25 during the IDA are compared and utilized as an example to show how weld strength affects the collapse response for a chevron CBF with strong beam. Table 7.7 limit states and their time of occurrence for these 2 models at collapse ground motion intensities for GM25. Model C1 with a weak weld design collapses under GM25 at the ground motion intensity corresponding to $S_T(C_u T_a) = 0.8g$. With a weak weld design, Weld 1-2 fractures before the brace buckles. As demonstrated in the pushover analysis of C1 (Figure 7.5), the strong beam resists the unbalanced force from the braces without excessive deformation and enables a larger force to develop in the tension brace (Brace 1-1). As a result, Weld 1-1 fractures later when the brace is in tension. At this time (17.49s), both 2 welds in the first story have fractured (Figure 7.18 (a)). The lateral resistance from brace re-engagement of Brace 1-2 and frame

action is not enough to prevent first story collapse (Figure 7.18 (b)). For model C2 with a strong weld strength at the same ground motion intensity, the first story weld do not fracture. Instead, Brace 1-1 and Brace 1-2 buckle under compression. The ground motion does not cause low cycle fatigue of the brace. Therefore, the structure does not collapse as the braces provide lateral resistance by post-buckling response (Figure 7.19). Model C2 does not collapse until GM25 is increased to the intensity corresponding $S_T(C_u T_a) = 1.1g$ when Brace 1-1 fails by low cycle fatigue (Figure 7.20).

The responses of model C3 and model C4 to GM14 during the IDA are studied to understand how the weld design strength affects the collapse response for a chevron CBF with a weak beam design. Table 7.8 shows the important limit states and their time of occurrence for these 2 models at collapse ground motion intensities for GM14. Model C4 with a strong weld design collapses at $S_T(C_u T_a) = 0.9g$. With a strong weld, Brace 1-1 buckles and later fractures due to low cycle fatigue (Figure 7.23 (a)). The first story collapses with Brace 1-2 intact, as a “long link EBF system”. At the same ground motion intensity, Weld 1-1 fractures in model C3. After weld fracture, Brace 1-1 becomes effective by brace re-engagement (Figure 7.21 (a)). Meanwhile, since the beam is not strong, considerable vertical deflection develops under the unbalanced brace force, relieving the demand on the tension brace (Brace 1-2). Therefore, Weld 1-2 does not fracture. With one brace effective via brace re-engagement and another brace intact, the first story develops stable response and does not collapse (Figure 7.21 (b)). Model C3 collapses at when GM14 is increase to intensity corresponding to $S_T(C_u T_a) = 1.2g$. After Weld 1-2 fractures, the structure has larger drift in the direction where the fractured connection is in tension without the benefit from brace re-engagement (Figure 7.22).

The responses of model X1 and model X2 to GM39 during the IDA are compared to show how the weld strength affects the collapse response for a split-X CBF. Table 7.9 shows the limit states and their time of occurrence for these 2 models at collapse ground motion intensities for GM39. Model X2 with a strong weld design collapses at $S_T(C_u T_a) = 0.5g$. With a strong weld design, Brace 1-2 buckles first. Weld 1-1 fractures soon after, despite a strong weld design (Figure 7.26 (a)). The reason is that, as shown in the pushover analysis (Figure 7.14), the second story braces with the first floor beam maintain the demand high on the tension brace (Brace 1-1). It should be noted that a “strong weld” design for the low-ductility CBF means the design strength has a relatively larger margin above the required strength. The definition of “strong weld” here does not mean the weld strength exceeds the capacity of the brace. As the fractured weld 1-1 is loaded in tension, it does not develop brace re-engagement. In this case, there is only one brace resisting the lateral force through post buckling response, leading to collapse of the first story (Figure 7.26 (b)). At the same ground motion intensity, model X1 develops weld fracture (Weld 2-1, 2-2) for both braces in the second story (Figure 7.24). Brace re-engagement of Brace 2-1 prevents a second story collapse. In the first story, Weld 1-1 fractures when the brace is in compression and this brace continues to be loaded in compression, so brace re-engagement prevents the first story from collapsing.

7.2.3.2 Effect of beam design strength

The following comparisons are made to study the effect of beam design strength: C1 vs. C3, C2 vs. C4, X1 vs. X3 and X2 vs. X4. It is found that the influence of beam design strength also depends on the weld strength and the brace configuration. For a chevron CBF with a weak weld (C1 vs. C3), a stronger beam leads to a lower collapse capacity. For a

chevron CBF with a strong weld (C2 vs. C4), a stronger beam design leads to a larger collapse capacity. For Split-X CBF (X1 vs. X2 and X3 vs. X4), the beam strength makes little difference on the collapse capacity.

The responses of model C1 and model C3 to GM21 during the IDA are investigated to understand how the beam strength affects the collapse response for a chevron CBF with a weak weld design. Table 7.10 shows the limit states and their time of occurrence for these 2 models at collapse ground motion intensities for GM21. At $S_T(C_u T_a) = 0.5g$, both model C1 and model C3 suffer from fracture of the compressive brace weld (Weld 1-2). As discussed before, the stronger beam will maintain the deformation demand on the tension brace and weld. Therefore, as the drift continues in one direction, model C1 with a stronger beam will suffer from fracture of Weld 1-1 (Figure 7.27 (a)) while model C3 will not (Figure 7.28 (a)). With one intact brace and another brace acting in compression by re-engagement, model C3 will survive GM21 of $S_T(C_u T_a) = 0.5g$ (Figure 7.27 (b)) while model C1 will collapse with only one brace effective from re-engagement (Figure 7.28 (b)).

The responses of model C2 and model C4 to GM18 during the IDA are studied to understand how beam strength affects collapse response for a chevron CBF with a strong weld design. Table 7.11 shows the limit states and their time of occurrence for these 2 models at collapse ground motion intensities for GM18. At $S_T(C_u T_a) = 0.9g$, buckling and subsequent fracture of Brace 1-1 occurred for both model C2 and model C4. The first story forms a “long link EBF system” with Brace 1-2 acting in tension and pulling the beam down to form a plastic hinge at the chevron point. Plastic analysis of this mechanism shows

that the force in Brace 1-2 is influenced by the plastic moment of the beam. With a stronger beam, model C2 develops a larger force in the brace, which helps it survive GM18 at $S_T(C_u T_a) = 0.9g$ (Figure 7.30 (b)). In comparison, model C4 develops a smaller force in the brace from this mechanism and collapse under GM18 at $S_T(C_u T_a) = 0.9g$ (Figure 7.32 (b)).

The responses of model X2 and model X4 to GM16 during IDA are studied to show how the beam strength affects the collapse response for split-X CBF. Table 7.12 shows the limit states and their time of occurrence for these 2 models at collapse ground motion intensities for GM16. Both model X2 and model X4 have Brace 1-2 buckling followed by Weld 1-1 fracture. Unlike the chevron CBF, the braces in the second story of the split-X CBF maintain the demand on the first story braces. Therefore, the stiffness and strength of the beam will have little influence on the demand on the first story tension brace and tension brace weld. For the same reason, a plastic hinge does not form in the beam. Therefore, the force that develops in the buckled Brace 1-2 is similar for the 2 models. The models behave in a similar manner (Figure 7.33 and Figure 7.34) and collapse under GM16 at the same ground motion intensity.

7.2.3.3 Effect of brace configuration

The following comparisons are made to study the effect of beam design strength: C1 vs. X1, C2 vs. X2. It is found that the influence of the brace configuration also depends on the weld strength. For a weak weld (C1 vs. X1), the brace configuration makes little difference on the collapse capacity. For a strong weld (C2 vs. X2), the chevron bracing leads to a larger collapse capacity.

The responses of model C1 and model X1 to GM19 during the IDA are studied to show how brace configuration affects the collapse response for CBFs with weak weld design. Table 7.13 shows the limit states and their time of occurrence for these 2 models at collapse ground motion intensities for GM19. For the story that collapses, both model C1 and model X1 have both welds in the story fractured (Figure 7.35 (a) and Figure 7.36 (a)). For both models, the lateral resistance is provided by compression brace re-engagement (Figure 7.35 (b) and Figure 7.36 (b)). Their response is similar and they collapse under GM19 at the same ground motion intensity.

The responses of model C2 and model X2 to GM23 during the IDA are studied to show how brace configuration affects the collapse response for a CBF with a strong weld design. Table 7.14 shows the limit states and their time of occurrence for these 2 models at collapse ground motion intensities for GM23. Model X2 with split-X brace configuration collapses at $S_T(C_u T_a) = 0.5g$. Both Brace 1-1 and 1-2 buckled (Figure 7.39 (a)). Weld 1-1 also fractured later because the demand on the first story tension brace is maintained. In comparison, the welds in model C2 does not fracture after the brace buckled because the flexibility of the beam relieves the demand on the braces (Figure 7.37 (a)). Therefore, model C2 does not collapse under GM23 at this ground motion intensity (Figure 7.37 (b)).

7.3 Collapse performance evaluation using ECUS GM set

IDA and collapse performance evaluation were conducted using the ECUS GM set presented in Chapter 5. The RTR variability is estimated from the IDA results, and in the IDA the ground motions are scaled by the using “Sa component scaling method” (Figure 6.4 (c)&(d)) (which also provides the Sa_c of each ground motion). Due to limitations on

the period in which could be used to develop the ECUS GM set (Chapter 5), the ECUS GM set is developed for the hazard defined at $T = 1s$. Therefore, spectral shape of this ground motion set peaks at 1s; hazard is defined at 1s, and $Sa(1s)$ is used as the intensity measure in the IDA; The IDA is conducted with ground motions that are scaled to have the same $Sa(1s)$. The results are shown in Figure 7.40.

7.3.1 Spectral shape effect

The FEMA GM set, as stated in section 5.2.1, is not selected for a specific site or a specific period. Therefore, this ground motion set is ε -neutral. Consequently, the shape of the median spectrum of the FEMA GM set is not representative of shape of the median spectrum of a ground motion set selected to represent the hazard at a given site and a given period (e.g. the ECUS GM set, Figure 5.19), which has a peak at the period of where the hazard is defined. The shape of the spectrum may have an important effect on the collapse capacity obtained from IDA. For a ground motions set scaled to the same Sa at the period of where the hazard is defined, the ground motion set with a median spectrum with a peaked shape will have smaller Sa at other periods. During the nonlinear response, the effective period of the structure will elongate. At the longer effective period, the GM set with a peaked shape has smaller spectral acceleration. Therefore, the response to the GM set with a peaked shape is expected to be smaller, resulting a larger collapse capacity.

To consider the spectral shape effect, the FEMA P695 methodology develops the SSF (Eq. (7.5)) to adjust the collapse capacity due to the difference between target ε value $\bar{\varepsilon}_0(T)$ and that of the FEMA set $\bar{\varepsilon}(T)_{record}$ as well as the period elongation effect. The period elongation effect is characterized by β_1 which is determined by an empirical formula (Eq.

(7.6)) as a function of μ_T from a pushover analysis and the procedure described in section 7.2.

$$SSF = \exp[\beta_1(\bar{\varepsilon}_0(T) - \bar{\varepsilon}(T)_{,record})] \quad (7.5)$$

$$\beta_1 = 0.14(\mu_T - 1)^{0.42} \quad (7.6)$$

Since the ECUS GM set was developed to represent the hazard at $T = 1s$, using ε values from the hazard deaggregation (Chapter 5), and directly addresses the spectral shape effect, the results of the IDA using the ECUS GM set can be used to examine whether the FEMA P695 methodology for the spectral shape effect applies to ECUS low-ductility CBF. The median collapse capacity for each of the 8 archetype models is calculated as the geometric mean $Sa_{c,m}(1s)$ of the collapse capacity for each ground motion $Sa_c(1s)^{(i)}$ from the IDA result using ECUS GM set (Eq. (7.7)).

$$Sa_{c,m}(1s) = \exp\left[\frac{1}{N} \sum_{i=1}^N \ln Sa_c(1s)^{(i)}\right] \quad (7.7)$$

It should be mentioned that the collapse margin ratio is a generic concept as the measure of a structure's margin against collapse. It can be calculated accordingly depending on the specific intensity measure used in the collapse performance assessment, which is not necessarily spectral acceleration at $C_u T_a$ as used in FEMA P695 methodology, as long as the intensity measure for the MCE and the median collapse capacity is consistent with each other. Since the intensity measure in the IDA using the ECUS GM set is $Sa(1s)$, the collapse margin ratio in this section is calculated as $Sa_{c,m}(1s)$ divided by S_{M1} as MCE intensity. To have a consistent comparison, the IDA with the FEMA GM set is performed

using “Sa component scaling method” with $Sa(1s)$ as the intensity. The median collapse capacity $Sa_{c,m}(1s)$ is obtained and the CMR is calculated. The SSF calculated from section 7.2 is used to factor the CMR for the FEMA ground motion to obtain the adjusted collapse margin ratio (ACMR). The results are compared in Table 7.15. It is found that the values of ACMR are considerably smaller than the CMR obtained from IDA using the ECUS GM set. This suggests the SSF from the FEMA P695 methodology is not applicable to ECUS low-ductility CBFs.

One reason why the SSF from FEMA P695 methodology is not applicable to account for the spectral shape effect for ECUS low-ductility CBFs is because it uses 80% base shear reduction rule to define the inelastic deformation capacity. The 80% base shear reduction rule is based on the idealized pushover curve for an RC MRF (Figure 7.1). For a low-ductility CBF, the pushover curve has significant strength reduction due to brace buckling or weld fracture at very small drift levels. But subsequently, the strength may have significant recovery in the base shear resistance due to secondary mechanisms such as brace re-engagement or CBF beam flexural response (Figure 7.3). According to 80% rule, the recovery response which is after the 80% of peak base shear does not count as inelastic deformation capacity or lead to period elongation effect. In fact, however, the recovery response after initial brace buckling or connection weld fracture may lead to a significant period elongation. Figure 7.41 shows the pushover response and the tangent first mode period, which is determined from eigenvalue analysis using the tangent stiffness matrix, at each load step during the pushover analysis. As can be seen, the value of tangent first mode period has a significant increase, which is an indication of the period elongation. The recovery response also plays an important role in the dynamic response of low-ductility

CBFs. As shown in Figure 7.42, the structure develops a stable hysteresis through brace re-engagement effect after weld fracture. The structure remains in this damage state for many cycles before it collapses. During this stage, there is a significant period elongation. As shown in Figure 7.43, the average tangent first mode period over the entire response duration is 3.92s compared to its initial first mode period of 0.80s. Therefore, the μ_T calculated from the 80% of the peak base shear appears to underestimate the inelastic deformation capacity of low-ductility CBF. As a result, the empirical formula developed based on μ_T is not adequate to characterize the period elongation effect and spectral shape effect for ECUS low-ductility CBFs.

7.3.2 RTR variability

The RTR variability $\sigma_{\ln(Sa_c)}$ calculated according to Eq. (6.7) and (6.8) is determined from the IDA results from both ECUS GM set and FEMA GM set. The results are listed in Table 7.16 along with the β_{RTR} according to the FEMA P695 methodology. It can be seen that $\sigma_{\ln(Sa_c)}$ obtained from collapse capacity from IDA for both FEMA and ECUS GM set is consistently larger than β_{RTR} from the FEMA P695 methodology. The FEMA P695 methodology is developed for IDA results for RC MRFs. The differences between the result from the FEMA P695 methodology and $\sigma_{\ln(Sa_c)}$ calculated from the IDA results can be attributed to the possibility that μ_T appears to underestimate the inelastic deformation capacity of low-ductility CBFs. While there are many causes for RTR variability, one of them is period elongation. The effect of period elongation can be understood from Figure 7.44 and Figure 7.45. Figure 7.45 shows the log standard deviation of the spectral acceleration $\sigma_{\ln(Sa(T))}$ for the ground motions in each of the 2 GM sets at all values of T

when all ground motions are scaled to a common $Sa(1s)$. With greater period elongation, the effective period will move further away from 1s where all ground motions have the same spectral acceleration $Sa(1s)$. Figure 7.45 shows the dispersion in Sa , represented by $\sigma_{\ln(Sa(T))}$, becomes greater, which contributes to more dispersion in collapse capacity. Since μ_T appears to underestimate the deformation capacity of low-ductility CBFs, the empirical formula based on μ_T also appears to underestimate the RTR variability. It can also be observed that the IDA results from the ECUS GM set have larger $\sigma_{\ln(Sa_c)}$ than the IDA results from the FEMA GM set. The reason is that the ECUS GM has more dispersion ($\sigma_{\ln(Sa(T))}$) in the period range beyond 1s (Figure 7.45).

7.4 Effect of modeling approach uncertainty on collapse performance

The effect of modeling approach is investigated by comparing the collapse capacity obtained from the same structure modeled in different ways. In particular, the effect of modeling brace re-engagement, beam strength deterioration and the lateral resistance of gravity system are investigated.

7.4.1 Effect of modeling brace re-engagement

IDA are performed using the ECUS GM set on archetype model C1 and C3 without including the brace re-engagement effect. The median collapse capacity $Sa_{c,m}$ is obtained and compared with that from models that include the brace re-engagement effect (Table 7.17).

Table 7.17 shows that including the brace re-engagement effect in the model does not necessarily always increase the collapse capacity. For example, model C1 (weak weld and

strong beam) has a lower collapse capacity when brace re-engagement is included. The reason is explained in Figure 7.46. When the compression brace is acting via brace re-engagement, the equilibrium of the forces in the vertical direction at the chevron point includes the gravity force G and the vertical component of the tension brace force $P_1 \sin(\theta)$ acting against the beam shears V_1 and V_2 and the vertical component of the compression brace force $P_2 \sin(\theta)$. To balance the upward compression brace force component $P_2 \sin(\theta)$ from brace re-engagement, a large force in the tension brace is required. In addition, a strong beam also develops larger shear forces, further increasing the force demand in the tension brace. As a result, the tension brace weld will fracture at a smaller drift level, which can reduce the collapse capacity. In comparison, when the brace re-engagement is not included, the upward compression brace force component $P_2 \sin(\theta)$ is essentially 0. The shears from the beam alone are not enough to make the tension brace force larger than the weld strength. Therefore, the tension brace remains intact and this behavior increases the collapse capacity. The IDA results for model C1 under GM16 (Figure 7.47) provide an example. At $Sa(1s) = 0.3g$, the model with brace re-engagement collapses. After Weld 1-2 fractures, Brace 1-2 develops re-engagement. Although the re-engagement briefly provides significant recovery of the lateral force resistance, the subsequent fracture of Weld 1-1 reduces the lateral resistance which leads to first story collapse (Figure 7.48). In comparison, the model without brace re-engagement has Weld 1-2 fracture, and the structure behaves like a “long link EBF system”, and develops stable hysteresis and does not collapse. It should be noted that for some ground motions, brace re-engagement leads to larger collapse capacity for model C1. In this case, a second weld in the first story does

not fracture. Overall, for model C1 (strong beam design) brace re-engagement tends to reduce the collapse capacity.

For model C3 with a weak beam, re-engagement tends to increase the collapse capacity. The reason is the small beam shears due to the weak beam, which results in less force demand on the tension brace, and delays the fracture of the second weld. The positive impact of brace re-engagement overcomes the negative impact and increases the collapse capacity.

In summary, brace re-engagement may have positive effect by keeping the compressive brace effective as well as a negative effect by contributions to conditions which cause the other brace weld to fracture. When the beam is strong, the negative effect overcomes the positive impact; and when the beam is weak, the positive effect is dominant.

7.4.2 Effect of modeling beam strength deterioration

IDA are performed using the ECUS GM set on the 4 chevron CBF models in which the beams are modeled using the fiber based element approach described in section 4.4.5. In this approach, the beam flexural strength deterioration due to local buckling is not modeled, but the axial force-moment interaction is included. Recall that the baseline model used for the previous IDA and the pushover analysis, the beams were modeled with the concentrated plastic hinge approach (CPH) at section 4.4.1.

The median collapse capacity of the 4 chevron CBF models using 2 different beam modeling approaches are compared in Table 7.18. It can be seen that modeling the beam using the CPH approach leads to a lower collapse capacity. The reason is that the “long

link EBF” system is a yielding prevention mechanism that often forms after one brace buckles and fractures. It relies on the beam flexural response. Therefore, beam plastic hinge formation and strength deterioration from local buckling are becomes an important limit state which contributes to collapse. The IDA result of model C2 under GM2 can be used as an example (Figure 7.51). Under $Sa(1s) = 0.6g$, Brace 1-2 buckles and later fractures. The system forms a “long link EBF” and the force in the remaining brace depends on the flexural response of the beam. When the beam is modeled with CPH, the hysteresis response of the beam hinge will deteriorate at large drift (Figure 7.53), leading to a reduction of the brace force and collapse (Figure 7.52). In comparison, when the beam is modeled with fiber elements, the strength of the beam hinge increases due to strain hardening. The “long link EBF” mechanism is stable and the brace force does not decrease and serve as collapse prevention. It should be noted that the axial force level in the beam is not high (around $0.1P_y$). The axial force-moment interaction is not significant. From the results, it can be seen that modeling the beam flexural strength deterioration is more important than modeling axial force-moment interaction for an assessment of the collapse capacity. Using the CPH approach to model beams in low-ductility CBFs is recommended.

7.4.3 Effect of modeling gravity load system

IDA are performed again using the ECUS GM set on model C1 in which the gravity load systems is modeled using 3 different approaches (model ii, iii and iv) described Figure 4.26 in section 4.4.5, and the results are compared with the result when gravity load system is modeled using model i (Table 7.19), as in the baseline model.

The results in Table 7.19 show that the gravity load system model has a significant impact on the collapse capacity. Just considering the continuity of the gravity columns (model ii) increases the collapse capacity substantially. Including the beam-column moment-rotation capacity (model iv), the collapse capacity of the system almost doubles. The results are corroborated by the pushover analysis of the structure with different gravity load system models (Figure 7.54). It can be seen that the lateral strength of the model after weld fracture significantly increases due to the lateral resistance of the gravity load system.

7.5 Effect of model parameter uncertainty on collapse performance

The effect of uncertainty for the 5 model parameters identified in Chapter 6 is studied by both sensitivity analysis and Monte Carlo Simulation. The analysis is performed on archetype model C1 and model C2 which represent the cases of chevron CBFs with strong beams and weak weld design or strong weld design, respectively.

7.5.1 Sensitivity study

The sensitivity study is performed by perturbing each of the 5 model parameters individually to its upper and lower values shown in Table 7.20 and conducting IDA for the ECUS GM set. The median collapse capacity $Sa_{c,m}(1s)$ of the perturbed model is obtained and compared with that of the median model, i.e., the model with median values for all these 5 model parameters. The upper and lower values are based on the statistical distributions for the parameters given in Table 6.6. As the brace weld strength R_c and brace LCF strength ε_0 follow lognormal distributions, their upper and lower values are calculated as plus and minus two log standard deviations from the median value, respectively, i.e., $\exp(\ln x_m \pm 2\delta_x)$, where x_m is the median value and δ_x is the coefficient of variation

(c.o.v.). The upper and lower values for the brace re-engagement strength are based on the upper and lower bound of the uniform distribution for F_{re} (section 4.4.1). The upper value for the brace initial imperfection e/L is set to 1/1000 which is the construction tolerance according to AISC. The upper value for brace yield strength $F_{y_{br}}$, which follows a normal distribution, is calculated as two standard deviations above the median, i.e., $\mu + 2\sigma$, where μ is the mean (median) and σ is the standard deviation. In the sensitivity analysis, the parameters for different elements (at different locations in the structure) are assumed to vary in the same pattern. For example, when the weld strength takes the upper value, the weld strength for all 6 brace connections is the upper value, equal to $2.64R_n$.

The results of the sensitivity analysis are shown in Figure 7.55. The vertical line indicates the median collapse capacity $Sa_{c,m}(1s)$ of the median model. It can be seen that for model C1 (weak weld design), the weld strength is the most influential parameter. The brace re-engagement strength and brace yield strength also have significant impact on the collapse capacity. The LCF strength and brace initial imperfection have little effect on the collapse capacity. For model C2 (strong weld design), the collapse capacity is most sensitive to the brace LCF strength. The weld strength also makes considerable impact, but only when the lower value is used. The brace yield strength and initial imperfection have little effect on collapse capacity. The brace re-engagement strength has no effect in this case. It can be seen that the sensitivity of each parameter depends on the median value which is related to the design value (e.g. the weld strength). The sensitivity of each parameter also depends on the value of the other parameters (e.g. the effect of LCF strength depends on the value of the weld strength), a trend also found in the study of the influence of design variation.

The IDA results are studied to provide some insight into the sensitivity of the collapse capacity to each the model parameters. It should be noted that the influence of model parameters varies between different ground motions (Figure 7.56). So the examples used to provide insight are from ground motions whose result conforms with the overall trend.

7.5.1.1 Effect of weld strength R_c

For model C1, a larger weld strength leads to a larger collapse capacity. The IDA result, for GM12 (Figure 7.57) is used as an example to explain the reason. At $Sa(1s) = 0.1g$, the model with the lower value of the weld strength has both Weld 1-1 and Weld 1-2 fractured, while the median model has only Weld 1-2 fractured (Figure 7.58). The reason is that, after the first weld fractures, it takes more drift to fracture the remaining brace weld. The weld in the median model is stronger so that the ground motion at this level of $Sa(1s)$ causes only one weld fracture. Unlike the model with the median and lower value weld strength, the weld strength in the higher value model is larger than the brace buckling strength (Figure 7.60(a)). As a result, at $Sa(1s) = 0.2g$, Brace 1-2 buckled and fractured, instead of Weld 1-2 fracture (Figure 7.59). Brace 1-1 remains intact. For the median model, GM12 at $Sa(1s) = 0.2g$ is enough to cause both welds to fracture and leads to collapse (Figure 7.59).

For model C2, the collapse capacity is the same for the median and upper value models. In both models, the weld strength is larger than the buckling strength of the corresponding brace (Figure 7.60(b)). The brace buckles and the weld does not fracture. The response of the 2 models is the same. For the lower value model, the weld strength in first story is smaller than the brace buckling strength. So, the weld fractures. The collapse capacity is

affected in the same way as the variation between model C1 with the upper value and the median value of the weld strength.

7.5.1.2 Effect of brace LCF strength ϵ_0

For model C1, the variation of the LCF strength has little effect, because the weld strength of the median model is smaller than the buckling strength of the braces in the first and second stories, where the collapse occurs. In this case, weld fracture instead of brace buckling will happen in these 2 stories. Thus, these braces do not develop LCF and the variation of their LCF strength will not have an effect. The minor difference in the collapse capacity is due to a few cases in which the third story brace buckles, because the weld strength for the third story braces has a large overstrength due to the minimum weld length in design requirements (see section 4.3.6). For example, in the IDA result for GM44 (Figure 7.61), Brace 3-2 buckles and subsequently fractures at $Sa(1s) = 0.8g$ for the model with lower value of the LCF strength (Figure 7.62 (b)). In comparison, Brace 3-2 buckles but does not fracture in the model with the upper value (Figure 7.62 (a)). The fracture of Brace 3-2 changes the subsequent response of the structure. The drift histories of the 2 models, they start to deviate from each other right after Brace 3-2 fractures (Figure 7.64). The 2 models also experience different limit states after Brace 3-2 fractures (Figure 7.63). The model with the lower value of LCF strength has both Weld 1-1 and 1-2 fracture and the first story collapses. For this example, we can see that the response of the story which collapses may be indirectly affected by events happening in other stories.

For model C2, however, the increase in the brace LCF strength leads a significant increase on the collapse capacity, because the weld strength is larger than the corresponding brace

buckling strength, which enables brace buckling. Collapse occurs due to the LCF fracture of the brace in the story that collapses for most of the cases. So, the LCF strength of the brace directly influences the collapse capacity. The IDA result for GM12 (Figure 7.65) can be used as an example. At $Sa(1s) = 0.3g$, Brace 1-1 in both models buckles. The brace in the median model develops low cycle fatigue and fractures while the brace in the model with the upper value of the LCF strength does not (Figure 7.66). The median model collapses in the first story as a result of Brace 1-1 fracture.

7.5.1.3 Effect of brace re-engagement strength F_{re}

For model C1, the influence of brace re-engagement strength is not monotonic. The collapse capacity of the median model is smaller than the collapse capacity of the models with the upper value and lower value of the re-engagement strength. The model with the lower value has the highest collapse capacity, because as explained in section 7.4.1, brace re-engagement has a positive impact of providing secondary brace resistance after the weld fractures, as well as a negative impact of creating a large force demand on the tension brace weld fracture. A lower brace re-engagement strength leads to a larger collapse capacity than the median value of the re-engagement strength because it reduces the force demand on the tension brace. The results for GM5 at $Sa(1s) = 0.6g$ can be used as an example to explain the difference between the model with median and lower values of brace re-engagement strength (Figure 7.67). Figure 7.68 shows the force histories of Brace 1-1 and Brace 1-2 for the median value and lower value models. Shortly after Weld 1-2 fractures at $t=4.03s$, Brace 1-2 start to re-engage. According to the equilibrium shown in Figure 7.46, a larger re-engagement strength for Brace 1-2 will lead to a larger tension force in Brace 1-1. In the median model, the tension force in Brace 1-1 exceeds the weld strength and

causes Weld 1-1 to fracture at $t=4.25s$. From then on, the median model does not have enough lateral resistance in the first story and collapses (Figure 7.69). In comparison, for the model with the lower value of brace re-engagement strength, the tension force in Brace 1-1 is not large enough to cause Weld 1-1 to fracture, which helps to prevent collapse. The IDA result for GM2 at $Sa(1s) = 0.5g$ can be used as an example to explain the difference between models with the median and upper values of brace re-engagement strength (Figure 7.70). For both models, the brace re-engagement strength is large enough to cause Weld 1-1 to fracture. But the larger brace re-engagement strength from Brace 1-2 from the model with the upper value (Figure 7.71(b)) will provide a larger lateral resistance to the first story (Figure 7.71(a)) and helps preventing collapse.

For C2 model, the variation of the brace re-engagement strength has no effect on the collapse capacity, because the weld strength is larger than the brace buckling strength, precluding weld fracture. Without weld fracture, brace re-engagement does not happen.

7.5.1.4 Effect of brace initial imperfection e/L

For both model C1 and model C2, the variation of e/L has little effect on the collapse capacity. The brace initial imperfection will affect the buckling strength of the brace. However, as can be seen in Figure 7.72, the buckling strength of the first story braces with 3 different values of e/L are all larger than the median weld strength for model C1 but smaller than that of model C2. This result means the first limit state of the first story brace in compression will always be weld fracture for model C1 and brace buckling for model C2 regardless of e/L . In other words, the change of e/L does not result in a change in the

sequence of limit states, or ultimately, the collapse mechanism in the first story. This result may explain the insensitivity the collapse capacity to e/L .

Also, the small effect of e/L on the collapse capacity does not show a clear trend because e/L often affects the response of the story that does not collapse, which may indirectly affect the response of the story that collapses. For example, Figure 7.73 shows the response of Brace 3-1 in model C1 with the median value and lower value of e/L to GM5 at $Sa(1s) = 0.4g$. Brace 3-1 buckles in the median value model. It turns out that buckling of Brace 3-1 change the response of the structure afterwards (Figure 7.74). The first story drift history of the 2 models begins to deviate at the instance of the buckling of Brace 3-1 (Figure 7.75). In some sense, the buckling of a third story brace in the median value model leads to the collapse at the first story.

7.5.1.5 Effect of brace yield strength $F_{y_{br}}$

The yield strength of the brace has a large effect on the collapse capacity when it is at the lower value in model C1. For model C2, it has little effect. The reason can be explained using Figure 7.76. The brace yield strength will change the buckling strength for the brace in compression. For model C1, the brace with the lower value of the yield strength will have a buckling strength below the weld strength while the buckling strength of first story brace with the median value and upper value of the yield strength will have a buckling strength larger than the weld strength. The change in the buckling strength will result in a change in the limit states which are reached. The IDA result for GM19 can be used as an example (Figure 7.77). For example, under GM19 at $Sa(1s) = 0.5g$, the first story braces in the model with the lower value for yield strength develop buckling and LCF fracture. In

comparison, the model with median value develops weld fracture before the first story braces buckle (Figure 7.78). In comparison, the change of the brace yield strength from the median value to the upper value does not cause a change in the limit states. Therefore, it has little effect in the collapse capacity as shown by the IDA results for GM19, in which the median value and upper value models collapse at the same $Sa(1s)$. Similarly, the variation of brace yield strength in model C2 does not lead to a change in the limit states that are reached. The first story brace buckles for all 3 models with different brace yield strengths. The variation in brace yield strength thus has limited influence on the collapse capacity of model C2.

7.5.1.6 Summary of sensitivity study

Generally, the weld strength and the LCF strength are the most important parameters affecting the collapse capacity. Some other observations are as follows.

1. The influence of each model parameter is not independent. There is interaction between different parameters. For example, the influence of the brace LCF strength is significant when the weld strength is large and not significant when the weld strength is small.
2. The influence of a parameter depends on the central value of its range of variation. In other words, the median value of a parameter also affects the influence of its variation. For example, when the weld strength is large enough, a further increase of weld strength will not affect the collapse capacity.
3. The influence of a parameter on the collapse capacity may not be monotonic, and the collapse capacity of a model with the median value of a parameter may not be

bounded by the collapse capacities corresponding to the upper and lower values. The influence of the brace re-engagement strength is an example.

4. If the variation of a parameter changes the sequence of limit states, the parameter will significantly affect the collapse capacity. For example, a change of the brace yield strength from the median value to the lower value in model C1 causes a change in the limit states that occur. The collapse capacity is therefore significantly affected.
5. The response in one story may affect the response in another story. The response in the story that collapses may be affected by the response of another story. An example is shown in Figure 7.63.
6. The influence of a parameter varies between different ground motions.

This sensitivity study shows that the interaction between different parameters is important to the collapse capacity. But the sensitivity analysis is not ideal for demonstrating this effect. In addition, the interaction of one parameter among different elements was seen in this sensitivity study since each parameter was varied in the same way for all elements. Therefore, Monte Carlo Simulation is used to systematically vary the model parameter values, treating them as truly random variables.

7.5.2 Monte Carlo Simulation

Monte Carlo Simulation (MCS) is used to assess the effect of the uncertainty in the model parameters on the collapse capacity. The procedure for the MCS is illustrated in Figure 6.6. In the MCS, each of the 5 model parameters (Table 6.6) for different elements of the model are treated as different random variables. For example, the weld strength R_c in Weld 1-1

and Weld 1-2 are treated as 2 different random variables. There are 5 model parameters (listed in Table 7.21) for 6 elements (i.e., 2 braces and connections in each of the 3 stories) resulting in 30 random variables. To consider the correlation between the model parameters in different elements, it is assumed that the correlation ρ for one model parameter between any 2 different elements is 0.5. The different model parameters are considered to be uncorrelated. For example, the correlation ρ between the weld strength for any 2 different elements (braces and connections) is 0.5 while the weld strength is not correlated to the LCF strength for any element (Figure 7.79). Samples of these random variables are generated according to their statistical distributions given in Table 6.6. The correlation between the random variables are ensured using the “simulated annealing” technique (Charpis and Panteli 2004) which rearranges the sequence of generated samples to achieve the desired correlation between multiple random variables. In this way, heterogeneous values of model parameters, i.e., different values for the same parameter for different elements (at different locations) are achieved in the MCS. One set of samples for the 30 random variables is termed a “sample model”. 20 sample models are generated and each of them is subjected to IDA for the entire ECUS GM set of 44 ground motions, which adds up to 880 IDAs. The results of the IDAs for the 20 sample models from the MCS are presented in Figure 7.80 for model C1 and Figure 7.81 for model C2.

7.5.2.1 Median collapse capacity

The median collapse capacity $Sa_{c,m}(1s)$ for each sample model is calculated from the IDA result using Eq. (7.7). Also, the median collapse capacity considering all 20 sample models is calculated as the median of the collapse capacities obtained from the IDA for the 880 GM-sample model pairs using Eq. (7.8), and is denoted as $Sa_{c,m,MCS}(1s)$. In Eq. (7.8),

$Sa_c(1s)^{(i,j)}$ is the collapse capacity of model j under GM i ; N is the number of ground motions and equals 44; M is the number of sample models and equals 20.

$$Sa_{c,m,MCS}(1s) = \exp\left[\frac{1}{N \times M} \sum_{i=1}^N \sum_{j=1}^M \ln Sa_c(1s)^{(i,j)}\right] \quad (7.8)$$

Figure 7.83 shows the $Sa_{c,m}(1s)$ for each sample model, $Sa_{c,m,MCS}(1s)$, which considers all 20 sample models together, and $Sa_{c,m}(1s)$ of the median model results for model C1 and C2. The median collapse capacity of the median model is from Table 7.15. Two major observations are made. First, $Sa_{c,m}(1s)$ shows appreciable variation among the sample models, which indicates considerable effect of the model parameter uncertainty. For example, $Sa_{c,m}(1s)$ for the sample models of model C1 ranges from 0.32g to 0.57g, which differ by a factor of 1.8. Second, $Sa_{c,m,MCS}(1s)$ is notably different from $Sa_{c,m}(1s)$ for the median model. For example, for model C1 $Sa_{c,m,MCS}(1s)$ is 0.44g while $Sa_{c,m}(1s)$ for the median model is only 0.38g.

To make sure the significant difference between $Sa_{c,m,MCS}(1s)$ and $Sa_{c,m}(1s)$ for the median model is not from an inadequate number of samples in the MCS, the $Sa_{c,m,MCS}(1s)$ is calculated with an increasing number of sample models, and the results are shown in Figure 7.82. As can be seen, when more than 10 sample models are included, $Sa_{c,m,MCS}(1s)$ varies within a range of 2% higher or lower than the result when 20 sample models are included. This result shows that the MCS with 20 sample models converges, and the difference between the $Sa_{c,m,MCS}(1s)$ considering 20 models and $Sa_{c,m}(1s)$ for the median model is of statistical significance.

There are two main reasons for the difference between the $Sa_{c,m,MCS}(1s)$ considering 20 models and $Sa_{c,m}(1s)$ for the median model. The first one is the effect of heterogeneous values of model parameters (for different elements). The second is the asymmetrical influence of a model parameter on the collapse capacity as it varies above and below the median value (as seen in Figure 7.55). The influence of the weld strength for the first story brace can be used as an example to explain both these 2 aspects. Figure 7.84 presents the strength of Weld 1-1 and Weld 1-2 for the 20 sample models in the MCS and for the median model for model C1. The value of $Sa_{c,m}(1s)$ for each model is shown by color coating. The distribution of the weld strength can be divided into 3 regions: Zone I where both welds are weak; Zone II where both welds are strong and Zone III for the rest. In Zone III, there are many models in which the strength of Weld 1-1 and Weld 1-2 are significantly different from each other (heterogeneous values). These models have collapse capacity consistently larger than the median model. For sample model 3, as an example, the strength of Weld 1-1 and Weld 1-2 is 355.7 kips and 272.7 kips, respectively. The strength of these 2 welds vary in an “opposite” manner with respect to the weld strength in the median model (301.6 kips). However, this opposite variation of the 2 weld strengths does not offset the effect (producing no effect on the collapse capacity), but instead, it increases the collapse capacity compared to the median model (Figure 7.85). The reason can be explained with the IDA results for GM5 (Figure 7.86). As shown in Figure 7.87, while Weld 1-2 in sample model 3 has early fracture due to the low strength, of the subsequent brace re-engagement of Brace 1-2 has no negative impact on the response of Brace 1-1, since the large strength of Weld 1-1 eliminates the possibility of Weld 1-1 fracture. This combination of different weld strengths results in responses that utilize the positive impact of brace re-engagement

and suppresses its negative impact. In comparison, the weld strength in the median model is not large enough to sustain the large tension demand arising from brace re-engagement. As a result, the weld for the tension brace fractures after re-engagement of the compression brace, severely limiting the subsequent lateral resistance. For this reason, although the individual weld strength parameter values of the sample models in Zone III are scattered around the median weld strength, the values of $Sa_{c,m}(1s)$ for the corresponding sample models are not scattered around $Sa_{c,m}(1s)$ of the median model.

In addition, the influence of weld strength is not symmetric with respect to the median value. The models in Zone II in Figure 7.84, weld strength above the median value result in a large increase in $Sa_{c,m}(1s)$ for the sample model. A decrease in the weld strength by the same amount however, does not lead to as large a decrease in $Sa_{c,m}(1s)$ for the models in Zone I. This result is because increasing the weld strength results in a change in the limit states that occur. The braces will buckle and fracture for the Zone II models and weld fracture will not occur. However, when the weld strength is less than that of the median model, the controlling limit state of weld fracture for the sample is the same as the median model.

The median model cannot represent the variation of controlling limit states and this limitation is of special importance for low-ductility CBFs, as the variation in the model parameters will cause a variation of the controlling limit states. Figure 7.88 presents the definition of some of the collapse modes that were observed. A collapse mode is the collapse mechanism and controlling limit states experienced before collapse, observed during the IDA. In the IDA for all 44 GMs, the median model of model C1 only exhibits 3

collapse modes with collapse mode 1 being dominant (Figure 7.89 (a), Figure 7.88). In comparison, the 20 sample models in the MCS exhibit 8 collapse modes under GM1 (Figure 7.89 (b), Figure 7.88). It can be seen that the median model fails to capture many possible collapse modes, which is an important reason for the bias in estimation of the median collapse response from the median model (i.e., $Sa_{c,m}(1s)$ for median model is different than $Sa_{c,m,MCS}(1s)$). Therefore, the median model is not representative of the median response of low-ductility CBF in the presence of model parameter uncertainty. The median model alone is inadequate to accurately capture the median collapse capacity.

7.5.2.2 Dispersion of collapse capacity

The log standard deviation of $Sa_c(1s)$ denoted as $\sigma_{\ln(Sa_c)}$, for each sample model is calculated from Eq. (6.8). The log standard deviation of $Sa_c(1s)$ considering all 20 sample models, denoted as $\sigma_{\ln(Sa_c),MCS}$, is calculated using Eq. (7.9), where $Sa_{m,MCS}(1s)$ is obtained from Eq. (7.8).

$$\sigma_{\ln(Sa_c),MCS} = \sqrt{\frac{\sum_{i=1}^N \sum_{j=1}^M [\ln Sa_c(1s)^{(i,j)} - \ln Sa_{m,MCS}(1s)]^2}{N \times M - 1}} \quad (7.9)$$

Figure 7.90 shows the $\sigma_{\ln(Sa_c)}$ for each sample model, $\sigma_{\ln(Sa_c),MCS}$ considering all 20 sample models, and $\sigma_{\ln(Sa_c)}$ for the median model. The $\sigma_{\ln(Sa_c)}$ for the median model is from Table 7.16. Figure 7.90 shows that $\sigma_{\ln(Sa_c),MCS}$ is slightly larger than $\sigma_{\ln(Sa_c)}$ for the median model, since the median model does not include the model parameter uncertainty. The dispersion of $Sa_c(1s)$ of the median model represents only RTR variability of the collapse capacity. The dispersion represented by $\sigma_{\ln(Sa_c),MCS}$ includes both RTR variability

and the effect of model parameter uncertainty. Assuming the RTR variability and model parameter uncertainty are statistically independent, the effect of model parameter uncertainty, denoted β_{MP} , can be quantified using Eq. (7.10), where $\sigma_{\ln(Sa_c)}$ is from the median model. β_{MP} is 0.18 and 0.24 for model C1 and C2 respectively.

$$\beta_{MP} = \sqrt{\sigma_{\ln(Sa_c),MCS}^2 - \sigma_{\ln(Sa_c)}^2} \quad (7.10)$$

β_{MP} is compared with β_{RTR} for model C1 and C2. It is found that β_{MP} is considerably smaller than β_{RTR} . This indicates that RTR variability is the dominating factor in the collapse capacity uncertainty. As discussed in Chapter 6, the model parameter uncertainty (MP) corresponds to only a part of design requirement uncertainty (DR) and test data uncertainty (TD) in from the FEMA P695 methodology (Figure 6.7). Here, β_{MP} is compared with a combination of the DR uncertainty and the TD uncertainty, denoted $\beta_{DR-TD} = \sqrt{\beta_{DR}^2 + \beta_{TD}^2} = \sqrt{0.5^2 + 0.5^2} = 0.71$. It is found that β_{MP} is much smaller than β_{DR-TD} . It should be noted that this study only includes the uncertainty of a limited number of model parameters. In addition, β_{DR} and β_{TD} also account for some sources of uncertainty other than model parameter uncertainty.

The dominance of RTR variability in the dispersion of Sa_c can also be seen in Figure 7.91 and Figure 7.92. Figure 7.91 presents the IDA result for sample model 1 of model C1 under 44 GMs and the IDA results for 20 sample models for GM1. It can be seen that variation of the ground motions lead to a larger dispersion in Sa_c . Figure 7.92 shows the $\sigma_{\ln(Sa_c)}$ for all sample models together under each ground motion individually. It can be seen that the

value of $\sigma_{\ln(Sa_c)}$ based only on the model variation is smaller than the values in Figure 7.90 which show the dispersion due to RTR variability. Even though the model parameter uncertainty increases the variation in the limit state sequence and collapse mode, (Figure 7.89 (b)), its influence is not as large as the RTR variability.

7.6 Discussion and summary of effect of various sources of uncertainty

The effects of all sources of uncertainty are summarized and compared in this section. The RTR variability and effect of model parameter uncertainty on the collapse capacity have been explicitly quantified. For each archetype model (C1, C2, C3, C4, X1, X2, X3, and X4), the log standard deviation of $Sa_c(1s)$ was calculated from Eq. (6.8), denoted previously as $\sigma_{\ln(Sa_c)}$, is here denoted β_{RTR_Sa} . The results are shown in Figure 7.93, where β_{RTR_Sa} is around 0.4 while β_{MP} is around 0.2 for the 5 parameters studied. It is shown that RTR variability dominates over the model parameter (MP) uncertainty in IDA. In addition, the β_{MP} is smaller than the combined β_{DR-TD} from the FEMA P695 methodology as shown earlier. As it is challenging to use MCS to estimate the effect of model parameter uncertainty for any specific archetype model, the β values in FEMA P695 methodology may be a simple way to account for the model parameter uncertainties and related uncertainties from design requirement (DR) and test data (TD) in collapse performance evaluation. Based on the results of the present study, it is recommended to use these β values to account for uncertainties from design requirement (DR) and test data (TD).

The effect of design variation (DV) is investigated in a qualitative way by comparing results for different archetype models with results from the MCS for archetype model C1. Figure 7.94 shows the median collapse capacity for the sample models for archetype model

C1 and for the median model of all 8 archetype models. The variation of the 8 archetype models represent the design variation while the 20 sample models represent effect of model parameter uncertainty. The figure shows that the variation among the sample models for model C1 is much greater than the variation between the 8 median models with different designs. So, the model parameter uncertainty appears to have greater impact than the design variation.

The effect of modeling approach (MA) is studied by repeating the calculation of the collapse capacity $Sa_{c,m}(1s)$ for the median model of model C1 with different modeling approaches used for the IDA. The modeling approaches and the results are given in Table 7.21. $Sa_{c,m}(1s)$ for the median model of model C1 obtained using different modeling approaches are compared with $Sa_{c,m}(1s)$ for the 20 sample models of model C1 in Figure 7.95. In particular, the modeling of the gravity load system has a larger effect on the $Sa_{c,m}(1s)$. For models of the gravity load system which have larger lateral force resistance (section 4.4.2), such as model ii, iii or iv, the collapse capacity becomes larger than the largest for the sample models using the baseline model (model i). As stated in Chapter 6, the MA uncertainty is not quantified directly; however, the results show that the MA may have a greater effect than the model parameter uncertainty.

7.7 Collapse performance evaluation using modified FEMA P695 methodology

Based on the results presented earlier, 3 major issues in applying the FEMA P695 methodology to evaluate the collapse performance of ECUS low-ductility CBFs are presented as follows.

1. The FEMA ground motion set, SSF and β_{RTR}

The FEMA ground motion set was not assembled to represent ECUS ground motion characteristics. In addition, the empirical formulas for SSF and β_{RTR} in FEMA P695 methodology are developed for more ductile west coast structures and west coast ground motions, which are not representative of low-ductility CBFs and ECUS ground motions. The results presented early show that SSF based on FEMA P695 formula is small (1.03 to 1.04) and β_{RTR} from FEMA P695 is smaller than $\beta_{RTR,Sa}$ for the IDA performed using ECUS GM set.

2. The method of calculating median collapse capacity

The FEMA P695 methodology defines the collapse capacity using $S_T(C_u T_a)$, which is the median spectral acceleration of the ground motion set at the approximate period for design, $C_u T_a$. However, β_{RTR} used to determine the collapse fragility function was determined from the dispersion in collapse capacity ($Sa_c(C_u T_a)$) from individual ground motion with the “Sa component scaling method” (FEMA 2009). To overcome this inconsistency, it is suggested that the median collapse capacity should be the median of Sa causing collapse for each ground motion, denoted as $Sa_c(C_u T_a)$ in the present study.

3. Consideration of model parameter uncertainty

In FEMA P695 methodology uses the median model (where the model parameters take median values) for the IDA used to obtain the median collapse capacity. The FEMA P695 methodology includes dispersion in the collapse capacity from various sources of uncertainty by predefined β values. In this study, which includes model

parameter uncertainty within a MCS, it is found that, while the predefined β values may be adequate for the dispersion of collapse capacity, the median collapse capacity may not be accurately quantified by the collapse capacity of the median model. The median collapse capacity should be obtained considering a set of samples models from a MCS instead of considering only the median model.

In addition, there are 2 important findings that are worth consideration in varying the FEMA P695 methodology.

1. Lateral resistance from the gravity load system

FEMA P695 methodology states that the lateral resistance from the gravity load system should not be included when assessing the structural collapse capacity, and the P- Δ effect should be considered. However, the results of this study show that including the lateral resistance from the gravity load system, even just the continuity of the gravity columns, significantly increases the collapse capacity for EUCS low-ductility CBFs. Therefore, it is worth investigating collapse performance of low-ductility CBFs when the contribution of gravity load system is included.

2. Intensity of the MCE hazard level

According to FEMA P695 methodology, the intensity of the MCE hazard level is based on the 2008 version of USGS national hazard map (Petersen et al. 2008). However, using the current seismological models and considering the expected site amplification effect in Philadelphia from various potential Site Class D sites, the ECUS GM set developed in Chapter 5 indicates a much lower MCE intensity for

Site Class D sites. The reason, as described in Chapter 5, is that ASCE MCE spectrum assumes peak amplification to happen at all periods, which gives an upper bound and conservative estimate for the site amplification in the design stage. It is worth investigating the implications of lower MCE intensity for various Philadelphia Site Class D sites (by considering the expected soil amplification effect) on the collapse performance of low-ductility CBFs in the ECUS.

5 variations of the FEMA P695 methodology are presented in Table 7.22. The specific variation is listed in comparison with the original FEMA P695 methodology. The 5 modified variations of FEMA P695 methodology are applied to evaluate the collapse performance of low-ductility CBFs in the ECUS.

In Mod1 variation, the median collapse capacity is defined as $Sa_{c,m}(C_u T_a)$, which is the geometric mean of the collapse capacity of each individual ground motion (in the FEMA GM set) $Sa_c(C_u T_a)$. Accordingly, the CMR is calculated as the ratio between $Sa_{c,m}(C_u T_a)$ and S_{MT} which is the spectral acceleration at the design period $C_u T_a$ from the MCE spectrum in ASCE7-10 (ASCE 2010). All other aspects remain the same as the original FEMA P695 methodology. Table 7.23 and Table 7.24 show the results of the collapse performance assessment using Mod1 variation. It is found that the ACMR is consistently larger than ACMR from the original methodology (Table 7.2). However, the performance groups of the archetype models still do not have satisfactory collapse performance.

In Mod2 variation, the median collapse capacity is defined as $Sa_{c,m}(1s)$, which is the geometric mean of the collapse capacity of each individual ground motion $Sa_c(1s)$ (in the ECUS GM set). Accordingly, the CMR is calculated as the ratio between $Sa_{c,m}(1s)$ and

S_{M1} , which is the spectral acceleration at the period of 1s from the MCE spectrum in ASCE7-10 (ASCE 2010). In addition, the RTR variability is $\beta_{RTR_{Sa}}$ calculated as $\sigma_{\ln(Sa_c)}$ using Eq. (6.8), which is the log standard deviation of the collapse capacity of each ground motion $Sa_c(1s)$ from the IDA results. All the other aspects of the calculations are the same as the original FEMA P695 methodology. Table 7.25 and Table 7.26 show the results of the collapse performance assessment using Mod2 variation. It should be noted that the CMR is equal to ACMR in this case since the ECUS GM set includes the spectral shape effect, and SSF is not calculated or included in the calculation. Hence, the obtained CMR can be directly compared with ACMR10 and ACMR20. It is found that the CMR (Table 7.25) calculated using the Mod 2 variation is consistently larger than the ACMR obtained using Mod1 variation (Table 7.23), which is likely due to an underestimation of the spectral shape effect using the empirical formulas from the FEMA P695 methodology. It is worth noting that β_{TOT} for Mod 2 variation (Table 7.25) are consistently larger than β_{TOT} used for the calculations for the original FEMA P695 methodology ($\beta_{TOT} = 0.82$, from Table 7.4) which results in larger ACMR10 and ACMR20 in Table 7.26 for the Mod 2 variation. However, the performance groups for the archetype models still do not have satisfactory collapse performance.

In Mod3 variation, the median collapse capacity is defined as $Sa_{c,m,MCS}(1s)$, which is median collapse capacity considering all 20 sample models in the MCS (Eq. (7.8)). Accordingly, the CMR is calculated as the ratio between $Sa_{c,m,MCS}(1s)$ and S_{M1} which is the spectral acceleration at the design period of 1s from the MCE spectrum in ASCE7-10. All other aspects of Mod3 variation calculations remain the same as for the Mod2 variation,

including the calculation of $\beta_{RTR_{Sa}}$ as well as β_{DR} , β_{TD} , and β_{MDL} . Table 7.27 and Table 7.28 show the results of the collapse performance assessment using the Mod3 variation. It should be noted that the average β_{TOT} (Table 7.27) and the corresponding ACMR10 (Table 7.28) considers the entire performance group of chevron CBF (C1, C2, C3, C4). However, since the MCS was performed on archetype model C1 and C2 only, the collapse assessment of an entire performance group could not be completed.

In Mod4 variation, the numerical model uses different approaches mentioned in section 4.4.2 and section 7.4.3, where the models (i, ii, iii, and iv) are described, to model the gravity load system. Only archetype model C1 is included. All the other aspects of the Mod4 variation remain the same as for the Mod2 variation. Table 7.29 and Table 7.30 show the results of the collapse performance assessment using Mod4 variation. The results in Table 7.29 show that including only the continuity of the gravity columns in model ii increases the CMR significantly to 3.63, compared to 2.61 for the baseline gravity load system model i. This CMR surpasses the ACMR10 of 3.23 (for performance group) (Table 7.26) by 12%. Although the other archetype models were not analyzed including the lateral resistance of the gravity load system, the results for model C1 show significant enhancement of collapse capacity. Therefore, it is suggested that the other archetype models will have satisfactory collapse performance when the lateral resistance of the gravity load system is included.

In Mod5 variation, the MCE hazard intensity is defined as the median spectral acceleration of the ECUS GM set at 1s. All other aspects of this calculation are the same as for the Mod2 variation. Table 7.31 and Table 7.32 show the results of the collapse performance

assessment using Mod5 variation. Comparison of S_{M1} in Table 7.31 with S_{M1} in Table 7.25 shows a significant decrease from using the ECUS GM set to define the MCE hazard intensity. It can be seen that due to the significant decrease in the MCE intensity, the CMR for each archetype model and the performance groups pass the acceptance thresholds by a large margin and the archetype models have satisfactory performance (Table 7.32).

The collapse performance evaluation results from different variations of the FEMA P695 methodology are summarized in Table 7.33. The probability of collapse under MCE for each archetype model is less than 20%, regardless of the method used. Using the original FEMA P695 methodology, the average probability of collapse for the performance group exceeds 10%. According to the results from variation Mod 4 and Mod5, the average probability of collapse under the MCE for the performance group is below 10%, if either one of the following conditions is met: 1. the lower MCE intensity is used, which is due to the more updated seismological analyses and, more importantly, the soil amplification effect based on the expected soil property for a generic Site Class D site in Philadelphia; 2. the contribution of lateral force resistance from the gravity load system is considered, even to a modest extent.

Table 7.1 Pushover analysis results and calculation of SSF for each archetype model

Archetype ID	C_0	V_{max} (kips)	W (kips)	T (s)	T_1 (s)	δ_y (in)	δ_u (in)	μ_T	SSF
C1	1.3	411.1	2812.5	0.551	0.744	1.03	1.30	1.26	1.04
C2	1.3	456.8	2812.5	0.551	0.745	1.15	1.45	1.27	1.04
C3	1.3	365.3	2812.5	0.551	0.798	1.05	1.29	1.23	1.03
C4	1.3	388.8	2812.5	0.551	0.799	1.12	1.36	1.22	1.03
X1	1.3	338.4	2812.5	0.551	0.770	0.91	1.14	1.26	1.03
X2	1.3	424.9	2812.5	0.551	0.769	1.14	1.62	1.43	1.04
X3	1.3	361.6	2812.5	0.551	0.776	0.98	1.22	1.24	1.03
X4	1.3	459.9	2812.5	0.551	0.775	1.25	1.79	1.43	1.04

Table 7.2 Median collapse capacity and CMR for each archetype model

Archetype ID	\hat{S}_{CT} (g)	S_{MT} (g)	CMR	SSF	ACMR
C1	0.58	0.26	2.22	1.04	2.31
C2	0.63	0.26	2.41	1.04	2.51
C3	0.60	0.26	2.30	1.03	2.36
C4	0.55	0.26	2.10	1.03	2.17
Average					2.34
X1	0.56	0.26	2.14	1.03	2.21
X2	0.53	0.26	2.03	1.04	2.11
X3	0.55	0.26	2.10	1.03	2.17
X4	0.54	0.26	2.07	1.04	2.15
Average					2.16

Table 7.3 Period-based ductility and RTR variability for each archetype model

Archetype ID	μ_T	β_{RTR}
C1	1.26	0.23
C2	1.27	0.23
C3	1.23	0.22
C4	1.21	0.22
X1	1.26	0.23
X2	1.43	0.24
X3	1.24	0.22
X4	1.43	0.24

Table 7.4 β values for various sources of uncertainty for different ratings and corresponding total uncertainty and acceptable CMR (selected rating is shown in italic)

β_{RTR}	β_{TD}		β_{MDL}		β_{DR}		β_{TOT}	ACMR10	AMCR20
	rating	value	rating	value	rating	value			
0.23	fair	0.35	fair	0.35	fair	0.35	0.65	2.30	1.73
0.23	fair	0.35	fair	0.35	poor	0.5	0.74	2.58	1.86
0.23	poor	0.5	fair	0.35	fair	0.35	0.74	2.58	1.86
<i>0.23</i>	<i>poor</i>	<i>0.5</i>	<i>fair</i>	<i>0.35</i>	<i>poor</i>	<i>0.5</i>	<i>0.82</i>	<i>2.87</i>	<i>2.00</i>
0.23	poor	0.5	poor	0.5	poor	0.5	0.90	3.17	2.13

Table 7.5 Comparison of adjusted CMR and acceptable CMR for each archetype model and performance group

Archetype ID	ACMR	ACMR10	AMCR20	Probability of collapse under MCE	Result
Performance Group No. PG-1 (chevron braced frame)					
C1	2.31		2.00	0.15	Pass
C2	2.51		2.00	0.13	Pass
C3	2.36		2.00	0.15	Pass
C4	2.17		2.00	0.17	Pass
Average	2.34	2.87		0.15	Fail
Performance Group No. PG-2 (split-X braced frame)					
X1	2.21		2.00	0.17	Pass
X2	2.11		2.00	0.18	Pass
X3	2.17		2.00	0.17	Pass
X4	2.15		2.00	0.18	Pass
Average	2.16	2.87		0.17	Fail

Table 7.6 Comparison of median collapse capacity from FEMA P695 methodology and actual collapse $Sa_{c,m}$

Archetype ID	FEMA P695 methodology		Based on individual ground motion	
	\hat{S}_{CT} (g)	CMR	$Sa_{c,m}(C_u T_a)$ (g)	CMR
Performance Group No. PG-1 (chevron braced frame)				
C1	0.58	2.22	0.61	2.32
C2	0.63	2.41	0.69	2.65
C3	0.60	2.30	0.66	2.53
C4	0.55	2.10	0.59	2.27
Average	0.59	2.26	0.64	2.44
Performance Group No. PG-2 (split-X braced frame)				
X1	0.56	2.14	0.61	2.35
X2	0.53	2.03	0.58	2.23
X3	0.55	2.10	0.64	2.44
X4	0.54	2.07	0.58	2.24
Average	0.55	2.09	0.60	2.31

Table 7.7 Comparison of collapse response under GM25 for chevron CBF models with strong beam design and different weld design strength

Model	Ground motion intensity	Location	Limit state	Time (s)	Collapse mode
C1	$S_T(C_u T_a) = 0.8g$	1-1	WF	17.49	
		1-2	WF	13.98	
		2-1	WF	16.71	
		2-2	WF	12.58	
		3-1	BB	13.28	
		3-2			
		1st story	Col	21.02	
C2	$S_T(C_u T_a) = 0.8g$	1-1	BB	13.00	
		1-2	BB	13.36	
		2-1			
		2-2			
		3-1	BB	14.66	
		3-2			
C2	$S_T(C_u T_a) = 1.1g$	1-1	BB	14.63	
			BF	16.51	
		1-2	BB	12.55	
		2-1			
		2-2	BB	12.57	
		3-1	BB	10.78	
		3-2	BB	10.34	
		1st story	Col	17.71	
BB: Brace Buckling BF: Brace Fracture Re: Brace re-engagement WF: Weld Fracture Col: Collapse					

Table 7.8 Comparison of collapse response under GM14 for chevron CBF models with weak beam design and different weld design strength

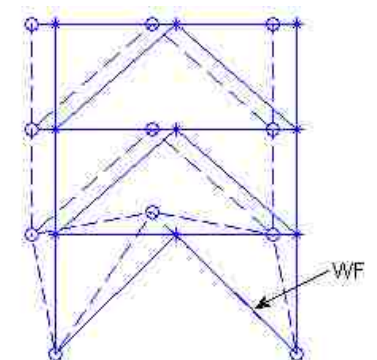
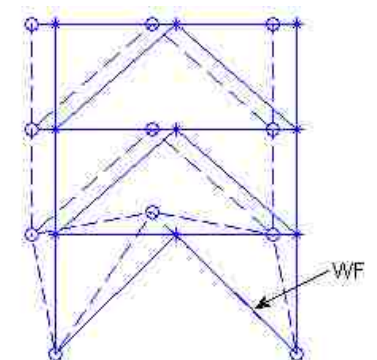
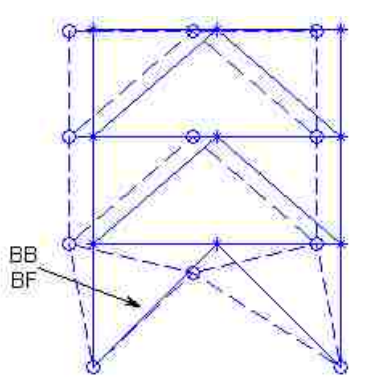
Model	Ground motion intensity	Location	Limit state	Time (s)	Collapse mode
C3	$S_T(C_u T_a) = 0.9g$	1-1	WF	10.13	
		1-2			
		2-1	WF	17.93	
		2-2	WF	16.55	
		3-1			
		3-2	BB	17.27	
C3	$S_T(C_u T_a) = 1.2g$	1-1			
		1-2	WF	9.73	
		2-1			
		2-2			
		3-1			
		3-2			
		1st story	Col	16.48	
C4	$S_T(C_u T_a) = 0.9g$	1-1	BB	10.13	
			BF	12.71	
		1-2			
		2-1			
		2-2			
		3-1			
		3-2	BB	12.8	
		1st story	Col	24.63	
BB: Brace Buckling BF: Brace Fracture Re: Brace re-engagement WF: Weld Fracture Col: Collapse					

Table 7.9 Comparison of collapse response under GM39 for split-X CBF models with different weld design strength

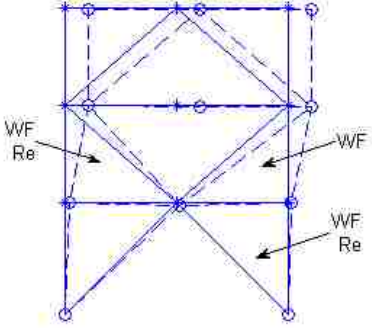
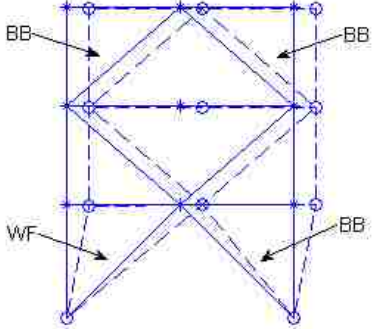
Model	Ground motion intensity	Location	Limit state	Time (s)	Collapse mode
X1	$S_T(C_u T_a) = 0.5g$	1-1			
		1-2	WF	12.2	
		2-1	WF	12.54	
		2-2	WF	12.2	
		3-1			
		3-2			
X1	$S_T(C_u T_a) = 0.6g$	1-1			
		1-2	WF	11.92	
		2-1	WF	11.89	
		2-2	WF	15.05	
		3-1			
		3-2			
		2 nd story	Col	20.71	
X2	$S_T(C_u T_a) = 0.5g$	1-1	WF	12.33	
		1-2	BB	12.21	
		2-1			
		2-2			
		3-1	BB	12.52	
		3-2	BB	12.28	
		1st story	Col	21.31	
		BB: Brace Buckling BF: Brace Fracture Re: Brace re-engagement WF: Weld Fracture Col: Collapse			

Table 7.10 Comparison of collapse response under GM21 for chevron CBF models with weak weld design and different beam design strength

Model	Ground motion intensity	Location	Limit state	Time (s)	Collapse mode
C1	$S_T(C_u T_a) = 0.5g$	1-1	WF	5.95	
		1-2	WF	4.54	
		2-1			
		2-2			
		3-1			
		3-2	BB	4.6	
		1st story	Col	9.01	
C3	$S_T(C_u T_a) = 0.5g$	1-1			
		1-2	WF	4.56	
		2-1			
		2-2			
		3-1			
		3-2	BB	4.63	
C3	$S_T(C_u T_a) = 0.7g$	1-1	WF	4.31	
		1-2			
		2-1	WF	5.03	
		2-2			
		3-1			
		3-2			
		1st story	Col	15.24	
BB: Brace Buckling BF: Brace Fracture Re: Brace re-engagement WF: Weld Fracture Col: Collapse					

Table 7.11 Comparison of collapse response under GM18 for chevron CBF models with strong weld design and different beam design strength

Model	Ground motion intensity	Location	Limit state	Time (s)	Collapse mode
C2	$S_T(C_u T_a) = 0.9g$	1-1	BB	6.64	
			BF	10.5	
		1-2	BB	6.9	
		2-1	BB	9.14	
		2-2			
		3-1	BB	6.49	
3-2	BB	6.2			
C2	$S_T(C_u T_a) = 1.1g$	1-1	BB	6.6	
			BF	11.08	
		1-2	BB	6.05	
		2-1			
		2-2	BB	8.23	
		3-1	BB	9.01	
		3-2	BB	6.22	
1st story	Col	11.57			
C4	$S_T(C_u T_a) = 0.9g$	1-1	BB	6.59	
			BF	10.18	
		1-2			
		2-1			
		2-2			
		3-1			
		3-2	BB	6.24	
1st story	Col	13.73			
BB: Brace Buckling BF: Brace Fracture Re: Brace re-engagement WF: Weld Fracture Col: Collapse					

Table 7.12 Comparison of collapse response under GM16 for split-X CBF models with different beam design strength

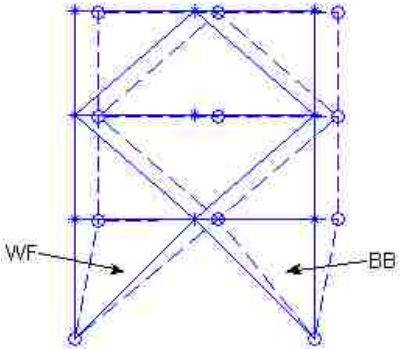
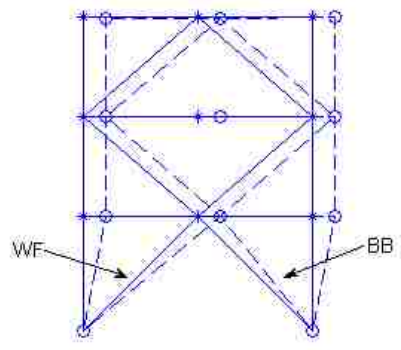
Model	Ground motion intensity	Location	Limit state	Time (s)	Collapse mode
X2	$S_T(C_u T_a) = 0.4g$	1-1	WF	7.81	
		1-2	BB	7.69	
		2-1			
		2-2			
		3-1			
		3-2			
		1st story	Col	29.78	
X4	$S_T(C_u T_a) = 0.4g$	1-1	WF	7.82	
		1-2	BB	7.7	
		2-1			
		2-2			
		3-1			
		3-2			
		1st story	Col	29.89	
BB: Brace Buckling BF: Brace Fracture Re: Brace re-engagement WF: Weld Fracture Col: Collapse					

Table 7.13 Comparison of collapse behavior under GM19 for models with weak weld design and different brace configuration

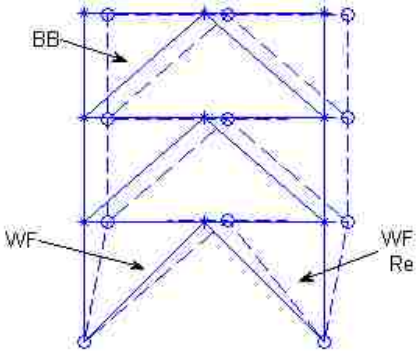
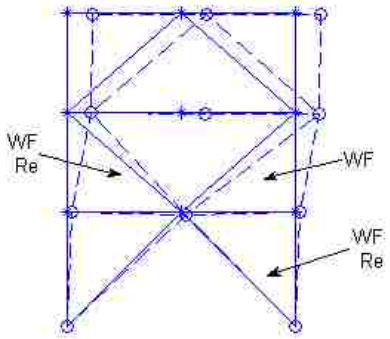
Model	Ground motion intensity	Location	Limit state	Time (s)	Collapse mode
C1	$S_T(C_u T_a) = 0.7g$	1-1	WF	4.62	
		1-2	WF	4.96	
		2-1			
		2-2			
		3-1	BB	4.68	
		3-2			
		1st story	Col	13.76	
X1	$S_T(C_u T_a) = 0.7g$	1-1			
		1-2	WF	4.64	
		2-1	WF	5.12	
		2-2	WF	4.64	
		3-1			
		3-2			
		1st story	Col	18	
BB: Brace Buckling BF: Brace Fracture Re: Brace re-engagement WF: Weld Fracture Col: Collapse					

Table 7.14 Comparison of collapse behavior under GM23 for models with strong weld design and different brace configuration

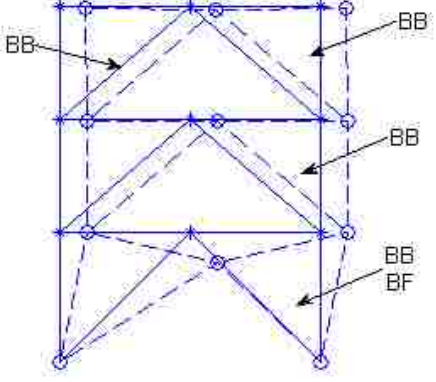
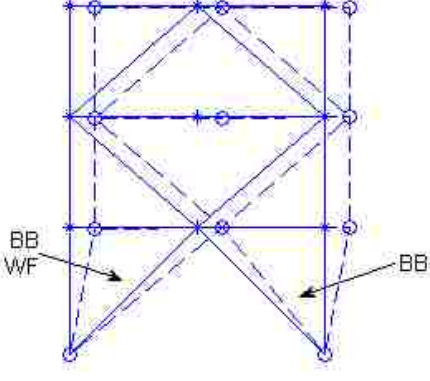
Model	Ground motion intensity	Location	Limit state	Time (s)	Collapse mode
C2	$S_T(C_u T_a) = 0.5g$	1-1	BB	4.77	
		1-2	BB	8.69	
		2-1	BB	6.57	
		2-2	BB	5.18	
		3-1	BB	4.67	
		3-2	BB	8.71	
C2	$S_T(C_u T_a) = 0.7g$	1-1			
		1-2	BB	5.17	
			BF	7.28	
		2-1			
		2-2	BB	5.2	
		3-1	BB	4.04	
		3-2	BB	3.48	
		1st story	Col	11.11	
X2	$S_T(C_u T_a) = 0.5g$	1-1	BB	4.76	
			WF	5.34	
		1-2	BB	5.23	
		2-1			
		2-2			
		3-1			
		3-2			
		1st story	Col	15.69	
BB: Brace Buckling BF: Brace Fracture Re: Brace re-engagement WF: Weld Fracture Col: Collapse					

Table 7.15 Comparison of collapse capacity from IDA using ECUS GM set and FEMA GM set and from FEMA P695 methodology

Archetype ID	ECUS		FEMA			
	$Sa_{c,m}(1s)$ (g)	CMR	$Sa_{c,m}(1s)$ (g)	CMR	SSF	ACMR
Performance Group No. PG-1 (chevron braced frame)						
C1	0.38	2.61	0.34	2.39	1.04	2.49
C2	0.44	3.08	0.37	2.54	1.04	2.64
C3	0.47	3.25	0.37	2.56	1.03	2.64
C4	0.43	3.02	0.35	2.44	1.03	2.51
Average	0.43	2.99	0.36	2.48		2.57
Performance Group No. PG-2 (split-X braced frame)						
X1	0.42	2.93	0.35	2.41	1.03	2.48
X2	0.40	2.74	0.33	2.30	1.04	2.39
X3	0.44	3.06	0.37	2.59	1.03	2.67
X4	0.43	2.97	0.35	2.42	1.04	2.52
Average	0.42	2.92	0.35	2.43		2.51

Table 7.16 Comparison of $\sigma_{\ln(Sa_c)}$ from IDA result for ECUS GM set and FEMA GM set and β_{RTR} from FEMA P695 methodology

Archetype ID	ECUS	FEMA	
	$\sigma_{\ln(Sa_c)}$	$\sigma_{\ln(Sa_c)}$	β_{RTR} according to FEMA P695 methodology
Performance Group No. PG-1 (chevron braced frame)			
C1	0.42	0.36	0.23
C2	0.37	0.27	0.23
C3	0.54	0.44	0.22
C4	0.50	0.29	0.22
Performance Group No. PG-2 (split-X braced frame)			
X1	0.38	0.35	0.23
X2	0.40	0.29	0.24
X3	0.40	0.39	0.22
X4	0.41	0.33	0.24

Table 7.17 Effect of brace re-engagement

Archetype Model	Modeling brace re-engagement	$Sa_{c,m}(1s)$ (g)
C1	yes	0.38
C1	no	0.39
C3	yes	0.47
C3	no	0.43

Table 7.18 Effect of beam strength deterioration

Model	$Sa_{c,m}(1s)$ (g)	
	CPH	Fiber
C1	0.38	0.41
C2	0.44	0.47
C3	0.47	0.47
C4	0.43	0.44

Table 7.19 Effect of gravity system modeling

Gravity system model	$Sa_{c,m}(1s)$ (g)
i	0.38
ii	0.52
iii	0.51
iv	0.71

Table 7.20 Variation of uncertain model parameters for sensitivity study

Uncertain model parameter	Physical meaning	Median	Upper value	Lower value
R_c	Brace weld connection strength	$1.45R_n$	$2.64R_n$	$0.80R_n$
ε_0	Brace low cycle fatigue (LCF) strength	ε_0	$1.82\varepsilon_0$	$0.55\varepsilon_0$
F_{re}	Brace re-engagement strength	$0.27P_y$	$0.38P_y$	$0.16P_y$
e/L	Brace initial imperfection	1/1500	1/1000	1/5000
$F_{y_{br}}$	Brace yield strength	$1.3F_y$	$1.51F_y$	F_y
<p>Notes;</p> <p>4. R_n is the nominal strength of the fillet weld connection from Eq. (4.4);</p> <p>5. P_y is the nominal yield strength of the brace cross section;</p> <p>6. ε_0 is from Eq. (4.28)</p>				

Table 7.21 Median collapse capacity of model C1 using different modeling approaches

Modeling approach	Inclusion of brace re-engagement	Beam modeling	Gravity system modeling	$Sa_{c,m}(1s)$ (g)
MA1 (baseline model)	Yes	CPH	i	0.38
MA2	No	CPH	i	0.39
MA3	Yes	Fiber	i	0.41
MA4	Yes	CPH	ii	0.52
MA5	Yes	CPH	iii	0.51
MA6	Yes	CPH	iv	0.71

Table 7.22 Summary of FEMA P695 methodology with variations

Variation	GM set	Median collapse capacity	RTR variability	Lateral resistance from gravity load system	MCE hazard intensity
Original	FEMA	$\hat{S}_{CT} = S_T(C_u T_a)$ when 22 ground motions caused collapse	β_{RTR} from Eq. (6.6)	no	ASCE MCE spectrum at $C_u T_a$
Mod 1	FEMA	$S_{a_{c,m}}(C_u T_a)$	β_{RTR} from Eq. (6.6)	no	ASCE MCE spectrum at $C_u T_a$
Mod 2	ECUS	$S_{a_{c,m}}(1s)$	$\beta_{RTR_{Sa}}$ from Eq. (6.8)	no	ASCE MCE spectrum at 1s
Mod 3	ECUS	$S_{a_{c,m,MCS}}(1s)$	$\beta_{RTR_{Sa}}$ from Eq. (6.8)	no	ASCE MCE spectrum at 1s
Mod 4	ECUS	$S_{a_{c,m}}(1s)$	$\beta_{RTR_{Sa}}$ from Eq. (6.8)	Yes	ASCE MCE spectrum at 1s
Mod 5	ECUS	$S_{a_{c,m}}(1s)$	$\beta_{RTR_{Sa}}$ from Eq. (6.8)	no	Median $S_a(1s)$ from ECUS GM set

Table 7.23 Median collapse capacity and ACMR for each archetype model using Mod1 variation of FEMA P695 methodology

Archetype ID	$Sa_{c,m}(C_u T_a)$ (g)	S_{MT} (g)	CMR ¹	SSF	ACMR
C1	0.61	0.26	2.32	1.04	2.41
C2	0.69	0.26	2.65	1.04	2.75
C3	0.66	0.26	2.53	1.03	2.61
C4	0.59	0.26	2.27	1.03	2.34
Average					2.53
X1	0.61	0.26	2.35	1.03	2.42
X2	0.58	0.26	2.23	1.04	2.32
X3	0.64	0.26	2.44	1.03	2.51
X4	0.58	0.26	2.24	1.04	2.33
Average					2.39
Note:					
1. $CMR = Sa_{c,m}(C_u T_a)/S_{MT}$					

Table 7.24 Performance evaluation for each archetype model using Mod1 variation of FEMA P695 methodology

Archetype ID	ACMR	ACMR10 ¹	AMCR20 ¹	Probability of collapse under MCE	Result
Performance Group No. PG-1 (chevron braced frame)					
C1	2.41		2	0.14	Pass
C2	2.75		2	0.11	Pass
C3	2.61		2	0.12	Pass
C4	2.34		2	0.15	Pass
Average	2.53	2.87		0.13	Fail
Performance Group No. PG-2 (split-X braced frame)					
X1	2.42		2	0.14	Pass
X2	2.32		2	0.15	Pass
X3	2.51		2	0.13	Pass
X4	2.33		2	0.15	Pass
Average	2.39	2.87		0.14	Fail
Note:					
1. ACMR10 and ACMR20 based on β_{TOT} calculated according to the original FEMA P695 methodology as shown in Table 7.4.					

Table 7.25 Summary of IDA result for each archetype model using Mod2 variation of FEMA P695 methodology

Archetype ID	$Sa_{c,m}(1s)$ (g)	S_{M1} (g)	CMR ¹	$\beta_{RTR_{Sa}}$	β_{TOT}^2
C1	0.38	0.14	2.61	0.42	0.89
C2	0.44	0.14	3.08	0.37	0.87
C3	0.47	0.14	3.25	0.54	0.96
C4	0.43	0.14	3.02	0.50	0.93
Average			2.99		0.91
X1	0.42	0.14	2.93	0.38	0.88
X2	0.40	0.14	2.74	0.40	0.89
X3	0.44	0.14	3.06	0.40	0.88
X4	0.43	0.14	2.97	0.41	0.89
Average			2.92		0.88

Note:
 1. $CMR = Sa_{c,m}(1s)/S_{M1}$
 2. β_{TOT} calculated using Eq. (6.3) in which β_{RTR} has the value from this table and the other β values are from the quality rating results described in section 7.2 (Table 7.4)

Table 7.26 Performance evaluation for each archetype model using Mod2 variation of FEMA P695 methodology

Archetype ID	CMR (AMCR ¹)	ACMR10 ²	AMCR20 ²	Probability of collapse under MCE	Result
Performance Group No. PG-1 (chevron braced frame)					
C1	2.61		2.12	0.14	Pass
C2	3.08		2.08	0.10	Pass
C3	3.25		2.24	0.11	Pass
C4	3.02		2.19	0.12	Pass
Average	2.99	3.23		0.12	Fail
Performance Group No. PG-2 (split-X braced frame)					
X1	2.93		2.09	0.11	Pass
X2	2.74		2.11	0.13	Pass
X3	3.06		2.11	0.10	Pass
X4	2.97		2.11	0.11	Pass
Average	2.92	3.10		0.11	Fail

Note:
 1. $CMR=AMCR$ in this case as the ECUS GM set considers the spectral shape effect
 2. $ACMR10$ and $ACMR20$ based on β_{TOT} from Table 7.25.

Table 7.27 Summary of IDA result for archetype model C1 and C2 using Mod3 variation of FEMA P695 methodology

Archetype ID	$Sa_{c,m,MCS}(1s)$ (g)	S_{M1} (g)	CMR ¹	β_{RTR_Sa}	β_{TOT} ²
C1	0.44	0.14	3.03	0.42	0.89
C2	0.47	0.14	3.23	0.37	0.87
Average			3.13		0.91 ³

Note:

1. $CMR = Sa_{c,m,MCS}(1s)/S_{M1}$
2. β_{TOT} calculated using Eq. (6.3) in which β_{RTR} has the value from this table and the other β values are determined from the quality rating results described in section 7.2 (Table 7.4)
3. Average β_{TOT} considering a complete performance group (C1, C2, C3 and C4) from Table 7.25.

Table 7.28 Performance evaluation for archetype model C1 and C2 using Mod3 variation of FEMA P695 methodology

Archetype ID	CMR (AMCR ¹)	ACMR10 ²	AMCR20 ²	Probability of collapse under MCE	Result
Performance Group No. PG-1 (chevron braced frame)					
C1	3.03		2.12	0.11	Pass
C2	3.23		2.08	0.09	Pass
Average	3.13	3.23 ³		0.10	Unknown

Note:

1. CMR=AMCR in this case as the ECUS GM set already considers the spectral shape effect
2. ACMR10 and ACMR20 based on β_{TOT} from Table 7.27.
3. ACMR10 corresponds to a complete performance group (C1, C2, C3 and C4) from Table 7.26.

Table 7.29 Summary of IDA result for archetype model C1 using Mod4 variation of FEMA P695 methodology

Gravity load system model	$Sa_{c,m}(1s)$ (g)	S_{M1} (g)	CMR ¹	$\beta_{RTR_{Sa}}$	β_{TOT} ²
i, LOC hinge	0.38	0.14	2.61	0.42	0.89
ii, LOC continuous	0.52	0.14	3.63	0.47	0.92
iii, LOC fiber	0.51	0.14	3.55	0.47	0.92
iv, Full	0.71	0.14	4.95	0.56	0.97

Note:

1. $CMR = Sa_{c,m}(1s)/S_{M1}$
2. β_{TOT} calculated using Eq. (6.3) in which β_{RTR} has the value from this table and the other β values are determined from the quality rating results described in section 7.2 (Table 7.4)

Table 7.30 Performance evaluation for each archetype model C1 using Mod4 variation of FEMA P695 methodology

Gravity load system model	CMR (AMCR ¹)	ACMR10 ²	AMCR20 ³	Probability of collapse under MCE
i, LOC hinge	2.61	3.23	2.12	0.14
ii, LOC continuous	3.63	3.23	2.17	0.08
iii, LOC fiber	3.55	3.23	2.16	0.08
iv, Full	4.95	3.23	2.26	0.05

Note:

1. CMR=AMCR in this case as the ECUS GM set already considers the spectral shape effect
2. ACMR10 corresponds to a complete performance group (C1, C2, C3 and C4) from Table 7.26.
3. ACMR20 based on β_{TOT} from Table 7.29.

Table 7.31 Summary of IDA result for each archetype model using Mod5 variation of FEMA P695 methodology

Archetype ID	$Sa_{c,m}(1s)$ (g)	S_{M1}^1 (g)	CMR ²	$\beta_{RTR_{Sa}}$	β_{TOT}^3
C1	0.38	0.07	5.78	0.42	0.89
C2	0.44	0.07	6.82	0.37	0.87
C3	0.47	0.07	7.20	0.54	0.96
C4	0.43	0.07	6.68	0.50	0.93
Average			6.62		0.91
X1	0.42	0.07	6.48	0.38	0.88
X2	0.40	0.07	6.08	0.40	0.89
X3	0.44	0.07	6.77	0.40	0.88
X4	0.43	0.07	6.59	0.41	0.89
Average			6.48		0.88

Note:

1. S_{M1} from median spectrum of ECUS GM set (Chapter 5) at 1s
2. $CMR = Sa_{c,m}(1s)/S_{M1}$
3. β_{TOT} calculated using Eq. (6.3) in which β_{RTR} has the value from this table and the other β values are determined from quality rating results described in Table 7.4

Table 7.32 Performance evaluation for each archetype model using Mod5 variation of FEMA P695 methodology

Archetype ID	CMR (AMCR ¹)	ACMR10 ²	AMCR20 ²	Probability of collapse under MCE	Result
Performance Group No. PG-1 (chevron braced frame)					
C1	5.78		2.12	0.02	Pass
C2	6.82		2.08	0.01	Pass
C3	7.20		2.24	0.02	Pass
C4	6.68		2.19	0.02	Pass
Average	6.62	3.23		0.02	Pass
Performance Group No. PG-2 (split-X braced frame)					
X1	6.48		2.09	0.02	Pass
X2	6.08		2.11	0.02	Pass
X3	6.77		2.11	0.02	Pass
X4	6.59		2.11	0.02	Pass
Average	6.48	3.10		0.02	Pass

Note:

1. CMR=AMCR in this case as the ECUS GM set already considers the spectral shape effect
2. ACMR10 and ACMR20 based on β_{TOT} from Table 7.31.

Table 7.33 Summary of performance evaluation result using different variations of FEMA P695 methodology

Variation	Result	
	Individual ($P_c < 20\%$)	Performance group ($P_c < 10\%$)
Original	Pass	Fail
Mod 1	Pass	Fail
Mod 2	Pass	Fail
Mod 3	Pass	Unknown ¹
Mod 4	Pass	Likely to pass ²
Mod 5	Pass	Pass

Note:

1. MCS not performed for each archetype model; average CMR for the entire performance group of chevron CBF cannot be obtained; average CMR for model C1 and C2 smaller than ACMR10 for the entire group
2. Large margin between CMR and ACMR10 for model C1 due to including the lateral resistance of gravity load system.

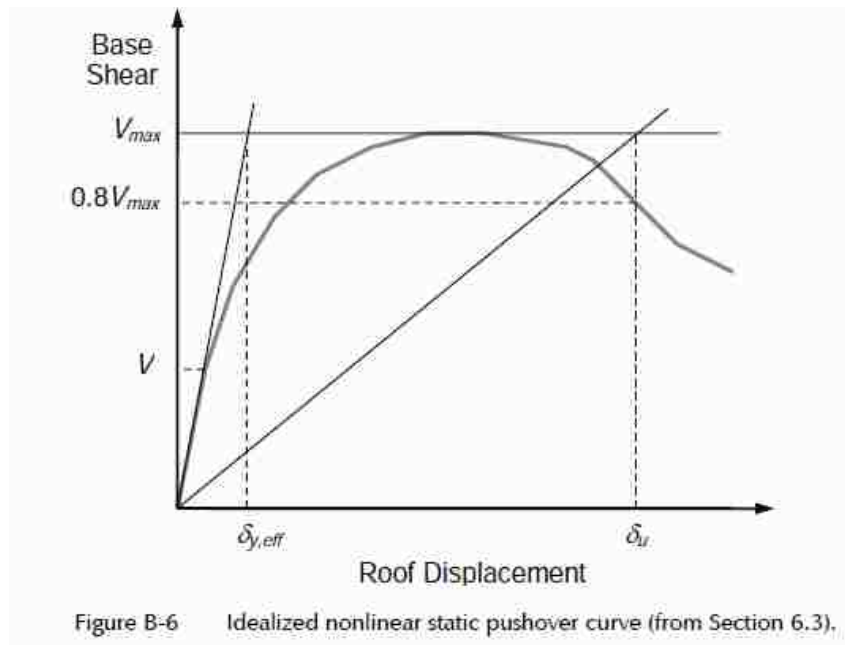


Figure 7.1 Idealized pushover curve and definition of δ_u according to 80% base shear reduction rule (FEMA 2009)

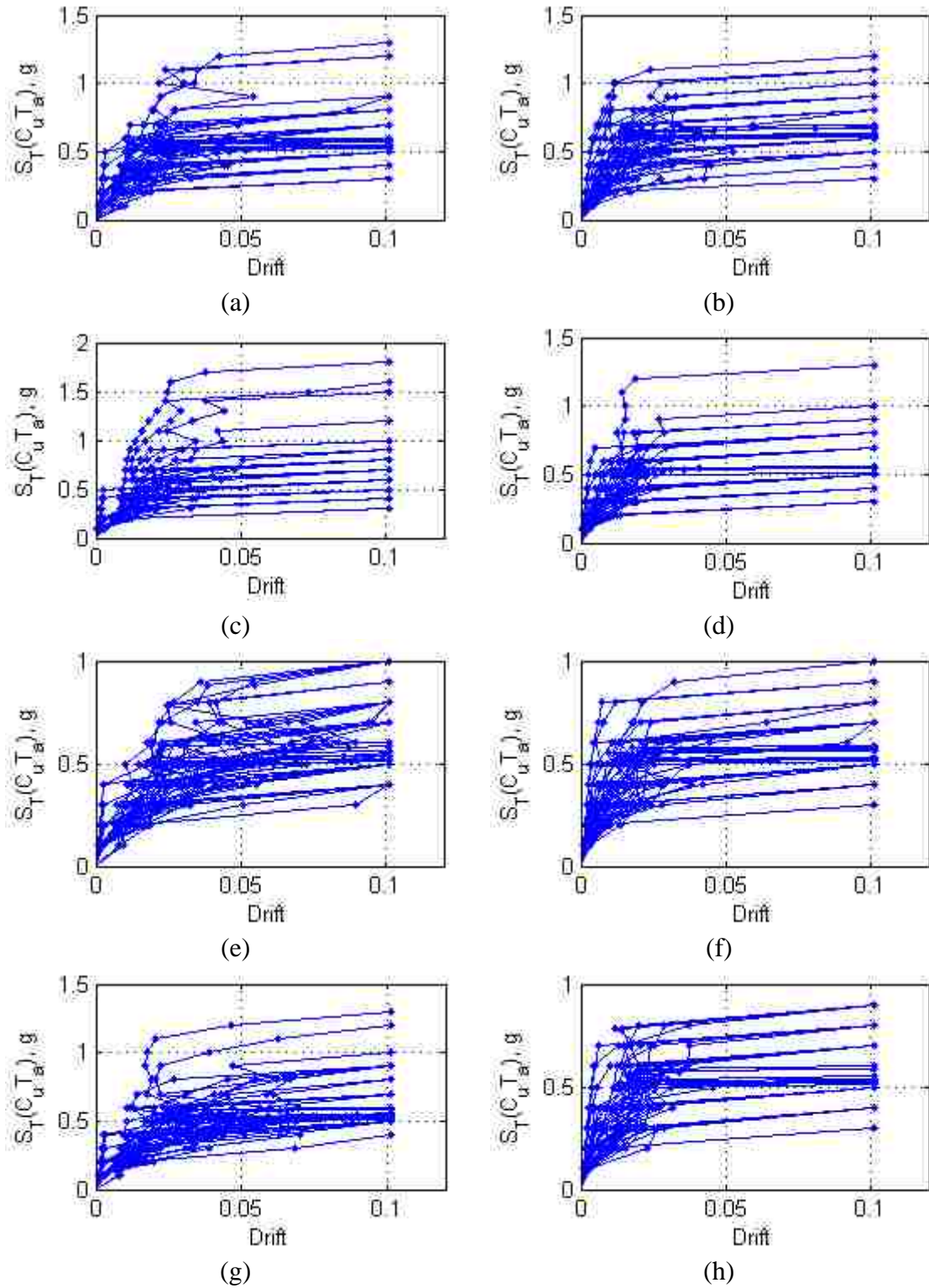
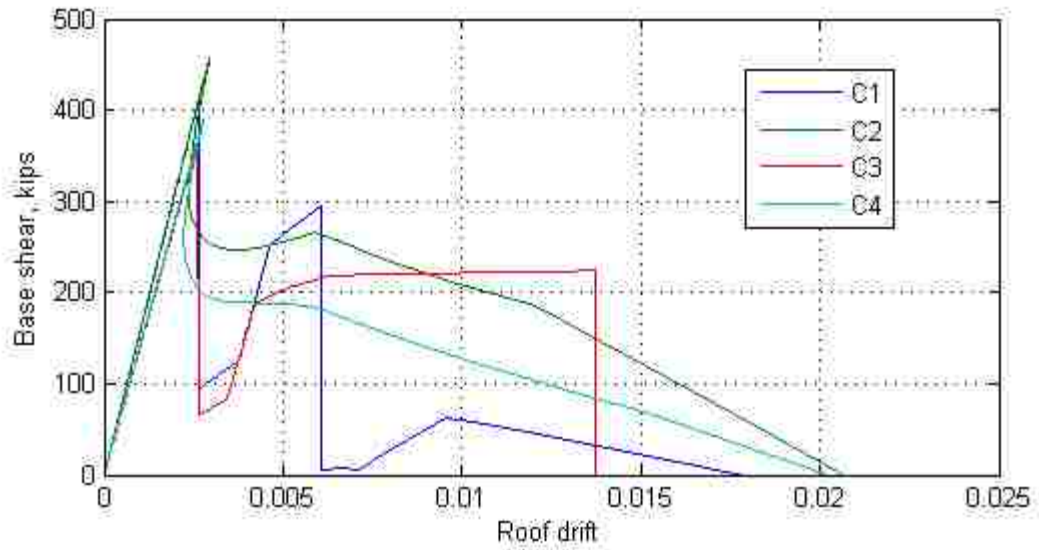
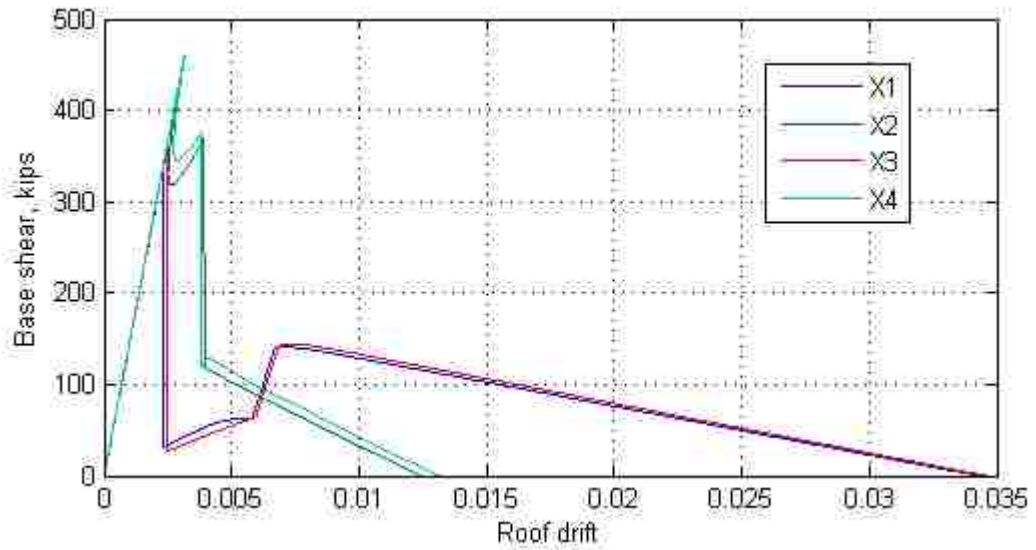


Figure 7.2 IDA results using PGV scaling method for archetype models: (a) C1; (b) C2; (c) C3; (d) C4; (e) X1; (f) X2; (g) X3; (h) X4



(a)



(b)

Figure 7.3 Pushover analysis results for: (a) archetype models with chevron bracing and (b) archetype models with split-X bracing

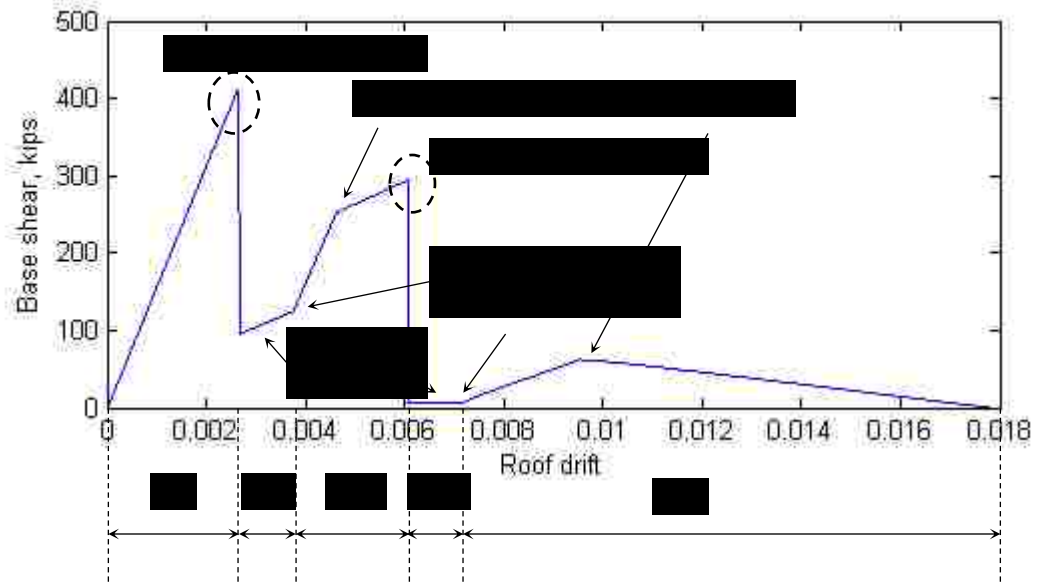


Figure 7.5 Pushover response for model C1

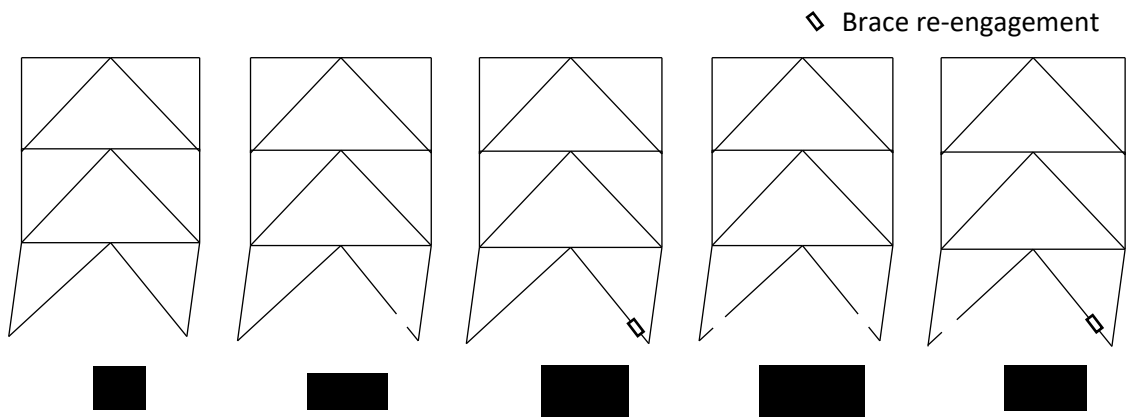


Figure 7.6 Stages of pushover response for model C1

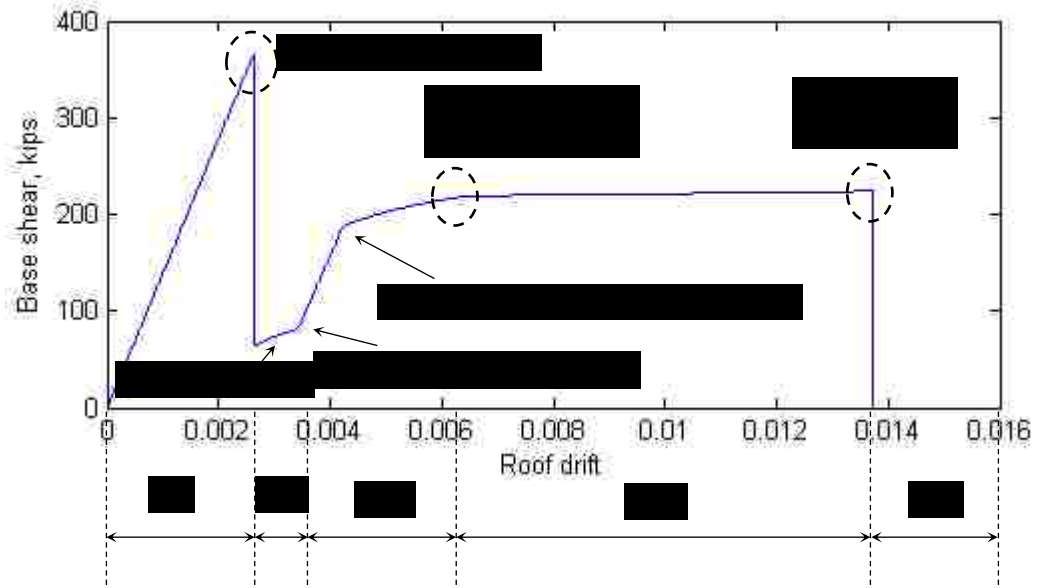


Figure 7.7 Pushover response for model C3

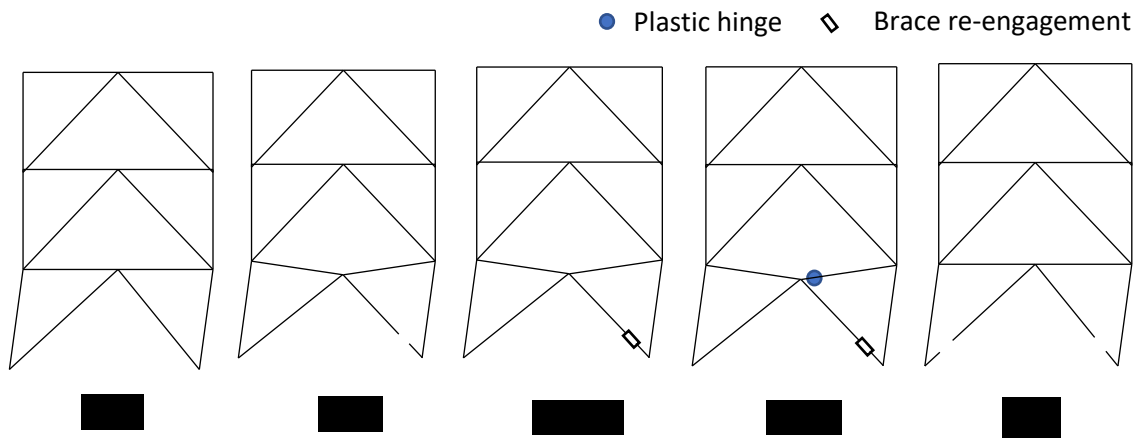


Figure 7.8 Stages of pushover response for model C3

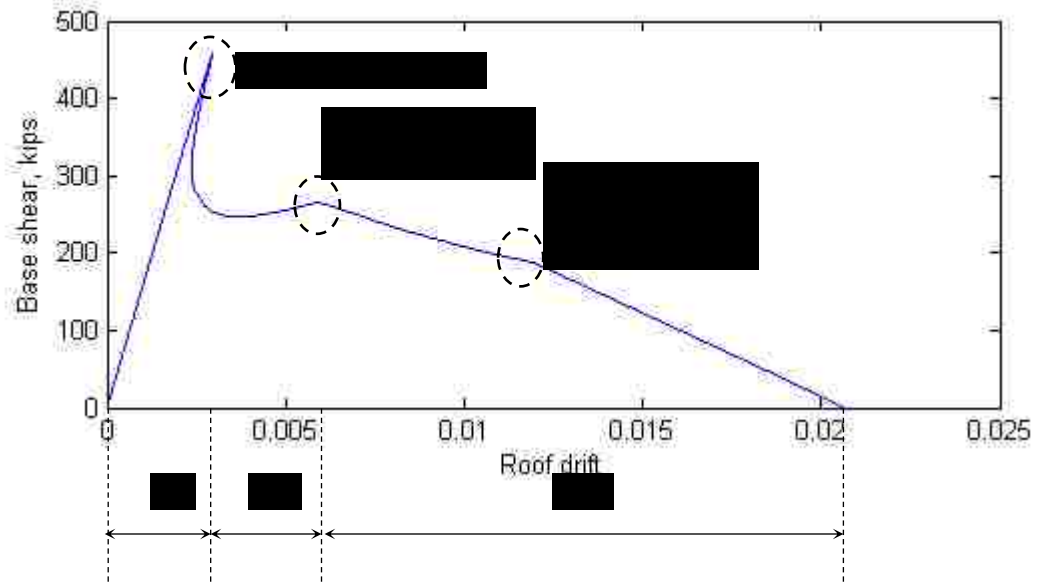


Figure 7.9 Pushover response for model C2

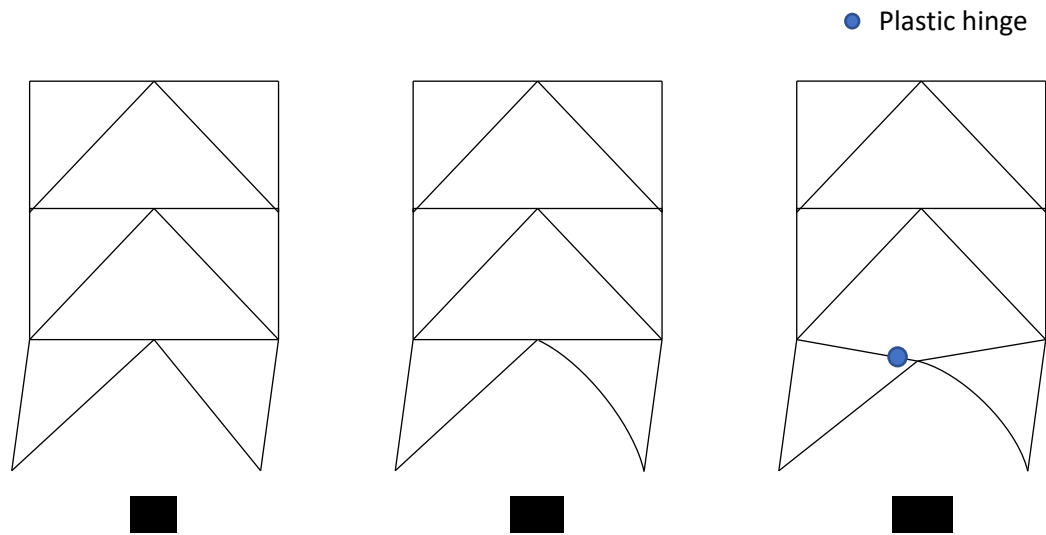


Figure 7.10 Stages of pushover response for model C2

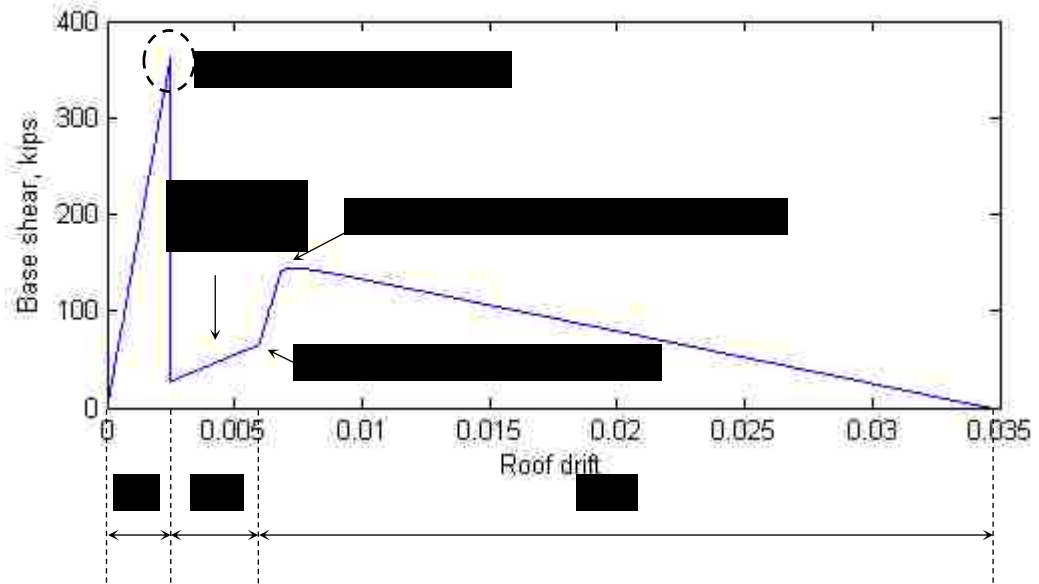


Figure 7.11 Pushover response for model X3

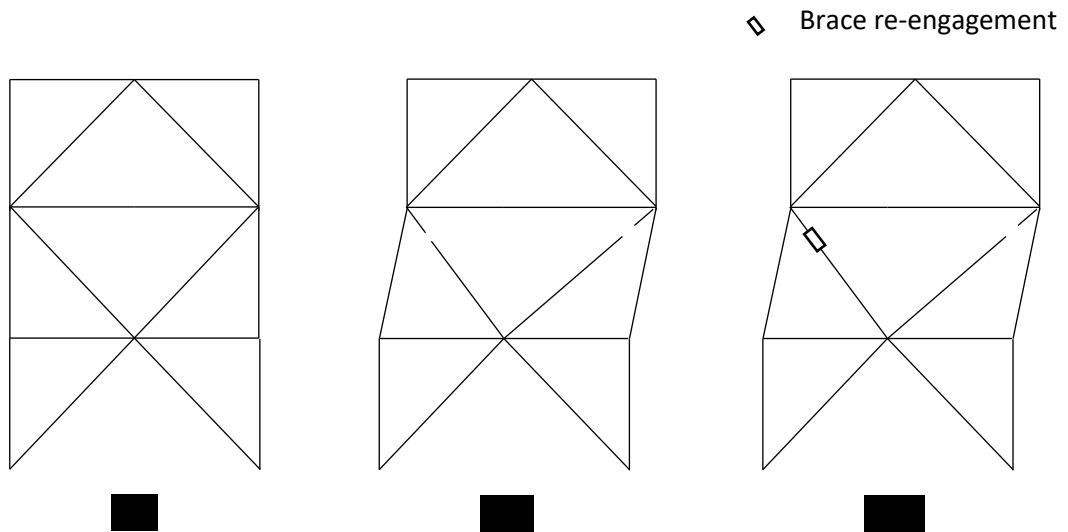


Figure 7.12 Stages of pushover response for model X3

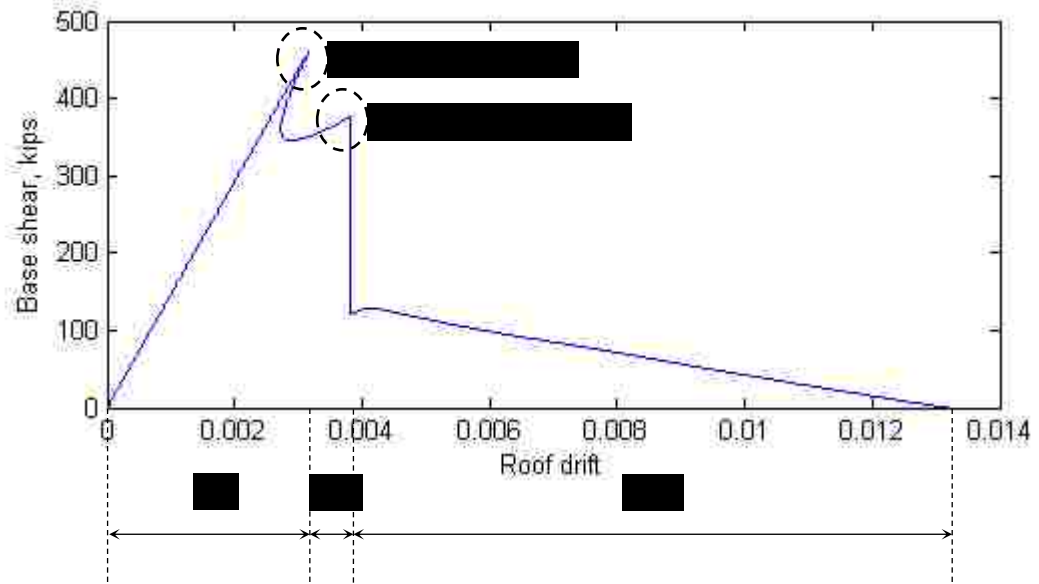


Figure 7.13 Pushover response for model X4

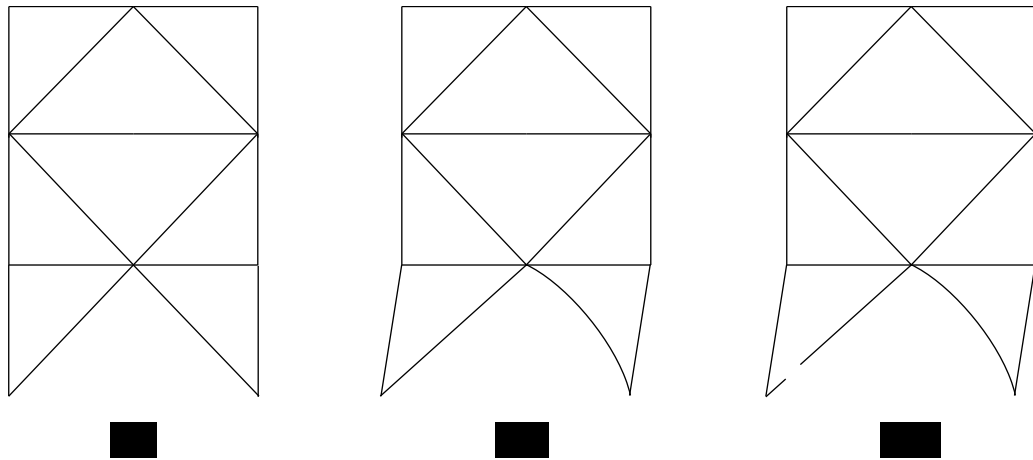


Figure 7.14 Stages of pushover response for model X4

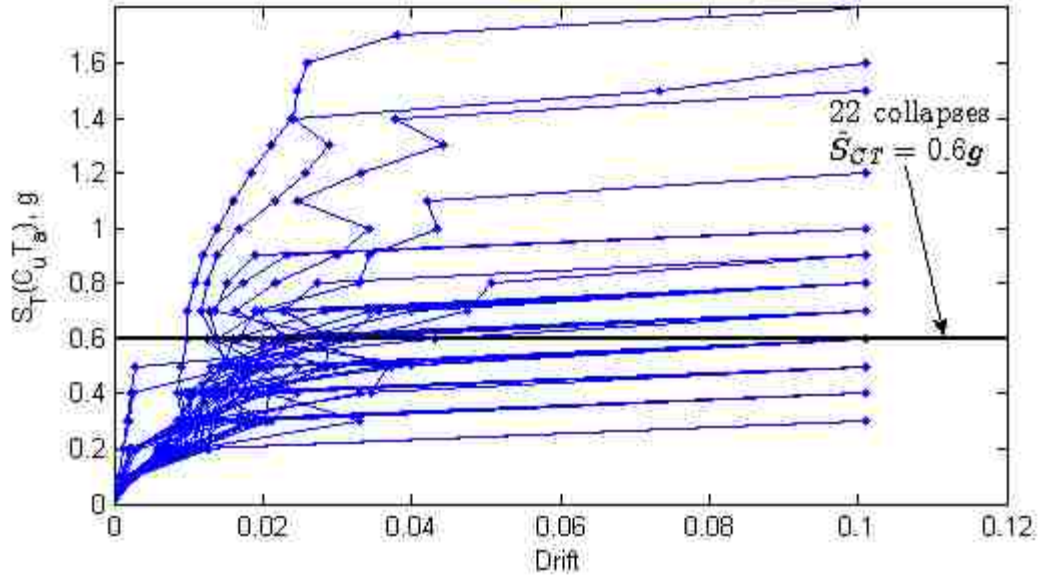


Figure 7.15 IDA result of C3 model ($\hat{S}_{CR} = 0.6g$ according to FEMA P695 methodology)

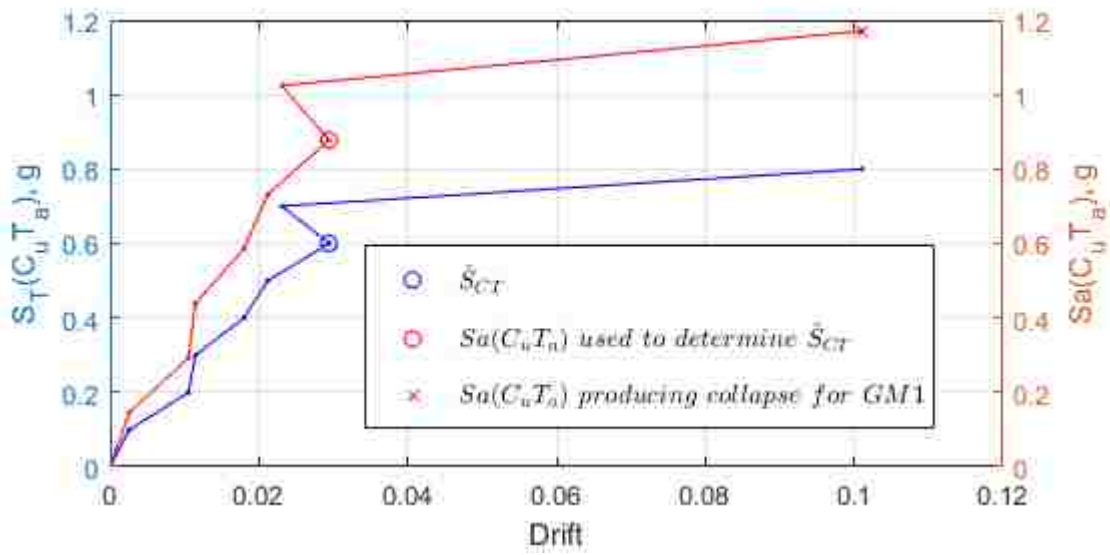


Figure 7.16 Median spectral acceleration for ground motion set $S_T(C_u T_a)$ vs. $Sa(C_u T_a)$ using IDA result for model C3 under GM1

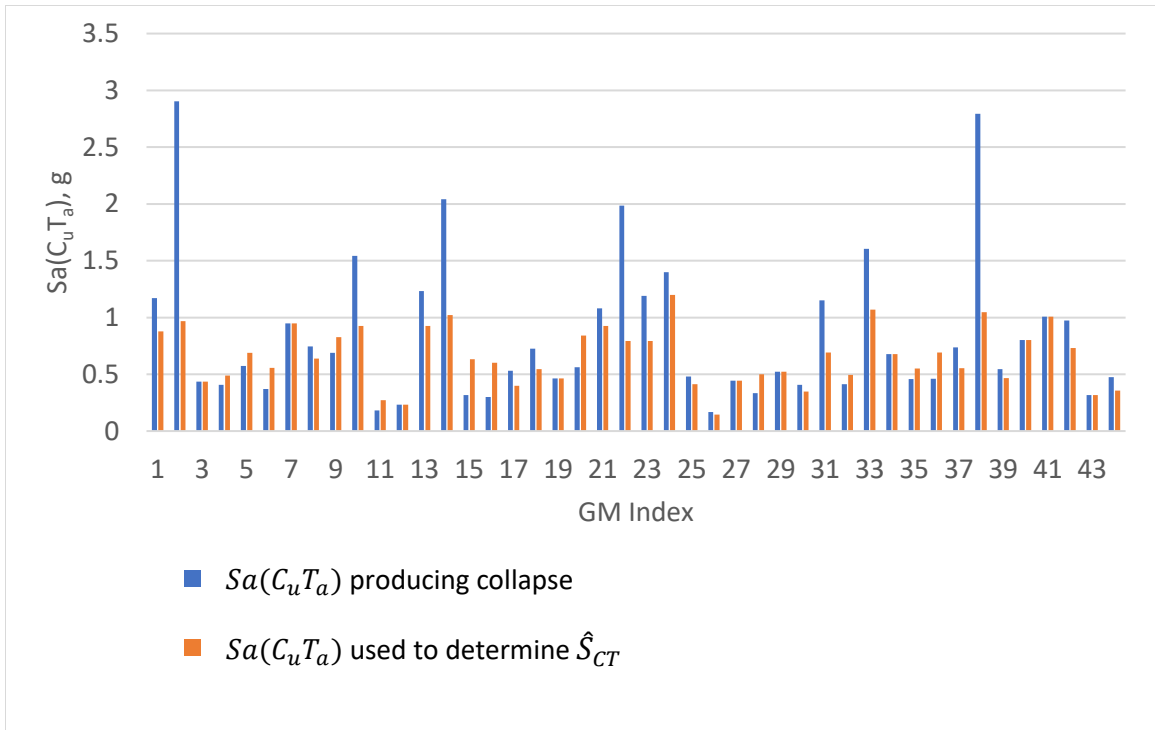
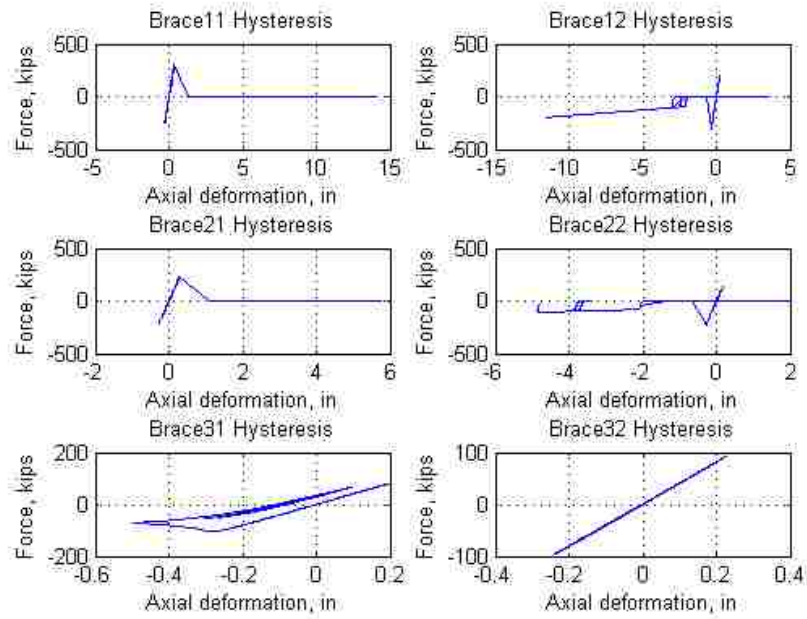
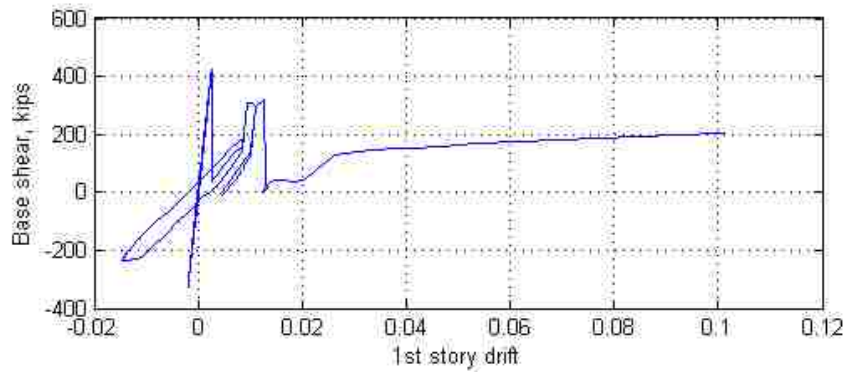


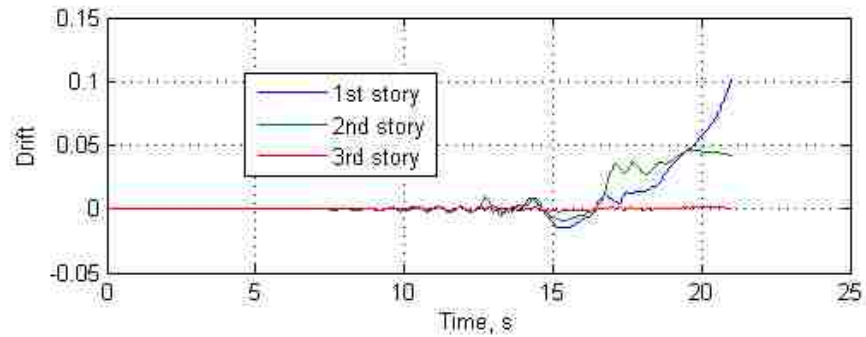
Figure 7.17 Comparison of $Sa(C_u T_a)$ causing collapse for each ground motion with $Sa(C_u T_a)$ for each ground motion used to calculate \hat{S}_{CT} using IDA results for model C3



(a)

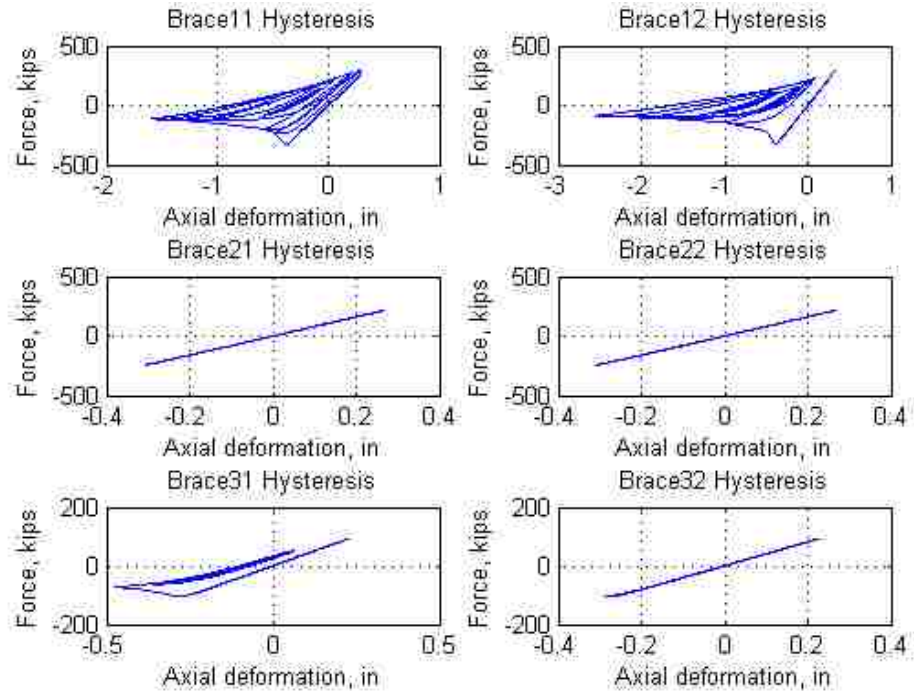


(b)

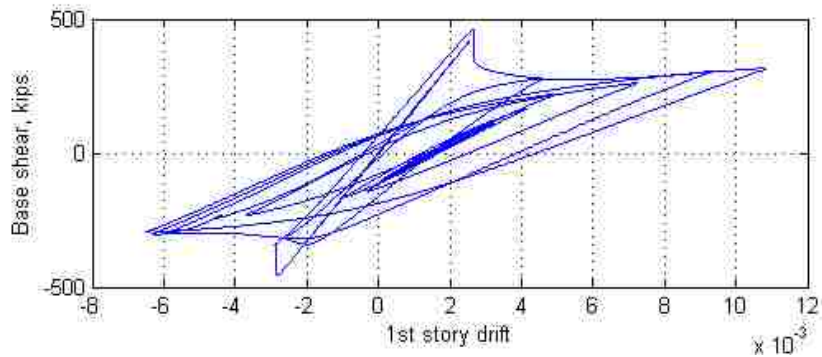


(c)

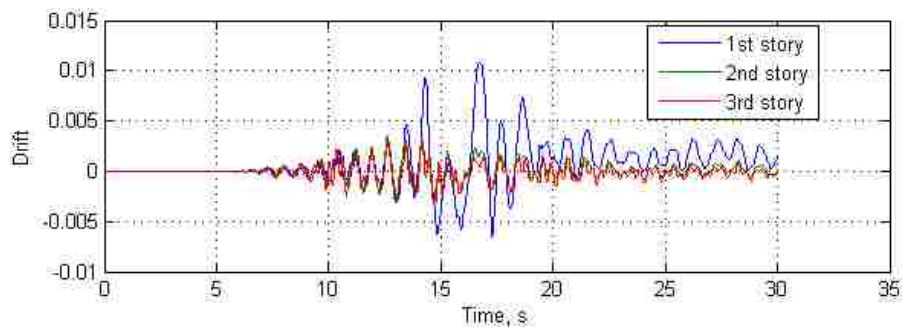
Figure 7.18 Response of archetype model C1 for GM25 at $S_T(C_u T_a) = 0.8g$: (a) brace hysteresis; (b) first story hysteresis; (c) drift history



(a)

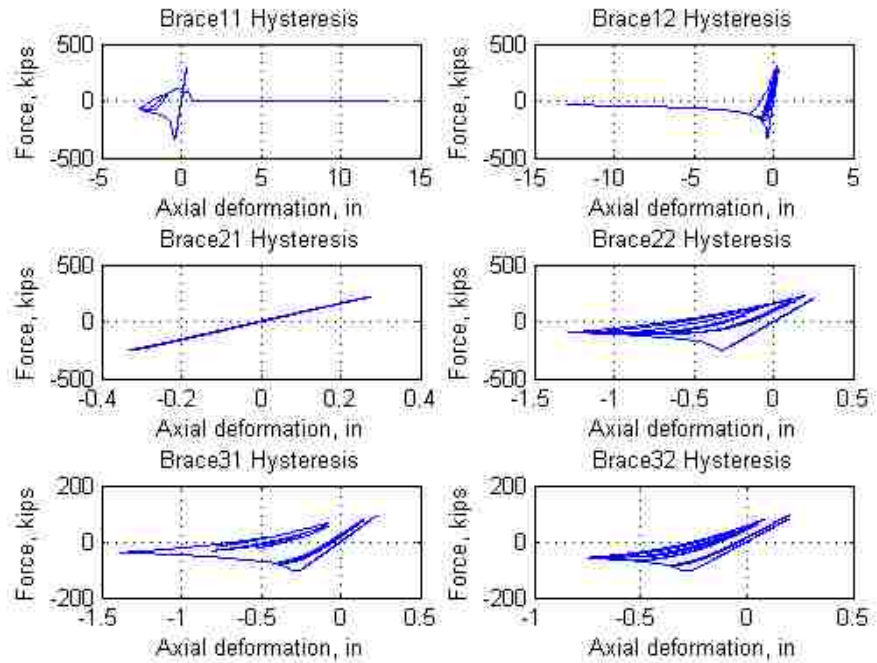


(b)

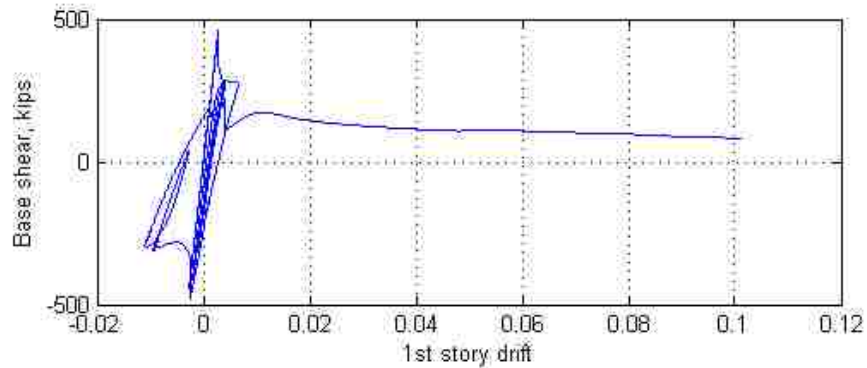


(c)

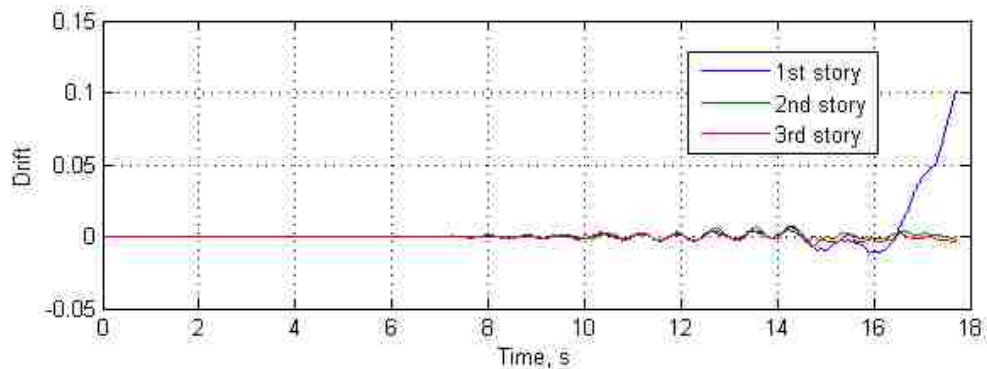
Figure 7.19 Response of archetype model C2 for GM25 at $S_T(C_u T_a) = 0.8g$: (a) brace hysteresis; (b) first story hysteresis; (c) drift history



(a)

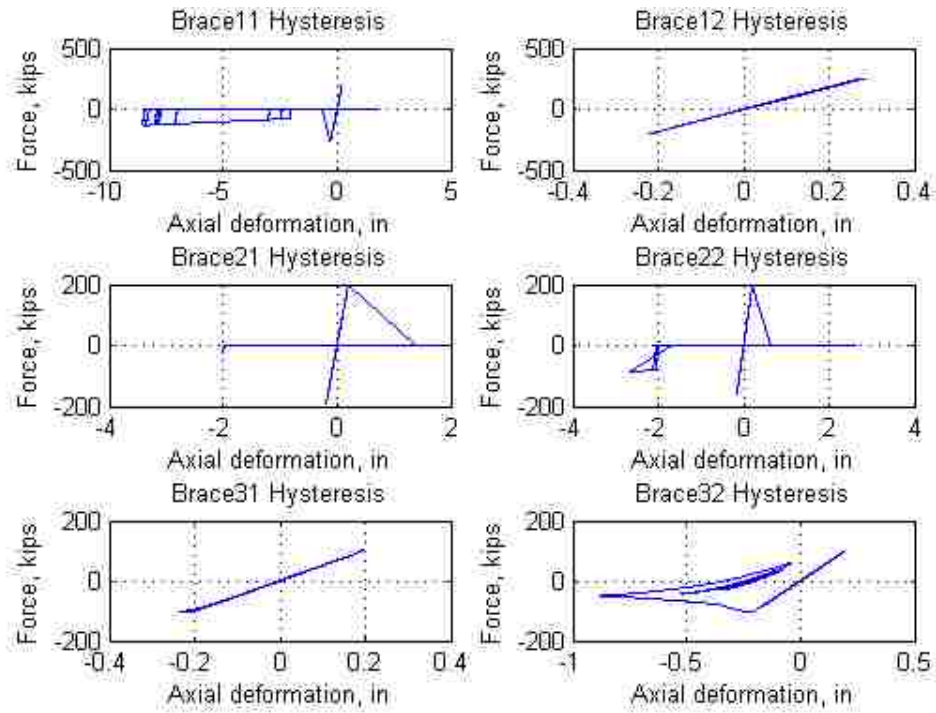


(b)

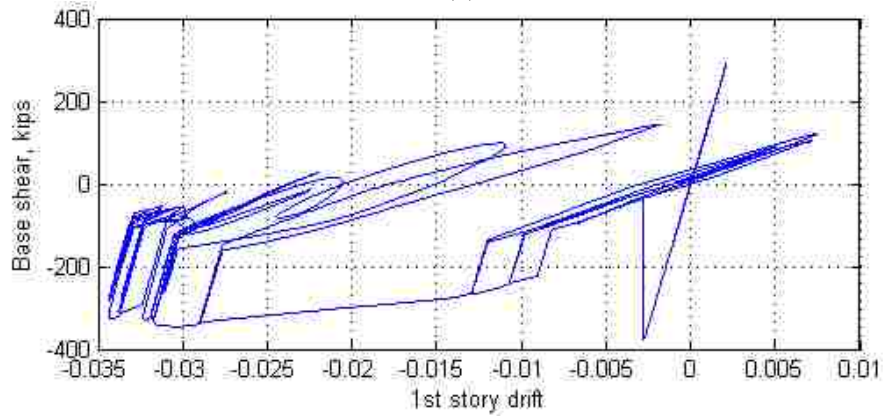


(c)

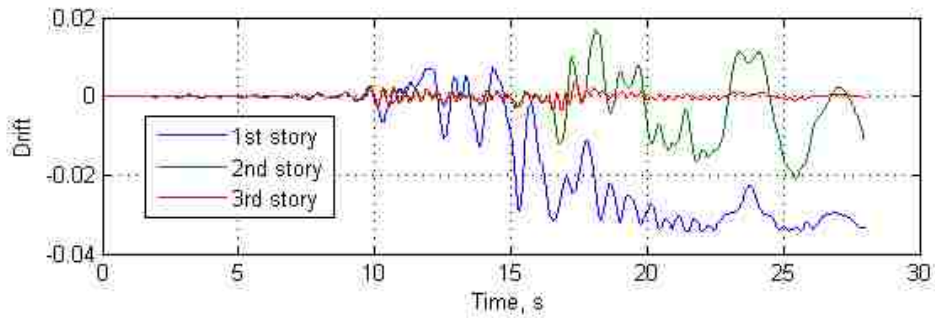
Figure 7.20 Response of archetype model C2 for GM25 at $S_T(C_uT_a) = 1.1g$: (a) brace hysteresis; (b) first story hysteresis; (c) drift history



(a)

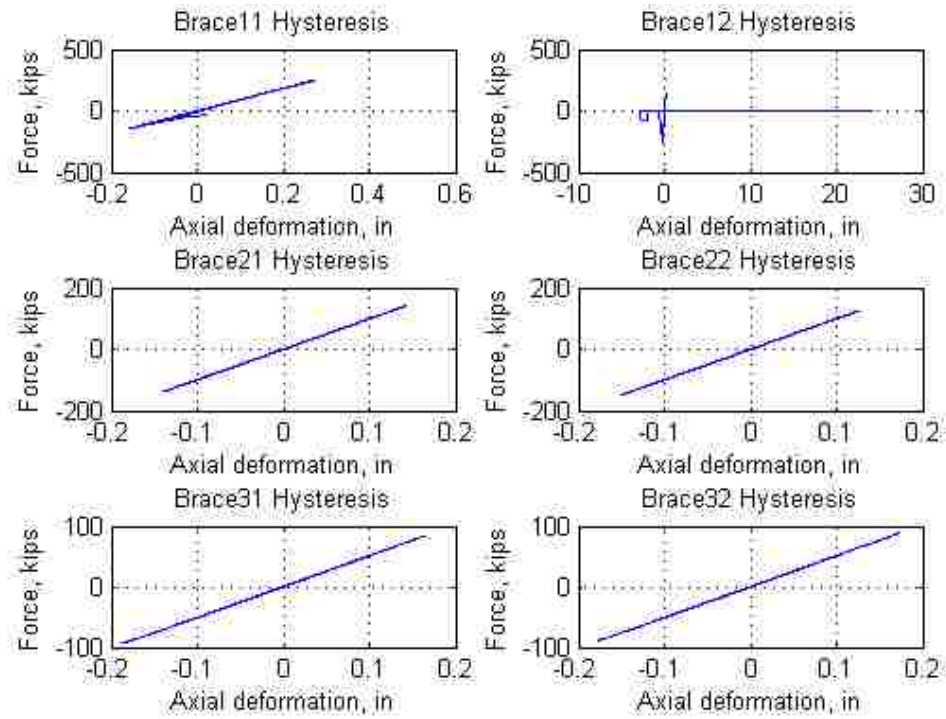


(b)

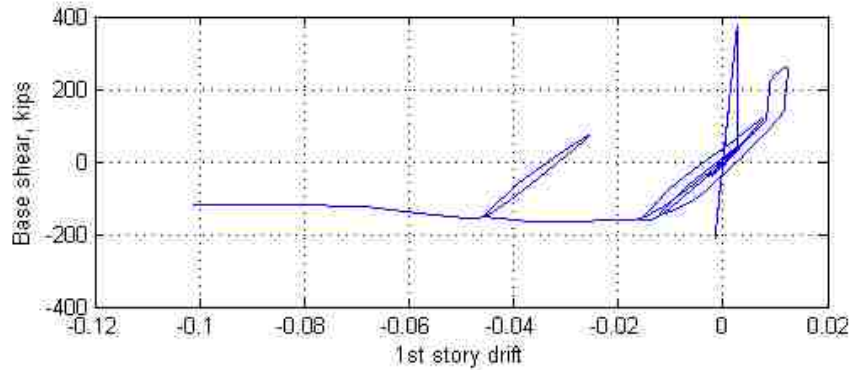


(c)

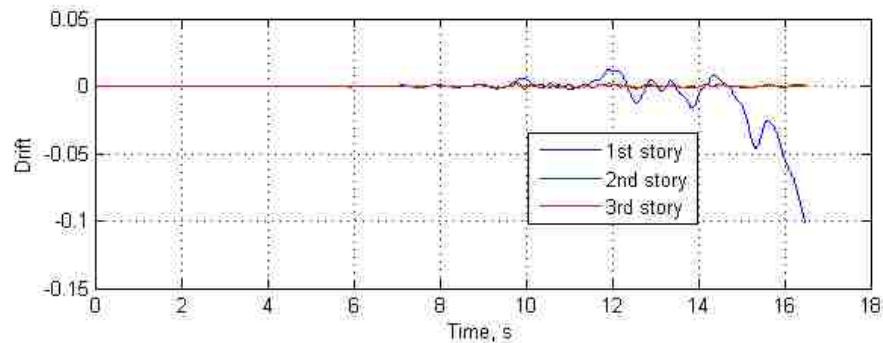
Figure 7.21 Response of archetype model C3 for GM14 at $S_T(C_u T_a) = 0.9g$: (a) brace hysteresis; (b) first story hysteresis; (c) drift history



(a)

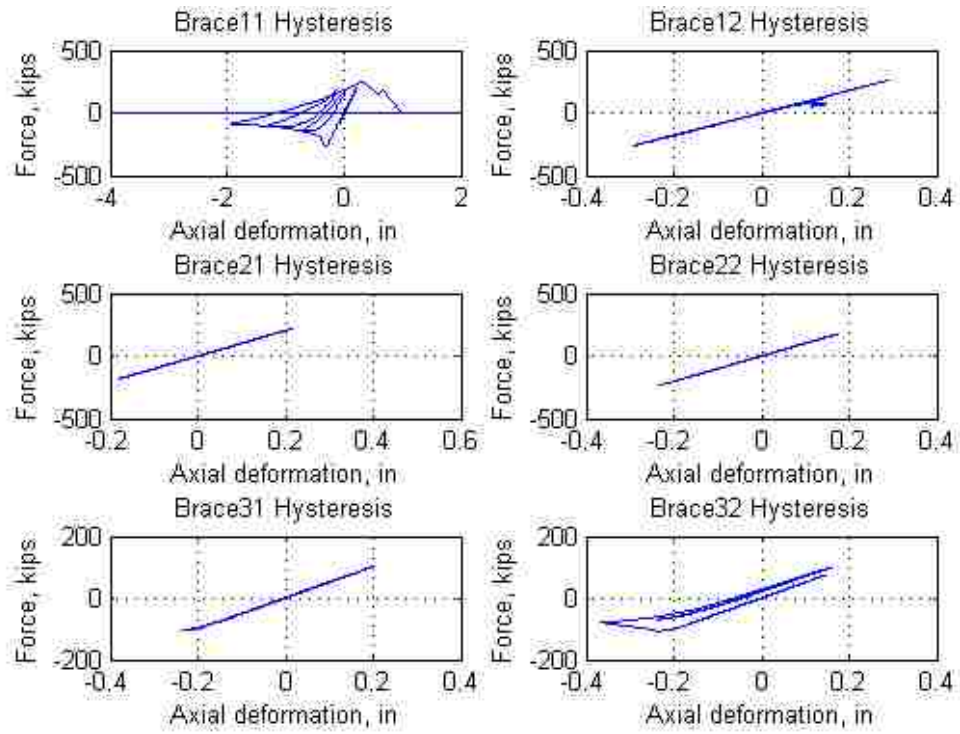


(b)

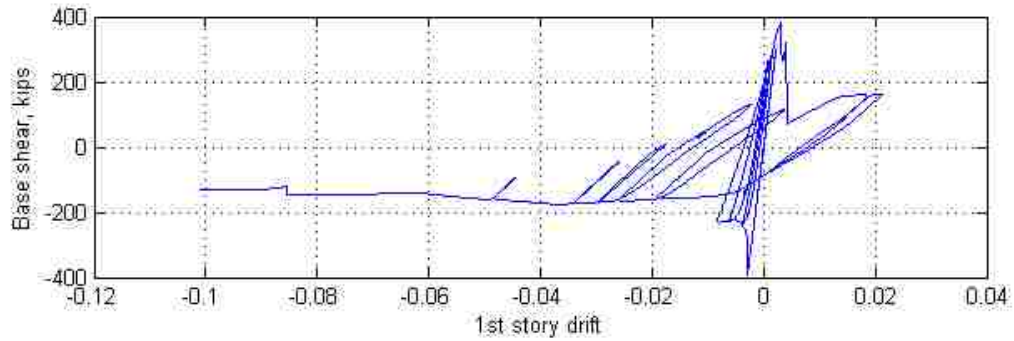


(c)

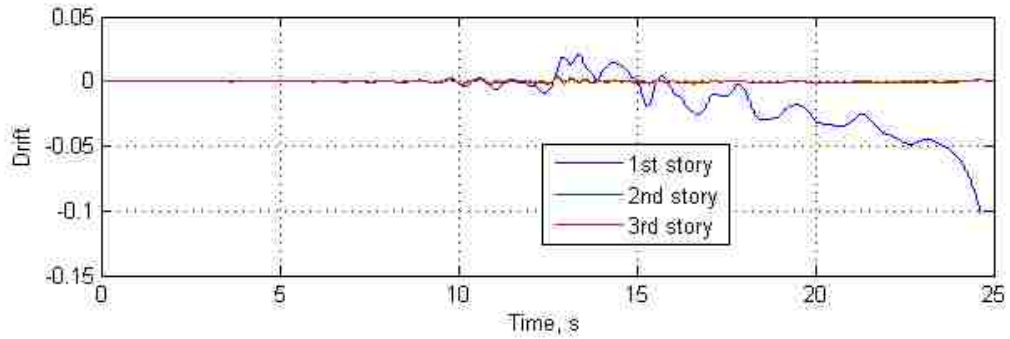
Figure 7.22 Response of archetype model C3 for GM14 at $S_T(C_u T_a) = 1.2g$: (a) brace hysteresis; (b) first story hysteresis; (c) drift history



(a)

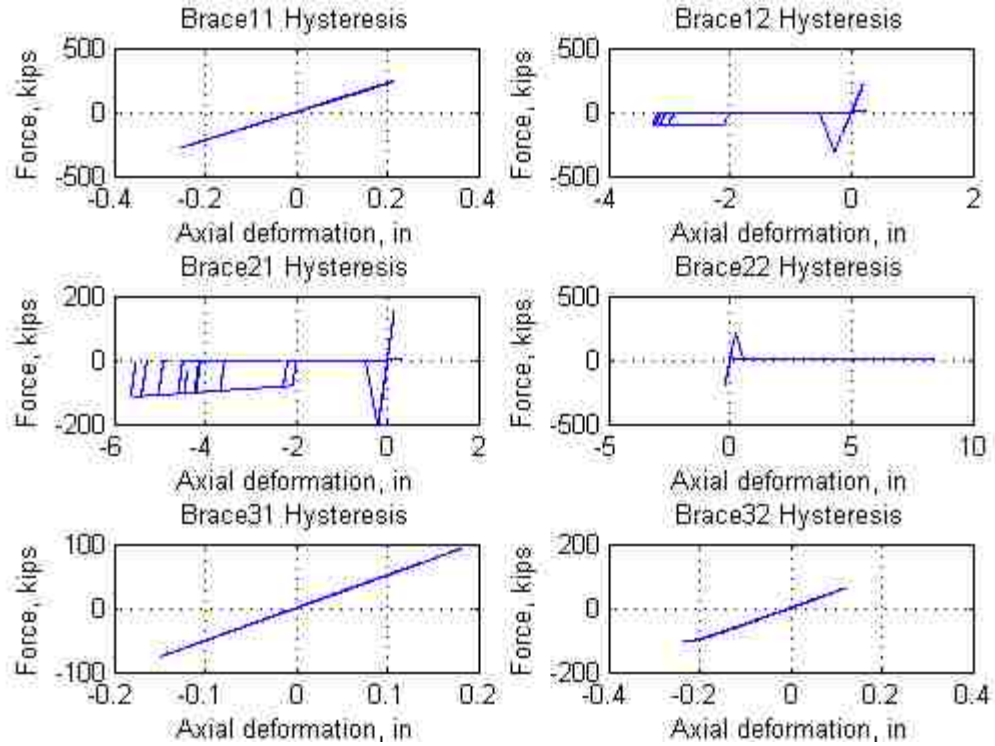


(b)

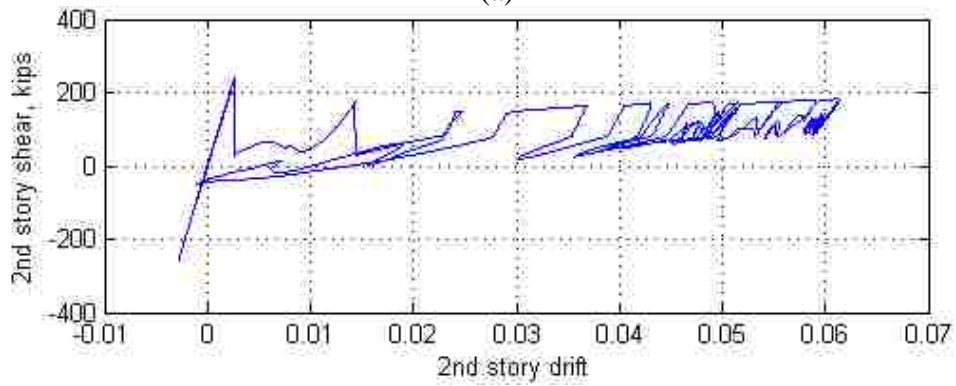


(c)

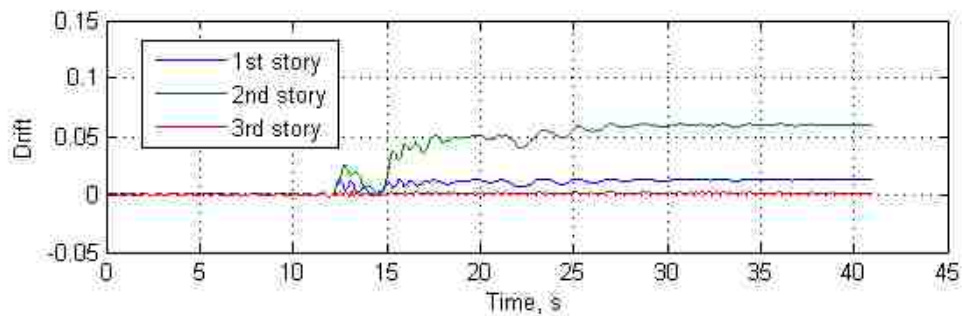
Figure 7.23 Response of archetype model C4 for GM14 at $S_T(C_u T_a) = 0.9g$: (a) brace hysteresis; (b) first story hysteresis; (c) drift history



(a)

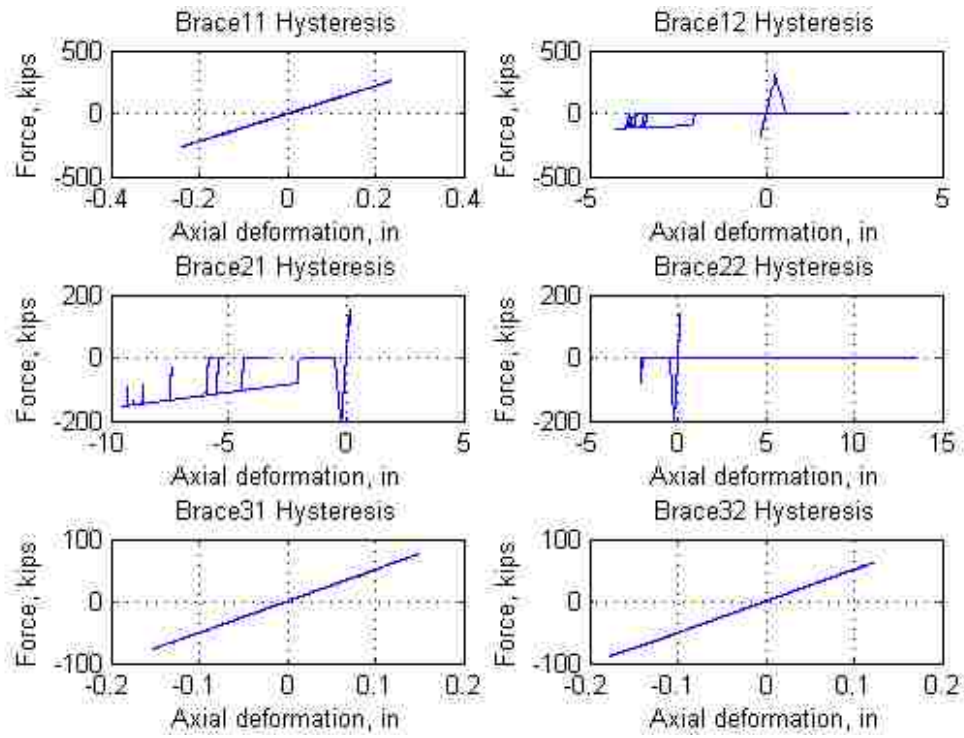


(b)

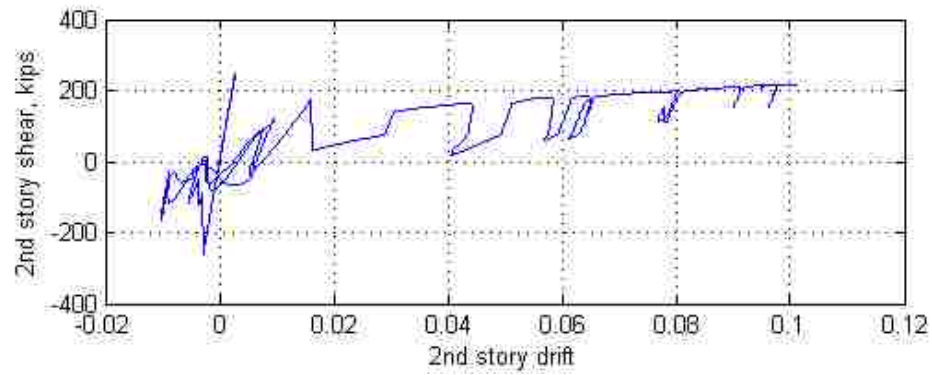


(c)

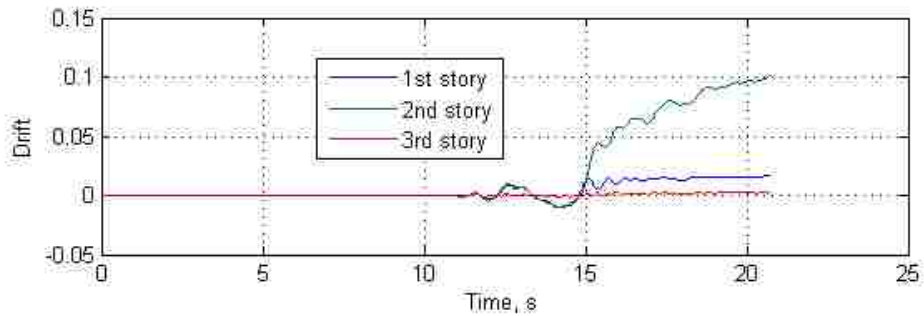
Figure 7.24 Response of archetype model X1 for GM39 at $S_T(C_u T_a) = 0.5g$: (a) brace hysteresis; (b) second story hysteresis; (c) drift history



(a)

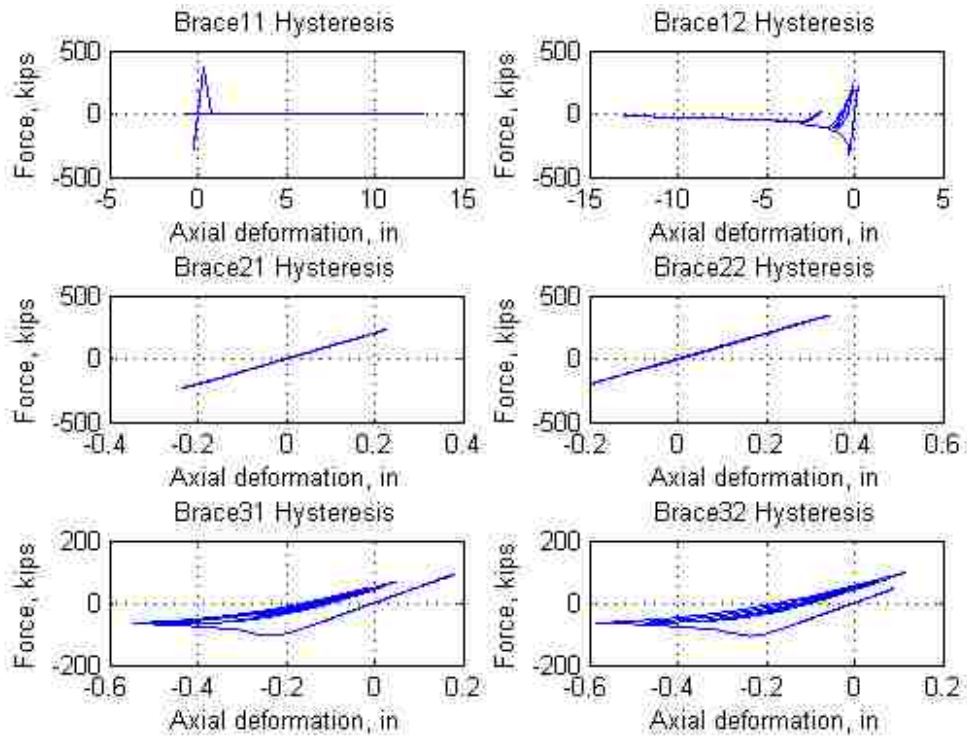


(b)

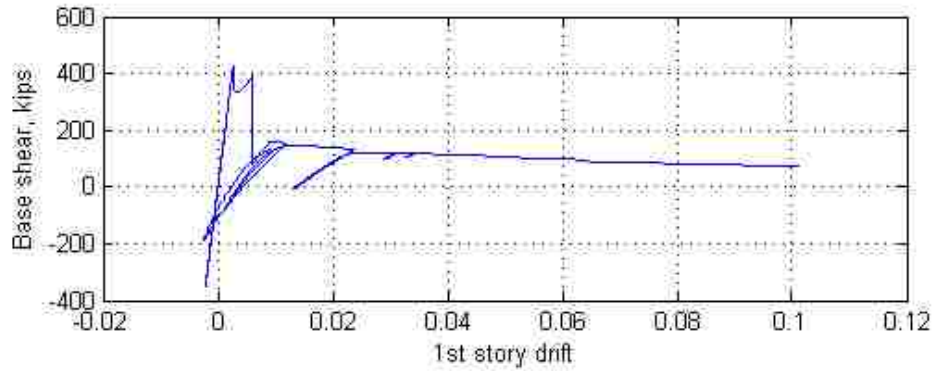


(c)

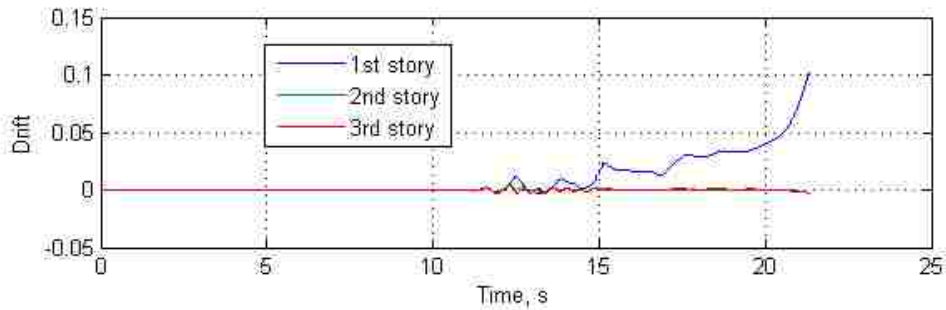
Figure 7.25 Response of archetype model X1 for GM39 at $S_T(C_u T_a) = 0.6g$: (a) brace hysteresis; (b) second story hysteresis; (c) drift history



(a)

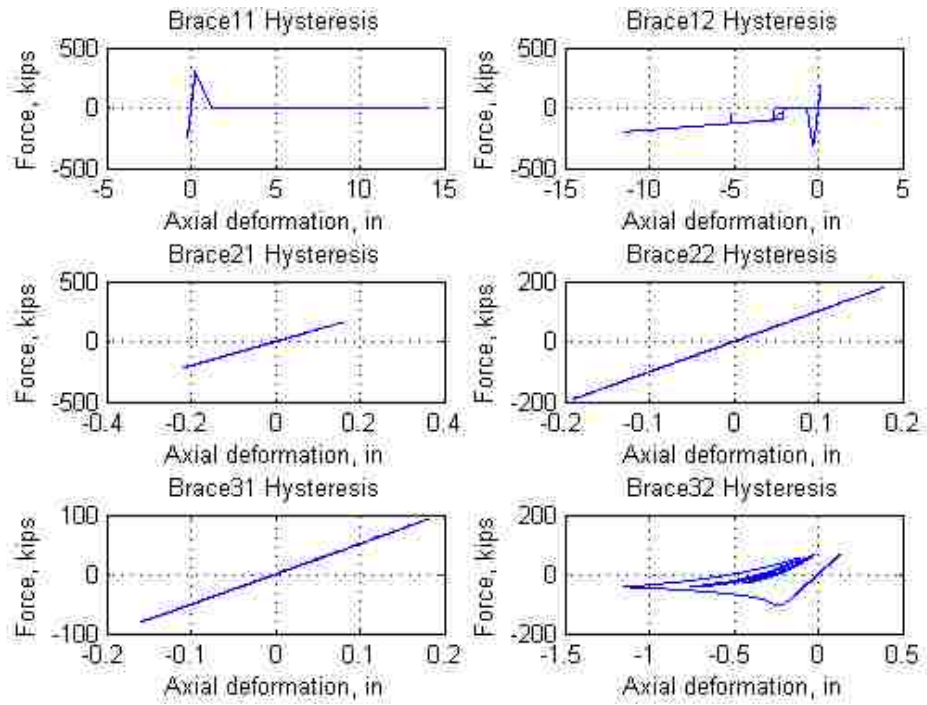


(b)

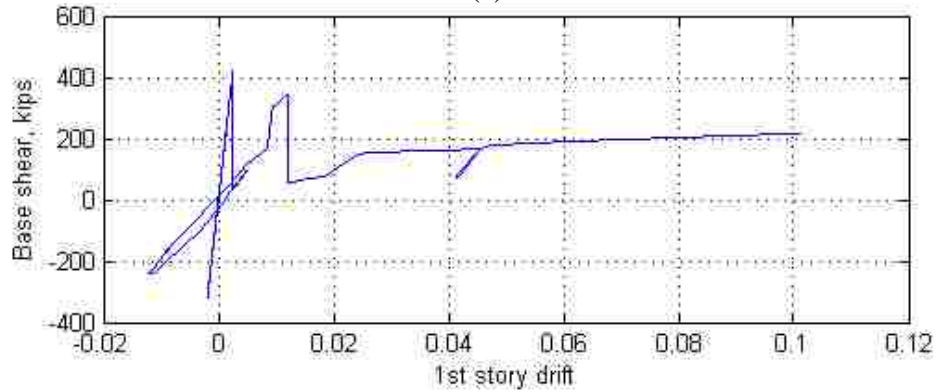


(c)

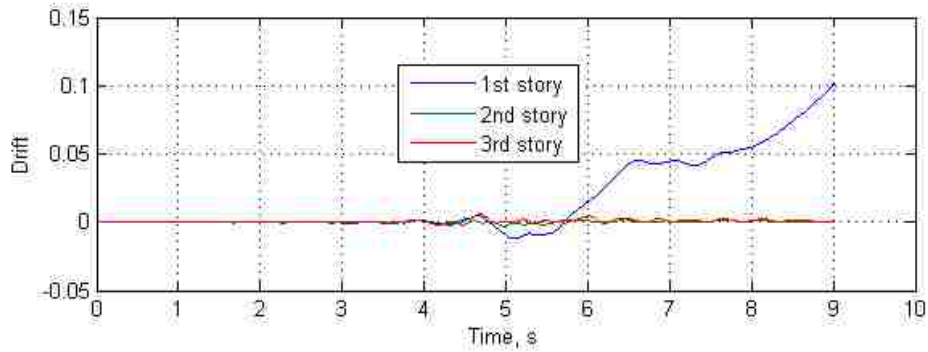
Figure 7.26 Response of archetype model X2 for GM39 at $S_T(C_u T_a) = 0.5g$: (a) brace hysteresis; (b) first story hysteresis; (c) drift history



(a)

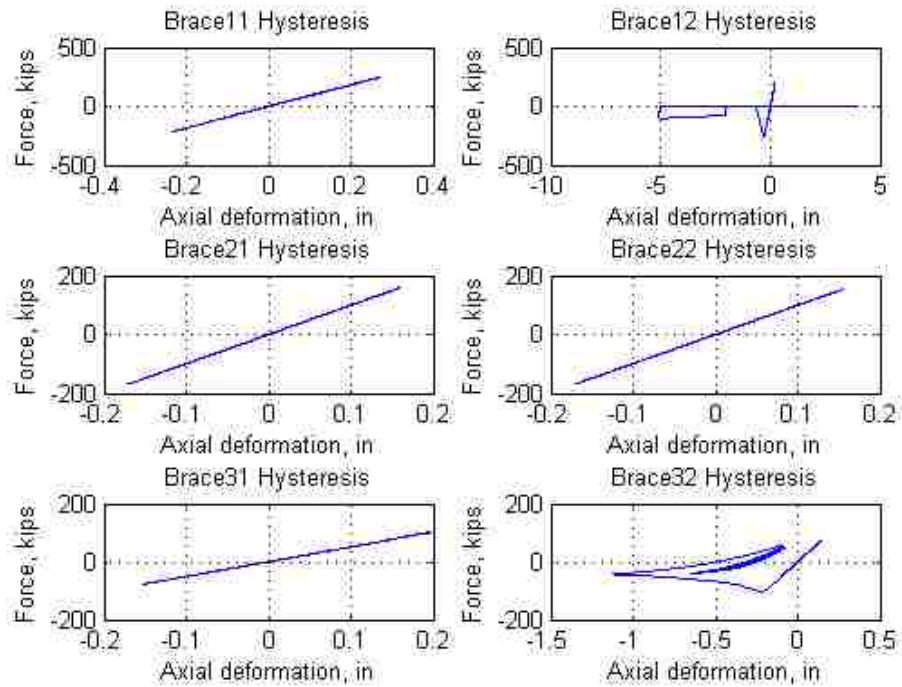


(b)

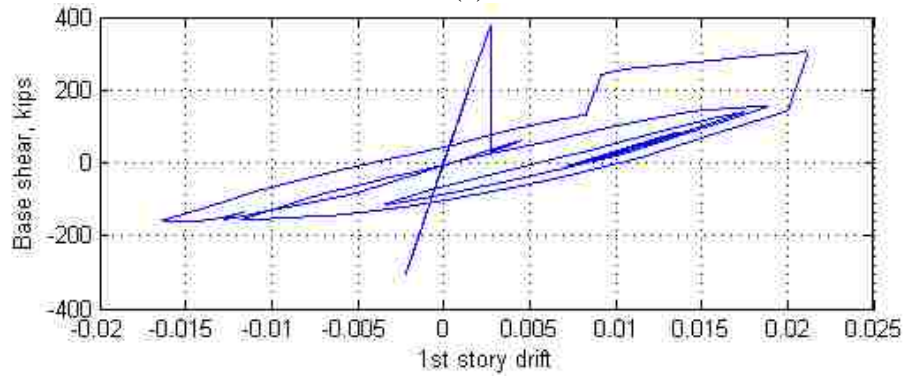


(c)

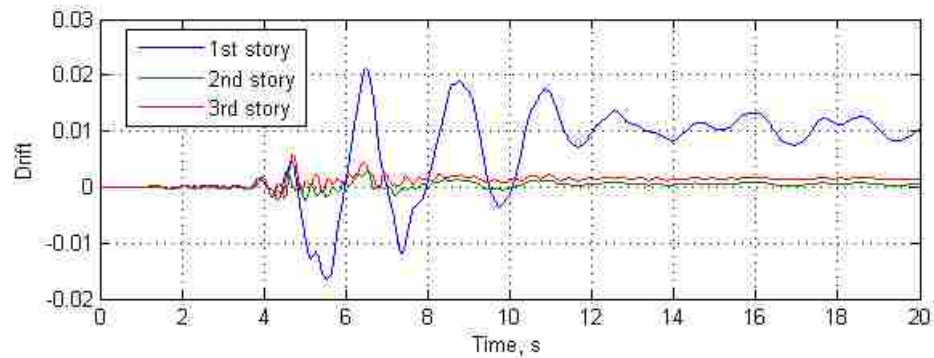
Figure 7.27 Response of archetype model C1 for GM21 at $S_T(C_u T_a) = 0.5g$: (a) brace hysteresis; (b) first story hysteresis; (c) drift history



(a)

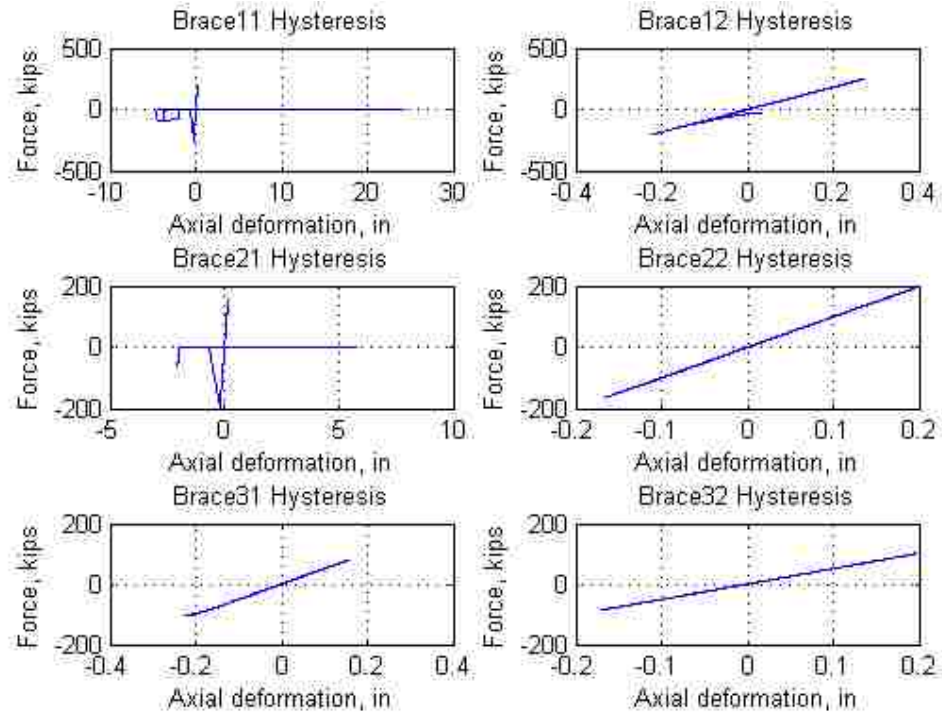


(b)

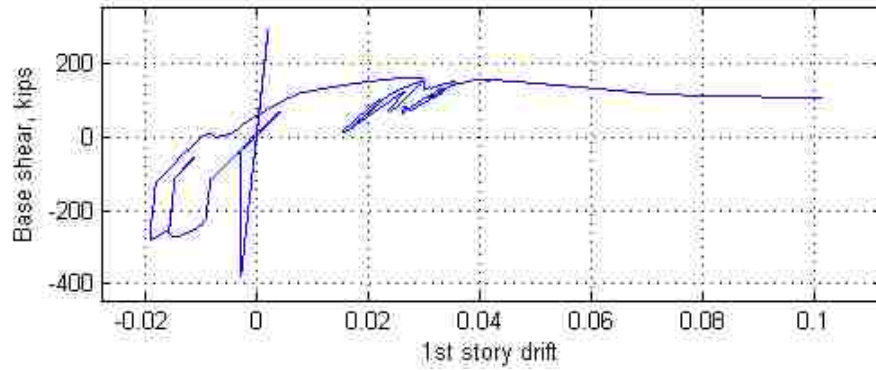


(c)

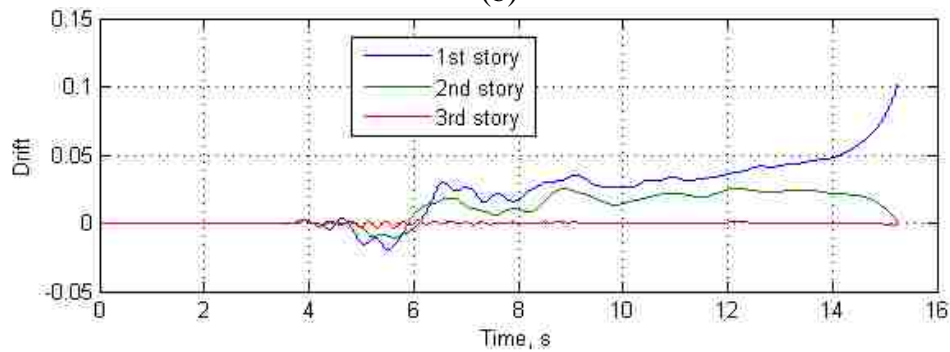
Figure 7.28 Response of archetype model C3 for GM21 at $S_T(C_u T_a) = 0.5g$: (a) brace hysteresis; (b) first story hysteresis; (c) drift history



(a)

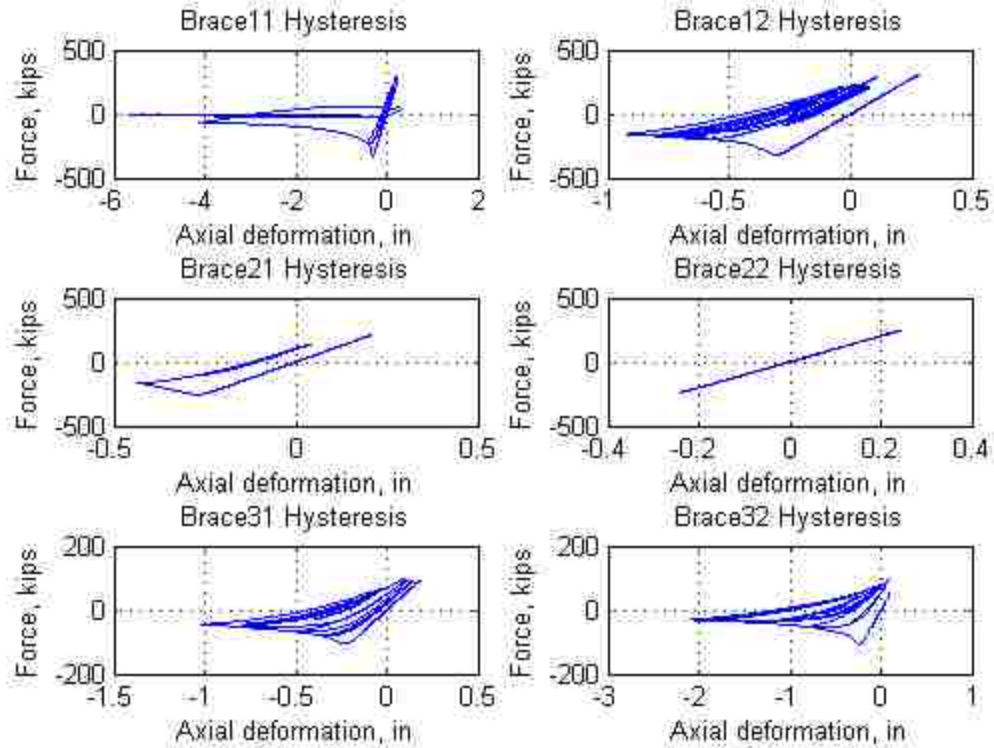


(b)

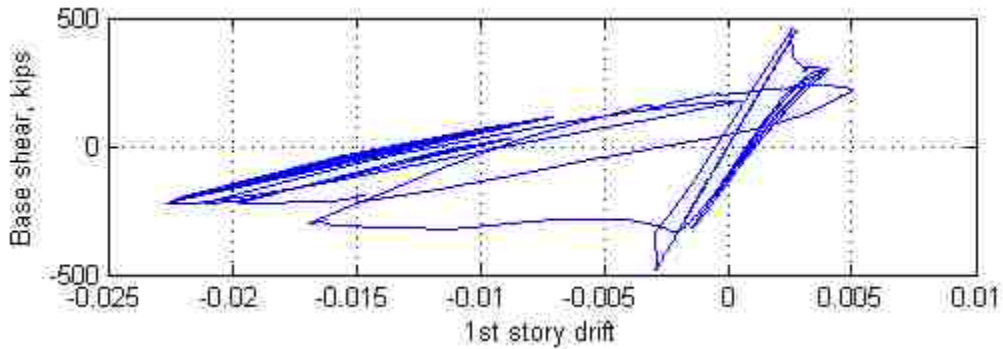


(c)

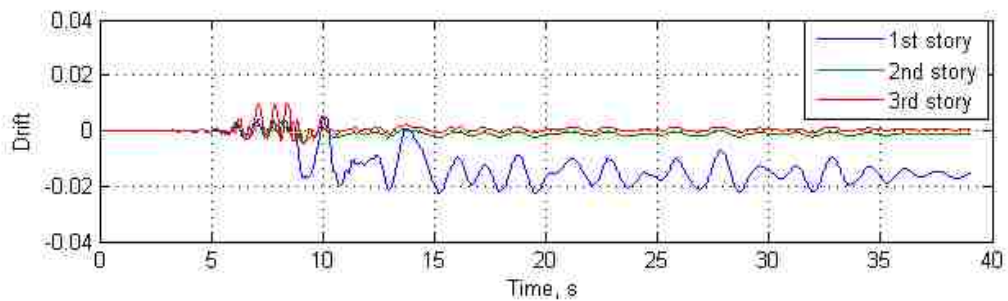
Figure 7.29 Response of archetype model C3 for GM21 at $S_T(C_u T_a) = 0.7g$: (a) brace hysteresis; (b) first story hysteresis; (c) drift history



(a)



(b)



(c)

Figure 7.30 Response of archetype model C2 for GM18 at $S_T(C_u T_a) = 0.9g$: (a) brace hysteresis; (b) first story hysteresis; (c) drift history

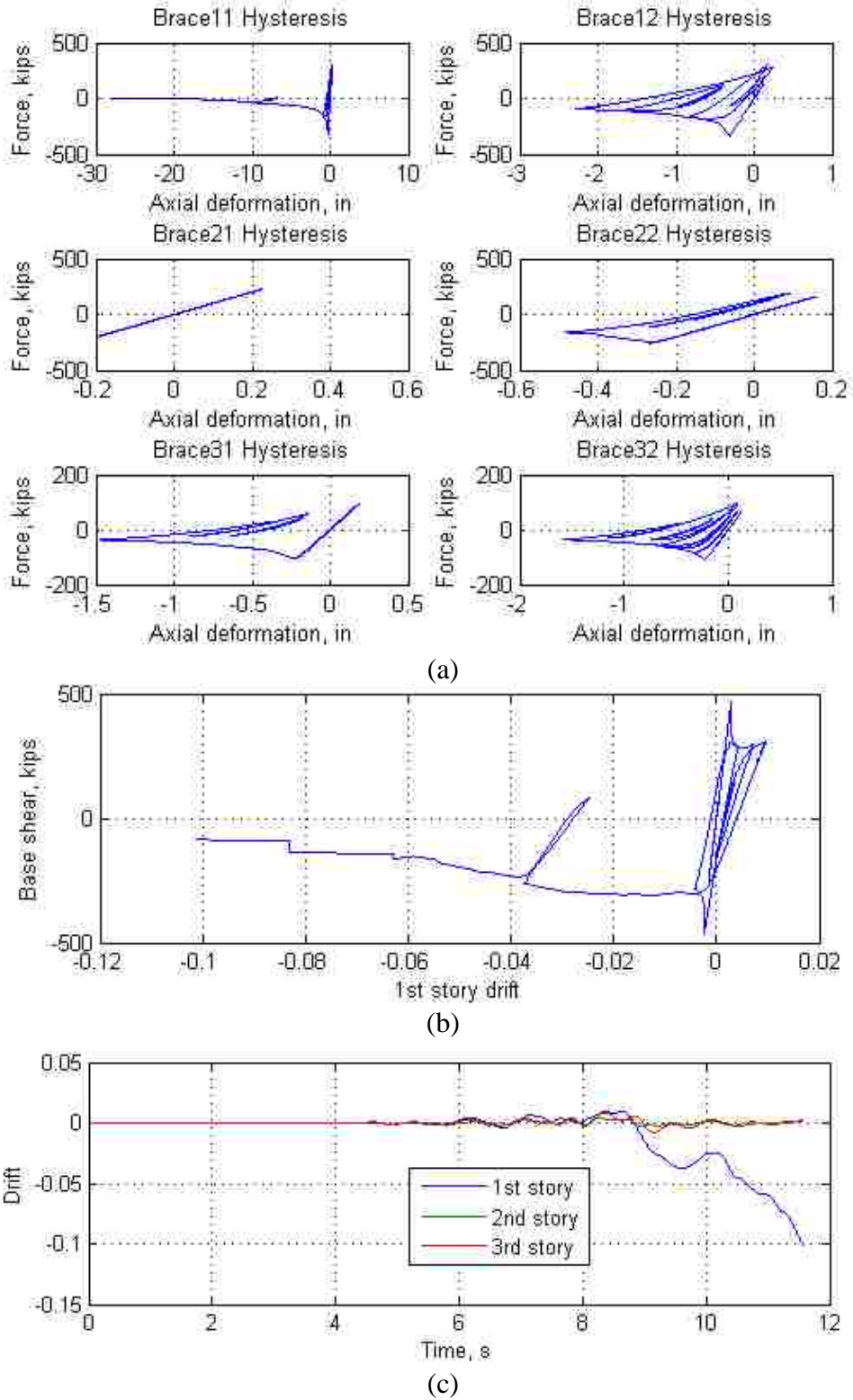
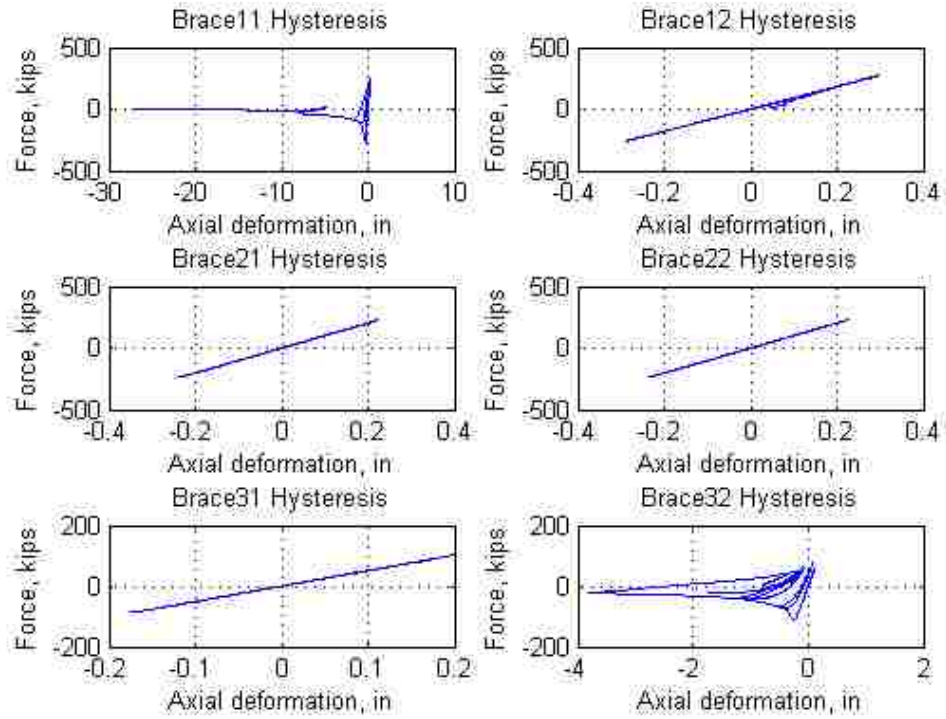
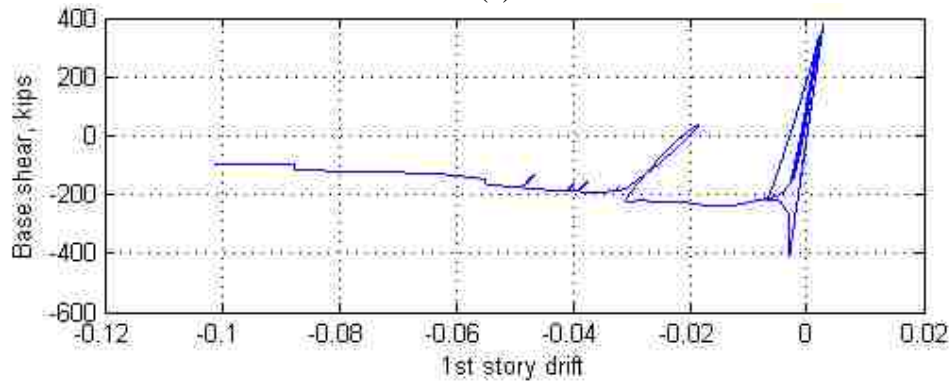


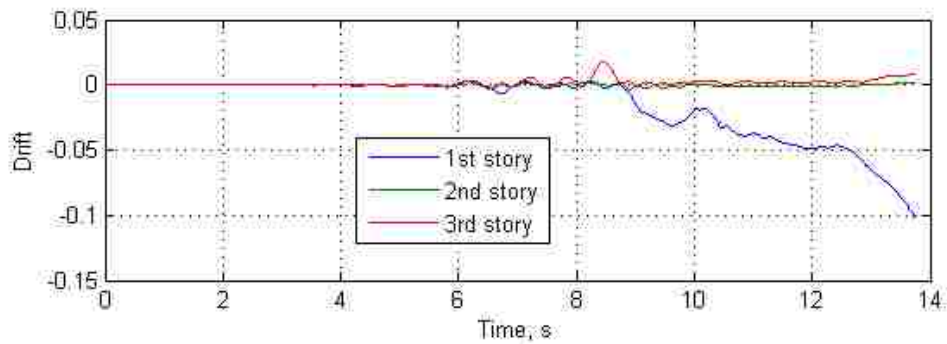
Figure 7.31 Response of archetype model C2 for GM18 at $S_T(C_u T_a) = 1.1g$: (a) brace hysteresis; (b) first story hysteresis; (c) drift history



(a)

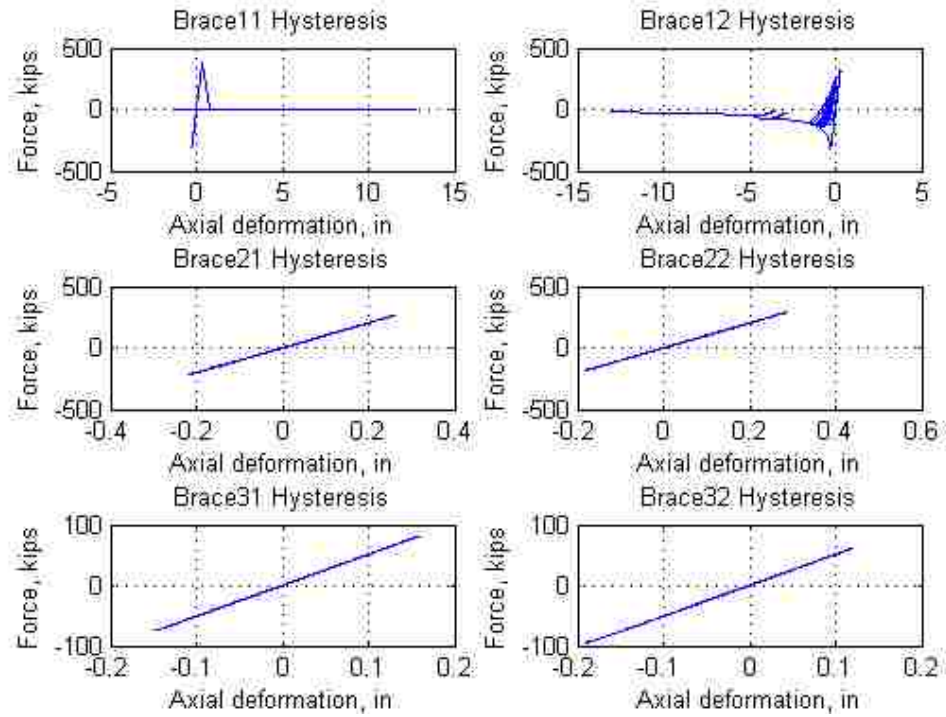


(b)

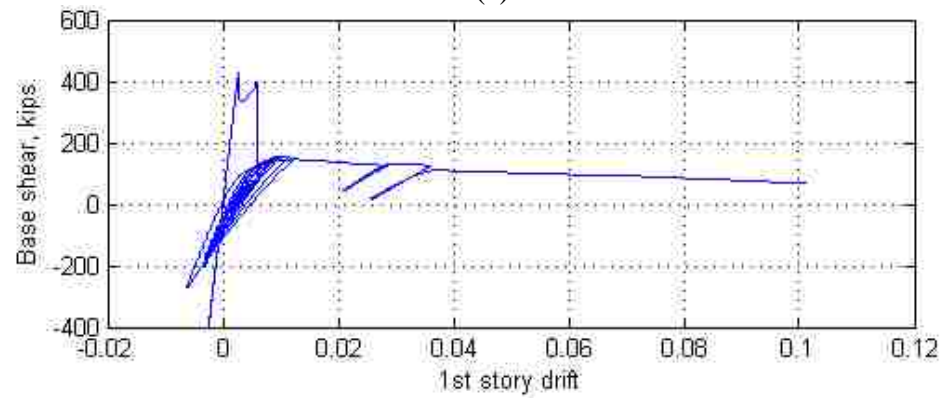


(c)

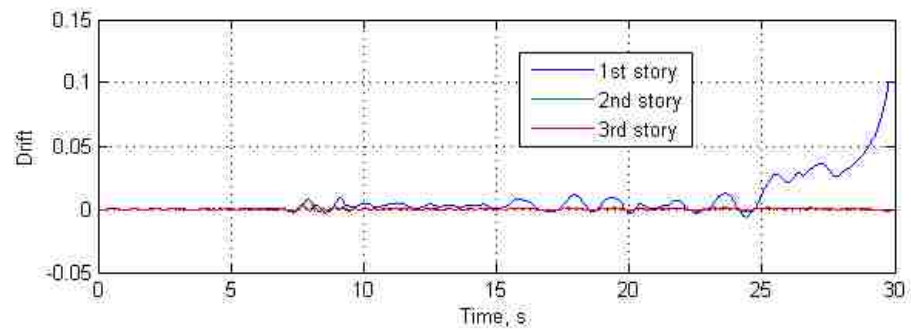
Figure 7.32 Response of archetype model C4 for GM18 at $S_T(C_u T_a) = 0.9g$: (a) brace hysteresis; (b) first story hysteresis; (c) drift history



(a)

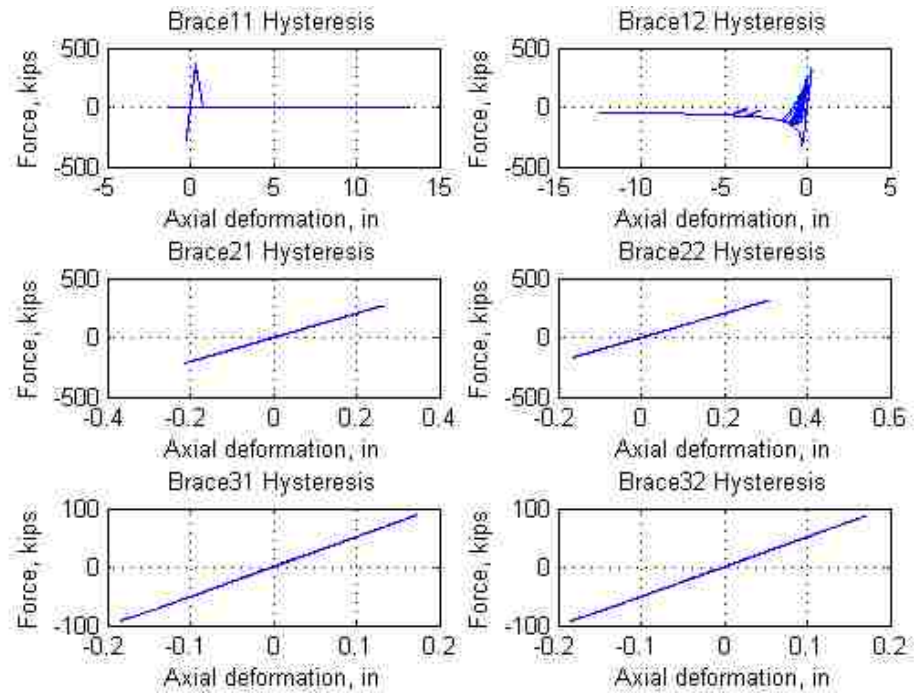


(b)

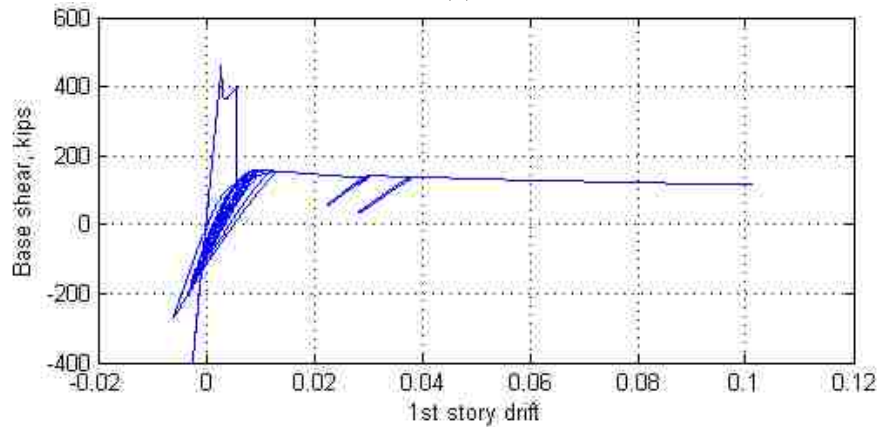


(c)

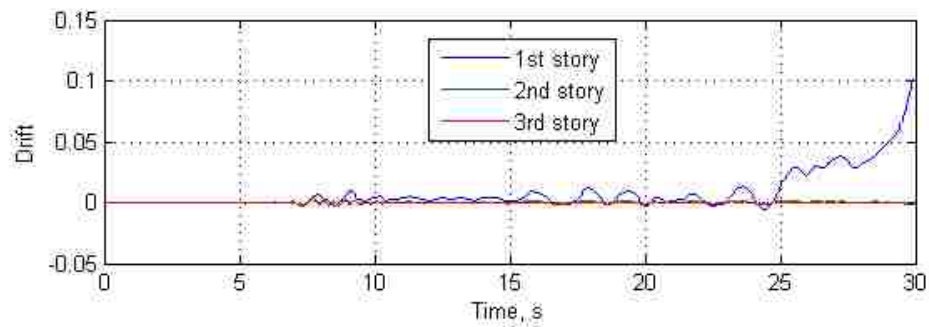
Figure 7.33 Response of archetype model X2 for GM16 at $S_T(C_u T_a) = 0.4g$: (a) brace hysteresis; (b) first story hysteresis; (c) drift history



(a)

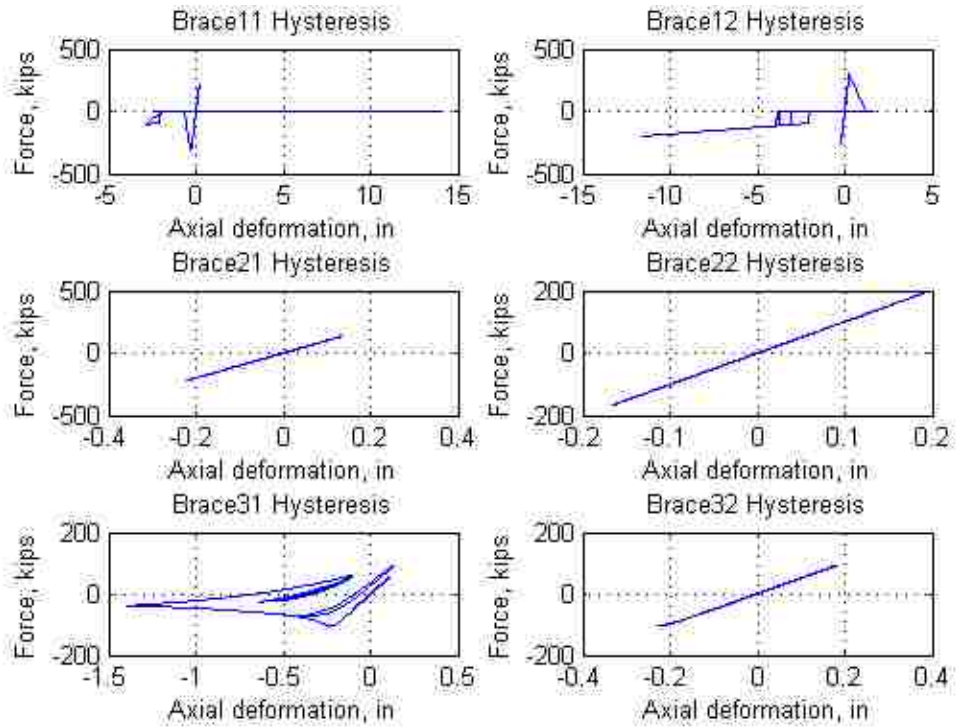


(b)

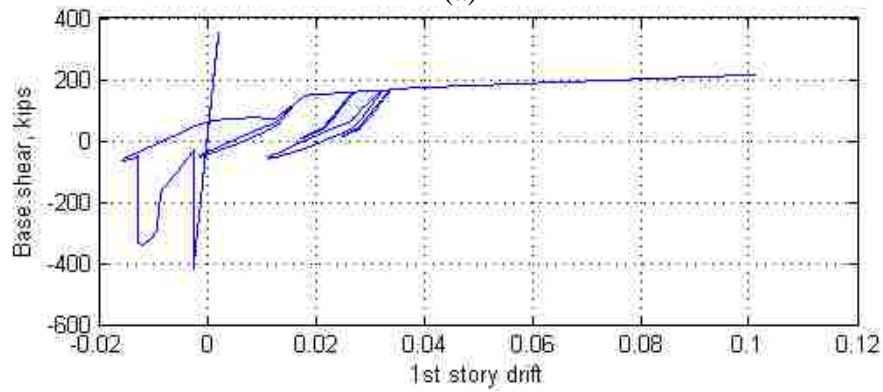


(c)

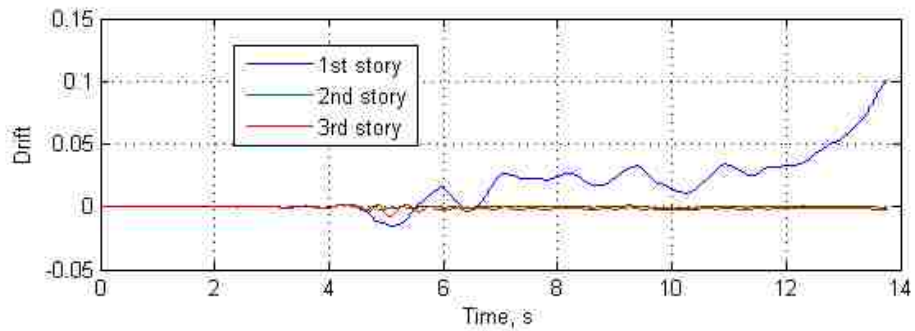
Figure 7.34 Response of archetype model X4 for GM16 at $S_T(C_u T_a) = 0.4g$: (a) brace hysteresis; (b) first story hysteresis; (c) drift history



(a)

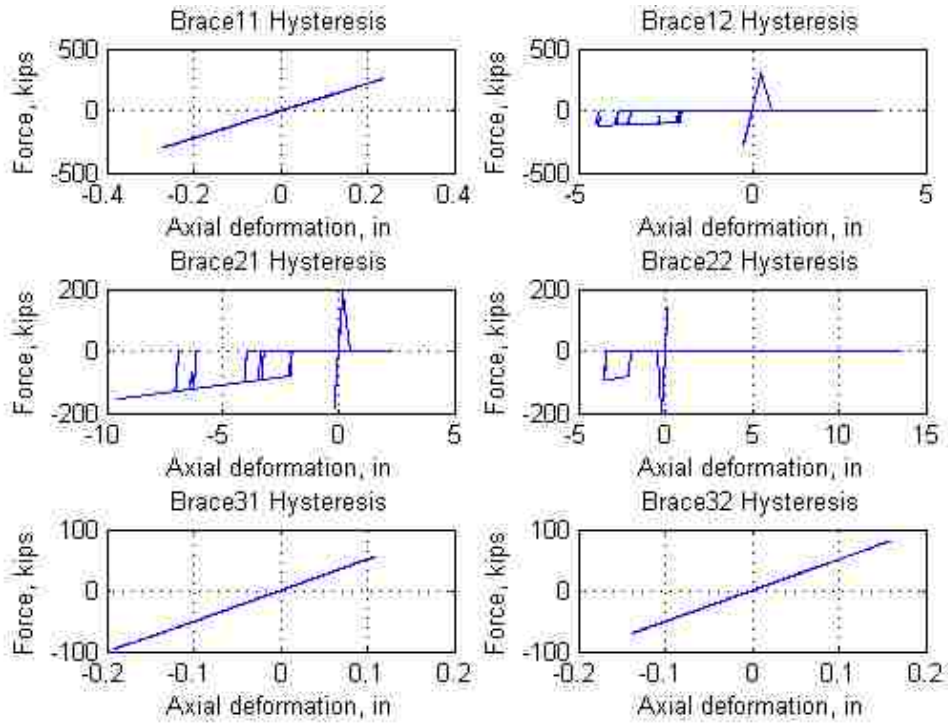


(b)

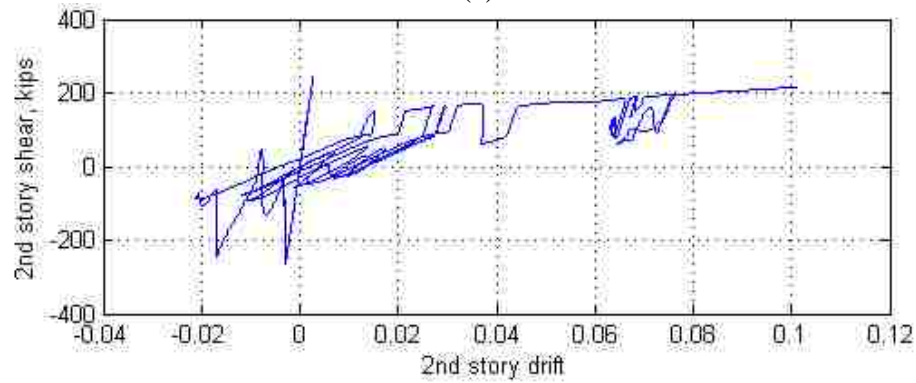


(c)

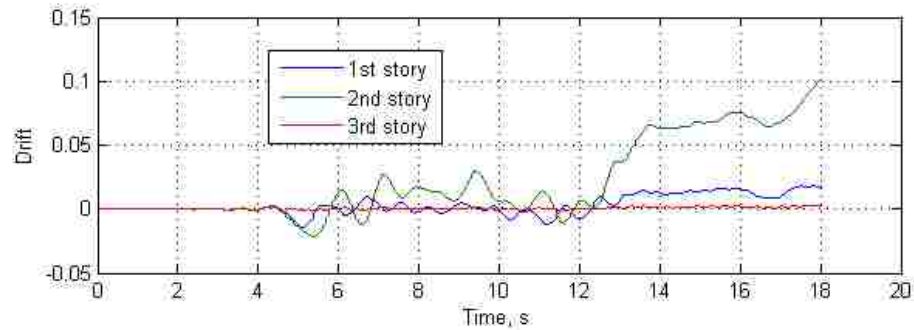
Figure 7.35 Response of archetype model C1 for GM19 at $S_T(C_u T_a) = 0.7g$: (a) brace hysteresis; (b) first story hysteresis; (c) drift history



(a)

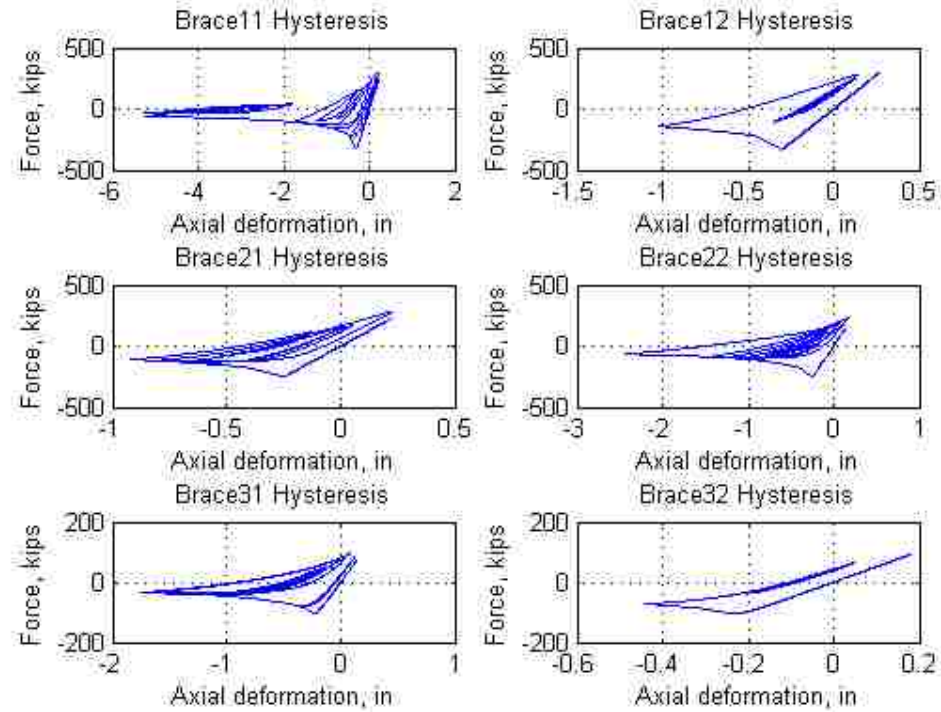


(b)

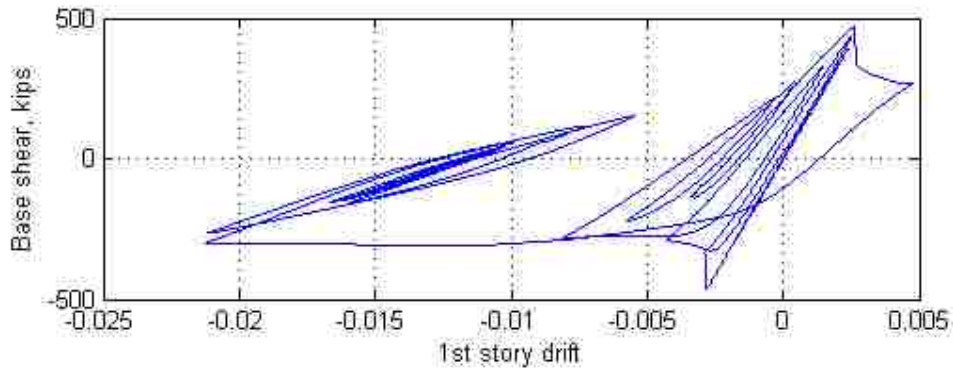


(c)

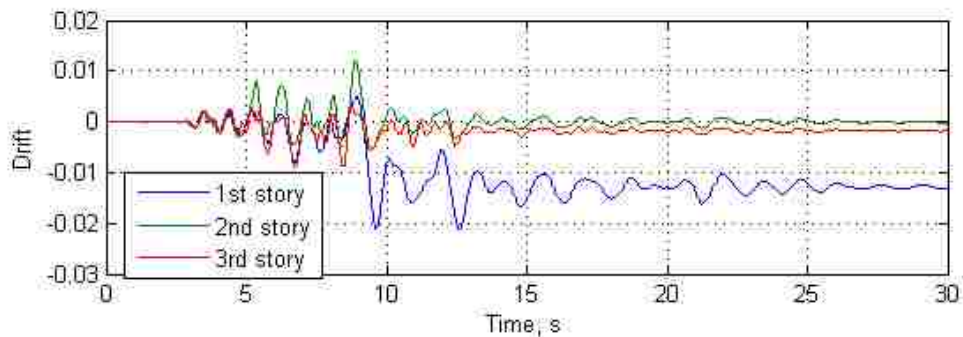
Figure 7.36 Response of archetype model X1 for GM19 at $S_T(C_u T_a) = 0.7g$: (a) brace hysteresis; (b) first story hysteresis; (c) drift history



(a)



(b)



(c)

Figure 7.37 Response of archetype model C2 for GM23 at $S_T(C_u T_a) = 0.5g$: (a) brace hysteresis; (b) first story hysteresis; (c) drift history

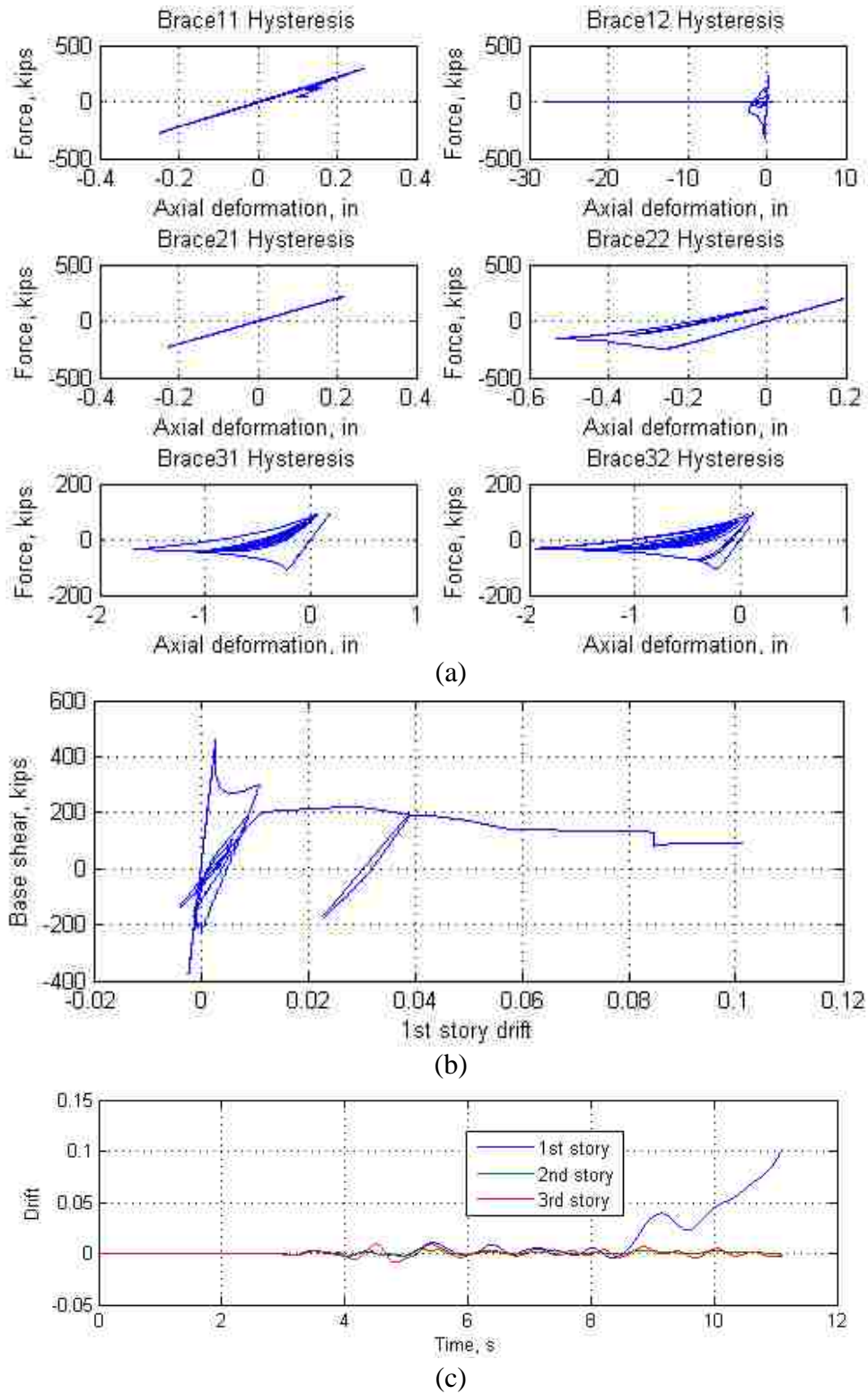
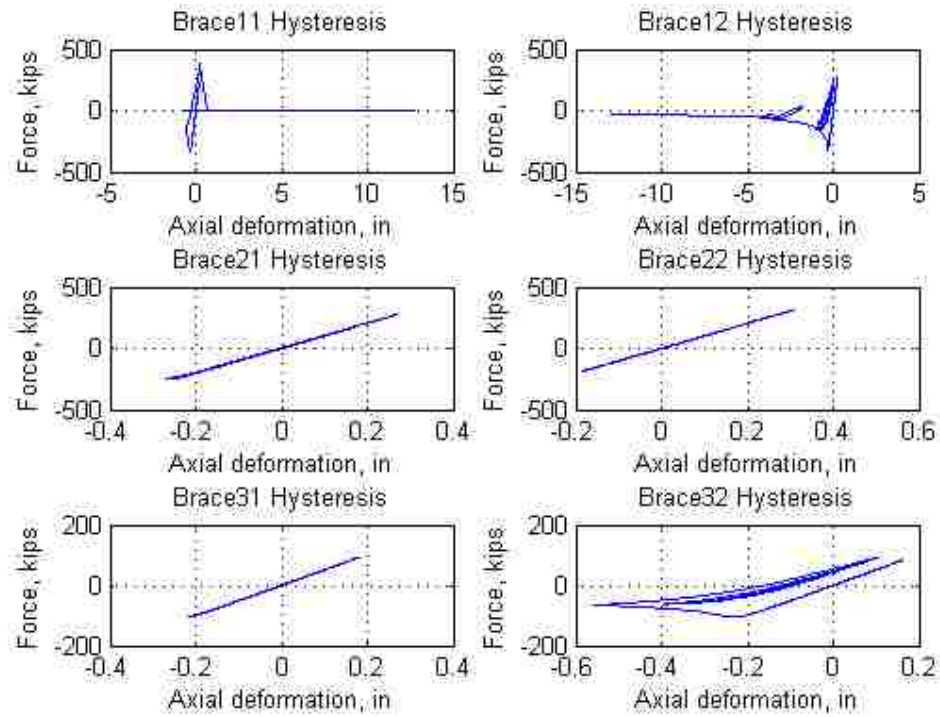
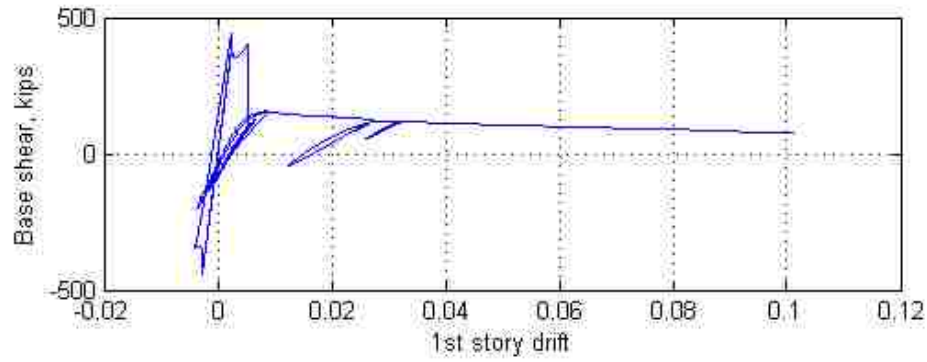


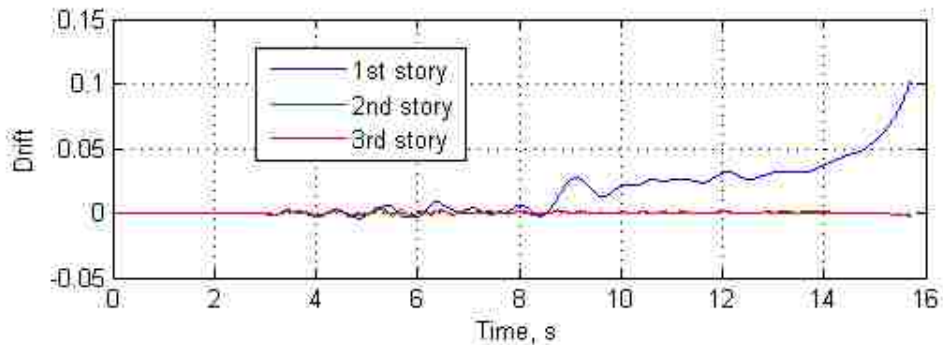
Figure 7.38 Response of archetype model C2 for GM23 at $S_T(C_u T_a) = 0.7g$: (a) brace hysteresis; (b) first story hysteresis; (c) drift history



(a)



(b)



(c)

Figure 7.39 Response of archetype model X2 for GM23 at $S_T(C_u T_a) = 0.5g$: (a) brace hysteresis; (b) first story hysteresis; (c) drift history

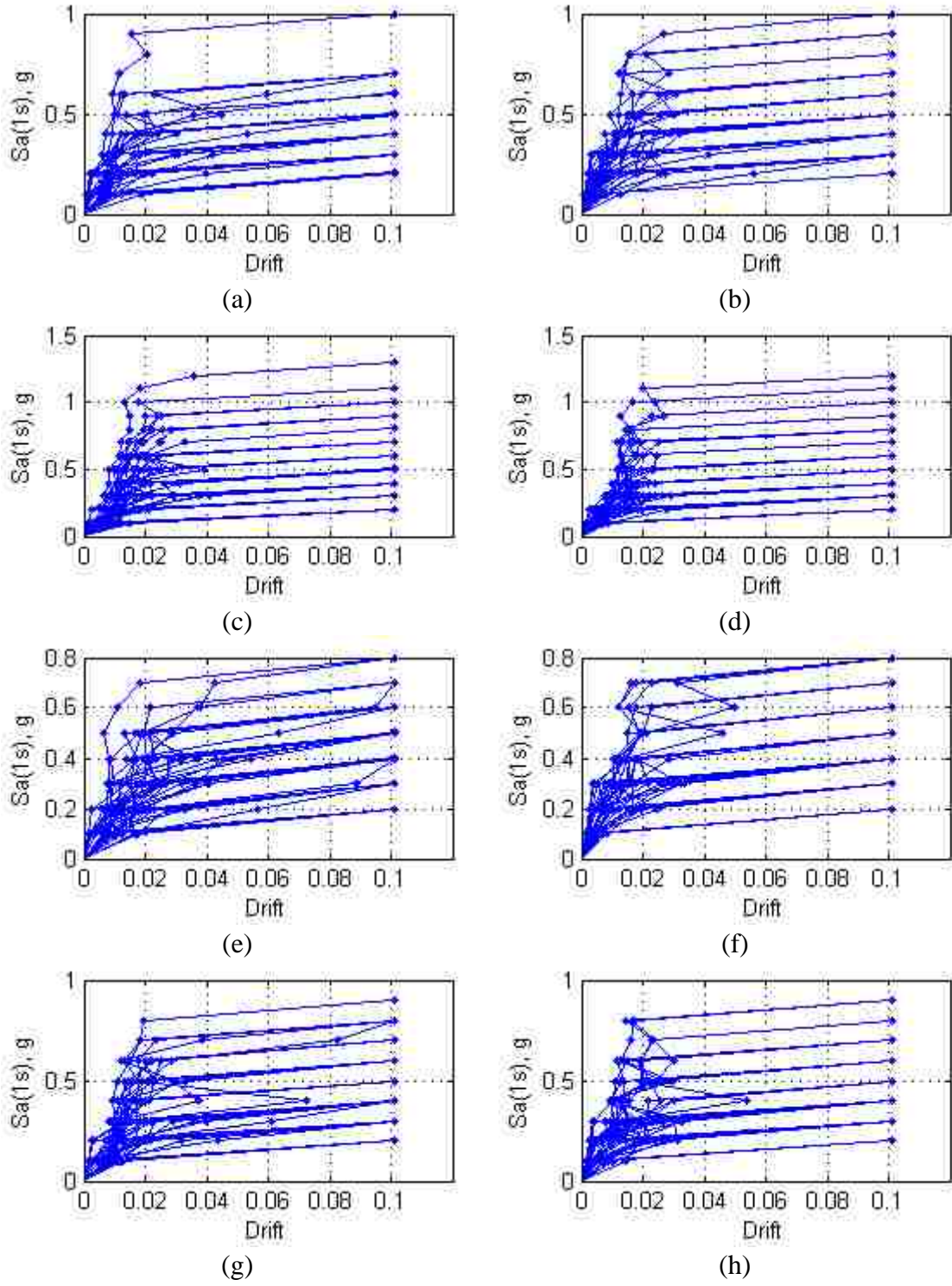


Figure 7.40 IDA results using ECUS GM set for model: (a) C1; (b) C2; (c) C3; (d) C4; (e) X1; (f) X2; (g) X3; (h) X4

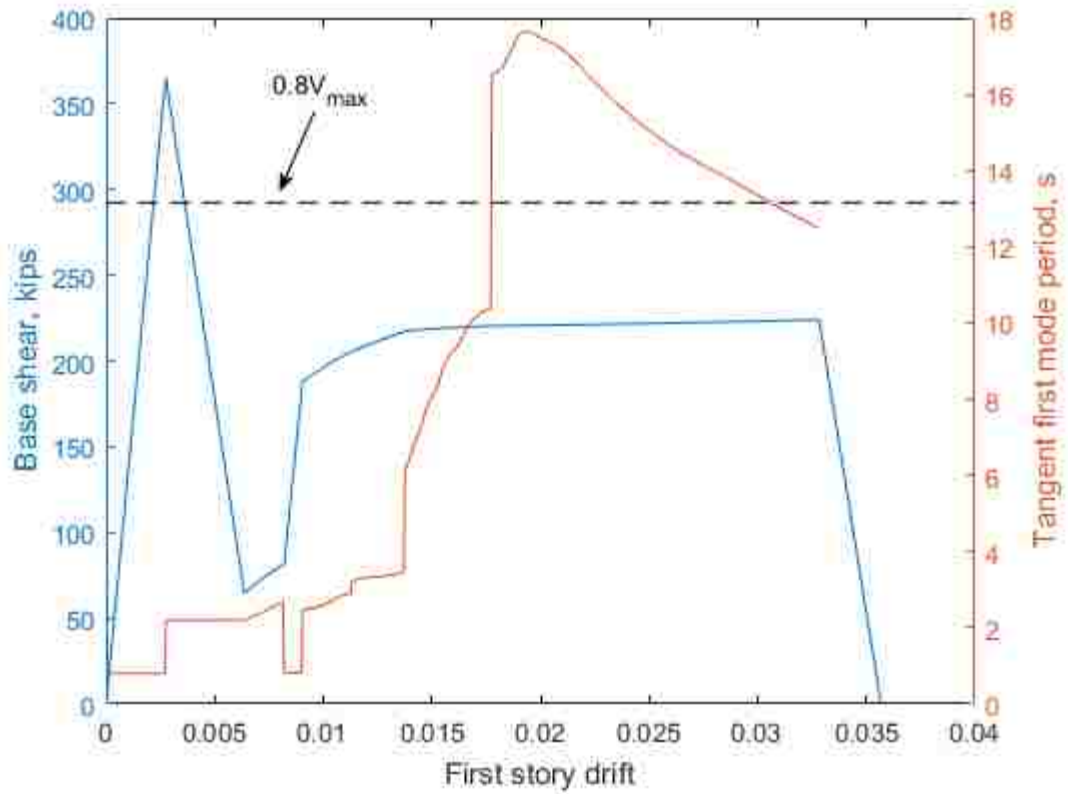


Figure 7.41 Response of the pushover analysis and tangent first mode period at each load step during the pushover analysis for model C3

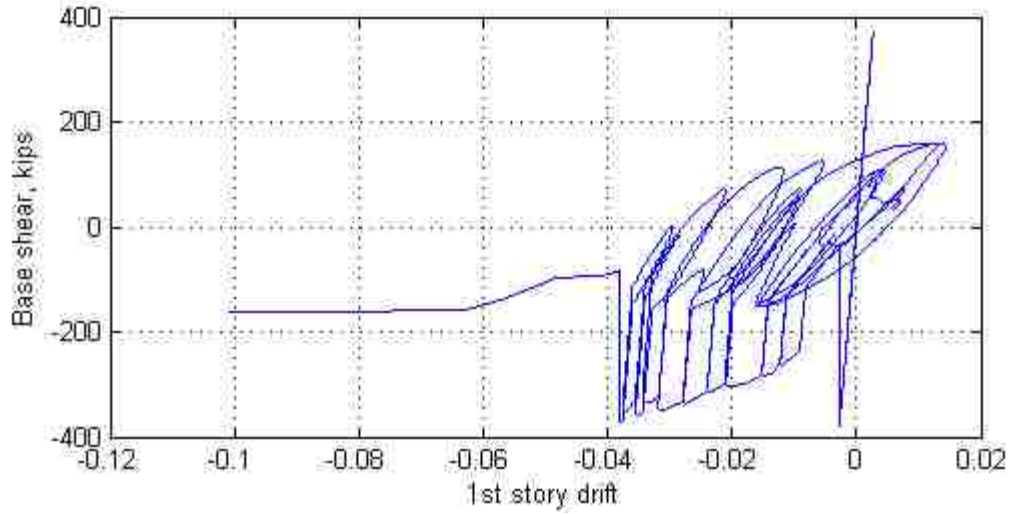


Figure 7.42 First story hysteresis response of model C3 under GM10 at $Sa(1s) = 1.0g$

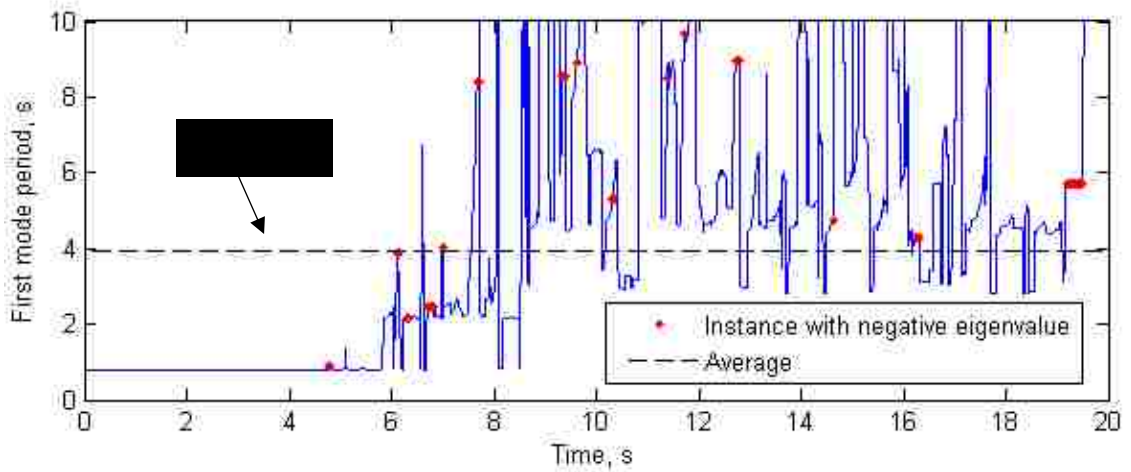
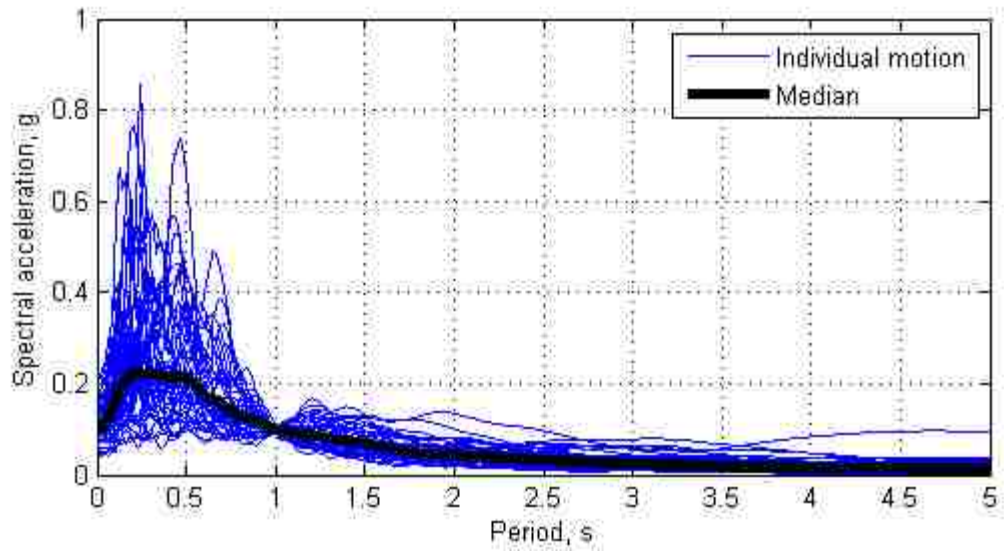
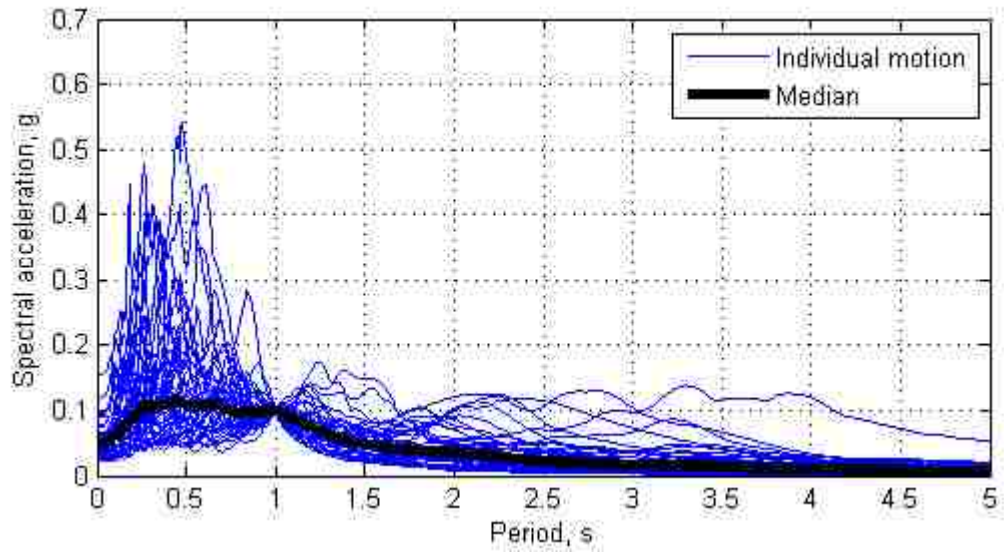


Figure 7.43 Tangent first mode period at each time step during the response of model C3 under GM10 at $Sa(1s) = 1.0g$ in IDA



(a)



(b)

Figure 7.44 Response spectrum of (a) FEMA set; (b) ECUS GM set when all ground motions are scaled to $Sa(1s)=0.1g$

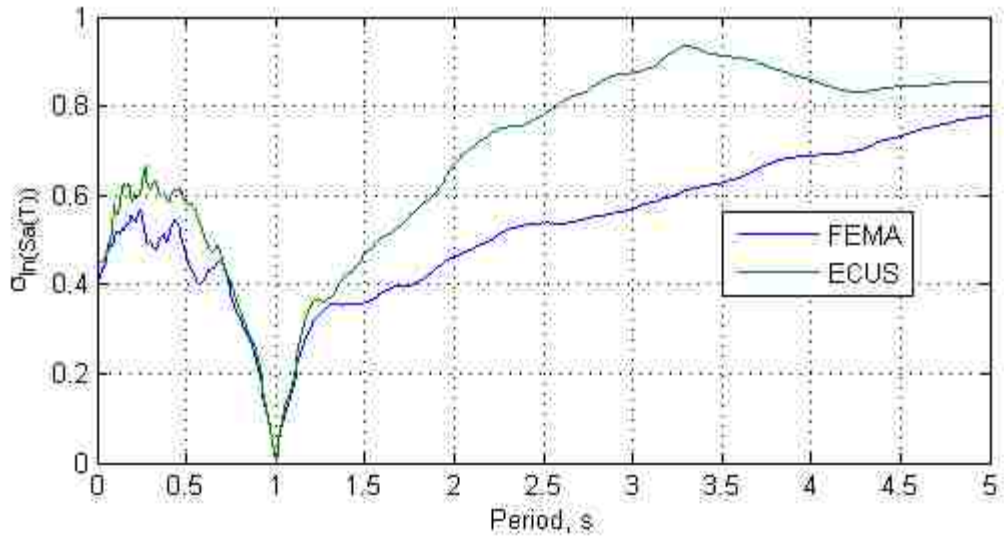


Figure 7.45 Comparison of standard deviation of $\ln(Sa)$ at each period between FEMA and ECUS GM set at $Sa(1s)=0.1g$ using “Sa component scaling method”

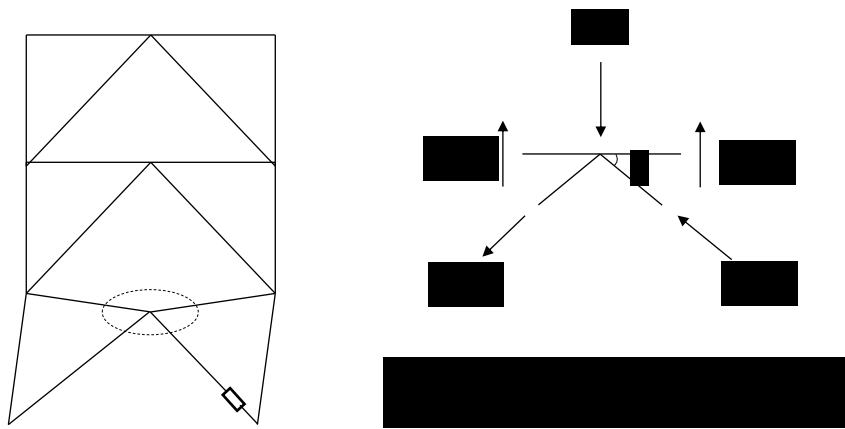


Figure 7.46 Illustration on brace re-engagement effect: free body diagram on chevron point

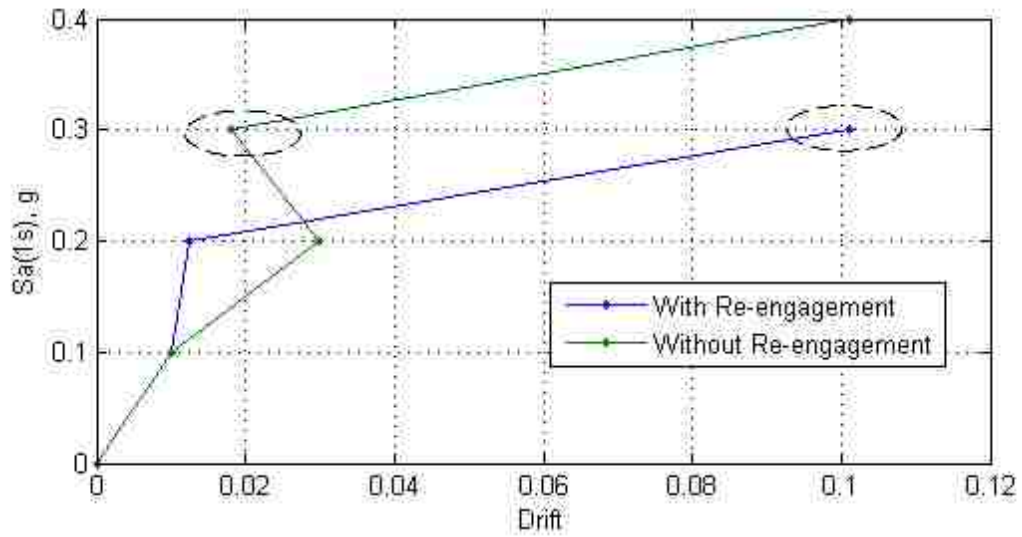


Figure 7.47 IDA results for model C1 under GM16 with and without modeling brace re-engagement

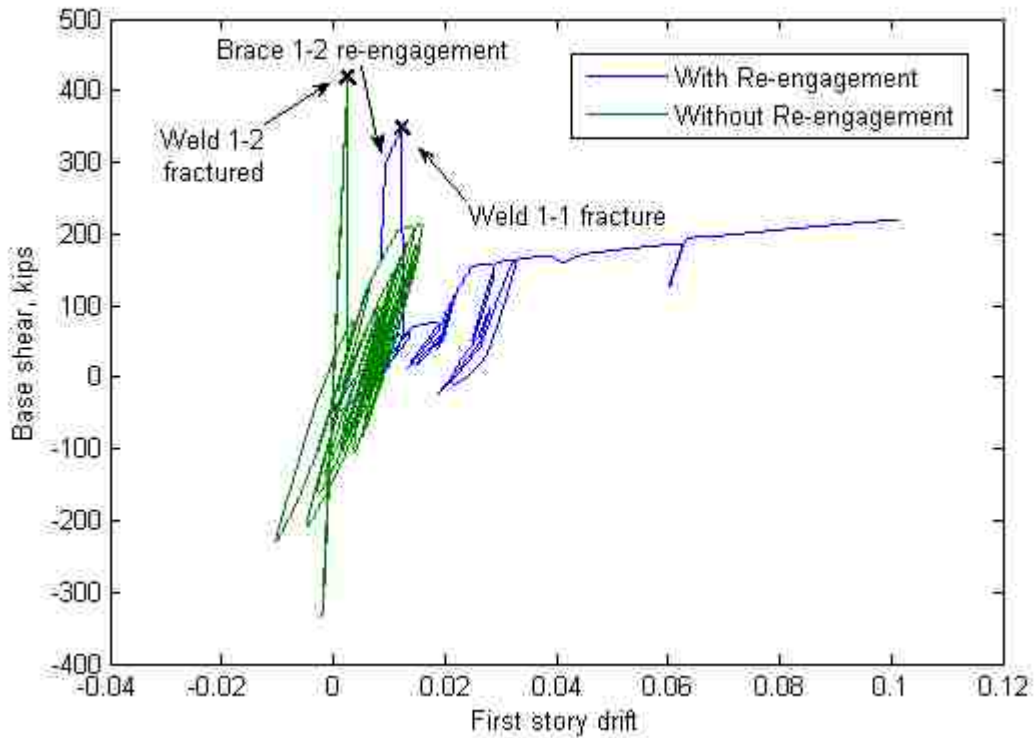


Figure 7.48 First story hysteresis of model C1 under GM16 at $S_a(1s)=0.3g$ with and without modeling brace re-engagement

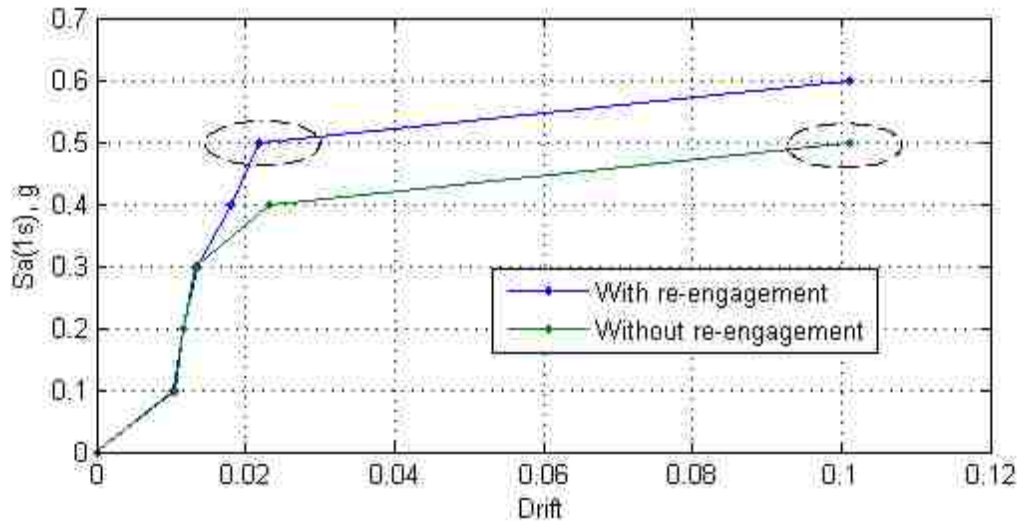


Figure 7.49 Comparison of IDA results for model C1 under GM25 with and without including brace re-engagement

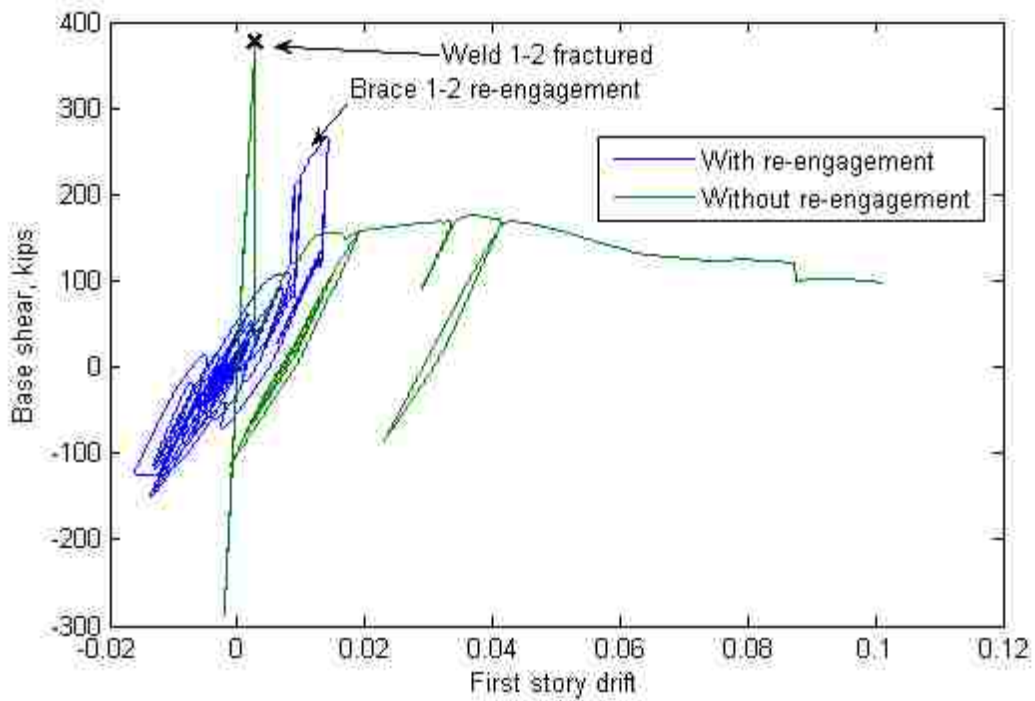


Figure 7.50 Comparison first story hysteresis of model C1 under GM25 at $S_a(1s)=0.5g$ with and without including brace re-engagement

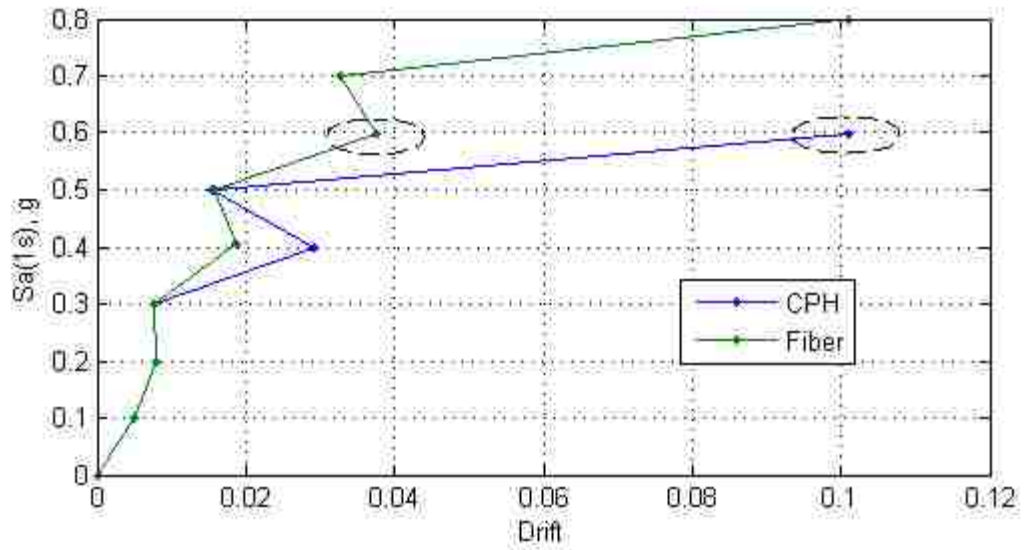


Figure 7.51 IDA results for model C2 under GM2 when CPH approach or fiber approach is used for beam modeling

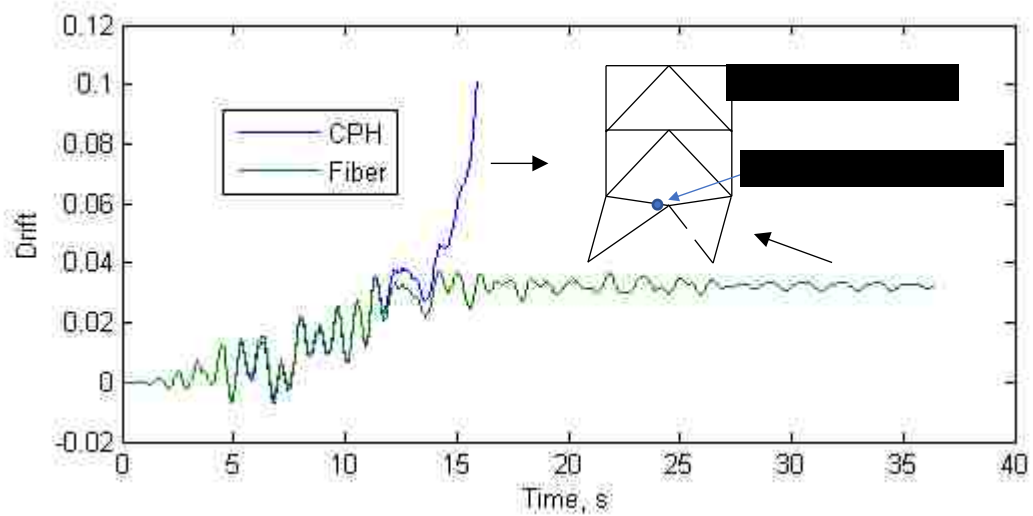


Figure 7.52 First story drift history of model C2 under GM2 at $S_a(1s)=0.6g$ when CPH approach or fiber approach is used for beam modeling

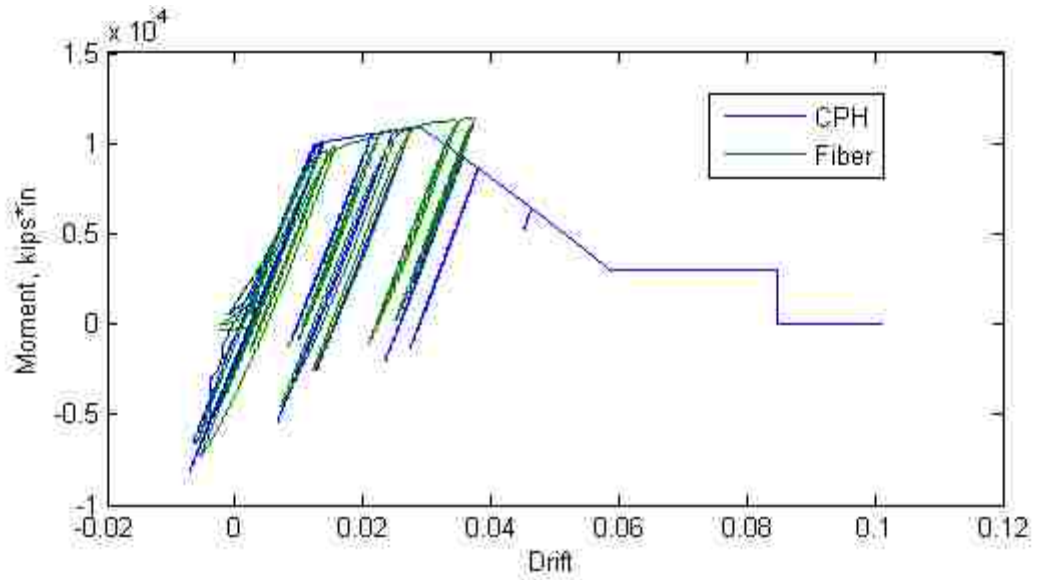


Figure 7.53 Beam moment response at chevron point of model C2 under GM2 at $S_a(1s)=0.6g$ when CPH approach or fiber approach is used for beam modeling

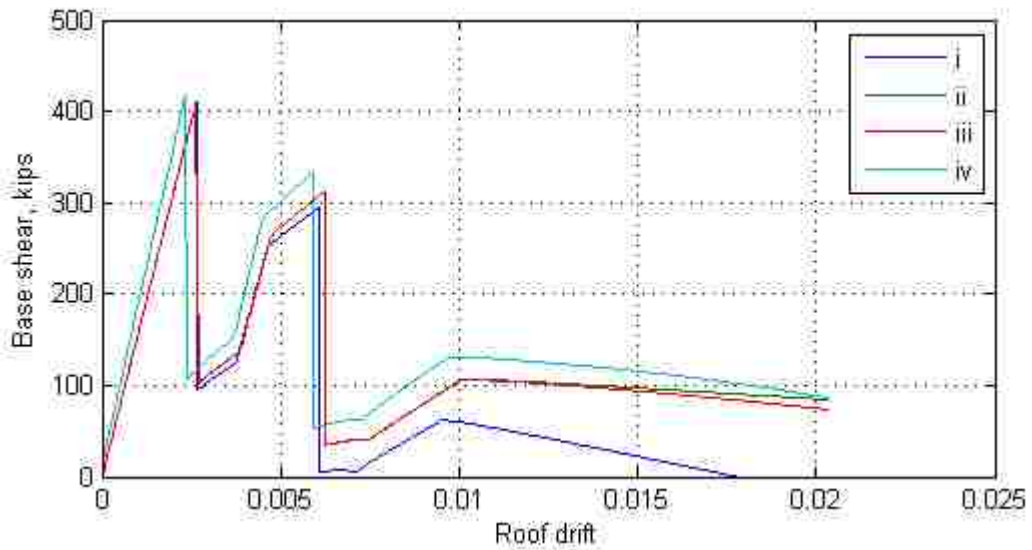
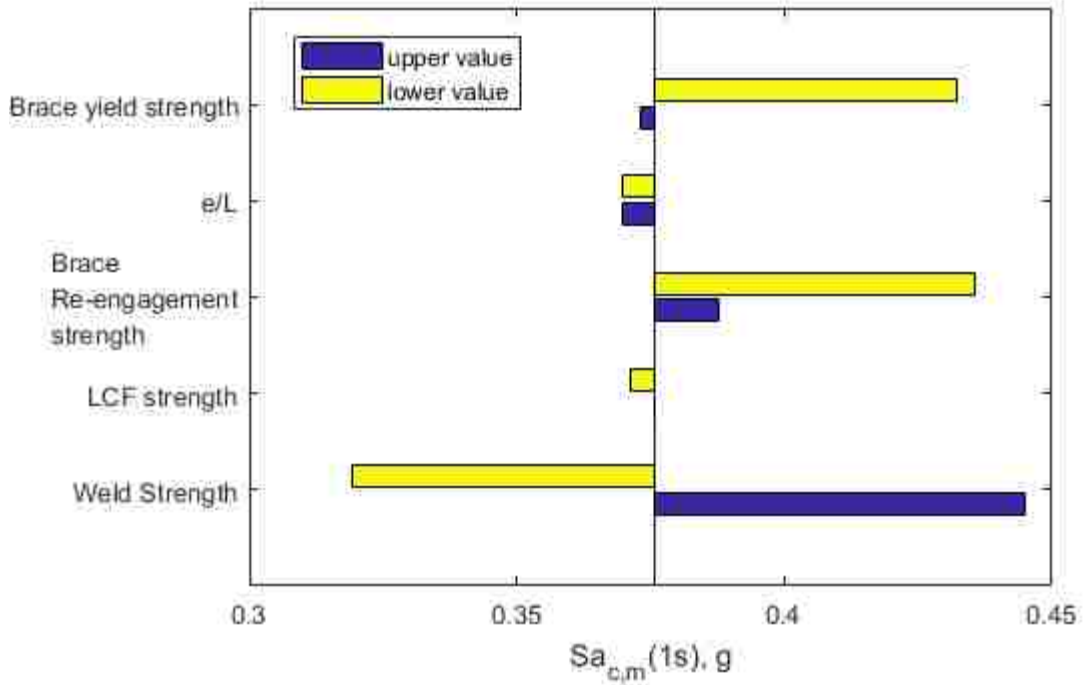
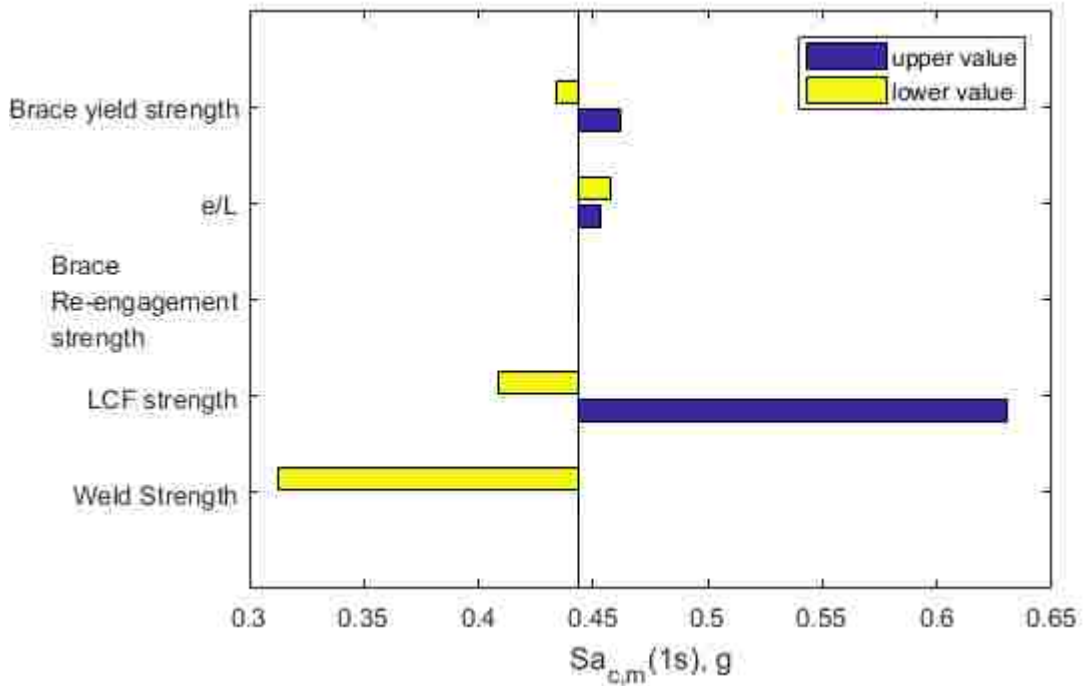


Figure 7.54 Pushover analysis results for C1 model with different gravity load system modeling approaches



(a)



(b)

Figure 7.55 Variation of median collapse capacity as individual model parameters are varied to lower and upper valued: (a) model C1; (b) model C2.

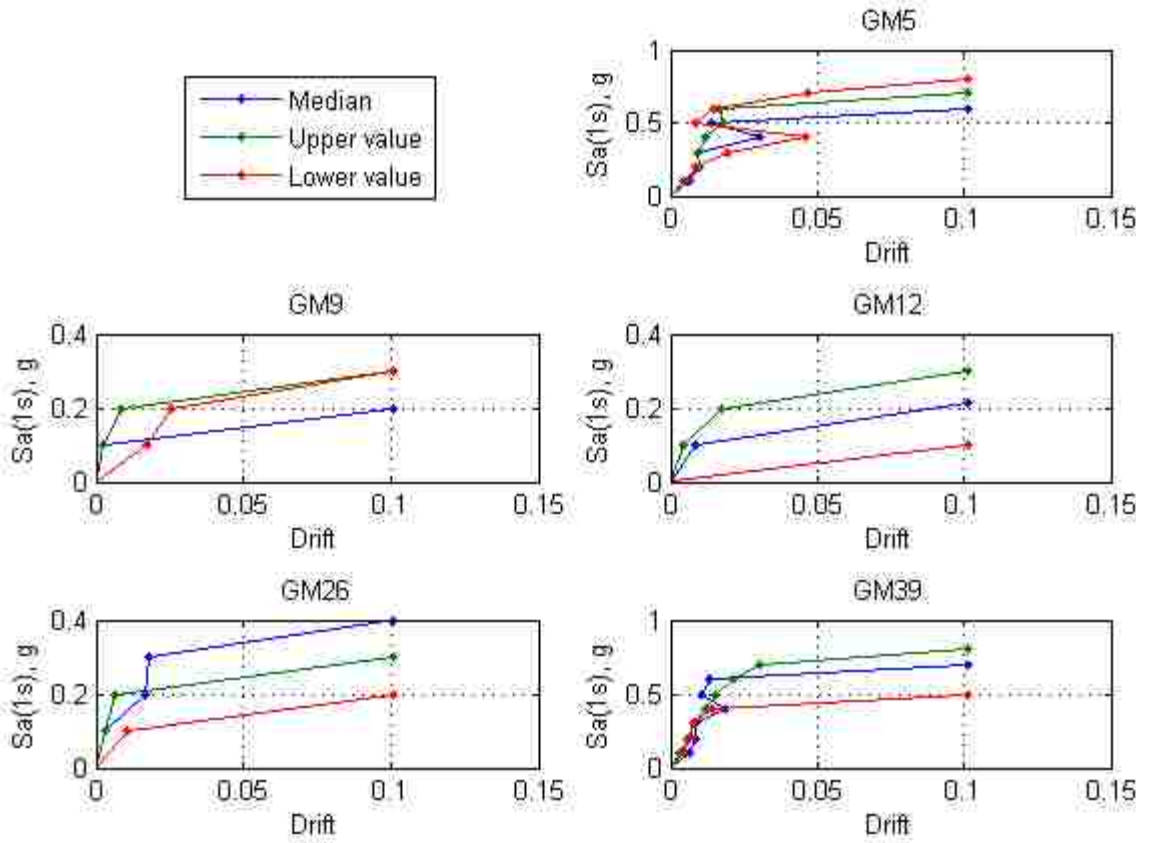


Figure 7.56 Effect of weld strength on the collapse capacity for model C1 for 5 ground motions

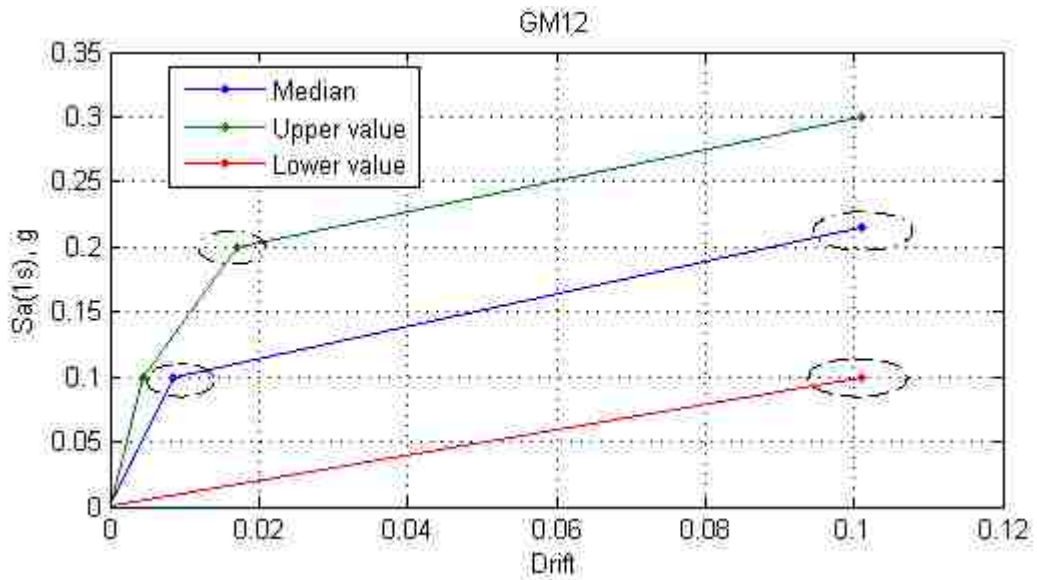


Figure 7.57 IDA for GM12 for model C1 with variation on weld strength

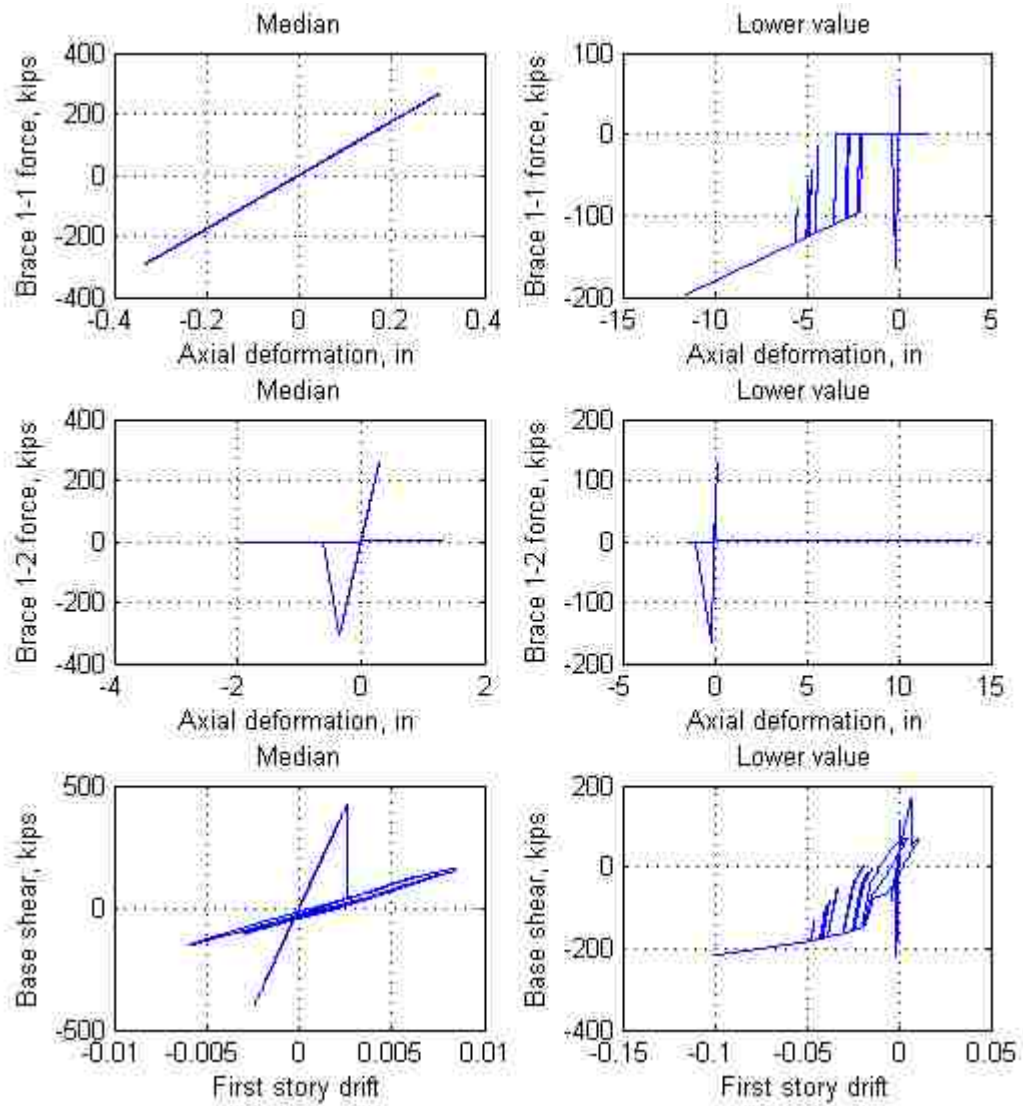


Figure 7.58 Response for GM12 at $S_a(1s)=0.1g$ for model C1 with median and lower value of weld strength

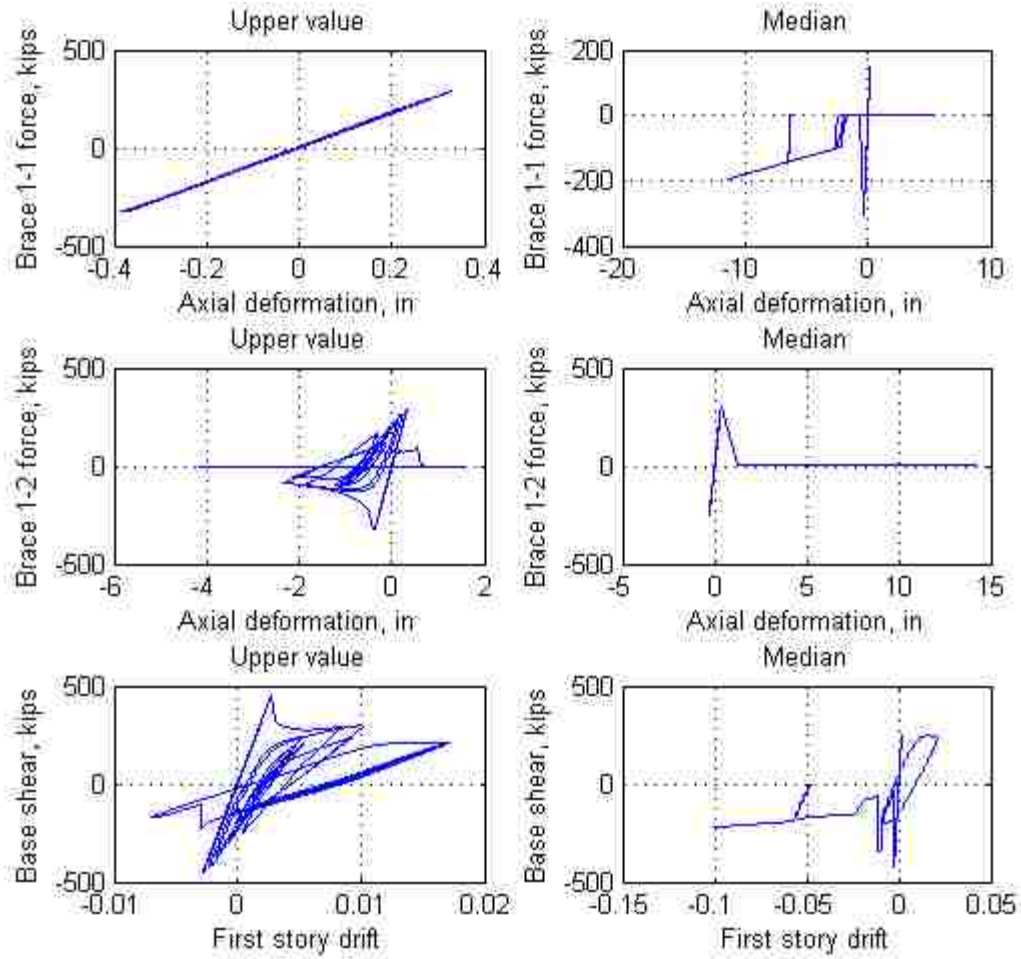
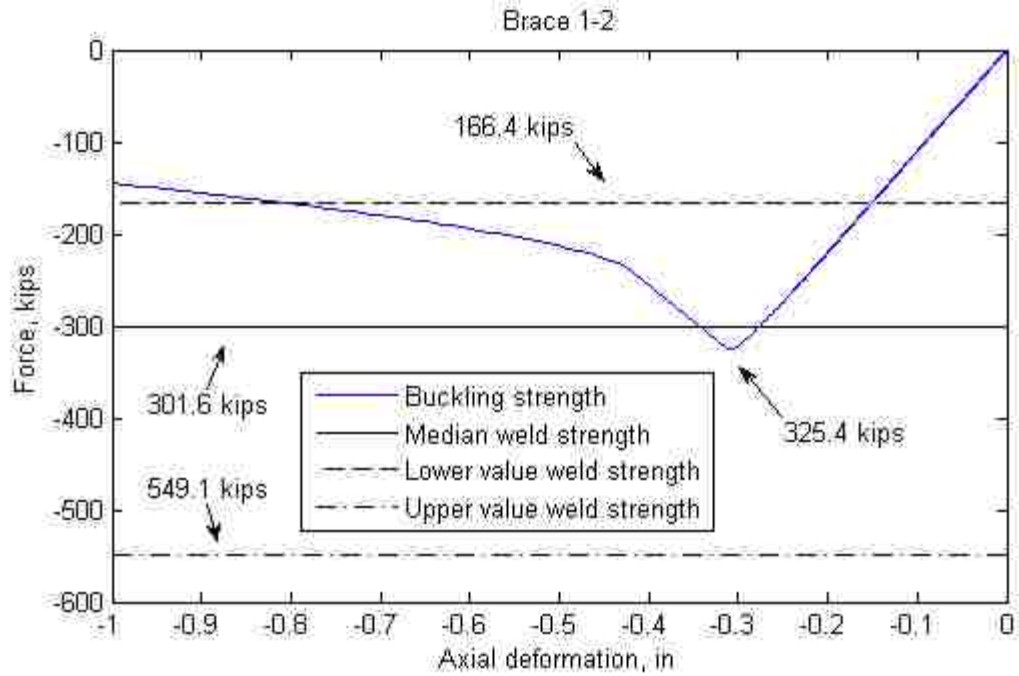
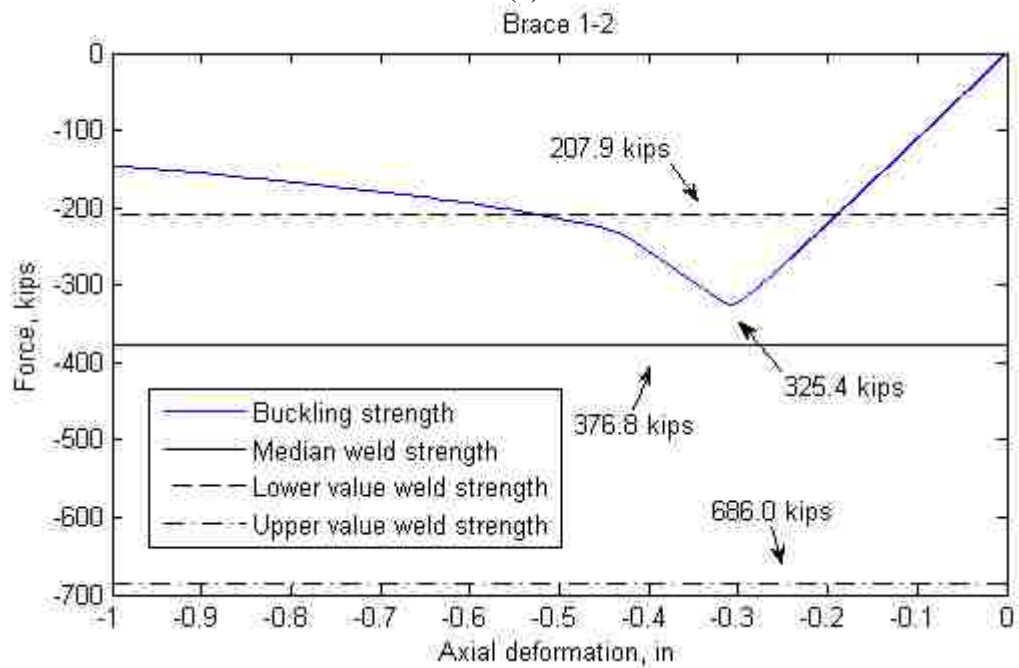


Figure 7.59 Response for GM12 at $S_a(1s)=0.2g$ for model C1 with median and upper value of weld strength



(a)



(b)

Figure 7.60 Brace 1-2 buckling strength with different Weld 1-2 strength in sensitivity analysis for (a) model C1; (b) model C2

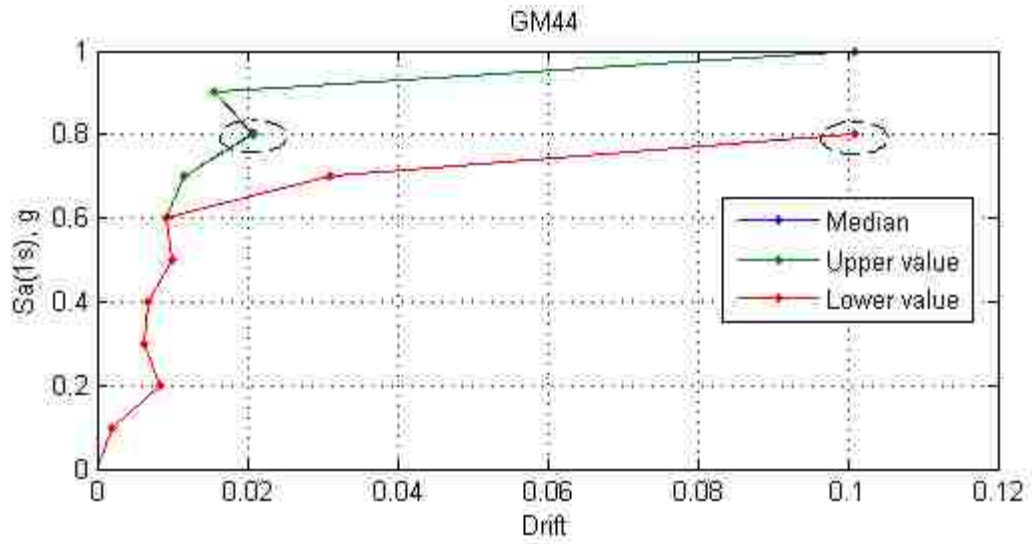


Figure 7.61 IDA result for GM44 for model C1 with different LCF strength

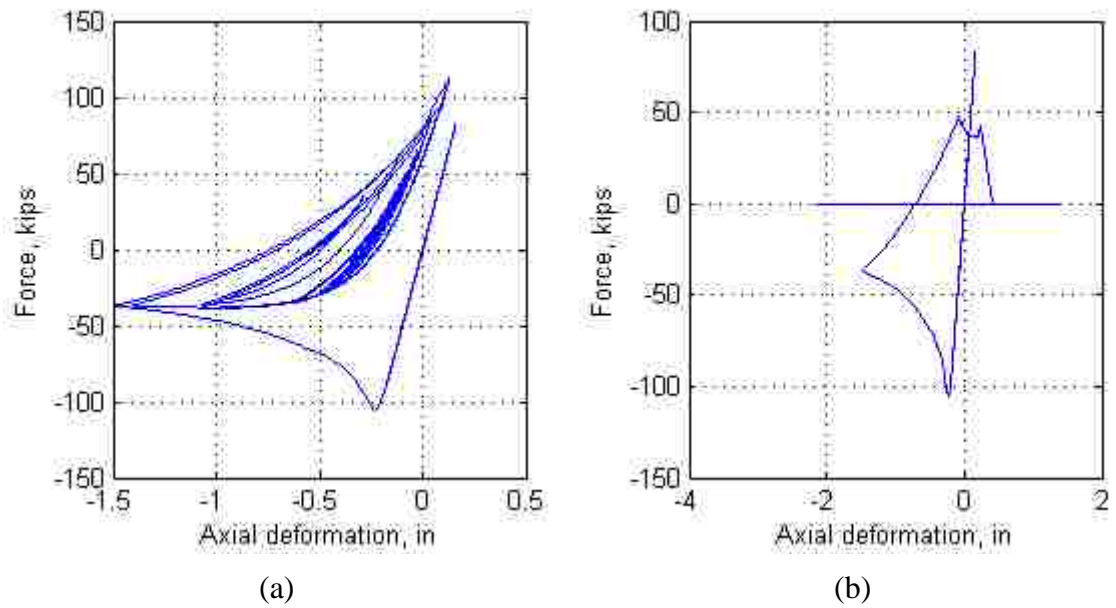


Figure 7.62 Brace 3-2 hysteresis with different brace LCF strength: (a) upper value; (b) lower value

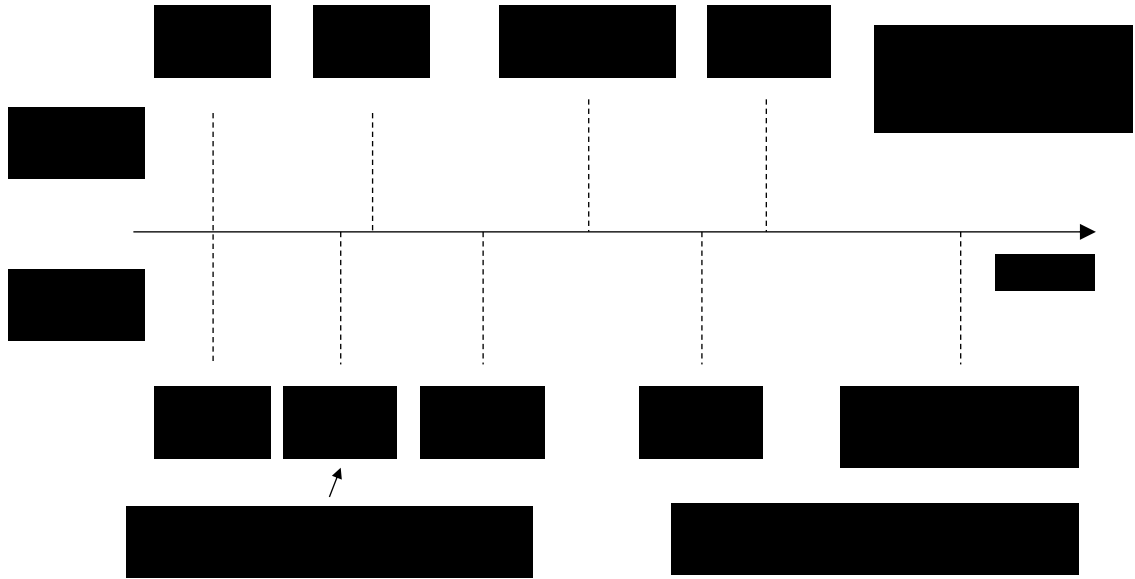


Figure 7.63 Timeline of important limit states for GM44 at $S_a=0.8g$ for model C1 with different LCF strength

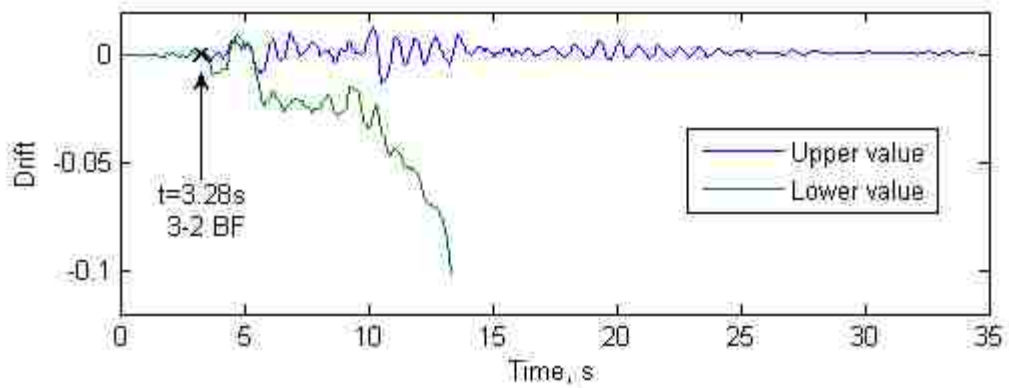


Figure 7.64 First story drift history for GM44 at $S_a=0.8g$ for model C1 with different LCF strength (BF: brace fracture)

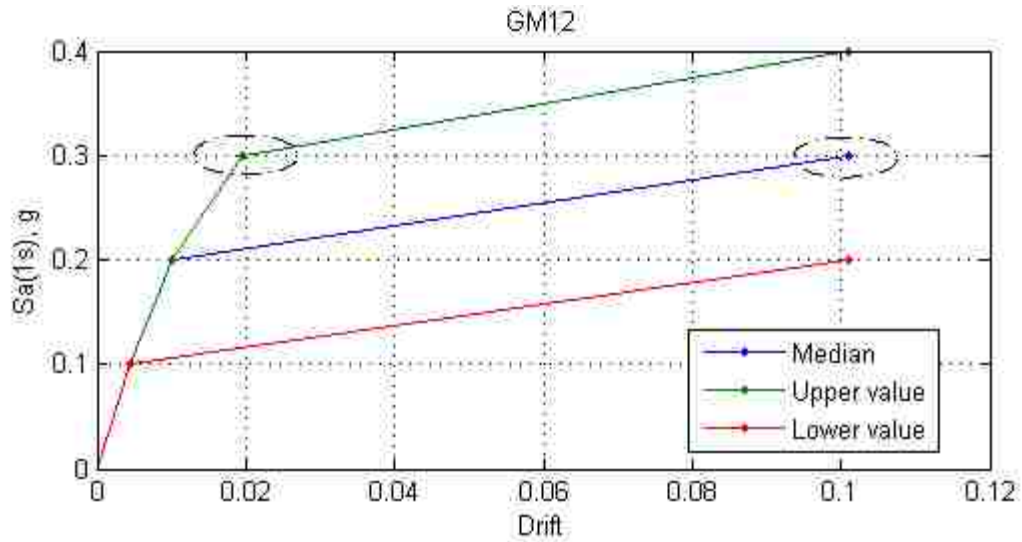


Figure 7.65 IDA result for GM12 for model C2 with different brace LCF strength

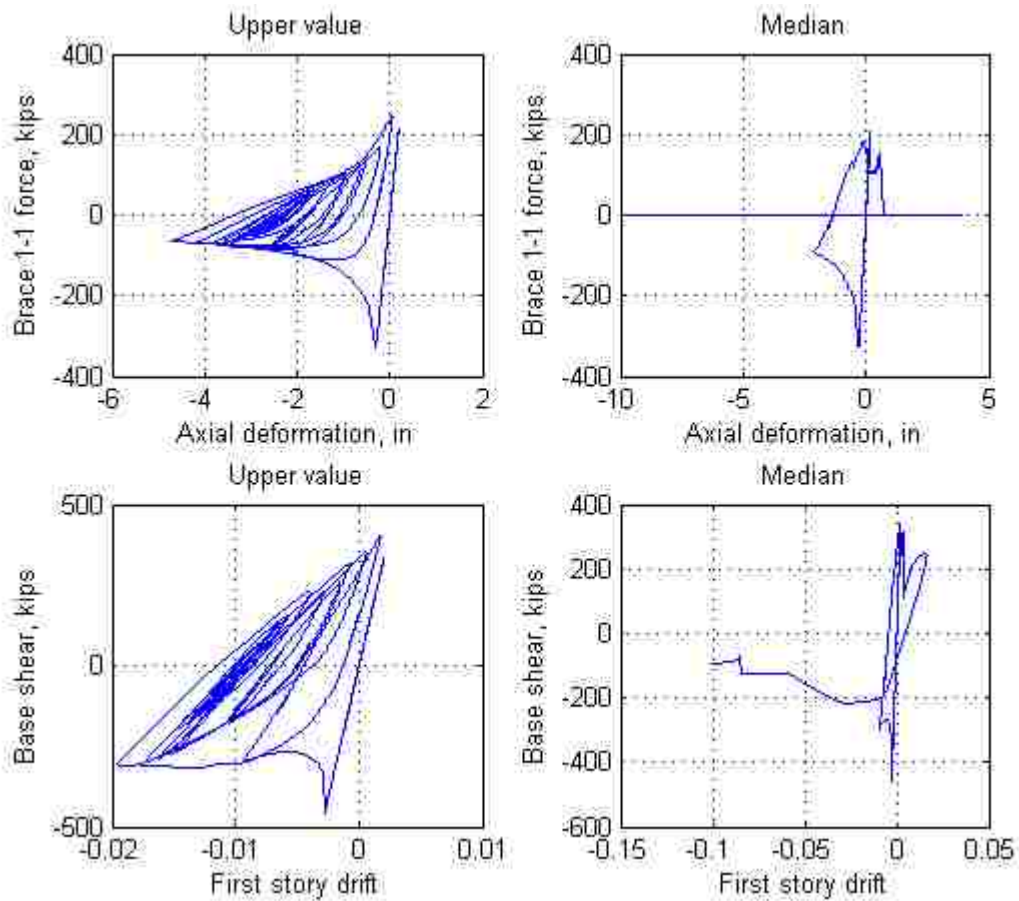


Figure 7.66 Brace 1-2 and first story hysteresis response for GM12 at $S_a=0.3g$ for model C2 with different LCF strength

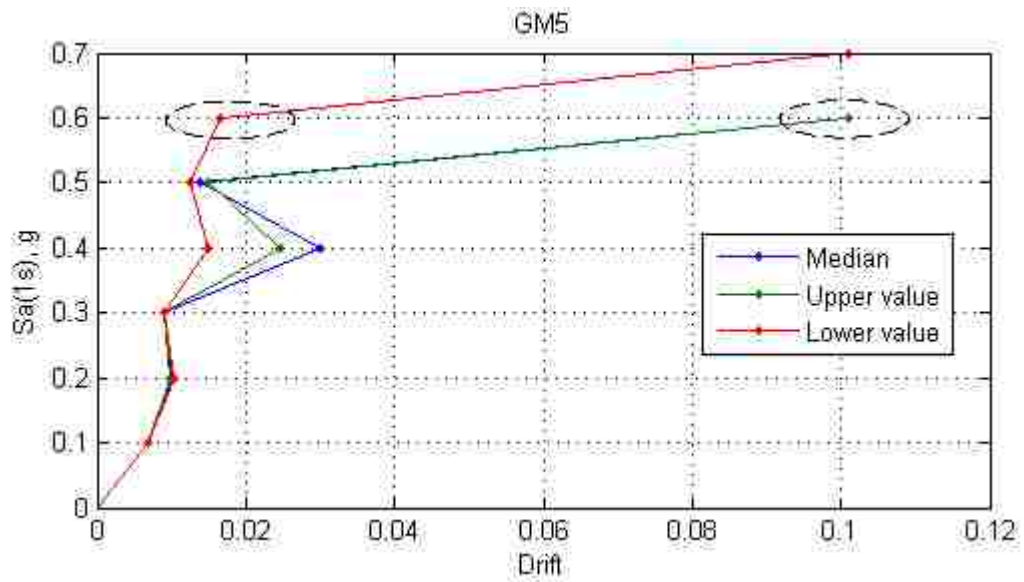


Figure 7.67 IDA result for GM5 for model C1 with different brace re-engagement strength

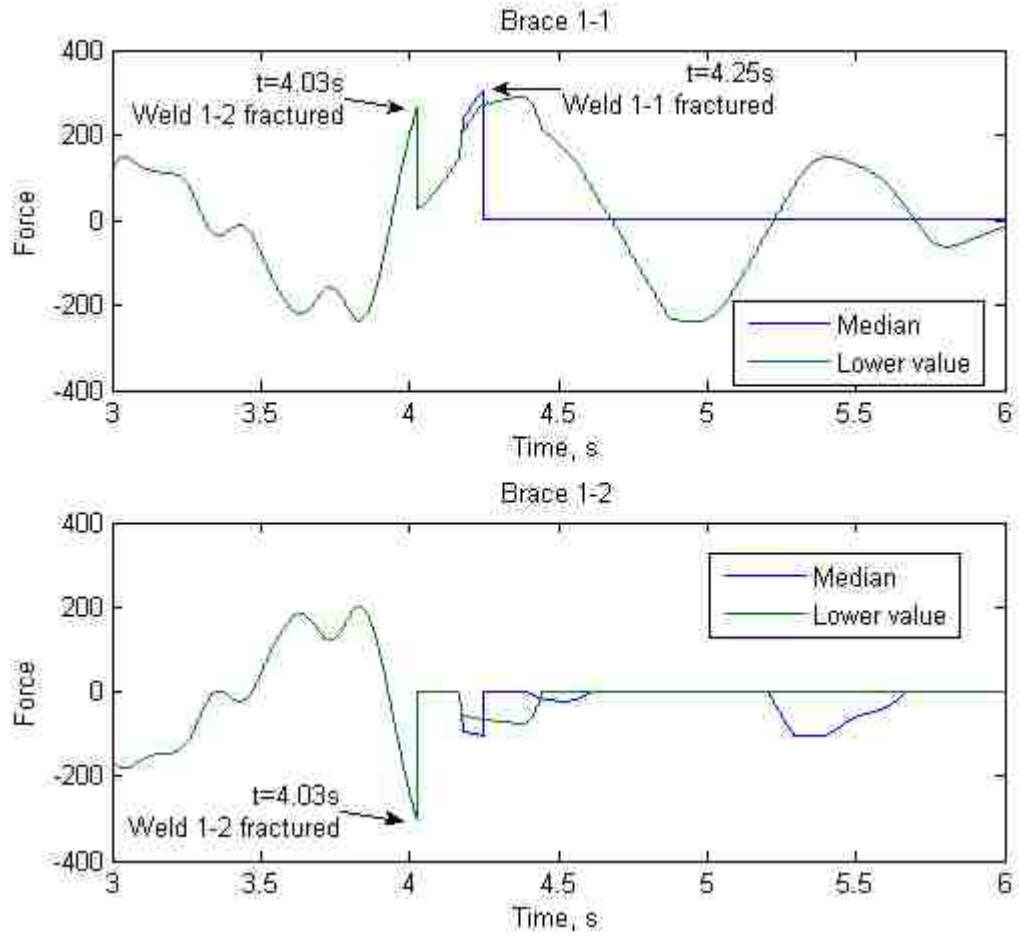


Figure 7.68 Force history of Brace 1-1 and Brace 1-2 for GM5 at $S_a=0.6g$ for model C1 with different brace re-engagement strength

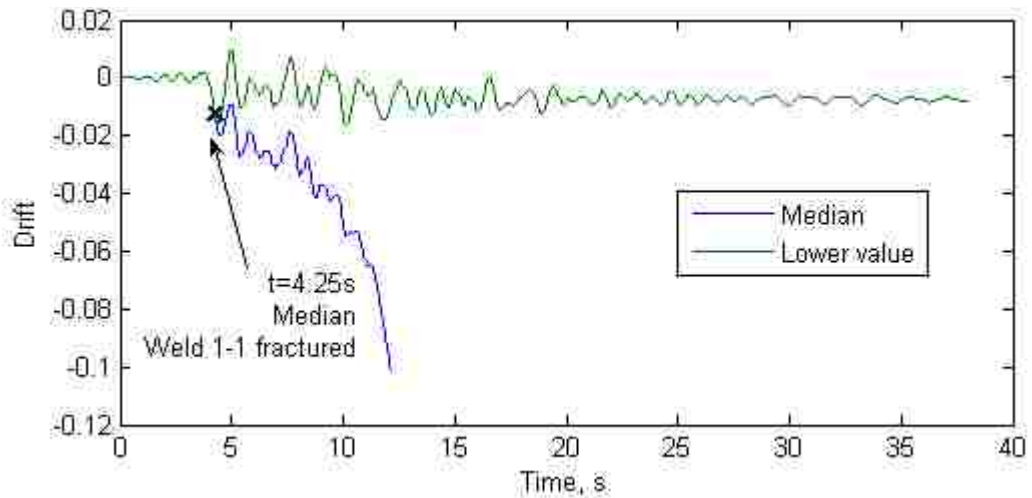


Figure 7.69 First story drift history for GM5 at $S_a=0.6g$ for model C1 with different brace re-engagement strength

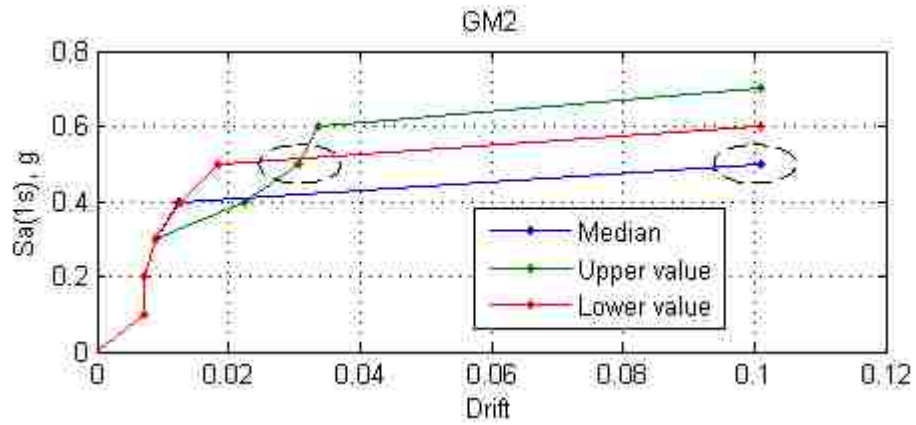
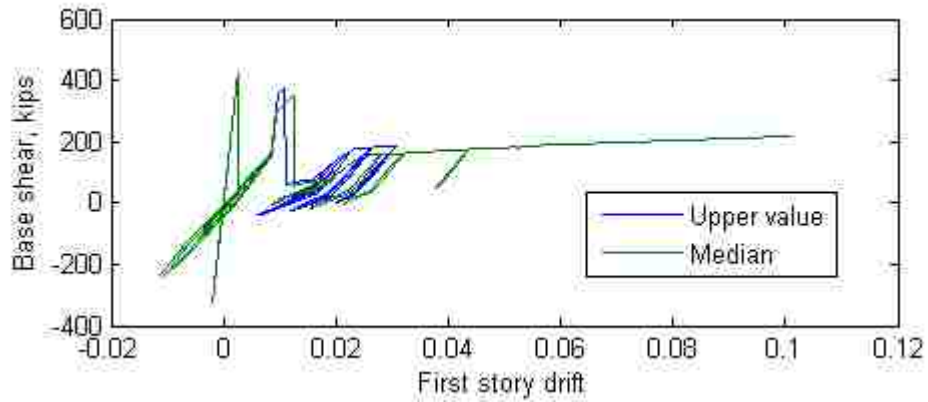
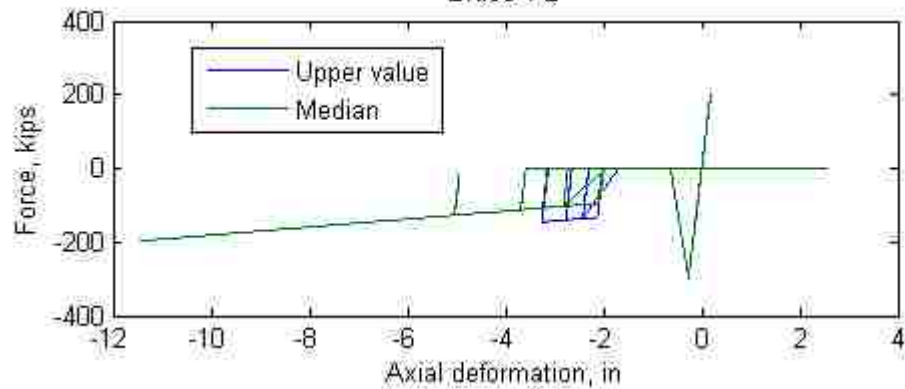


Figure 7.70 IDA result for GM2 for model C1 with different brace re-engagement strength



(a)
Brace 1-2



(b)

Figure 7.71 Comparison of (a) First story and (b) Brace 1-2 hysteresis response for GM2 at $S_a=0.5g$ for model C1 with different brace re-engagement strength

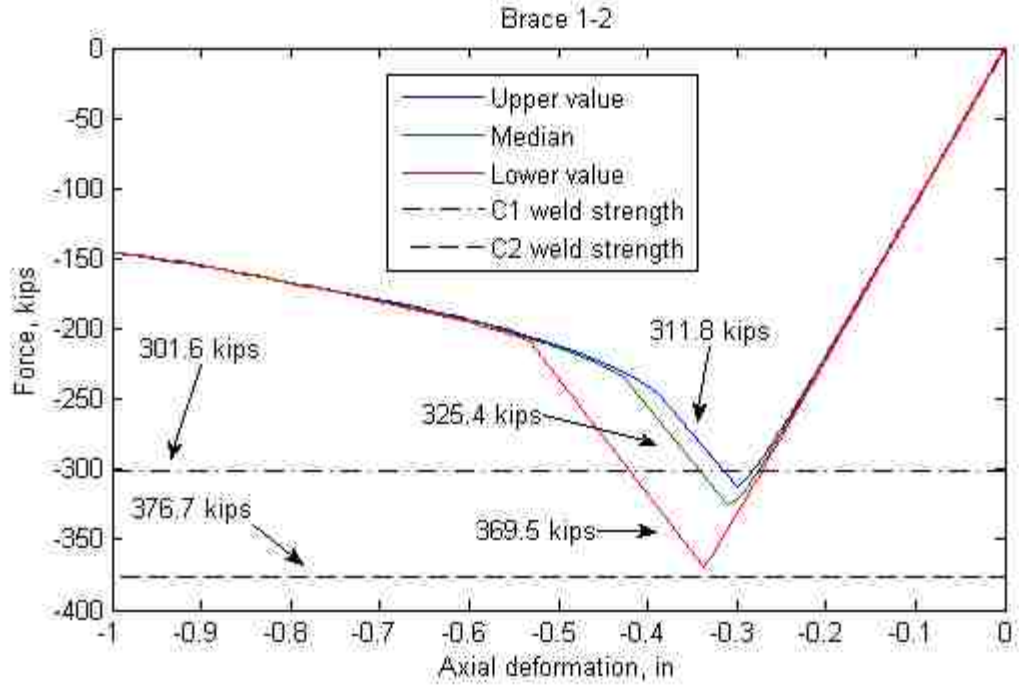


Figure 7.72 Buckling strength of Brace 1-2 with different e/L value and Weld 1-2 strength in mode C1 and model C2

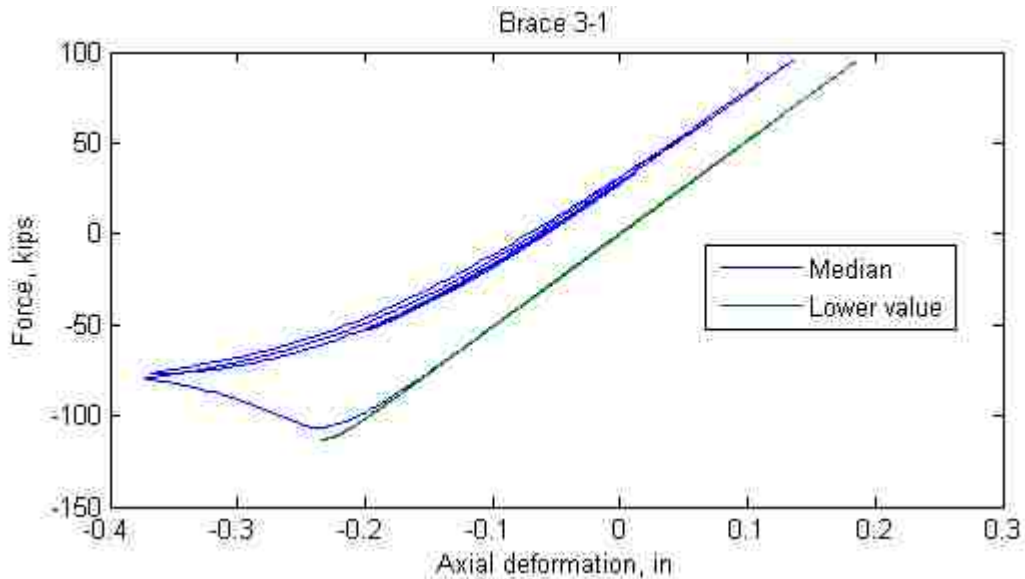


Figure 7.73 Brace 3-1 hysteresis response for GM5 at $S_a=0.4g$ for model C1 with different brace initial out of straightness (e/L)

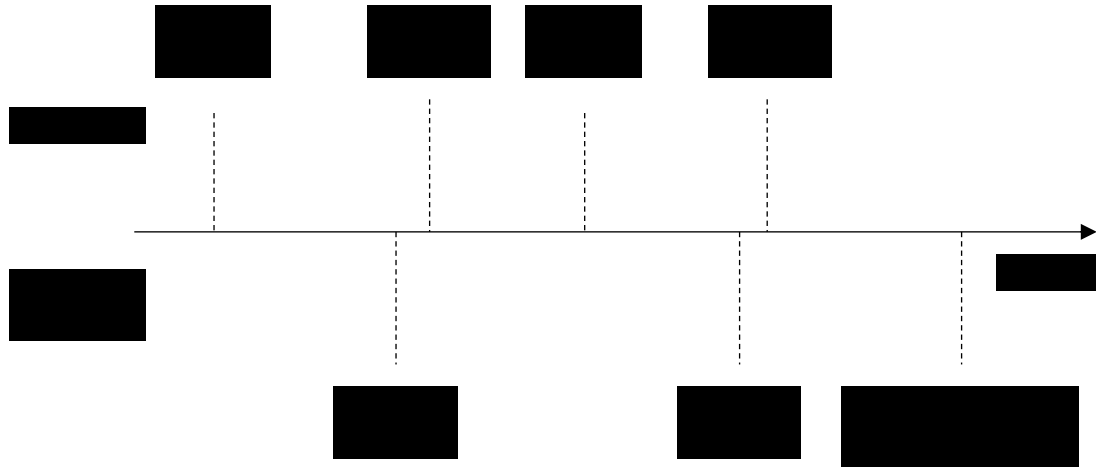


Figure 7.74 Timeline of limit states for GM5 at $S_a=0.4g$ for model C1 with different brace initial out of straightness (e/L)

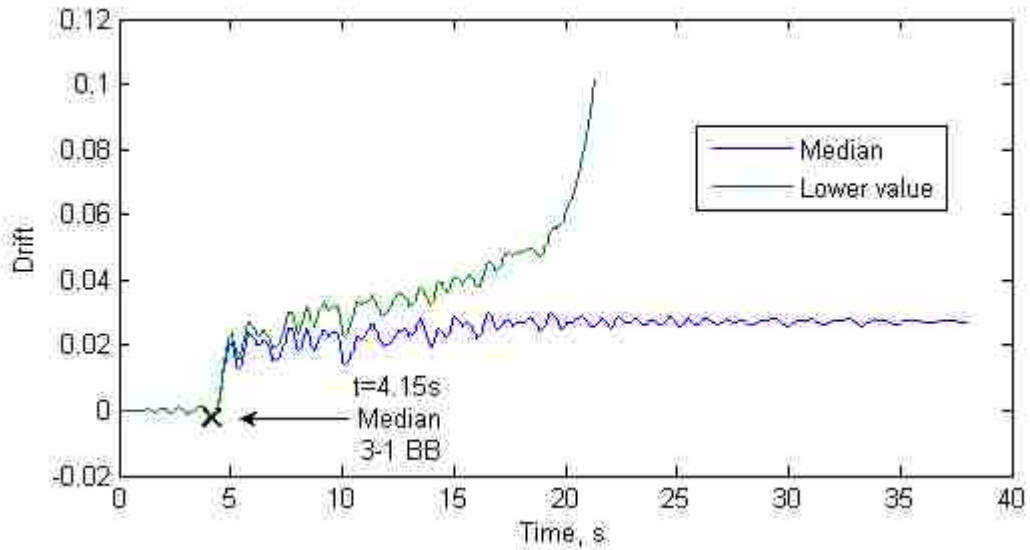


Figure 7.75 First story drift history for GM5 at $S_a=0.4g$ for C1 model with different brace initial out of straightness (e/L)

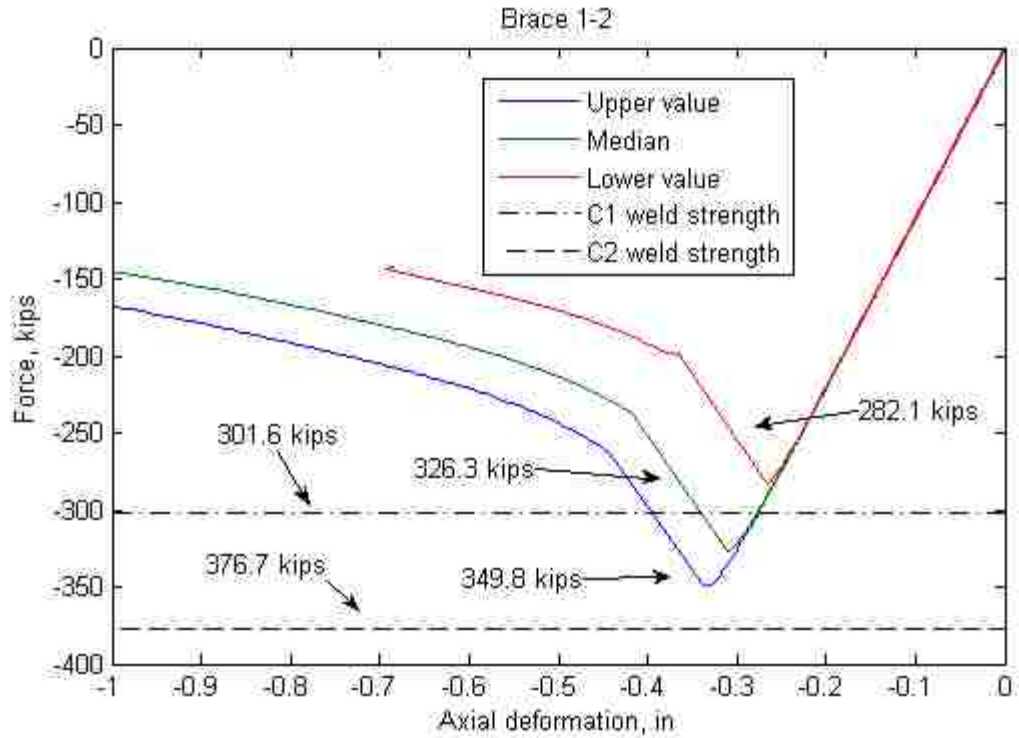


Figure 7.76 Buckling strength of Brace 1-2 with different yield strength and weld 1-2 strength in model C1 and model C2

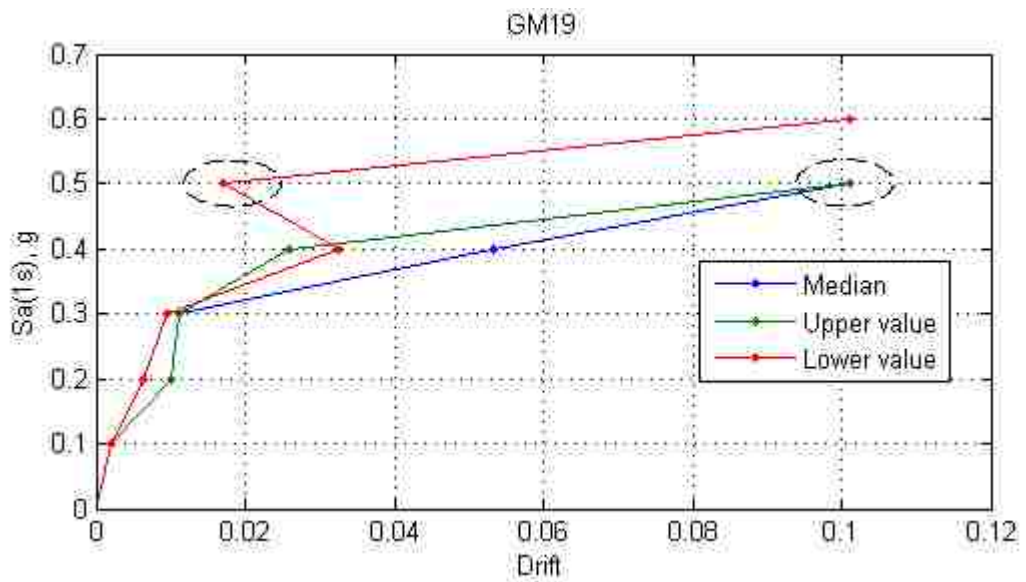


Figure 7.77 IDA result for GM19 for model C1 with different brace yield strength

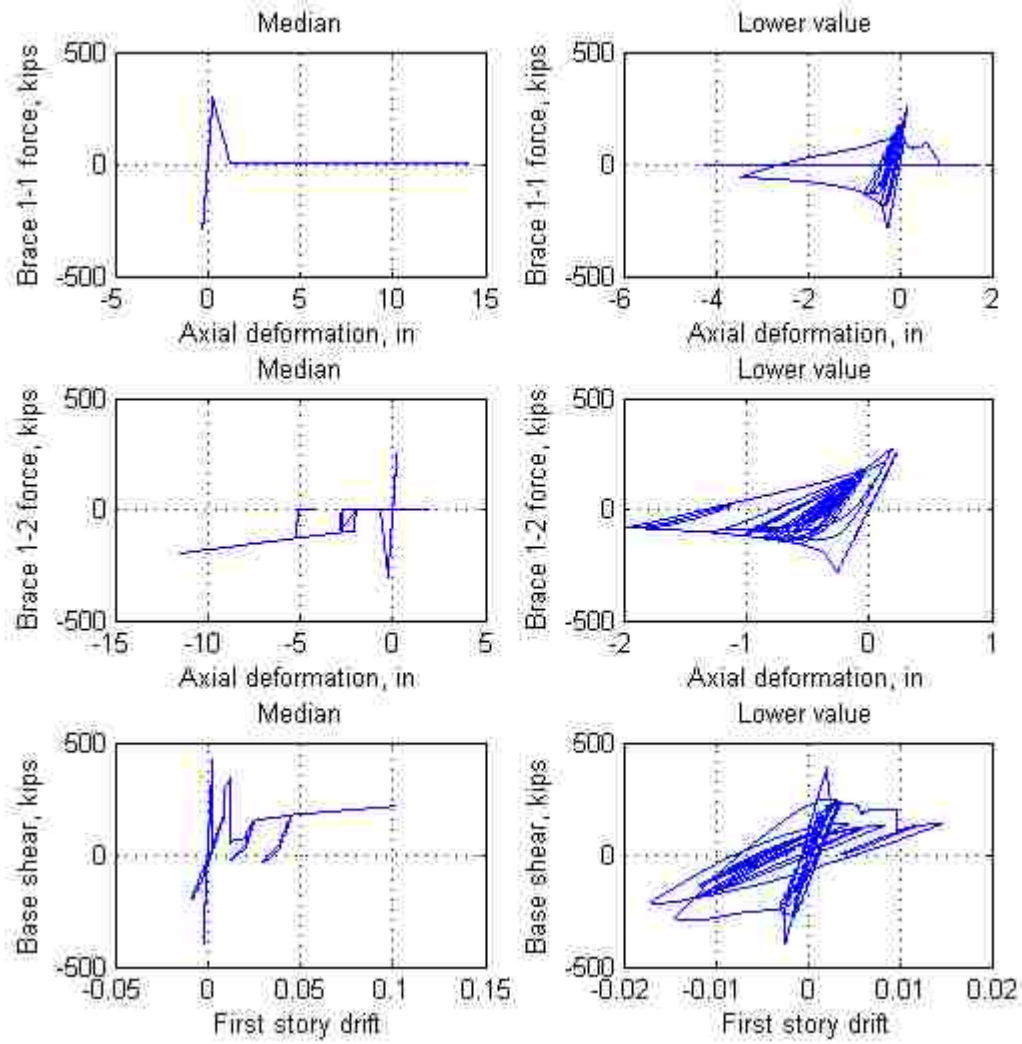


Figure 7.78 Brace 1-1, Brace 1-2, and first story hysteresis response for GM19 at $S_a=0.5g$ for model C1 with different brace yield strength

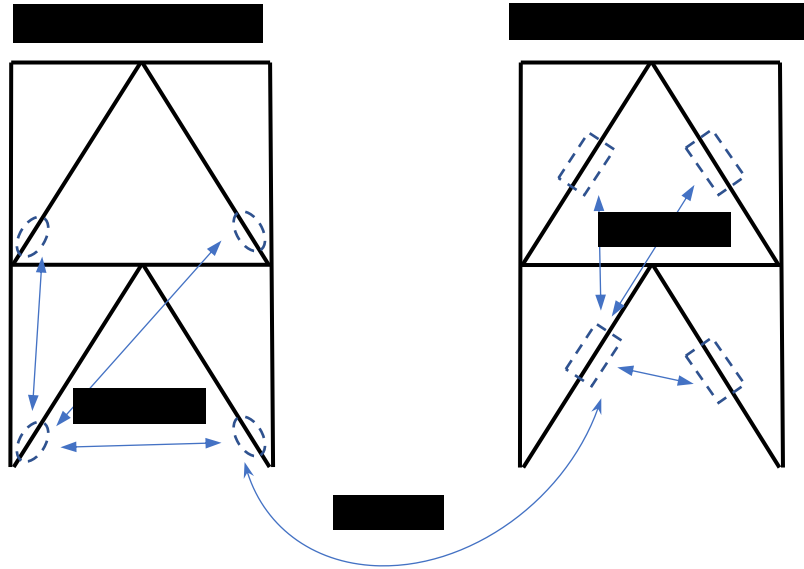


Figure 7.79 Correlation between random variables in MCS

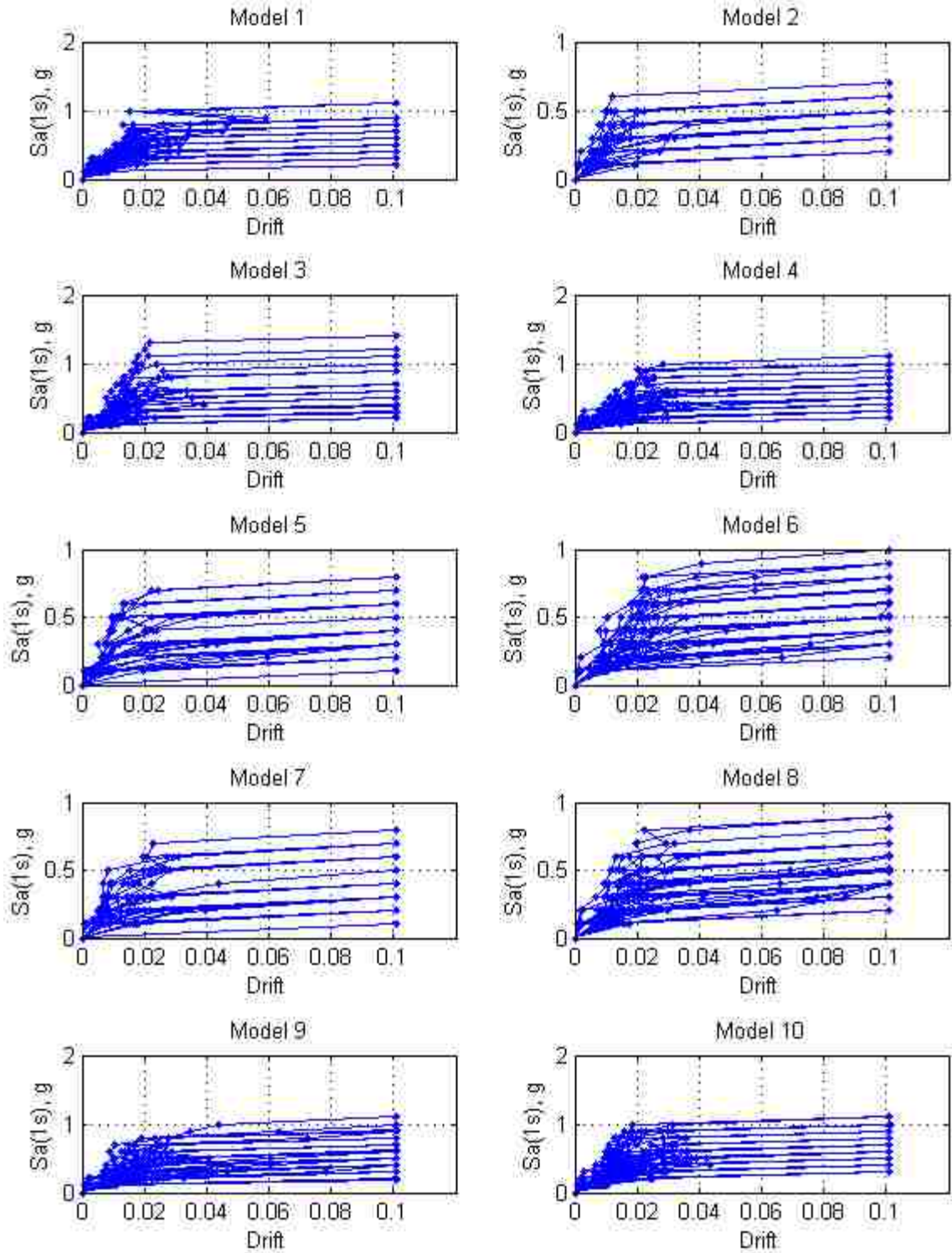


Figure 7.80 IDA results for 20 sample models for model C1

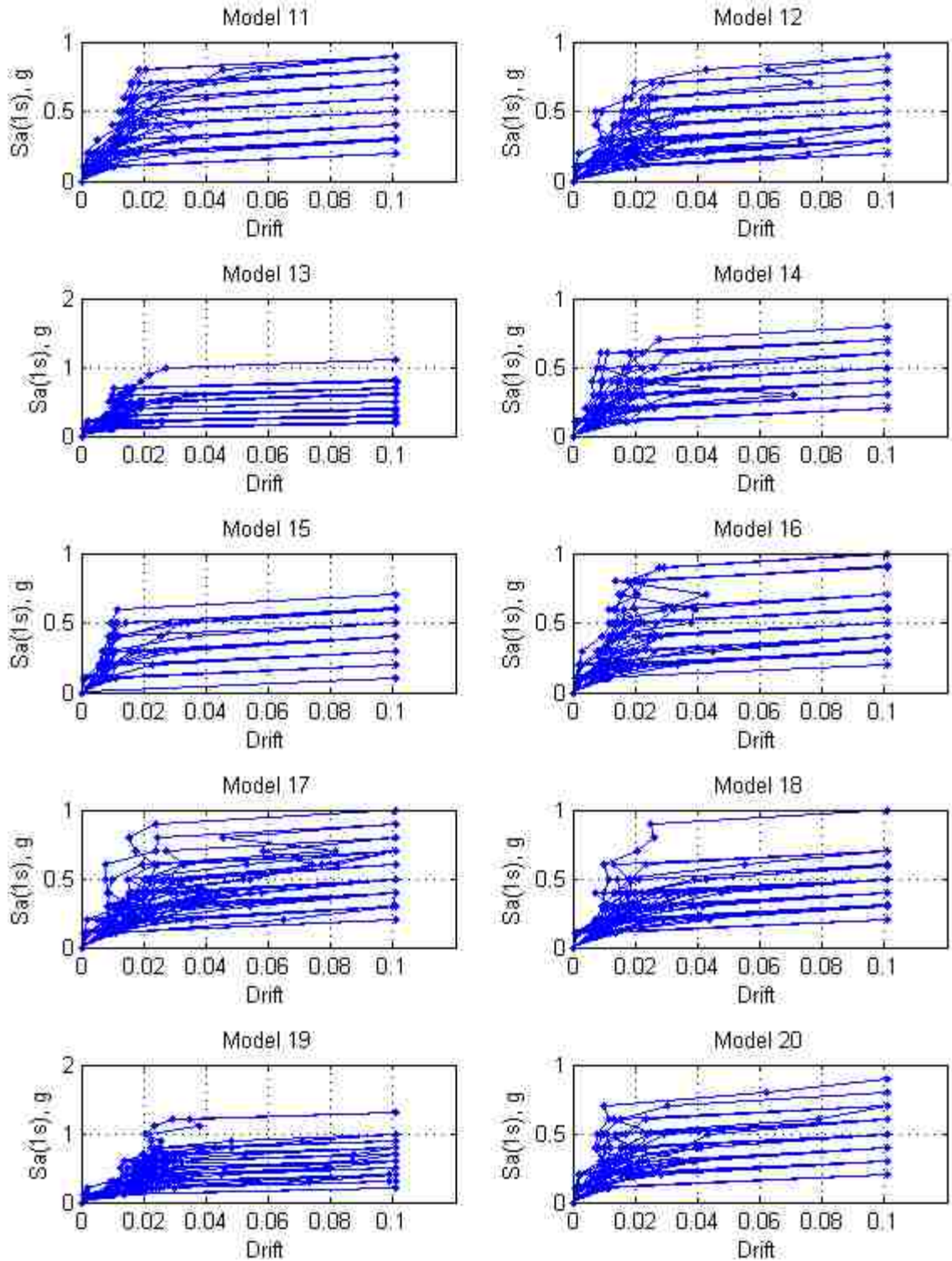


Figure 7.80 IDA results for 20 sample models for model C1 (continued)

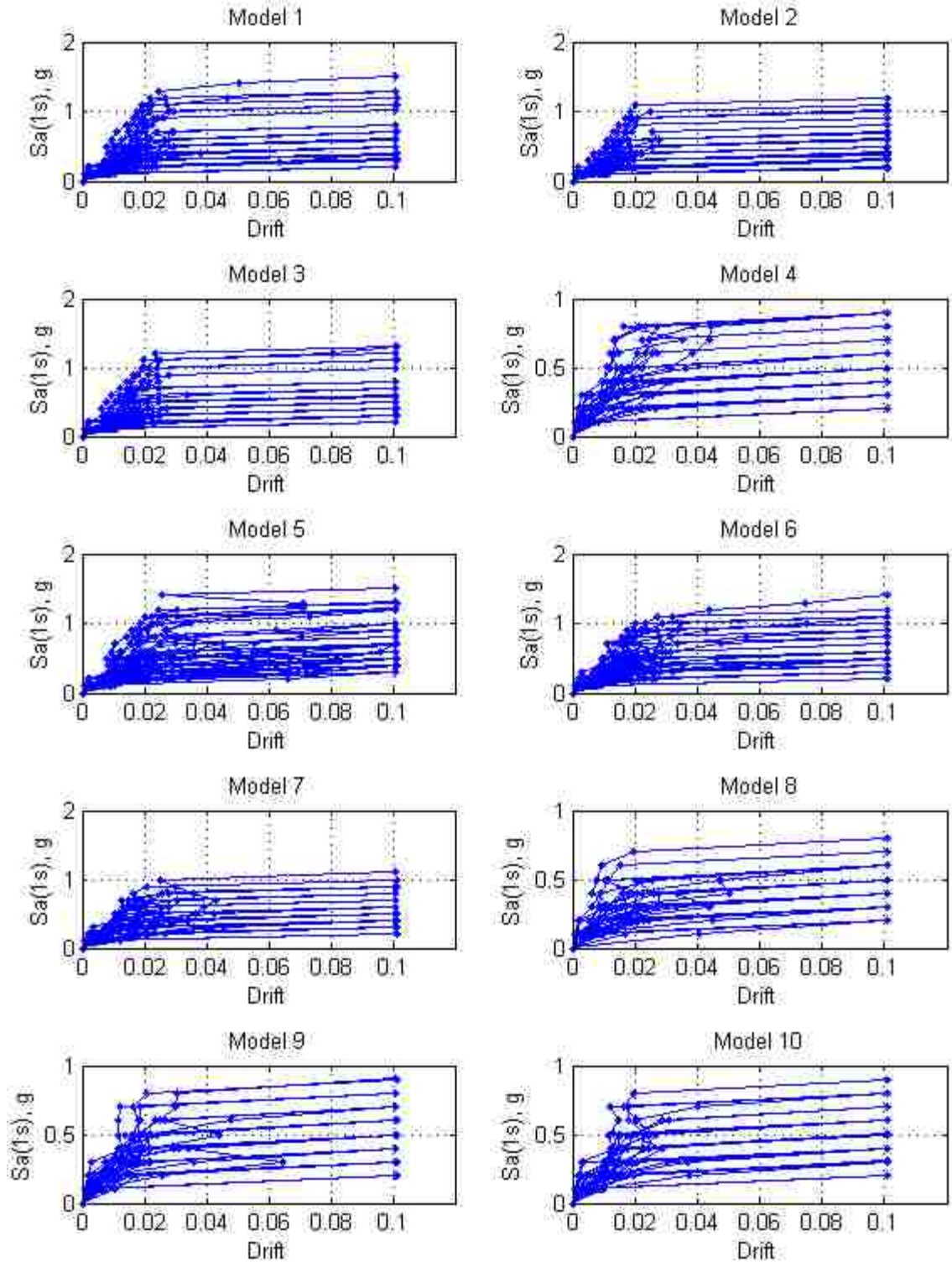


Figure 7.81 IDA results for 20 sample models for model C2

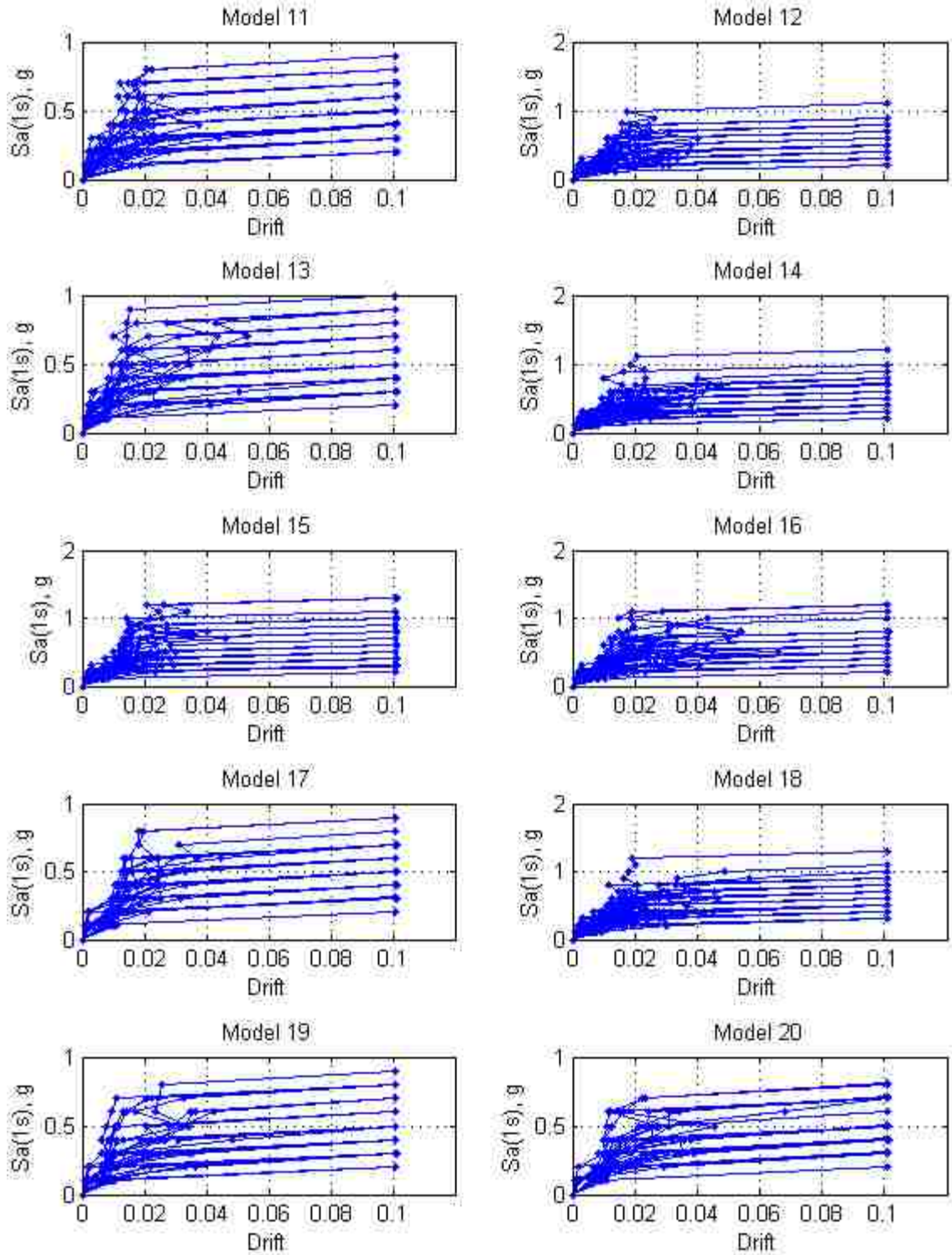
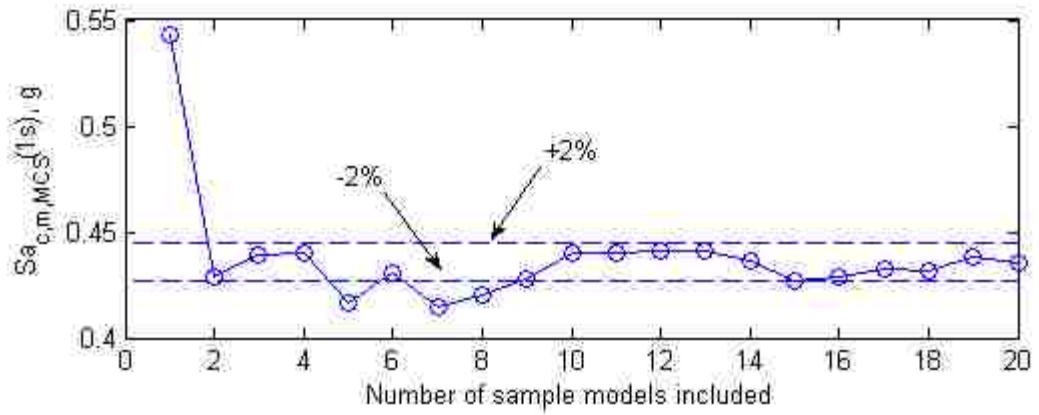
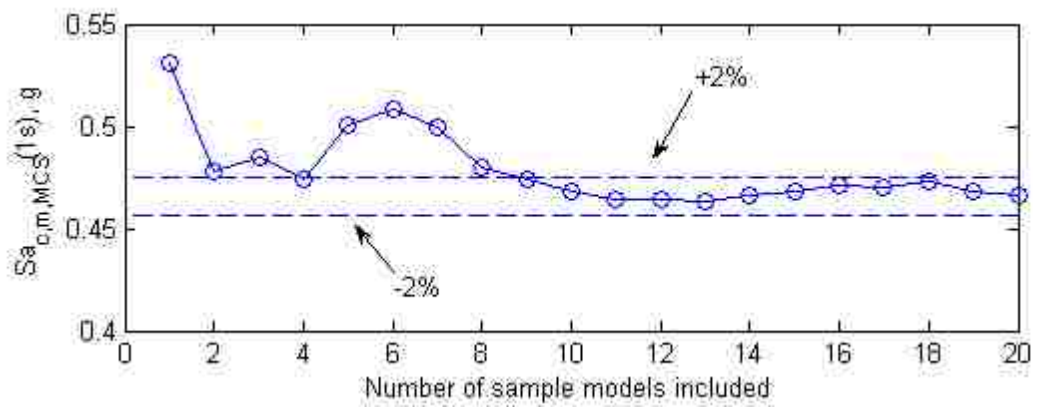


Figure 7.81 IDA results for 20 sample models for model C2 (continued)

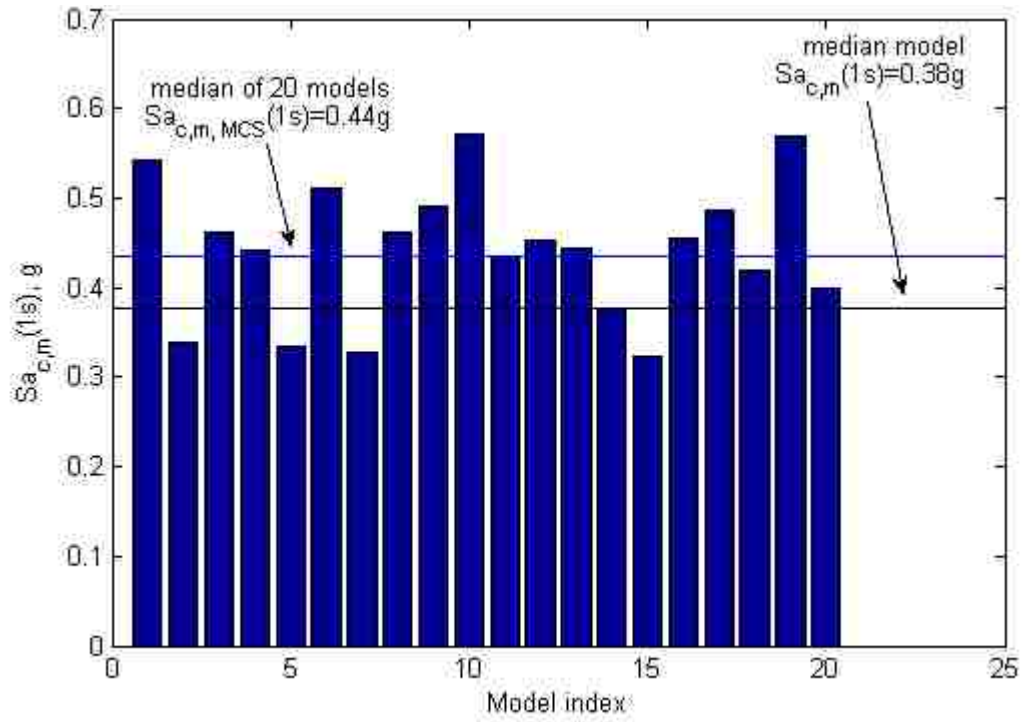


(a)

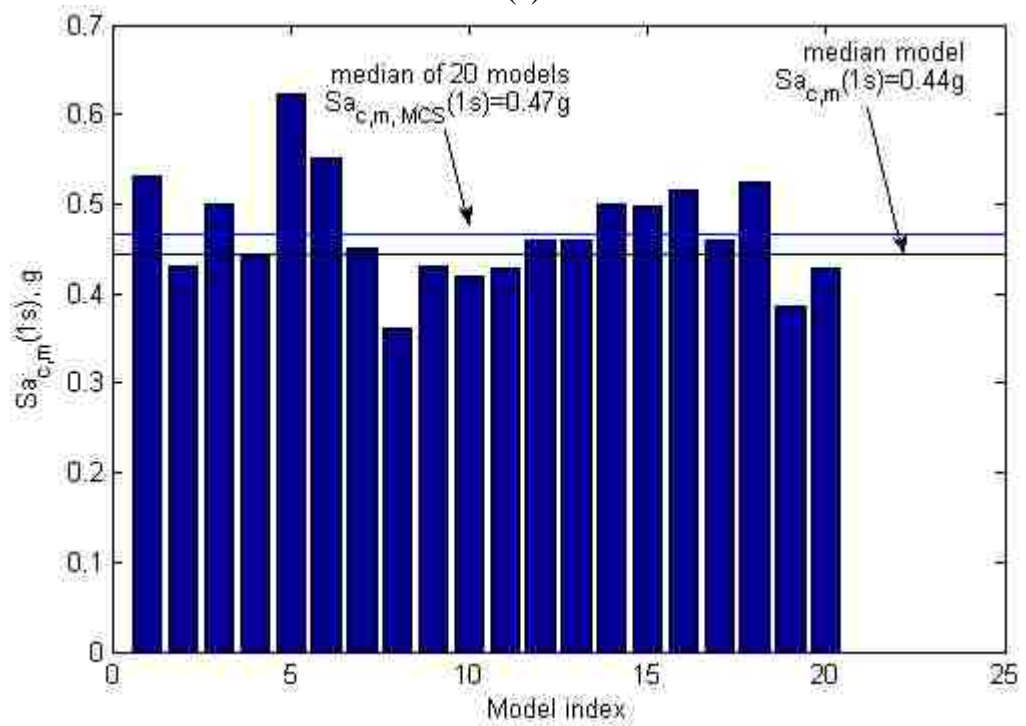


(b)

Figure 7.82 Median collapse capacity with different number of sample models included
 (a) C1 model; (b) C2 model



(a)



(b)

Figure 7.83 Median collapse capacity for each sample model, median collapse capacity considering all 20 sample models, and median collapse capacity of median model for: (a) model C1 and (b) model C2

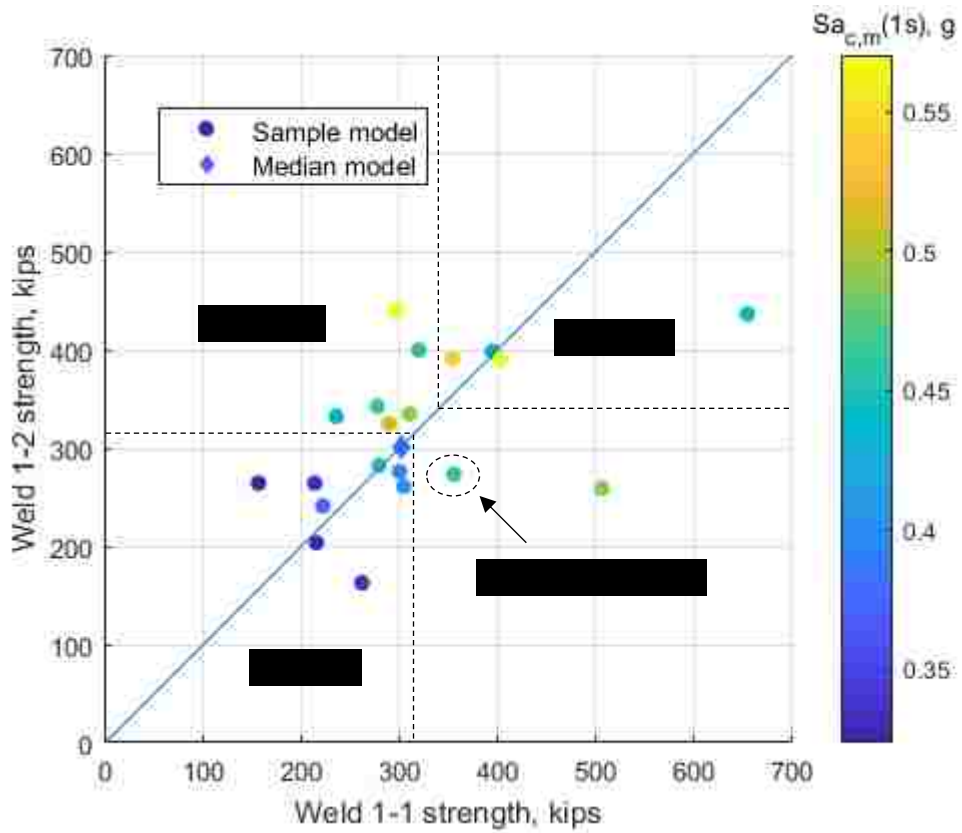


Figure 7.84 First story weld strength and corresponding $Sa_{c,m}(1s)$ for each of the 20 sample models and for the median model for model C1

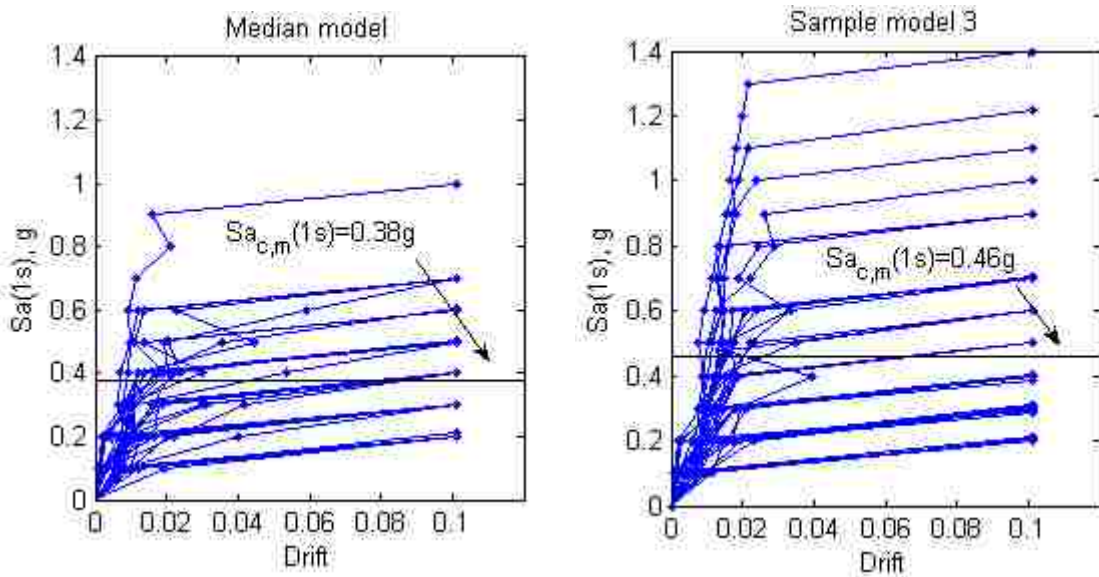


Figure 7.85 IDA results for sample model 3 and median model of model C1

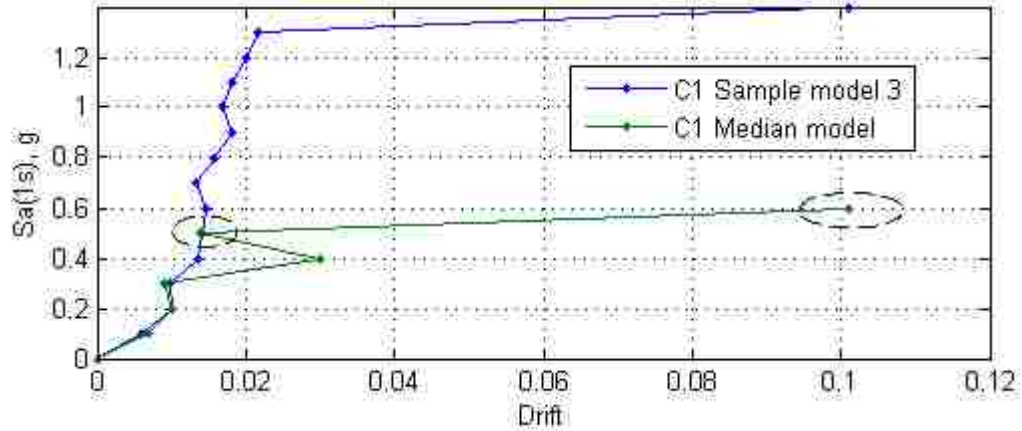


Figure 7.86 IDA result for of GM5 for sample model 3 and median model of model C1

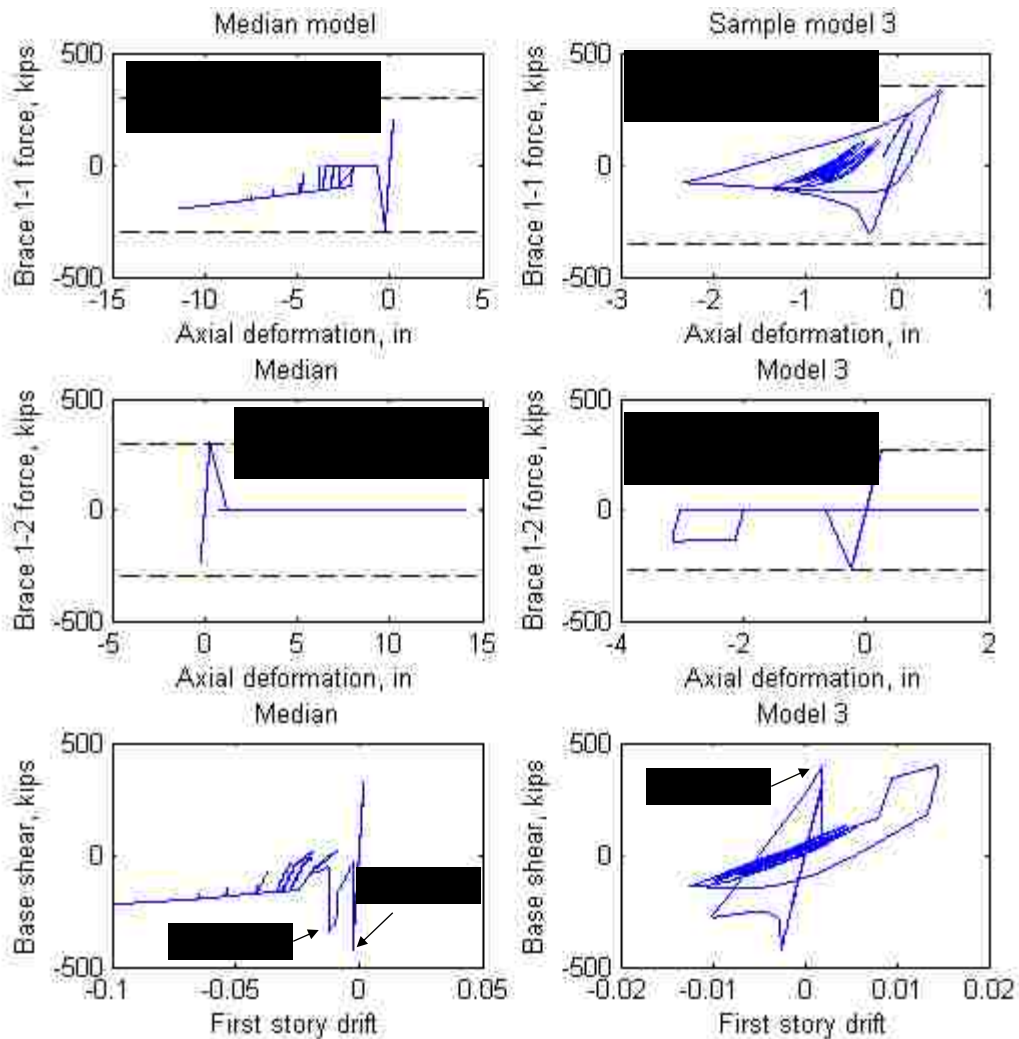


Figure 7.87 Comparison of first story brace response and first story hysteresis between sample model 3 and median model for model C1 for GM5 at $S_a(1s)=0.5g$

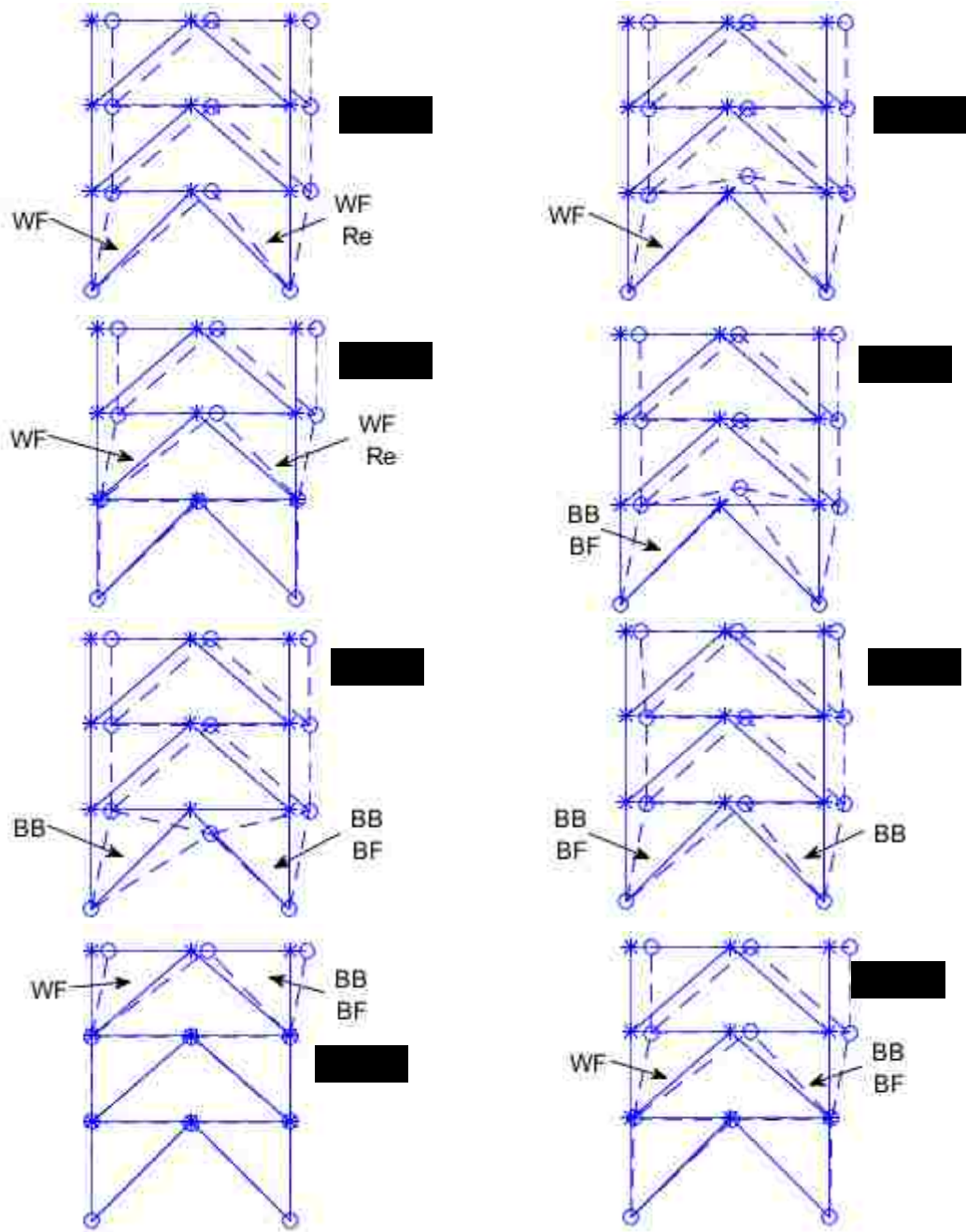
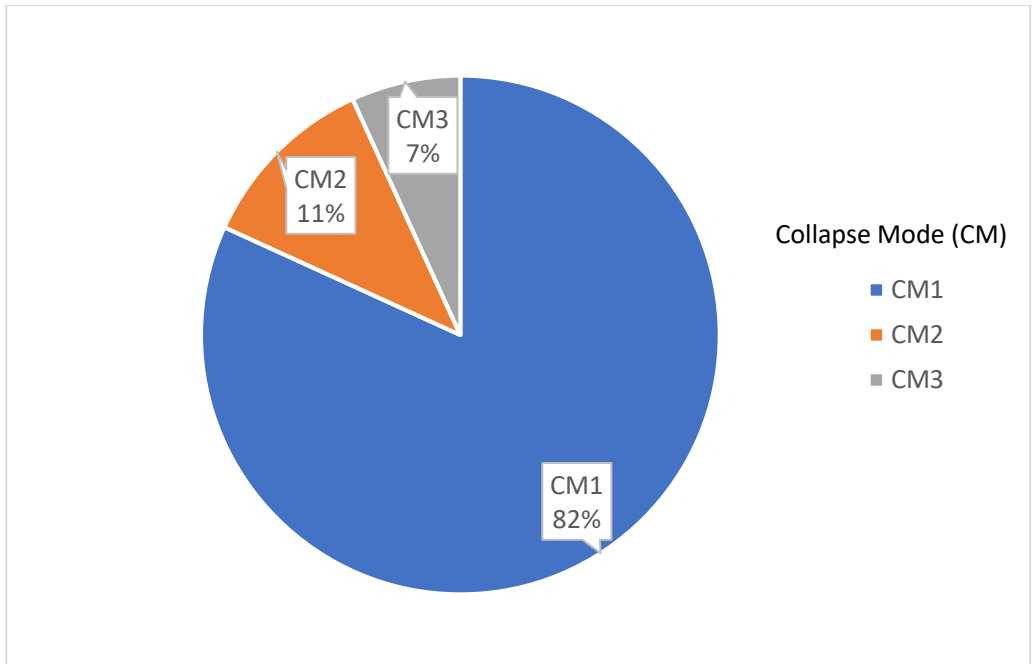
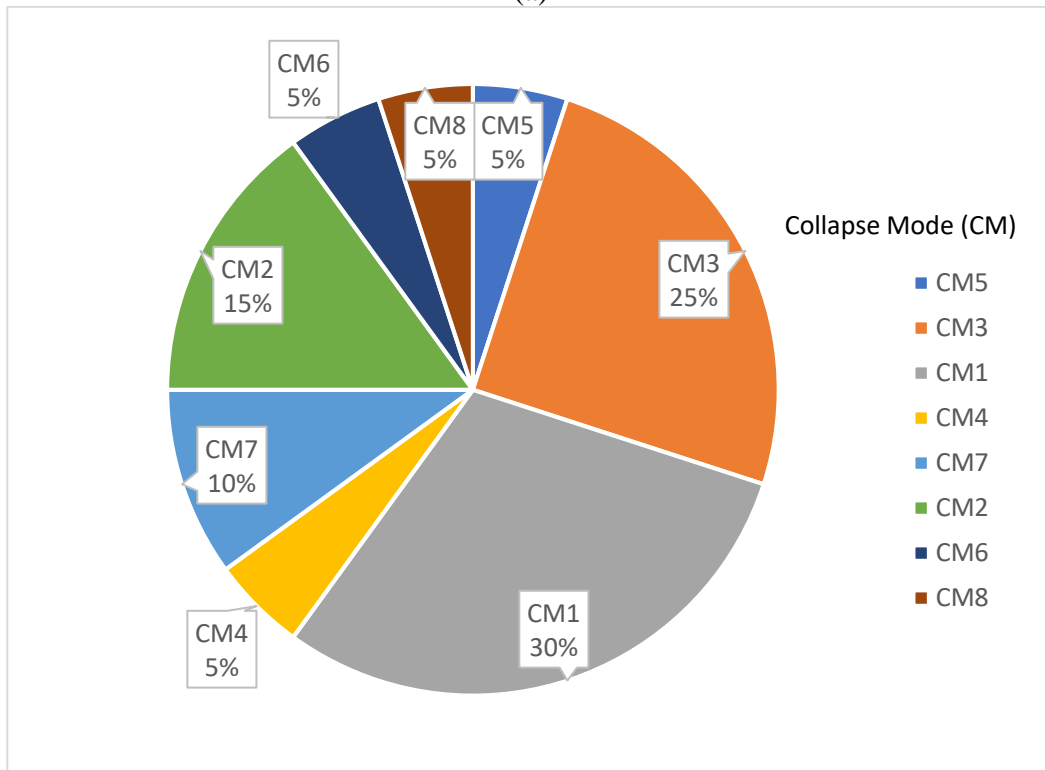


Figure 7.88 Notation for some collapse modes observed in IDA



(a)



(b)

Figure 7.89 Percentage of collapse modes exhibited in (a) IDA of median model (model C1) under 44 GMs; (b) IDA of 20 sample models (model C1) in MCS under GM1

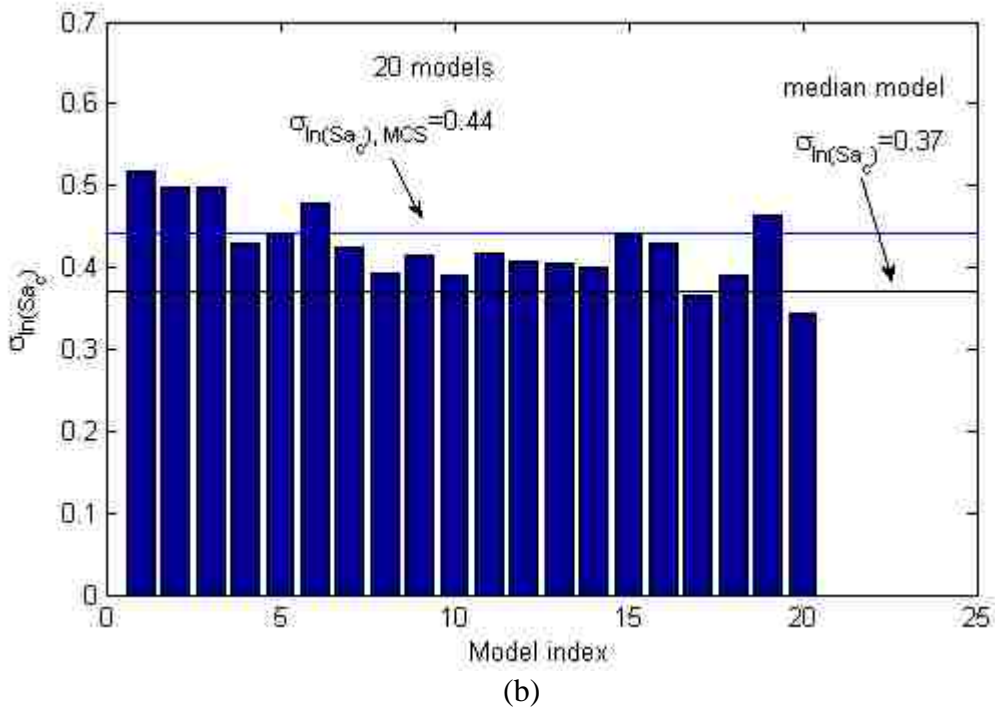
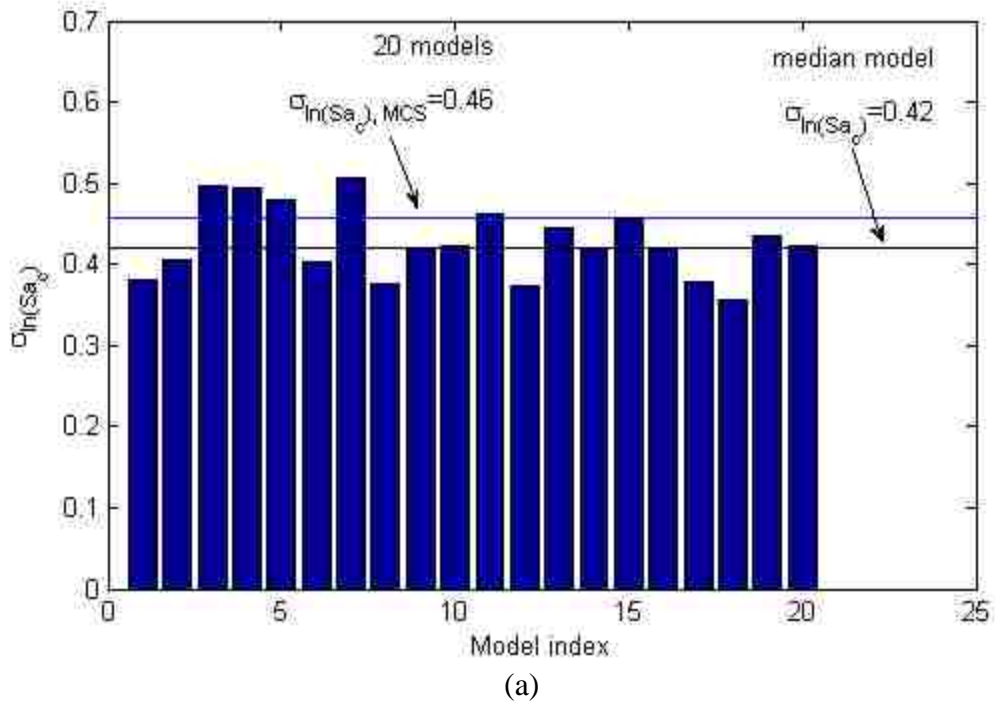


Figure 7.90 Log standard deviation of collapse capacity for each sample model $\sigma_{\ln(Sa_c)}$, for median model $\sigma_{\ln(Sa_c)}$, and log standard deviation considering all sample models $\sigma_{\ln(Sa_c),MCS}$.

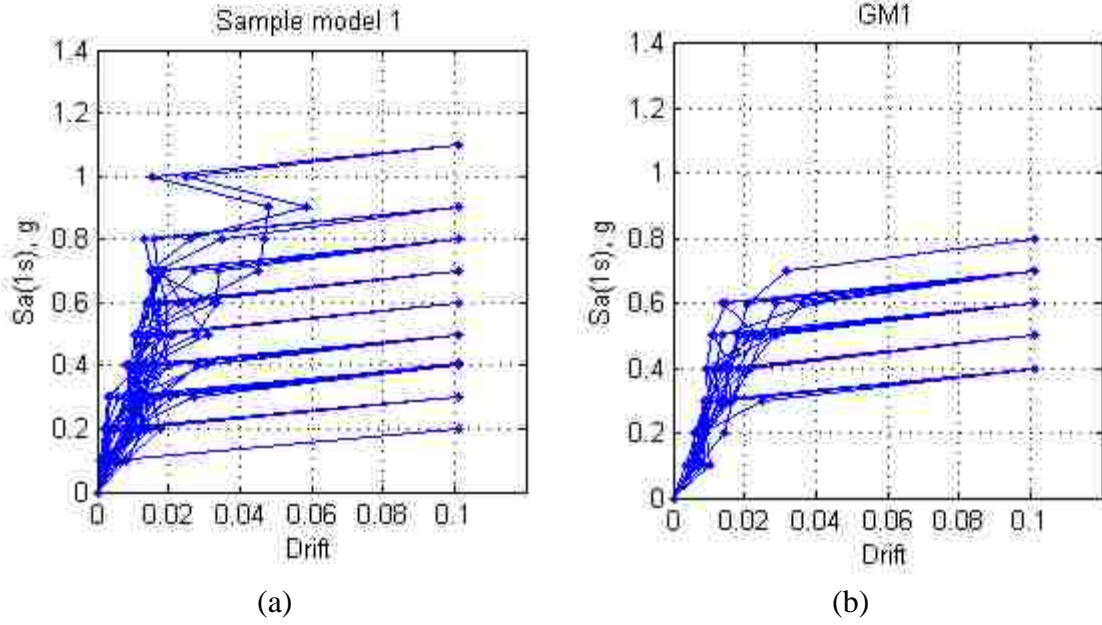
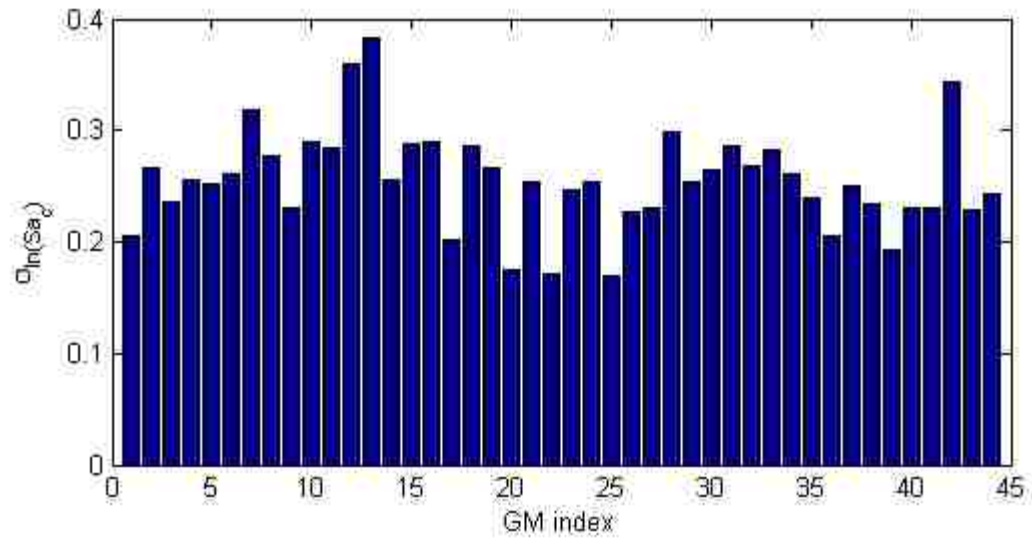
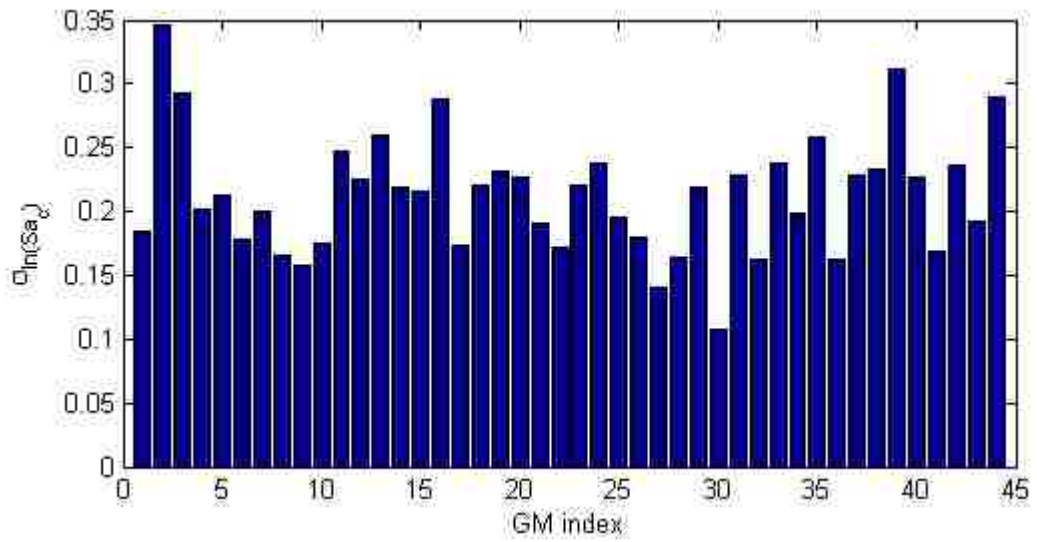


Figure 7.91 IDA results for: (a) sample model 1 under 44 GMs; (b) 20 sample models under GM1



(a)



(b)

Figure 7.92 Log standard deviation of collapse capacity from different sample models under each GM: (a) model C1; (b) model C2

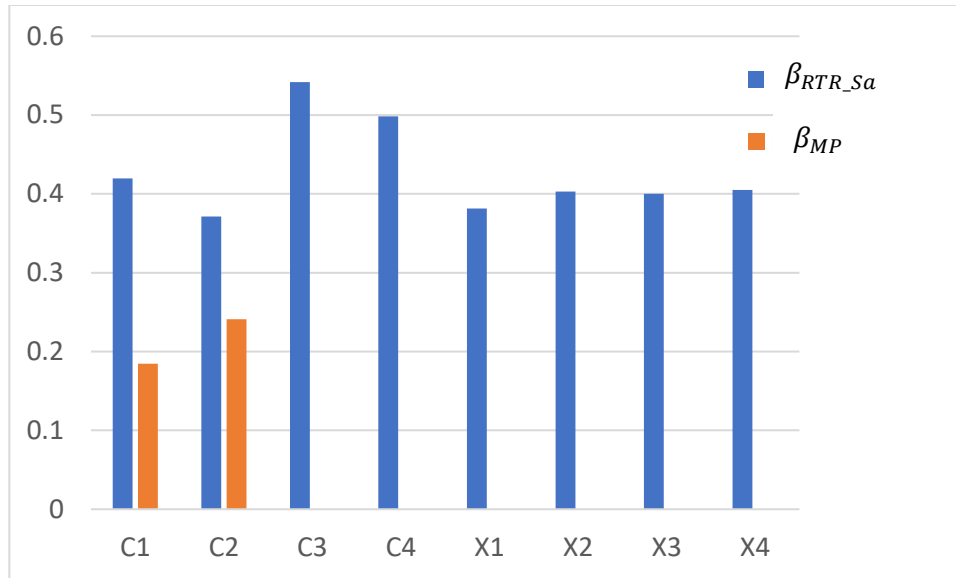


Figure 7.93 Comparison of RTR variability β_{RTR_Sa} and model parameter uncertainty β_{MP}

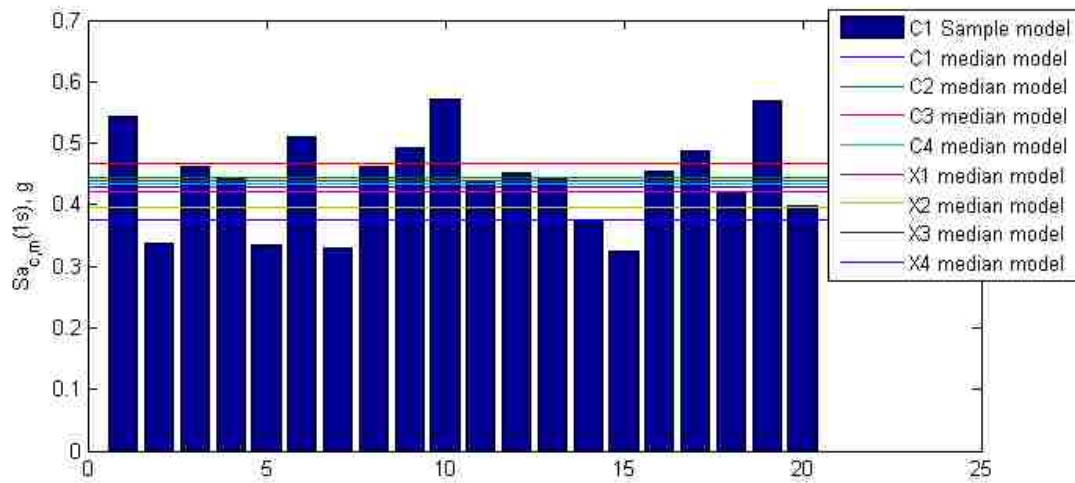


Figure 7.94 Median collapse capacity for each sample model of archetype model C1 and median collapse capacity for the median model of each archetype model

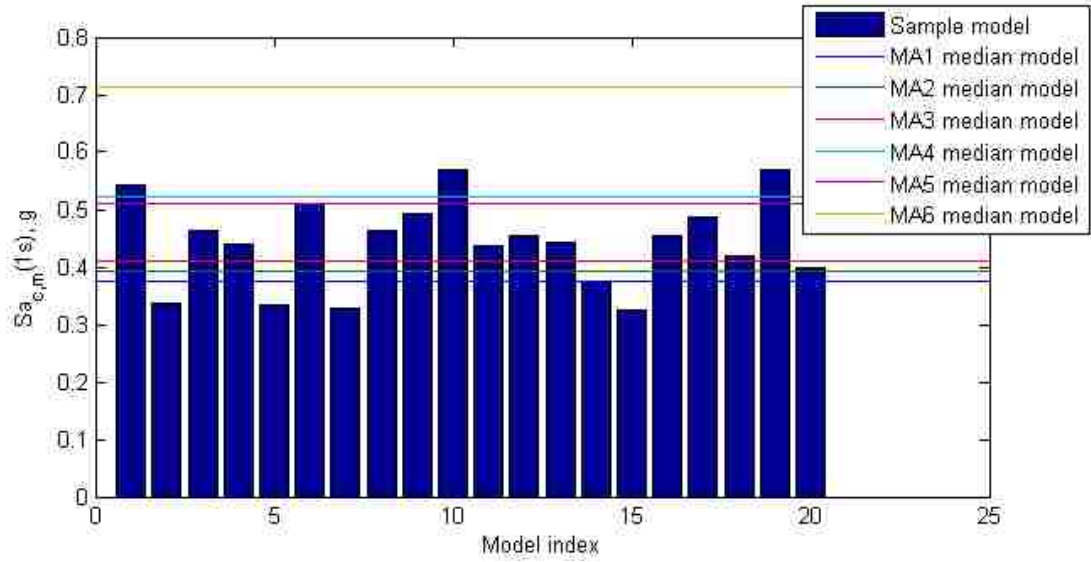


Figure 7.95 Median collapse capacity for each sample model of the baseline model (MA1) for archetype model C1 and for the median model with different modeling approaches for archetype model C1

Chapter 8

Summary and conclusions

8.1 Summary

8.1.1 Motivation

The seismic design of low-ductility CBFs in the mid-Atlantic east coast region of the United States (ECUS) is usually based on a Response Modification Factor R equal to 3, without any seismic detailing to promote ductile behavior. Low-ductility CBFs constitute a notable portion of the building inventory in low to moderate seismic zones such as the ECUS. However, there is inadequate understanding on their seismic response and performance in the context of the ECUS seismic hazard environment.

In particular, the collapse performance of low-ductility CBFs in the ECUS entails significant uncertainty. The seismic design of low-ductility CBFs in the ECUS does not enforce a controlled sequence of yielding and other limit states due to the flexibility and non-prescriptive nature of the design provision. Recent experimental investigations of low-ductility CBFs show they develop limit states that are not observed in CBFs designed for ductile seismic response (i.e. Special CBFs). Therefore, the effect of various sources of uncertainty on the collapse performance of low-ductility CBFs was investigated in this research.

FEMA P695 (FEMA 2009) provides a methodology to evaluate the collapse performance of structures considering the effects of uncertainties. Many aspects of the FEMA P695

methodology are based on ductile reinforced concrete (RC) moment resisting frames (MRFs) designed for the west coast of the United States. It is not clear if the FEMA P695 methodology applies to evaluating the collapse performance of ECUS low-ductility CBFs.

Therefore, this research has been conducted to evaluate the seismic performance of low-ductility CBFs in the context of the ECUS seismic hazard environment, with special attention to the collapse performance and how it is affected by the various sources of uncertainty.

8.1.2 Research objective

To advance knowledge on the seismic response and performance of low-ductility concentrically braced frames (CBFs) in the ECUS, the following research objectives are established:

1. Investigate the non-collapse performance of low-ductility CBFs through a case study of an existing ECUS CBF that was significantly damaged during the 2011 Virginia earthquake.
2. Develop numerical models for low-ductility CBFs for collapse response analysis. The numerical models need to capture the unique limit states of low-ductility CBF that are important to collapse response (e.g. weld fracture and brace re-engagement).
3. Investigate the effect and sensitivity of various sources of uncertainty (e.g., design approach, model parameters, modeling approach, and ground motions) on the collapse capacity of low-ductility CBFs

4. Examine the application of the FEMA P695 methodology to assess the collapse capacity of ECUS low-ductility CBFs in the presence of various sources of uncertainty and propose modifications that could improve applicability to ECUS low-ductility CBFs.
5. Evaluate the collapse performance of low-ductility CBFs under the ECUS seismic hazard environment.

8.1.3 Research scope

The following research tasks were performed in this research:

1. Response simulation of an existing ECUS CBF in the MSC building during the 2011 Virginia earthquake and performance evaluation.

Damage reconnaissance of the MSC building was performed after the 2011 Virginia earthquake. A numerical model was developed in SAP2000 to simulate the response of the structure during the earthquake. The model was validated using dynamic properties of the building from field vibration testing. The response simulation results were consistent with the damage from the earthquake. A nonlinear model was developed in OpenSees for fragility analysis. The fragility curves for structural as well as non-structural damage were developed. The probability of having structural damage and various types of non-structural damage was obtained for different hazard levels. The influence of a potential retrofit strategy on the seismic performance was also investigated.

2. Development of prototype building design and numerical model for collapse simulation of low-ductility CBFs

The design of multiple existing CBF designs were reviewed from which 3 key design variables were identified: weld design strength in the brace connections, beam design strength and brace configuration. The prototype building design along with 8 design variants were developed. The 8 design variants were used as 8 archetype models in the subsequent seismic collapse assessment. Numerical models of the low-ductility CBF system were developed for collapse simulation. The models represent the important and unique limit states of low-ductility CBFs and were validated by experimental results.

3. Development of an ECUS ground motion set for seismic collapse performance assessment

A set of ECUS ground motions was developed for the seismic collapse performance assessment of the prototype building. A set of 44 synthetic ground motion is first developed at the rock level using seismic hazard deaggregation results for Philadelphia. The ground motion simulation used current seismological models developed in the recent NGA East project (Goulet et al. 2011). The ground motion set was also developed according to the target ε values from the deaggregation results and directly considers the effect of spectral shape. To consider the effect of soil amplification, a set of representative soil profiles in Philadelphia was developed and used to perform site response analysis with the rock ground motion set as input. The resulting ground

motion set at the ground surface level, denoted as the ECUS GM set, was used for the subsequent seismic collapse assessment.

4. Identify and categorize different sources of uncertainty in seismic collapse performance assessment of ECUS low-ductility CBFs

The various sources of uncertainty that affect the collapse capacity of ECUS low-ductility CBFs were identified. Different strategies were proposed to evaluate the effect of different categories of uncertainty. The categorization is compared with that of the FEMA P695 methodology (FEMA 2009).

5. Investigate the effects of various sources of uncertainty on the seismic collapse performance of ECUS low-ductility CBFs

The effect of design variation (i.e., alternative designs based on engineering practice) was investigated by performing IDA on the 8 archetype models and carefully examining their response. IDA were performed using the FEMA GM set and ECUS GM set to study the effect of uncertainty due to ground motion variation for a given hazard level (RTR variability). The effect of modeling approach uncertainty was studied by comparing the IDA results for the same archetype model with different modeling approaches. The model parameter uncertainty was studied by sensitivity analysis and Monte Carlo Simulation (MCS).

6. Examine the application of the FEMA P695 methodology to ECUS low-ductility CBFs and propose modifications.

The FEMA P695 methodology was examined during the process of investigating the effect of uncertainty. Specifically, the following 5 aspects were examined:

- The method to calculate median collapse capacity from IDA results in the FEMA P695 methodology
- The formula to calculate SSF and β_{RTR} in the FEMA P695 methodology
- The usage of a median model to estimate the median response and collapse capacity in the presence of model parameter uncertainty
- The inclusion of lateral resistance from the gravity load system
- MCE hazard intensity considering current seismological models and expected soil amplification for Site Class D sites in Philadelphia

Possible modifications of the FEMA P695 methodology for ECUS low-ductility CBFs were investigated, and collapse performance of the archetype models was assessed with different versions of a modified FEMA P695 methodology.

8.2 Research findings

8.2.1 Findings in Chapter 3

Through damage reconnaissance and response simulation, it was found that seismic damage to the MSC building during the 2011 Virginia earthquake can be attributed to the following aspects:

1. The ground motion was significantly amplified by the soil beneath the building;
2. The building is strongly coupled in torsion and translation in its mode shape as a result of floor eccentricity and storage content distribution;

3. The bi-directional earthquake demand exacerbated the combined effect of torsion and translation response and caused more severe damage in the east perimeter than the west perimeter of the building.

From fragility analysis, it was found that the structure is more vulnerable in N-S direction than the E-W direction. Although the ground motion intensity to cause structural damage in the steel mezzanine of the MSC building is not high, due to low seismic hazard level at the site of the building, the probability of having structural damage under the DBE earthquake is not high. However, the probability of non-structural damage from motion of the storage cabinets is considerable under the DBE and higher hazard level ground motions. This result reveals a significant risk in terms of the normal functioning of this storage warehouse. It is also found that retrofit of the structure with stronger braces will increase the fragility for non-structural damage.

8.2.2 Findings in Chapter 4

Through a review of a number of existing designs, it is found that low-ductility CBFs in the ECUS have a lot of design variation. The developed numerical models are able to represent the important and unique limit states of low-ductility CBFs such as weld failure, and brace re-engagement. The numerical models are also robust for the nonlinear dynamic analysis needed for collapse simulation.

8.2.3 Findings in Chapter 5

The developed ECUS ground motion set conforms to site-specific hazard characteristics of Philadelphia and accounts for the spectral shape effect. The ground motion set indicates a

lower MCE intensity level than the MCE spectrum for Site Class D in Philadelphia in ASCE7-10 (ASCE 2010).

8.2.4 Findings in Chapters 6 and 7

The various sources of uncertainty in the current study are categorized differently than in the FEMA P695 document (FEMA 2009). The types of uncertainty considered in this study are related to but do not exactly correspond those in FEMA P695. Categorization of uncertainty in FEMA P695 methodology does not facilitate explicit quantification of the effects of various sources of uncertainty.

Low-ductility CBFs do not have satisfactory collapse performance according to the FEMA P695 methodology. The probabilities of collapse under the MCE for the 8 archetype buildings are between 0.13 and 0.18.

For ECUS low-ductility CBFs, the FEMA P695 methodology for calculating the median collapse capacity from IDA results, which uses the median spectral acceleration of the ground motion set as the hazard intensity, produces a median collapse capacity consistently smaller than the geometric mean of the collapse capacity for each ground motion in the ground motion set.

Design variation will lead to changes in the sequence of limit states that occur in low-ductility CBFs. The influence on the collapse capacity from design variations in the brace connection (i.e., weld strength), beam strength, and brace configuration are not independent from each other. For chevron CBFs, when the beam strength increases as the

brace connection weld strength increases, or when the beam strength decreases as the brace connection weld strength decreases, a larger collapse capacity can be achieved.

The FEMA P695 methodology does not reasonably represent the spectral shape effect and record-to-record variability for ECUS low-ductility CBFs. The empirical formulas in the FEMA P695 methodology to calculate SSF and β_{RTR} should not be used for ECUS low-ductility CBFs. One important reason is the underestimation of the inelastic deformation capacity of the structure by μ_T determined using the reduction in the base shear to 80% of the peak base shear as the criterion. In low-ductility CBFs, the response after brace buckling or weld fracture is important and contributes to resisting collapse.

Modeling brace re-engagement does not always increase the collapse capacity. Brace reengagement can have either positive or negative impact on the collapse capacity.

It is more important to model the beam flexural strength deterioration than axial force-moment interaction. It is recommended to model the beam using a concentrated plastic hinge (CPH) approach which includes deterioration, rather than using a fiber section approach in numerical models for collapse simulation of low-ductility CBF.

Modeling the lateral resistance of the gravity load system significantly increases the collapse capacity of low-ductility CBFs. If only the gravity column continuity is included, the collapse capacity of the structure is increased significantly.

From sensitivity analysis of the model parameter uncertainty, it is found that the brace connection weld strength and brace LCF strength are more influential on the collapse capacity than other parameters. The influences of the model parameters are interdependent.

From the Monte Carlo Simulation (MCS), it is found that the IDA of the median model does not provide the median collapse capacity of a set of sample models that include the variation of model parameters. MCS is needed to capture the unbiased median collapse capacity in the presence of model parameter uncertainty for low-ductility CBFs. The RTR variability dominates the dispersion of the collapse capacity even when the model parameter uncertainty is included. The quantified value of the model parameter (MP) uncertainty, β_{MP} is smaller than a combination of the design requirement (DR) uncertainty β_{DR} and test data (TD) uncertainty β_{TD} , from the FEMA P695 methodology, which together include the model parameter uncertainty as well as to other uncertainties. It is inferred that the β values in the FEMA P695 methodology for DR and TD uncertainty are conservative relative to the MP uncertainty included here. It is recommended to use β_{DR} , β_{TD} and β_{MDL} from the FEMA P695 document to address the respective sources of uncertainty in a seismic collapse performance evaluation.

By comparing the effects of various sources of uncertainty, it is found that modeling approach (MA) uncertainty causes a larger variation in the collapse capacity than model parameter (MP) uncertainty. It is also found that the impact of design variation (DV) is smaller than that of MP uncertainty.

Three modifications are proposed to improve the applicability of the FEMA P695 methodology to ECUS low-ductility CBFs. 1. It is suggested that the median collapse capacity be calculated as the geometric mean of the collapse capacity for each ground motion; 2. It is suggested to use the ECUS ground motion set to capture the effects of spectral shape and RTR variability; 3. MCS is needed to capture the median collapse

capacity in the presence of model parameter uncertainty (but due to the limited number of parameters that can be practically incorporated in the MCS, the dispersion of the collapse capacity should be based on the β values from the FEMA P695 methodology).

By using a modified version of the FEMA P695 methodology (Mod 3 version), it is found that the low-ductility CBFs are possible to have collapse margin larger than ACMR10 (on average having less than 10% probability of collapse). If either the contribution of lateral resistance from the gravity load system or the potential fact that the MCE intensity from current seismological models and expected soil amplification effect for Site Class D sites in Philadelphia is lower than the MCE spectrum for Site Class D sites in ASCE 7-10 (ASCE 2010) is considered, low-ductility CBFs may have a large collapse margin over the acceptance threshold.

8.3 Conclusions

The following conclusions can be drawn based on the result of this dissertation:

- The FEMA P695 methodology (FEMA 2009) should not be used directly to evaluate the collapse capacity of low-ductility CBF in the ECUS.
- Low-rise low-ductility CBFs in the Philadelphia area may achieve satisfactory collapse performance if either one of the following premises is true: 1. the gravity load system is as effective in resisting lateral load as indicated by the models used in this study (even if considering only the gravity column continuity); 2. The MCE hazard intensity considering current seismological models and expected soil

amplification effect for Site Class D sites in Philadelphia is lower than indicated by the ASCE MCE spectrum for Site Class D (ASCE 2010).

8.4 Original contributions

- Identified the potential cause for the seismic damage of the MSC building during the 2011 Virginia earthquake and evaluated its seismic fragility and performance
- Developed numerical models with accuracy and robustness for collapse simulation of low-ductility CBFs
- Develop a set of ECUS ground motions that considers current seismicity, uncertainty in seismic hazard sources, spectral shape, and soil amplification effects for collapse performance evaluation
- Identify different sources of uncertainty affecting the collapse performance of low-ductility CBFs
- Presents a rationale for categorization of uncertainty and using predefined β values to address uncertainty in FEMA P695 methodology
- Investigated the effects of various sources of uncertainty on the collapse capacity of low-ductility CBFs
- Explicitly quantified the effect of model parameter uncertainty on the collapse capacity and compared with the predefined β values in the FEMA P695 methodology;
- Evaluated the collapse performance of low-ductility CBFs within the ECUS seismic hazard environment

- Proposed modifications to improve the applicability of the FEMA P695 methodology to the collapse performance assessment of low-ductility CBFs in the ECUS
- Advanced the understanding of the seismic response of ECUS low-ductility CBF through study of static and dynamic response of numerical models in a broad parametric space

8.5 Limitation and recommended future research

This research focuses on only one prototype 3-story CBF building. The performance of mid-rise and high-rise CBFs should be investigated.

This study only considers the seismic condition in Philadelphia, PA. Other major cities in the ECUS will have different seismic settings, and may have different structural design practices. Hence, seismic performance of CBFs in other cities should also be considered.

This study uses a set of sample soil profiles to broadly represent Site Class D building site in Philadelphia. The result of this study may not be representative for a particular site with deep soil profile that may produce more severe site response. In this case, the probability of collapse may be higher than indicated by the results of this study. More measurements of site soil conditions and specific site response analyses are needed.

There are important limit states in low-ductility CBFs that were not modeled. For example, the low cycle fatigue of the brace connection weld is not considered. In addition, weld fracture was assumed to happen at only one end of the brace close to the beam-column

connection. The potential brace re-engagement that could happen at the chevron point was not modeled. Modeling techniques for these limit states should be developed.

This study considers only the uncertainty of a limited number of model parameters and design variables. The effect of uncertainty in other model parameters and design variables should also be studied. It is possible that the dispersion in collapse capacity is larger than indicated by the β values in the FEMA P695 methodology, when all the uncertainty is exhaustively considered. In this case, the acceptable collapse margin ratio will increase and the low-ductility CBFs may no longer have satisfactory collapse performance.

Due to current limitations of the seismic hazard deaggregation tools used in this research, the ECUS GM set was developed at $T = 1s$, which is not the first mode period of the structure. Techniques should be developed to deaggregate the hazard at various periods (such as the fundamental period T_1) and develop GM sets at other periods, to assess whether periods other than 1s are more critical.

References

- AISC. (1997). *Seismic provisions for structural steel buildings*. Chicago, IL.
- AISC. (2010a). *Seismic provisions for structural steel buildings*. Chicago, IL.
- AISC. (2010b). *Specification for Structural Steel Buildings*. Chicago, Illinois.
- Applied Technology Council. (1978). *ATC 3-06 Tentative Provisions for the Development of Seismic Regulations for Buildings: A Cooperative Effort with the Design Professions, Building Code Interests, and the Research Community*. United States. Government Printing Office.
- ASCE. (2007). *ASCE/SEI 41 06: Seismic Rehabilitation of Existing Building*. Reston, VA.
- ASCE. (2010). *ASCE 7-10: Minimum design loads for buildings and other*. Reston, VA.
- Atkinson, G. M. (2004). "Empirical Attenuation of Ground-Motion Spectral Amplitudes in Southeastern Canada and the Northeastern United States." *Bulletin of the Seismological Society of America*, Seismological Society of America, 94(6), 2419–2423.
- Atkinson, G. M. (2007). "Challenges in seismic hazard analysis for continental interiors." *Special Paper 425: Continental Intraplate Earthquakes: Science, Hazard, and Policy Issues*, Geological Society of America, 329–344.
- Atkinson, G. M., and Boore, D. M. (1995). "Ground-motion relations for eastern North America." *Bulletin of the Seismological Society of America*, The Society, 85(1), 17–30.

Atkinson, G. M., and Boore, D. M. (2014). “The Attenuation of Fourier Amplitudes for Rock Sites in Eastern North America.” *Bulletin of the Seismological Society of America*, Seismological Society of America, 104(1), 513–528.

Atkinson, G. M., Goda, K., and Assatourians, K. (2011). “Comparison of Nonlinear Structural Responses for Accelerograms Simulated from the Stochastic Finite-Fault Approach versus the Hybrid Broadband Approach.” *Bulletin of the Seismological Society of America*, Seismological Society of America, 101(6), 2967–2980.

Baker, J. W., and Cornell, C. A. (2006). “Spectral shape, epsilon and record selection.” *Earthquake Engineering & Structural Dynamics*, 35(9), 1077–1095.

Bausher, E., and Pazzaglia, F. (2015). *Ground Acceleration-Prone Soils in Philadelphia County, PA; Input to Risk-Based Models of Earthquake Hazards in the Central and Eastern United States*. Bethlehem.

Beavers, J. E., Eatherton, M. R., Gilsanz, R. E., Ricles, J. M., and Lin, Y. (2012). “The August 23, 2011 Magnitude 5.8 Virginia Earthquake in the Eastern United States - An Engineering Perspective.” *Proceedings of 15th World Conference on Earthquake Engineering*, Lisbon, Portugal.

Bjorhovde, R. (1988). “Columns: From Theory to Practice.” *Engineering Journal of American Institute of Steel Construction*, 25(1).

Bjorhovde, R., and Birkemoe, P. C. (1979). “Limit states design of HSS columns.” *Canadian Journal of Civil Engineering*, NRC Research Press Ottawa, Canada , 6(2), 276–291.

Boatwright, J., and Seekins, L. (2011). “Regional Spectral Analysis of Three Moderate Earthquakes in Northeastern North America.” *Bulletin of the Seismological Society of America*, Seismological Society of America, 101(4), 1769–1782.

Boore, D. M. (2003). “Simulation of Ground Motion Using the Stochastic Method.” *Seismic Motion, Lithospheric Structures, Earthquake and Volcanic Sources: The Keiiti Aki Volume*, Birkhäuser Basel, Basel, 635–676.

Boore, D. M. (2013). “FUNDAMENTALS of ENGINEERING SEISMOLOGY: GROUND MOTIONS FROM SIMULATIONS.”
<http://www.daveboore.com/short_course_lectures_and_labs.html>.

Boore, D. M., Campbell, K. W., and Atkinson, G. M. (2010). “Determination of Stress Parameters for Eight Well-Recorded Earthquakes in Eastern North America.” *Bulletin of the Seismological Society of America*, Seismological Society of America, 100(4), 1632–1645.

Bradley, B. A. (2013). “A critical examination of seismic response uncertainty analysis in earthquake engineering.” *Earthquake Engineering & Structural Dynamics*, 42(11), 1717–1729.

Bradley, C. R. (2016). “Experimental Investigation of Post-Elastic Failure Mechanisms in Low-Ductility Braced Frames and the Implications for Collapse Performance.” Tufts University.

Bradley, C. R., Fahnestock, L. A., Hines, E. M., and Sizemore, J. G. (2015). "Full-Scale Cyclic Testing of an Ordinary Concentrically-Braced Frame." *Structures Congress 2015*, American Society of Civil Engineers, Portland, OR, 702–713.

BSSC. (2009). *NEHRP Recommended Provisions for Seismic Regulations for New Buildings and Other Structures*. Washington D.C.

Burks, L. S., Zimmerman, R. B., and Baker, J. W. (2015). "Evaluation of Hybrid Broadband Ground Motion Simulations for Response History Analysis and Design." *Earthquake Spectra*, Earthquake Engineering Research Institute , 31(3), 1691–1710.

Campbell, K. W., and Bozorgnia, Y. (2003). "Updated Near-Source Ground-Motion (Attenuation) Relations for the Horizontal and Vertical Components of Peak Ground Acceleration and Acceleration Response Spectra." *Bulletin of the Seismological Society of America*, Seismological Society of America, 93(1), 314–331.

Carr, A. J. (2004). "Ruaumoko—a program for inelastic time-history analysis." Christchurch, New Zealand.

Carter, C. J. (2009). "Connections and collapse resistance in R = 3 braced frames." Illinois Institute of Technology.

Celik, O. C., and Ellingwood, B. R. (2010). "Seismic fragilities for non-ductile reinforced concrete frames – Role of aleatoric and epistemic uncertainties." *Structural Safety*, 32(1), 1–12.

Chang, M., and Pakzad, S. N. (2014). "Observer Kalman Filter Identification for Output-Only Systems Using Interactive Structural Modal Identification Toolsuite." *Journal of Bridge Engineering*, 19(5), 4014002.

Chapman, M. C. (2013). "On the Rupture Process of the 23 August 2011 Virginia Earthquake." *Bulletin of the Seismological Society of America*, 103(2A), 613–628.

Chapman, M. C. (2015). "Magnitude, recurrence interval, and near-source ground-motion modeling of the Mineral, Virginia, earthquake of 23 August 2011." *Geological Society of America Special Papers*, Geological Society of America, 509, SPE509-02.

Charnpis, D. C., and Panteli, P. L. (2004). "A heuristic approach for the generation of multivariate random samples with specified marginal distributions and correlation matrix." *Computational Statistics*, Springer-Verlag, 19(2), 283–300.

Charney, F. A. (2008). "Unintended Consequences of Modeling Damping in Structures." *Journal of Structural Engineering*, 134(4), 581–592.

Choi, E., DesRoches, R., and Nielson, B. (2004). "Seismic fragility of typical bridges in moderate seismic zones." *Engineering Structures*, 26(2), 187–199.

Chu, X., Ricles, J. M., and Pakzad, S. N. (2017). "Seismic Fragility Analysis of the Smithsonian Institute Museum Support Center." *Earthquake Spectra*, 33(1), 85–108.

Chu, X., Ricles, J. M., Pakzad, S. N., Martin, J. R., and Shahidi, S. G. (2014). "Damage Reconnaissance and Seismic Response Prediction of an East Coast U.S. Building

Subjected to 2011 Virginia Earthquake.” *ASCE Structures Congress Proceedings*, Boston, Ma, 1324–1335.

Computer and Structures, I. (2010). “SAP2000 Manual (Version 14.1.0).”

Davaran, A., Tremblay, R., Beland, T., Fahnestock, L. A., and Hines, E. M. (2014). “Experimental Behavior of Low-Ductility Brace Connection Limit States.” *Structures Congress 2014*, American Society of Civil Engineers, Boston, Ma, 2429–2441.

Dietrich, E. (2012). *Personal communication*.

Dong, B., Sause, R., and Ricles, J. M. (2016). “Seismic Response and Performance of a Steel MRF Building with Nonlinear Viscous Dampers under DBE and MCE.” *Journal of Structural Engineering*, 142(6), 4016023.

Dooley, R. T. (1957). “Coefficient of friction of painted structural steel surfaces.” Georgia Institute of Technology.

EERI. (2011). “*Learning from Earthquakes: The Mw 5.8 Virginia Earthquake of August 23, 2011.*” *EERI Special Earthquake Report*.

Elkady, A., and Lignos, D. G. (2015). “Effect of gravity framing on the overstrength and collapse capacity of steel frame buildings with perimeter special moment frames.” *Earthquake Engineering & Structural Dynamics*, 44(8), 1289–1307.

Ellingwood, B. R., Celik, O. C., and Kinali, K. (2007). “Fragility assessment of building structural systems in Mid-America.” *Earthquake Engineering & Structural Dynamics*, 36(13), 1935–1952.

FEMA. (2009). *Quantification of Building Seismic Performance Factors (FEMA P695)*.

Fisher, J. W., Ravindra, M. K., Kulak, G. L., and Galambos, T. V. (1978). "Load and resistance factor design criteria for connectors." *ASCE Journal of the Structural Division*, 104(9), 1427–1441.

Goggins, J., and Salawdeh, S. (2013). "Validation of nonlinear time history analysis models for single-storey concentrically braced frames using full-scale shake table tests." *Earthquake Engineering & Structural Dynamics*, 42(8), 1151–1170.

Goulet, C. A., Kishida, T., Ancheta, T. D., Cramer, C. H., Darragh, R. B., Silva, W. J., Hashash, Y. M. A., Harmon, J., Stewart, J. P., Wooddell, K. E., and Youngs, R. R. (2014). *PEER NGA-East Database*. Berkeley, Ca.

Goulet, C., Abrahamson, N., and Bozorgnia, Y. (2011). *NGA-East Final Project Plan*. Berkeley, Ca.

Gryniuk, M. C. (2008). "Seismic Performance of Low-ductility Chevron Braced Steel Frames in Moderate Zone." Tufts University.

Gryniuk, M. C., and Hines, E. M. (2004). *Safety and Cost Evaluation of a Steel Concentrically Braced Frame Student Residence Facility in the Northeastern United States*. Cambridge, MA.

Hanks, T. C., and Kanamori, H. (1979). "A moment magnitude scale." *Journal of Geophysical Research*, 84(B5), 2348.

- Haselton, C. B. (2007). "Assessing seismic collapse safety of modern reinforced concrete moment frame buildings." Stanford University.
- Hashash, Y. M. A., Groholski, D. R., and Phillips, C. (2014). "DEEPSOIL v5.1 user manual and tutorial." Urbana, IL.
- Hines, E. M., Aboosaber, M., and Robinson, H. J. (2011). "Modeling Reserve System Performance for Low Ductility Braced Frames." *Engineering Mechanics Institute Annual Conference*, Boston, Ma.
- Hines, E. M., Appel, M. E., and Cheever, P. J. (2009). "Collapse Performance of Low-Ductility Chevron Braced Steel Frames in Moderate Seismic Regions." *AISC Engineering Journal*, 46(3), 149–180.
- Horton, J. W., and Williams, R. A. (2012). "The 2011 Virginia earthquake: What are scientists learning?" *Eos Trans. AGU*, 93(33).
- Hough, S. E. (2012). "Initial Assessment of the Intensity Distribution of the 2011 Mw 5.8 Mineral, Virginia, Earthquake." *Seismological Research Letters*, 83(4).
- Hsiao, P.-C., Lehman, D. E., and Roeder, C. W. (2012). "Improved analytical model for special concentrically braced frames." *Journal of Constructional Steel Research*, 73, 80–94.
- Ibarra, L. F., Medina, R. A., and Krawinkler, H. (2005). "Hysteretic models that incorporate strength and stiffness deterioration." *Earthquake Engineering & Structural Dynamics*, John Wiley & Sons, Ltd., 34(12), 1489–1511.

- International Code Council. (1997). *International Building Code*. Country Club Hills, IL.
- Jehel, P., Leger, P., and Ibrahimbegovic, A. (2014). “Initial versus tangent stiffness-based Rayleigh damping in inelastic time history seismic analyses.” *Earthquake Engineering & Structural Dynamics*, 43(3), 467–484.
- Karamanci, E., and Lignos, D. G. (2014). “Computational Approach for Collapse Assessment of Concentrically Braced Frames in Seismic Regions.” *Journal of Structural Engineering*, 140(8), A4014019.
- Kayen, R. E., Carkin, B. A., Corbett, S. C., Zangwill, A., Estevez, I., and Lai, L. (2015). *Shear Wave Velocity and Site Amplification Factors for 25 Strong-Motion Instrument Stations Affected by the M5.8 Mineral, Virginia, Earthquake of August 23, 2011*.
- Kinali, K., and Ellingwood, B. R. (2007). “Seismic fragility assessment of steel frames for consequence-based engineering: A case study for Memphis, TN.” *Engineering Structures*, 29(6), 1115–1127.
- Kramer, S. L. (1996). *Geotechnical earthquake engineering*. Prentice Hall.
- Kulkarni, R. B., Youngs, R. R., and Coppersmith, K. J. (1984). “Assessment of confidence intervals for results of seismic hazard analysis.” *Proceedings of the Eighth World Conference on Earthquake Engineering*, San Francisco, California, 263–270.
- Lesik, D. F., and Kennedy, D. J. L. (1990). “Ultimate strength of fillet welded connections loaded in plane.” *Canadian Journal of Civil Engineering*, NRC Research Press Ottawa, Canada , 17(1), 55–67.

Li, G., and Fahnestock, L. A. (2013). "Seismic Response of Single-Degree-of-Freedom Systems Representing Low-Ductility Steel Concentrically Braced Frames with Reserve Capacity." *Journal of Structural Engineering*, 139(2), 199–211.

Lignos, D. G., and Krawinkler, H. (2011). "Deterioration Modeling of Steel Components in Support of Collapse Prediction of Steel Moment Frames under Earthquake Loading." *Journal of Structural Engineering*, 137(11), 1291–1302.

Lignos, D. G., Krawinkler, H., and Whittaker, A. S. (2011). "Prediction and validation of sidesway collapse of two scale models of a 4-story steel moment frame." *Earthquake Engineering & Structural Dynamics*, John Wiley & Sons, Ltd., 40(7), 807–825.

Liu, J., and Astaneh-Asl, A. (2000). "Cyclic Testing of Simple Connections Including Effects of Slab." *Journal of Structural Engineering*, 126(1), 32–39.

Liu, J., Sabelli, R., Brockenbrough, R. L., and Fraser, T. P. (2007). "Expected Yield Stress and Tensile Strength Ratios for Determination of Expected Member Capacity in the 2005 AISC Seismic Provisions." *Engineering Journal of American Institute of Steel Construction*, 44(1).

Luco, N., and Bazzurro, P. (2007). "Does amplitude scaling of ground motion records result in biased nonlinear structural drift responses?" *Earthquake Engineering & Structural Dynamics*, 36(13), 1813–1835.

Manson, S. S. (1965). *Fatigue- a complex subject - some simple approximations*. Cleveland, OH.

Marsteller, R., Mueller, K., Ericksen, J., and Hewitt, C. (2002). "Chevron bracing in low rise buildings." *Modern Steel Construction*, 42(4), 26–30.

Marzocchi, W., Taroni, M., and Selva, J. (2015). "Accounting for Epistemic Uncertainty in PSHA: Logic Tree and Ensemble Modeling." *Bulletin of the Seismological Society of America*, Seismological Society of America, 105(4), 2151–2159.

McGuire, R. K., Silva, Walter, J., and Costantino, C. J. (2001). *Technical basis for revision of regulatory guidance on design ground motions. Rpt. NUREG/CR-6728*. Washington DC.

McKenna, F., Fenves, G. L., and Scott, M. H. (2000). "Manual of Open System for Earthquake Engineering (OpenSees)."

Metelli, G. (2013). "Theoretical and experimental study on the cyclic behaviour of X braced steel frames." *Engineering Structures*, 46, 763–773.

Miner, M. A. (1945). "Cumulative damage in fatigue." *Journal of Applied Mechanics*, 12(3), 159–164.

Motazedian, D., and Atkinson, G. M. (2005). "Stochastic Finite-Fault Modeling Based on a Dynamic Corner Frequency." *Bulletin of the Seismological Society of America*, Seismological Society of America, 95(3), 995–1010.

Nelson, T. A. (2007). "Performance of a 9-story low-ductility moment resisting frame under moderate seismic demands." Tufts University.

Nikolaou, S., Go, J. E., Beyzaei, C. Z., Moss, C., and Deming, P. W. (2012). “Geo-Seismic Design in the Eastern United States: State of Practice.” *Geotechnical Engineering State of the Art and Practice*, American Society of Civil Engineers, Reston, VA, 828–854.

Nordenson, G. J. P., and Bell, G. R. (2000). “Seismic Design Requirements for Regions of Moderate Seismicity.” *Earthquake Spectra*, 16(1), 205–225.

Pan, Y., Agrawal, A. K., Ghosn, M., and Alampalli, S. (2010). “Seismic Fragility of Multispan Simply Supported Steel Highway Bridges in New York State. II: Fragility Analysis, Fragility Curves, and Fragility Surfaces.” *Journal of Bridge Engineering*, American Society of Civil Engineers, 15(5), 462–472.

PEER. (2006). *PEER NGA Database*. Berkeley, Ca.

PEER. (2015). *NGA-East: Median Ground-Motion Models for the Central and Eastern North America Region*. Berkeley, Ca.

Peruš, I., and Fajfar, P. (2005). “On the inelastic torsional response of single-storey structures under bi-axial excitation.” *Earthquake Engineering & Structural Dynamics*, 34(8), 931–941.

Petersen, M. D., Frankel, A. D., Harmsen, S. C., Mueller, C. S., Haller, K. M., Wheeler, R. L., Wesson, R. L., Zeng, Y., Boyd, O. S., Perkins, D. M., Luco, N., Field, E. H., Wills, C. J., and Rukstales, K. S. (2008). *USGS Open-File Report 2008-1128: Documentation for the 2008 Update of the United States National Seismic Hazard Maps*.

Petersen, M. D., Moschetti, M. P., Powers, P. M., Mueller, C. S., Haller, K. M., Frankel, A. D., Zeng, Y., Rezaeian, S., Harmsen, S. C., Boyd, O. S., Field, N., Chen, R., Rukstales, K. S., Luco, N., Wheeler, R. L., Williams, R. A., and Olsen, A. H. (2014). *USGS Open-File Report 2014-1091: Documentation for the 2014 Update of the United States National Seismic Hazard Maps*.

Petersen, M. D., Moschetti, M. P., Powers, P. M., Mueller, C. S., Haller, K. M., Frankel, A. D., Zeng, Y., Rezaeian, S., Harmsen, S. C., Boyd, O. S., Field, N., Chen, R., Rukstales, K. S., Luco, N., Wheeler, R. L., Williams, R. A., and Olsen, A. H. (2015). "The 2014 United States National Seismic Hazard Model." *Earthquake Spectra*, Earthquake Engineering Research Institute , 31(S1), S1-S30.

Rabbat, B. G., and Russell, H. G. (1985). "Friction Coefficient of Steel on Concrete or Grout." *Journal of Structural Engineering*, American Society of Civil Engineers.

Roke, D. A. (2010). "Damage-Free Seismic-Resistant Self-Centering Concentrically-Braced Frames." Lehigh University.

Sen, A. D. (2014). "Seismic Performance of Chevron Concentrically Braced Frames with Weak Beams." University of Washington.

Sen, A. D., Roeder, C. W., Berman, J. W., Lehman, D. E., Li, C.-H., Wu, A.-C., and Tsai, K.-C. (2016a). "Experimental Investigation of Chevron Concentrically Braced Frames with Yielding Beams." *Journal of Structural Engineering*, 142(12), 4016123.

Sen, A. D., Sloat, D., Ballard, R., Johnson, M. M., Roeder, C. W., Lehman, D. E., and Berman, J. W. (2016b). "Experimental Evaluation of the Seismic Vulnerability of Braces

and Connections in Older Concentrically Braced Frames.” *Journal of Structural Engineering*, 142(9), 4016052.

Shahidi, S. G., Pakzad, S. N., Ricles, J. M., Martin, J. R., Olgun, C. G., and Godfrey, E. A. (2015). “Behavior and damage of the Washington Monument during the 2011 Mineral, Virginia, earthquake.” *Geological Society of America Special Papers*, Geological Society of America, 509, 235–252.

Shahjouei, A., and Pezeshk, S. (2015). “Synthetic Seismograms Using a Hybrid Broadband Ground-Motion Simulation Approach: Application to Central and Eastern United States.” *Bulletin of the Seismological Society of America*, Seismological Society of America, 105(2A), 686–705.

Shen, J., Rou, W., Akbas, B., Seker, O., and Uckan, E. (2015). “Near-collapse behavior of steel buildings with non-ductile concentrically braced frames.” *Journal of Constructional Steel Research*, 113, 101–114.

Shenton III, H. W. (1996). “Criteria for Initiation of Slide, Rock, and Slide-Rock Rigid-Body Modes.” *Journal of Engineering Mechanics*, American Society of Civil Engineers, 122(7), 690–693.

Silva, W., Gregor, N., and Darragh, R. (2002). *DEVELOPMENT OF REGIONAL HARD ROCK ATTENUATION RELATIONS FOR CENTRAL AND EASTERN NORTH AMERICA*. El Cerrito, Ca.

Simpson, B., Mahin, S. A., and Lai, J.-W. (2013). *Summary of Test Results for Non-Seismic Concentric Braced Frame Specimen at NEES Berkeley Laboratory*. Berkeley, Ca.

Sizemore, J. G., Davaran, A., Fahnestock, L. A., Tremblay, R., and Hines, E. M. (2014). “Seismic Behavior of Low-Ductility Concentrically-Braced Frames.” *Structures Congress 2014*, American Society of Civil Engineers, Boston, Ma, 2369–2380.

Sizemore, J. G., Fahnestock, L. A., Hines, E. M., and Bradley, C. R. (2015). “Full-Scale Cyclic Testing of a Low-Ductility Concentrically-Braced Frame.” *8th International Conference on Behavior of Steel Structures in Seismic Areas*, Shanghai, China.

Stoakes, C. D., and Fahnestock, L. A. (2011). “Cyclic Flexural Testing of Concentrically Braced Frame Beam-Column Connections.” *Journal of Structural Engineering*, 137(7), 739–747.

Stoakes, C. D., and Fahnestock, L. A. (2012). “Cyclic flexural analysis and behavior of beam-column connections with gusset plates.” *Journal of Constructional Steel Research*, 72, 227–239.

Talwani, P. (1999). “Fault geometry and earthquakes in continental interiors.” *Tectonophysics*, 305(1–3), 371–379.

Tilashalski, M., Guney Olgun, C., Rodriguez-Marek, A., Godfrey, E. A., Chapman, M. C., Shamsalsadati, S., and Eddy, M. A. (2015). “Regional Geology and Seismic Site Amplification in the Washington, DC, Metropolitan Area.” *IFCEE 2015*, ASCE, 1278–1287.

Uriz, P. (2005). “Towards earthquake resistant design of concentrically braced steel structures.” University of California, Berkeley.

Uriz, P., and Mahin, S. A. (2008). *Toward Earthquake-Resistant Design of Concentrically Braced Steel-Frame Structures*. Berkeley, Ca.

Vamvatsikos, D., and Cornell, C. A. (2002). “Incremental dynamic analysis.” *Earthquake Engineering & Structural Dynamics*, John Wiley & Sons, Ltd., 31(3), 491–514.

Vamvatsikos, D., and Cornell, C. A. (2004). “Applied Incremental Dynamic Analysis.” *Earthquake Spectra*, 20(2), 523–553.

Vita

Xin Chu was born in Wuhan, China to Tong Chu and his wife Xiaolin Xia in 1989. He attended Tongji University in Shanghai from 2007 to 2011 where he earned a Bachelor of Science degree in Civil Engineering with focus on Bridge Engineering. He started to pursue his PhD in Lehigh University in August 2011. He will receive his PhD degree in Structural Engineering in August 2017. He will be joining Thornton Tomasetti in the New York City as a senior engineer upon finishing his study in Lehigh.